NASA Technical Memorandum 110421 USAATCOM Technical Report 96-A-008

IN-01
93248

# A Comparison of Lifting-Line and CFD Methods with Flight Test Data from a Research Puma Helicopter

William G. Bousman, *Aeroflightdynamics Directorate, U.S. Army Aviation and Troop Command, Ames Research Center, Moffett Field, California*
Colin Young, *Defence Research Agency (Aerospace Division), Farnborough, United Kingdom*
François Toulmay, *Eurocopter France, Marignane, France*
Neil E. Gilbert, *Aeronautical and Maritime Research Laboratory, Melbourne, Australia*
Roger C. Strawn, *Aeroflightdynamics Directorate, U.S. Army Aviation and Troop Command, Ames Research Center, Moffett Field, California*
Judith V. Miller, *Defence Research Agency (Aerospace Division), Farnborough, United Kingdom*
Thomas H. Maier, *Aeroflightdynamics Directorate, U.S. Army Aviation and Troop Command, Ames Research Center, Moffett Field, California*
Michel Costes and Philippe Beaumier, *ONERA, Châtillon, France*

October 1996

National Aeronautics and
Space Administration

**Ames Research Center**
Moffett Field, CA 94035-1000

US Army
Aviation and Troop Command

**Aeroflightdynamics Directorate**
Moffett Field, CA 94035-1000

NASA Technical Memorandum 110421 USAATCOM Technical Report 96-A-008

# A Comparison of Lifting-Line and CFD Methods with Flight Test Data from a Research Puma Helicopter

William G. Bousman, Colin Young, François Toulmay, Neil E. Gilbert, Roger C. Strawn, Judith V. Miller, Thomas H. Maier, Michel Costes, and Philippe Beaumier

October 1996

National Aeronautics and
Space Administration

US Army
Aviation and Troop Command

# FOREWORD

A joint program was undertaken in 1987 by investigators in England, France, Australia, and the United States to examine the accuracy of computational fluid dynamics (CFD) model predictions of the flow about a rotor blade on a helicopter in forward flight. The focus of this program was on the accuracy of the CFD predictions; however, lifting-line methods were also evaluated as they are a necessary first step in the CFD computation. Three cases were selected from experimental data obtained on an Aérospatiale Puma with modified swept-tip blades flown at the Royal Aircraft Establishment (RAE) at Bedford (Riley and Miller, 1983; Riley, 1986) and these were used to assess the CFD model accuracy. A workshop was held at RAE Farnborough in May 1988 and the results were presented at the European Rotorcraft Forum in September 1989 (Jones et al., 1990; Strawn et al., 1989; Bousman et al., 1989).

A second phase of correlation using the research Puma flight test data was agreed upon in 1989. The work was expanded considerably with a stronger focus on the lifting-line methods which must provide an accurate basis for the CFD calculations. A workshop was held at Ames Research Center in May 1990 to examine the predictions of the various calculation methods. Participants at this workshop were Colin Young, Judith Miller, and John Riley from England; François Toulmay, Andre Desopper, and C. T. Tran from France; Neil Gilbert from Australia; and Bill Bousman, Roger Strawn, Tom Maier, and Francisco Hernandez from the United States. The workshop employed a common graphic interface and data base for all of the calculations, but even with this aid the workshop participants were able to examine only half the available data base in the time available. At the end of the workshop, however, the participants agreed upon an outline for a final report and sections of the report were assigned to each participant. The result of this collaboration is the present document.

The present report has been a long time in preparation for a variety of reasons. A portion of the work dealing with the lifting-line methods has already been published (Young et al., 1991), but much of what is contained here is new material. Not all of the original participants have been able to contribute fully to this document. C. T. Tran died in 1992, John Riley retired from his job at the Defence Research Agency (DRA) in Bedford, formerly the RAE, and Andre Desopper and Francisco Hernandez have changed organizations and no longer have the time to write their sections nor comment on the complete report. Fortunately, Michel Costes and Philippe Beaumier have been able to author some of the missing sections even though they did not participate in the original workshop.

Colin Young wrote the section on the RAE/WHL analysis, the vacuum modal calculations, and all of the sections in Task 1 dealing with blade moments and loads. Tom Maier and Neil Gilbert wrote the section on the CAMRAD analyses and Robert Toffoletto assisted Gilbert with Appendix C. François Toulmay wrote the section on the METAR/R85 analysis, the trim and performance sections in Tasks 1 and 3, the vibratory loads section in Task 1 (with Bill Bousman), and the appendix on power computation. Roger Strawn wrote the description of FPR, the section on calculated airfoil characteristics for Task 1, the CFD comparisons for the autorotational case in Task 2, and improvements that can be expected in coupling methods. Judith Miller wrote the section describing the TSP code plus the CFD comparisons for the level flight case in Task 2. Michel Costes and Philippe Beaumier wrote two of the sections describing the blade airloads for Task 1. Finally, Bill Bousman wrote many of the section introductions, the Task 3 section dealing with airloads and motion (with Neil Gilbert), the Task 3 section dealing with airfoil characteristics, the flight data descriptions, the recommendations, the summary, and

the documentation appendix. He also took primary responsibility for editing of the report. All of the individual authors reviewed a final draft of the report and offered many useful comments which have been incorporated in the report.

# CONTENTS


SUMMARY 1

1 INTRODUCTION 4

2 ANALYTICAL MODELS 6

2.1 Lifting-Line Models . . . . . 6

2.1.1 RAE/WHL Analysis . . . . . 6

2.1.2 CAMRAD Family . . . . . 9

2.1.3 METAR/R85 Analysis . . . . . 10

2.1.4 Comparison of Lifting-Line Methods . . . . . 12

2.2 CFD Models . . . . . 13

2.2.1 FPR Code . . . . . 13

2.2.2 TSP Code . . . . . 14

3 MODAL CALCULATIONS IN A VACUUM 17

4 ANALYTICAL MODELING OF LIFTING-LINE METHODS (TASK 3) 20

4.1 Introduction . . . . . 20

4.2 Airfoil Characteristics . . . . . 21

4.3 Comparison of Analytical Methods . . . . . 24

4.3.1 Trim and Performance . . . . . 28

4.3.2 Airloads and Motions . . . . . 43

4.4 Summary of Analytical Modeling Investigation (Task 3) . . . . . 94

5 COMPARISON OF LIFTING-LINE METHODS WITH FLIGHT TEST DATA (TASK 1) 97

5.1 Introduction . . . . . 97

5.2 Advance Ratio Sweep (Flight 525) . . . . . 98

5.2.1 Flight Data . . . . . 98

5.2.2 Comparison of Analysis and Experiment . . . . . 119

5.2.3 Summary of Advance Ratio Sweep (Flight 525) Comparisons . . . . . 192

5.3 Reference Case (Flight 123) . . . . . 195

5.3.1 Introduction . . . . . 195

5.3.2 Flight Data . . . . . 196

5.3.3 Comparison of Analysis and Experiment . . . . . 203
5.3.4 Summary of Reference Case Investigation . . . . . 230
5.4 Autorotational Case (Flight 487) . . . . . 230
5.4.1 Flight Data . . . . . 230
5.4.2 Comparison of Analysis and Experiment . . . . . 247
5.4.3 Summary of Autorotational Flight Case Calculations . . . . . 252
5.5 Puma Airfoil . . . . . 253
5.5.1 Introduction . . . . . 253
5.5.2 Puma Airfoil Measurements . . . . . 253
5.5.3 Airfoil Analysis . . . . . 255
5.5.4 Puma Airfoil Summary . . . . . 259
**6 COMPARISON OF HYBRID METHODS WITH FLIGHT TEST DATA (TASK 2)** 262
6.1 Introduction . . . . . 262
6.2 Autorotational Case (Flight 487, Counter 11) . . . . . 264
6.2.1 Azimuthal Histories of Section Lift . . . . . 264
6.2.2 Azimuthal Histories of Section Moment . . . . . 266
6.2.3 Chordwise Pressure Distributions . . . . . 268
6.3 High-Speed Level Flight Case (Flight 525, Counter 21) . . . . . 268
6.3.1 Azimuthal Histories of Section Lift . . . . . 273
6.3.2 Azimuthal Histories of Section Moment . . . . . 273
6.3.3 Chordwise Pressure Distributions . . . . . 273
6.4 Comparison of Hybrid CFD Methods with Lifting-Line Calculations . . . . . 277
6.5 Coupling Method Improvements (Flight 488, Counter 9) . . . . . 283
6.6 Summary of Hybrid CFD Calculations . . . . . 286
**7 CONCLUSIONS** 288
**8 RECOMMENDATIONS** 293
**APPENDIX A— RESEARCH PUMA DOCUMENTATION** 295
Puma Research Aircraft Configurations . . . . . 295
Rotor Geometry . . . . . 296

Structural Properties . . . . . 297
Lag Damper . . . . . 312
Control System . . . . . 312
Fuselage Aerodynamic Force and Moments . . . . . 312

**APPENDIX B— POWER BREAKDOWN USING THE ENERGY METHOD** 315

**APPENDIX C— DIFFERENCES BETWEEN CAMRAD AND CAMRAD/JA ROTOR WAKE MODELS** 319

**REFERENCES** 324

# TABLES


| | | |
|---|---|---|
| 1 | Predicted modal frequencies and shapes | 17 |
| 2 | Task 3 modeling complexity | 20 |
| 3 | Lift equation stall boundary and coefficient | 22 |
| 4 | Drag equation boundary angle and coefficients | 23 |
| 5 | Pitching moment equation boundary angle and coefficients | 23 |
| 6 | Calculated collective pitch at $0.75R$ | 29 |
| 7 | Calculated lateral cyclic pitch | 31 |
| 8 | Calculated cyclic pitch angles in amplitude and phase | 32 |
| 9 | Calculated longitudinal cyclic pitch | 33 |
| 10 | Calculated longitudinal forces for Task 3 cases | 35 |
| 11 | Calculated lateral forces for Task 3 cases | 36 |
| 12 | Calculated profile power for Task 3 cases | 38 |
| 13 | Calculated induced power for Task 3 cases | 39 |
| 14 | Calculated parasite power for Task 3 cases | 40 |
| 15 | Calculated thrust-dependent power for Task 3 cases | 41 |
| 16 | Calculated shaft power for Task 3 cases | 42 |
| 17 | Flight 525 correlation cases | 98 |
| 18 | Pressure transducer locations, x/c | 99 |
| 19 | Measured and calculated collective pitch angles for Flight 525 | 123 |
| 20 | Measured and calculated cosine (lateral) cyclic pitch for Flight 525 | 125 |
| 21 | Measured and calculated sine (longitudinal) cyclic pitch for Flight 525 | 125 |
| 22 | Comparison of Flight 123 and 525 counters | 196 |
| 23 | Unspecified trim parameters and shaft torque for Flight 123, Counter 9 | 207 |
| 24 | Trim conditions for Counter 11, Flight 487 | 231 |
| 25 | Unspecified trim parameters and shaft torque for Flight 487, Counter 11 | 247 |
| 26 | Summary of airfoil comparison cases | 258 |
| A-1 | Puma blade geometry | 296 |
| A-2 | Puma hub/blade geometry | 297 |
| A-3 | Blade twist distribution | 299 |

A-4 Mass distribution . . . . . 301
A-5 Blade c.g. offset . . . . . 303
A-6 Extensional stiffness distribution . . . . . 305
A-7 Flap and chord stiffness distribution . . . . . 307
A-8 Torsional stiffness distribution . . . . . 308
A-9 Torsional inertia distribution . . . . . 310

C-1 Modifications to reduce differences between CAMRAD and CAMRAD/JA near-wake models . . . . . 321
C-2 Aerodynamic segment boundaries for CAMRAD and CAMRAD/JA models . . . . . 321
C-3 Effect of near-wake model changes on induced and total power for forward flight with circulation and motion iterations excluded . . . . . 322
C-4 Effect of near-wake model changes on induced and flap angles for forward flight with circulation and motion iterations included . . . . . 322
C-5 Effect of near-wake model changes on induced power and coning angle for hover with circulation and motion iterations included . . . . . 323

# FIGURES


1 Top view of the FPR grid for the swept-tip Puma blade calculations. . . . . 14

2 Comparison of modal frequencies calculated by the RAE/WHL and CAMRAD/JA analyses. . . . . 19

3 Comparison of lift coefficient from look-up tables with data from Harris (1981). . . . 25

4 Comparison of drag coefficient from look-up tables with data from Harris (1981). . . . 26

5 Comparison of pitching moment coefficient from look-up tables with data from Harris (1981). . . . . 27

6 Calculated collective pitch for the Task 3 cases. . . . . 29

7 Calculated lateral cyclic pitch for the Task 3 cases. . . . . 31

8 Calculated longitudinal cyclic pitch for the Task 3 cases. . . . . 33

9 Calculated longitudinal forces for Task 3 cases. . . . . 35

10 Calculated lateral forces for Task 3 cases. . . . . 36

11 Calculated profile power for Task 3 cases. . . . . 38

12 Calculated induced power for Task 3 cases. . . . . 39

13 Calculated parasite power for Task 3 cases. . . . . 40

14 Calculated thrust-dependent power for Task 3 cases. . . . . 41

15 Calculated shaft power for Task 3 cases. . . . . 42

16 Normal force distribution as a function of azimuth and blade radius for Case 1; all harmonics. . . . . 44

17 Angle-of-attack distribution as a function of azimuth and blade radius for Case 1; all harmonics. . . . . 45

18 Normal force distribution as a function of azimuth and blade radius for Case 1; harmonics 3 and above. . . . . 47

19 Comparison of analytical methods for Case 1 for four parameters; all harmonics. Flap angle not shown for the RAE/WHL analysis. . . . . 48

20 Normal force distribution as a function of azimuth and blade radius for Case 2; all harmonics. . . . . 49

21 Comparison of radial distribution of steady normal force for Cases 1 and 2. . . . . 50

22 Normal force distribution as a function of azimuth and blade radius for Case 3; all harmonics. . . . . 51

23 Normal force distribution as a function of azimuth and blade radius for Case 3; harmonics 3 and above. . . . . 52

24 Comparison of the radial distribution of steady normal force for Case 3. . . . . 53

25 Angle-of-attack distribution as a function of azimuth and blade radius for Case 3; all harmonics. . . . . 54

26 Comparison of angle-of-attack distribution as a function of azimuth for Cases 1 and 3; $0.85R$, harmonics 2 and above. . . . . 55

27 Normal force distribution as a function of azimuth and blade radius for Case 4; all harmonics. . . . . 57

28 Normal force distribution as a function of azimuth and blade radius for Case 5; all harmonics. . . . . 58

29 Comparison of normal force distribution as a function of azimuth for Cases 3 and 5; $0.85R$, all harmonics. . . . . 59

30 Angle-of-attack distribution as a function of azimuth and blade radius for Case 5; all harmonics. . . . . 60

31 Comparison of angle of attack as a function of azimuth for Cases 3 and 5; $0.85R$, harmonics 2 and above. . . . . 61

32 Section pitching moment distribution as a function of azimuth and blade radius for Case 5; all harmonics. . . . . 62

33 Angle-of-attack distribution and section pitching moment as a function of azimuth for Case 5; $0.98R$. . . . . 63

34 Normal force and Mach number distributions at two radial stations and comparison with RAE equation stall boundary (heavy dashed line). Two-dimensional section lift at constant angle of attack shown as dotted lines. . . . . 64

35 Normal force distribution as a function of azimuth and blade radius for Case 6; all harmonics. . . . . 65

36 Normal force distribution as a function of azimuth and blade radius for Case 7; all harmonics. . . . . 66

37 Comparison of normal force distribution as a function of azimuth for Cases 5 and 7; $0.85R$, all harmonics. . . . . 67

38 Angle-of-attack distribution as a function of azimuth and blade radius for Case 7; all harmonics. . . . . 68

39 Comparison of angle of attack as a function of azimuth for Cases 5 and 7; $0.85R$, harmonics 2 and above. . . . . 69

40 Section pitching moment distribution as a function of azimuth and blade radius for Case 7; all harmonics. . . . . 70

41 Comparison of section pitching moment as a function of azimuth for Cases 5 and 7; $0.95R$, all harmonics. . . . . 71

42 Normal force distribution as a function of azimuth and blade radius for Case 8; all harmonics. . . . . 72

43 Comparison of normal force distribution as a function of azimuth for Cases 7 and 8; $0.85R$, all harmonics. . . . . 73

44 Comparison of angle of attack as a function of azimuth for Cases 7 and 8; $0.85R$, harmonics 2 and above. . . . . 74

45 Comparison of section pitching moment as a function of azimuth for Cases 7 and 8; $0.95R$, all harmonics. . . . . 75

46 Normal force distribution as a function of azimuth and blade radius for Case 9; all harmonics. . . . . 77

47 Comparison of normal force distribution as a function of azimuth for Cases 3, 8, and 9; $0.85R$, all harmonics. . . . . 78

48 Normal force distribution as a function of azimuth and blade radius for Case 9; harmonics 3 and above. . . . . 79

49 Comparison of normal force distribution as a function of azimuth for Cases 3, 8, and 9; $0.85R$, harmonics 3 and above. . . . . 80

50 Angle-of-attack distribution as a function of azimuth and blade radius for Case 9; all harmonics. . . . . 81

51 Comparison of angle of attack as a function of azimuth for Cases 3, 8 and 9; $0.85R$, harmonics 2 and above. . . . . 82

52 Section pitching moment distribution as a function of azimuth and blade radius for Case 9; all harmonics. . . . . 84

53 Comparison of section pitching moment as a function of azimuth for Cases 8 and 9; $0.95R$, all harmonics. . . . . 85

54 Normal force distribution as a function of azimuth and blade radius for Case 10; all harmonics. . . . . 86

55 Comparison of normal force distribution as a function of azimuth for Cases 3, 9, and 10; $0.85R$, all harmonics. . . . . 87

56 Normal force distribution as a function of azimuth and blade radius for Case 10; harmonics 3 and above. . . . . 88

57 Comparison of normal force distribution as a function of azimuth for Cases 3, 9, and 10; $0.85R$, harmonics 3 and above. . . . . 89

58 Angle-of-attack distribution as a function of azimuth and blade radius for Case 10; all harmonics. . . . . 90

59 Comparison of angle of attack as a function of azimuth for Cases 3, 9 and 10; $0.85R$, harmonics 2 and above. . . . . 91

60 Section pitching moment distribution as a function of azimuth and blade radius for Case 10; all harmonics. . . . . 92

61 Comparison of section pitching moment as a function of azimuth for Cases 9 and 10; $0.95R$, all harmonics. . . . . 93

62 Structural and pressure instrumentation installed on the research Puma blade. . . . . 99

63 Section lift and pitching moment as a function of azimuth and advance ratio for Flight 525; $0.95R$. Correlation cases shown by thickend lines. . . . . 101

64 Section lift and pitching moment as a function of azimuth at low speed; $\mu = 0.098$. . 102

65 Upper surface pressure as a function of azimuth at low speed; $0.95R$, $\mu = 0.098$. . . 103

66 Section lift and pitching moment as a function of azimuth at high speed; $\mu = 0.402$. . 104

67 Upper surface pressure as a function of azimuth at high speed; $0.95R$, $\mu = 0.402$. $M = 1$ boundary shown as heavy dotted line. . . . . 106

68 Flap bending moment distribution as a function of azimuth and advance ratio; $0.57R$, 1–32 harmonics. . . . . 107

69 Flap bending moment distribution as a function of azimuth and blade radius for $\mu =$ 0.098 and 0.402, 1–32 harmonics. . . . . 108

70 Chord bending moment distribution as a function of azimuth and advance ratio; $0.55R$, 1–32 harmonics. . . . . 109

71 Chord bending moment distribution as a function of azimuth and blade radius for $\mu =$ 0.098 and 0.402, 1–32 harmonics. . . . . 110

72 Torsion moment distribution as a function of azimuth and advance ratio; $0.126R$, 1–32 harmonics. . . . . 111

73 Torsion moment distribution as a function of azimuth and blade radius for $\mu = 0.098$ and 0.402, 1–32 harmonics. . . . . 113

74 Pitch-link load distribution as a function of azimuth and advance ratio, 1–32 harmonics. 114

75 Blade pitch angle distribution at $0.75R$ as a function of azimuth and advance ratio. . 115

76 Collective pitch angle at $0.75R$ as a function of advance ratio. . . . . 115

77 Lateral and longitudinal pitch angles as a function of advance ratio. . . . . 116

78 Pitch angle with control motions removed; 2–32 harmonics. . . . . 116

79 Flap angle distribution as a function of azimuth and advance ratio for Blade 1. . . . . 117

80 First harmonic blade flapping as a function of advance ratio. . . . . 117

81 Lead-lag angle distribution as a function of azimuth and advance ratio for Blade 1. . 118

82 Shaft angle as a function of azimuth for three different measurements. . . . . 119

83 Computed trim rotor thrust compared to aircraft gross weight as a function of advance ratio. . . . 120

84 Comparison of measured and calculated first harmonic flapping as a function of advance ratio for Flight 525. . . . 121

85 Aircraft gross weight, gross weight plus fuselage and stabilizer download, and coning-based thrust as functions of advance ratio. . . . 122

86 Comparison of measured and calculated collective pitch angle at blade pitch bearing as a function of advance ratio for Flight 525. . . . 123

87 Comparison of measured and calculated cyclic pitch angles at the blade pitch bearing as a function of advance ratio for Flight 525. . . . 125

88 Comparison of measured and calculated blade coning as a function of advance ratio for Flight 525. . . . 126

89 Comparison of measured and calculated blade steady lag angle as a function of advance ratio for Flight 525. . . . 127

90 Comparison of measured and calculated first harmonic lead-lag angles as functions of advance ratio for Flight 525. . . . 128

91 Comparison of calculated X-forces as a function of advance ratio for Flight 525. . . . 129

92 Comparison of calculated Y-forces as a function of advance ratio for Flight 525. . . . 130

93 Comparison of calculated pitch moments with values derived from test data as functions of advance ratio for Flight 525. . . . 131

94 Comparison of calculated roll moments with values derived from test data as functions of advance ratio for Flight 525. . . . 132

95 Comparison of measured and calculated shaft torque as a function of advance ratio for Flight 525. . . . 134

96 Comparison of measured and calculated section normal force as a function of azimuth and advance ratio; $0.95R$, Flight 525. . . . 135

97 Comparison of measured and calculated section pitching moment as a function of azimuth and advance ratio; $0.95R$, Flight 525. . . . 136

98 Comparison of measured and calculated section normal force as a function of azimuth; $\mu = 0.098$, $0.95R$, Flight 525. . . . 138

99 Comparison of measured and calculated section normal force as a function of azimuth; $\mu = 0.182$, $0.95R$, Flight 525. . . . 139

100 Comparison of measured and calculated section normal force as a function of azimuth; $\mu = 0.307$, $0.95R$, Flight 525. . . . 140

101 Comparison of measured and calculated section normal force as a function of azimuth; $\mu = 0.362$, $0.95R$, Flight 525. . . . 141

102 Comparison of measured and calculated section normal force as a function of azimuth; $\mu = 0.402$, $0.95R$, Flight 525. . . . . 142

103 Comparison of measured and calculated section normal force as a function of radius at four azimuths; $\mu = 0.402$, Flight 525. . . . . 144

104 Comparison of measured and calculated section pitching moment as a function of azimuth; $\mu = 0.098$, $0.95R$, Flight 525. . . . . 145

105 Comparison of measured and calculated section pitching moment as a function of azimuth; $\mu = 0.182$, $0.95R$, Flight 525. . . . . 146

106 Comparison of measured and calculated section pitching moment as a function of azimuth; $\mu = 0.307$, $0.95R$, Flight 525. . . . . 147

107 Comparison of measured and calculated section pitching moment as a function of azimuth; $\mu = 0.362$, $0.95R$, Flight 525. . . . . 148

108 Comparison of measured and calculated section pitching moment as a function of azimuth; $\mu = 0.402$, $0.95R$, Flight 525. . . . . 149

109 Comparison of measured and calculated section pitching moment as a function of radius at four azimuths; $\mu = 0.402$, Flight 525. . . . . 150

110 Comparison of calculated section normal force as a function of azimuth and radial station at $\mu = 0.098$; Flight 525. . . . . 152

111 Comparison of calculated section pitching moment as a function of azimuth and radial station at $\mu = 0.098$; Flight 525. . . . . 153

112 Comparison of calculated section normal force as a function of azimuth and radial station at $\mu = 0.402$; Flight 525. . . . . 154

113 Comparison of calculated section pitching moment as a function of azimuth and radial station at $\mu = 0.402$; Flight 525. . . . . 155

114 Comparison of measured and calculated blade flapping as a function of azimuth and advance ratio for Flight 525; 1–36 harmonics. . . . . 157

115 Comparison of measured and calculated blade lead-lag motion as a function of azimuth and advance ratio for Flight 525; 1–36 harmonics. . . . . 158

116 Comparison of measured and calculated flap bending moment as a function of azimuth at $0.20R$; $\mu = 0.098$, Flight 525, 1–36 harmonics. . . . . 159

117 Comparison of measured and calculated flap bending moment as a function of azimuth at $0.57R$; $\mu = 0.098$, Flight 525, 1–36 harmonics. . . . . 161

118 Comparison of measured and calculated flap bending moment as a function of azimuth at $0.78R$; $\mu = 0.098$, Flight 525, 1–36 harmonics. . . . . 162

119 Comparison of measured and calculated chord bending moment as a function of azimuth at $0.122R$; $\mu = 0.098$, Flight 525, 1–36 harmonics. . . . . 163

120 Comparison of measured and calculated chord bending moment as a function of azimuth at $0.55R$; $\mu = 0.098$, Flight 525, 1–36 harmonics. . . . . 164

121 Comparison of measured and calculated harmonic amplitude of chord bending moment at $0.55R$; $\mu = 0.098$, Flight 525. . . . . 165

122 Comparison of measured and calculated torsion moment as a function of azimuth at $0.126R$; $\mu = 0.098$, Flight 525, 1–36 harmonics. . . . . 167

123 Comparison of measured and calculated torsion moment as a function of azimuth at $0.55R$; $\mu = 0.098$, Flight 525, 1–36 harmonics. . . . . 168

124 Comparison of measured and calculated pitch-link load as a function of azimuth; $\mu = 0.098$, Flight 525. . . . . 169

125 Comparison of measured and calculated flap bending moment as a function of azimuth at $0.20R$; $\mu = 0.182$, Flight 525. . . . . 171

126 Comparison of measured and calculated flap bending moment as a function of azimuth at $0.67R$; $\mu = 0.182$, Flight 525. . . . . 172

127 Comparison of measured and calculated chord bending moment as a function of azimuth at $0.55R$; $\mu = 0.182$, Flight 525. . . . . 173

128 Comparison of measured and calculated torsion moment as a function of azimuth at $0.33R$; $\mu = 0.182$, Flight 525. . . . . 174

129 Comparison of measured and calculated flap bending moment as a function of azimuth and blade radius; $\mu = 0.307$, Flight 525. . . . . 176

130 Comparison of measured and calculated chord bending moment as a function of azimuth and blade radius; $\mu = 0.307$, Flight 525. . . . . 177

131 Comparison of measured and calculated torsion moment as a function of azimuth and blade radius; $\mu = 0.307$, Flight 525. . . . . 178

132 Comparison of measured and calculated flap bending moment as a function of azimuth and blade radius; $\mu = 0.362$, Flight 525. . . . . 180

133 Comparison of measured and calculated chord bending moment as a function of azimuth and blade radius; $\mu = 0.362$, Flight 525. . . . . 181

134 Comparison of measured and calculated torsion moment as a function of azimuth and blade radius; $\mu = 0.362$, Flight 525. . . . . 182

135 Comparison of measured and calculated flap bending moment as a function of azimuth and blade radius; $\mu = 0.402$, Flight 525. . . . . 183

136 Comparison of measured and calculated chord bending moment as a function of azimuth and blade radius; $\mu = 0.402$, Flight 525. . . . . 184

137 Comparison of measured and calculated torsion moment as a function of azimuth and blade radius; $\mu = 0.402$, Flight 525. . . . . 186

138 Comparison of calculated hub 4/rev X-force as a function of advance ratio for Flight 525. . . . . 187

139 Comparison of calculated hub 4/rev Y-force as a function of advance ratio for Flight 525. 188

140 Comparison of calculated hub 4/rev vertical shears and values derived from blade measurements as a function of advance ratio for Flight 525. . . . . 189

141 Modal fit of blade flap bending moment data using nine calculated modes; $\mu = 0.402$. 191

142 Comparison of calculated hub 4/rev roll moment and values derived from blade measurements as a function of advance ratio for Flight 525. . . . . 192

143 Comparison of calculated hub 4/rev pitch moment and values derived from blade measurements as a function of advance ratio for Flight 525. . . . . 193

144 Comparison of calculated 4/rev shaft torque as a function of advance ratio for Flight 525. 194

145 Structural instrumentation on the standard Puma blade. . . . . 197

146 Shaft angle of attack for Flight 123 compared with Flight 525 angle-of-attack schedule. 197

147 Flight 123 first harmonic flapping compared with Flight 525 values. . . . . 198

148 Flight 123 collective pitch angles compared with Flight 525 values. . . . . 198

149 Flight 123 cyclic pitch angles compared with Flight 525 values. . . . . 199

150 Flight 123 coning angles compared with Flight 525 values. . . . . 200

151 Flight 123 lead-lag angles compared with Flight 525 values. . . . . 200

152 Comparison of midspan flap bending moment distributions for flights 525 and 123 as functions of azimuth and advance ratio. Comparison cases shown with a thickened line. 201

153 Comparison of flap bending moment radial distribution for flights 525 and 123; $\mu = 0.307$ (Flight 525), $\mu = 0.321$ (Flight 123). . . . . 202

154 Comparison of measured flap bending moments for flights 525 and 123 at $0.35R$ and $0.55R$; $\mu = 0.307$ (Flight 525), $\mu = 0.321$ (Flight 123). . . . . 204

155 Comparison of measured chord bending moments for flights 525 and 123 at $0.73R$; $\mu = 0.307$ (Flight 525), $\mu = 0.321$ (Flight 123). . . . . 205

156 Comparison of measured torsion moments for flights 525 and 123 at $0.33R$; $\mu = 0.307$ (Flight 525), $\mu = 0.321$ (Flight 123). . . . . 206

157 Calculated normal force as a function of azimuth and blade radius; Flight 123, $\mu = 0.321$. 208

158 Calculated normal force as a function of azimuth at $0.95R$; Flight 123, $\mu = 0.321$. . . 209

159 Calculated pitching moment as a function of azimuth and blade radius; Flight 123, $\mu = 0.321$. . . . . 211

160 Calculated pitching moment as a function of azimuth at $0.95R$; Flight 123, $\mu = 0.321$. 212

161 Comparison of calculated radial distributions of lift for a rectangular-tip and swept-tip blade; $\psi = 0°$. . . . . 213

162 Comparison of section lift for a rectangular-tip and swept-tip blade; $0.95R$. . . . . 215

163 Comparison of vibratory section lift for a rectangular-tip and swept-tip blade; $0.95R$, harmonics 3 and above. . . . . 216

164 Comparison of section pitching moment for a rectangular-tip and swept-tip blade; $0.95R$. 217

165 Comparison of measured and calculated flap bending moments as a function of azimuth for Flight 123; $0.35R$, $\mu = 0.321$. . . . . 219

166 Comparison of measured and calculated flap bending moment harmonics for Flight 123; $0.35R$, $\mu = 0.321$. . . . . 220

167 Comparison of measured and calculated flap bending moments as a function of azimuth for Flight 123; $0.75R$, $\mu = 0.321$. . . . . 221

168 Comparison of measured and calculated chord bending moments as a function of azimuth for Flight 123; $0.73R$, $\mu = 0.321$. . . . . 222

169 Comparison of measured and calculated chord bending moment harmonics for Flight 123; $0.73R$, $\mu = 0.321$. . . . . 223

170 Comparison of measured and calculated torsion moments as a function of azimuth for Flight 123; $0.33R$, $\mu = 0.321$. . . . . 225

171 Comparison of measured and predicted flap bending moments for flights 525 and 123; $0.35R$. . . . . 226

172 Comparison of measured and predicted flap bending moments for flights 525 and 123; $0.75R$. . . . . 227

173 Comparison of measured and predicted chord bending moments for flights 525 and 123; $0.73R$. . . . . 228

174 Comparison of measured and predicted torsion moments for flights 525 and 123; $0.33R$. 229

175 Instrumentation on Flight 487. . . . . 231

176 Comparison of root pitch angle for flights 487 and 525. Zeroth and first harmonic approximation included for Flight 487. . . . . 232

177 Comparison of blade flapping for flights 487 and 525. Zeroth and first harmonic approximation included for Flight 487. . . . . 233

178 Section normal force and pitching moments; Flight 487. . . . . 235

179 Upper surface pressures as a function of azimuth; $0.95R$, Flight 487. Sonic line shown as heavy dashed line. . . . . 236

180 Offset plot of upper surface pressures as a function of azimuth; $0.95R$, Flight 487. . . 237

181 Lower surface pressures as a function of azimuth; $0.95R$, Flight 487. Sonic line shown as heavy dashed line. . . . . 239

182 Offset plot of lower surface pressures as a function of azimuth; $0.95R$, Flight 487. . . 240

183 Comparison of normal force and pitching moment for flights 487 and 525; $0.95R$. . . 241

184 Chordwise pressure distributions at four radial stations; $\psi = 78°$, Flight 487. Critical $M^2C_p$ shown as heavy dashed line on y-axis. . . . . 242

185 Chordwise pressure distributions at four radial stations; $\psi = 85°$, Flight 487. Critical $M^2C_p$ shown as heavy dashed line on y-axis. . . . . 243

186 Comparison of flap bending moments on flights 487 and 525; $0.46R$. . . . . 244

187 Comparison of chord bending moments on flights 487 and 525; $0.55R$. . . . . 245

188 Comparison of torsion moments on flights 487 and 525; $0.33R$. . . . . 246

189 Comparison of experiment and calculation section normal force for the Flight 487 condition. . . . . 248

190 Comparison of experiment and calculation section pitching moment for the Flight 487 condition. . . . . 250

191 Comparison of measured and calculated flap bending moments for Flight 487; $0.46R$. 251

192 Comparison of measured and calculated chord bending moments for Flight 487; $0.55R$. 251

193 Comparison of measured and calculated torsion moments for Flight 487; $0.33R$. . . . 252

194 Swept tip planform of research Puma. Chordwise pressure transducer sections shown by dashed lines and feather axis by dotted line. . . . . 254

195 Puma section profile created by translation of inboard profile and fairing; $0.95R$, vertical scale 4.4 X horizontal scale. . . . . 254

196 Comparison of theoretical profiles and 1982 measurements for four stations. Vertical scale 1.7 X horizontal scale. . . . . 256

197 Comparison of theoretical profile with 1982 and 1989 measurements; $0.95R$. Vertical scale 2.4 X horizontal scale. . . . . 257

198 Comparison plot of the Puma airfoil sections and the NACA 0012 section. Vertical scale 3.8 X horizontal scale. . . . . 257

199 Viscous calculation results; $M_\infty = 0.60$, $\alpha = 6.0°$. NACA 0012: $C_l = 0.8244$, $C_d = 0.02333$, $C_m = 0.02612$; Puma airfoil: $C_l = 0.7840$, $C_d = 0.02349$, $C_m = 0.02904$. 259

200 Viscous calculation results; $M_\infty = 0.80$, $\alpha =$; Puma airfoil: $C_l = 0.4599$, $C_d = 0.03022$, $C_m = -0.02514$. . . . . 260

201 Viscous calculation results; $M_\infty = 0.84$, $\alpha = 0.5°$. NACA 0012: $C_l = 0.1175$, $C_d = 0.04216$, $C_m = -0.02706$; Puma airfoil: $C_l = 0.1469$, $C_d = 0.02222$, $C_m = -0.02649$. . . . . 260

202 Schematic of the combined rotor airloads prediction scheme of Tung et al. (1986). . . 263

203 Comparison of hybrid CFD analyses with experiment for section lift; Flight 487. . . . 265

204 Comparison of hybrid CFD analyses with experiment for section moment; Flight 487. 267

205 Chordwise pressure comparison of experimental measurements and CFD hybrid predictions for Flight 487; $\psi = 30°$. . . . . 269

206 Chordwise pressure comparison of experimental measurements and CFD hybrid predictions for Flight 487; $\psi = 90°$. . . . . 270

207 Chordwise pressure comparison of experimental measurements and CFD hybrid predictions for Flight 487; $\psi = 120°$. . . . . 271

208 Chordwise pressure comparison of experimental measurements and CFD hybrid predictions for Flight 487; $\psi = 270°$. . . . . 272

209 Comparison of hybrid CFD analyses with experiment for section lift; Flight 525. . . . 274

210 Comparison of hybrid CFD analyses with experiment for section moment; Flight 525. 275

211 Chordwise pressure comparison of experimental measurements and CFD hybrid predictions for Flight 525; $\psi = 30°$. . . . . 276

212 Chordwise pressure comparison of experimental measurements and CFD hybrid predictions for Flight 525; $\psi = 120°$. . . . . 278

213 Chordwise pressure comparison of experimental measurements and CFD hybrid predictions for Flight 525; $\psi = 150°$. . . . . 279

214 Chordwise pressure comparison of experimental measurements and CFD hybrid predictions for Flight 525; $\psi = 270°$. . . . . 280

215 Comparison of CAMRAD/JA and FPR-CAMRAD/JA with flight test measurements at $0.95R$ and $0.978R$; Flight 487, Counter 11. . . . . 281

216 Comparison of CAMRAD/JA and FPR-CAMRAD/JA with flight test measurements at $0.95R$ and $0.978R$; Flight 525, Counter 21. . . . . 282

217 Comparison of TSP and TSP-RAE/WHL with flight test measurements at $0.95R$ and $0.978R$; Flight 487, Counter 11. . . . . 284

218 Comparison of TSP and TSP-RAE/WHL with flight test measurements at $0.95R$ and $0.978R$; Flight 525, Counter 21. . . . . 285

A-1 Comparison of standard Puma blade and modified swept-tip blade. . . . . 295

A-2 Standard and swept-tip blade twist distribution. . . . . 298

A-3 Standard and swept-tip blade mass distribution. . . . . 300

A-4 Standard and swept-tip blade c.g distribution with respect to root quarter chord. . . . . 302

A-5 Standard and swept-tip blade EA distribution. . . . . 304

A-6 Standard and swept-tip blade flap stiffness distribution. . . . . 306
A-7 Standard and swept-tip blade chord stiffness distribution. . . . . 307
A-8 Standard and swept-tip blade torsional stiffness distribution. . . . . 308
A-9 Standard and swept-tip blade torsional inertia with respect to section shear center. . . . 309
A-10 Hydraulic damper force response characteristics from bench tests. . . . . 313

C-1 General representation of near wake geometry. . . . . 319
C-2 CAMRAD and CAMRAD/JA representation of near-wake panel. . . . . 320

# SUMMARY

A collaborative effort by investigators in the United States, the United Kingdom, France, and Australia is reported here. The purpose of the collaborative study was to make a detailed assessment of the accuracy of Computational Fluid Dynamics (CFD) methods for the prediction of the airloads on a helicopter blade in high-speed flight. As of 1990 the state-of-the-art of CFD analysis was restricted to cases where the trim condition, blade dynamic and elastic response, and a portion of the inflow must either be specified as constants or computed by an analysis external to the CFD calculation. Typically this external computation is obtained with a comprehensive analysis based on lifting-line theory. The external computation is then coupled to the CFD calculation and a hybrid solution is obtained following a number of iterations between the two analyses.

The assessment of CFD predictive accuracy was approached by examining not only the accuracy of the hybrid calculation but also by examining the accuracy of the lifting-line methods in isolation, that is, outside of the hybrid calculation. In addition, because of the sensitivity of the hybrid calculation to modeling assumptions in the lifting-line methods, the problem of predictive accuracy was further investigated by examining the influence of various modeling assumptions on the lifting-line calculation. These three components, then, (1) the effects of analytical modeling assumptions, (2) the accuracy of the lifting-line methods in isolation, and (3) the accuracy of the hybrid calculation, comprise the body of this report.

An Introduction to the present effort is provided as Section 1. Following this, Section 2 briefly describes the analytical methods used. The four lifting-line methods include two methods in use in the United States and Australia: CAMRAD/JA and its predecessor CAMRAD; a method developed jointly by Westland and the RAE (now the DRA) in the United Kingdom which is referred to in this study as the RAE/WHL analysis; and a method developed by Aérospatiale (now Eurocopter France) which is referred to here as the METAR/R85 code. The two CFD analyses used are the FPR code, in use in the United States, and the TSP code, in use in the United Kingdom. The hybrid calculations couple FPR with CAMRAD/JA and TSP with the RAE/WHL analysis.

Section 3 compares modal and frequency calculations for three of the lifting-line methods and this comparison indicates that the same structural model has been implemented satisfactorily by each code.

The sensitivity of the lifting-line methods to various modeling assumptions is examined in Section 4 for a single high-speed flight condition. There are no data for this case. This examination is based on a stepwise approach that starts with a simplified model and builds to the full-complexity or 'all-up' model. The simplified model assumes that the rotor is represented by a rigid, hinged blade and the aerodynamics are represented by a uniform wake, linear aerodynamics, no unsteady flow, and no yawed flow corrections. Modeling complexity is increased in a stepwise manner by adding: (1) a prescribed wake, (2) nonlinear airfoil characteristics (tables), (3) unsteady aerodynamics, (4) radial or yawed flow effects, (5) elastic bending modes, and (6) elastic torsion modes. Based on this approach it is observed that the modeling step that has the most significant effect on the blade airloads is the change from a uniform to a prescribed wake. For the moderate flight condition studied here the influence of nonlinear aerodynamics is essentially nonexistent on the blade lift but does significantly influence the blade pitching moment. Unsteady aerodynamics is shown to have little effect on lift but, again, affects

the pitching moment. Radial or yawed flow effects are small, for the most part. The addition of blade flexibility influences the airloads to a limited degree with similar effects caused by both blade bending and torsion.

The lifting-line methods in isolation are examined in Section 5 by comparison with flight-test data obtained on a research Puma with a swept-tip blade under a joint Anglo-French program. The major focus of the comparison is an airspeed sweep from 0.1 to 0.4 advance ratio and comparisons are made with the airloads measured near the blade tip, bending and torsion moments, pitch-link loads and vibratory rotor forces and moments. There is, in general, a good prediction of the blade normal force at lower advance ratios for the lifting-line methods that include a free wake and for all of the methods at high speed. However, the prediction of the section pitching moment near the blade tip is much less satisfactory. The flap bending moments, particularly in the central section of the blade, are well predicted by most of the analyses, but the chord moments are poorly predicted. The prediction of the torsion moments and pitch-link loads is only fair and, in general, all of the analyses underpredict the torsion moments. By inference, these methods will also underpredict the elastic torsional deflection in the blade as well.

The effect of tip sweep on the predictive ability of the lifting-line methods was a concern in this study and the approach taken was to examine data obtained on a Puma with the conventional rectangular-tip blade and use these data as baseline or control case. The lifting-line methods are compared with these data for a single advance ratio in Section 5.3. It is shown that the primary effect of sweep is on section pitching moments near the blade tip and, hence, on the torsion moments inboard on the blade. In general, where lifting-line methods show good predictive capability this holds true for either the rectangular-tip or swept-tip blade. The converse is also true that when the predictive capability is poor it is poor regardless of configuration.

Two flight conditions were selected for hybrid calculations, one from the level flight airspeed sweep discussed in Section 5.1 and one for an autorotational dive condition. The lifting-line method predictions in isolation for this latter case are discussed in Section 5.4. The prediction of blade airloads and structural moments is noticeably poorer for this dive condition than for the high-speed level flight case, but it is unclear to what degree this is related to the higher advance ratio and higher tip Mach number for this condition.

Finally, Section 5 concludes with an examination of the blade airfoil characteristics in Section 5.5. Blade profile measurements are compared with the ordinate data that are used by the CFD methods and good agreement is observed. The modified airfoil at the tip of the Puma blade is similar to an NACA 0012 airfoil section and, based on that similarity, the lifting-line methods have all used airfoil tables or data based on the NACA 0012 section. The limitations of this assumption are examined by using both a potential flow and a Navier-Stokes flow solver to obtain two-dimensional airfoil characteristics for a variety of angles of attack and Mach numbers. This comparison suggests that the tables or equations used by the lifting-line methods in this section are, for the most part, satisfactory.

Section 6 presents the results of the hybrid calculations for the two flight conditions examined. The first case is an autorotational dive condition with $\mu = 0.43$ and $M_{90} = 0.92$ while the second case is a high-speed level flight case with $\mu = 0.40$ and $M_{90} = 0.83$. The airloads predicted by these hybrid calculations are, in general, no better than those predicted by the lifting-line methods

in isolation and particularly for the section pitching moments the predictions are worse. The hybrid coupling procedure is examined in more detail in Section 6.5 and although some improvements can be obtained it is concluded that the present 'loose-coupled' procedure does not provide accurate prediction of the airloads on a helicopter blade at high speed.

Summary sections are included throughout the report and the most important results of the collaborative effort are contained in Section 7, Conclusions, and Section 8, Recommendations. Documentation of the research Puma rotor and aircraft is contained in Appendix A of this study. Appendix B discusses various approaches to categorizing rotor power and Appendix C examines details of the near-wake representation used by CAMRAD and CAMRAD/JA.

# 1 INTRODUCTION

Computational fluid dynamics (CFD) models have provided great insight in recent years into the flow over a rotor blade in forward flight, particularly for unsteady transonic flows at high speed and close blade-vortex interactions at moderate speeds. Present methods, however, compute only the effects of the blade self-induced flows, that is, the effects of the rotor blade's own wake. For a lifting rotor in forward flight it is also necessary to account for the flow induced by the wakes of previous blades and the effects of structural deformation on angle of attack. It is expected that in the future the entire calculation will be made using a unified flow method, but for the present such a computation can only be done by using hybrid methods that combine the CFD analysis with an appropriate comprehensive analysis based on lifting-line theory (Caradonna, 1990).

The first demonstration of a hybrid approach for rotors in forward flight compared calculations using a lifting-line method and a finite-difference code with measurements obtained in a wind tunnel test of a 1/7th-scale model of an AH-1G rotor (Tung et al., 1986). In this calculation the blade angle of attack was calculated by the lifting-line method in the normal fashion except that the component of the induced flow resulting from the blade self-induced wake within the CFD method computational domain was removed. The angle-of-attack values that exclude the blade self-induced flow were referred to as partial angles of attack and were then used in the finite-difference method to calculate the blade lift. The finite-difference lift was then transferred to the lifting-line analysis in lieu of table look-up values, and a relaxation scheme was employed to allow convergence between the two methods. The two methods then were coupled in lift and it was demonstrated that the convergence process was quite rapid.

In 1987, it was decided to examine the accuracy of these hybrid methods for the prediction of the flow over a full-scale rotor blade using pressure data obtained on a research Puma in flight (Riley and Miller, 1983; Riley, 1986). As a first step in a collaborative study, comparisons were made between three lifting-line methods for the prediction of the partial angles of attack. Then, one set of partial angles was selected as a baseline, and the blade pressures were computed using three different CFD methods. In essence, this study examined the first two steps in the hybrid calculation, but did not examine the coupling of the methods. The results of these calculations were compared in a workshop at DRA Farnborough in May 1988. Two general conclusions were reached from this workshop (Jones et al., 1990; Bousman et al., 1989; Strawn et al., 1989). First, the three CFD methods, in general, showed good agreement with each other, but did not provide a satisfactory prediction of the flight test measurements. Second, while the lifting-line methods showed fairly good agreement in the prediction of rotor lift, the calculated partial angles differed substantially.

Following the 1988 workshop, a second collaborative effort was proposed that would focus on the problems revealed in the first workshop. In particular, it was apparent that much more needed to be learned about the accuracy of the lifting-line methods before these methods could be coupled with the CFD calculations. For the second collaboration, then, three tasks were proposed:

*Task 1* Compare the predictions of lifting-line methods over a range of airspeeds for the research Puma and examine, not just the measured pressures, but the blade structural response as well.

*Task 2* Compare hybrid predictions for two flight points: a high-speed level flight case and an autorotational dive case.

*Task 3* Examine the modeling assumptions in the lifting-line calculation for one hypothetical flight condition as these assumptions are varied in a stepwise fashion.

A workshop was held in May 1990 at Ames Research Center to report on the three tasks. This report is the result of that workshop. The report is organized to first discuss the various analyses used. Following this, comparisons are made between the lifting-line methods to assess how well the rotor blade structure was modeled. The three tasks are then discussed, but in the order of Task 3, Task 1, and Task 2. This re-ordering of the tasks has been done to allow insights gained in the evaluation of modeling assumptions (Task 3) to be used in evaluating the accuracy of the lifting-line methods (Task 1). Because of the length of the report intermediate summaries are provided for many of the individual sections. A conclusions section is provided at the end of the report that assesses the results from the three tasks from an integrated perspective. This is followed with recommendations for further work. Appendices are included that provide model property documentation, a derivation of the method used for power comparisons in Task 3, and an examination of subtle differences in the CAMRAD and CAMRAD/JA wake models.

The work reported here is, to some extent, dated. The analytical models that were used for these comparisons have, for the most part, evolved on a more or less continuous basis over the past six years. This is particularly true for the METAR/R85 analysis, but a number of changes have also been made to the RAE/WHL analysis as well. The CAMRAD analyses, on the other hand, are relatively static. Improvements to CAMRAD/JA are to be found in the CAMRAD II software rather than in CAMRAD/JA. The authors believe, however, that the conclusions in Section 7 are generally valid today, as are the recommendations of Section 8.

# 2 ANALYTICAL MODELS

Two types of analytical models were used in the studies reported here: lifting-line models and CFD models. The lifting-line models used are, in general, comprehensive analyses that iteratively obtain a complete solution for the equations describing the rotor and the flight vehicle. The solution includes the effects of blade aerodynamics, the rotor wake, and the blade motions and elastic deformations.

The CFD methods used here compute the blade aerodynamic loads using full potential or small-disturbance methods and are more adaptable than the lifting-line methods that must use tabulated aerodynamic data to determine the loads. This adaptability, however, is compromised to a degree by the absence of a boundary-layer model that can properly represent viscous effects. The CFD computation includes the influence of the blade's own near wake, that is, part of the self-induced flows, but does not compute the flow induced by the remaining part of the wake, by the wakes of the other blades, or by the blade motions. For an accurate calculation, therefore, the CFD methods must be coupled to a lifting-line computation to account for effects outside their computational domain.

This section first discusses the lifting-line methods used and, following this discussion, describes the CFD models.

## 2.1 Lifting-Line Models

The lifting-line models used in the present correlation study are briefly described here. Each of these models iteratively obtains a steady-state solution for the entire rotor that accounts for the blade aerodynamics, the rotor wake, and the blade motions and elastic deformations.

Sufficient detail is provided in this section to allow a general idea of each of the lifting-line model's structure, assumptions, and limits of applicability. A detailed discussion of these models, however, is beyond the scope of this report and the cited references should be examined.

### 2.1.1 RAE/WHL Analysis

The RAE/WHL lifting-line analysis was developed jointly by the DRA (formerly the RAE) and Westland Helicopters Limited (WHL) and was described briefly in Bousman et al. (1989). However, some changes have been made to the analysis recently and the description of the method is repeated in this section with increased emphasis on the options used for the Puma calculations.

A modal approach is adopted to represent the elasticity of the blades in the analysis. The method as developed by S. P. King at WHL is used, which allows a blade of a very general geometry to be treated. The shear center of the blade consists of a series of straight line segments that can be orientated in any direction; thus sweep and precone can be introduced anywhere along the blade. Secondary load paths, consisting of linear and rotational springs to earth, can be attached directly to the blade or may be positioned at the end of a weightless arm. A linear spring remote from the blade is normally used to model the control system of the rotor with the geometry of the arm the same as the aircraft pitch horn. The root end of the blade can be built-in or have up to three mutually perpendicular hinges, with or without restraint. The modes are normally calculated with steady loads applied, representing the mean

blade lift and drag, so that the displacement of the modes becomes a small perturbation about the steady state position. The calculated modes are fully coupled in flap, lag and torsion, and a maximum of eight are normally used in a calculation of the rotor performance. A method for calculating the modes of a bearingless rotor system also exists.

The forced response equation is derived to a consistent order of accuracy throughout and is fully compatible with the blade modes. The equation is complicated and is split into five main forcing terms: the aerodynamic forcing, the Coriolis force, the cyclic inertia force, the nonlinear stiffness forcing, and the cyclic stiffening force. The aerodynamic, Coriolis and cyclic inertia forcing are always included in a calculation but the nonlinear stiffness and the cyclic stiffening terms are optional.

The four contributions to the forced response equation arising from the blade dynamics are fairly easy to calculate as they are composed of functions of the pitch angle and its derivatives, and the modal displacements, slopes and curvatures. The Coriolis force is an inplane force due to the blade flapping while the cyclic inertia arises from the azimuthal variation of the blade pitch. The cyclic stiffening is due also to the pitch variation and is a series of terms to account for the difference between the local blade pitch and the collective pitch at which the modes are calculated. The nonlinear terms are a collection of expressions which cannot be included conveniently in any other group. Most calculations made using the analysis omit the cyclic stiffening and nonlinear stiffness terms as they are of second order and should not be important. However, some more recent calculations have shown that the inclusion of the torsion mode terms in the expressions improved the correlation of the predicted torsion moments with test data. The calculations made for the Puma helicopter therefore include the torsion mode forcing in the cyclic stiffening and nonlinear stiffness integrals.

The aerodynamic forcing is much more difficult to calculate than the contributions from the blade dynamics. The features that must be accounted for include the effect of a swept tip, the unsteady aerodynamics, the rotor wake, the fuselage flow field, and the variation of the airfoil section along the span of the blade.

The effect of a swept tip and radial flow on the aerodynamics of a rotor blade is one of the more recent improvements to the analysis since both were neglected in the original model. Blade sweep is accounted for by resolving the velocities through the local quarter chord sweep into tangential and normal components. The angle of attack and lift curve slope are factored according to the usual sweep rules and then the calculated lift, drag and pitching moment coefficients factored similarly. Radial flow effects are calculated in a similar fashion but for a straight blade. The accounting for the blade sweep had a large effect on the calculated loads for the Puma but the inclusion of radial flow had only a small influence on the loads calculated for a standard Puma blade.

The unsteady aerodynamic effects are modeled by Wagner functions for attached flow and there are two representations of dynamic stall. The first method uses a time delay model (Beddoes, 1975) which assumes that there are two distinct time constants which determine when the lift and pitching moment coefficients diverge once the airfoil exceeds the static angle for maximum lift. The second dynamic stall model uses a leading-edge velocity criterion (Beddoes, 1977), but is only applicable at low Mach number. A new unsteady aerodynamic model has been developed by Leishman and Beddoes (1986), and is to be incorporated into the analysis when testing is complete. The calculations presented in this report use the time delay model for dynamic stall throughout.

The rotor induced velocity can be calculated by one of five methods: uniform downwash based on momentum theory, a Glauert distribution, the vortex ring model, the vortex ring model with an interactive near wake, and a spiral vortex model made up of curved elements. The development of the various methods and the effect on the calculated blade stresses are described in Young (1982). All the calculations for Task 1 of the workshop were made using the vortex ring model with the interactive near wake as this option represents the best compromise between accuracy and computer efficiency.

The original vortex ring model was developed by WHL over twenty years ago (Cook, 1970). Two half vortex rings originate from the root and tip of the reference blade, and a series of complete vortex rings form the wake from the other blades of the rotor. The strength of the rings takes a prescribed value related to the rotor thrust and geometry. The center of each ring was initially placed on a line extending downstream and was uniformly spaced in the vertical direction according to the mean flow through the rotor disk. The model has undergone some extensive changes since its inception. The rings are no longer positioned on a straight line downstream but are moved so that the intersection in plan view in the rotor disk and the tangency to the blade corresponds to a spiral wake. The vertical spacing of the rings is no longer uniform and the rings are positioned as though they had passed through a representative induced velocity field, a free-stream velocity component and, optionally, a fuselage flow field. No physical core size is given to the vortices but they are not allowed to approach the blade closer than 5% of the blade chord which effectively limits the maximum induced velocity.

The main drawback to the original vortex ring wake model was that the loading on the advancing side of the disk was too negative at moderate to high advance ratio and the interactive near wake was developed to improve the correlation with experiment. The interactive near wake replaced the two half vortex rings with a series of half vortex rings whose strength is related to the radial load distribution on the blade. The strength does not vary along the length of the half ring; thus the history of the loading is neglected but the influence of the rings diminishes very rapidly and only the portion of the ring very near the blade has any measurable effect. Relating the strength of the ring to the loading on the blade means that the tip vortex changes sign when the loading becomes negative and the predictions at high advance ratio are improved greatly.

The fuselage flow field can be calculated internally in the analysis using a single source or externally to the program using a panel method originally developed for fixed wing aircraft. The panel method is preferred as a better representation of the fuselage shape is possible. The inclusion of the fuselage induced velocity distribution can have a considerable influence on the predicted blade loads and vibrational characteristics of the rotor and are included whenever possible. All the calculation made for Task 1 include the fuselage flow field calculated by the panel method.

Modern rotor designs generally use a variation of the blade airfoil section in the spanwise sense. A thin section may be employed at the tip, for example, to reduce noise and alleviate adverse compressibility effects. The analysis can use a maximum of eight airfoil sections. However, multiple airfoils are not employed for the Puma calculations. The airfoil section does change on the Puma blade because the increased chord in the swept tip region reduces the thickness/chord ratio but the section characteristics are not known and the same airfoil is used over the complete span.

The forced response equation was solved using the Z-transform in the original analysis. The Z-transform is similar to a Laplace transform but uses sampled rather than continuous data. Two hold

circuits can be used: the zero-order hold which assumes that the data do not change between samples and the first-order hold which assumes that the forcing changes linearly. The calculations made for the Puma, however, replaced the Z-transform with a modified fourth-order Runge-Kutta technique which proved more stable for the swept-tip blade.

The rotor was trimmed by matching the measured first harmonic flapping angle and assuming the thrust was equal to the weight of the aircraft. All the calculations were made using an azimuth increment of 5°.

### 2.1.2 CAMRAD Family

CAMRAD (Comprehensive Analytical Model of Rotorcraft Aerodynamics and Dynamics) and the more recent Johnson Aeronautics version, CAMRAD/JA, are comprehensive codes that allow the solution of a number of problems for a wide range of rotorcraft configurations in a single, consistent analysis (Johnson, 1981a; Johnson, 1981b; Johnson, 1986; Johnson, 1988).

The first step in running the CAMRAD family of codes is to obtain a trim solution in which the control positions and the aircraft orientation are determined for the specified operating condition. The periodic blade motion is calculated and then the rotor performance, aerodynamic and structural loads, and rotor noise may be calculated.

The structural model of the rotor is based on engineering beam theory for rotating wings with large pitch and pretwist. A single load path is assumed and the blade is considered to have a straight, undeformed elastic axis—a recognized deficiency in modeling a swept tip. The blade motion is described by rotating flap/lag and nonrotating uncoupled torsion free vibration modes, equivalent to a Galerkin analysis. The baseline model for the Puma correlation studies reported here used six bending modes with a pinned boundary condition together with two torsion modes, one for a rigid blade with control system flexibility and the other for a rigid controls system with spanwise torsional flexibility. The baseline model was used for all calculations except Task 3, Cases 1–9. For Cases 1–8 of Task 3 the blade dynamics were represented by a single mode about the flap hinge and with prescribed torsional motion, but no flexibility. For Case 9 six bending modes were included with a pinned boundary condition and, again, prescribed torsional motion. Case 10 incorporated the baseline model. Structural moments were calculated using a modal summation procedure for all the results shown here.

The rotor aerodynamic model is based on lifting-line theory, and uses steady two-dimensional airfoil characteristics provided in tables of section lift, drag, and pitching moment, defined over a grid of angle-of-attack and Mach number values. These tables are derived either from analytical expressions or from experimental data in the form of tables used in the C81 rotorcraft analysis program. The NACA 0012 tabulated values of Davis (1974) have been used here, with the exception of Task 3 which used formulas based on RAE wind tunnel data.

The rotor aerodynamic model for the Puma includes static stall, a yawed flow correction, and unsteady aerodynamic forces derived from thin airfoil theory, these forces being set to zero for stalled flow. For the swept tip, allowance is made for offsets of both the aerodynamic center and the center of gravity from the straight, undeformed elastic axis. However, the airfoil section is effectively sheared at discrete radial stations, and the vortices are considered to originate at the elastic axis.

There are three levels of wake model in CAMRAD and CAMRAD/JA: uniform inflow, nonuniform inflow with a prescribed wake geometry, and nonuniform inflow with a free wake geometry (for forward flight only). Uniform inflow here refers to an empirical model based on momentum theory that includes, for forward flight, a linear variation of the inflow over the rotor disk. The usual procedure is to begin by calculating the trimmed uniform inflow solution and then, as required, calculate the trimmed prescribed wake solution, followed by the trimmed free wake solution. Finite-length, straight-line vortex elements are used for the tip vortices, with an azimuth increment of 15°. The inboard wake is divided into near and far wake regions with the same azimuth increment. In the near wake, which extends azimuthally for 60° directly behind the blade, the inboard vorticity is represented in CAMRAD by 15 panels distributed along the blade and in CAMRAD/JA by 18 panels, with a greater concentration toward the tip, where the greater loading variations occur. The multiple panels in the near wake are replaced by a single panel in the far wake. The far wake regions extend for three revolutions. By collapsing all the wake panels to finite-strength line segments, a lattice model of the rotor wake is produced. The tip vortex is represented by a uniform core radius (nondimensionalized by rotor radius) of 0.035 for interactions outboard of 88% span. The core size is increased to 0.100 for points inboard of 76% of span to reduce the magnitude of these interactions. The core size transitions linearly between these two span stations. In addition to an empirically chosen spanwise varying core size, the modeling of blade vortex interaction is improved in CAMRAD/JA by using second-order lifting-line theory (three-quarter-chord collocation point).

Modeling of the far wake distribution of vorticity in CAMRAD/JA was improved for cases where negative loading occurs along the tip of the blade in high speed flight. In these cases the circulation distribution results in a positive inboard maximum and a negative outboard maximum, with the positive peak being the greater of the two. The CAMRAD model calculates a tip vortex based on the maximum circulation, resulting in the wrong sign and magnitude. The dual peak model in CAMRAD/JA calculates a weak tip vortex from the negatively loaded outboard section, and a stronger trailed line vortex from the inboard positively loaded section.

### 2.1.3 METAR/R85 Analysis

R85 is a general purpose rotor code (Allongue and Krysinski, 1990; Arnaud et al., 1991) which can be used as a submodel of a comprehensive helicopter model or for the simulation of an isolated rotor. In the present case, the Puma main rotor was modeled as an isolated rotor.

The blades are regarded as flexible beams in the sense of classical engineering beam theory, with only three degrees of freedom: flapwise bending, chordwise bending, and torsion. Due to convergence problems, the torsional deflections were not taken into account for the calculations here, but the torsion loads were calculated by integration of the inertial and aerodynamic forces.

The beam is approximated by a series of rigid linear segments, and elastic deflections are simulated by finite rotations in pitch, flap and chord at segment junctions with concentrated stiffness replacing the actual distributed stiffness (Mykelstad's model). For the calculation of kinetic energy and inertial forces, each segment is regarded as a rigid body with its own mass, center of gravity, and full inertial tensor. Unlike previous analyses, R85 rejects the linearized theory of modal response and solves the blade motion problem using the exact Lagrange equations. The usual set of orthogonal blade modes is thus replaced by a series of arbitrary generalized deflection functions compatible with hub kinematics. The spanwise integration of kinetic energy and elastic energy or, more precisely, their derivatives with respect

to generalized coordinates, is the computational price paid for the elimination of improper assumptions inherent in modal theory such as the linearization of deflections and overlooking of the azimuthal pitch variation.

To maximize the computational efficiency, it is necessary to reduce the number of generalized deflection functions as far as possible. It has been found that choosing modal deflections as generalized deflections makes it possible to obtain a good accuracy with a very limited number of degrees of freedom. Therefore, the Puma calculations were performed using seven coupled rotating blade modes as generalized deflections:

- four flapwise modes
- three chordwise modes

The accuracy and convergence of the solution is assessed by comparing two independent calculations of the blade loads:

- integration of aerodynamic and inertial forces
- elastic forces derived from beam curvature

The flexible blade calculation is initialized by means of a rigid blade calculation. The aerodynamic model is common to the rigid and flexible calculations and is based on lifting-line theory, the blade being represented by its quarter-chord line including tip sweep and anhedral. The spanwise distribution of circulation is approximated by a step function with a trailed vortex emitted at each junction of two segments, and the timewise variation of circulation is considered as a step function with a shed vortex released at evenly distributed azimuthal stations. The wake is thus represented by a lattice composed of quadrilateral cells.

The circulation over a cell is constant and is equal to that of the blade at the station and time of emission (Kelvin's theorem of vorticity conservation). The induced velocity is integrated in closed form using the Biot-Savart law for incompressible flow over linear segments. For high-speed level flight, the wake can be truncated after three revolutions without appreciable error.

The wake geometry may be prescribed by various models according to the case considered. The model of Kocurek and Tangler (1977) is used in hover. In forward flight a simplified version of the model of Egolf and Landgrebe (1984) or a classical, undistorted wake model is used. The latter model, which is a submodel of R85, is called METAR and has proved sufficient for high-speed cruise conditions.

The airfoil characteristics were obtained from tabulated airfoil polars derived from wind tunnel tests (Davis, 1974). Compressibility effects are therefore included and power, drag, and pitching moment outputs can be derived.

The Mach number, angle of attack, and aerodynamic chord are computed in the local reference frame attached to the quarter-chord line, which may differ from the pitch axis because of sweep or anhedral.

Various corrections may be applied to the airfoil data: Reynolds number correction on the drag coefficient, radial flow correction on the maximum lift coefficient and the radial skin friction, transonic extrapolation if the tables do not extend to the required Mach number, and linear unsteady effects on the pitching moment $C_m$. The main options and data used are the following:

- 25 spanwise stations
- 36 time steps per turn (10° azimuthal increment)
- 108 wake steps (3 turns)
- prescribed distorted wake
- NACA 0012 tables
- Reynolds number and radial flow corrections
- Unsteady $C_m$ including pitch, plunge, and fore/aft motions
- near wake domain: $0° \leq \psi_{age} \leq 50°$

Eight harmonics are calculated for the flexible modes. Rigid blade calculations (Task 3) are performed with five harmonics in flap, no harmonics in lead/lag (that is, static lag only), and one harmonic in pitch.

To minimize the computational effort, the METAR inflow is calculated in the rigid blade step, and induced velocities are held constant during the following flexible blade calculation step.

### 2.1.4 Comparison of Lifting-Line Methods

The four lifting-line methods have some common features but also differ from one another in several important respects.

The RAE/WHL analysis and the two CAMRAD analyses use modes in the solution of the forced response equation. The RAE/WHL input modes are fully coupled in flap, lag and torsion whereas CAMRAD uses input modes that are coupled in flap and lag, but the torsion modes are uncoupled. Although CAMRAD uses uncoupled input modes the degrees of freedom are fully coupled during the solution process. The METAR/R85 analysis does not use modes but solves the equations of motion directly, although the torsional motion is neglected because of convergence problems.

CAMRAD, CAMRAD/JA, and the METAR/R85 analyses have a similar wake model that employs straight line vortex elements to form a lattice. The CAMRAD analyses can use a free wake model which is especially useful at low speed but the METAR/R85 wake uses a prescribed geometry. The RAE/WHL method, however, uses a combination of half and complete vortex rings which are positioned as though they had passed through a representative velocity field. The strength of the half vortex rings, which originate from the reference blade, is related to the loading on the blade but the complete vortex rings take a prescribed strength.

All the analyses model unsteady aerodynamic effects for attached flow. CAMRAD and CAMRAD/JA use a method derived from thin airfoil theory, METAR/R85 treats the problem as a first-order differential equation, whereas the RAE/WHL method uses Wagner functions. The modeling of dynamic stall differs widely in the three methods but no stall cases were considered for the Puma correlation.

Radial flow effects were included in all the analyses but the representation in the RAE/WHL method was not very refined.

The fuselage flow field is included in the RAE/WHL analysis but not in any of the others. The main effect of the flow field is to produce an upwash around the front of the disk, which tends to keep the vortices trailed from the blades nearer to the tip path plane.

There are substantial differences in the analyses used for the collaborative exercise with the Puma data, and the strengths and merits of each approach will become obvious when making the comparisons. However, the development of rotor loads prediction methods is an evolutionary process and the results presented in this report are indicative of the state of the analyses at the time of the 1990 workshop. Further enhancements have been made to these analyses in the light of ongoing verification against flight test and model test data.

## 2.2 CFD Models

The CFD models used in the present correlation study are briefly described here. These models solve for the rotor flow field using either small-disturbance or full-potential methods and require as input the partial angle-of-attack angles computed by the lifting line methods.

The descriptions in this section provide a general idea of how each of these methods works. However, it is necessary to consult the cited references if additional information is required for any of these analyses.

### 2.2.1 FPR Code

The Full-Potential Rotor code (FPR) solves the unsteady, three-dimensional, full-potential equation in strong conservation form. The code employs a finite-difference scheme with first-order backward differencing in time and second-order central differencing in space. The temporal density derivative is locally linearized about the old time levels in a manner that preserves the conservative form. Stability in regions of supersonic flow is obtained by biasing the density calculation in the upwind direction.

A spanwise series of parallel O-grids are used for the basic grid system. Rotor flows are computed by assigning an appropriate rotational coordinate velocity to each grid point. As a result, the rotor and the attached finite-difference grid move through still air. On the surface of the blade, a transpiration velocity condition is used to simulate angle-of-attack conditions (including wake-induced inflow angles). At the outer radial boundary of the O-grid, a nonreflection boundary condition is used to prevent the accumulation of numerical disturbances.

Typical grid sizes for the Puma flight-test calculations are 80 points in the chordwise direction, 25 in the spanwise direction, and 25 in the direction normal to the rotor surface. Figure 1 shows a top view of the FPR grid for the swept-tip Puma blade.

The finite-difference grid extends approximately seven chords inward from the rotor tip and two chords outward from the tip in the spanwise direction. The outer radial boundary of the O-grid is located five chords from the surface of the blade. Constant time steps were used corresponding to $0.25^\circ$ of rotor

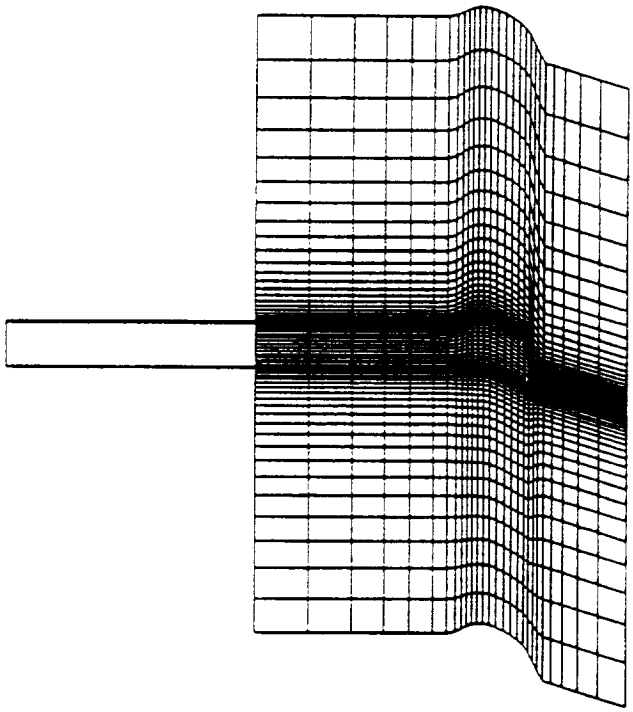

Figure 1. Top view of the FPR grid for the swept-tip Puma blade calculations.

azimuthal angle per time step. Unsteady calculations for a complete 360° of rotor azimuth required approximately 1200 CPU seconds on a CRAY YMP computer system. A more complete description of the FPR code can found in (Strawn and Caradonna, 1987; Bridgeman et al., 1982). Significant improvements to the original differencing algorithm in FPR are detailed in (Bridgeman et al., 1989).

### 2.2.2 TSP Code

The transonic small perturbation (TSP) code in use at the RAE solves an equation for quasi-steady three-dimensional flow around the tip region of a helicopter rotor blade at an arbitrary, but specified, azimuth angle. Separate calculations are performed for each required azimuth station value.

The equation solved by the code is given by

$$\frac{\partial^2\phi}{\partial x^2}\left[1-{M_T}^2{u_1}^2-(\gamma+1){M_T}^2u_1\frac{\partial\phi}{\partial x}-(\gamma-1){M_T}^2u_2\frac{\partial\phi}{\partial y}\right]$$
$$+\frac{\partial^2\phi}{\partial y^2}\left[1-{M_T}^2{u_2}^2-(\gamma-1){M_T}^2u_1\frac{\partial\phi}{\partial x}-(\gamma+1){M_T}^2u_2\frac{\partial\phi}{\partial y}\right]$$
$$+\frac{\partial^2\phi}{\partial z^2}\left[1-(\gamma-1){M_T}^2\left(u_1\frac{\partial\phi}{\partial x}+u_2\frac{\partial\phi}{\partial y}\right)\right]$$
$$-2\frac{\partial^2\phi}{\partial x\partial y}{M_T}^2\left[u_1u_2+u_1\frac{\partial\phi}{\partial y}+u_2\frac{\partial\phi}{\partial x}\right]-2{M_T}^2\frac{\partial\phi}{\partial z}\left(u_1\frac{\partial^2\phi}{\partial x\partial z}+u_2\frac{\partial^2\phi}{\partial y\partial z}\right)$$
$$+\frac{{M_T}^2}{A}\left(u_1+\mu\sin\psi\right)\frac{\partial\phi}{\partial y}-\frac{{M_T}^2}{A}\left(u_2+\mu\cos\psi\right)\frac{\partial\phi}{\partial x}=0 \qquad (2\text{-}1)$$

where $x$, $y$, and $z$ are coordinates in the rotating blade in the chordwise, spanwise, and vertical directions, respectively; $u_1$, $u_2$ are the local velocities in the chordwise and spanwise directions; $M_T$ is the tip Mach number due to rotation, $\mu$ is the advance ratio; $\psi$ is the azimuth angle (with $\psi = 0$ at the back of the disk); and $A$ is the aspect ratio $(R/c)$.

The differential equation is subject to the surface boundary condition

$$\frac{\partial\phi}{\partial z}=\left(u_1+\frac{\partial\phi}{\partial x}\right)\frac{\partial z_s}{\partial x}+\left(u_2+\frac{\partial\phi}{\partial y}\right)\frac{\partial z_s}{\partial y} \qquad (2\text{-}2)$$

The grid on which the equation is solved is obtained by an algebraic transformation which maps the semi-infinite space around the outer section of the rotor blade onto a rectangular box $-1 \le X \le 1$, $0 \le Y \le 1$, $-1 \le Z \le 1$ with the rotor blade lying in the $Z = 0$ plane and $Y = 0$ being the inboard station of the rotor tip. In the physical space, the gridlines are swept with the leading and trailing edges of the tip, and then swept off the tip parallel to each other, asymptotically parallel with the inboard blade quarter-chord line. For each coordinate direction in turn, the gridlines are clustered around the blade tip, the blade leading and trailing edges, and the blade surface respectively. A total of 112,545 gridpoints are used: 61 in the chordwise direction, 45 radially and 41 vertically. On the blade itself, there are typically 33 points along the chord and 35 radially on the swept tip.

The differential equation is discretised with the streamwise components of the derivatives being switched from central to backward differences (in the sense of the local flow direction) in the supersonic regions.

The wake is assumed to be a plane vortex sheet skewed in the direction of the resultant free-stream flow. Jump conditions on the velocity potential are imposed across the vortex sheet. For the far-field boundary conditions, the pressure is assumed to have recovered to the appropriate free-stream value.

The resulting difference equations are solved by an iterative relaxation technique, with sweeps in each of the coordinate directions at each iteration step. The calculation starts on a coarse grid with every alternate gridpoint removed, and uses an initial solution which is zero everywhere. When convergence is obtained on the coarse grid, the solution is interpolated to the fine grid and further iterations performed.

The pressure coefficient is calculated from the potential values by the equation

$$C_P = \frac{-2}{\left({u_1}^2 + {u_2}^2\right)} \left( u_1 \frac{\partial \phi}{\partial x} + u_2 \frac{\partial \phi}{\partial y} \right)$$
$$- \frac{1}{\left({u_1}^2 + {u_2}^2\right)} \left[ \left( \frac{\partial \phi}{\partial x} \right)^2 + \left( \frac{\partial \phi}{\partial y} \right)^2 - {M_T}^2 \left( u_1 \frac{\partial \phi}{\partial x} + u_2 \frac{\partial \phi}{\partial y} \right)^2 \right] \qquad (2\text{-}3)$$

Further details of the code and early comparison cases performed using it can be found in Grant (1979) and in the report of the 1988 Workshop (Jones et al., 1990). Refinements to the code since the 1988 Workshop include the facility to calculate consecutively a series of different azimuth cases, using the solution from the previous case as a starting value in the iterative process. This reduces the number of iterations needed, especially for the coarse-grid calculation.

# 3 MODAL CALCULATIONS IN A VACUUM

The equation of motion for a rotor blade can be solved in several ways but there are two widely used methods. The first solves the equation by direct integration along the span and around the azimuth. The second method calculates the natural modes of the blade as an intermediate stage and then uses the modes in solving the simpler forced response equation. The R85 analysis employs the first method, while CAMRAD, CAMRAD/JA and the RAE/WHL analysis use modes in one form or another.

The RAE/WHL modes analysis calculates fully coupled modes, i.e, modes that can have flap, lag and torsional deflections. The modes are orthogonal to one another, an attribute that reduces greatly the complexity of the forced response equation. CAMRAD and CAMRAD/JA, which have identical models of the rotor dynamics, both use three different types of modes: coupled flap/lag modes, an uncoupled elastic control system rigid blade torsion mode, and uncoupled rigid control system elastic torsion modes. These modes are the degrees of freedom used by the trim and eigenanalysis. The modal frequencies that are computed by the eigenanalysis are coupled flap/lag/torsion modes. The R85 analysis, which uses direct integration of the blade equations, does not need blade modes and uses arbitrary shape functions to represent the blade elastic displacements. However experience with the method has shown that convergence is quicker when the shape functions correspond to the natural mode shapes although the modal frequencies play no part in the calculation. Modes are used therefore in all the analyses to some extent and this section compares the modal frequencies and mode shapes calculated by the three methods.

The modal calculations shown here are for the swept-tip blade of Tasks 1 and 2, not the rectangular blade of Task 3. The comparison is made in three parts. The first part compares the calculated frequencies of CAMRAD, the RAE/WHL method, and R85. The second part is a comparison of the tip deflections calculated by the RAE/WHL and R85 analyses, and the third part is a comparison of the modal frequencies calculated by CAMRAD and the RAE/WHL method over a range of rotor speeds.

The frequencies calculated by the CAMRAD, RAE/WHL, and R85 analyses are shown in the second, third, and seventh columns of table 1.

The frequencies calculated by the three methods generally show good agreement, particularly for the flapping modes. The R85 method computes a 1st lag frequency that is about twice that computed

Table 1. Predicted modal frequencies and shapes

| Mode | CAMRAD | RAE/WHL | | | | METAR/R85 | | | |
|---|---|---|---|---|---|---|---|---|---|
| | $\omega$ | $\omega$ | Tip deflection | | | $\omega$ | Tip deflection | | |
| | per/rev | per/rev | flap | lag | torsion | per rev | flap | lag | torsion |
| 1st lag | 0.2315 | 0.2372 | −0.0000 | 1.0000 | −0.0000 | 0.4406 | −0.0097 | 1.0000 | −0.0001 |
| 1st flap | 1.0227 | 1.0277 | 1.0000 | −0.0001 | −0.0000 | 1.0278 | 1.0000 | 0.0130 | −0.0000 |
| 2nd flap | 2.8850 | 2.8974 | 1.0000 | −0.0300 | −0.0668 | 2.8899 | 1.0000 | −0.0377 | −0.0292 |
| 2nd lag | 4.7372 | 4.7405 | 0.1620 | 1.0000 | −0.4988 | 4.8287 | 0.1780 | 1.0000 | −0.1133 |
| 1st torsion | 5.1764 | 5.0261 | −0.0301 | 0.0170 | 1.0000 | 6.5090 | 0.0250 | −0.0020 | 1.0000 |
| 3rd flap | 5.7354 | 5.7478 | 0.5346 | −0.0654 | 1.0000 | 5.6201 | 1.0000 | −0.1526 | −1.4290 |

by the other methods and this is caused by a restraint around the lag hinge that was added to introduce curvature near the lag damper attachment. In addition, the 1st torsion mode computed by R85 is about 30% higher than the other methods and this is a result of assuming the control system is rigid.

The tip displacements calculated by the RAE/WHL and R85 analyses are compared in columns 4 to 6 and 8 to 10 of table 1. The R85 calculations were made for a rotor speed of 265 rpm compared to 259.6 rpm for the RAE/WHL calculation. The first flap mode show no lag displacement in the RAE/WHL calculation and about 1% for the R85 analysis. Similar results are observed for the first lag mode. The second flap mode, as calculated with the RAE/WHL method, shows about 3% lag tip deflection which is quite close to that computed by R85. The torsional component, however, $-0.07$, is considerably larger than the $-0.03$ computed by R85. Similarly, for the second lag mode, flap deflections of 0.16 and 0.18 show good agreement for the RAE/WHL and R85 methods, but the computed torsional displacement is substantially greater for the RAE/WHL method, $-0.50$ compared to $-0.11$ for R85 and this is presumably a consequence of control system flexibility that is present in the RAE/WHL analysis, but not the R85 calculation. Both methods show a first torsion mode with little flap or lag content, although, as mentioned above, the R85 frequency is 30% greater. The highest frequency mode compared, the third flap mode, is highly coupled in flap, lag, and torsion and the two methods are quite comparable. The RAE/WHL and R85 modal calculation methods therefore show consistency with each other when the differences in the models are taken into account.

Modal frequencies computed by the RAE/WHL and CAMRAD analyses are compared in figure 2. There is very close agreement between the two analyses for these modal calculations and this agreement is seen at all rotor speeds.

The representation of the dynamics of the rotor blade differs considerably in each of the methods examined—CAMRAD, R85 and RAE/WHL—but the resulting frequencies and mode shapes are consistent and any differences can be easily explained.

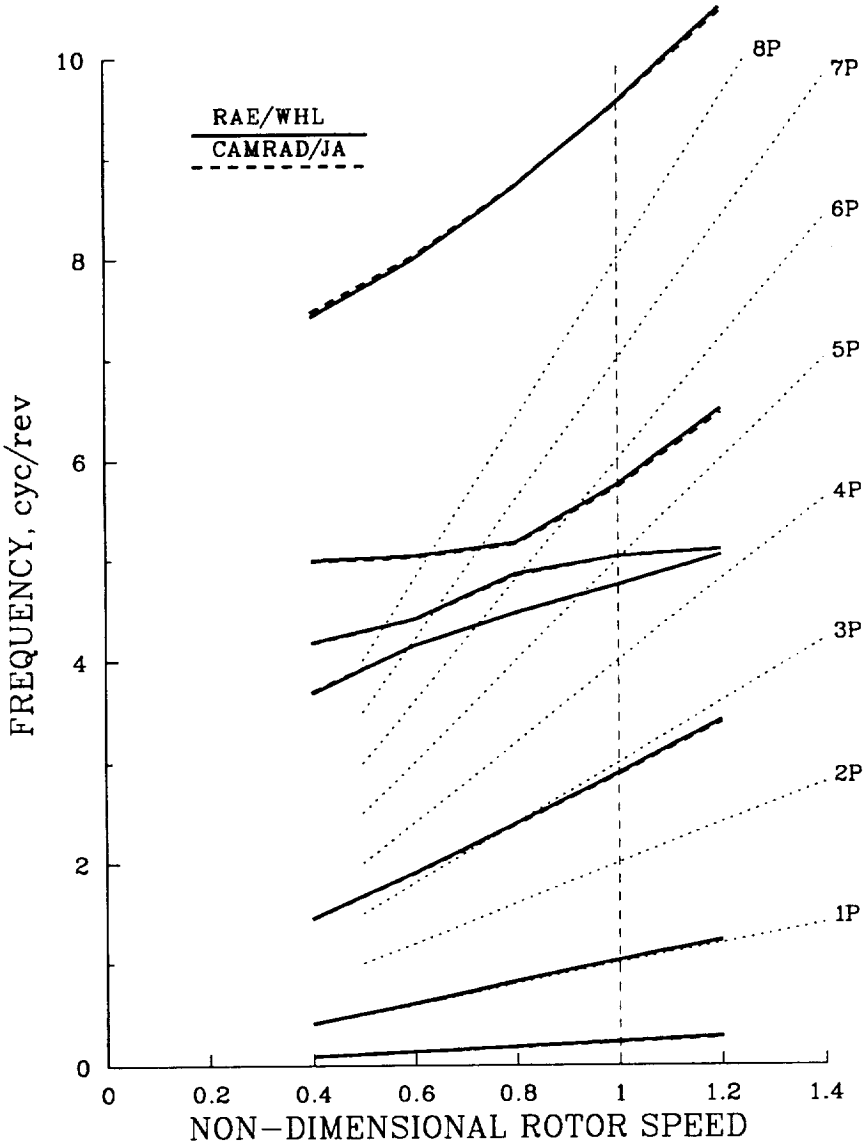


Figure 2. Comparison of modal frequencies calculated by the RAE/WHL and CAMRAD/JA analyses.

# 4 ANALYTICAL MODELING OF LIFTING-LINE METHODS (TASK 3)

## 4.1 Introduction

The third task defined for the collaborative effort was to compare the predictions of the four lifting-line methods as modeling sophistication was increased from a simple, baseline model to a full, "all up" model. Ten levels of sophistication or modeling complexity were specified as shown in table 2. At the simplest level the analytical models used a uniform wake without sine or cosine variation in the inflow, linear aerodynamics, no unsteady aerodynamics or radial flow, and the rotor dynamics were represented by a rigid blade with a single flapping hinge. At the most complex level the analytical models incorporated all of the features used in the Task 1 and 2 calculations except that a rectangular blade planform was used instead of the swept-tip planform.

An isolated rotor trim condition was selected to simplify the comparisons as much as possible. For these calculations the trim was specified as $\mu = 0.381$, $C_T/\sigma = 0.0799$, $M_{90} = 0.863$, $\alpha_s = -6.8°$, $\beta_{1c} = 0.392°$, and $\beta_{1s} = -0.074°$. This trim condition was arbitrarily selected to match the Case 3 trim from the first collaboration (Bousman et al., 1989), but there are no available flight data for this case for a Puma with a rectangular blade. Note that by selecting an isolated rotor trim condition external fuselage forces and moments such as caused by fuselage aerodynamic loads or tail rotor forces are not included in the trim calculation.

Case 1, or the baseline case, was the simplest condition examined. The blade aerodynamic properties were defined:

$$\frac{dc_l}{d\alpha} = \frac{5.7}{\sqrt{1 - M^2}} \tag{4-1}$$

$$c_{d_0} = 0.01 \tag{4-2}$$

$$c_{m_0} = 0.0 \tag{4-3}$$

Table 2. Task 3 modeling complexity

| Case | Root Cutout | Wake | Airfoil Tables | Unsteady Aero | Radial Flow | Bending Modes | Torsion Modes |
|---|---|---|---|---|---|---|---|
| 1 | $0.228R$ | Uniform | Constant | No | No | No | No |
| 2 | $0.40R$ | Uniform | Constant | No | No | No | No |
| 3 | $0.228R$ | Prescribed | Constant | No | No | No | No |
| 4 | $0.40R$ | Prescribed | Constant | No | No | No | No |
| 5 | $0.228R$ | Prescribed | NACA 0012 | No | No | No | No |
| 6 | $0.40R$ | Prescribed | NACA 0012 | No | No | No | No |
| 7 | $0.228R$ | Prescribed | NACA 0012 | Yes | No | No | No |
| 8 | $0.228R$ | Prescribed | NACA 0012 | Yes | Yes | No | No |
| 9 | $0.228R$ | Prescribed | NACA 0012 | Yes | Yes | Yes | No |
| 10 | $0.228R$ | Prescribed | NACA 0012 | Yes | Yes | Yes | Yes |

without any unsteady aerodynamics in the calculation or any accounting for radial flow or sweep effects. The blade was assumed to be rigid with a flap hinge located at $0.0386R$. The first and second moments of inertia were obtained from the blade properties in Appendix A. Case 2 was identical to Case 1 except the root cutout was changed from $0.228R$ to $0.40R$ to eliminate all reverse flow effects.

Each of the analytical methods was able to adapt to the Case 1 and 2 model requirements with the exception of the METAR/R85 analysis which was required to retain a coincident lag hinge for all of the rigid blade calculations (Cases 1–8).

Case 3 differs from Case 1 in that a prescribed wake is used instead of the uniform wake. In all other respects the modeling is unchanged. The prescribed wakes used in the CAMRAD, CAMRAD/JA, and METAR/R85 analyses are similar in that they are based on a vortex-lattice model. The RAE/WHL analysis is quite different, however, in that the wake is represented by a series of partial and full vortex rings. Case 4 is the same as Case 3 except for the extension of the root cutout to $0.40R$.

The modeling change that distinguishes Case 5 from Case 3 is that the linear aerodynamics of Case 3 are replaced with the nonlinear equations described in Section 4.2. Case 6 is the same as Case 5 except for the $0.40R$ root cutout.

Case 7 differs from Case 5 in that unsteady aerodynamic terms are incorporated in the analysis. Case 8 differs from Case 7 in that the radial or yawed flow terms are used in the analyses.

Case 9 adds blade bending flexibility to the analyses although the torsion degree of freedom is not included. The number of modes used, for those analyses that use bending modes, was a choice of the analyst. Case 10 adds the torsion degree of freedom to the computation, with the exception of METAR/R85 which could not achieve convergence for this case.

The comparisons made under Task 3 provide an improved understanding of aspects of the lifting-line models that are important for airloads prediction. Note, however, that the sequence of modeling steps used here does affect the conclusions obtained as the problem is nonlinear. The Case 10 results would, of course, be identical regardless of the order of the steps, but some of the intermediate conclusions made here could be modified if a different order was used.

The airfoil characteristics used for this task are discussed in Section 4.2. The comparison of the methods is discussed in Section 4.3 and this is done in two parts: a comparison of the unspecified trim parameters and power required in Section 4.3.1 and the blade airloads and motions in Section 4.3.2. Summary comments are provided in Section 4.4.

## 4.2 Airfoil Characteristics

The blade steady lift, drag, and pitching moment characteristics are represented by linear functions for Cases 1–4. For Cases 5–10 nonlinear aerodynamics are incorporated in the four models. The nonlinear aerodynamics in the two CAMRAD analyses and METAR/R85 are normally represented by look-up tables where the lift, drag, and pitching moment are stored as functions of angle of attack and Mach number. The implementation in the RAE/WHL analysis is different in that the aerodynamics are based on empirical functions below stall and equations derived from oscillating airfoil data above stall.

To reduce confounding effects of using different nonlinear aerodynamic section properties a set of modified airfoil tables was developed for the CAMRAD analyses so that the blade aerodynamic properties would match the RAE/WHL functions below stall. Above stall it was necessary to blend these special tables into the C81 NACA 0012 deck (Davis, 1974). Similarly, the METAR/R85 code was modified directly to include the RAE/WHL formulas. Thus, below stall, the nonlinear aerodynamics used by the four methods should obtain identical results. However, above the stall boundary, the RAE/WHL analysis will compute different results from the other methods.

The RAE/WHL empirical equations are described in the paragraphs below and tables are provided that provide both the coefficients of the equations as well as the stall boundary that is associated with the equations. Below stall, the RAE/WHL model for section lift is represented by the equation:

$$C_L = \frac{dC_L(M)}{d\alpha}\alpha \qquad \alpha \leq \alpha_L \tag{4-4}$$

The stall angle boundary and the $dC_L(M)/d\alpha$ values are shown in table 3 as a function of Mach number. For negative angles of attack the sign of $\alpha_L$ is reversed, of course.

Table 3. Lift equation stall boundary and coefficient

| Mach number | $dC_l/d\alpha$ | $\alpha_L$ |
|---|---|---|
| 0.30 | 0.110 | 14.3 |
| 0.35 | 0.113 | 13.5 |
| 0.40 | 0.116 | 12.5 |
| 0.45 | 0.119 | 11.2 |
| 0.50 | 0.122 | 10.0 |
| 0.55 | 0.128 | 8.7 |
| 0.60 | 0.134 | 7.5 |
| 0.65 | 0.138 | 5.8 |
| 0.70 | 0.155 | 4.2 |
| 0.75 | 0.170 | 2.8 |
| 0.80 | 0.220 | 1.3 |
| 0.85 | 0.300 | 0.0 |
| 0.90 | 0.380 | 0.0 |
| 0.95 | 0.380 | 0.0 |

The RAE/WHL model for the section drag coefficient is represented by

$$C_D = C_{DO} + K_D\alpha^2 \qquad \alpha \leq \alpha_D \tag{4-5}$$

$$C_D = C_{DO} + K_D\alpha^2 + K_{DD}(\alpha - \alpha_D)^2 \qquad \alpha > \alpha_D \tag{4-6}$$

The $\alpha_D$ boundary and the $K_D$ and $K_{DD}$ coefficients are shown in table 4. The sign of $\alpha_D$ is changed for negative angles of attack.

Table 4. Drag equation boundary angle and coefficients

| Mach number | $C_{D_0}$ | $K_D$ | $K_{DD}$ | $\alpha_D$ |
|---|---|---|---|---|
| 0.30 | 0.0088 | 0.000070 | 0.0019 | 11.50 |
| 0.35 | 0.0088 | 0.000055 | 0.0019 | 9.75 |
| 0.40 | 0.0088 | 0.000040 | 0.0019 | 8.00 |
| 0.45 | 0.0088 | 0.000040 | 0.0019 | 6.90 |
| 0.50 | 0.0088 | 0.000040 | 0.0019 | 5.80 |
| 0.55 | 0.0088 | 0.000040 | 0.00275 | 5.20 |
| 0.60 | 0.0088 | 0.000040 | 0.0036 | 4.70 |
| 0.65 | 0.0088 | 0.000040 | 0.0036 | 3.35 |
| 0.70 | 0.0088 | 0.000040 | 0.0036 | 3.35 |
| 0.75 | 0.0090 | 0.000040 | 0.0040 | 3.35 |
| 0.80 | 0.0125 | 0.006250 | 0.0000 | 3.35 |
| 0.85 | 0.0270 | 0.010000 | 0.0000 | 3.35 |
| 0.90 | 0.0500 | 0.015040 | 0.0000 | 3.35 |
| 0.95 | 0.0500 | 0.015040 | 0.0000 | 3.35 |

The RAE/WHL model for the section pitching moment coefficient is represented by

$$C_M = K_M \alpha \qquad \alpha \leq \alpha_M \tag{4-7}$$

$$C_M = K_M \alpha + K_{MM}(\alpha - \alpha_M)^2 \qquad \alpha > \alpha_M \tag{4-8}$$

This equation applies below the lift stall boundary, $\alpha_L$. The $\alpha_M$ boundary and the $K_M$ and $K_{MM}$ coefficients are shown in table 5. The signs of $\alpha$ and $\alpha_M$ are changed for negative angles of attack.

Table 5. Pitching moment equation boundary angle and coefficients

| Mach number | $K_M$ | $K_{MM}$ | $\alpha_M$ |
|---|---|---|---|
| 0.30 | 0.0003 | 0.00032 | 5.00 |
| 0.35 | 0.0003 | 0.00051 | 5.00 |
| 0.40 | 0.0003 | 0.00070 | 5.00 |
| 0.45 | 0.0003 | 0.00085 | 4.25 |
| 0.50 | 0.0003 | 0.00100 | 3.50 |
| 0.55 | 0.0003 | 0.00105 | 2.75 |
| 0.60 | 0.0003 | 0.00110 | 2.00 |
| 0.65 | 0.0003 | 0.00110 | 1.20 |
| 0.70 | 0.0003 | 0.00110 | 0.70 |
| 0.75 | 0.0000 | −0.00110 | 1.00 |
| 0.80 | −0.0150 | 0.00000 | 0.00 |
| 0.85 | −0.0450 | 0.00000 | 0.00 |
| 0.90 | −0.0450 | 0.00000 | 0.00 |
| 0.95 | −0.0450 | 0.00000 | 0.00 |

The accuracy of the equations used in the RAE/WHL analysis is assessed by comparing the predicted section properties to experimental data. Based on McCroskey's assessment of NACA 0012 data (McCroskey, 1987) the data from Harris (1981) were used for these purposes. Included in this comparison are the section properties from the C81 deck for the NACA 0012 (Davis, 1974) although these are only used above the stall boundary for this task. However, the C81 section properties will be used for all computations in Tasks 1 and 2 for the CAMRAD and METAR/R85 analyses so their inclusion here is of interest even for characteristics below the stall angle.

The section lift calculated with the two sets of tables is compared with data from Harris in figure 3 for five Mach numbers. The wind tunnel data are for two Reynolds numbers, $3 \times 10^6$ and $9 \times 10^6$, except for the $M = 0.3$ case ($Re = 3 \times 10^6$ only). The Puma, for the Task 3 trim condition, has a Reynolds number at $0.75R$ that varies around the azimuth from $3.8 \times 10^6$ to $8.5 \times 10^6$. In general the section lift computed from the tables agrees fairly well with the Harris data. At low Mach number the RAE/WHL equations overpredict $C_{l_{max}}$, but there is good agreement at intermediate Mach numbers. At $M = 0.80$ and as angle of attack becomes greater than two degrees the section lift becomes significantly overpredicted using the table look-up. Note that the table values based on the RAE formulas are valid only up to the $\alpha_L$ value in table 3. Beyond $\alpha_L$ the tables revert to the C81 NACA 0012 tables.

The section drag calculated with the NACA 0012 tables and the tables based on the RAE formulas is compared with data from Harris in figure 4. At the lowest Mach number, $M = 0.30$, the rise in drag coefficient with angle of attack is predicted better with the RAE/WHL equations than with the NACA 0012 tables. For higher Mach numbers both sets of tables show good agreement with the data, particularly in the contraction of the "drag bucket" with Mach number. The minimum drag coefficient is predicted to be slightly higher for the C81 tables; however, both predictions lie between the $Re = 3 \times 10^6$ and $Re = 9 \times 10^6$ measurements.

The section pitching moment calculated with the standard NACA 0012 tables and the RAE/WHL model is compared with the data in figure 5. Over the range $0.30 \leq M \leq 0.70$ the tables based on the RAE/WHL model show good agreement with measured pitching moments, both in the amount of positive pitching moment seen below the stall break and the angle of attack of the stall break. The C81 NACA 0012 tables, on the other hand, reflect these characteristics poorly. At $M = 0.80$ both sets of tables show reasonable agreement with the slope at low angles of attack, but do not show the reversal in moment at higher angles that were obtained in the experiment.

The C81 NACA 0012 airfoil characteristics below stall, shown in figures 3–5, are not used for the Task 3 calculations in this section and, therefore, their accuracy or inaccuracy is of little importance for the present examination of the effects of modeling assumptions on the lifting-line methods. However, tables based on the C81 NACA 0012 airfoil characteristics shown here are used in Section 5 and the poor prediction of the pitching moment below stall for Mach numbers less than 0.70 will significantly influence the prediction of aerodynamic pitching moment and torsional response.

## 4.3 Comparison of Analytical Methods

The comparison of the analytical methods for the ten cases is divided into two sections. In Section 4.3.1 scalar parameters such as power and the collective and cyclic trim values are examined

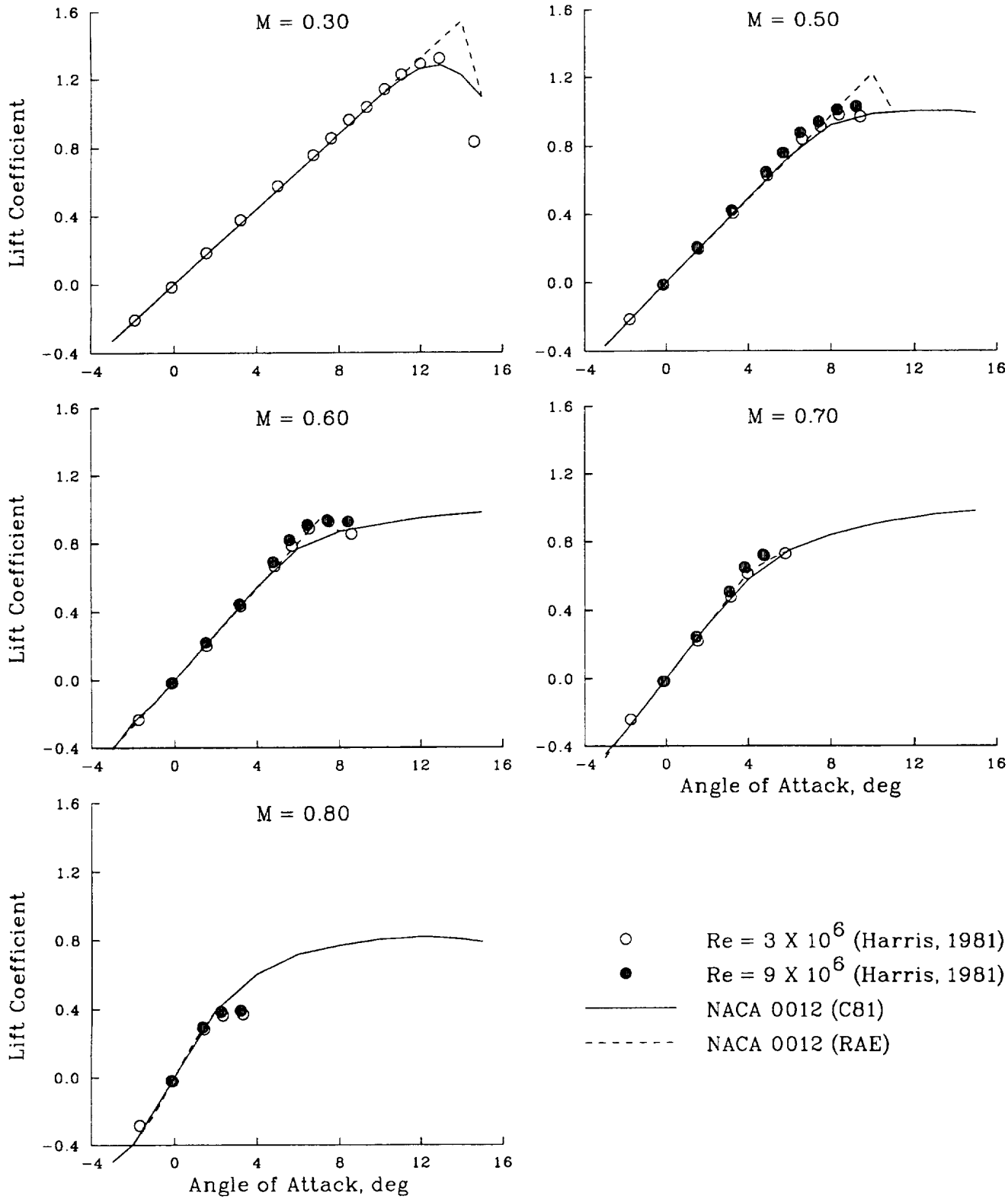


Figure 3. Comparison of lift coefficient from look-up tables with data from Harris (1981).

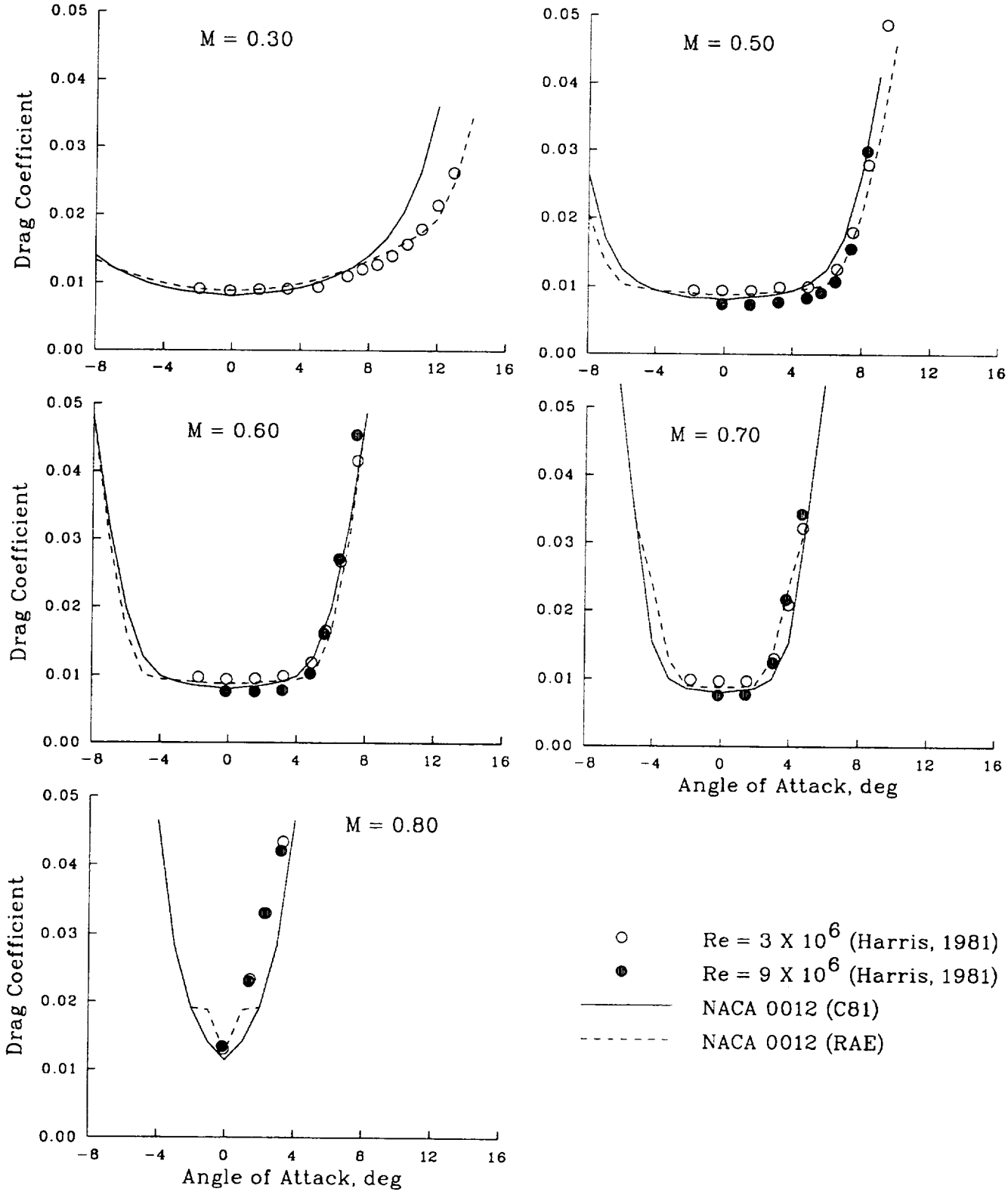


Figure 4. Comparison of drag coefficient from look-up tables with data from Harris (1981).

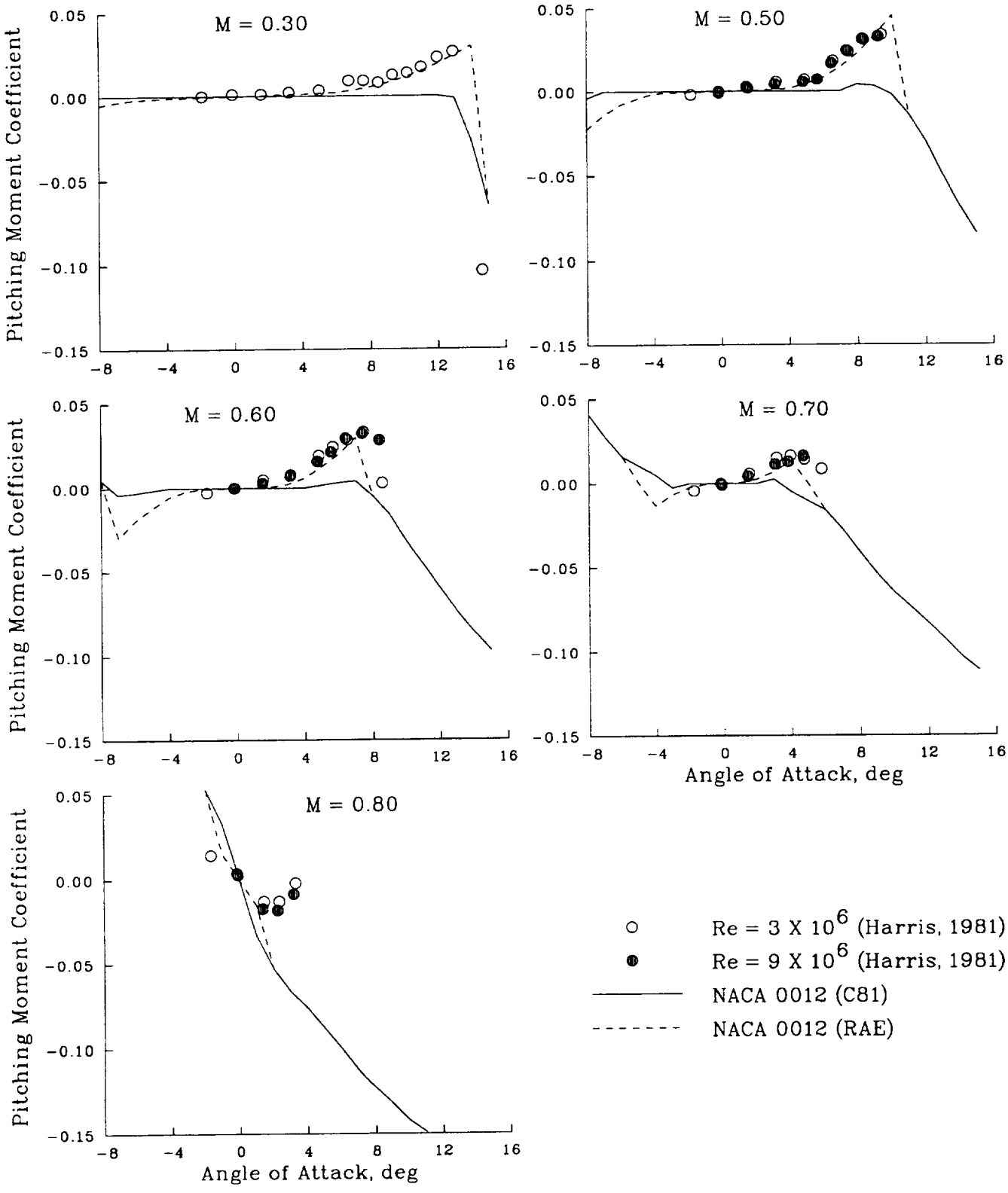


Figure 5. Comparison of pitching moment coefficient from look-up tables with data from Harris (1981).

while in Section 4.3.2 distributed parameters such as blade airloads and motions are assessed. For the scalar parameters in Section 4.3.1 it is convenient to examine the behavior of one parameter for all of the ten cases and in this fashion gain insight into the difference in the methods. However, for the distributed parameters it is more convenient to compare the methods one case at a time for all of the parameters.

### 4.3.1 Trim and Performance

*Unprescribed Trim Variables*

Four trim parameters were prescribed for the Task 3 cases: rotor thrust, shaft angle of attack, and the first harmonic cosine and sine flap angles. Other variables, such as blade collective pitch, the cosine and sine cyclic angles, and the X- and Y-forces are obtained as part of the solution process and, as they are not prescribed in the trim calculation, they make a good basis for comparison of the models.

*Collective Pitch*

The collective pitch angles calculated at $0.75R$ are shown in figure 6 for the Task 3 cases and the values are tabulated in table 6. Note that the table includes the value for all ten cases, but the figure excludes the large root cutout cases as, in general, the effect of reverse flow is slight. Cases 1 and 2 provide a sound baseline with only elementary formulas for the induced flow and the airfoil data. All of the analyses use the same aerodynamics and differ only in the following features:

- geometrical simplification (such as neglecting the flap hinge offset, or linearizing sine and cosine functions of angles)
- simplification of the inertial tensor
- accuracy of spanwise force integration
- algorithm for trim solution

Case 2 is even more basic than Case 1 because the $0.40R$ root cutout eliminates the reversed flow region.

The four analyses give results in close agreement for Cases 1 and 2. The major difference is the larger influence of the root cutout for CAMRAD/JA which shows a $0.7^\circ$ increase in collective pitch compared to the $0.3^\circ$ to $0.4^\circ$ increments seen in the other three analyses.

Introducing nonuniform inflow (Cases 3 and 4) increases the collective pitch for all analyses. This confirms a well-known shortcoming of the uniform inflow assumption, namely the underestimation of the average induced velocity. CAMRAD, RAE/WHL, and METAR/R85 are still in close agreement for the collective pitch, the discrepancy being not larger than $0.26^\circ$ for Case 4. This result is not surprising for CAMRAD and METAR/R85 which use approximately the same vortex-lattice modelization of the wake, but most encouraging is the fact that RAE/WHL is converging to the same result with a quite different model based on vortex half rings.

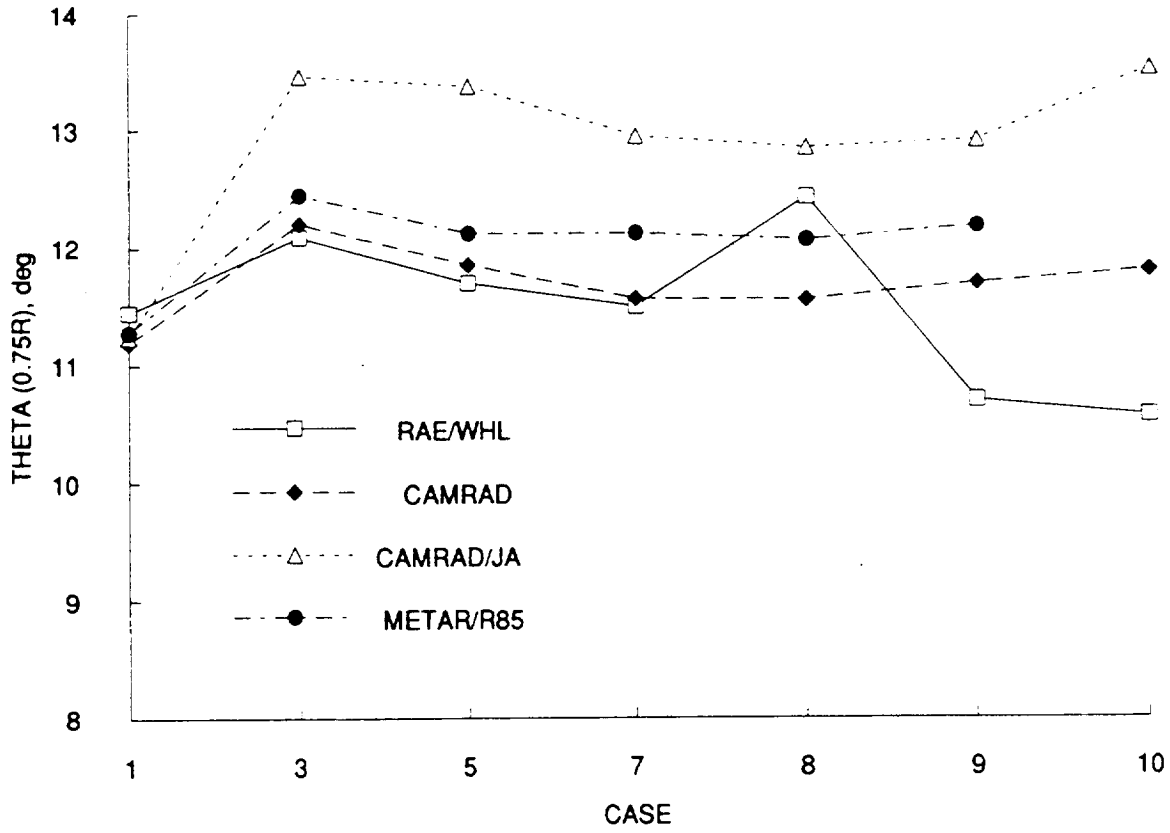


Figure 6. Calculated collective pitch for the Task 3 cases.

The collective pitch given by CAMRAD/JA appears larger by more than 1° and this increment is seen consistently with respect to the other analyses for Case 3 and above (except for Case 8 for the RAE/WHL analysis). The primary difference between CAMRAD/JA and CAMRAD is in the implementation of second-order lifting-line theory and it seems likely that the difference seen here is related to this implementation.

Table 6. Calculated collective pitch at $0.75R$

| Case | $\theta_{.75R}$, deg | | | |
|---|---|---|---|---|
| | RAE/WHL | CAMRAD | CAMRAD/JA | METAR/R85 |
| 1 | 11.44 | 11.19 | 11.24 | 11.28 |
| 2 | 11.82 | 11.46 | 11.93 | 11.61 |
| 3 | 12.08 | 12.20 | 13.46 | 12.45 |
| 4 | 12.68 | 12.56 | 14.08 | 12.82 |
| 5 | 11.69 | 11.85 | 13.37 | 12.12 |
| 6 | 12.27 | 12.26 | 14.13 | 12.45 |
| 7 | 11.49 | 11.56 | 12.94 | 12.12 |
| 8 | 12.42 | 11.55 | 12.84 | 12.06 |
| 9 | 10.69 | 11.69 | 12.90 | 12.17 |
| 10 | 10.56 | 11.80 | 13.51 | – |

Switching from linear airfoil characteristics to airfoil tables (Cases 5 and 6) does not alter the above mentioned conclusions. For all methods except CAMRAD/JA, the collective pitch is reduced by 0.4°. The gap between CAMRAD/JA and the other analyses increases since the collective pitch is reduced by less than 0.1° in this particular method (Case 5 minus Case 3).

The influence of unsteady aerodynamics on collective pitch can be assessed by comparing Cases 5 and 7. The collective pitch is slightly reduced, by 0.2° to 0.4°, except for METAR/R85, which is unchanged. The equations of linear unsteady aerodynamics for an airfoil undergoing a pure pitch oscillation based on the work of Theodorsen and Wagner conserve the static lift for a given static pitch, but the combination of an unsteady incidence with a time-varying velocity can lead to an augmented lift, even for a quasi-steady model of the velocity. This explains the reduced collective pitch required to achieve a constant trimmed lift. Due to the moderate lift and moderate advance ratio, dynamic stall is not involved in this case.

The impact of yawed or radial flow sweep (Case 8) on collective pitch is very small according to all the codes except the RAE/WHL analysis. The reason for this exception is not understood.

Introducing the blade bending instead of the rigid blade assumption (Case 9) does not change the collective pitch significantly except, again, for the RAE/WHL code.

The effect of blade torsion (Case 10) on collective pitch shows a number of differences between the codes. CAMRAD and CAMRAD/JA both show an increase in the trim collective with this increase larger for CAMRAD/JA. The RAE/WHL analysis, on the other hand, shows a decrease in trim collective. Case 10 was not calculated with METAR/R85 due to convergence problems when torsion was included.

*Lateral Cyclic Pitch*

The lateral cyclic angles calculated by the four analyses are shown in figure 7 for the Task 3 cases and the values are shown in table 7. The values predicted by RAE/WHL, CAMRAD and CAMRAD/JA are generally quite consistent.

METAR/R85 gives a higher value for Cases 1 through 8 because of the lead-lag hinge, which is not removed as for the other codes. The number of calculated harmonics is simply set to zero, but the static lag angle is still calculated.

Significant differences between codes are observed with respect to unsteady aerodynamics (Case 7) and, to a lesser degree, with respect to sweep (Case 8).

The change in lateral cyclic pitch observed in Case 9 should not be misinterpreted: it is not due to blade bending but rather to the lag angle which is introduced at the same time (except for METAR/R85 where static lag is always included). The effective azimuth is retarded with respect to the hub azimuth, and the pitch control has to compensate by a lead phasing equal to the static lag angle. This effect is shown in table 8 where the blade cyclic angles are shown in terms of amplitude and phase.

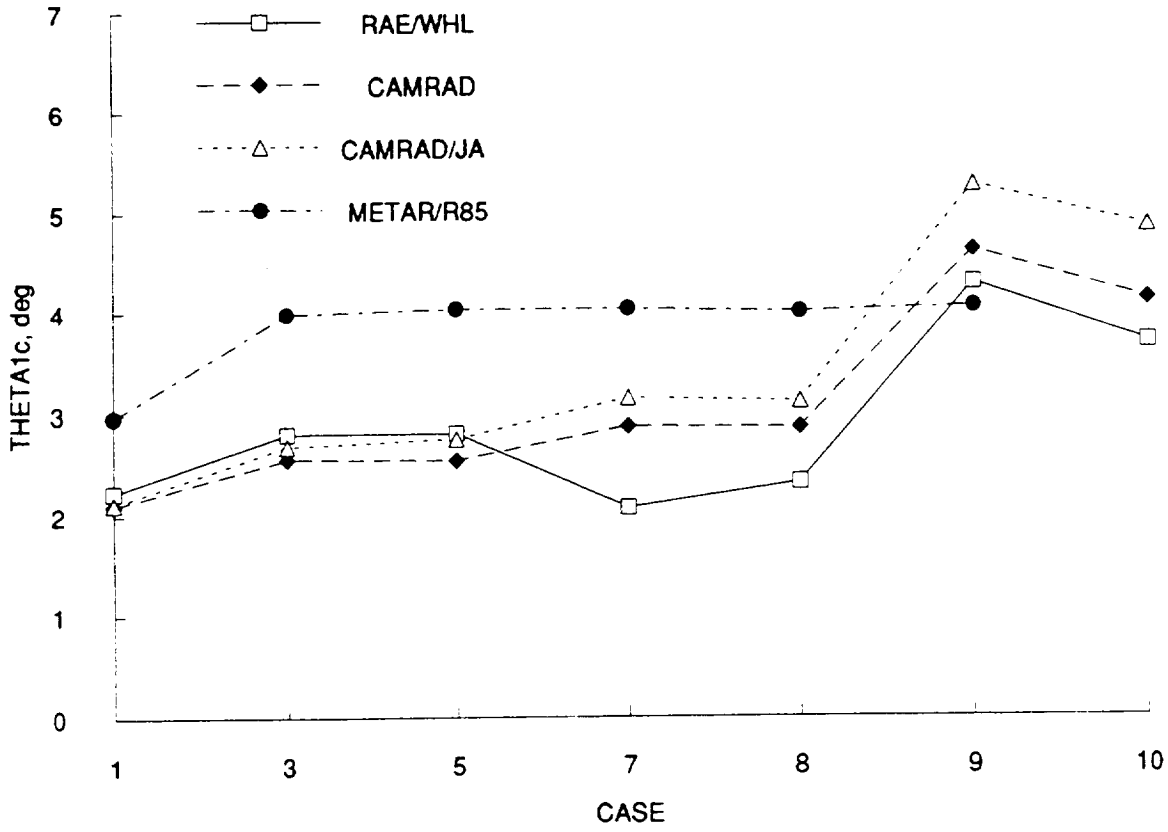


Figure 7. Calculated lateral cyclic pitch for the Task 3 cases.

On the other hand, the change in $\theta_{1c}$ observed in Case 10 can only be explained by the blade torsion. The RAE/WHL, CAMRAD and CAMRAD/JA analyses all show the same effect in the addition of the torsion degree of freedom.

Table 7. Calculated lateral cyclic pitch

| Case | $\theta_{1c}$, deg | | | |
|---|---|---|---|---|
| | RAE/WHL | CAMRAD | CAMRAD/JA | METAR/R85 |
| 1 | 2.23 | 2.10 | 2.12 | 2.97 |
| 2 | 2.27 | 2.18 | 2.18 | 3.07 |
| 3 | 2.80 | 2.55 | 2.68 | 3.99 |
| 4 | 2.93 | 2.53 | 2.65 | 3.93 |
| 5 | 2.81 | 2.54 | 2.75 | 4.03 |
| 6 | 2.93 | 2.54 | 2.73 | 3.99 |
| 7 | 2.07 | 2.87 | 3.15 | 4.03 |
| 8 | 2.31 | 2.86 | 3.11 | 4.00 |
| 9 | 4.28 | 4.61 | 5.26 | 4.04 |
| 10 | 3.70 | 4.12 | 4.85 | – |

Table 8. Calculated cyclic pitch angles in amplitude and phase

| Case | RAE/WHL | | CAMRAD | | CAMRAD/JA | | METAR/R85 | |
|---|---|---|---|---|---|---|---|---|
| | ampl. | phase | ampl. | phase | ampl. | phase | ampl. | phase |
| 1 | 8.56 | −75 | 8.29 | −75 | 8.34 | −75 | 8.31 | −69 |
| 3 | 9.53 | −73 | 9.67 | −75 | 11.01 | −76 | 9.76 | −66 |
| 5 | 9.24 | −72 | 9.36 | −74 | 11.11 | −76 | 9.53 | −65 |
| 7 | 9.33 | −77 | 9.16 | −72 | 10.75 | −73 | 9.53 | −65 |
| 8 | 10.16 | −77 | 9.15 | −72 | 10.62 | −73 | 9.47 | −65 |
| 9 | 10.36 | −66 | 9.48 | −61 | 10.96 | −61 | 9.54 | −65 |
| 10 | 10.52 | −69 | 9.03 | −63 | 10.76 | −63 | – | – |

*Longitudinal Cyclic Pitch*

The longitudinal cyclic pitch angles computed by the four analyses are illustrated in figure 8 and tabulated in table 9. The trends in longitudinal cyclic bear some resemblance to those observed in the collective pitch and are also connected with results for the lateral cyclic pitch.

Nonuniform inflow increases the magnitude of the longitudinal cyclic (Case 3). This is because the uniform inflow formula (Case 1) neglects the lateral gradient of inflow while the more realistic vortex models all produce larger velocities on the retreating blade side and this makes a larger $\theta_{1s}$ necessary to trim the rotor.

In the same way as for the collective pitch, CAMRAD/JA gives a much larger negative value than the other models.

The unsteady models (Case 7) again display contradictory trends due to different lift/pitch transfer (see table 8). CAMRAD and CAMRAD/JA show a reduced amplitude and a retarded phase, while RAE/WHL shows an augmented amplitude and anticipated phase.

The effect of radial flow (Case 8) is, again, very small except for RAE/WHL . . . the reason for this exception is unknown.

The change in longitudinal cyclic observed in Case 9 is again a result of the static lag angle, and not dependent upon blade bending.

For blade torsion (Case 10), the trends are not consistent. The sine component of blade torsion may be more difficult to predict than the cosine, possibly because of pitching moment divergence on the advancing blade side.

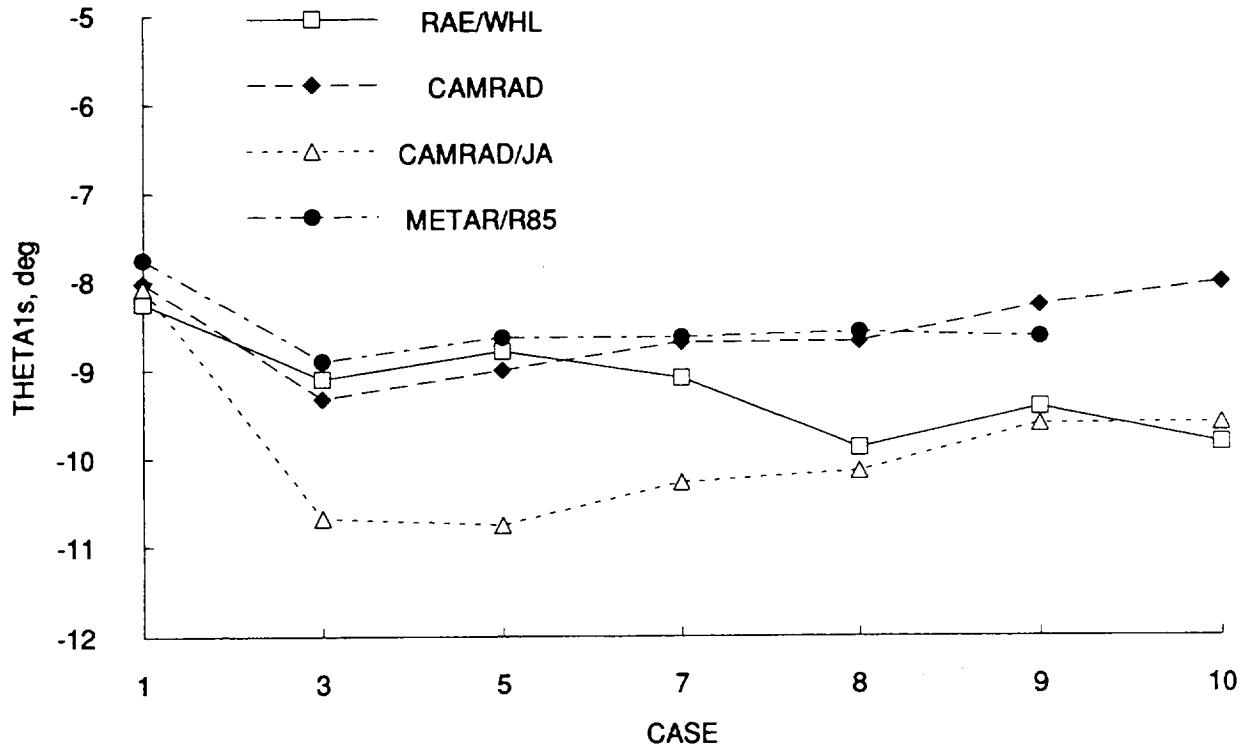


Figure 8. Calculated longitudinal cyclic pitch for the Task 3 cases.

Table 9. Calculated longitudinal cyclic pitch

| Case | $\theta_{1s}$, deg | | | |
|---|---|---|---|---|
| | RAE/WHL | CAMRAD | CAMRAD/JA | METAR/R85 |
| 1 | −8.26 | −8.02 | −8.07 | −7.76 |
| 2 | −8.44 | −8.16 | −8.40 | −7.94 |
| 3 | −9.11 | −9.33 | −10.68 | −8.91 |
| 4 | −9.39 | −9.42 | −10.96 | −9.04 |
| 5 | −8.80 | −9.01 | −10.76 | −8.64 |
| 6 | −9.09 | −9.16 | −11.28 | −8.76 |
| 7 | −9.10 | −8.70 | −10.28 | −8.64 |
| 8 | −9.89 | −8.69 | −10.15 | −8.58 |
| 9 | −9.43 | −8.28 | −9.62 | −8.64 |
| 10 | −9.85 | −8.03 | −9.61 | – |

*Longitudinal Force and Lateral Force*

The longitudinal and lateral forces calculated by the four analyses are shown in figures 9 and 10 and the tabulated values are given in tables 10 and 11. The longitudinal or X-force is positive forward, and the lateral or Y-force is positive to the right, that is, to the retreating blade side on the Puma rotor. The longitudinal and lateral forces are expressed in the shaft axes. The tables and the plots appear to show large differences between codes. It is noted, however, that a 500 N difference represents only a $0.5^\circ$ rotation of the thrust vector—the agreement is, in fact, good.

Comparing Case 3 with Case 1 indicates that the thrust vector is more inclined forward and toward the retreating blade when nonuniform inflow is applied. This result was not expected since the rotor disk is always trimmed to the same flap angle. The variation in the X-force produced by CAMRAD/JA is twice as much as that produced by the other codes, thereby confirming the peculiar behavior of its inflow model.

The thrust vector is tilted somewhat more forward and to the left-hand side as a result of introducing nonlinear aerodynamics for Case 5, but the codes do not agree on the amplitude of this effect. The impact of unsteady aerodynamics (Case 7) on inplane forces is small for all of the codes.

The effect of sweep (Case 8) is consistent for all codes except RAE/WHL. The skin friction drag caused by the radial flow produces a global inplane drag which reduces the propulsive force. Rotor performance is significantly affected by the radial drag, as discussed below.

Blade bending (Case 9) does not alter the inplane forces according to CAMRAD, CAMRAD/JA, and METAR/R85. This confirms the general opinion that the relatively small blade deformations have little impact on steady and 1/rev components of aerodynamic forces. However, the RAE/WHL analysis departs from this conclusion with a noticeable impact on both the X- and Y-forces.

Most surprising is the small effect of blade torsion (Case 10) on inplane forces observed with all the codes. It was assumed above, in the discussion of the trim longitudinal cyclic pitch, that torsion is compensated by a modified cyclic pitch to obtain a constant flap angle. Apparently this compensation also works for inplane forces.

*Power and Performance*

Most analysts accept the breakdown of shaft power into three components: parasite power, induced power, and profile power. This approach is based on energy conservation expressed in nonrotating coordinates as discussed in Appendix B. However, the power breakdown used at the RAE recognizes only two terms, the thrust-dependent power and rotational power, which are calculated in rotating coordinates (Young, 1989).

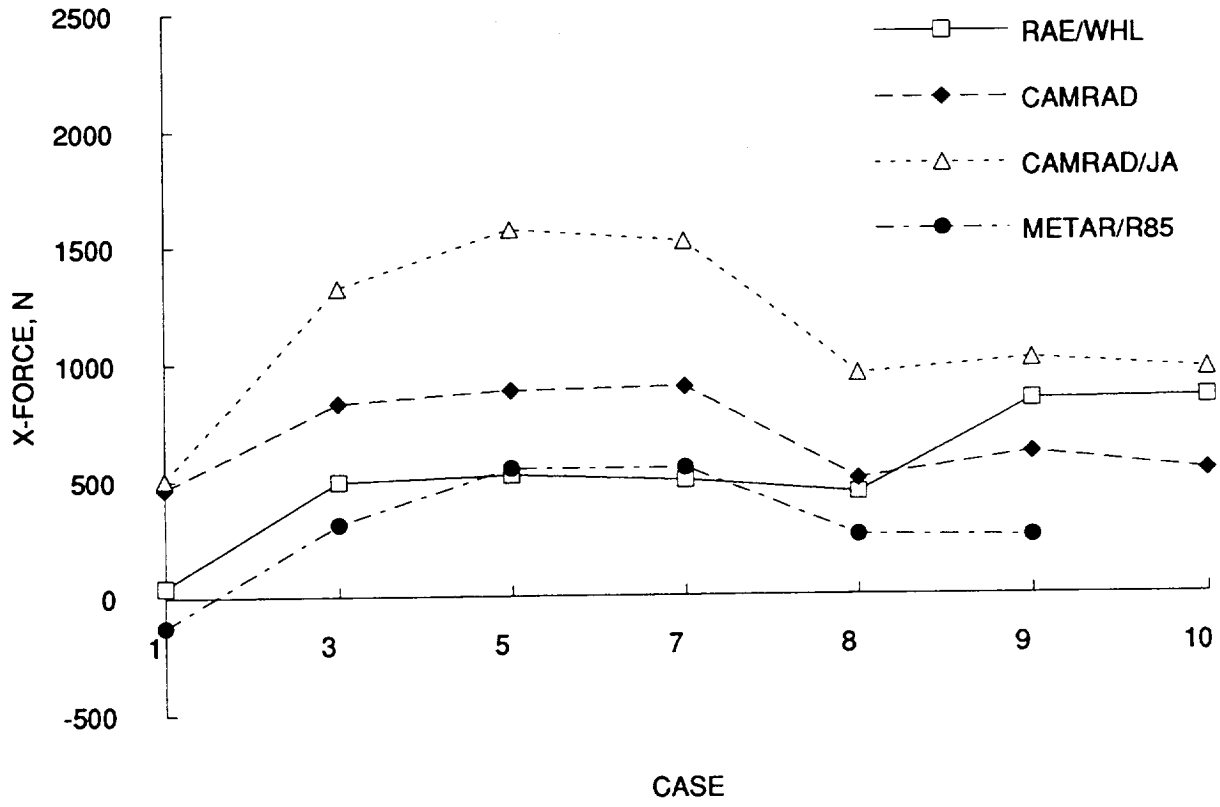


Figure 9. Calculated longitudinal forces for Task 3 cases.

Table 10. Calculated longitudinal forces for Task 3 cases

| Case | X-force, newtons | | | |
|---|---|---|---|---|
| | RAE/WHL | CAMRAD | CAMRAD/JA | METAR/R85 |
| 1 | 41.4 | 466.1 | 505.7 | −130.0 |
| 2 | 420.3 | 797.2 | 847.8 | 281.0 |
| 3 | 494.4 | 831.0 | 1319.5 | 307.0 |
| 4 | 788.1 | 1189.1 | 1656.8 | 739.0 |
| 5 | 519.4 | 884.0 | 1569.4 | 551.0 |
| 6 | 855.4 | 1237.3 | 2060.0 | 867.0 |
| 7 | 495.0 | 897.9 | 1514.7 | 551.0 |
| 8 | 438.8 | 498.6 | 949.9 | 253.0 |
| 9 | 838.8 | 610.6 | 1008.7 | 249.0 |
| 10 | 846.8 | 530.9 | 964.8 | – |

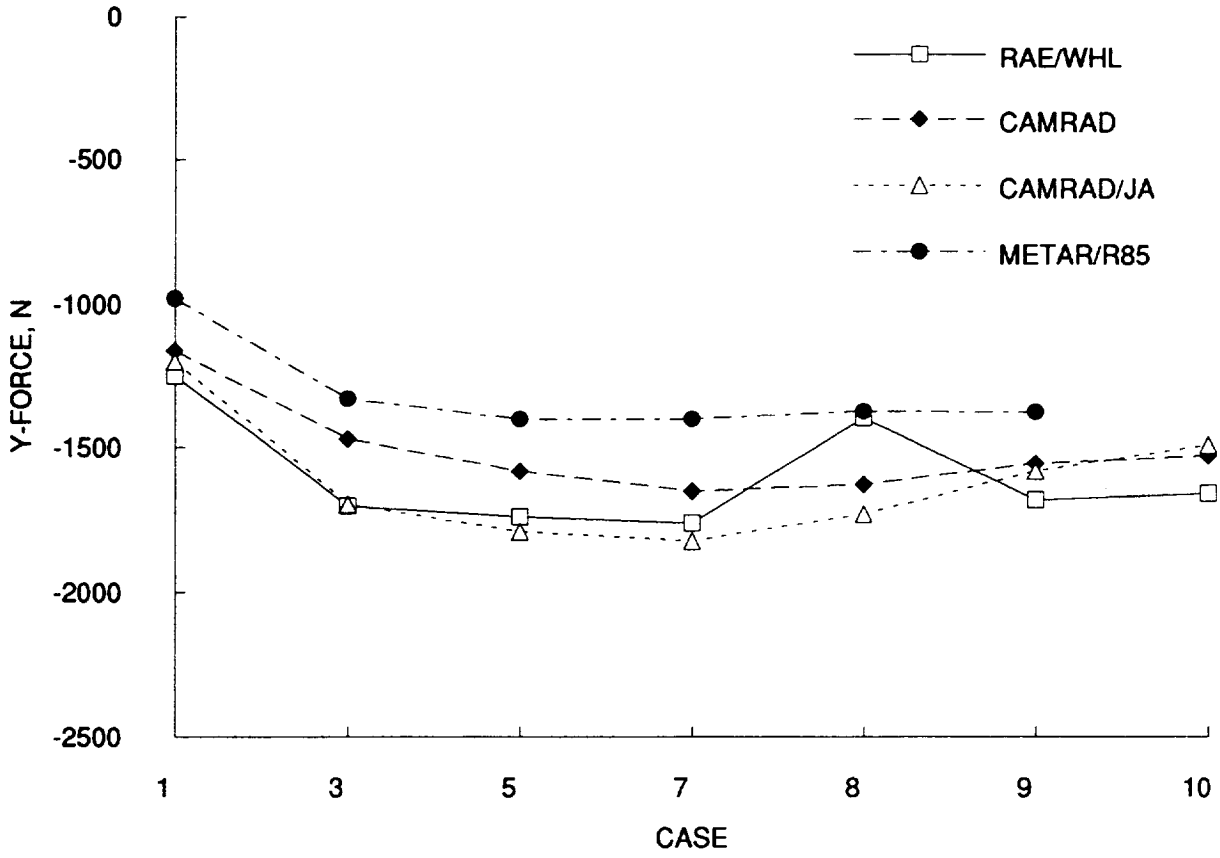


Figure 10. Calculated lateral forces for Task 3 cases.

Table 11. Calculated lateral forces for Task 3 cases

| Case | Y-force, newtons | | | |
|---|---|---|---|---|
| | RAE/WHL | CAMRAD | CAMRAD/JA | METAR/R85 |
| 1 | −1250.4 | −1162.4 | −1198.7 | −979.0 |
| 2 | −1231.4 | −1218.8 | −1210.3 | −1005.0 |
| 3 | −1702.9 | −1470.6 | −1696.9 | −1329.0 |
| 4 | −1693.1 | −1473.1 | −1595.5 | −1288.0 |
| 5 | −1741.2 | −1583.7 | −1790.9 | −1402.0 |
| 6 | −1750.1 | −1539.9 | −1761.9 | −1350.0 |
| 7 | −1761.4 | −1651.5 | −1822.3 | −1402.0 |
| 8 | −1399.8 | −1630.4 | −1731.2 | −1376.0 |
| 9 | −1683.8 | −1557.6 | −1583.0 | −1378.0 |
| 10 | −1660.2 | −1530.3 | −1491.9 | – |

*Profile Power.* The profile power calculated by the analyses is shown in figure 11 for the cases with the normal root cutout and tabulated values for all cases are shown in table 12. The RAE calculated rotational power is also included here although it is calculated differently (see Appendix B). As expected, rotational power is always lower than profile power by some 40 to 50 kw, this difference being interpreted as the power associated with translation of inplane forces. The agreement between CAMRAD and CAMRAD/JA is excellent for all cases.

The profile power calculated with METAR/R85 is lower than for the CAMRAD family except for Cases 1 and 2 where the agreement is very good. The difference in profile power for successive cases is the same for METAR/R85 and RAE/WHL, except for the effect of sweep: radial drag increases inplane drag, thus profile power is increased but not the rotational power.

*Induced Power.* The induced power calculated by the analyses is shown in figure 12 for the cases with the normal root cutout and the values for all cases are given in table 13. No calculations are shown for the RAE/WHL code as no equivalent quantity exists. CAMRAD and METAR/R85 give results in close agreement but CAMRAD/JA predicts a much higher induced power as soon as the nonuniform inflow is introduced. This is another consequence of the second-order lifting-line theory which produces a larger inflow than the other methods.

The greater induced power calculated by CAMRAD/JA relative to CAMRAD has been investigated in detail for Case 3 and the results are provided in Appendix C. Differences remained even when the modeling capability of CAMRAD/JA was limited to that provided by CAMRAD, as far as it is possible to control through user input. A stepwise elimination of the remaining differences through coding changes provide some insight into the different near-wake models used by the two analyses.

*Parasite Power.* The parasite power calculated by the analyses is shown in figure 13 for the cases with a normal root cutout and the values for all of the cases are tabulated in table 14. Calculations for parasite power are not included in the RAE/WHL analysis. It is observed that the shape of curves is very similar to that of the X-force which is expected as parasite power is the scalar product $V \cdot T$ (see Appendix B). However, the slight offset in X-force between METAR/R85 and CAMRAD as seen in figure 9 is not readily explained.

*Thrust-Dependent Power.* For analyses based on the energy method, the sum of induced and parasite contributions is compared to the thrust-dependent power as defined in Appendix B. The calculated thrust-dependent power for the cases with the normal root cutout is shown in figure 14 and the values for all cases are tabulated in table 15. As expected, the RAE/WHL thrust-dependent power is larger than in CAMRAD and METAR/R85, the difference being interpreted as the contribution of the inplane forces to parasite power. Again, CAMRAD/JA shows much higher induced power than the other codes, except for Cases 1 and 2.

*Shaft Power.* Shaft power is the sum of the profile, induced, and parasite powers for CAMRAD, CAMRAD/JA, and METAR/R85, and the sum of profile ("rotational") and thrust-dependent power for the RAE/WHL analysis. The shaft power is shown in figure 15 for the cases with the nominal root cutout and the values for all cases are tabulated in table 16.

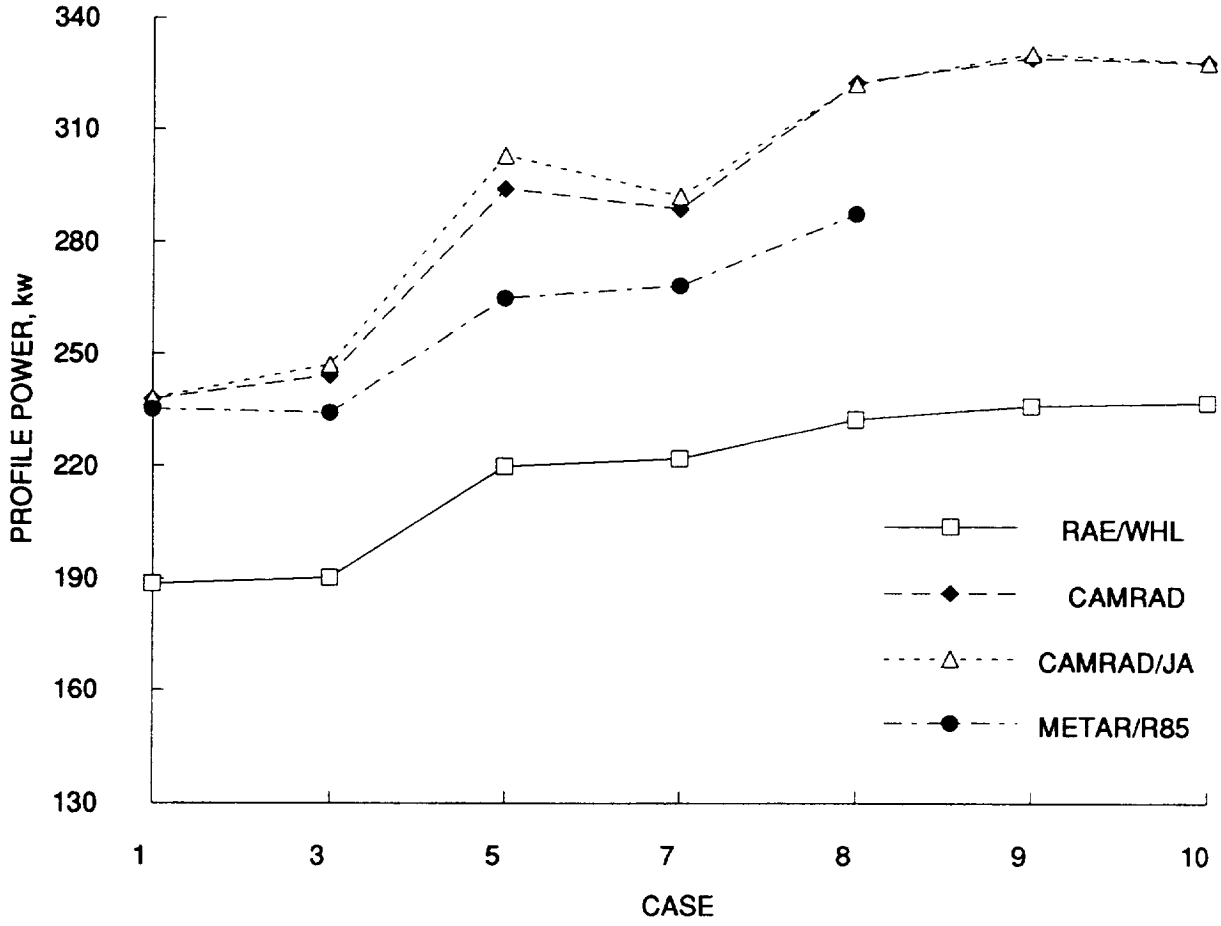


Figure 11. Calculated profile power for Task 3 cases.

Table 12. Calculated profile power for Task 3 cases

| Case | Profile power, kw | | | |
|---|---|---|---|---|
| | RAE/WHL[a] | CAMRAD | CAMRAD/JA | METAR/R85 |
| 1 | 188.6 | 237.8 | 238.1 | 235.1 |
| 2 | 184.6 | 226.2 | 226.5 | 223.3 |
| 3 | 190.2 | 244.0 | 247.0 | 234.1 |
| 4 | 184.8 | 231.4 | 236.9 | 222.3 |
| 5 | 219.7 | 293.9 | 302.7 | 264.8 |
| 6 | 227.8 | 300.9 | 319.5 | 265.2 |
| 7 | 221.7 | 288.6 | 292.0 | 268.2 |
| 8 | 232.1 | 322.3 | 322.2 | 287.3 |
| 9 | 235.7 | 329.1 | 330.3 | – |
| 10 | 236.6 | 327.7 | 327.9 | – |

[a]Rotational power.

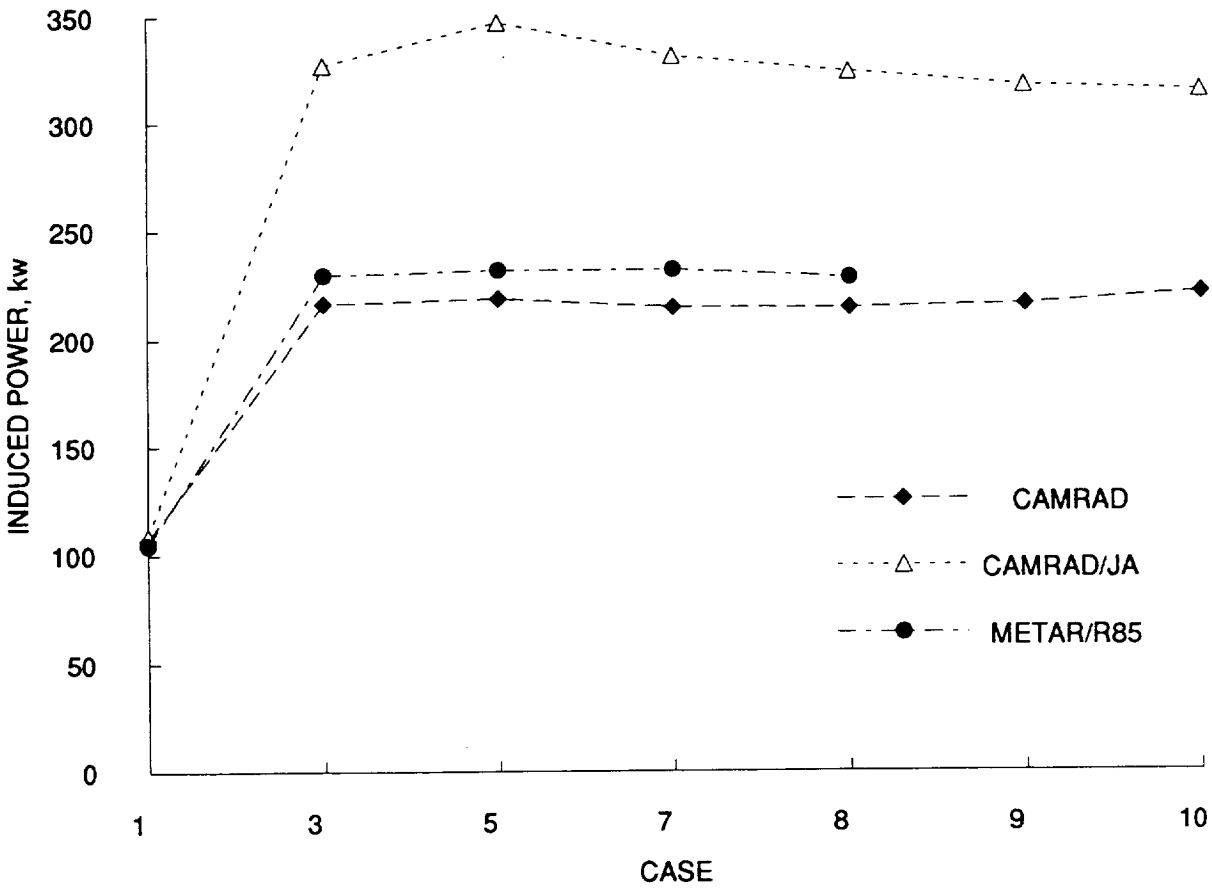


Figure 12. Calculated induced power for Task 3 cases.

Table 13. Calculated induced power for Task 3 cases

| Case | Induced power, kw | | |
|---|---|---|---|
| | CAMRAD | CAMRAD/JA | METAR/R85 |
| 1 | 106.7 | 108.6 | 104.5 |
| 2 | 106.6 | 161.6 | 107.7 |
| 3 | 216.6 | 327.0 | 229.5 |
| 4 | 228.4 | 370.5 | 234.1 |
| 5 | 218.7 | 346.8 | 231.5 |
| 6 | 234.0 | 400.0 | 237.0 |
| 7 | 214.6 | 331.0 | 231.5 |
| 8 | 214.2 | 323.3 | 227.8 |
| 9 | 215.7 | 316.9 | – |
| 10 | 220.7 | 314.2 | – |

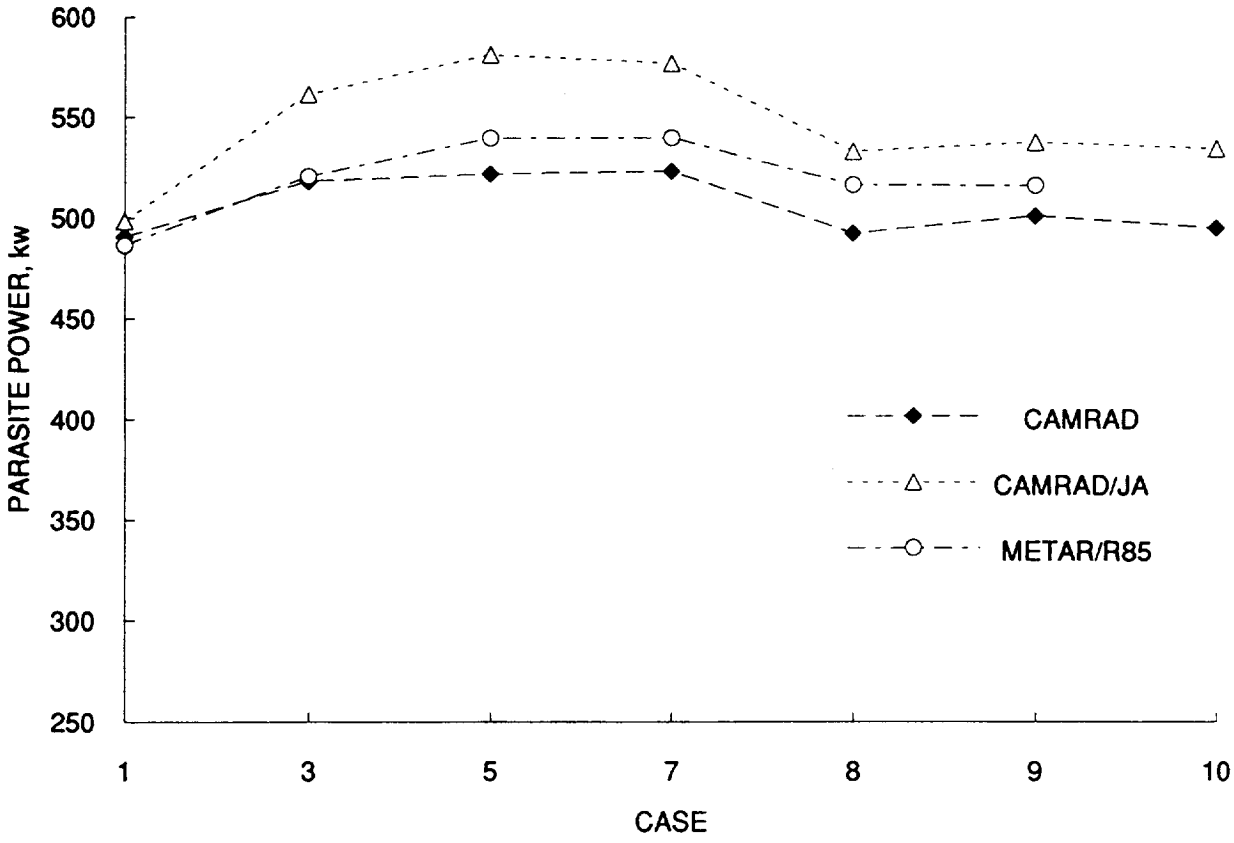


Figure 13. Calculated parasite power for Task 3 cases.

Table 14. Calculated parasite power for Task 3 cases

| Case | Parasite power, kw | | |
|---|---|---|---|
| | CAMRAD | CAMRAD/JA | METAR/R85 |
| 1 | 490.7 | 498.5 | 486.4 |
| 2 | 516.3 | 525.1 | 518.5 |
| 3 | 518.0 | 561.6 | 520.6 |
| 4 | 545.8 | 587.8 | 554.3 |
| 5 | 522.1 | 581.0 | 539.6 |
| 6 | 549.5 | 619.0 | 564.3 |
| 7 | 523.2 | 576.8 | 539.6 |
| 8 | 492.2 | 533.0 | 516.3 |
| 9 | 500.9 | 537.6 | 515.9 |
| 10 | 494.8 | 534.2 | – |

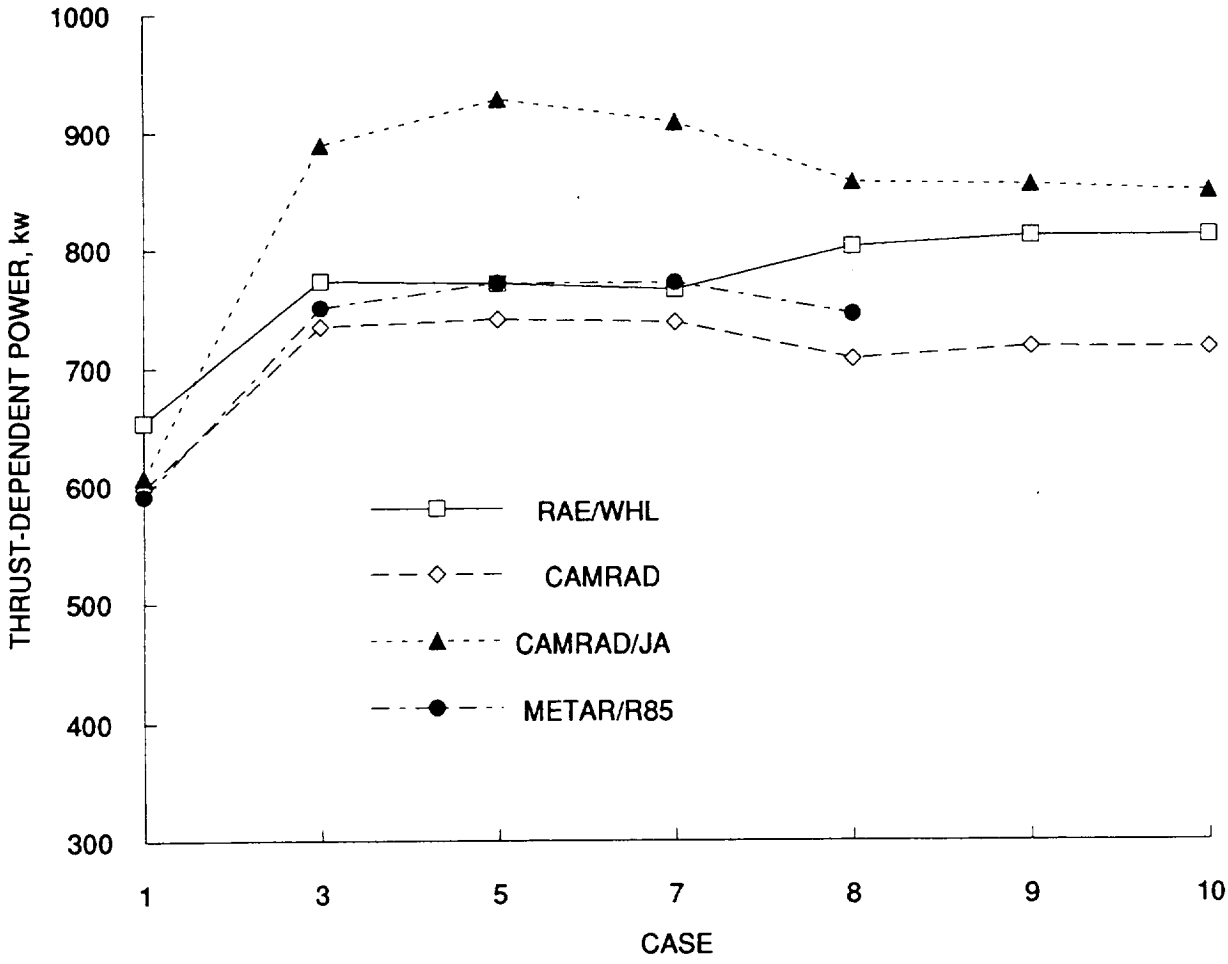


Figure 14. Calculated thrust-dependent power for Task 3 cases.

Table 15. Calculated thrust-dependent power for Task 3 cases

| Case | Thrust-Dependent power, kw | | | |
|---|---|---|---|---|
| | RAE/WHL | CAMRAD[a] | CAMRAD/JA[a] | METAR/R85[a] |
| 1 | 654.2 | 597.4 | 607.2 | 590.9 |
| 2 | 674.5 | 622.9 | 686.7 | 626.2 |
| 3 | 772.7 | 734.6 | 888.6 | 750.1 |
| 4 | 818.6 | 774.2 | 958.2 | 788.4 |
| 5 | 770.6 | 740.8 | 927.8 | 771.1 |
| 6 | 818.1 | 783.5 | 1019.0 | 801.3 |
| 7 | 765.2 | 737.8 | 907.7 | 771.1 |
| 8 | 801.4 | 706.4 | 856.4 | 744.1 |
| 9 | 810.6 | 716.6 | 854.5 | – |
| 10 | 810.5 | 715.5 | 848.4 | – |

[a]Sum of induced and parasite powers.

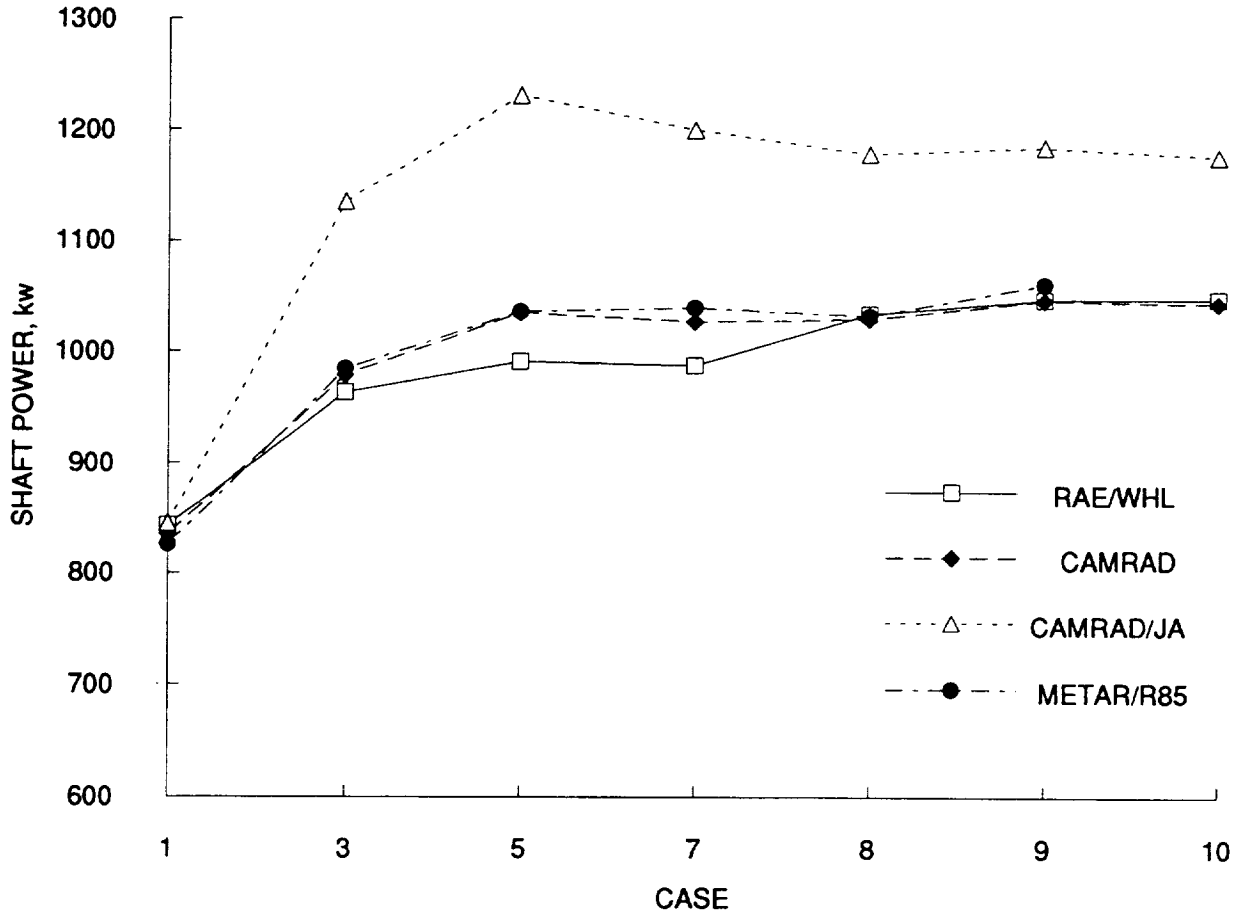


Figure 15. Calculated shaft power for Task 3 cases.

Table 16. Calculated shaft power for Task 3 cases

| Case | Shaft power, kw | | | |
|---|---|---|---|---|
| | RAE/WHL | CAMRAD | CAMRAD/JA | METAR/R85 |
| 1 | 842.8 | 835.2 | 845.2 | 826.0 |
| 2 | 859.1 | 849.1 | 913.2 | 849.5 |
| 3 | 962.9 | 978.6 | 1135.6 | 984.2 |
| 4 | 1003.4 | 1005.6 | 1195.1 | 1010.7 |
| 5 | 990.3 | 1034.7 | 1230.6 | 1035.9 |
| 6 | 1045.9 | 1084.4 | 1338.6 | 1066.5 |
| 7 | 986.9 | 1026.4 | 1199.7 | 1039.3 |
| 8 | 1033.5 | 1028.7 | 1178.5 | 1031.4 |
| 9 | 1046.3 | 1045.7 | 1184.7 | 1060.4 |
| 10 | 1047.1 | 1043.2 | 1176.3 | – |

The separation of shaft power into constituent parts, that is, into parasite, induced, and profile powers as calculated by the CAMRAD analyses and METAR/R85, or into thrust-dependent and rotational powers as done in the RAE/WHL analysis is valuable only to the degree that it provides insight into prediction differences observed. In the end the only calculation of importance is the prediction of shaft power as shown in figure 15. In this regard it is useful to note that the CAMRAD and METAR/R85 analyses are very consistent, with less than 2% difference in all cases. The RAE/WHL predictions are well matched with the others for Case 1 and 3 and Cases 8 and 9, but differences of about –4 or –5% are observed for Cases 5 and 7. CAMRAD/JA, on the other hand, calculates a shaft power 13% higher than the other methods and an examination of the power breakdown shows that approximately 9% of the value is in induced power and 4% in parasite power. The differences between CAMRAD and CAMRAD/JA are related to the wake model as discussed in Appendix C.

### 4.3.2 Airloads and Motions

*Case 1*

The Case 1 calculation was the most fundamental case examined and used simplified aerodynamics for the blade and wake, as well as a simplified representation of the blade dynamic properties. The blade aerodynamics were represented by linear equations, while unsteady flow, dynamic stall, and yawed flow were not modeled. The wake was assumed to be uniform, without harmonic variation. No tip loss factor was used in these calculations. The blade was assumed to be rigid with mass and inertia properties that matched the Puma rectangular blade. Three of the analyses included a flap hinge for the dynamic model, but not a lag hinge. The METAR/R85 analysis, however, required that the lag hinge be retained in the rotor representation and, in this respect, differed from the other models.

The lift calculated by the four analyses is shown in figure 16 as a surface plot where the independent variables are blade azimuth and blade radius. The radial grid shown corresponds to the calculated grid used by each analysis while a 5° step size is used for the azimuth grid. Note that the RAE/WHL analysis used 36 harmonics in its computation, METAR/R85 used 18 harmonics, and the two CAMRAD analyses used 12 harmonics. The measure of lift used here, $M^2C_L$, is a nondimensionalization based on the speed of sound rather than local velocity, that is

$$M^2C_L = \frac{2L}{\rho a^2 c} \tag{4-9}$$

where $L$ is the unit lift on the blade, $\rho$ is the density, $a$ is the speed of sound, and $c$ is the section chord. This form of nondimensionalization is useful in that the azimuthal behavior of $M^2C_L$ is the same as dimensional lift.

Azimuthally, the lift distribution for this simple case is dominated by a reduction in lift near the end of the first quadrant and, near the blade tip, there is a small region of negative lift. The reduced lift is a consequence of the need to maintain roll moment balance on the rotor. Radially, the lift increases towards the blade tip for most azimuths and the absence of a tip loss factor is clearly shown.

The distribution of blade angle of attack that corresponds to figure 16 is shown in figure 17. The angle of attack is a minimum near 90°, where the local airspeed is highest. It is a maximum at 270°. Inboard on the blade, in the third and fourth quadrants, the local velocity is quite low and computed

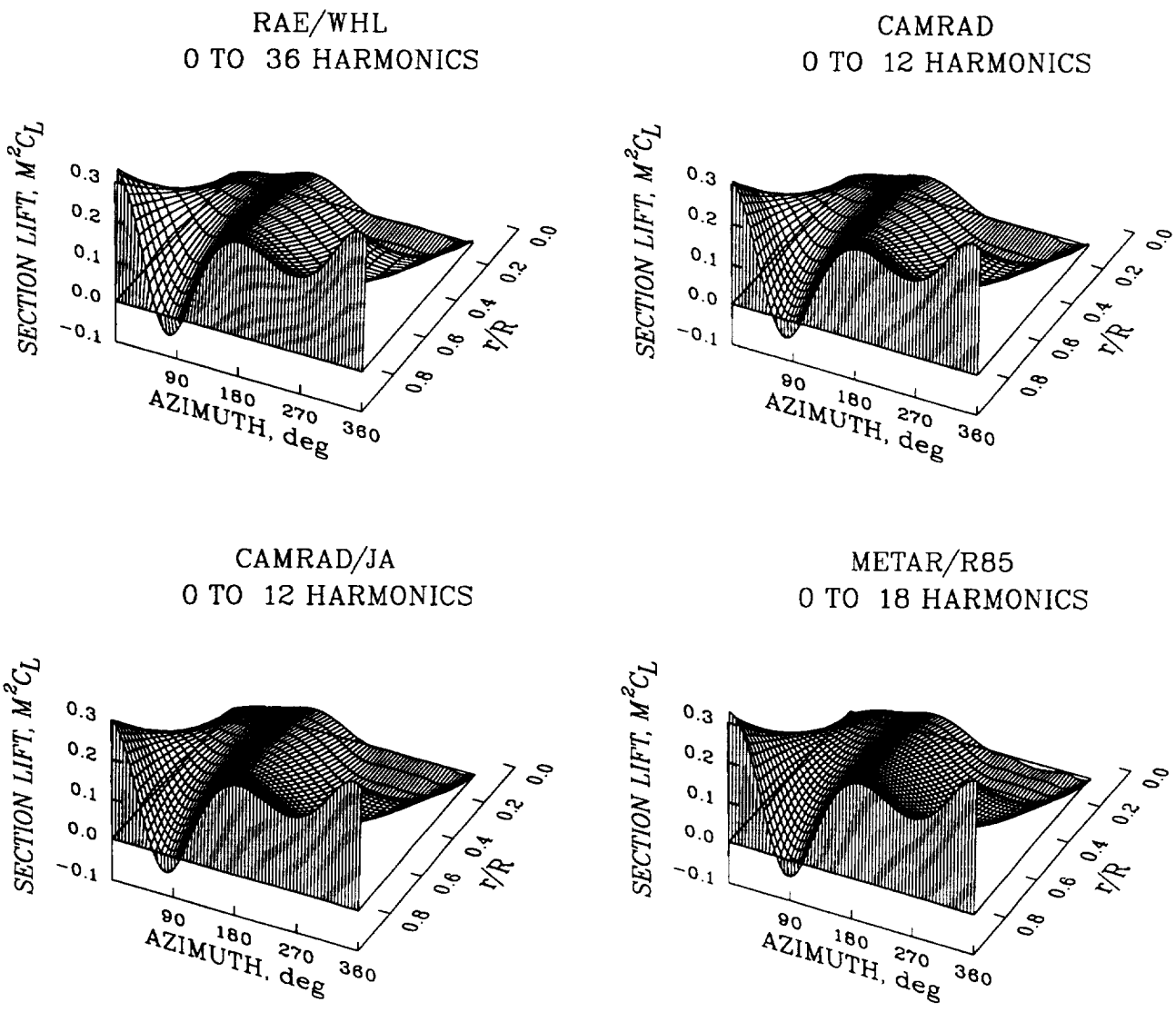


Figure 16. Normal force distribution as a function of azimuth and blade radius for Case 1; all harmonics.

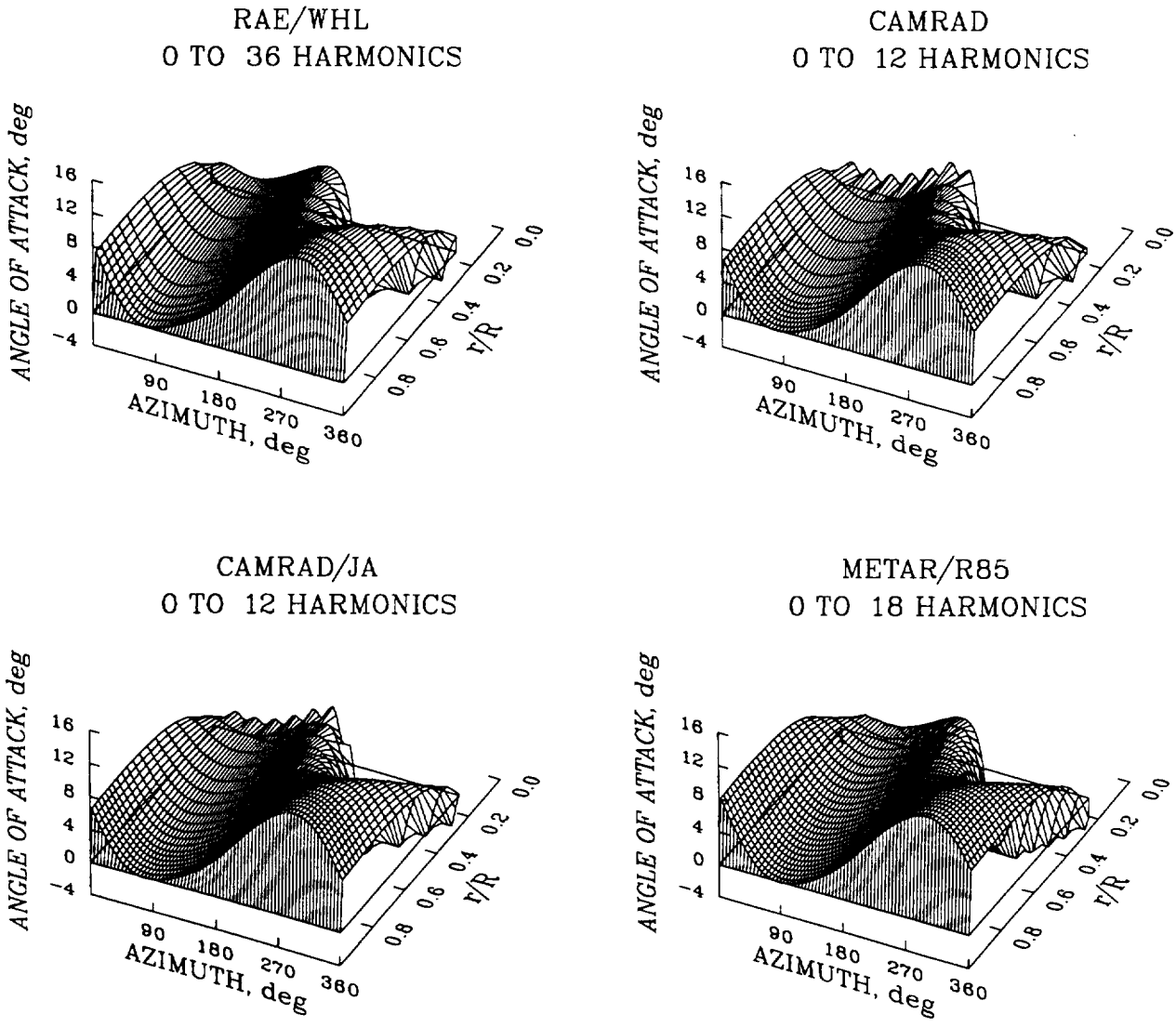


Figure 17. Angle-of-attack distribution as a function of azimuth and blade radius for Case 1; all harmonics.

angles of attack can be quite large, but these are not shown in the figure which cuts off the plot at the scale limit. The CAMRAD analyses show an oscillation in angle of attack at the most inboard station and it is believed that this is related to the solution method. Because the local dynamic pressure is so low at these inboard stations, small changes in angle of attack do not have a significant influence on the computed loads. The distribution of higher harmonic airloads, that is, harmonics at 3/rev and above, is shown in figure 18. These higher harmonic airloads are the source of vibration for the aircraft. As is seen here, these vibratory airloads are dominated by the third harmonic. It is probably useful to note that no blade elasticity is included in these computations so that there is no aeroelastic contribution to the 3/rev loads. The amplitude and phase of these loads is a consequence of the large variation in local velocity around the rotor disk. In this sense, then, the vibratory loading is induced by the requirements for trim in forward flight.

The predictions of the four analyses for various parameters are compared in figure 19. In general, very good agreement is achieved for the four analyses for this simplified case. The METAR/R85 calculation shows a slight phase lag when compared to the other analyses and this is simply a result of the steady lag deflection that is included in that analysis. However, the difference in blade flapping observed for the METAR/R85 analysis is surprising as this difference is primarily in blade coning which is directly related to blade thrust. The reason for this coning difference is unknown.

*Case 2*

The distribution of the airloads for Case 2 is shown in figure 20. This case differs from Case 1 in that the root cutout is changed from $0.228R$ to $0.40R$. This change in root cutout removes the reverse flow region from the calculation and, because there is less blade area, slightly increases the lift per unit span as shown in figure 21 which compares the steady lift calculated in this case with that computed for Case 1.

*Case 3*

The uniform wake model of Case 1 was replaced with a prescribed wake model for Case 3, but no other modeling changes were made. The RAE/WHL analysis uses a series of half vortex rings attached to the blade and full vortex rings within the wake to represent the wake induced flows. The other methods are based on a vortex-lattice model. Figure 22 shows the distribution of normal force for Case 3 for the four analytical models. Substantial differences are seen between these results and the uniform wake calculations of Case 1. Most noticeable in this figure is the drop-off in blade lift that occurs at the blade tip for each of the analyses and, particularly for the RAE/WHL and METAR/R85 analyses, indications of vortical loading in the first and fourth quadrants.

The differences between Cases 1 and 3 are more apparent if the higher harmonics of the loading are examined, as shown in figure 23. The largely 3/rev character observed in Case 1 is now modulated, particularly towards the blade root. Except for the two CAMRAD analyses, which have essentially the same wake model, substantial difference are now seen between the various analyses.

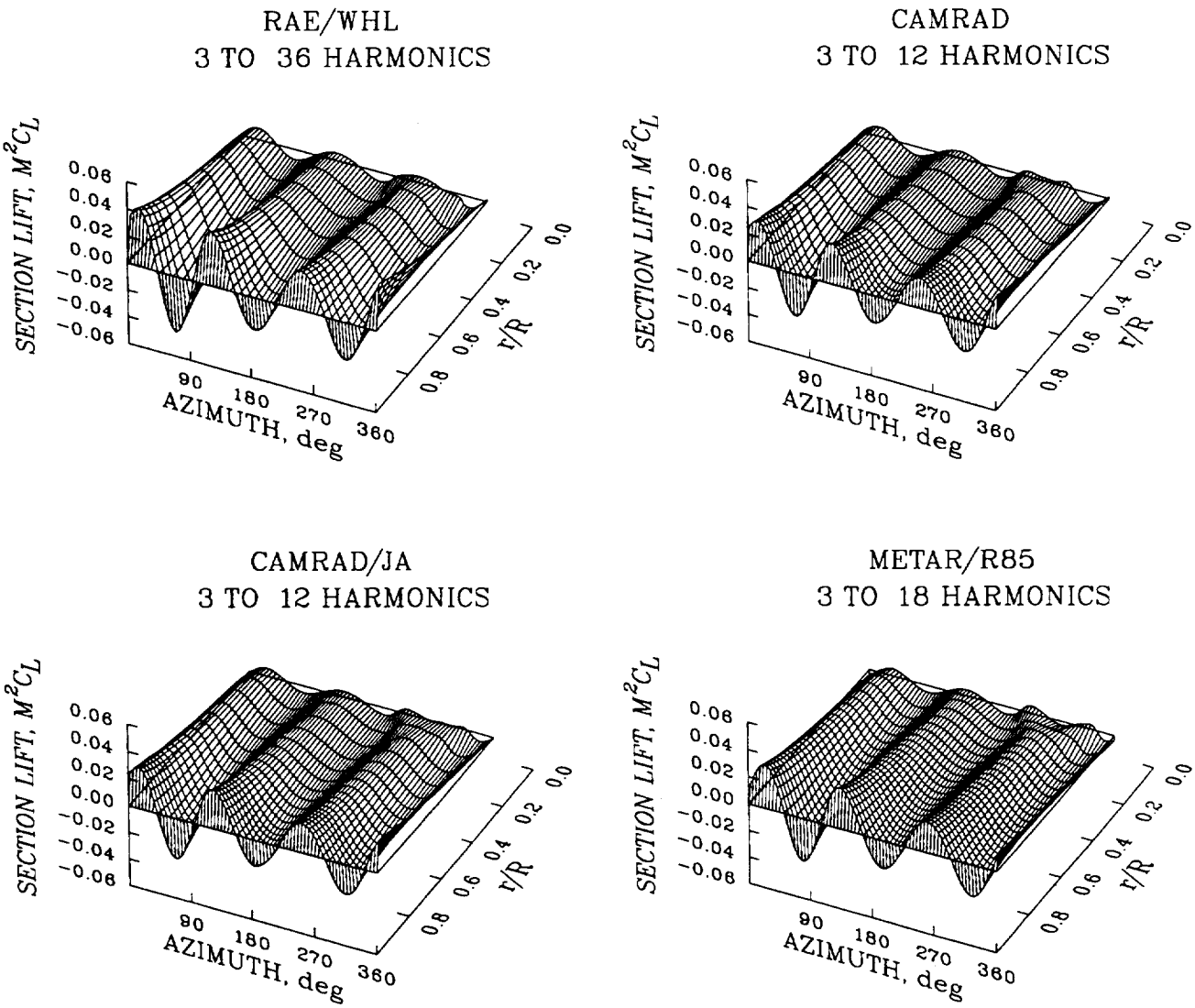


Figure 18. Normal force distribution as a function of azimuth and blade radius for Case 1; harmonics 3 and above.

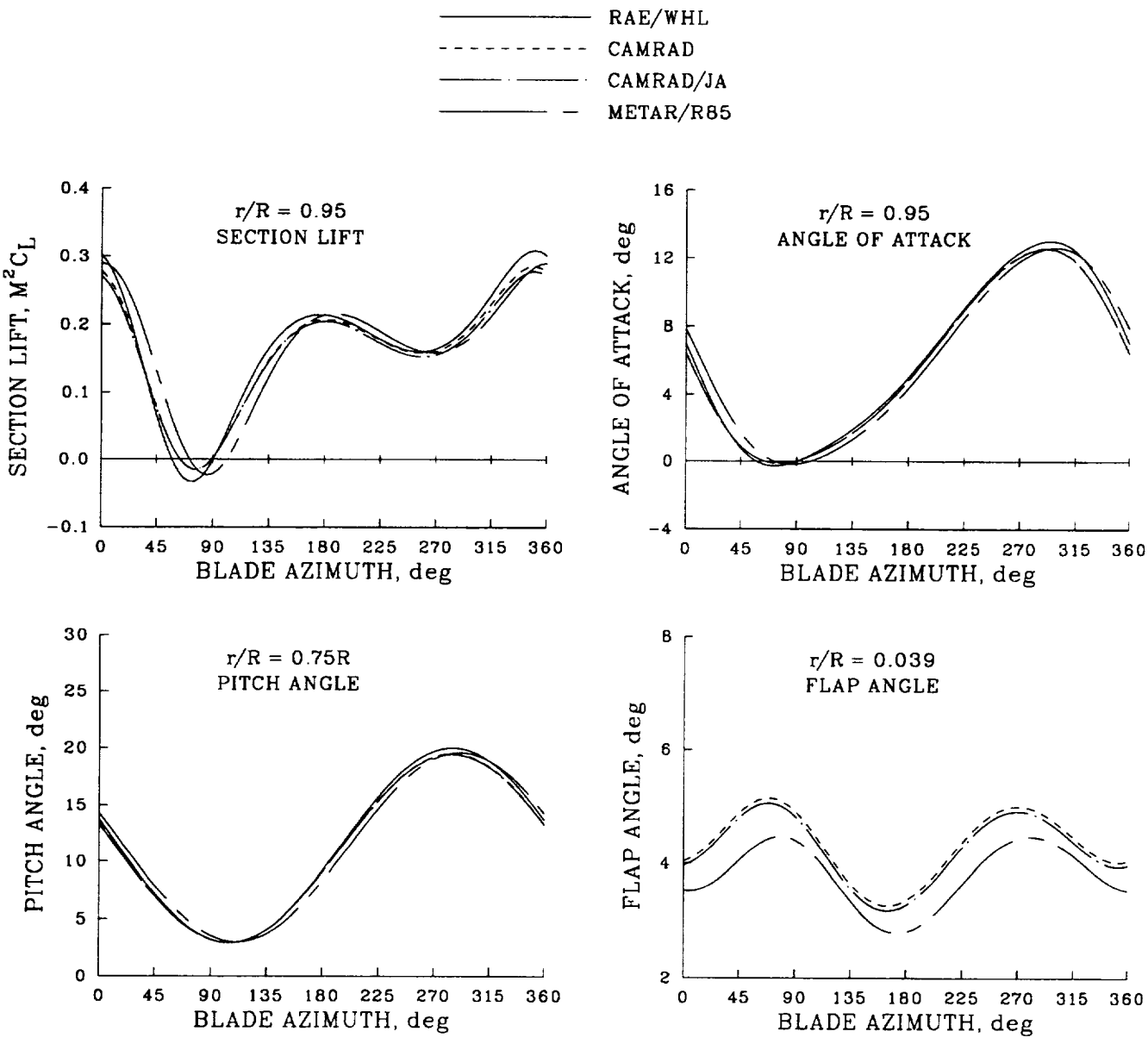


Figure 19. Comparison of analytical methods for Case 1 for four parameters; all harmonics. Flap angle not shown for the RAE/WHL analysis.

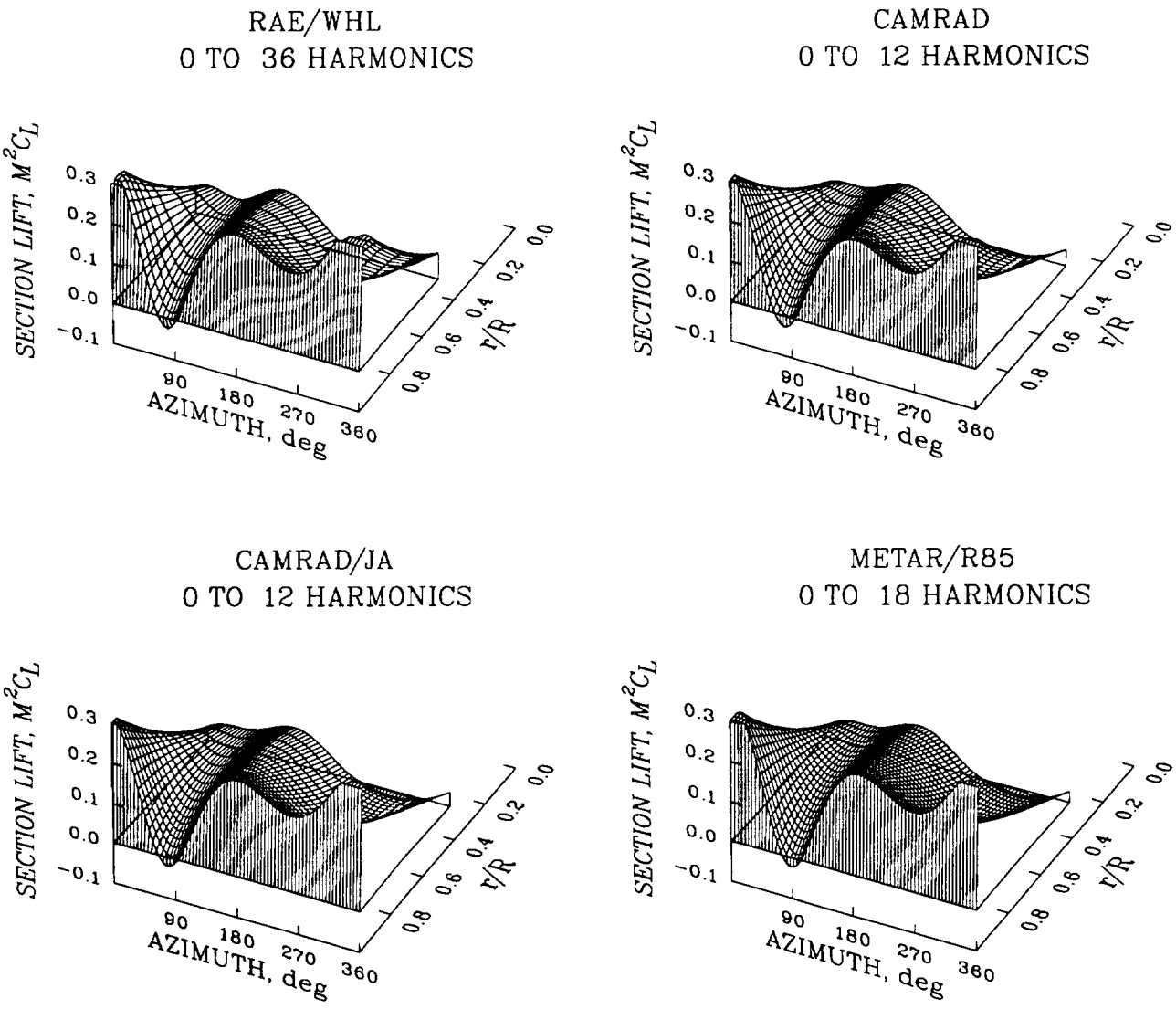


Figure 20. Normal force distribution as a function of azimuth and blade radius for Case 2; all harmonics.

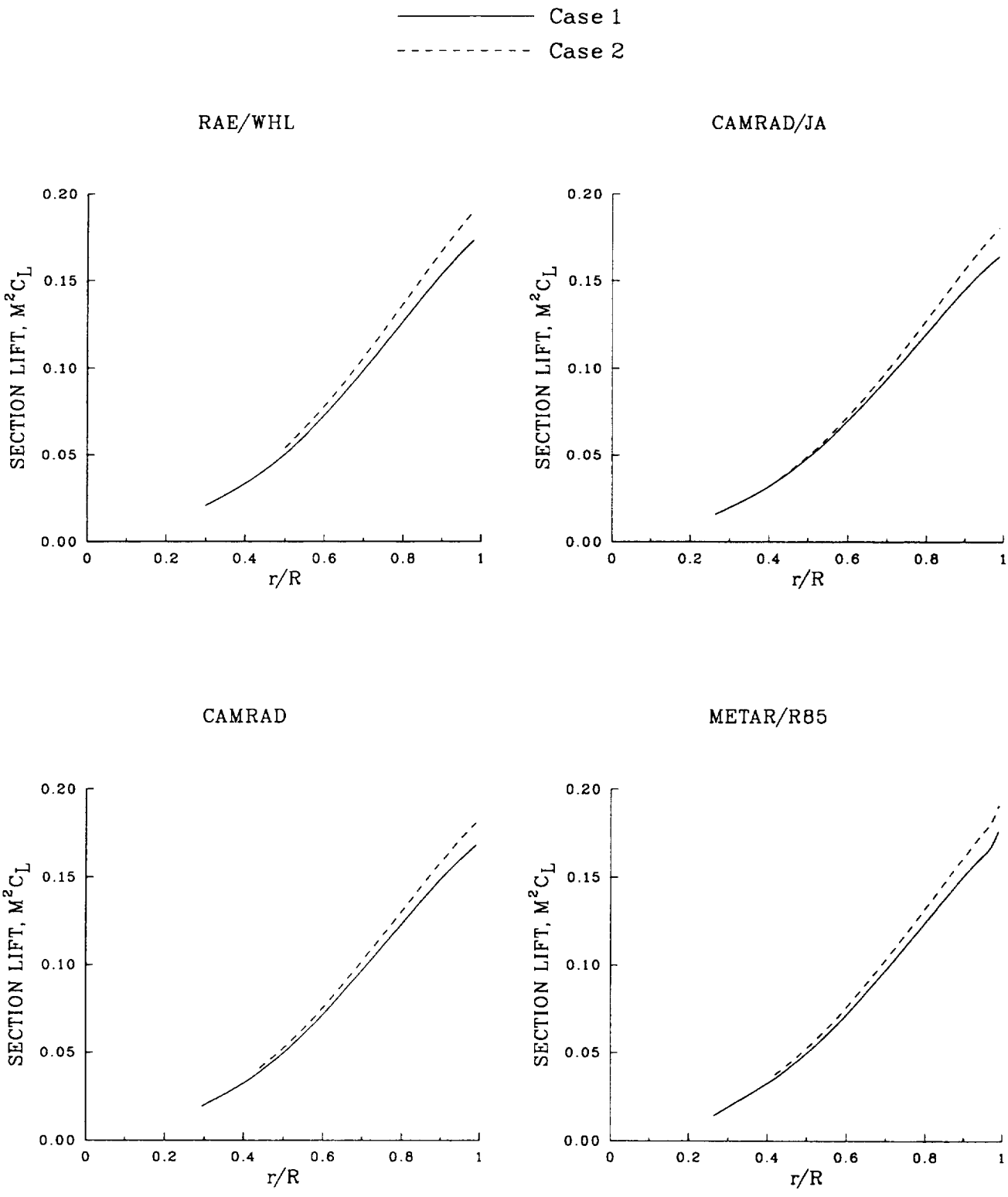


Figure 21. Comparison of radial distribution of steady normal force for Cases 1 and 2.

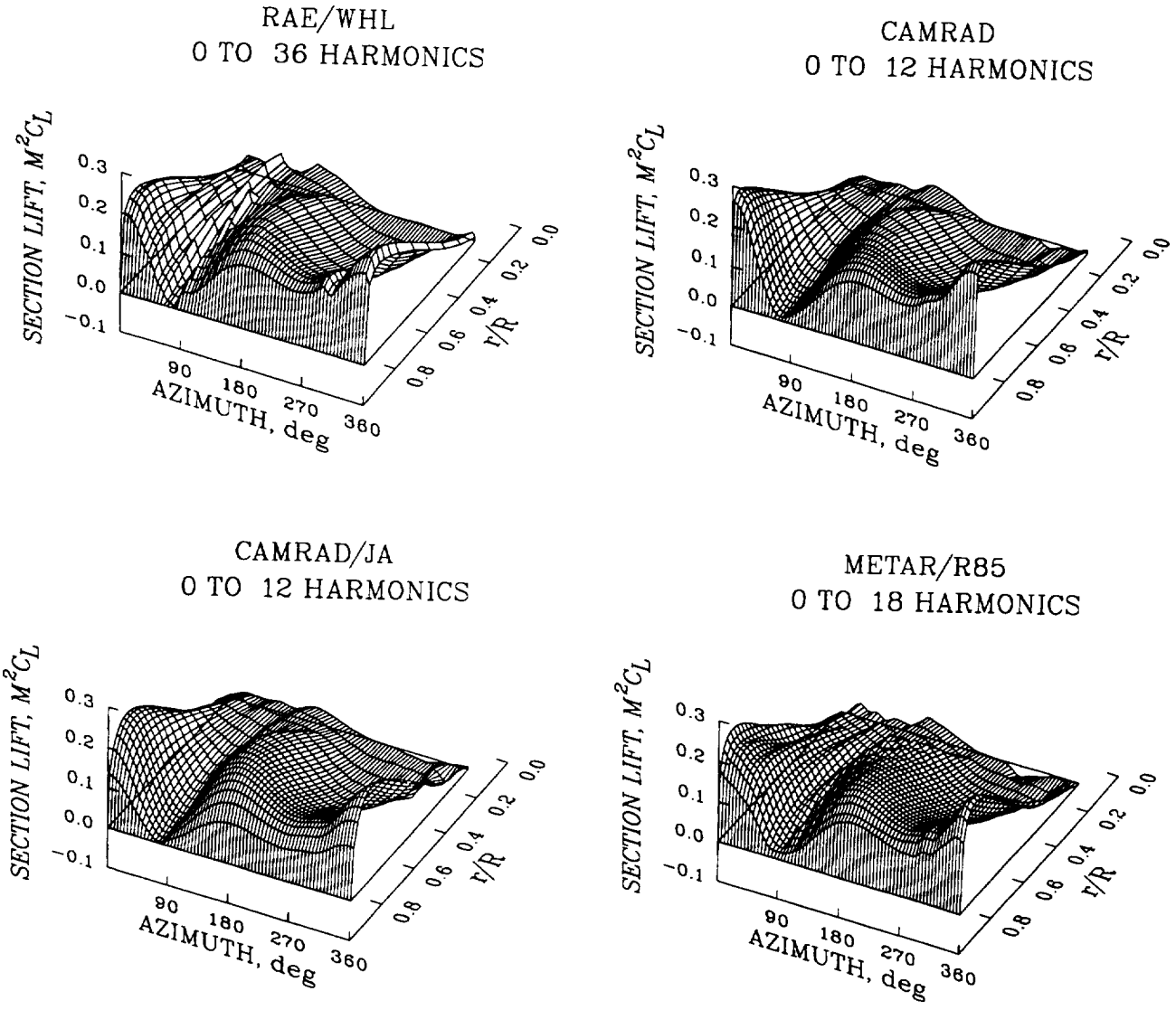


Figure 22. Normal force distribution as a function of azimuth and blade radius for Case 3; all harmonics.

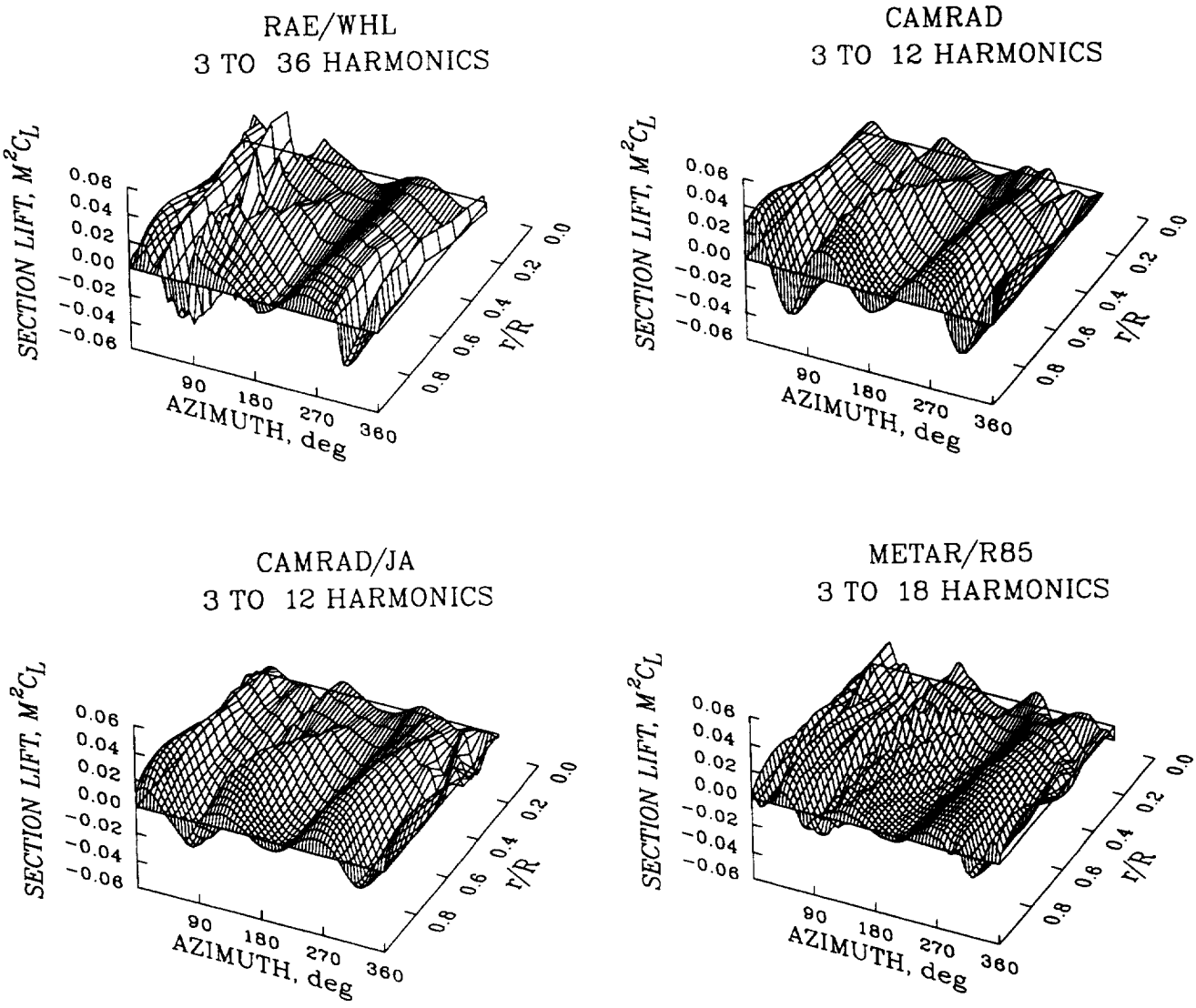


Figure 23. Normal force distribution as a function of azimuth and blade radius for Case 3; harmonics 3 and above.

The reduction in blade lift that occurs at the blade tip is a consequence of coupling of the prescribed wake to the lifting-line analysis. Figure 24 compares the radial distribution of steady normal force as computed by the four analyses. The inboard prediction of lift is similar for all methods, but the methods vary in their prediction of the lift drop-off at the blade tip. The lift predicted by CAMRAD/JA starts to decrease at $0.90R$ while the lift for CAMRAD is maintained past $0.95R$. The difference in the lift drop-off is believed to be a result of differences in the solution method. CAMRAD/JA is considered accurate to second order in its lift prediction while CAMRAD is only accurate to first order (Bousman et al., 1989). The other two methods show a drop off that is approximately halfway between the two CAMRAD predictions.

The significant changes that occur in the distribution of lift from Case 1 to Case 3 are caused by the wake model. Some insight into these changes can be obtained by looking at the angle-of-attack distributions shown in figure 25 and comparing these distributions to Case 1 (figure 17). All of the analyses show a reduction in angle of attack near the blade tip and the largely 1/rev character noted in figure 17 now includes higher harmonic effects. This is most noticeable for the RAE/WHL analysis which shows substantial changes in the angle of attack in the first and fourth quadrants caused by vorticity in the wake. This is seen in the other analyses as well, but is more subdued. A detailed comparison between Cases 1 and 3 is shown in figure 26 for the $0.85R$ radial station. The steady and first harmonic angle-of-attack variation has been removed in this figure to better illustrate the effects of the prescribed wake model. Each of the analyses shows a substantial variation in angle of attack

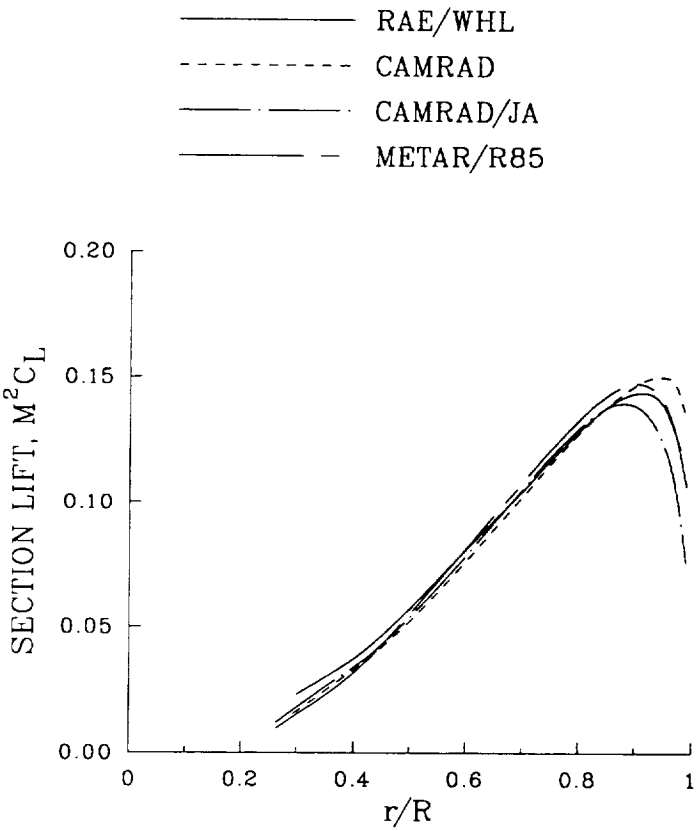


Figure 24. Comparison of the radial distribution of steady normal force for Case 3.

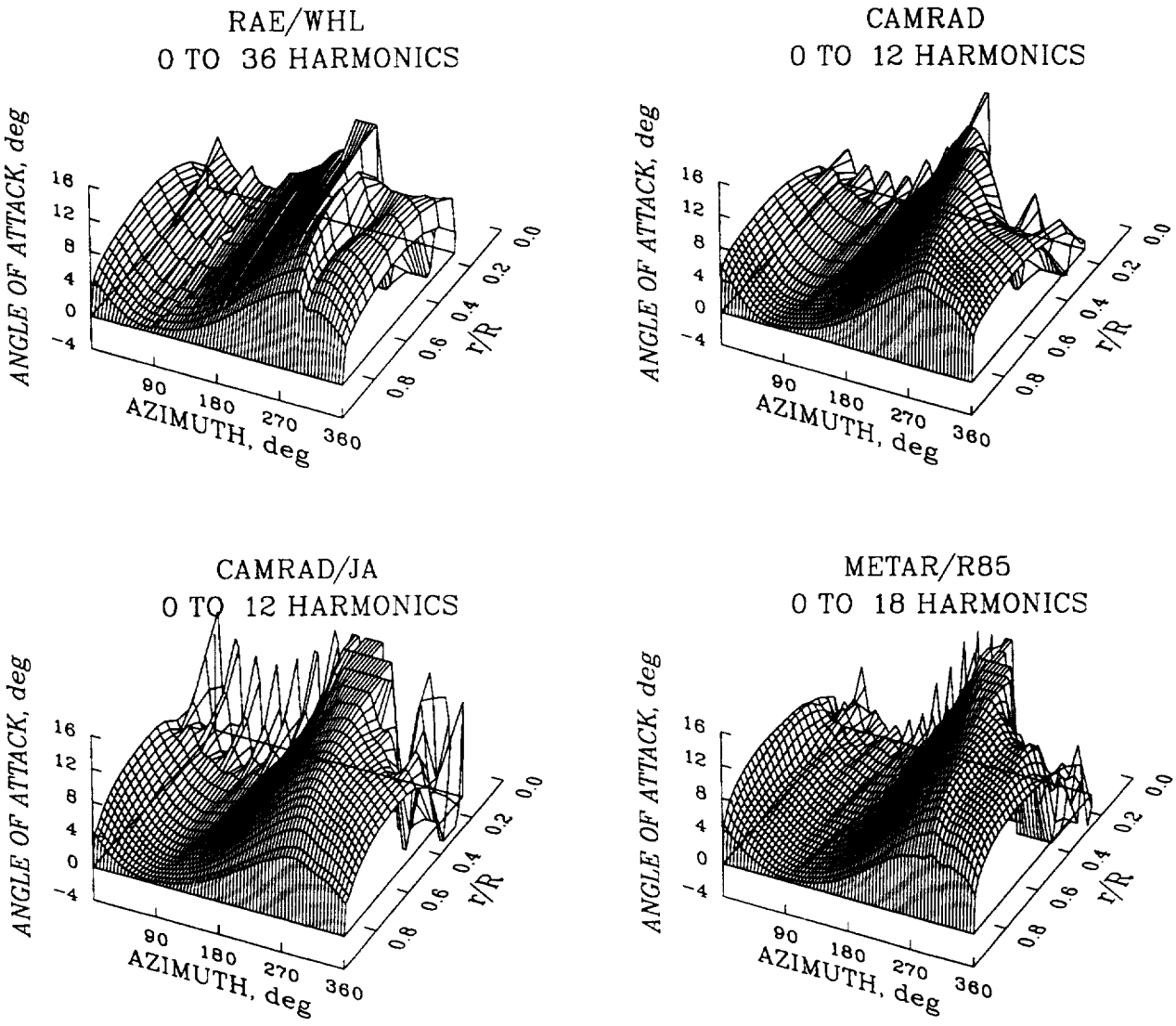


Figure 25. Angle-of-attack distribution as a function of azimuth and blade radius for Case 3; all harmonics.

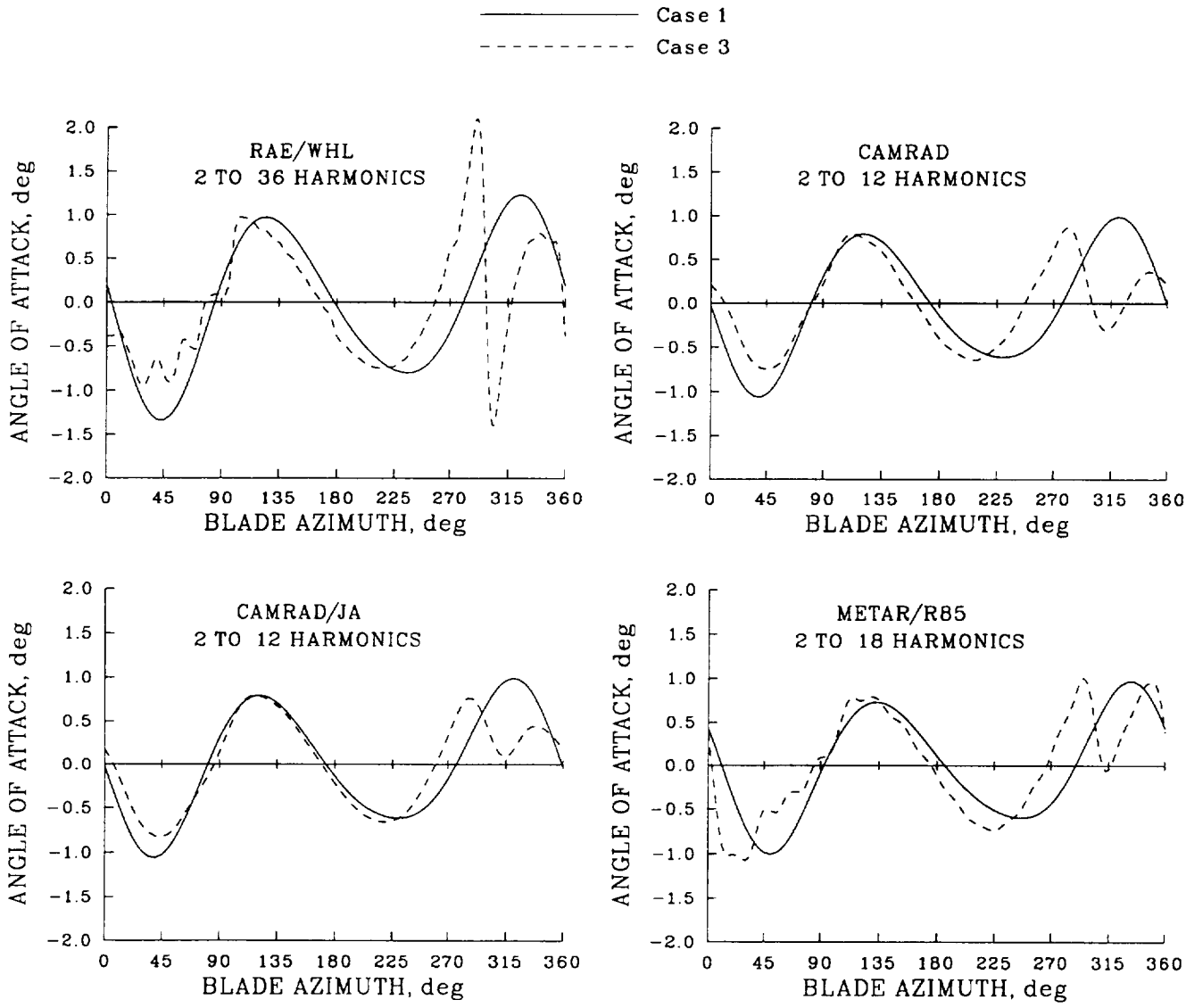


Figure 26. Comparison of angle-of-attack distribution as a function of azimuth for Cases 1 and 3; $0.85R$, harmonics 2 and above.

on the retreating side of the disk caused by the vorticity from the previous blades. The variation in angle of attack occurs at about $\psi = 300°$ at this blade radius and appears first as an upwash and then a downwash. In the case of the RAE/WHL analysis the change in angle of attack is much larger than is seen with the vortex-lattice methods.

The RAE/WHL analysis also shows the effects of discrete vortex loading on the advancing side and this is seen as well in the METAR/R85 prediction, but to a lesser extent. For this radial station the effects of at least four tip vortices are seen in the first quadrant. The higher frequency, vortical loading computed with the wake models in the RAE/WHL and METAR/R85 analyses is partly a result of the smaller azimuthal stepsize used in the solution: 5° for the RAE/WHL analysis and 10° for the

METAR/R85 analysis. However, most of the effects shown here are retained even if only the first 12 harmonics of the angle of attack are plotted.

*Case 4*

The distribution of the airloads for Case 4 is shown in figure 27. This case differs from Case 3 in that the root cutout is changed from $0.228R$ to $0.40R$. The effect of increasing the root cutout is to slightly increase the steady lift on the blade but, in general, these effects are slight. The differences between the two $0.40R$ root cutout cases, Case 2 and Case 4, are essentially the same as seen in comparing Cases 1 and 3.

*Case 5*

Case 5 differs from Case 3 in that the aerodynamic forces and moments on the blade are computed using nonlinear aerodynamics rather that the linear model. Figure 28 shows the distribution of normal force for Case 5 for the four analytical models. The normal force distributions are essentially unchanged from Case 3 (see figure 22), indicating that the blade is operating largely in the linear aerodynamic regime, at least as far as the normal force or lift is concerned. Using a slice of data at $0.85R$, the effects of the modeling change are examined by comparing the Case 5 results with Case 3 in figure 29. Except for a slight increase in normal force for the CAMRAD/JA calculations the results are the same for the two cases.

The angle-of-attack distribution is also essentially unchanged from Case 3 as indicated by the surface plot in figure 30. Comparing the Case 5 results with Case 3, figure 25, slight changes are seen inboard in the third quadrant for the CAMRAD analyses and METAR/R85, where the dynamic pressure is low and the airloads are small. Note that the calculated angles of attack in these plots are not plotted beyond the scale limits and this results in a squared-off or clipped appearance to the angle-of-attack distributions. The computed angles of attack at $0.85R$ are compared in figure 31 where the steady and first harmonic have been removed to accentuate the effects of higher harmonics. Except for small differences in the fourth quadrant of the CAMRAD/JA calculation no effect of nonlinear aerodynamics is seen in the calculation of angle of attack.

The distribution of the section pitching moment is shown in figure 32 for the four analyses. The largest pitching moments are observed near the blade tip in the first and second quadrants. There are some surprising differences between the analyses, considering that the computed moments are based solely on steady airfoil section properties and, for many angles of attack, the same airfoil section properties were used by the four analyses. The angle of attack, near the blade tip, approaches zero near 90°, where the Mach number is a maximum, but is positive on either side of 90°. The airfoil section pitching moment behavior in Section 4.2 shows that the pitching moment becomes quite negative for $M > 0.7$ at angles of attack greater than zero so the two-humped behavior shown by the CAMRAD analyses and METAR/R85 appears to result from the compensating effects of the decrease in angle of attack and the increase in Mach number as the azimuth approaches 90°. It is believed that the positive moment in RAE/WHL analysis is a result of a coding error.

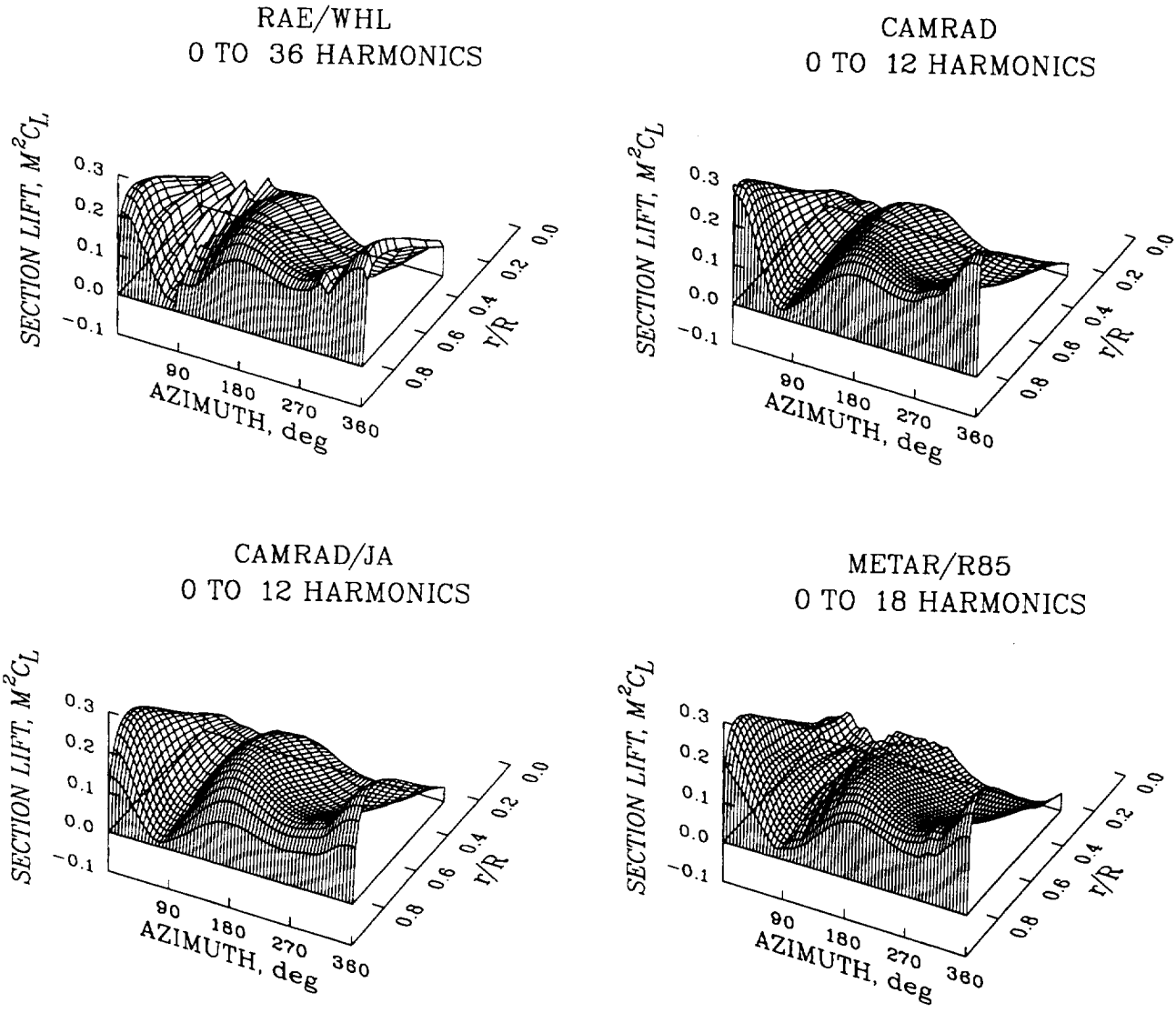


Figure 27. Normal force distribution as a function of azimuth and blade radius for Case 4; all harmonics.

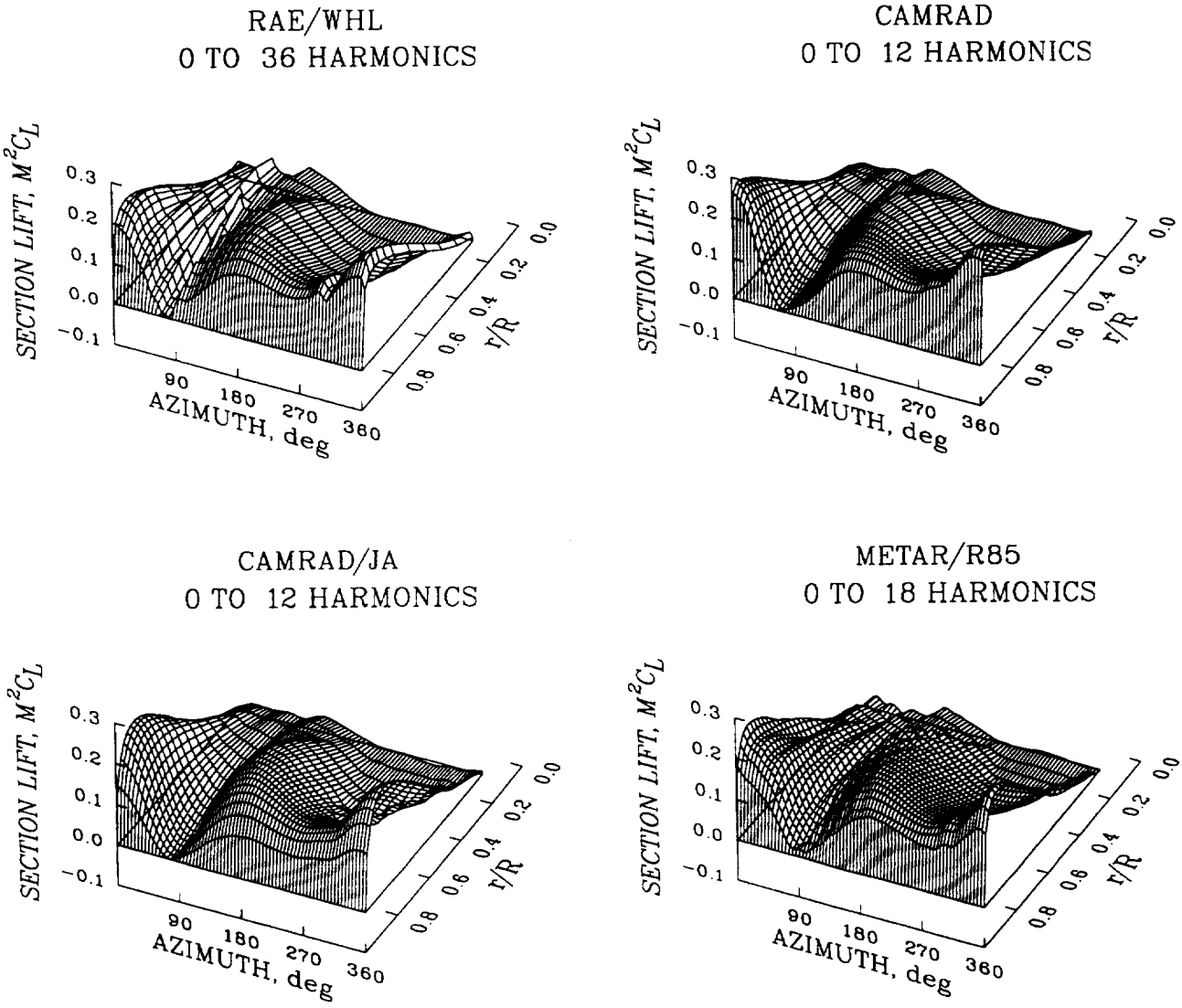


Figure 28. Normal force distribution as a function of azimuth and blade radius for Case 5; all harmonics.

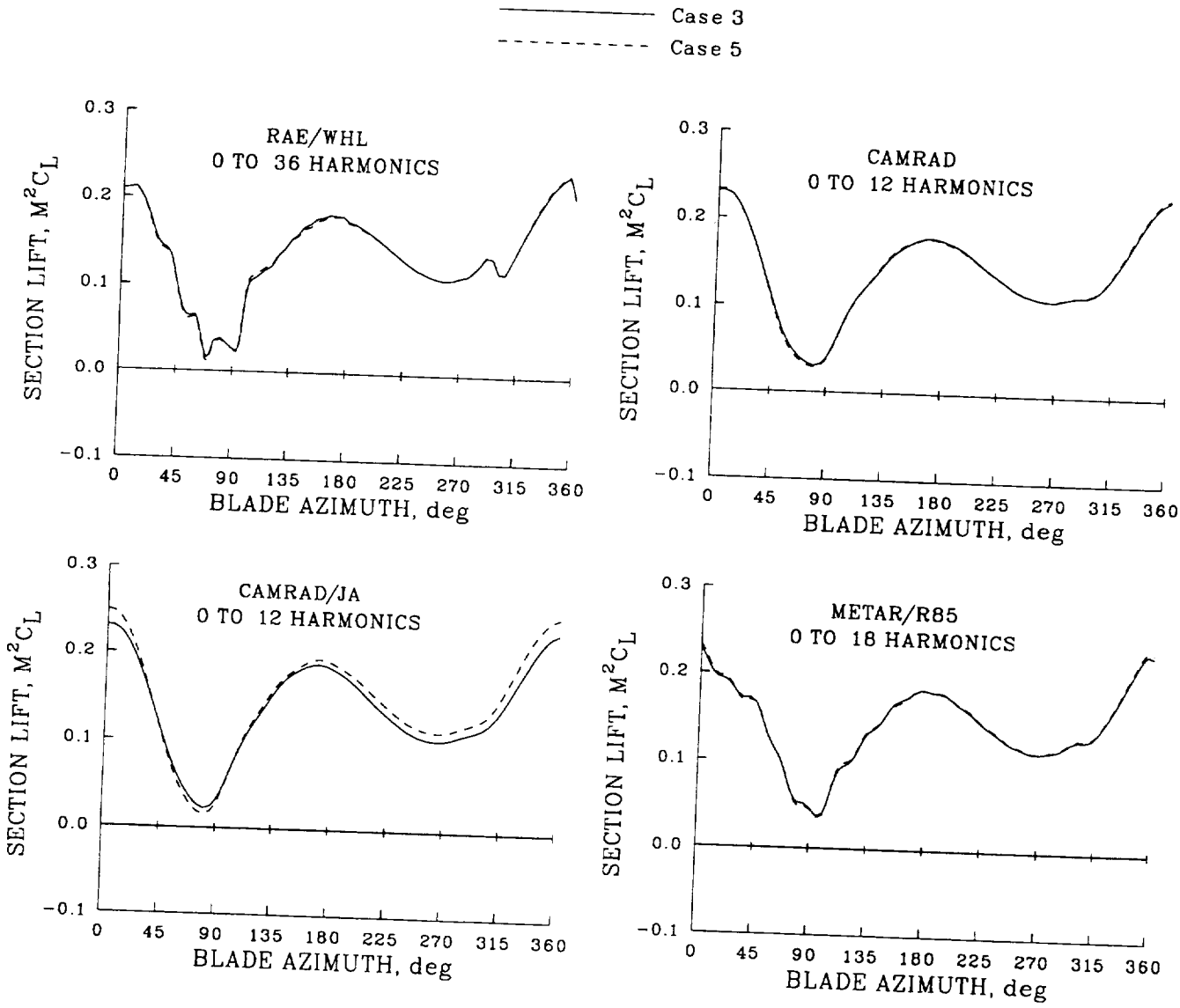


Figure 29. Comparison of normal force distribution as a function of azimuth for Cases 3 and 5; $0.85R$, all harmonics.

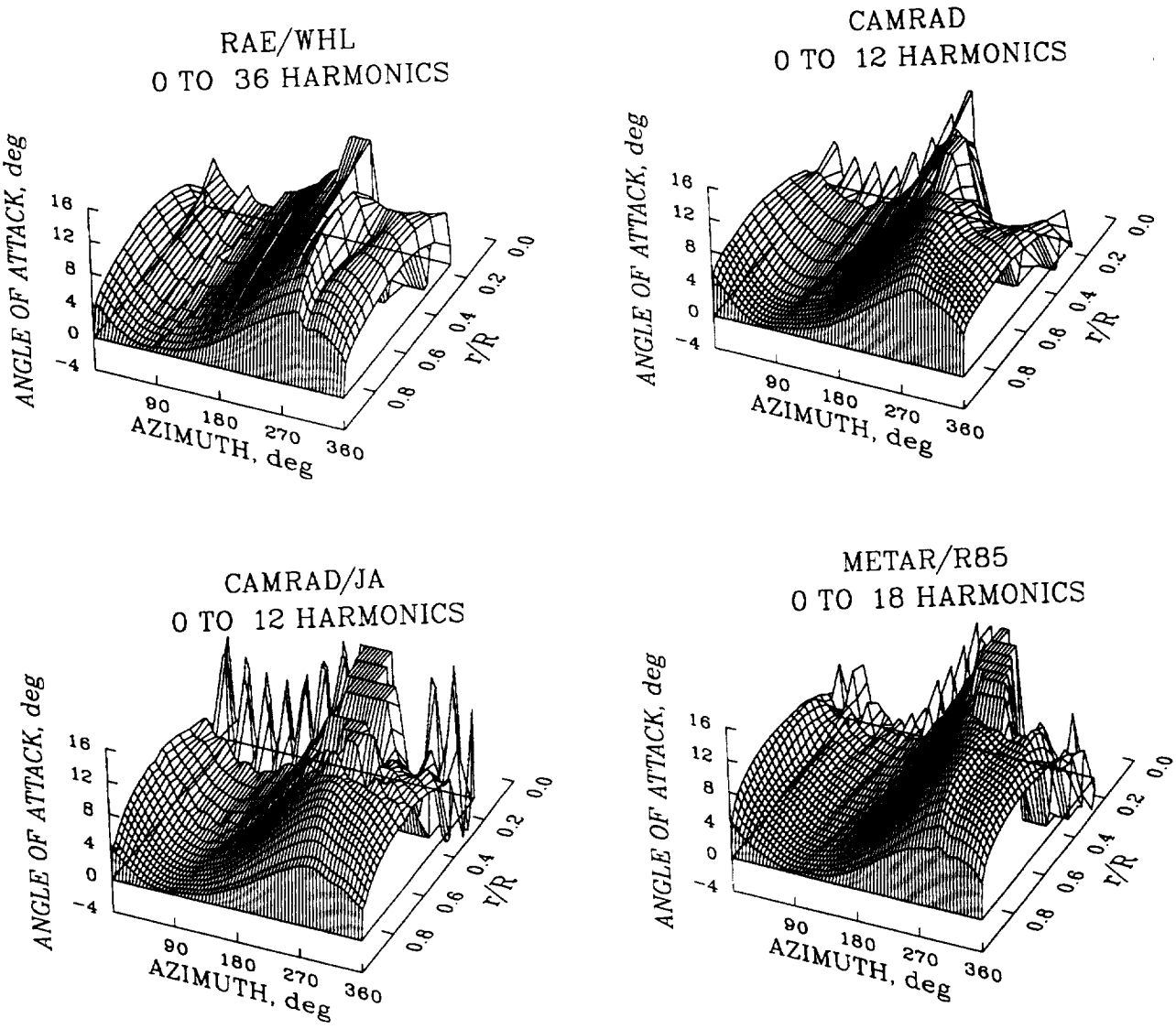


Figure 30. Angle-of-attack distribution as a function of azimuth and blade radius for Case 5; all harmonics.

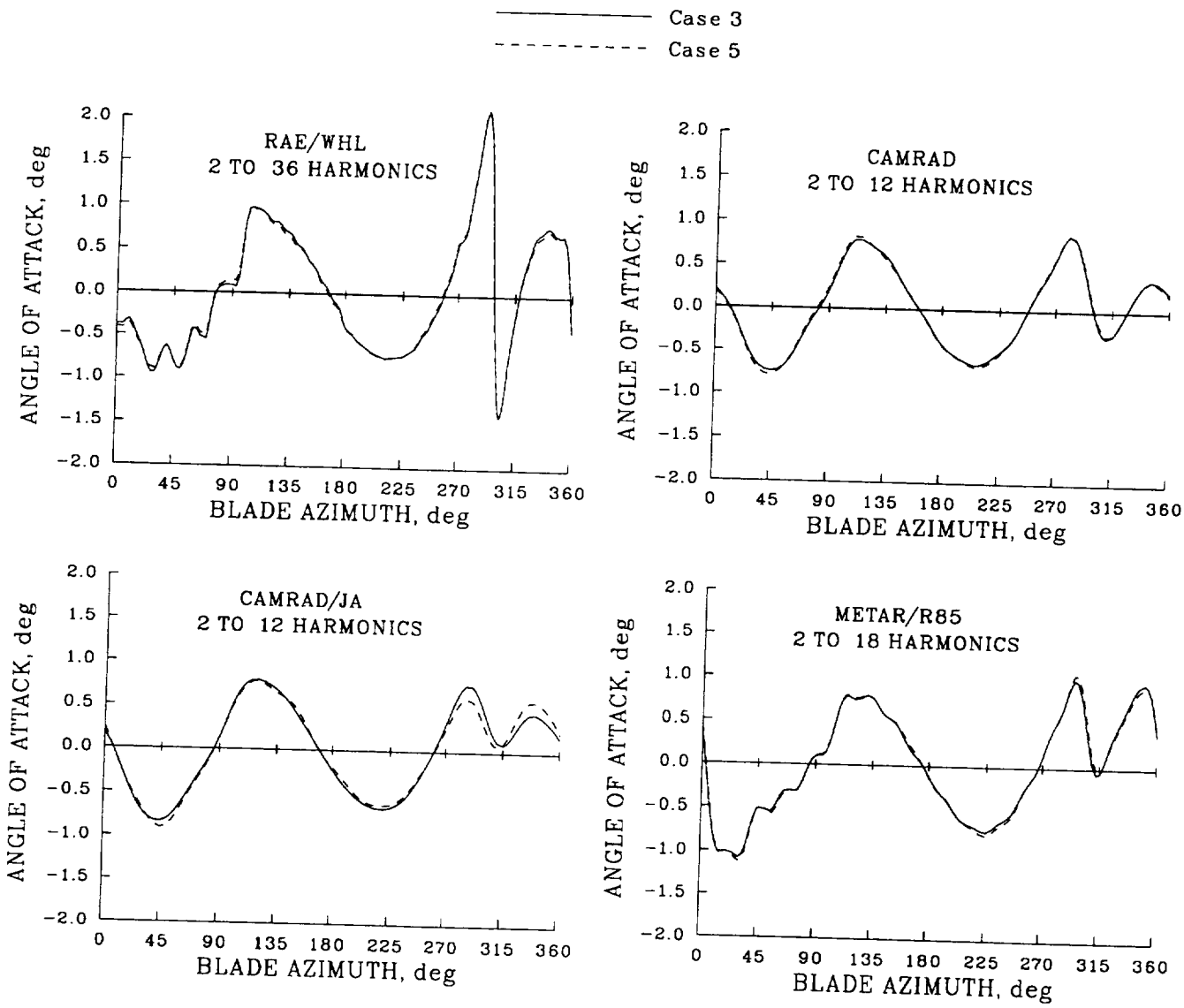


Figure 31. Comparison of angle of attack as a function of azimuth for Cases 3 and 5; $0.85R$, harmonics 2 and above.

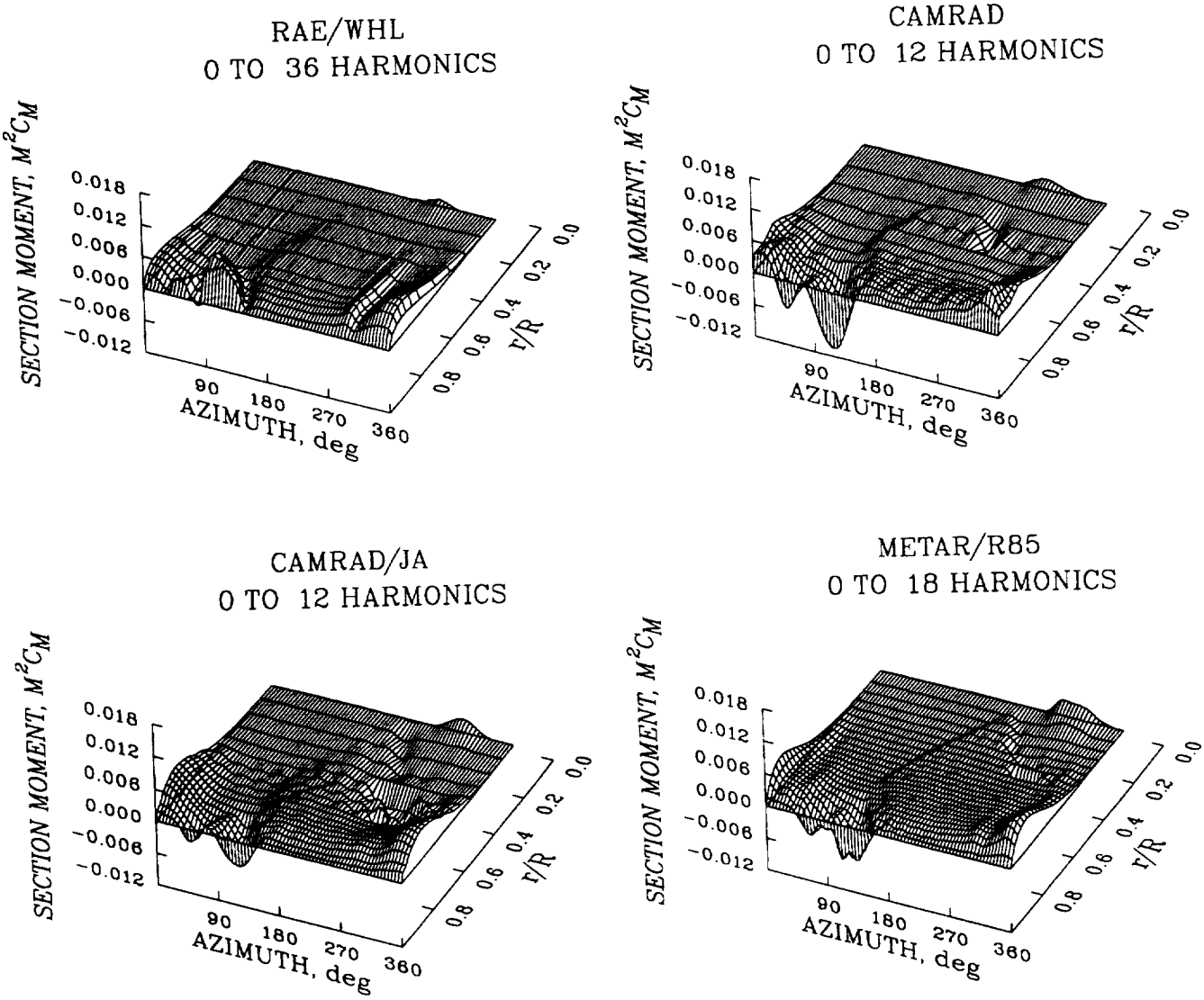


Figure 32. Section pitching moment distribution as a function of azimuth and blade radius for Case 5; all harmonics.

The blade tip pitching moment is examined in greater detail in figure 33 where the angle of attack and pitching moment are plotted as functions of rotor azimuth at $0.98R$. The angle of attack is decreasing in the first quadrant and, as the angle nears one degree, there is a rapid decrease in the moment for the CAMRAD predictions while the RAE/WHL analysis shows a positive moment. These moments reduce to zero at about 70°, where the angle of attack is zero, and then increase again as the angle of attack becomes more positive. At about 135° the Mach number has decreased and the moment returns to a nominal value. The difference in behavior for these analyses looks like an error in the coefficient sign, but this cannot be true in a global sense as all the analyses show the positive moment that occurs in the fourth quadrant inboard on the blade in the reverse flow region (see figure 32).

The nonlinear aerodynamic tables used by the CAMRAD analyses and METAR/R85 are, as mentioned before, based on the RAE/WHL equations described in Section 4.2. However, these equations are only used for angles of attack below the stall boundary defined in table 3. Above the stall boundary the section coefficient data are based on the C81 NACA 0012 deck that is valid for all angles of attack (Davis, 1974). Above the stall boundary, each analyst faired or patched the RAE/WHL equations into the C81 deck and, in some cases, there may be small perturbations in the section properties at these boundaries. Figure 34 shows the $C_L$ values computed by the four analyses at two radial stations as a function of the section Mach number. This figure includes an overplot of the angles of attack from the NACA 0012 deck that provide the equivalent $C_L$. In addition, the RAE/WHL stall boundary is plotted on these figures to show the range of applicability of the RAE/WHL equations. Near the blade tip, all of the analyses predict that the computed angles of attack and Mach number are within the domain of the RAE/WHL equations and, therefore, the analytical predictions are directly comparable. Inboard, at $0.60R$, however, the analyses show that angles of attack are reached on the retreating side that exceed

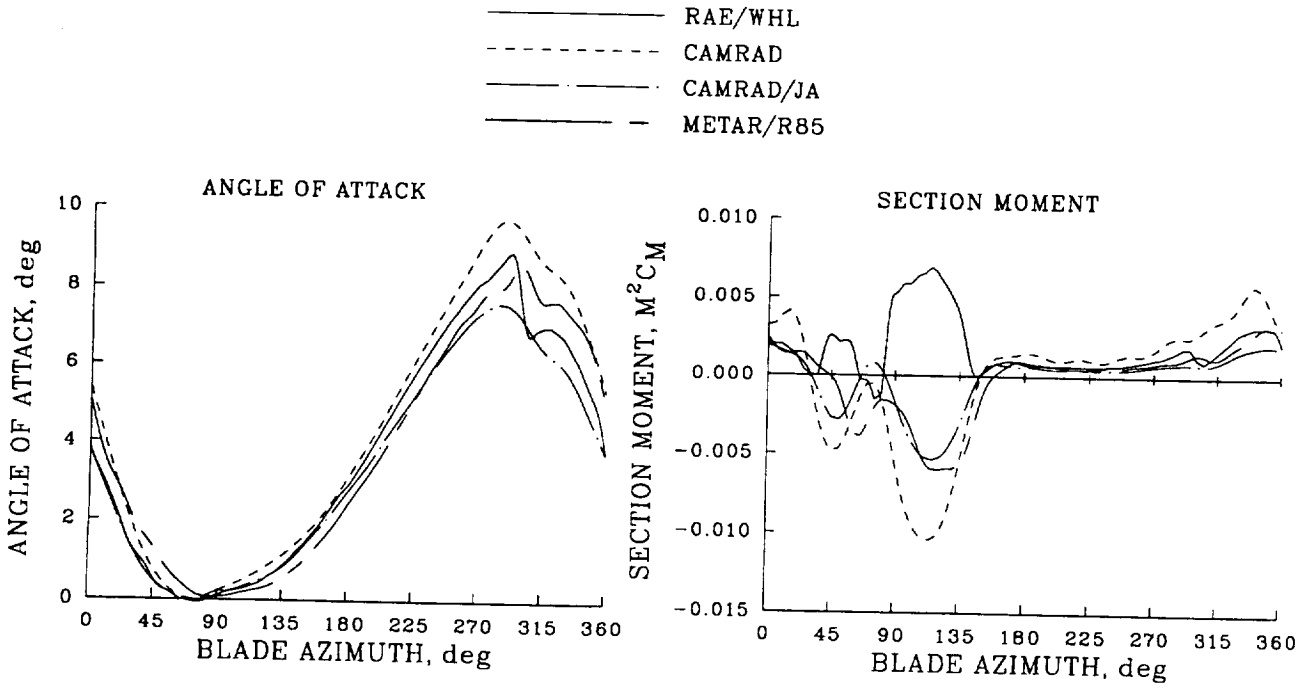


Figure 33. Angle-of-attack distribution and section pitching moment as a function of azimuth for Case 5; $0.98R$.

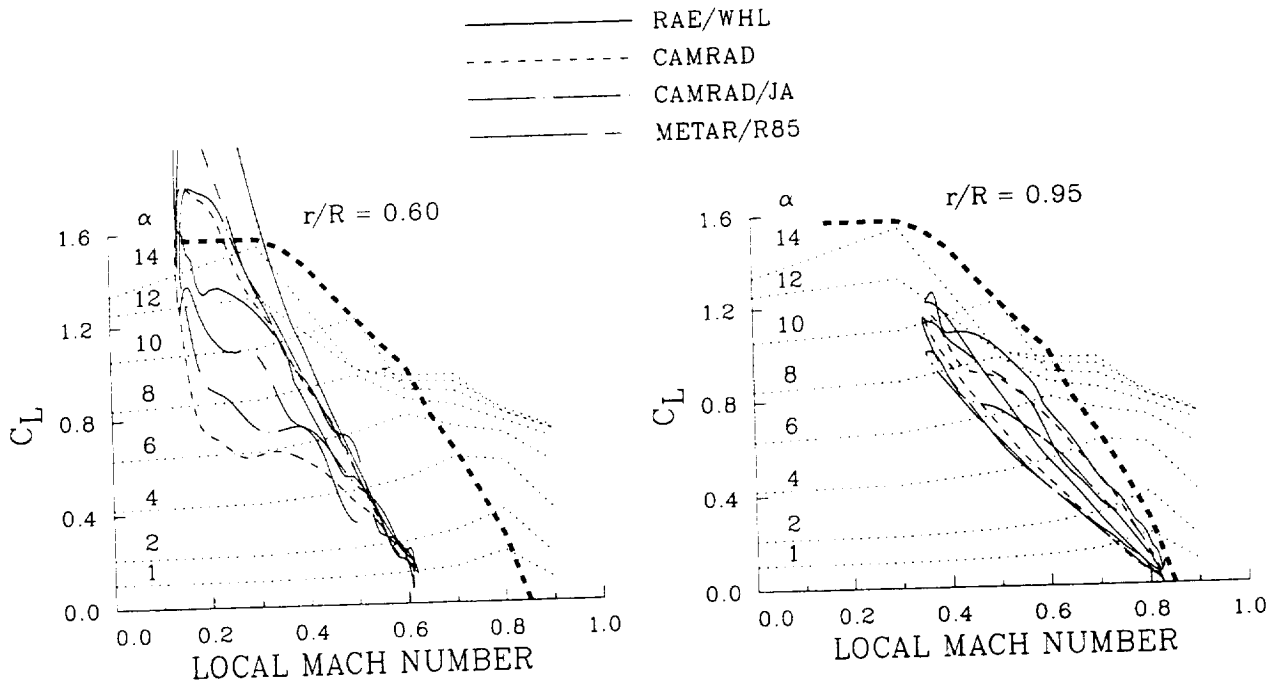


Figure 34. Normal force and Mach number distributions at two radial stations and comparison with RAE equation stall boundary (heavy dashed line). Two-dimensional section lift at constant angle of attack shown as dotted lines.

the RAE/WHL stall boundary and, in these cases, differences may occur in predicted results that are a consequence of differences in the tables (or equations) used.

*Case 6*

The distribution of the airloads for Case 6 is shown in figure 35. This case differs from Case 5 in that the root cutout is changed from $0.228R$ to $0.40R$. The effect of increasing the root cutout is to slightly increase the steady lift on the blade but, in general, these effects are slight. The differences between Cases 4 and 6, due to the addition of nonlinear aerodynamics, are essentially the same as the differences between Cases 3 and 5.

*Case 7*

Case 7 differs from Case 5 in that the computation of the aerodynamic forces on the blade includes unsteady aerodynamic terms in the equations. As with Case 5, the analyses used the same section coefficient data to compute the steady aerodynamic forces and moments, but the unsteady aerodynamic computation is different for each analysis. Figure 36 shows the distribution of normal force for Case 7 for the four analytical models. The normal force distributions are essentially unchanged from Case 5 (see figure 28), indicating that, for these conditions, unsteady aerodynamics do not significantly influence the blade lift. Again, a slice of data at $0.85R$ is examined in figure 37 to look in detail at the effects of adding the unsteady aerodynamics terms. The RAE/WHL and CAMRAD analyses show minor differences in the lift around the azimuth, and a slight reduction in the lift variation caused by the

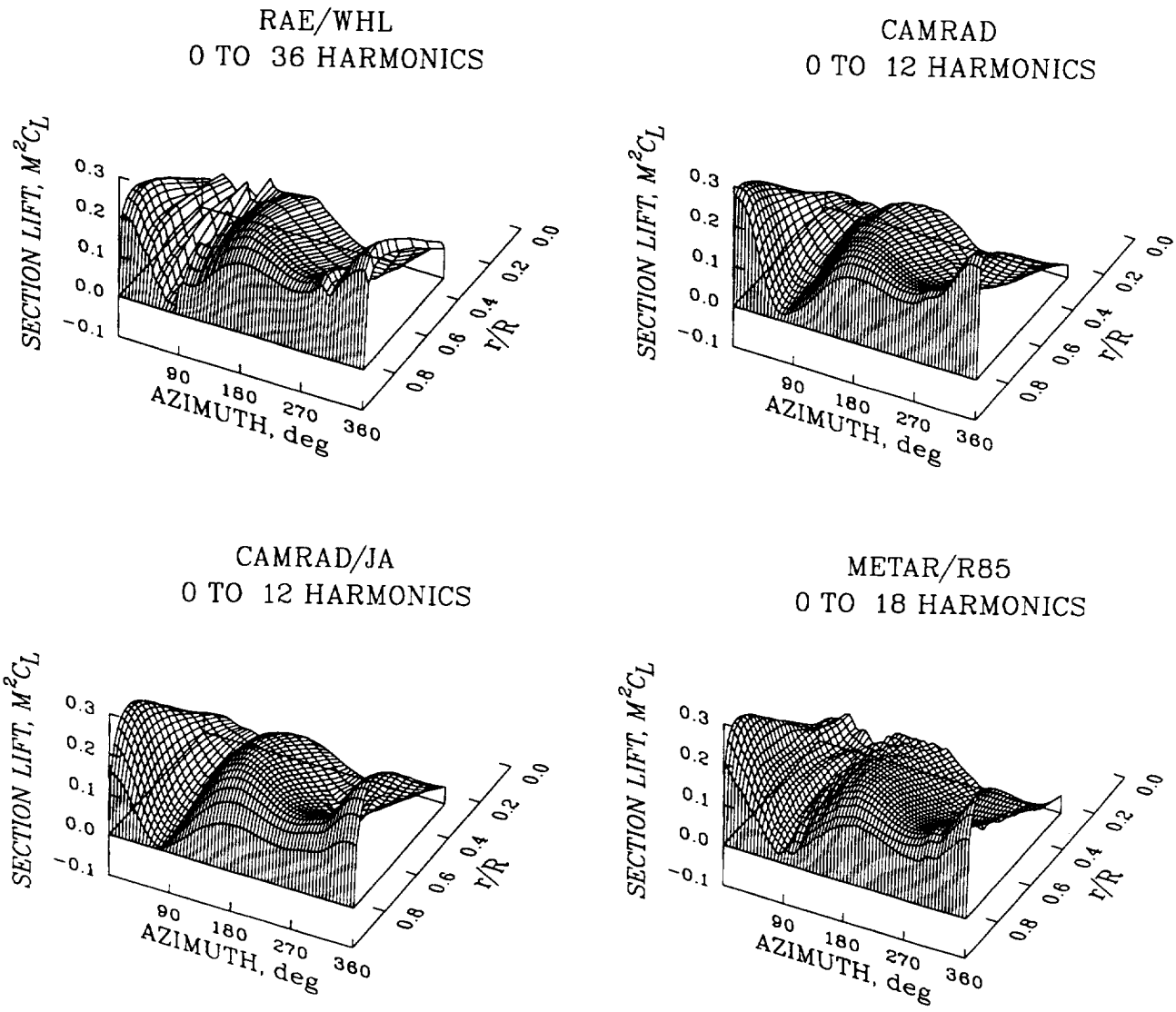


Figure 35. Normal force distribution as a function of azimuth and blade radius for Case 6; all harmonics.

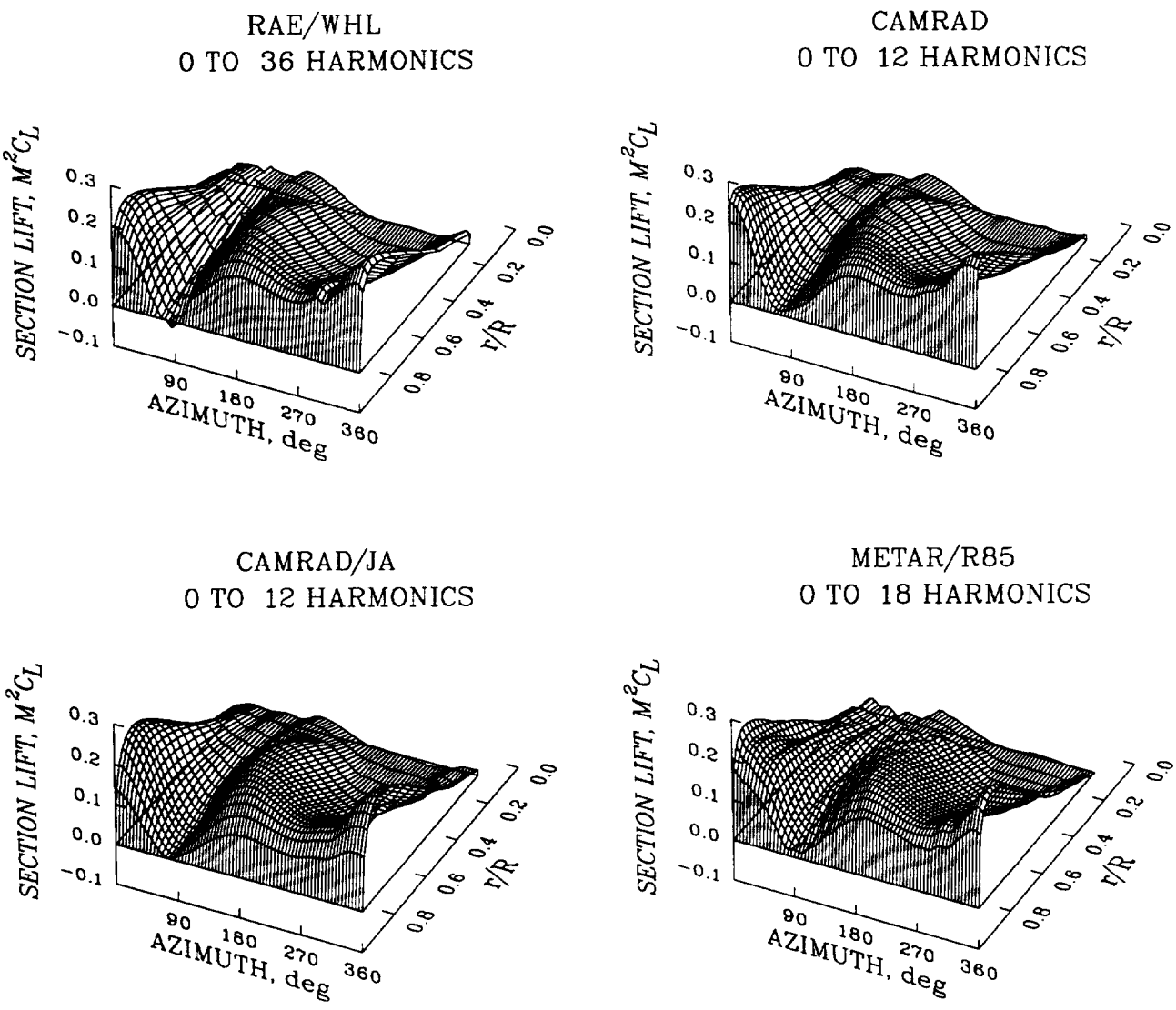


Figure 36. Normal force distribution as a function of azimuth and blade radius for Case 7; all harmonics.

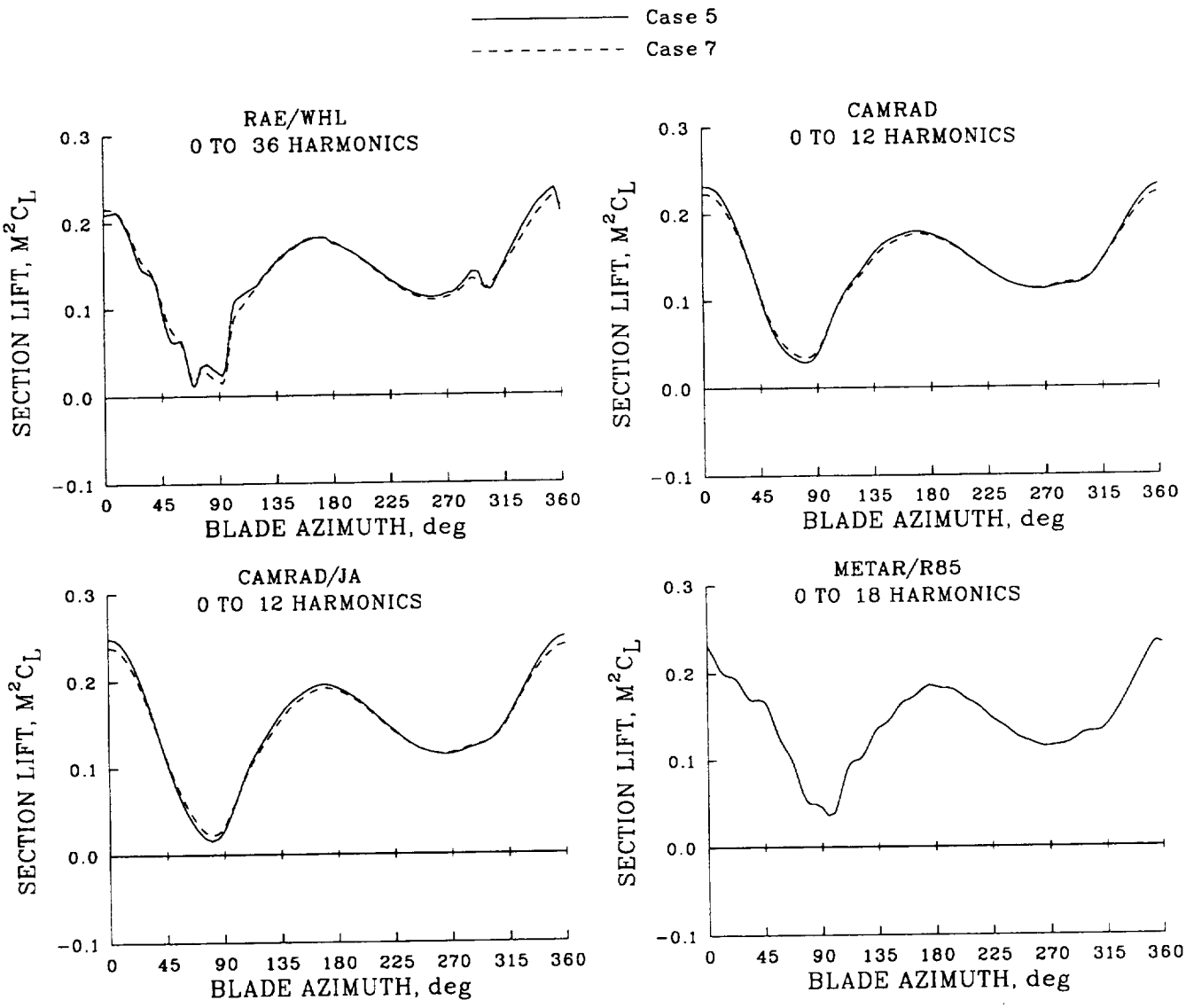


Figure 37. Comparison of normal force distribution as a function of azimuth for Cases 5 and 7; $0.85R$, all harmonics.

tip vorticity of previous blades is apparent in the RAE/WHL analysis. METAR/R85 does not include unsteady lifting terms in its equations so no difference is seen for this analysis between the two cases.

The angle-of-attack distribution is also essentially unchanged from Case 5 as indicated by the surface plot in figure 38. Comparing the Case 7 results with Case 5, figure 30, slight changes are seen inboard in some of the calculations but the dynamic pressure is quite low at these locations and the effect of angle-of-attack changes is slight. The computed angles of attack at $0.85R$ are compared in figure 39 where the steady and first harmonic have been removed to accentuate the effects of higher harmonics. The RAE/WHL analysis shows a slight reduction in the loading caused by blade tip vorticity from previous blades while the other analyses show little effect of the modeling change for this radial station.

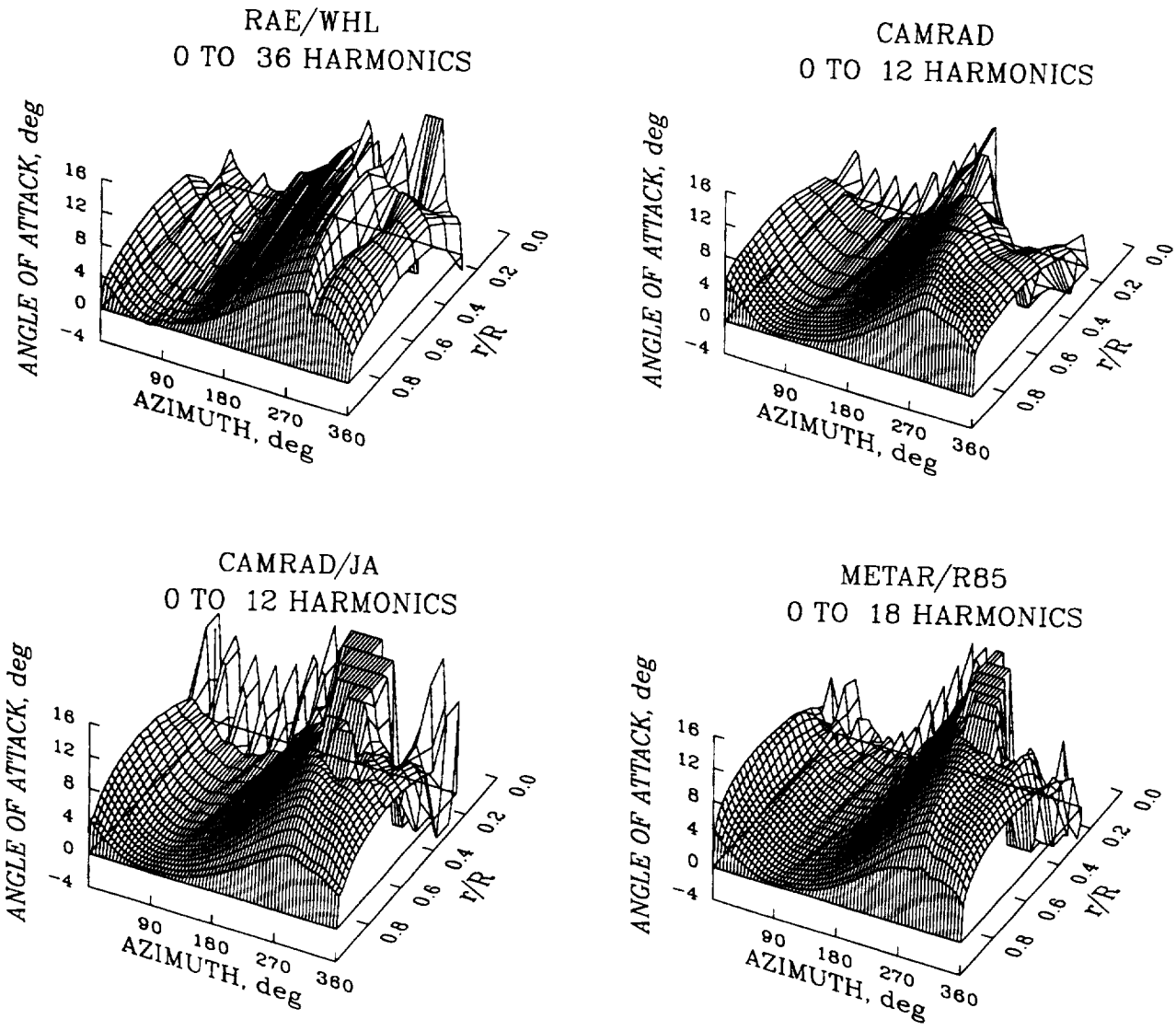


Figure 38. Angle-of-attack distribution as a function of azimuth and blade radius for Case 7; all harmonics.

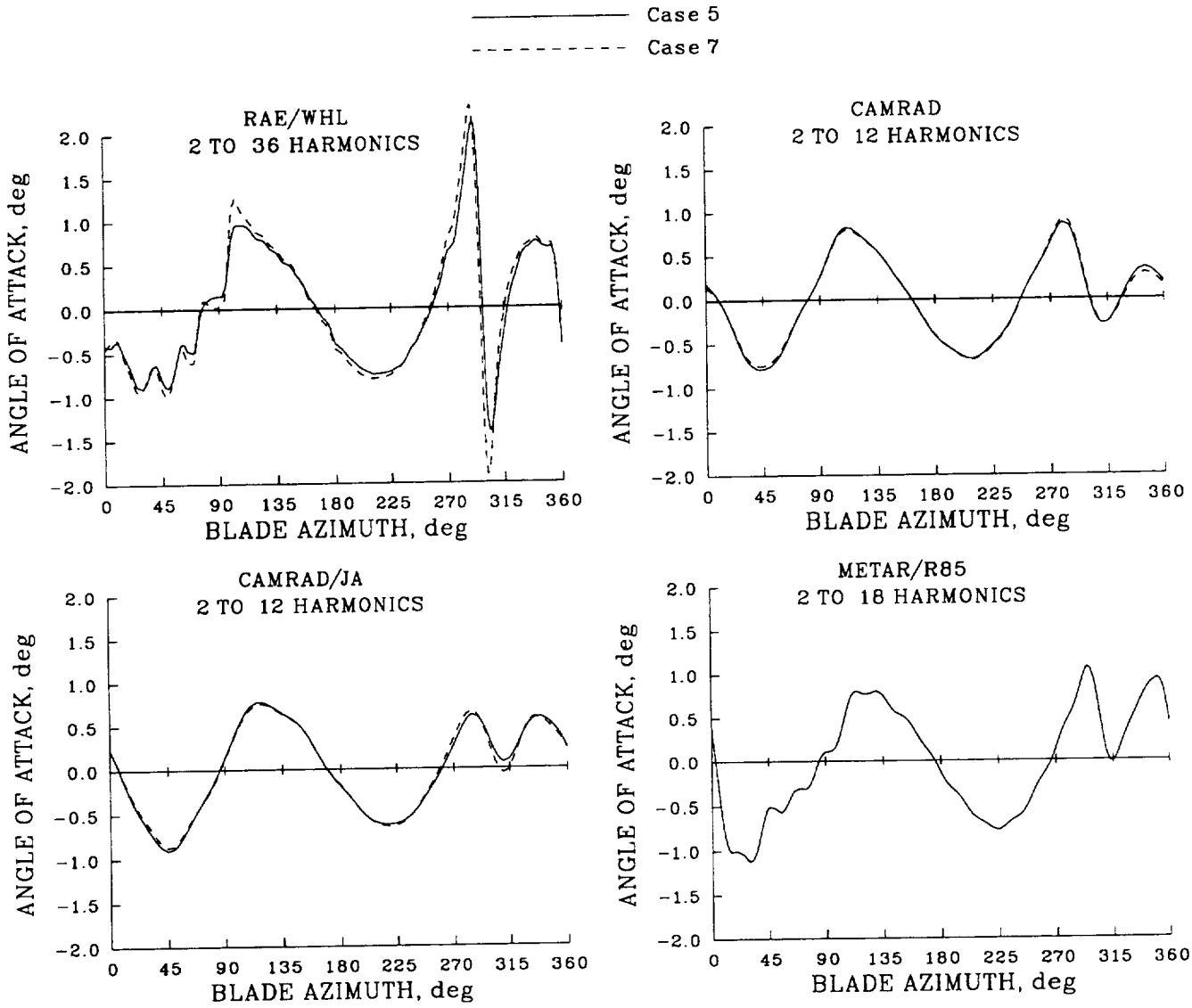


Figure 39. Comparison of angle of attack as a function of azimuth for Cases 5 and 7; $0.85R$, harmonics 2 and above.

The distribution of the section pitching moment is shown in figure 40 for the four analyses. The effects of including unsteady aerodynamics on the section pitching moments are substantial for all of the analyses; compare with Case 5, figure 32. These changes are interesting considering the absence of any observed differences in the lift distribution and suggest that the most important effects of unsteadiness are in the blade pitch rate terms. These changes, which are greatest near the blade tip, are examined in detail in figure 41. The RAE/WHL analysis shows a reversal in the pitching moment near the blade tip due to unsteady aerodynamics and this change is quite substantial—larger than the effects of unsteadiness seen in the other analyses. The CAMRAD analyses and METAR/R85 show similar effects, with a slight increase in the variation of section moment around the azimuth.

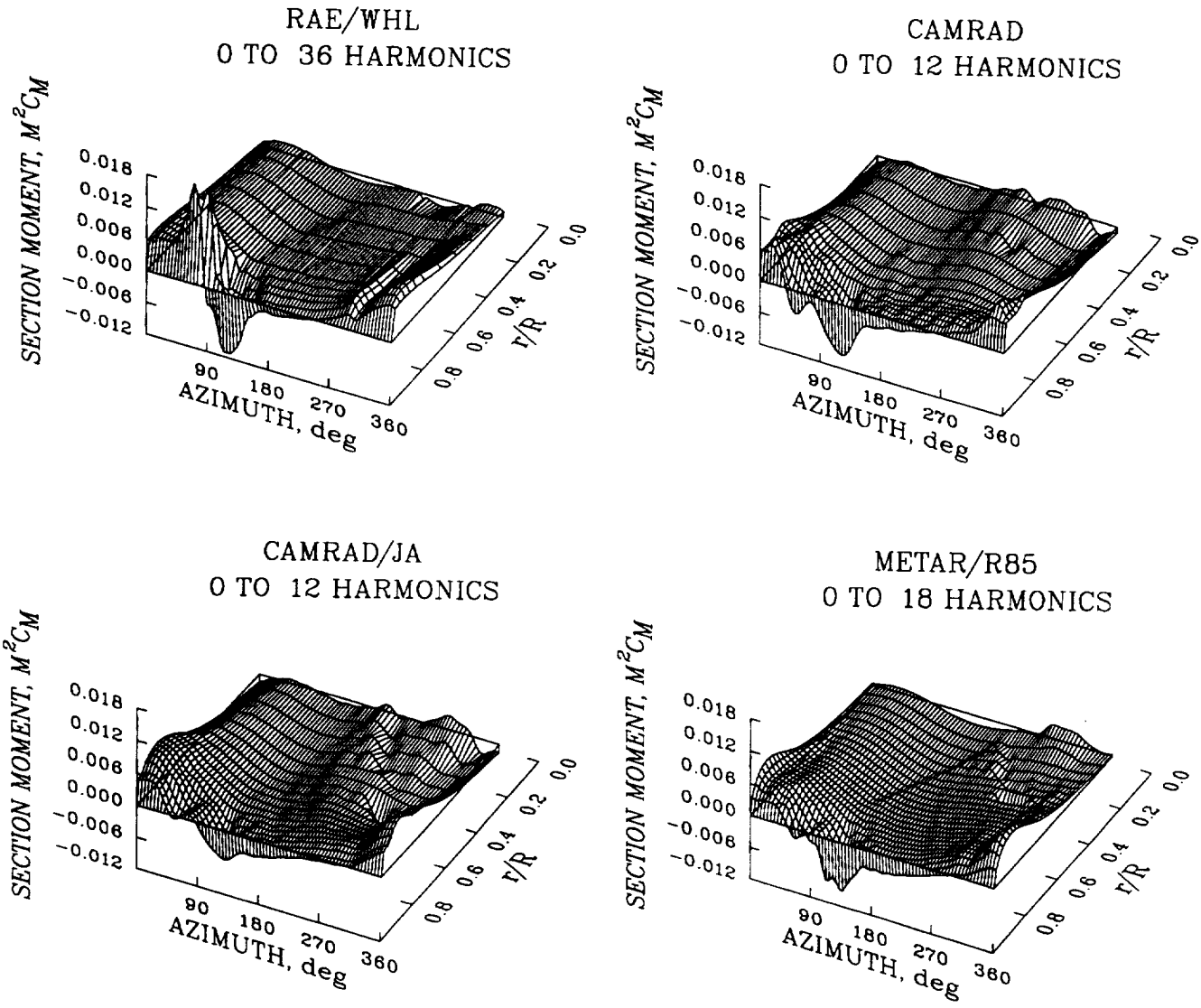


Figure 40. Section pitching moment distribution as a function of azimuth and blade radius for Case 7; all harmonics.

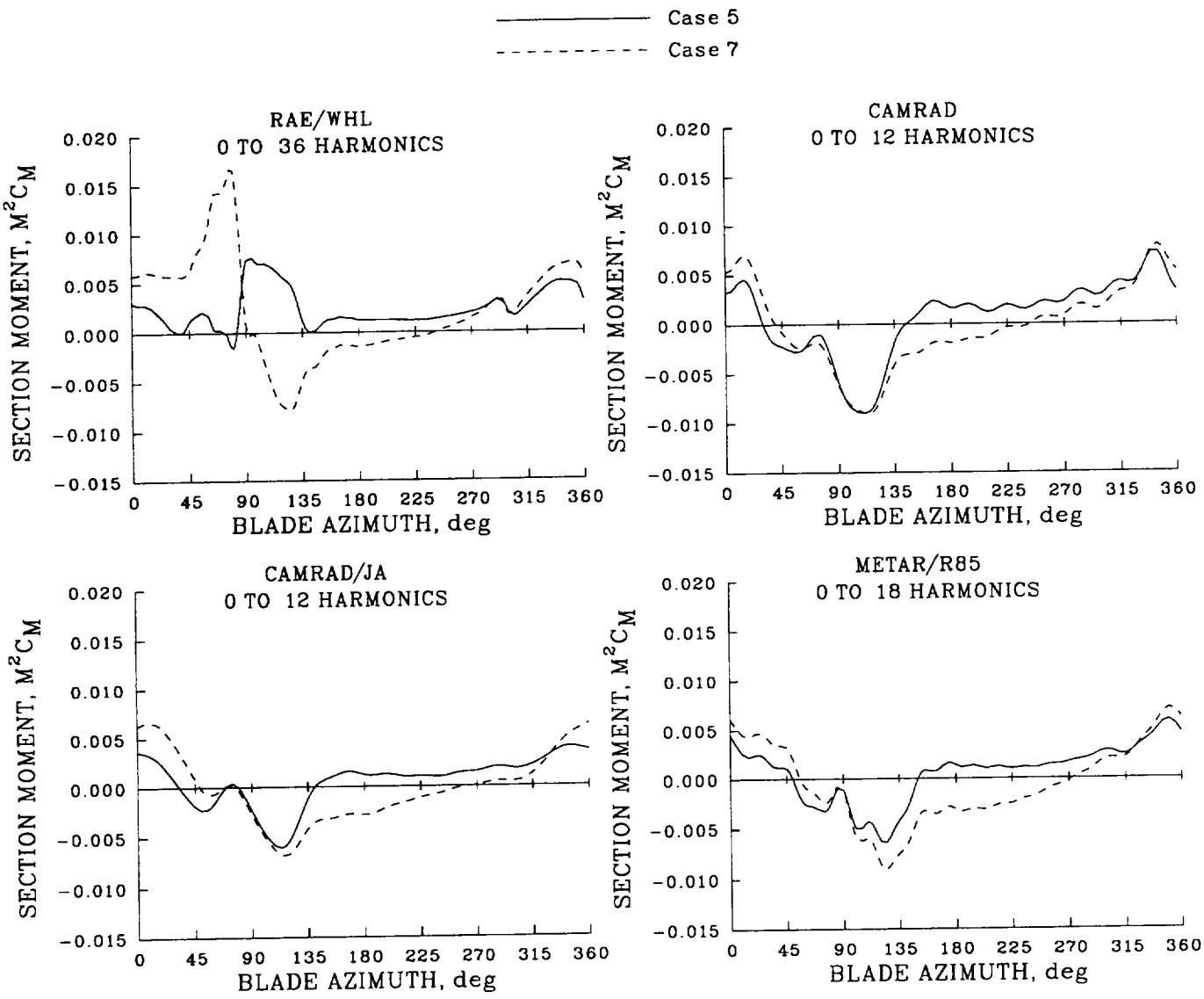


Figure 41. Comparison of section pitching moment as a function of azimuth for Cases 5 and 7; $0.95R$, all harmonics.

*Case 8*

Case 8 differs from Case 7 in that the computation of the aerodynamic forces on the blade includes yawed or radial flow effects. Figure 42 shows the distribution of normal force for Case 8 for the four analytical models. The normal force distributions show little change from Case 5 (see figure 36), indicating that, for these conditions, radial or yawed flow does not significantly influence the blade lift. As before, a slice of data at $0.85R$ is examined in figure 43 to look in detail at the effects of adding the yawed flow terms. The RAE/WHL analysis shows a small increment in lift at this station with the inclusion of the radial flow terms, but the other analyses are not influenced by the modeling changes.

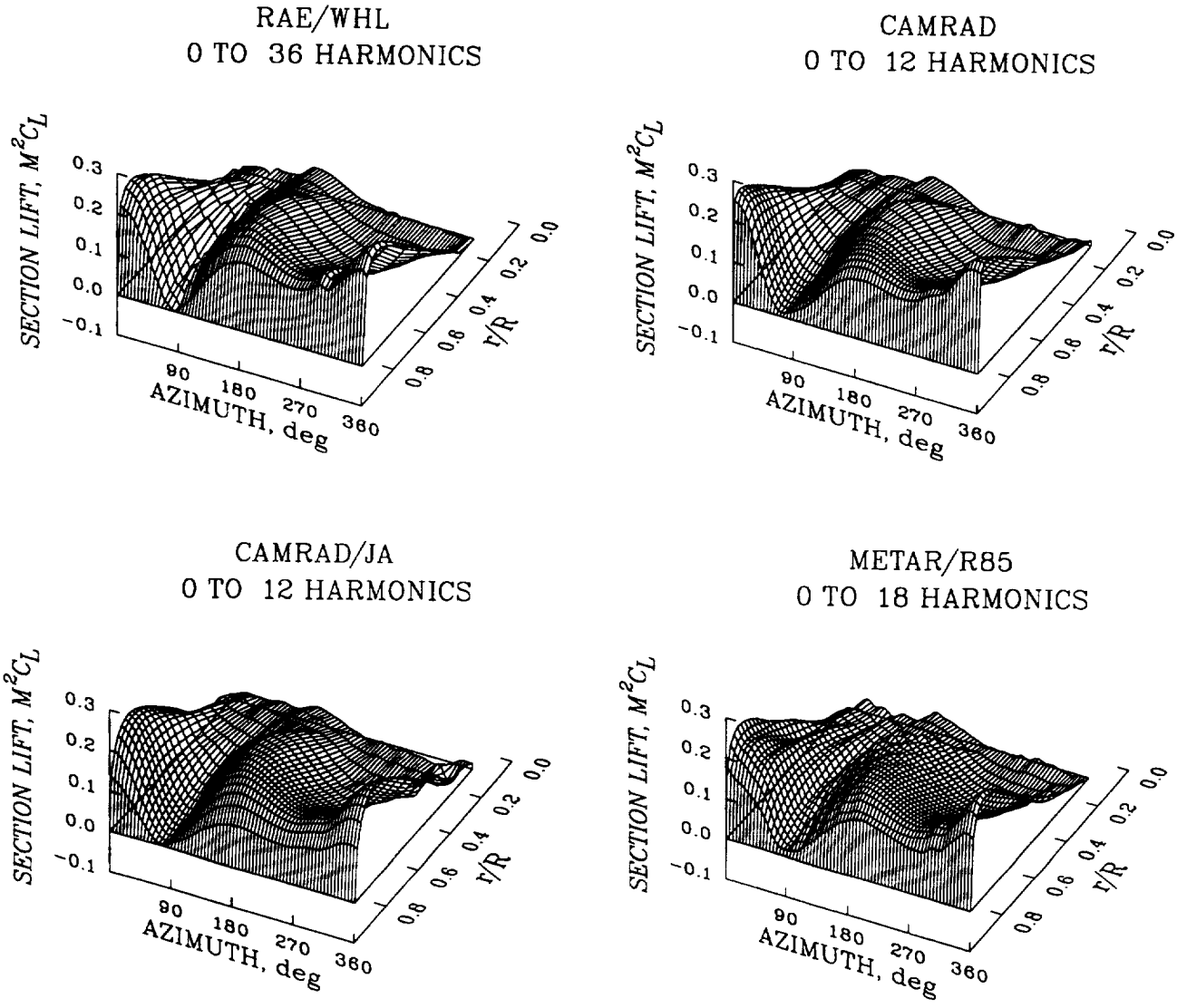


Figure 42. Normal force distribution as a function of azimuth and blade radius for Case 8; all harmonics.

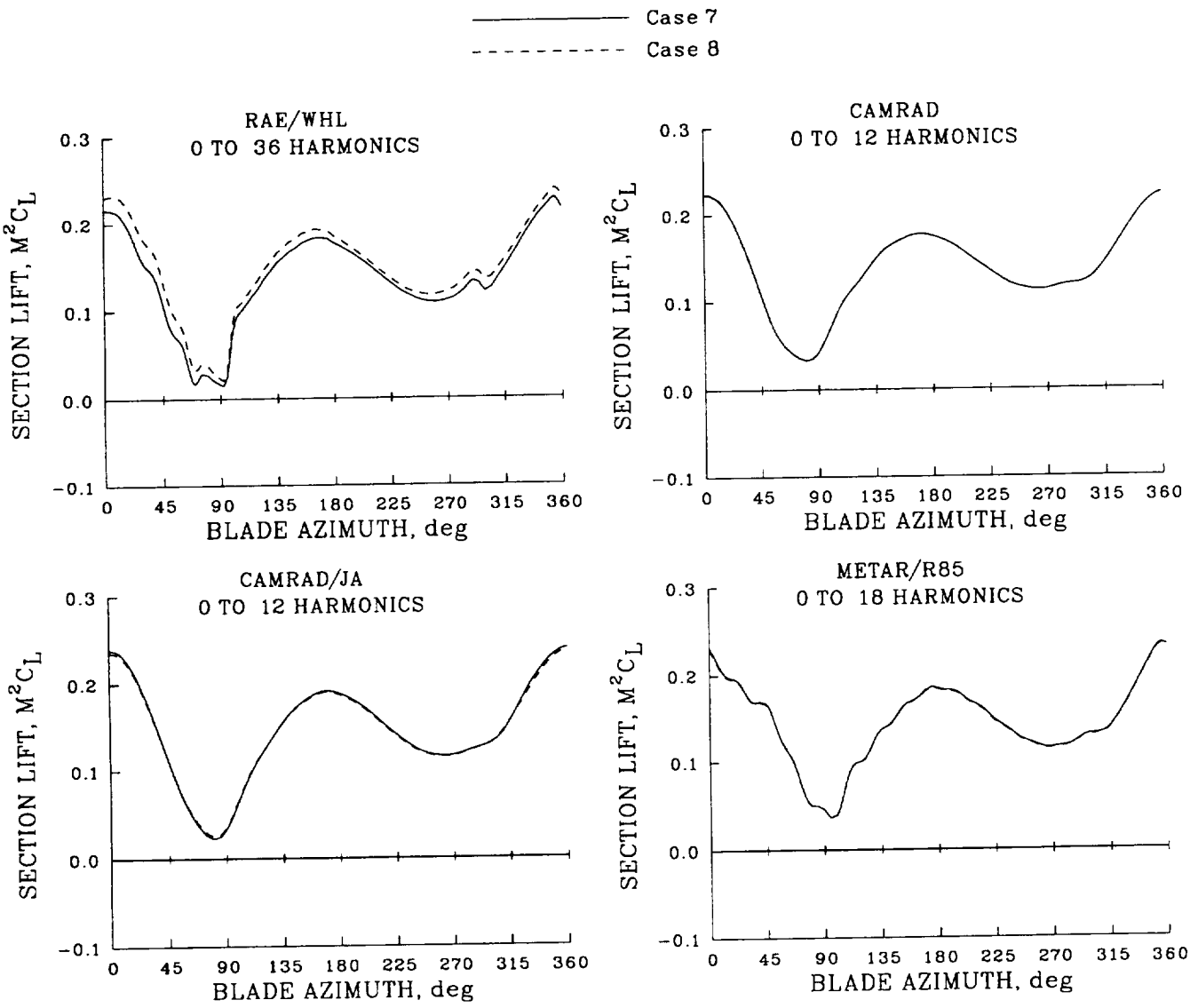


Figure 43. Comparison of normal force distribution as a function of azimuth for Cases 7 and 8; $0.85R$, all harmonics.

The angle of attack for Case 8 is compared with Case 7 in figure 44. Small changes in the angle-of-attack excursions are observed for the RAE/WHL and CAMRAD/JA analyses. The other analyses show no influence of radial flow on the angle of attack at this radial station.

Radial flow effects show little influence on the section pitching moments for this trim condition. Figure 45 compares the pitching moment computed for Case 8 with the Case 7 values for the four analyses. Fairly small changes are seen, particularly near $\psi = 0°$, but for the most part these changes are slight.

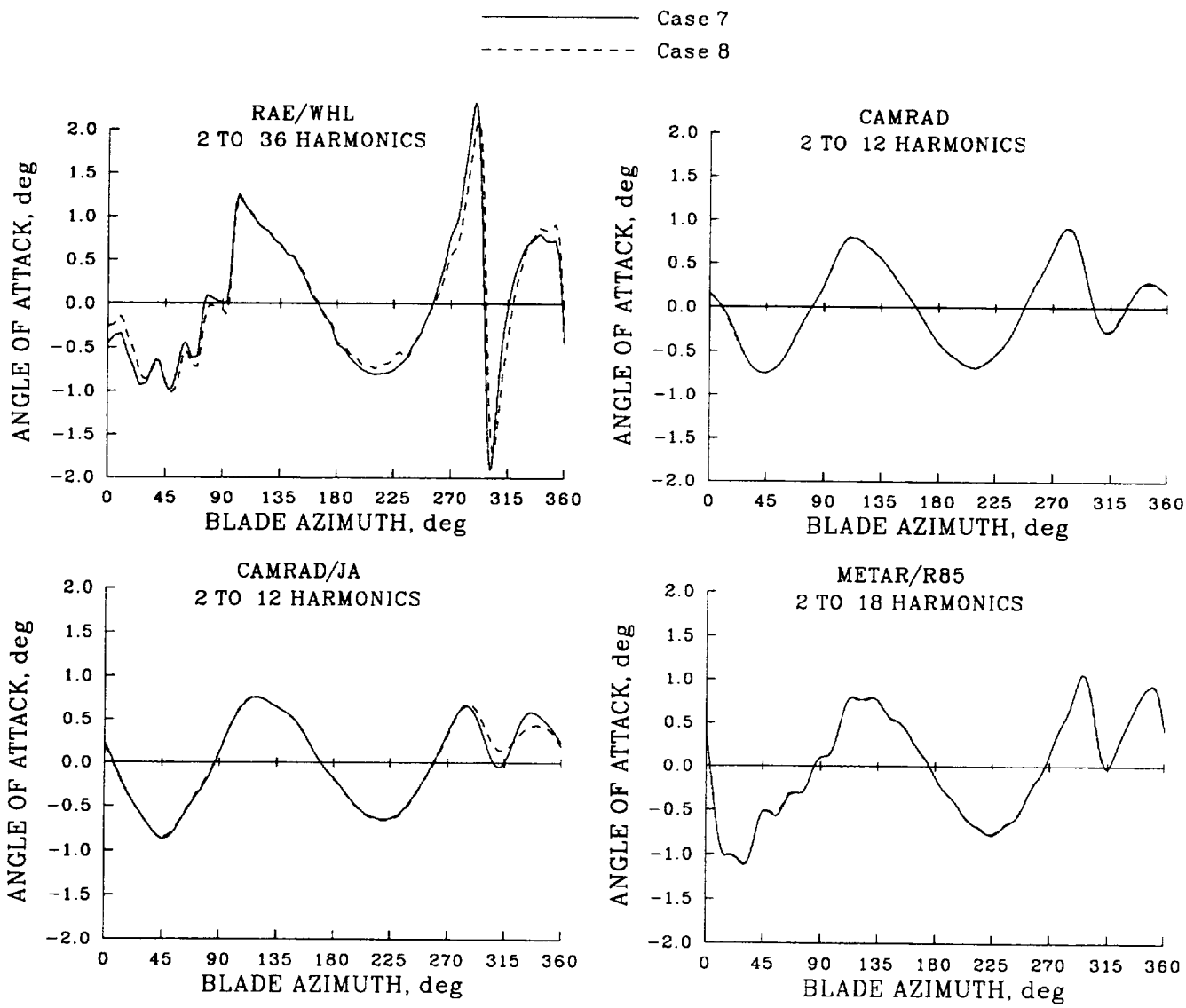


Figure 44. Comparison of angle of attack as a function of azimuth for Cases 7 and 8; $0.85R$, harmonics 2 and above.

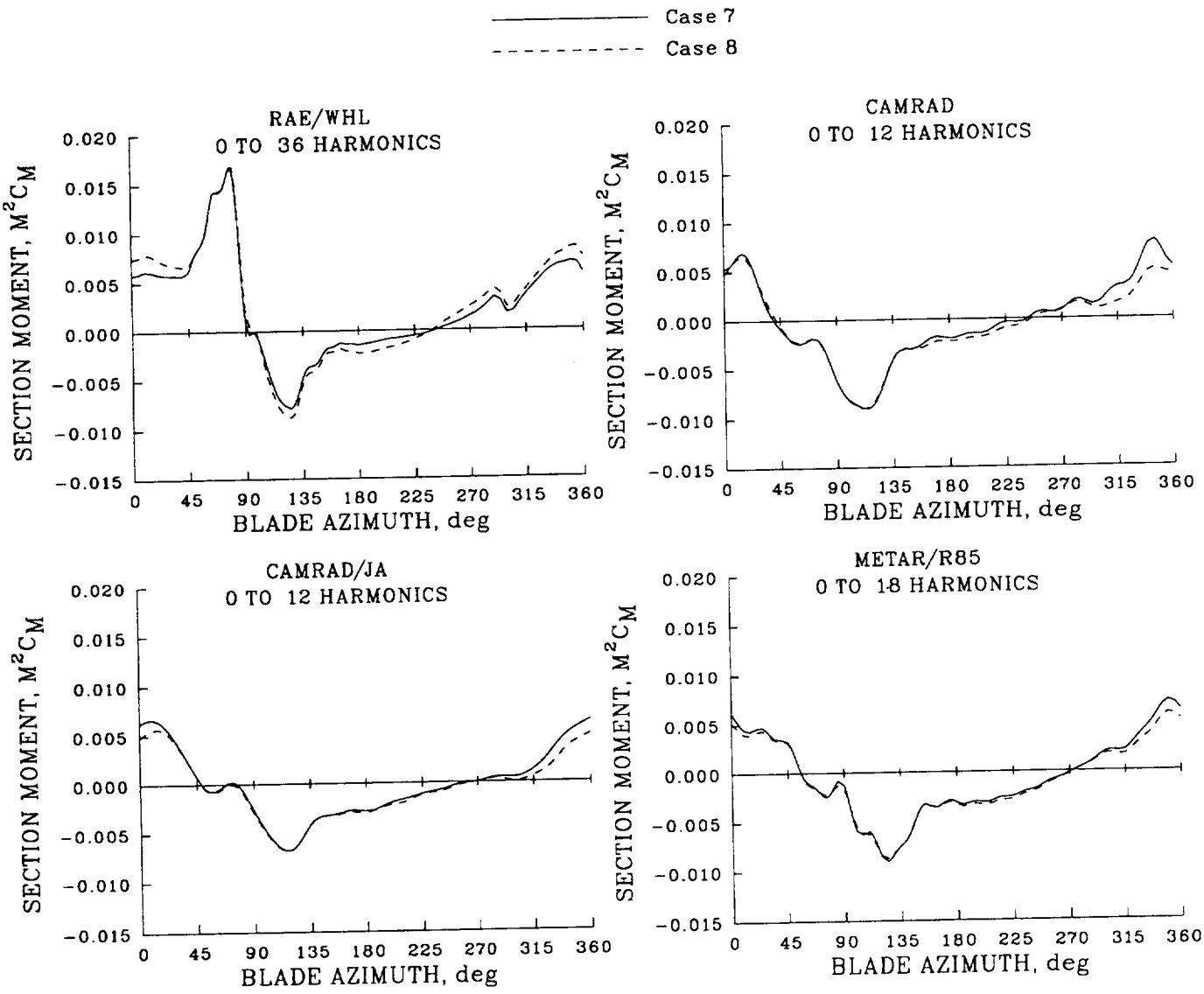


Figure 45. Comparison of section pitching moment as a function of azimuth for Cases 7 and 8; $0.95R$, all harmonics.

*Case 9*

Case 9 differs from Case 8 in changes made to the blade structural model. For the computations for Cases 1 to 8 the blade was modeled as a rigid beam with a hinge at the root to allow flap motion. (The METAR/R85 analysis was an exception in that it included a lag hinge as well.) For Case 9 a lag hinge was added to the RAE/WHL and CAMRAD analyses and blade flexibility was represented by multiple bending modes. Figure 46 shows the distribution of normal force for Case 9 for the four analytical models. Qualitatively, the distribution is similar to the Case 7 results shown in figure 36 or, for that matter, the Case 3 results, figure 22. Examining the normal force at $0.85R$, as shown in figure 47, it is apparent that the major effect of adding a lag hinge and blade flexibility is that the normal force is phase shifted by about $15^\circ$ or $20^\circ$. These results, compared with Case 3, show only small changes in the normal force for the various changes to the aerodynamic model.

The vibratory loads, that is, harmonics 3 and above, provide a more sensitive assay of the effects of aerodynamic and aeroelastic modeling changes. Figure 48 shows the distribution of the normal force for the four analyses with the steady and first two harmonics removed. A comparison with Case 3, figure 23, is particularly interesting as few changes are evident, even in these higher harmonic loads, as a consequence of the aerodynamic and aeroelastic modeling changes. A direct comparison of the vibratory loading, at $0.85R$, is shown in figure 49. As noted previously, the RAE/WHL vortex ring wake shows strong vortex loading on both the advancing and retreating sides of the disk. The aerodynamic modeling changes made from Case 3 to Case 8 slightly reduce the peak loads, particularly some of the higher harmonic content of these loads but, in general, these effects are slight. With the addition of blade flexibility, Case 9, the vortex loading is further reduced although the dominant 3/rev character remains the same. The calculated section normal force at this radial station is very similar for the two CAMRAD analyses. Almost no effects of the aerodynamic modeling changes from Case 3 to Case 8 are seen in the predictions. The inclusion of a lag hinge and blade flexibility, Case 9, shows a phase shift of about $20^\circ$ and the amplitude of the vibratory loads are reduced by about 10%. A lag hinge was included in the METAR/R85 calculations for all of the cases and no phase shift is observed for these results. Essentially no change is seen in the METAR/R85 predicted normal force because of aerodynamic modeling changes and only a small decrease in the normal force on the retreating side of the rotor is seen when blade flexibility is added to the model.

The angle-of-attack distribution for Case 9 is shown in figure 50 and qualitatively appears much the same as for the previous cases. (Angle of attack was not computed by METAR/R85 for this case.) The Case 9 angle of attack at $0.85R$ is compared in more detail with Cases 3 and 8 in figure 51. Only harmonics 2 and above are shown in this comparison to accentuate the differences caused by modeling changes. As can be seen, the angle-of-attack differences are quite small, whether caused by aerodynamic modeling changes or by blade flexibility.

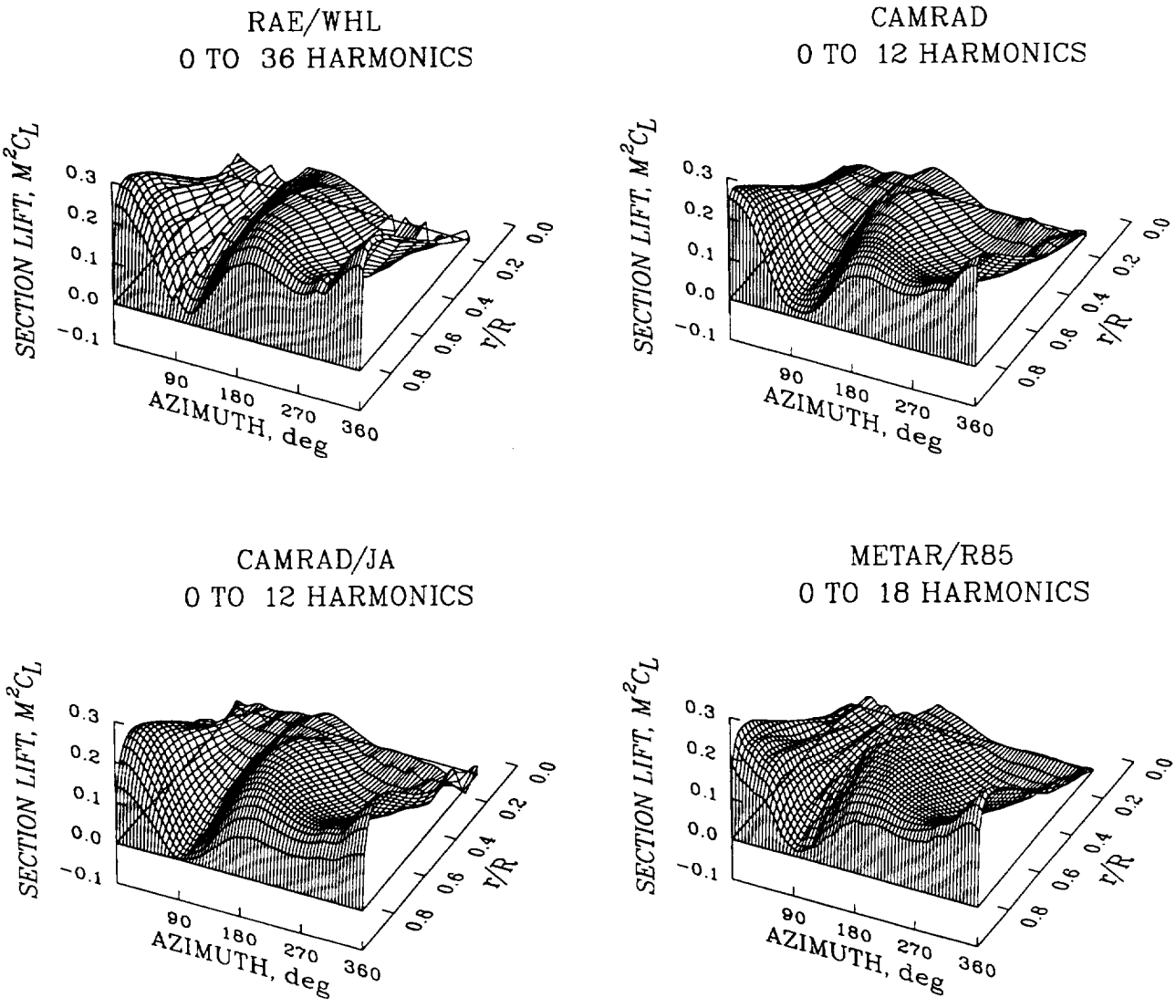


Figure 46. Normal force distribution as a function of azimuth and blade radius for Case 9; all harmonics.

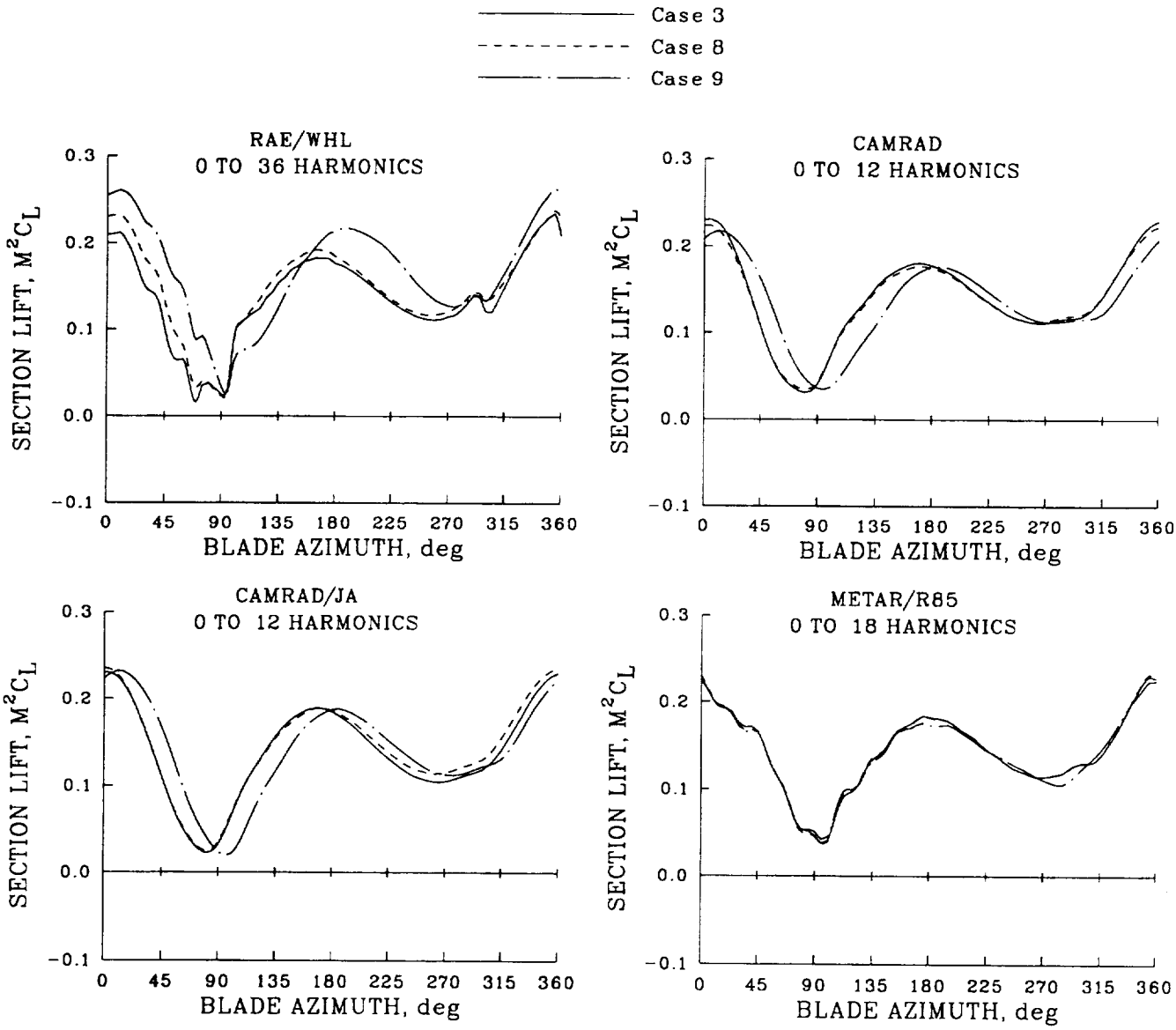


Figure 47. Comparison of normal force distribution as a function of azimuth for Cases 3, 8, and 9; $0.85R$, all harmonics.

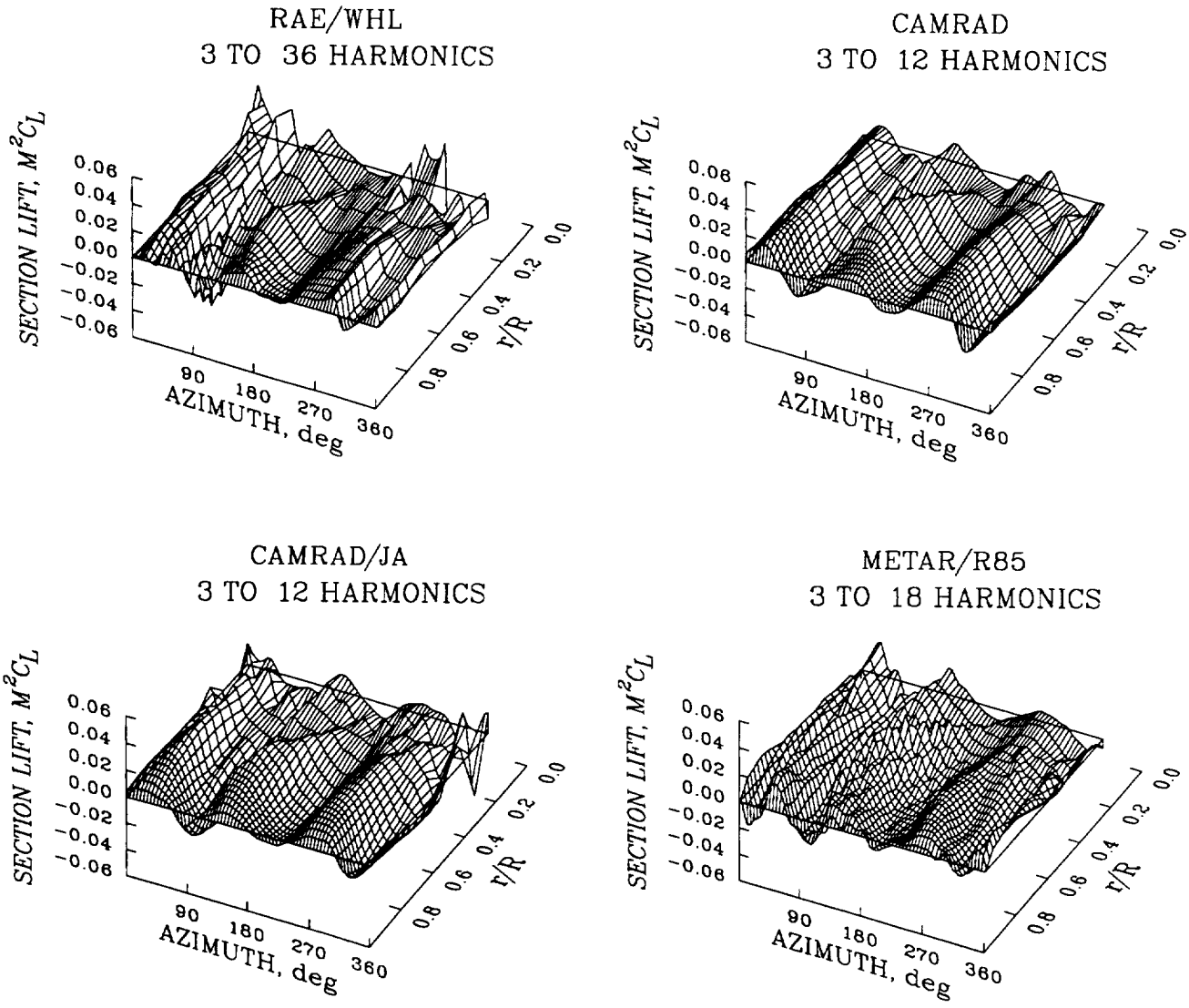


Figure 48. Normal force distribution as a function of azimuth and blade radius for Case 9; harmonics 3 and above.

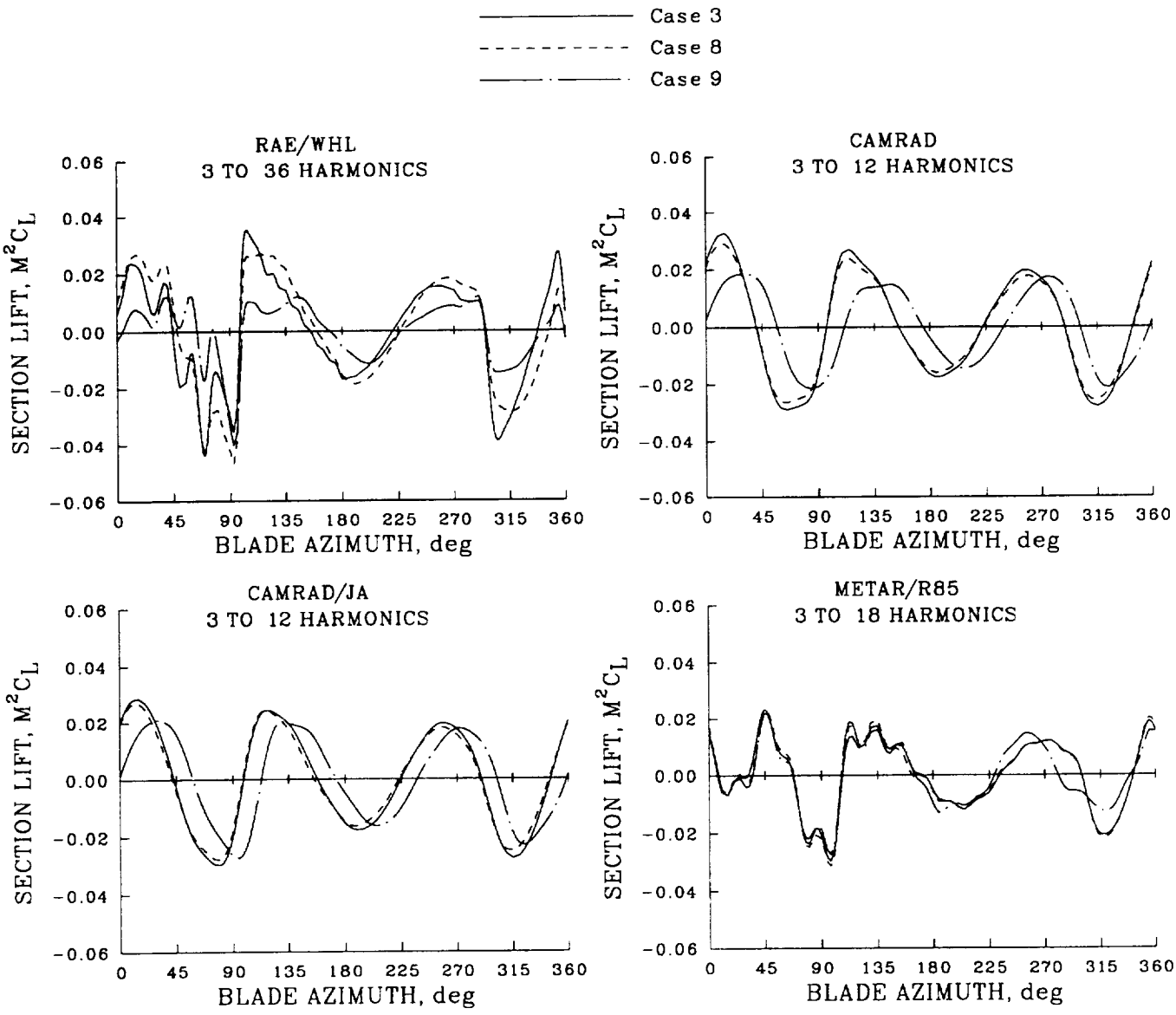


Figure 49. Comparison of normal force distribution as a function of azimuth for Cases 3, 8, and 9; $0.85R$, harmonics 3 and above.

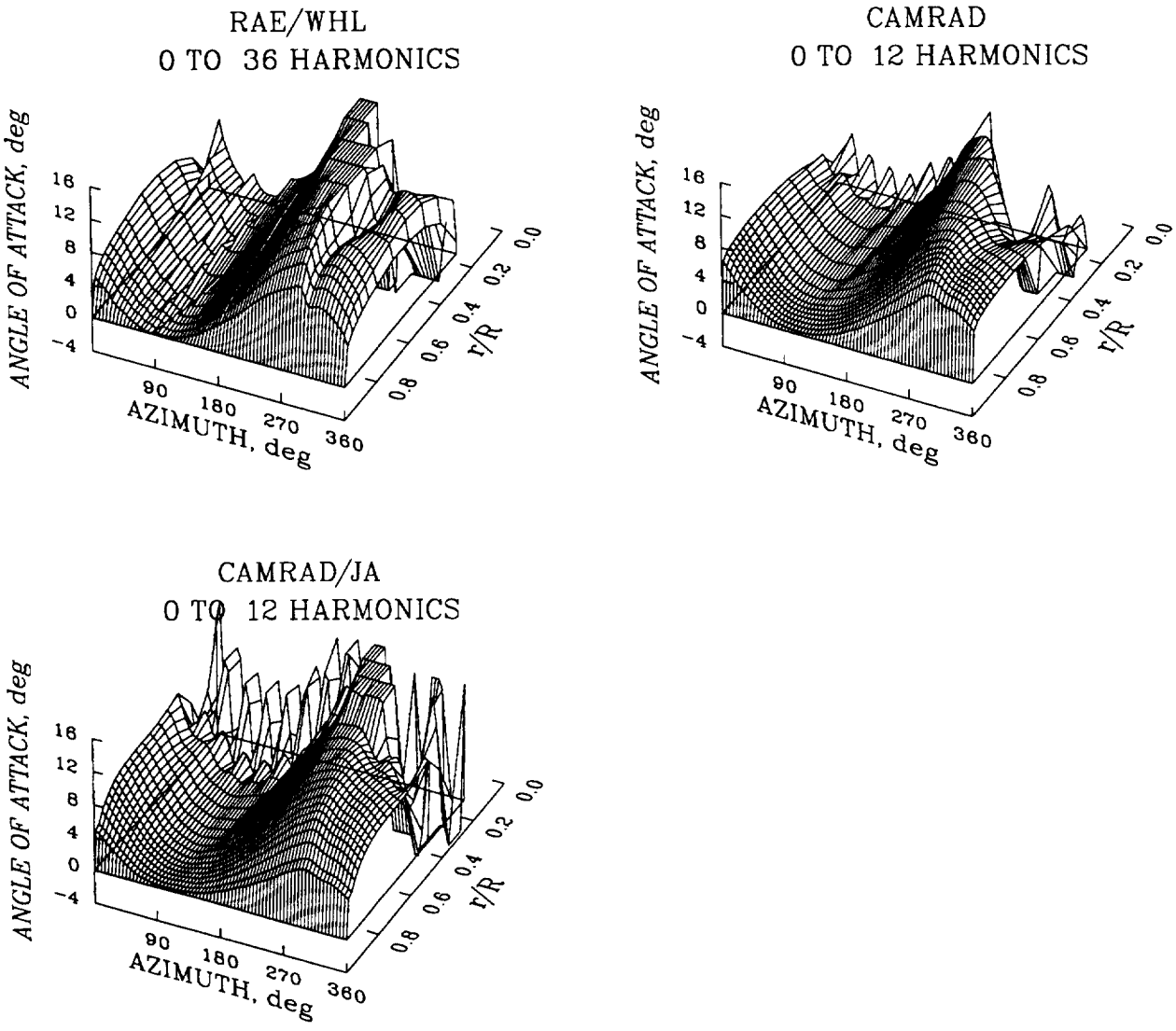


Figure 50. Angle-of-attack distribution as a function of azimuth and blade radius for Case 9; all harmonics.

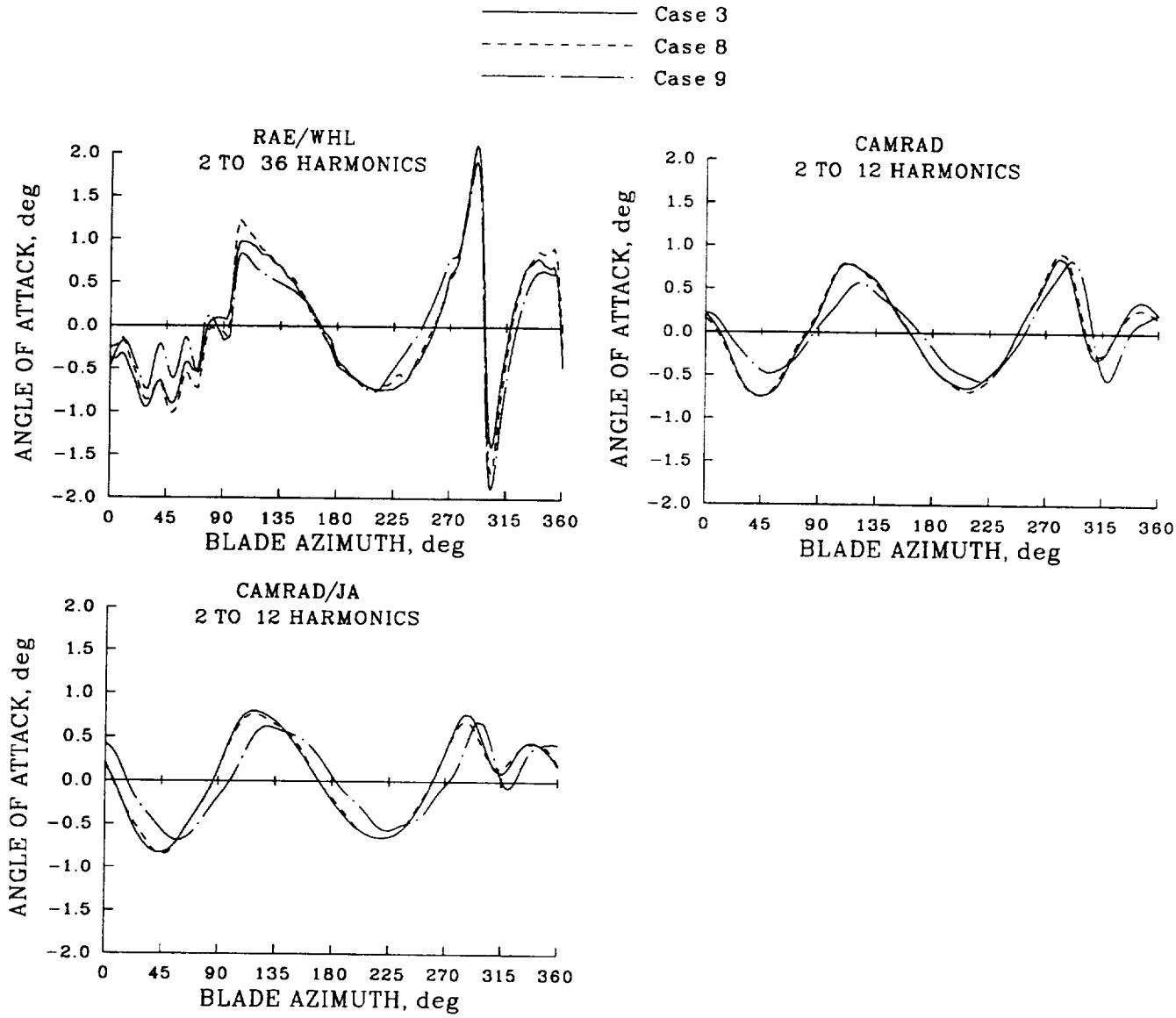


Figure 51. Comparison of angle of attack as a function of azimuth for Cases 3, 8 and 9; $0.85R$, harmonics 2 and above.

The distribution of the section pitching moment is shown in figure 52 for the four analyses. A number of changes are noted when comparing these predictions with Case 7, figure 40. The peak section moment near the tip predicted by the RAE/WHL analysis is reduced considerably with the addition of blade flexibility; however, the vortex-induced loads on the retreating side are largely unchanged. The computed values at the two innermost stations are incorrect because of an implementation error in the model but this has a negligible effect on the blade moment. The CAMRAD analyses and METAR/R85 section moments are similar to the Case 7 values. However, CAMRAD and METAR/R85 show that the first negative peak is increased in Case 9 and the second negative peak is reduced. The effects of blade flexibility (and the lag hinge) are examined in more detail in figure 53. At this radial station, blade bending flexibility reduces the peak section moment for the RAE/WHL and CAMRAD analyses, while the moments are substantially increased (in the negative sense) for the METAR/R85 analysis.

*Case 10*

Case 10 differs from Case 9 in the addition of torsional flexibility. The METAR/R85 analysis was unable to obtain a converged solution for this case so no results are shown. Figure 54 shows the distribution of normal force for Case 10 for the three analytical models. Qualitatively, the distribution is similar to the Case 9 results shown in figure 46 as well as the Case 3 results, figure 22. Examining the normal force at $0.85R$, as shown in figure 55, it is seen that only slight changes occur for the RAE/WHL analysis, but that the CAMRAD analyses predict a slight decrease in the normal force on the advancing side of the rotor.

The vibratory load distribution, harmonics 3 and above, is shown in figure 56. Qualitatively, only slight changes are seen between this case and Case 9, figure 48. A direct comparison of the vibratory loading, at $0.85R$, is shown in figure 57. The effect of blade bending flexibility was to reduce the higher harmonic airloads, as noted above. However, the addition of torsion flexibility does not appear to significantly increase or decrease the vibratory loads for the RAE/WHL analysis. For the CAMRAD analyses, however, the addition of torsion flexibility substantially increases the vibratory loads. Whereas the effect of bending flexibility (Case 9) was to reduce the vibratory loads by 10% with respect to the Case 3 results, the effect of torsion flexibility (Case 10) is to increase the vibratory loads by 10% with respect to the Case 3 loads.

The angle-of-attack distribution for Case 10 is shown in figure 58 and qualitatively appears much the same as for the previous cases. The Case 10 angle of attack at $0.85R$ is compared in more detail with Cases 3 and 9 in figure 59. Only harmonics 2 and above are shown in this comparison to accentuate the differences caused by modeling changes. Each of the analyses shows the effects of torsional flexibility and, in some cases, differences greater than $0.5^\circ$ are observed.

The distribution of the section pitching moment is shown in figure 60 for the three analyses. Qualitatively, the calculated section moments are very similar to those shown for Case 9, figure 52. The effects of torsion flexibility are examined in more detail in figure 61 for a radial station near the blade tip. Over most of the rotor azimuth, little effect of torsion flexibility is seen on the section moment. Only in the second quadrant are differences seen and, for the most part, the analyses show a more positive moment in this region.

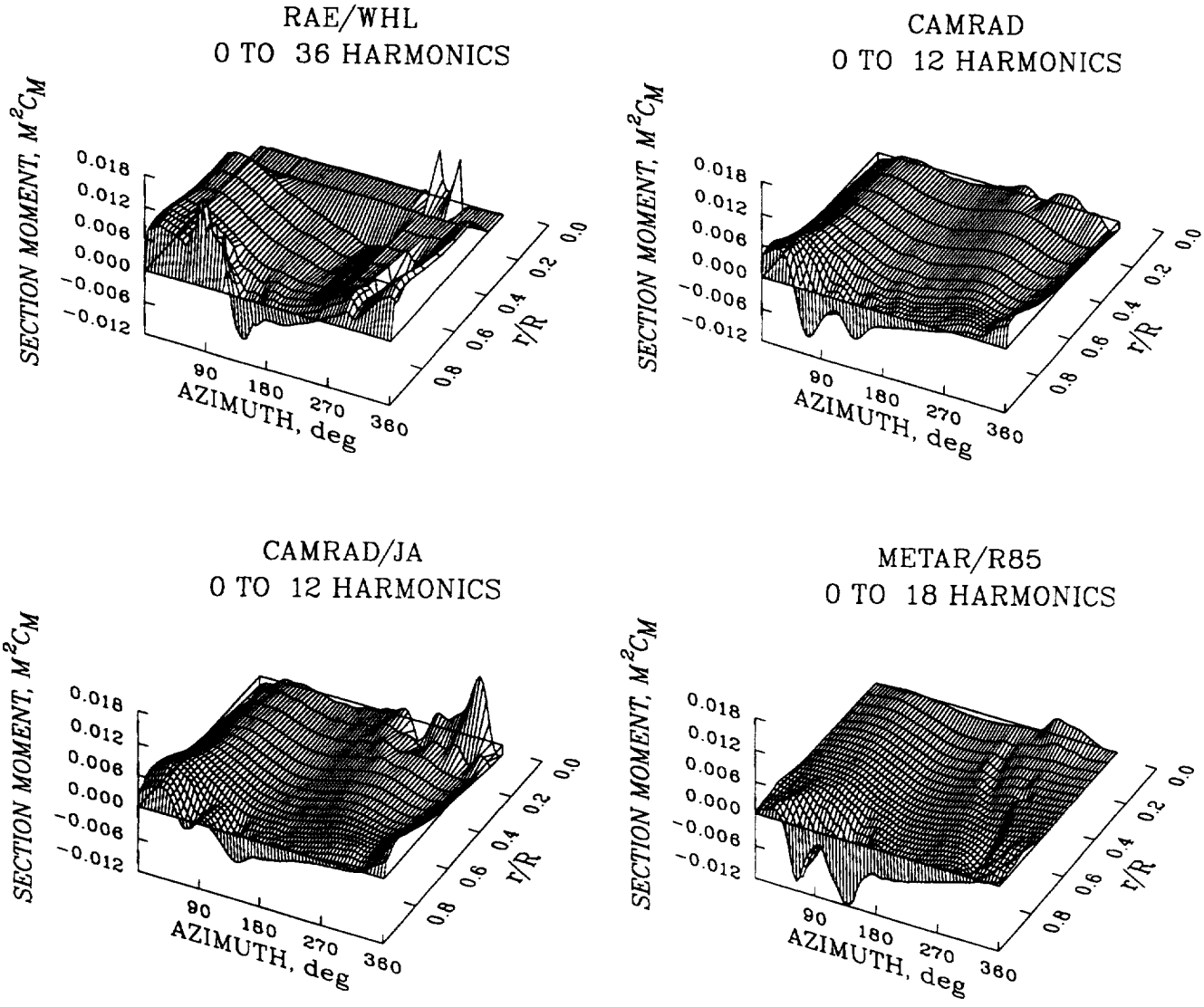


Figure 52. Section pitching moment distribution as a function of azimuth and blade radius for Case 9; all harmonics.

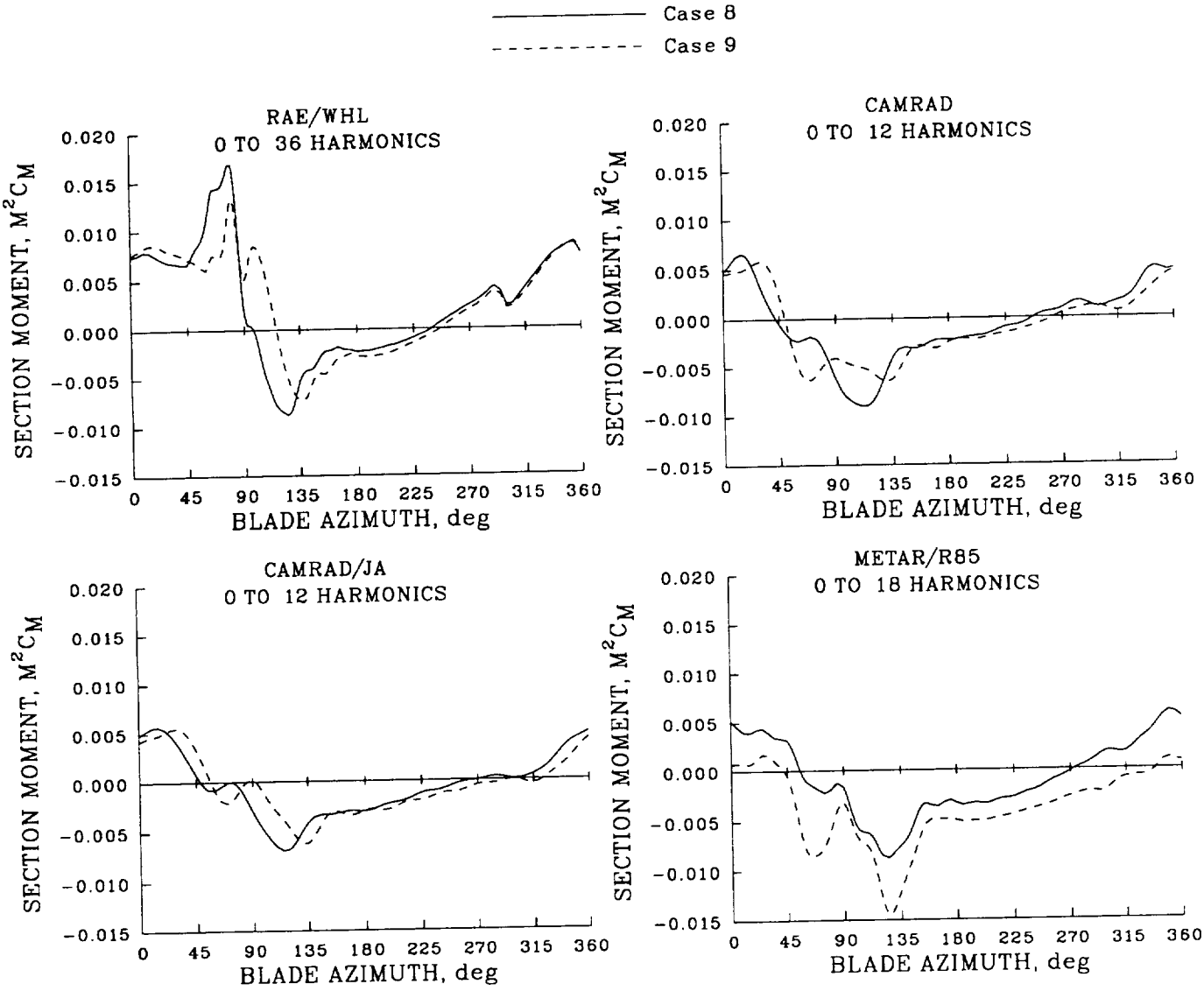


Figure 53. Comparison of section pitching moment as a function of azimuth for Cases 8 and 9; $0.95R$, all harmonics.

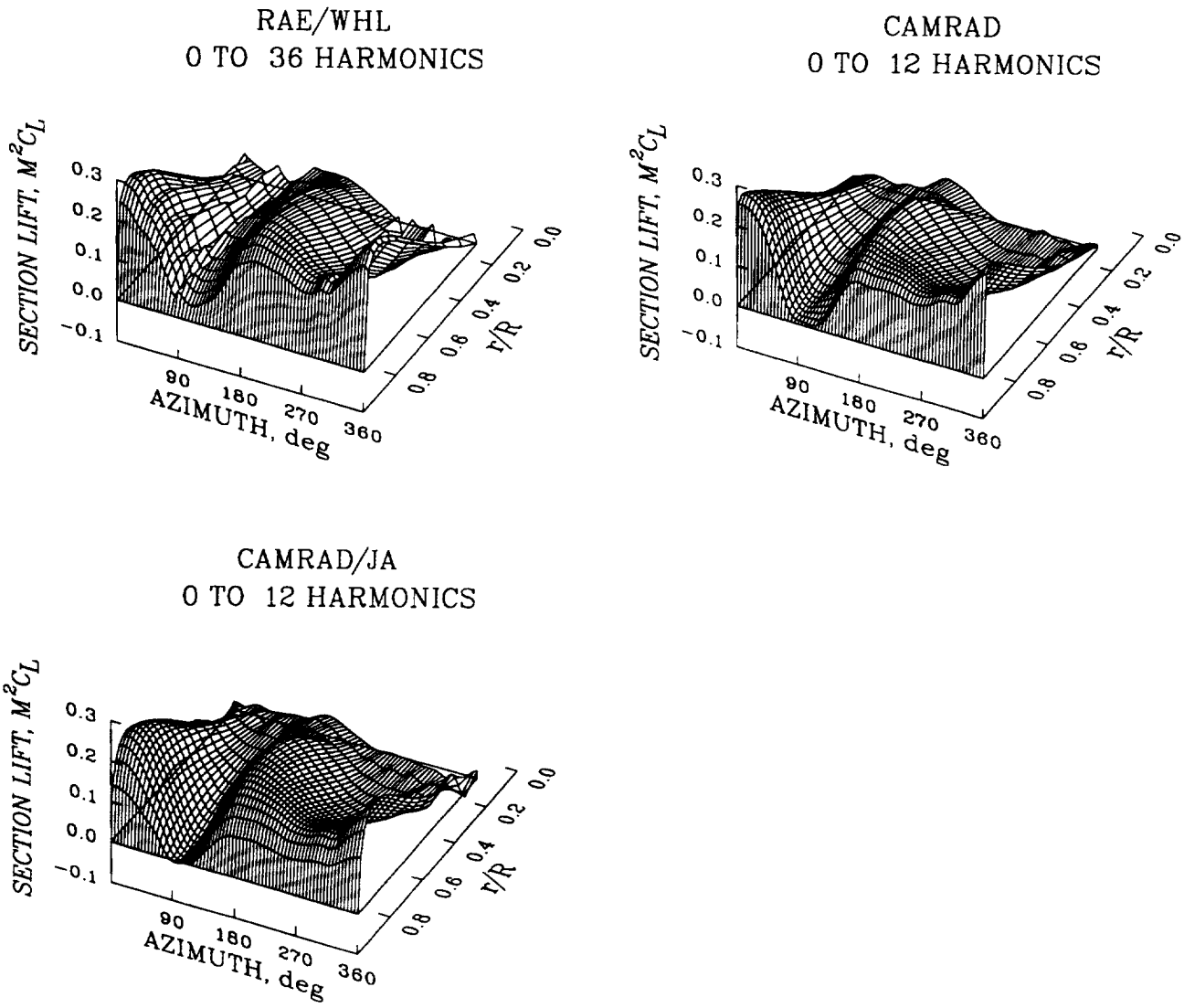


Figure 54. Normal force distribution as a function of azimuth and blade radius for Case 10; all harmonics.

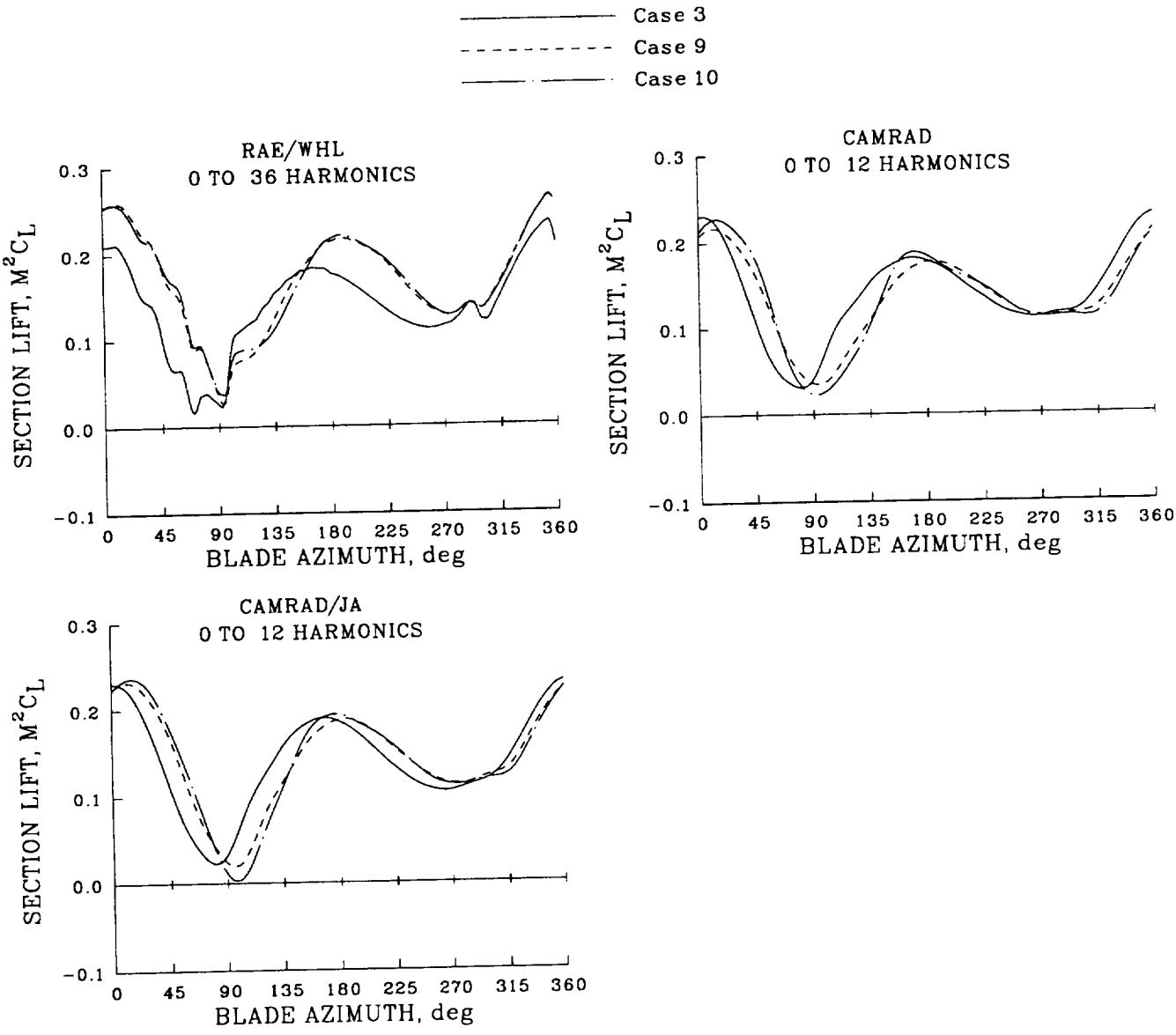


Figure 55. Comparison of normal force distribution as a function of azimuth for Cases 3, 9, and 10; $0.85R$, all harmonics.

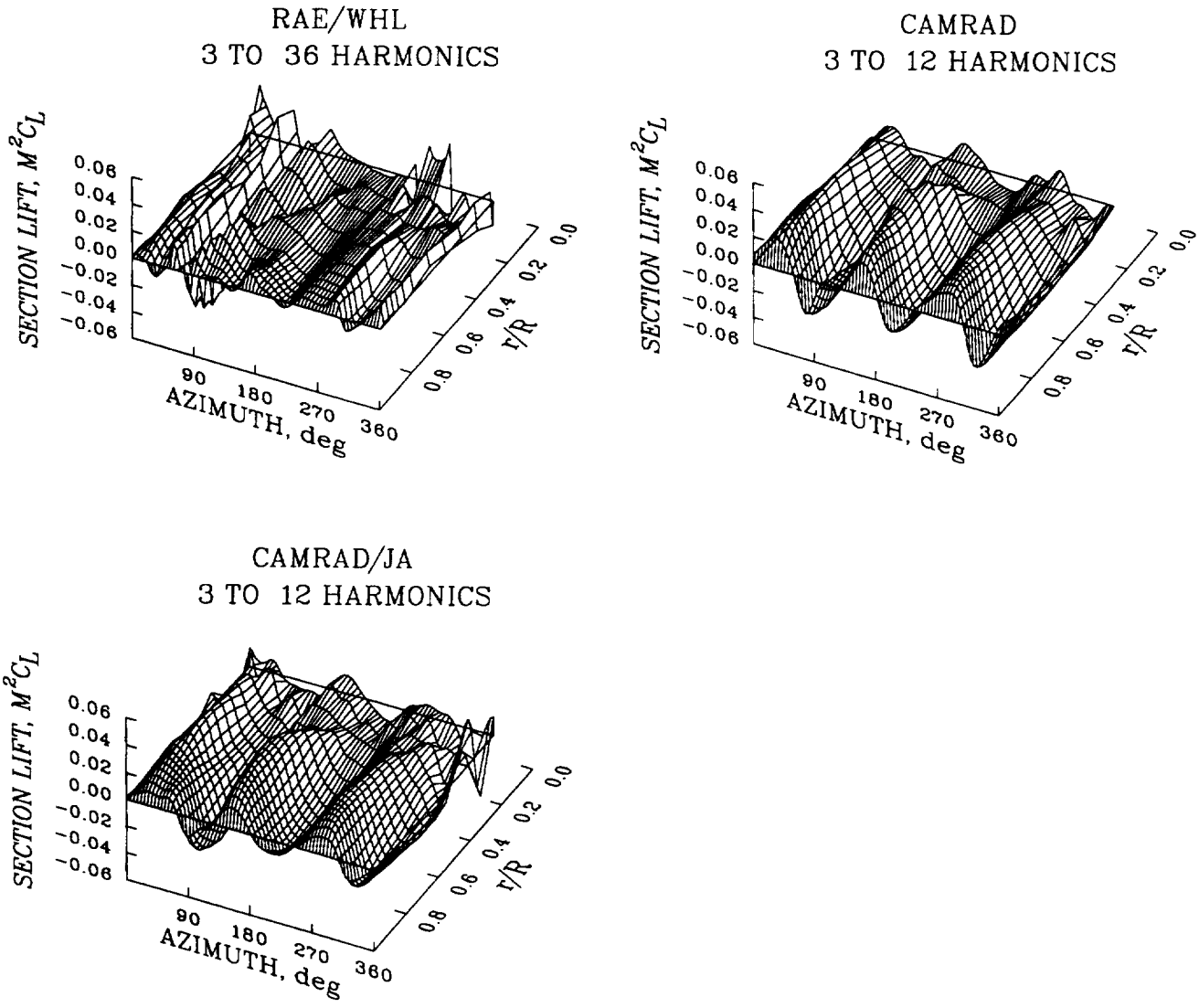


Figure 56. Normal force distribution as a function of azimuth and blade radius for Case 10; harmonics 3 and above.

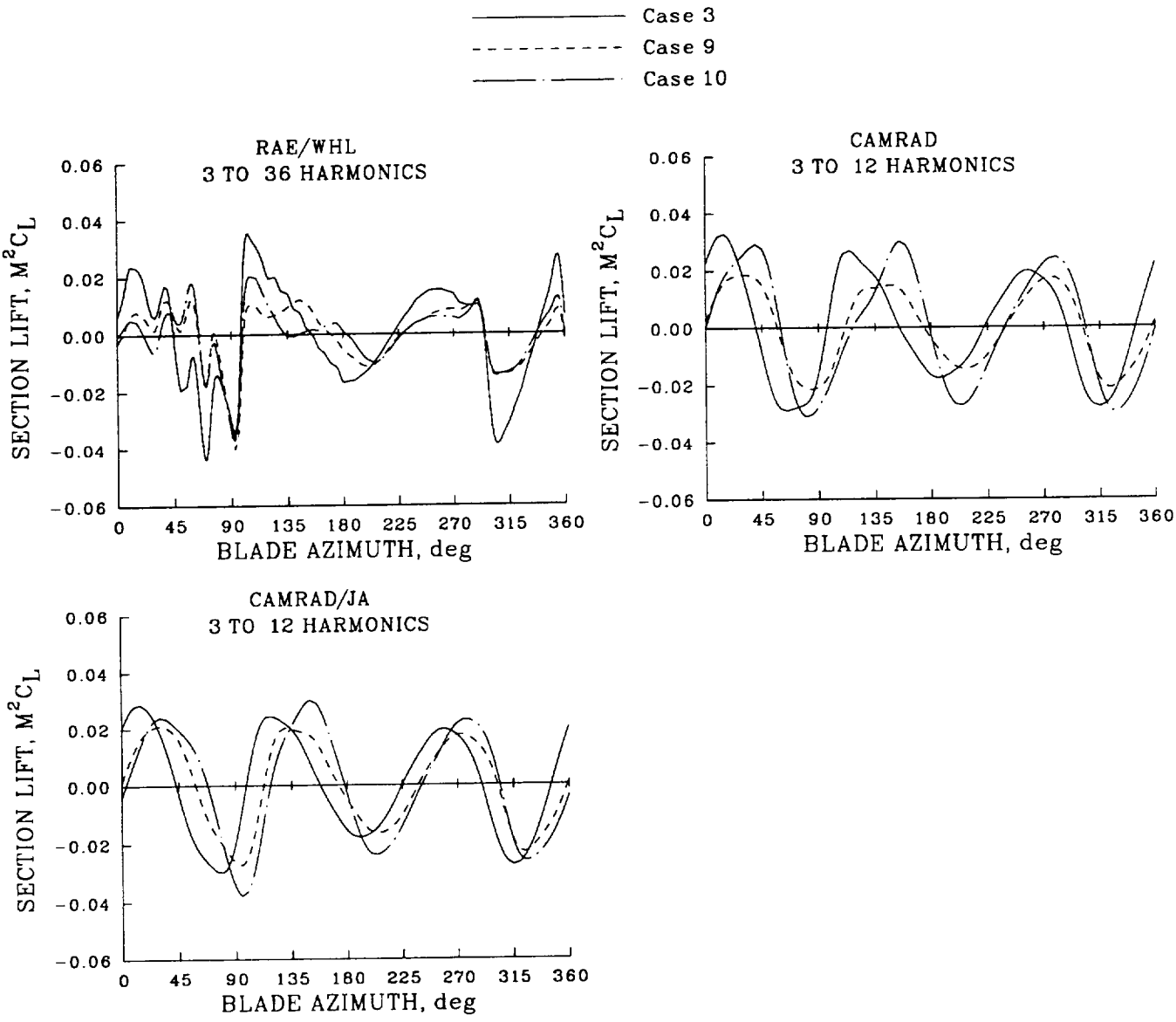


Figure 57. Comparison of normal force distribution as a function of azimuth for Cases 3, 9, and 10; $0.85R$, harmonics 3 and above.

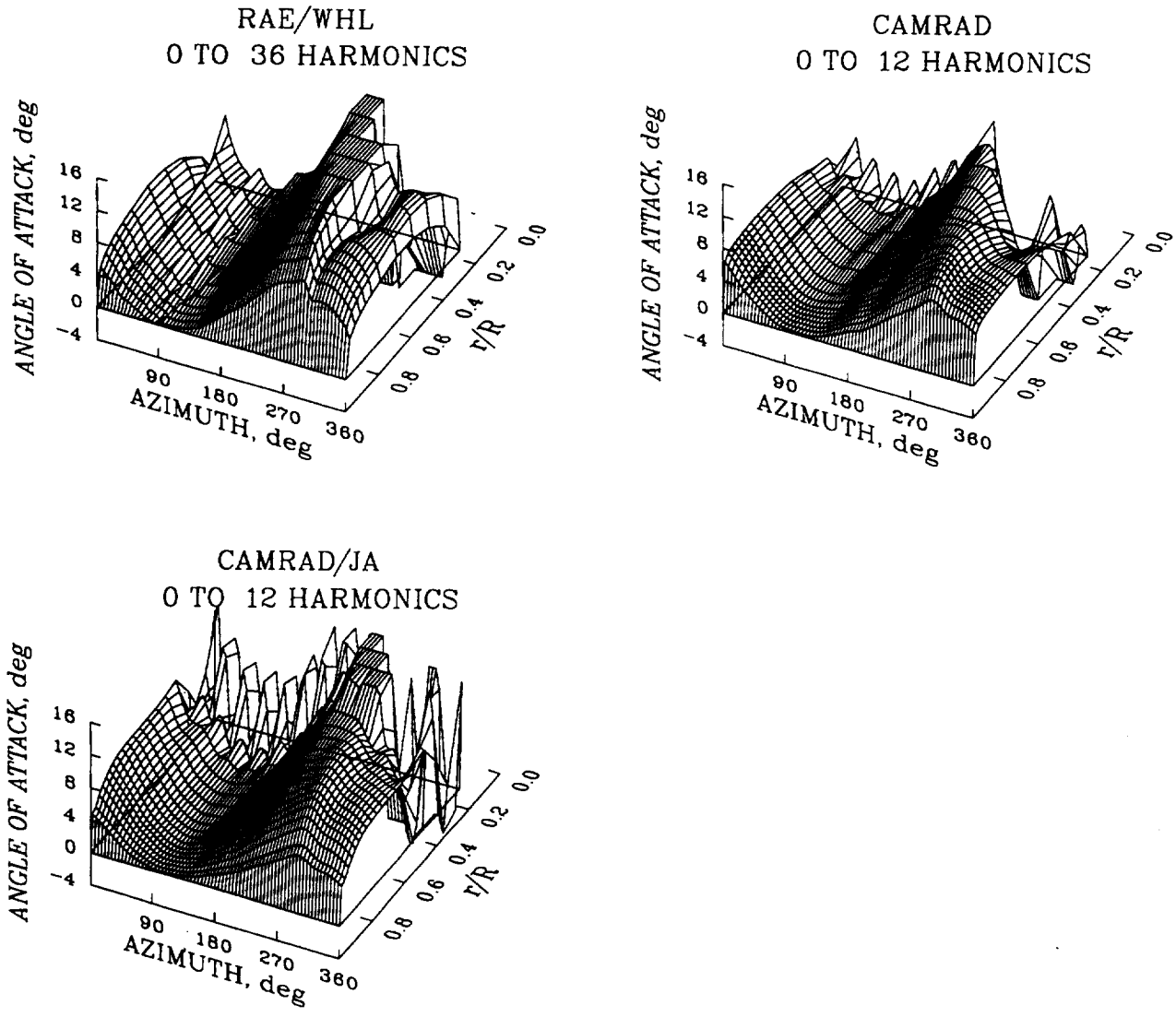


Figure 58. Angle-of-attack distribution as a function of azimuth and blade radius for Case 10; all harmonics.

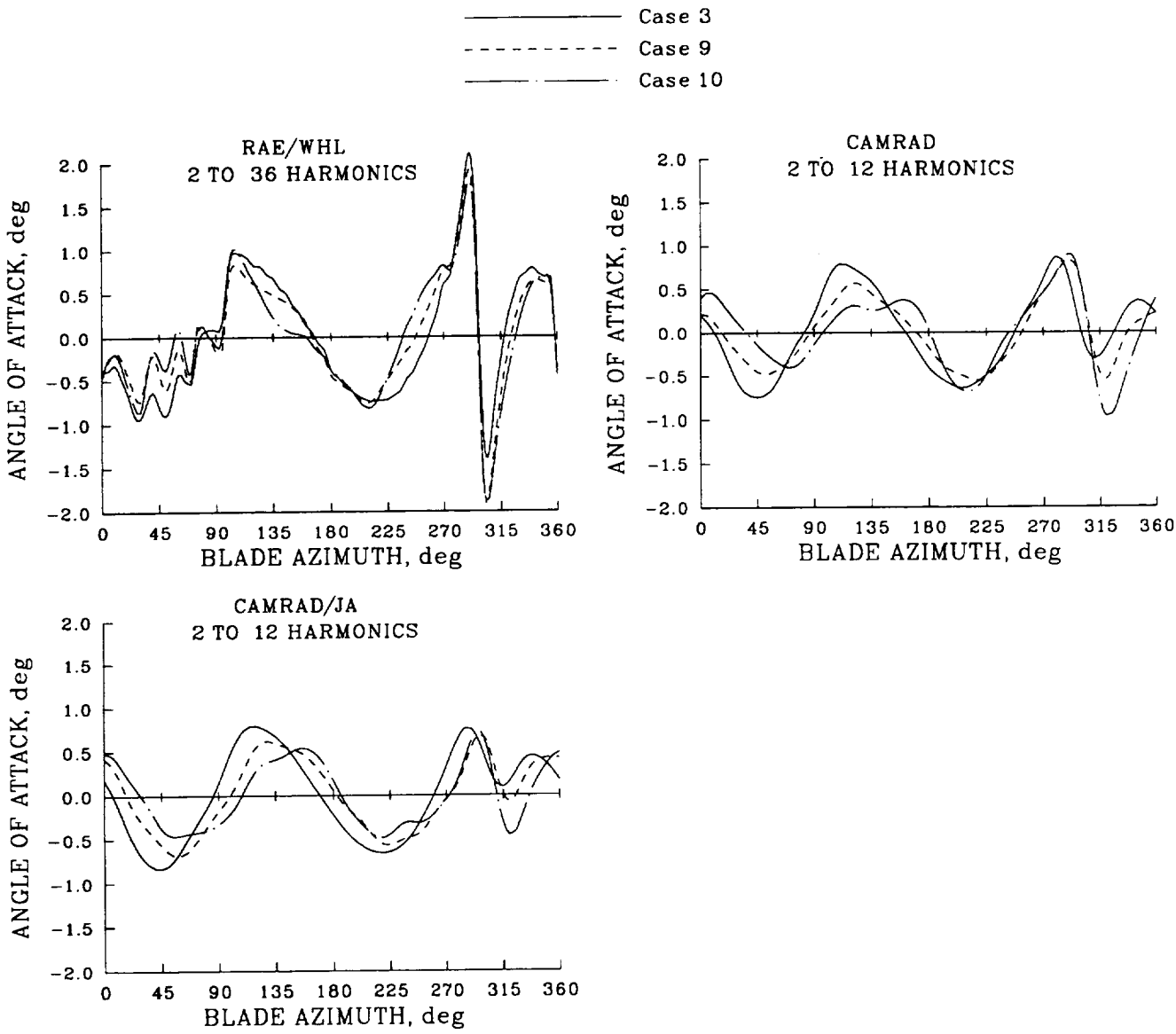


Figure 59. Comparison of angle of attack as a function of azimuth for Cases 3, 9 and 10; $0.85R$, harmonics 2 and above.

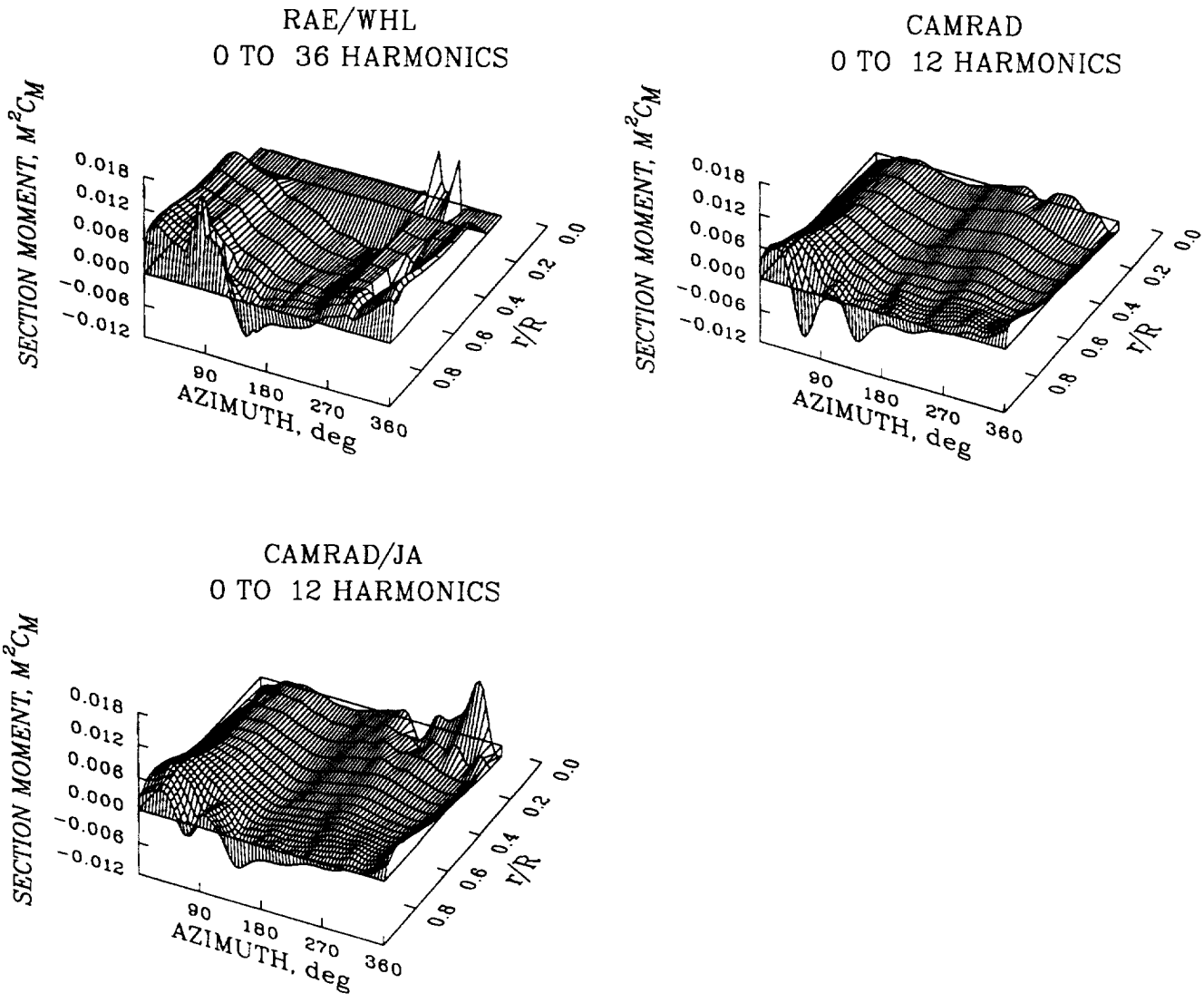


Figure 60. Section pitching moment distribution as a function of azimuth and blade radius for Case 10; all harmonics.

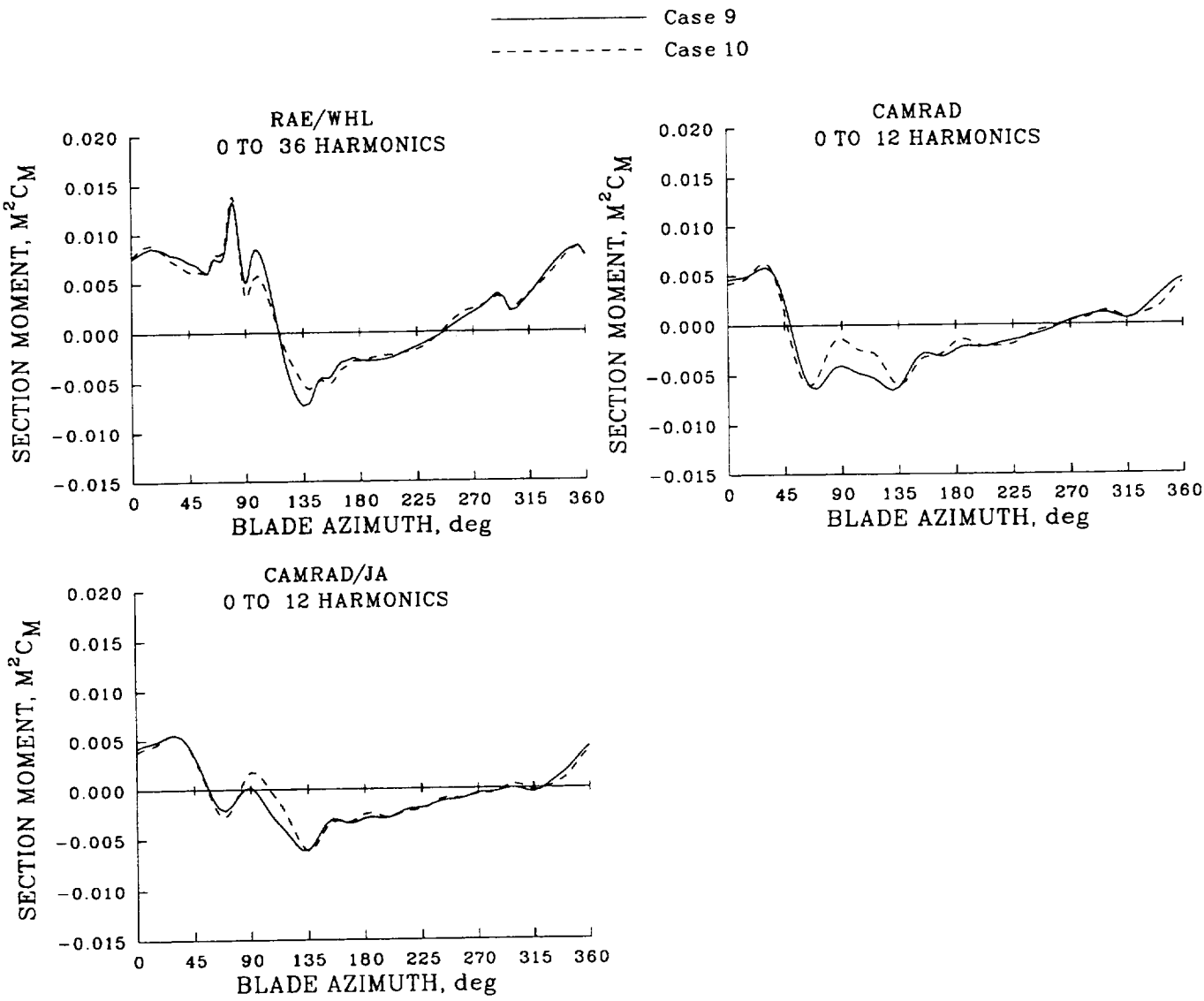


Figure 61. Comparison of section pitching moment as a function of azimuth for Cases 9 and 10; $0.95R$, all harmonics.

## 4.4 Summary of Analytical Modeling Investigation (Task 3)

The four analytical methods examined here show very good agreement for Case 1, which is both the simplest case examined and a baseline for the rest of the computations. The good agreement is seen for trim and performance parameters as well as for the radial and azimuthal distribution of lift. This good agreement provides a useful reference point for all subsequent comparisons.

The harmonics of the airloading at 3/rev and above, those loads that are a source of vibration for the aircraft, are very similar for the four analyses. The vibratory loading, for this very simple case, is clearly seen to be a consequence of the rotor trim. In this sense, the prediction of helicopter vibration at high speed starts from a baseline of trim-induced vibratory loading that will either be increased or decreased as modeling features are added to the analyses.

Cases 2, 4, and 6 (with respect to Cases 1, 3, and 5 respectively) examine the effect of the reversed flow region on the computation by increasing the root cutout from the Puma's dimensional root cutout at 22.8% radius to 40% to accommodate the reversed flow region which, at this trim condition, extends to $0.38R$. Except for a slight increase in blade unit lift, to account for the reduced blade area, there are no changes observed as a result of the increased cutout.

The modeling change made in going from Case 1 to Case 3 is the replacement of the uniform inflow wake with a prescribed wake. The wakes incorporated in each of the four analyses are different and there was no attempt to "match" the computations beyond the need for each analysis to achieve a converged solution to the trim values. The CAMRAD analyses and METAR/R85 each model the wake using a vortex-lattice representation although there are differences in the details of the implementation for each analysis. The RAE/WHL analysis uses a series of vortex rings and half rings to represent the wake vorticity. Despite the differences in the wake models the results in terms of trim and performance are basically equivalent for this flight condition.

The second-order lifting-line method of CAMRAD/JA gives a much greater inflow with larger gradients in the longitudinal and lateral directions of the rotor disk than the other methods. Using CAMRAD as the reference for Case 3, the CAMRAD/JA analysis predicts that the induced power is 51% higher, the parasite power 8% higher, the profile power 1% higher and the total shaft power 16% higher. It cannot be concluded from this code-to-code comparison whether the second-order lifting-line method is more or less realistic than the other analyses, but it is nevertheless encouraging to observe that the classical vortex-lattice methods (CAMRAD and METAR/R85) and the vortex-ring method of RAE/WHL converge to similar results.

The inclusion of concentrated vorticity in the wake models for Case 3 affects the distribution of the angle of attack, particularly in the first and fourth quadrants where the influence of the tip vortices from previous blades is greatest. However, it is important to note that the changes in angle of attack resulting from the prescribed wake models are substantially smaller than the angle-of-attack variation caused by rotor trim. The largest changes are, for each of the analyses, in the fourth quadrant and these differences are especially large for the RAE/WHL analysis.

Nonlinear aerodynamic characteristics are included in the models with the change from Case 3 to Case 5. The nonlinear characteristics, at least below stall, are made roughly uniform between the

analyses by incorporating the equations that are normally used in the RAE/WHL analysis into the other models. This was done for the CAMRAD analyses by creating a new set of tables for interpolation based on the RAE/WHL equations and for METAR/R85 by directly modifying the program. A slight increase in profile power is seen for all of the analyses, as expected, and the four methods predict similar trim and performance results. Essentially no changes are seen in the distribution of blade lift or the angle-of-attack distribution and, hence, the inflow angles. However, the pitching moments, based on static airfoil characteristics are quite different between the RAE/WHL analysis and the other methods and this is apparently the result of a coding error in the program.

Unsteady aerodynamic effects are incorporated in the analyses in going from Case 5 to Case 7. However, the METAR/R85 analysis models unsteadiness only in the pitching moment and not the lift. As the required rotor thrust and the pitch and roll moments are the same for each analysis, the variation in the collective and cyclic trim angles provides insight into the effects of the unsteady aerodynamic models. In this respect it is interesting to see that the RAE/WHL and CAMRAD analyses show the same reduction in collective pitch angle caused by augmented lift, but the phasing of this lift, as reflected in the cyclic angles, is opposite with the RAE/WHL analysis showing an anticipated response and the CAMRAD family a retarded response. This reflects the lack of maturity of dynamic lift models, even in the restricted framework of the unstalled regime. Little effect of unsteady aerodynamics is seen on the performance, however.

The effects of unsteady aerodynamic modeling in the calculation of the lift distribution is very slight and the vibratory airloads are unchanged. The calculated blade pitching moments are affected by the unsteady aerodynamic models, however. At the rear of the rotor disk, where the blade pitch rate is most negative, all of the analyses show an increase in pitching moment and at the front of the disk a decrease in pitching moment. Smaller changes are observed where the pitch rate is near zero. The RAE/WHL analysis, which showed very different static pitching moment characteristics for Case 5, shows predictions more like the other analyses after the addition of unsteady aerodynamics, although the variation in pitching moment near the blade tip is greater than is seen for the three other analyses.

Case 8 differs from Case 7 in the addition of yawed or radial flow effects in the analytical models. In this flight condition, radial flow modifies mainly the X-force with a reduction of propulsive force and parasite power at a given flap angle. On the other hand, the profile power is augmented by nearly the same amount so that the total power is almost unchanged. If the rotor was to be trimmed to a given propulsive force, then the parasite power would recover its initial value and the profile power increment would remain so that the global rotor efficiency would, in fact, deteriorate. These trends can be clearly seen with the CAMRAD family and METAR/R85. For the RAE/WHL analysis, however, the different power breakdown used makes the differences more difficult to see, but the influence of radial flow is larger, with an increased shaft power for the same blade flapping. The effects of radial flow on the airloads are very slight.

Cases 1 through 8 have examined aerodynamic modeling effects, retaining a simple rigid, hinged blade for the computations. For Case 9, the influence of blade bending modes is examined by adding flap and chord bending degrees of freedom. The RAE/WHL and CAMRAD analyses also add a lag hinge; the METAR/R85 analysis has included a lag hinge for all Task 3 calculations. Compared to a rigid, flapping blade, the difference in performance remains quite small. The cyclic pitch angles exhibit a change in phase of about 11 or 12 degrees for the RAE/WHL and CAMRAD analyses, but this is a

result of adding the lag hinge and no phase change is observed for the METAR/R85 analysis. All of the analyses show similar trends for performance and trim.

The blade airloads are changed with the addition of blade flexibility although these changes are fairly small. The largest change is, of course, the phase shift in the loading caused by the addition of the lag hinge. The RAE/WHL and CAMRAD analyses show about a 10% reduction in the vibratory blade lift, while METAR/R85 shows hardly any effect on lift. The pitching moments are reduced slightly for the RAE/WHL analysis and unchanged for the CAMRAD analyses, while a negative shift is seen for the METAR/R85 analysis.

Case 10 differs from Case 9 in the addition of torsional flexibility. For this case the METAR/R85 analysis would not converge so that the effects of the torsional degree of freedom are assessed using just the RAE/WHL and CAMRAD analyses.

The torsion degree of freedom does not play a large role in rotor performance for this moderate velocity and moderate lift flight condition according to the RAE/WHL and the CAMRAD analyses. However, the collective pitch angle required for this trim condition does vary with the RAE/WHL analysis showing a decrease and the CAMRAD analyses an increase. The amplitude and phasing of the cyclic trim angles also change with the RAE/WHL analysis showing an increase in the cyclic trim and the CAMRAD analyses a decrease.

The blade angles of attack and airloads are changed with the inclusion of the torsion degrees of freedom and these changes are of the same magnitude as those observed in going from Case 8 to Case 9, except that the vibratory airloads have increased by about 10% rather than being reduced by 10%. The blade pitching moments near the tip show some influence as well, particularly on the advancing side where the RAE/WHL analysis shows a slight reduction in the loads and the CAMRAD analyses a slight increase.

# 5 COMPARISON OF LIFTING-LINE METHODS WITH FLIGHT TEST DATA (TASK 1)

## 5.1 Introduction

Three sets of calculations were made with the lifting-line methods for Task 1 of the cooperative program: a set of calculations based on an airspeed sweep from Flight 525 that were the basis of the assessment; a set of reference calculations based on one airspeed from Flight 123 for a Puma with a rectangular-tip blade; and a set of calculations for an autorotational dive condition, Flight 487, that provided the basis for the CFD solutions reported in Section 6.

The primary purpose of the lifting-line methods assessment was to examine the accuracy of these methods over a range of forward flight speeds. For this purpose cases were selected from Flight 525 that included data for sixteen advance ratios from $\mu = 0.098$ to $\mu = 0.402$. Lifting-line predictions were then made for five of the sixteen advance ratios and comparisons with the flight test data are presented in Section 5.2. The highest speed case, $\mu = 0.402$, was also used as a basis for CFD computations and this is discussed in Section 6.3.

The Flight 123 case that is discussed in Section 5.3 was selected to provide a reference or baseline case with the standard Puma blade without the swept tip. Prior to the initiation of the cooperative effort that is reported here it was believed that the effects of the swept tip of the research Puma might confuse both the interpretation of available flight test data and the calculations. It was concluded, therefore, that it would be valuable to make calculations for one flight condition from Flight 123 and, through comparison with Flight 525, examine the effects of tip sweep on both the lifting-line predictions and the flight test data.

Calculations were also made for the research Puma for an autorotational dive condition on Flight 487 that achieved an advance ratio of $\mu = 0.429$ and an advancing tip Mach number of $M_{90} = 0.922$. These calculations are discussed in Section 5.4 and provide a basis for the CFD computations reported in Section 6.2.

The standard Puma airfoil section is similar to a NACA 0012 and, as a consequence, NACA 0012 section data are used as airfoil tables in the lifting-line calculations. The modifications that were made to the research Puma to sweep the tip and increase blade area outboard also influenced the airfoil profile at the outboard sections. Section 5.5 describes the various airfoil sections and summarizes measurements that were made of the swept-tip profile and some theoretical, two-dimensional calculations that were made to assess the swept-tip airfoil modifications.

Finally, some summary comments concerning the predictions for Task 1 are provided in Section 5.6.

The computed blade airloads and structural loads that are compared with flight test data in this section were, in general, not obtained for the same radial stations. However, the radial spacing used by these analyses for the computed loads is quite fine and, when direct comparisons are shown in this section as a function of the rotor azimuth, linear interpolation has been used with the theoretical data to

provide a direct comparison with the experimental measurements at the indicated radial station. Errors introduced by the use of linear interpolation are small in comparison to differences seen between the analyses and the data. In a number of cases, comparisons are made between experimental measurements obtained on different rotor configurations and, again, linear interpolation is used for one or the other data sets. In these cases, the data set for which interpolation was used is indicated.

## 5.2 Advance Ratio Sweep (Flight 525)

### 5.2.1 Flight Data

Data were obtained at sixteen advance ratios for Flight 525 with level flight test points from $\mu = 0.098$ to 0.402. Five of these cases were chosen for correlation and these are shown in table 17 where 'Counter' refers to the test point or condition. A trim condition was specified equivalent to isolated rotor trim in a wind tunnel, that is, five trim variables were specified: airspeed, rotor thrust, $C_T/\sigma$, shaft angle of attack, $\alpha_s$, and the first harmonic flapping angles measured at the blade hinge, $\beta_{1c}$ and $\beta_{1s}$. The flapping angle harmonic coefficients, $\beta_{1c}$ and $\beta_{1s}$, are defined as a conventional (positive) Fourier series. Positive $\beta_{1c}$ represents tilting of the rotor disk forward and positive $\beta_{1s}$ represents tilting of the rotor disk to the right (clockwise rotation). Although the shaft angle and flapping angles are directly measured, the rotor thrust is not measured and, instead, is assumed to be the same as the aircraft weight. The purpose in selecting an isolated rotor trim as a basis for these comparisons was to simplify the problem as much as possible and remove confounding factors.

Table 17. Flight 525 correlation cases

| Counter | 3 | 7 | 12 | 17 | 21 |
|---|---|---|---|---|---|
| $\mu$ | 0.0978 | 0.1821 | 0.3074 | 0.3619 | 0.4019 |
| $M_{90}$ | 0.6481 | 0.6983 | 0.7702 | 0.8026 | 0.8265 |
| $C_T/\sigma$ | 0.0700 | 0.0694 | 0.0701 | 0.0700 | 0.0699 |
| $\alpha_s$, deg | −1.10 | −2.70 | −5.70 | −7.40 | −9.05 |
| $\beta_{1c}$, deg | −0.223 | −0.732 | 0.040 | 0.116 | 0.437 |
| $\beta_{1s}$, deg | −0.319 | −0.293 | −0.082 | 0.078 | 0.222 |
| $C_Q/\sigma$ | 0.00409 | 0.00410 | 0.00608 | 0.00846 | 0.01085 |
| $\Omega$, rpm | 254.9 | 254.6 | 253.9 | 254.0 | 254.1 |

The blade instrumentation for Flight 525 is shown in figure 62. Flap bending moments were measured on the strain-gauge blade at eleven radial stations: $0.20R$, $0.26R$, $0.30R$, $0.36R$, $0.41R$, $0.46R$, $0.57R$, $0.62R$, $0.67R$, $0.78R$, and $0.83R$. The distribution of chord bending moment stations was more sparse: $0.122R$, $0.33R$, and $0.55R$. Torsion moments were measured at $0.126R$, $0.33R$, and $0.55R$. Surface pressures were measured on the tip section of the pressure blade as indicated in figure 62. The radial and chord locations of these transducers are given in table 18. Note that there were no lower surface measurements at $0.89R$.

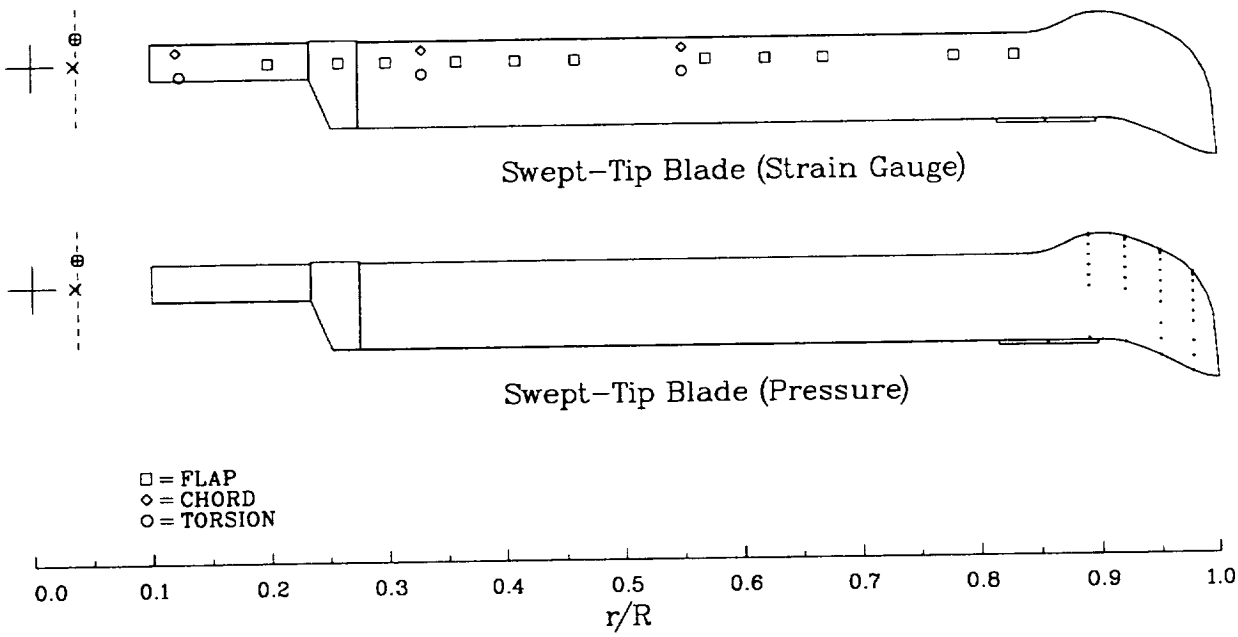


Figure 62. Structural and pressure instrumentation installed on the research Puma blade.

Table 18. Pressure transducer locations, x/c

| $0.89R$ | | $0.92R$ | | $0.95R$ | | $0.978R$ | |
|---|---|---|---|---|---|---|---|
| U | L | U | L | U | L | U | L |
| $0.000c$ | | $0.000c$ | | $0.000c$ | | $0.000c$ | |
| | | $0.002c$ | | $0.002c$ | | $0.002c$ | |
| $0.005c$ | | $0.005c$ | | $0.005c$ | | $0.005c$ | |
| | | $0.010c$ | | $0.010c$ | | $0.010c$ | |
| $0.020c$ | | $0.020c$ | | $0.020c$ | | $0.020c$ | |
| | | $0.040c$ | | $0.040c$ | | $0.040c$ | |
| $0.100c$ | | $0.100c$ | $0.100c$ | $0.100c$ | $0.100c$ | $0.100c$ | $0.100c$ |
| $0.200c$ | | $0.200c$ | $0.200c$ | $0.200c$ | $0.200c$ | $0.200c$ | $0.200c$ |
| $0.300c$ | | $0.300c$ | $0.300c$ | $0.300c$ | $0.300c$ | $0.300c$ | $0.300c$ |
| $0.400c$ | | $0.400c$ | $0.400c$ | $0.400c$ | $0.400c$ | $0.400c$ | $0.400c$ |
| $0.550c$ | | $0.550c$ | $0.550c$ | $0.550c$ | $0.550c$ | $0.550c$ | $0.550c$ |
| | | | | $0.700c$ | $0.700c$ | $0.700c$ | $0.700c$ |
| | | | | $0.850c$ | $0.850c$ | $0.850c$ | $0.850c$ |
| $1.000c$ | | $1.000c$ | | $1.000c$ | | $1.000c$ | |

A general notion of the section lift and pitching moment behavior near the blade tip can be obtained from an examination of these parameters at $0.95R$ as a function of airspeed. Figure 63 shows the lift and pitching moment as surface plots as functions of azimuth and advance ratio where the five advance ratios selected for correlation are emphasized by thickened lines. At low speed the airloads near the blade tip are dominated by the vorticity in the rotor wake that causes a down-up pulse on the advancing side of the rotor and an up-down pulse on the retreating side. As the airspeed increases, this vorticity loading decreases and the pulse-like signatures from this loading are largely gone by $\mu = 0.3$. As the airspeed is further increased an area of reduced section lift is seen on the advancing side of the rotor and for $\mu > 0.3$ this lift becomes negative. The section moment at high speed is characterized by a large positive moment over the rear of the disk that becomes negative at the beginning of the second quadrant.

The lift and pitching moment were obtained from the pressure measurements by a trapezoidal integration in the mapped coordinates $\sqrt{x/c}(c_p)$ as a function of $\sqrt{x/c}$ which is considered more accurate than the integration of $c_p$ as a function of $x/c$. The blade chord force was not computed. Strictly speaking, this integration provides the section normal force, not lift, but the two terms are used interchangeably here. The pitching moment is defined at all radial stations relative to the local quarter chord. The applied torsional moment seen by the blade at any station will, of course, include the couple induced by the normal force and the offset (if any) of the the local quarter chord from the blade's torsion axis which is assumed to be coincident with the unswept quarter chord. In all cases the data were obtained from a single rotor revolution.

The lift and pitching moment are examined in more detail for the low-speed case, $\mu = 0.098$, in figure 64. Lift variations on the advancing and retreating sides of the rotor disk induced by vorticity in the wake are clearly seen in this figure. As expected, the peak loading on the advancing side is seen at the most outboard station, $0.978R$, initially and then moves inboard, while on the retreating side the peak is first encountered at the most inboard station, $0.92R$, and then moves outboard. In terms of the integrated pressures it is unclear whether this vorticity is primarily caused by the tip vortex of the previous blade or the combined vorticity of intertwined tip vortices as suggested by calculations using the CAMRAD/JA free wake model (Bousman and Maier, 1992). An examination of the upper surface pressure time histories is shown in figure 65 where the individual pressure time histories have been offset and ordered from leading edge to trailing edge on the airfoil. Near the leading edge of the blade there is an indication of a second oscillation in the loading, both on the advancing and retreating sides, but this secondary oscillation is much smaller than the primary vorticity loading that is seen over the forward portion of the airfoil.

The section lift and moment for the high speed case, $\mu = 0.402$, are shown in figure 66. The section lift varies greatly on the advancing side to maintain a trimmed flight condition. Less variation is seen on the retreating side. At the rear of the disk the lift shows a rapid decrease towards the blade tip while on the front of the disk there is almost no change seen in moving from $0.92R$ to $0.978R$. A small change in lift seen at $0.95R$ just past $315^\circ$ is believed a result of a minor slip ring malfunction for the pressure tranducers at this station. The largest pitching moments are seen on the advancing side of the disk with a maximum in the moment in the first quadrant and a minimum in the second quadrant. In the first quadrant the pitching moment is observed to increase as the blade tip is approached.

SECTION LIFT

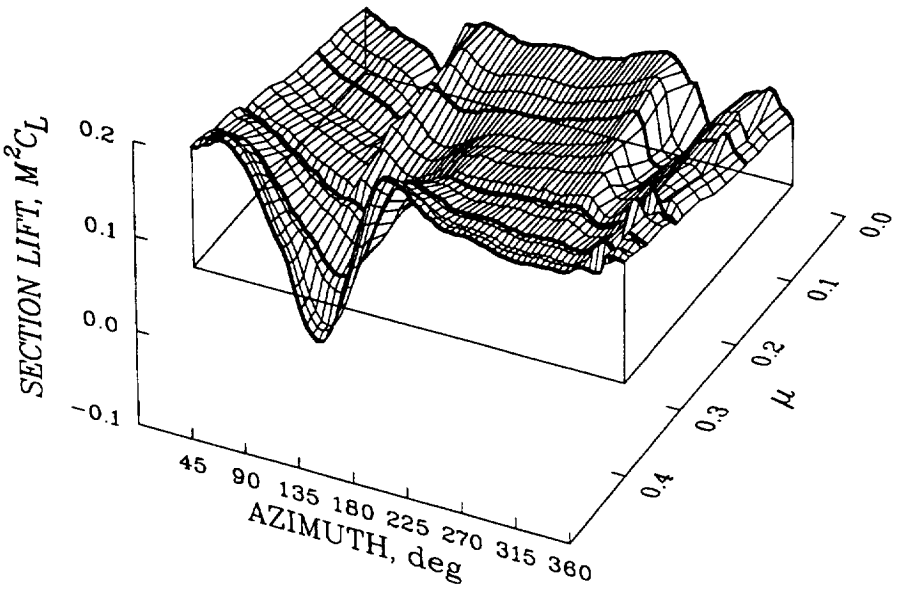


SECTION MOMENT

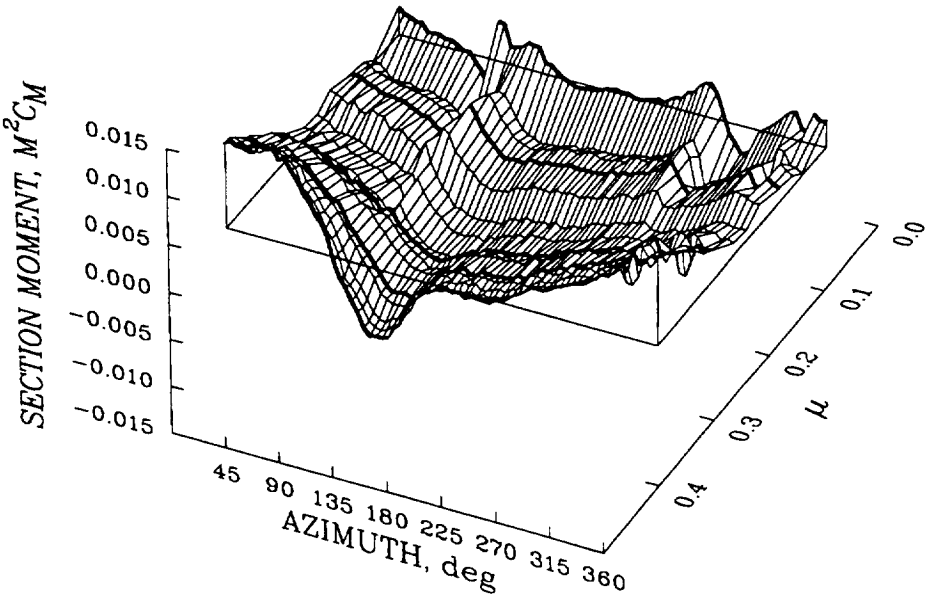


Figure 63. Section lift and pitching moment as a function of azimuth and advance ratio for Flight 525; $0.95R$. Correlation cases shown by thickend lines.

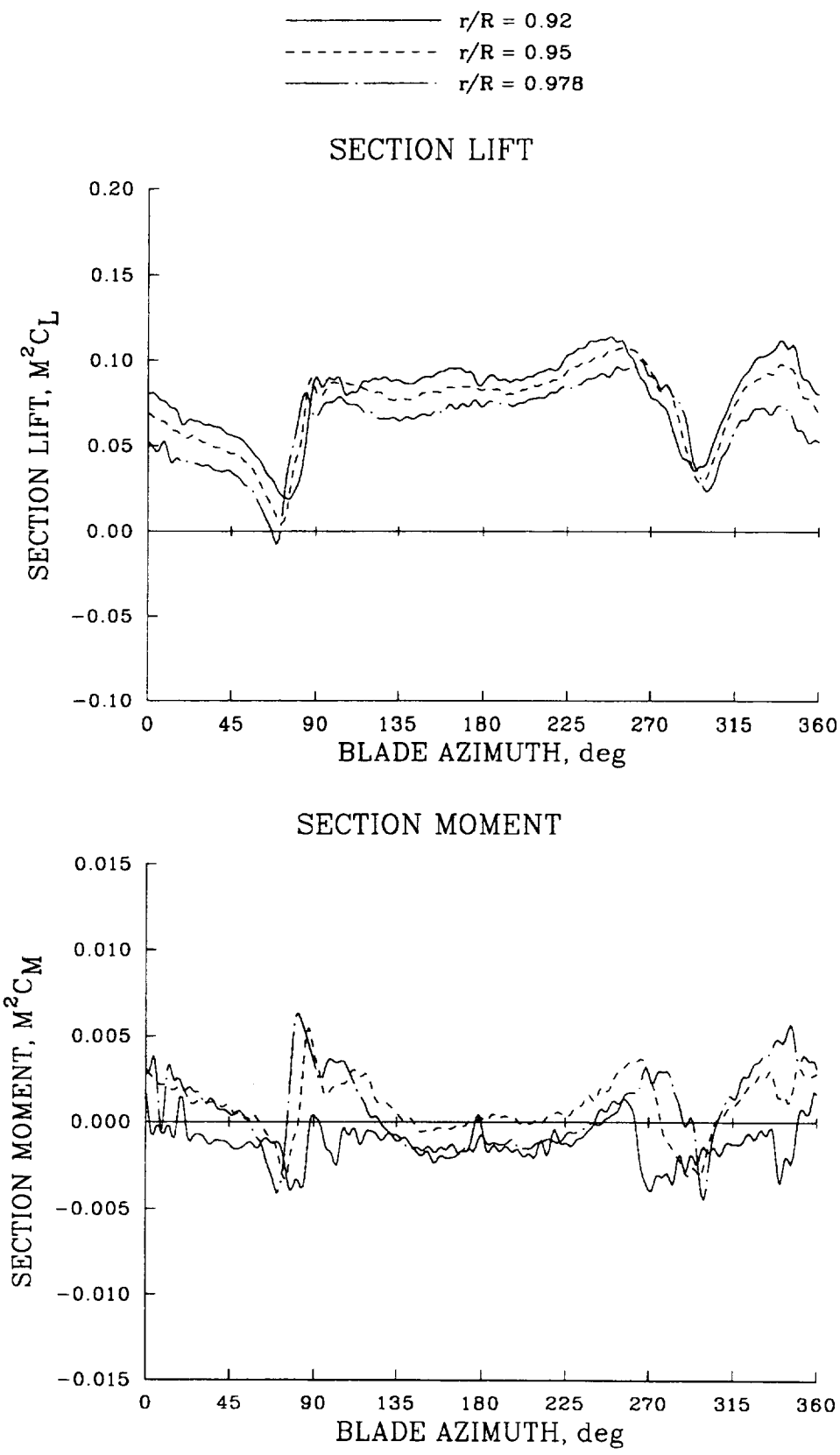


Figure 64. Section lift and pitching moment as a function of azimuth at low speed; $\mu = 0.098$.

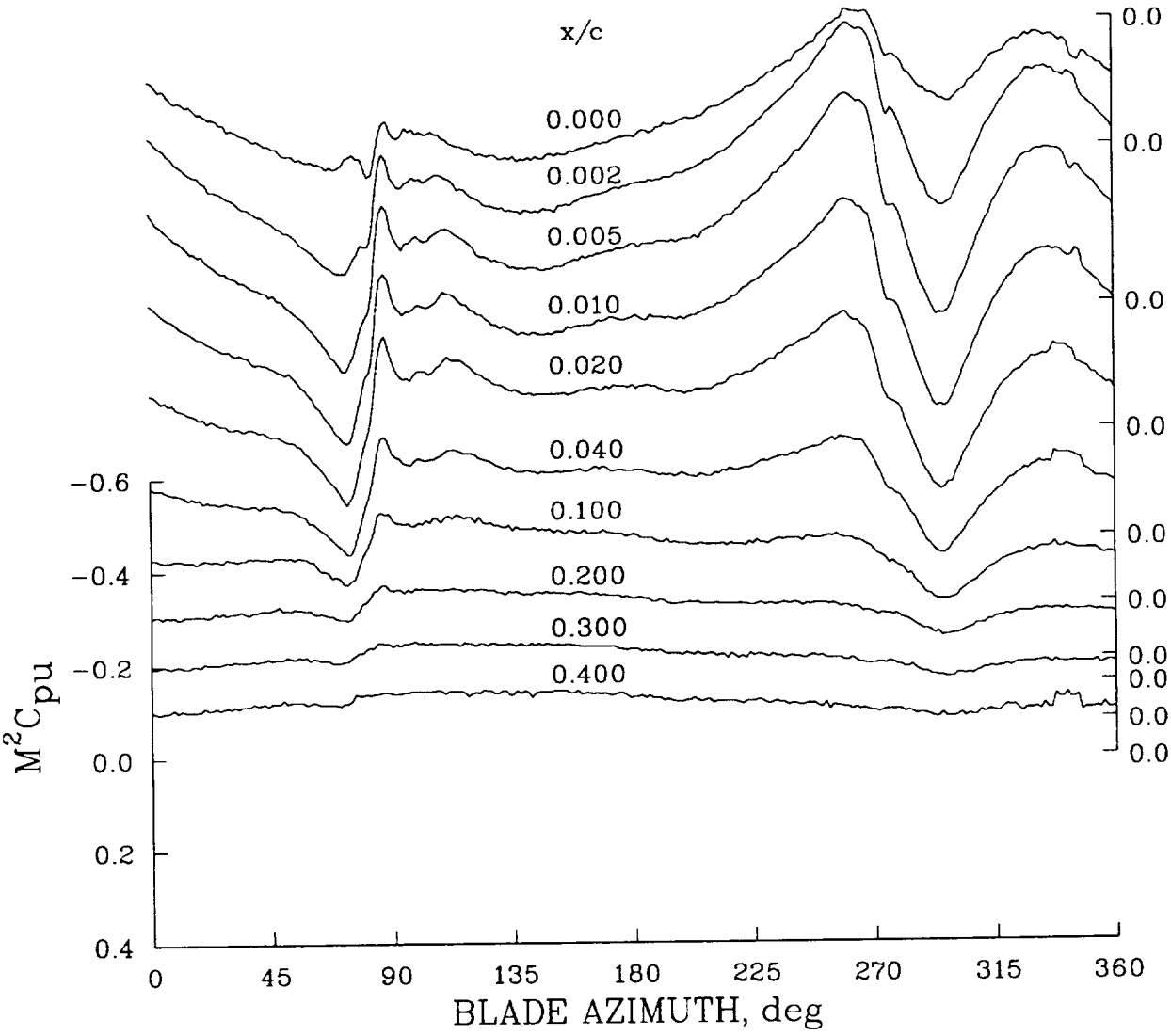


Figure 65. Upper surface pressure as a function of azimuth at low speed; $0.95R$, $\mu = 0.098$.

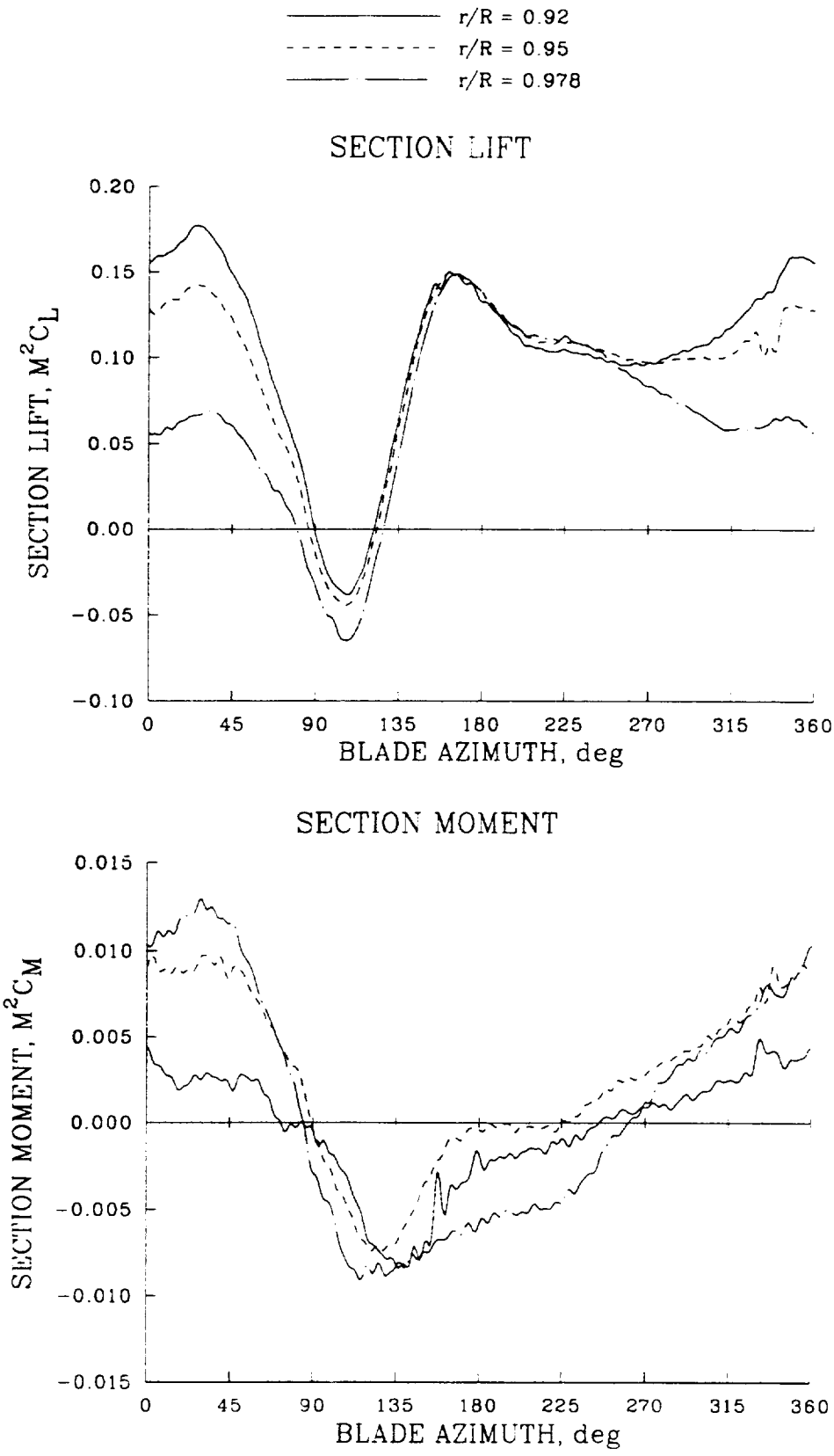


Figure 66. Section lift and pitching moment as a function of azimuth at high speed; $\mu = 0.402$.

The upper surface pressures on the forward portion of the airfoil at $0.95R$ are shown in figure 67. Included in this plot is the $M = 1$ boundary which indicates regions of supercritical flow. For the most part these supercritical flows occur very near the leading edge of the airfoil at the rear of the disk where the angle of attack is quite high. Little supercritical flow is observed at the beginning of the second quadrant, probably because of the sweep in the blade tip.

The flap bending moment variation with airspeed is shown in figure 68. Although not readily visible in this surface plot the dominant 3/rev loading is greatest at the low- and high-speed extremes and lowest in the middle range of airspeeds. The extensive flap bending moment instrumentation installed on the blade provides considerable resolution in the flap bending moment distribution, and the azimuthal and radial distributions of flap bending moment are shown at the low and high airspeeds in figure 69. The 3/rev character of the loading is seen at both low and high speeds and is the dominant component at nearly all blade stations. The largest loading is observed near the mid portion of the blade. Excursions in the measurements at the rear of the disk for the low-speed condition are believed to be related to instrumentation or slip-ring problems.

The bias or zero setting for all structural measurements were obtained with the aircraft on the ground and, therefore, included static moments. No corrections have been made for these static moments and, therefore, the steady or zero harmonic components are not included in these figures nor in any of the comparisons with calculation.

The bending moment nondimensionalization used here is analogous to a blade aerodynamic loading coefficient $C_T/\sigma$, that is,

$$\frac{C_{FM}}{\sigma} = \frac{M_\beta}{\pi\sigma\rho V_T^2 R^3} \tag{5-1}$$

where $M_\beta$ is the flap bending moment, $\sigma$ is the rotor solidity, $\rho$ is the density of air, $V_T$ is the tip speed, and $R$ is the blade radius.

The chord bending moment variation with airspeed is shown in figure 70 for a midspan station. The dominant loading at the center of the blade is 4/rev and this loading increases rapidly with advance ratio. The chord bending moment was measured at only three stations so that azimuthal/radial plots of the distribution do not show the richness in detail that was seen for the flap bending moment. Figure 71 shows the chord bending distribution for the low- and high-speed conditions. The amplitude of chord bending is relatively low for the low-speed case and instrumentation noise at the outer radial station makes it difficult to interpret the bending moment distribution. At the maximum speed the chord bending moments are quite pronounced and it is interesting to note that the 4/rev character changes to primarily a 3/rev loading near the blade root. The chord bending moment nondimensionalization used here is the same as for the flap bending moment.

The torsion moment variation with airspeed is shown in figure 72 for a blade root location. The torsion loading is relatively low for the low advance ratio case and increases with airspeed. At the maximum airspeed a strong positive moment is seen in the first quadrant and this moment becomes negative at about 90° and there is a peak in the negative torsion moment at about 135°. The moment then returns to a positive value with a 4/rev oscillation superimposed. The torsion moment on the

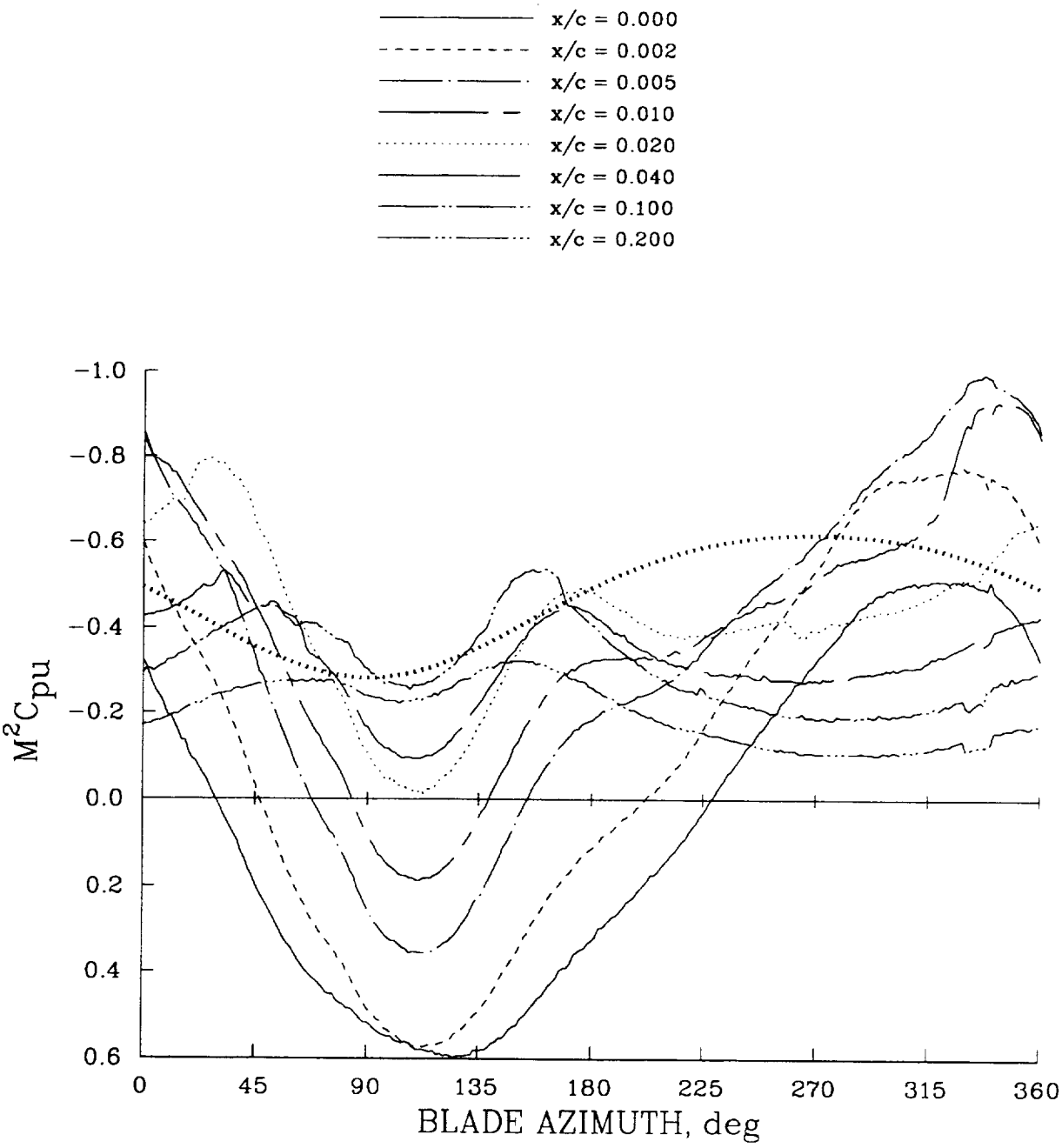


Figure 67. Upper surface pressure as a function of azimuth at high speed; $0.95R$, $\mu = 0.402$. $M = 1$ boundary shown as heavy dotted line.

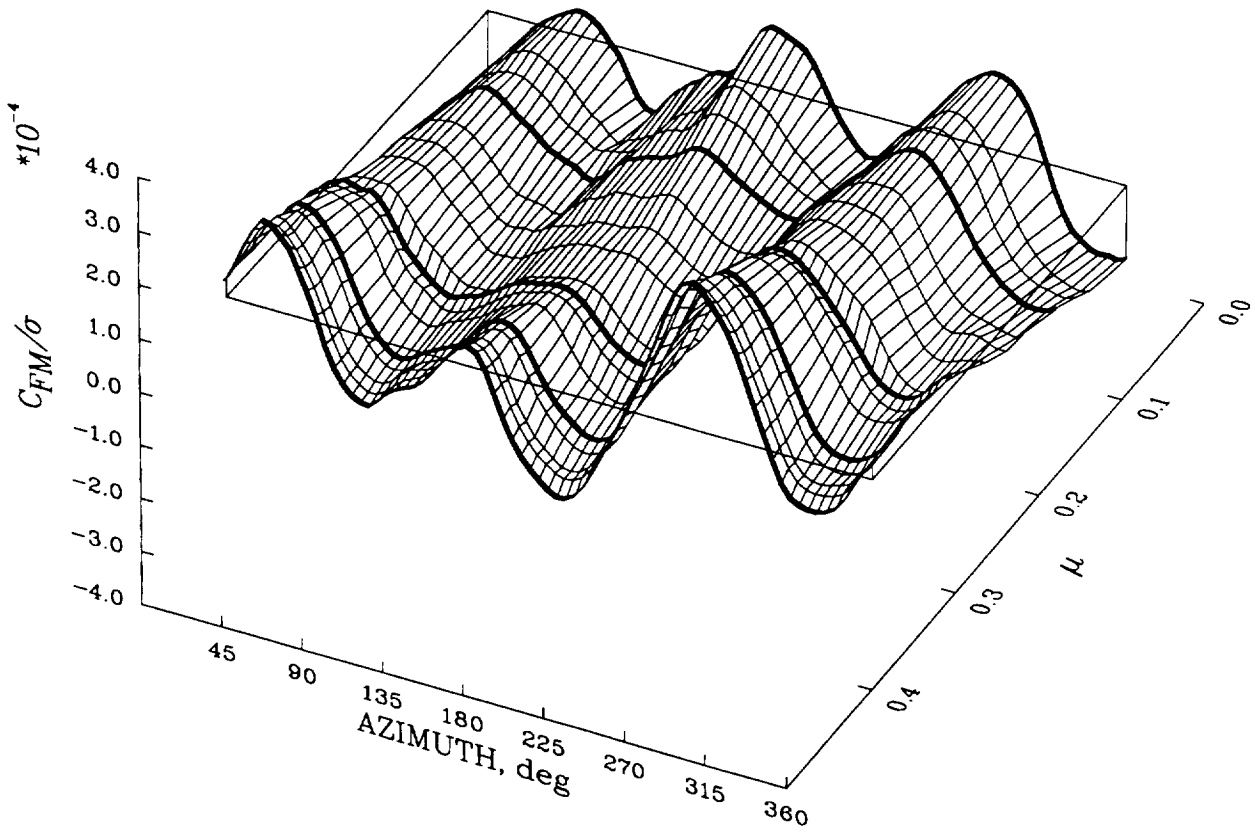


Figure 68. Flap bending moment distribution as a function of azimuth and advance ratio; $0.57R$, 1–32 harmonics.

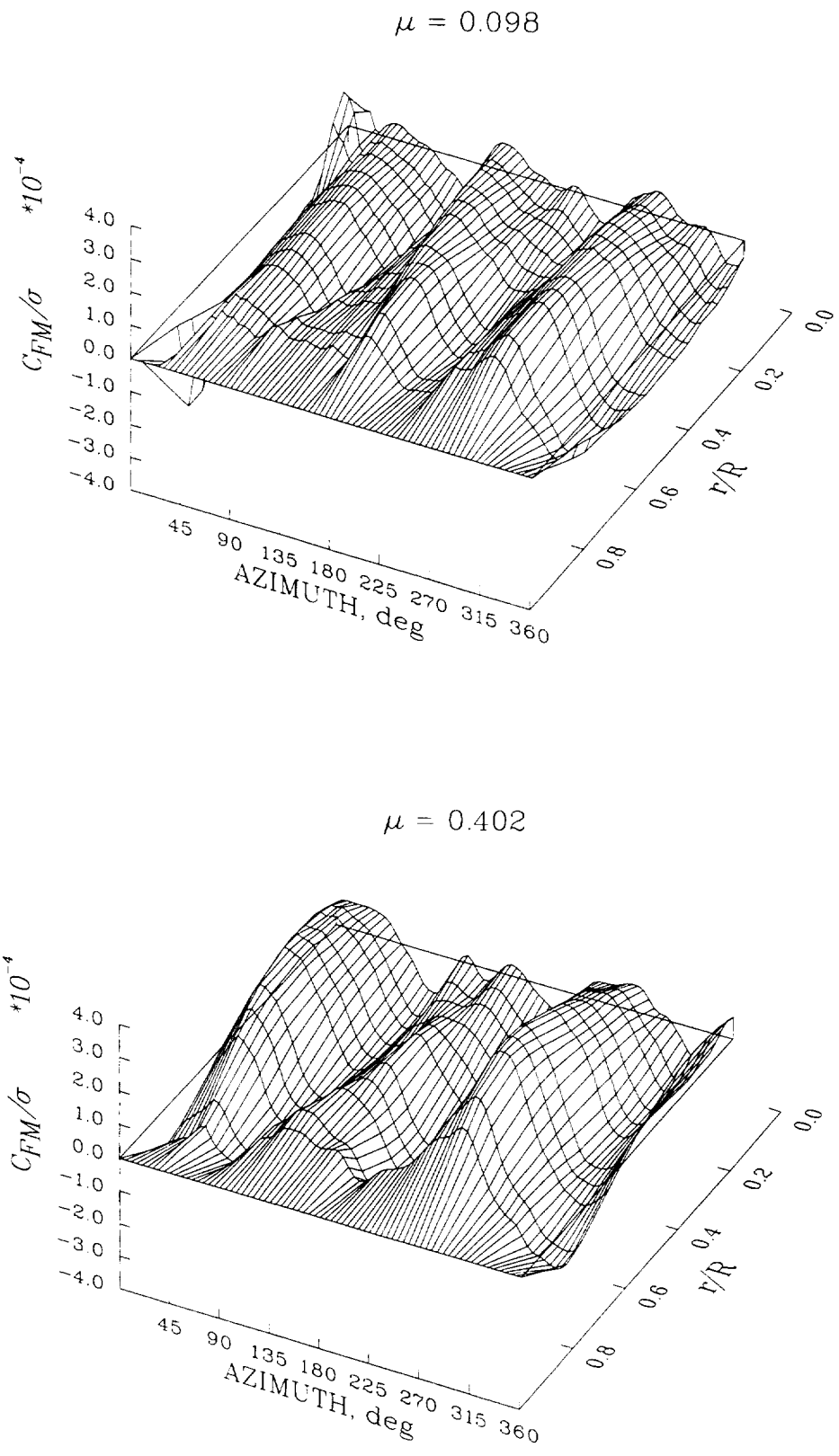


Figure 69. Flap bending moment distribution as a function of azimuth and blade radius for $\mu = 0.098$ and 0.402, 1–32 harmonics.

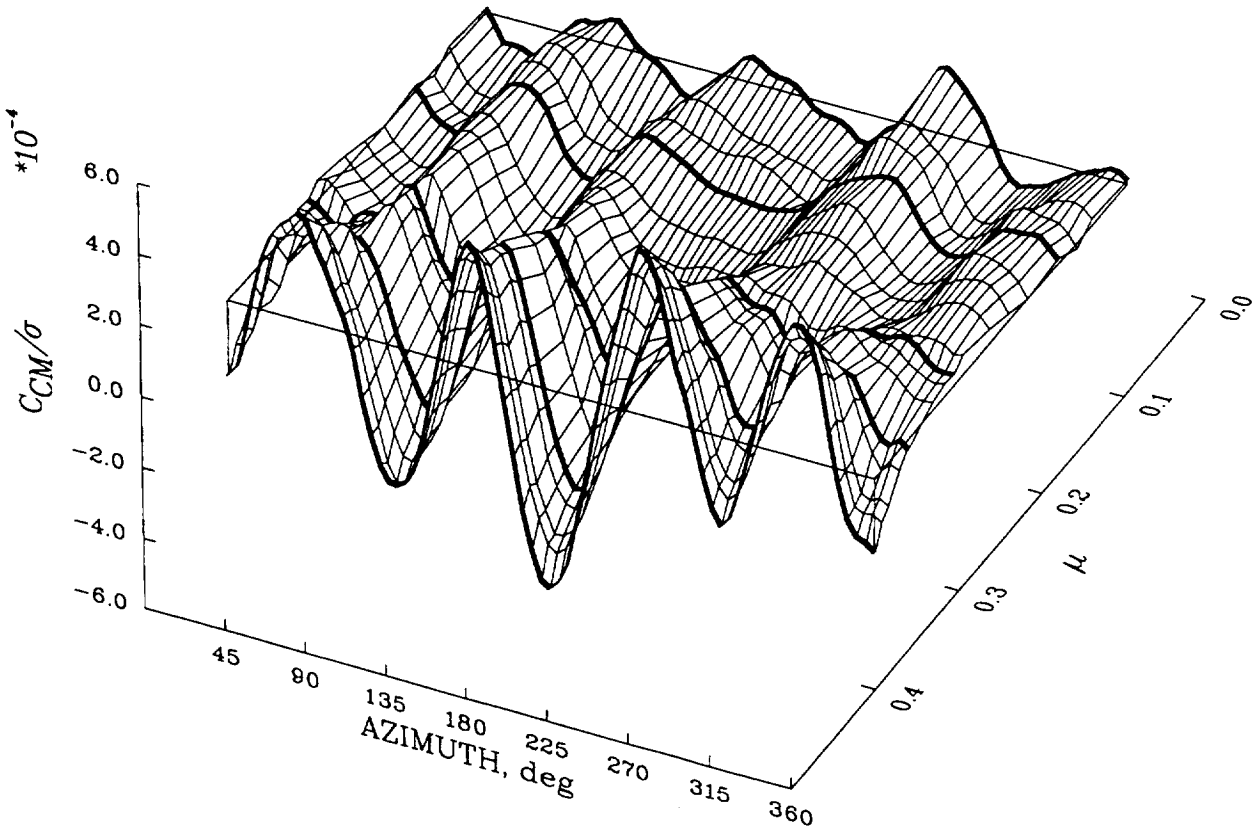


Figure 70. Chord bending moment distribution as a function of azimuth and advance ratio; $0.55R$, 1–32 harmonics.

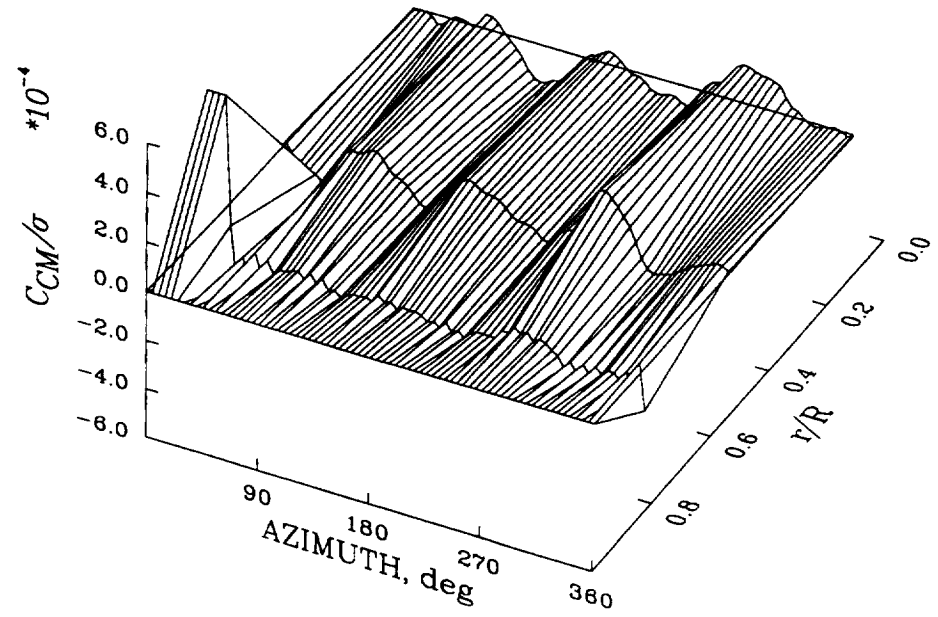


$\mu = 0.402$

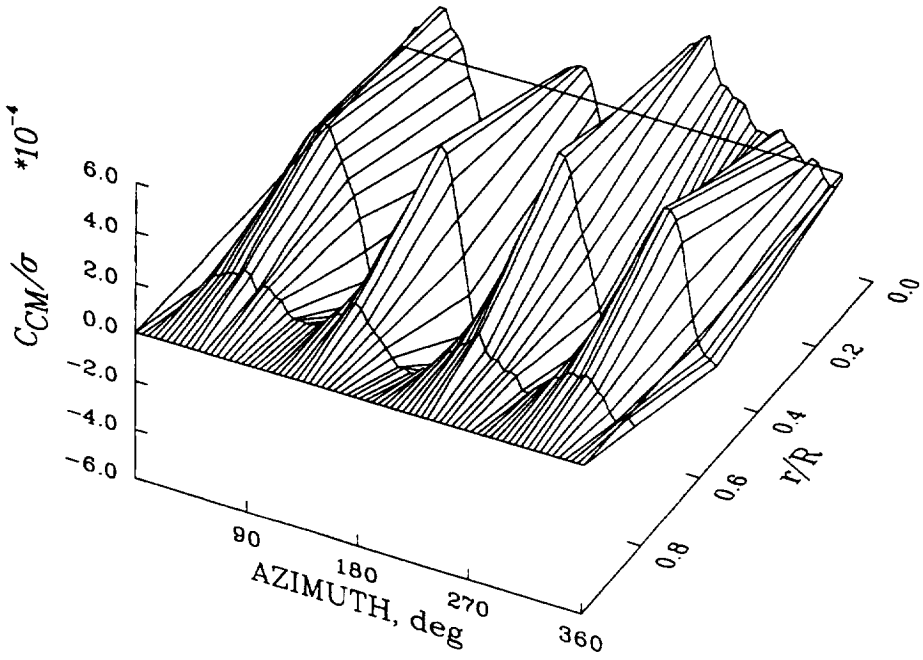


Figure 71. Chord bending moment distribution as a function of azimuth and blade radius for $\mu = 0.098$ and 0.402, 1–32 harmonics.

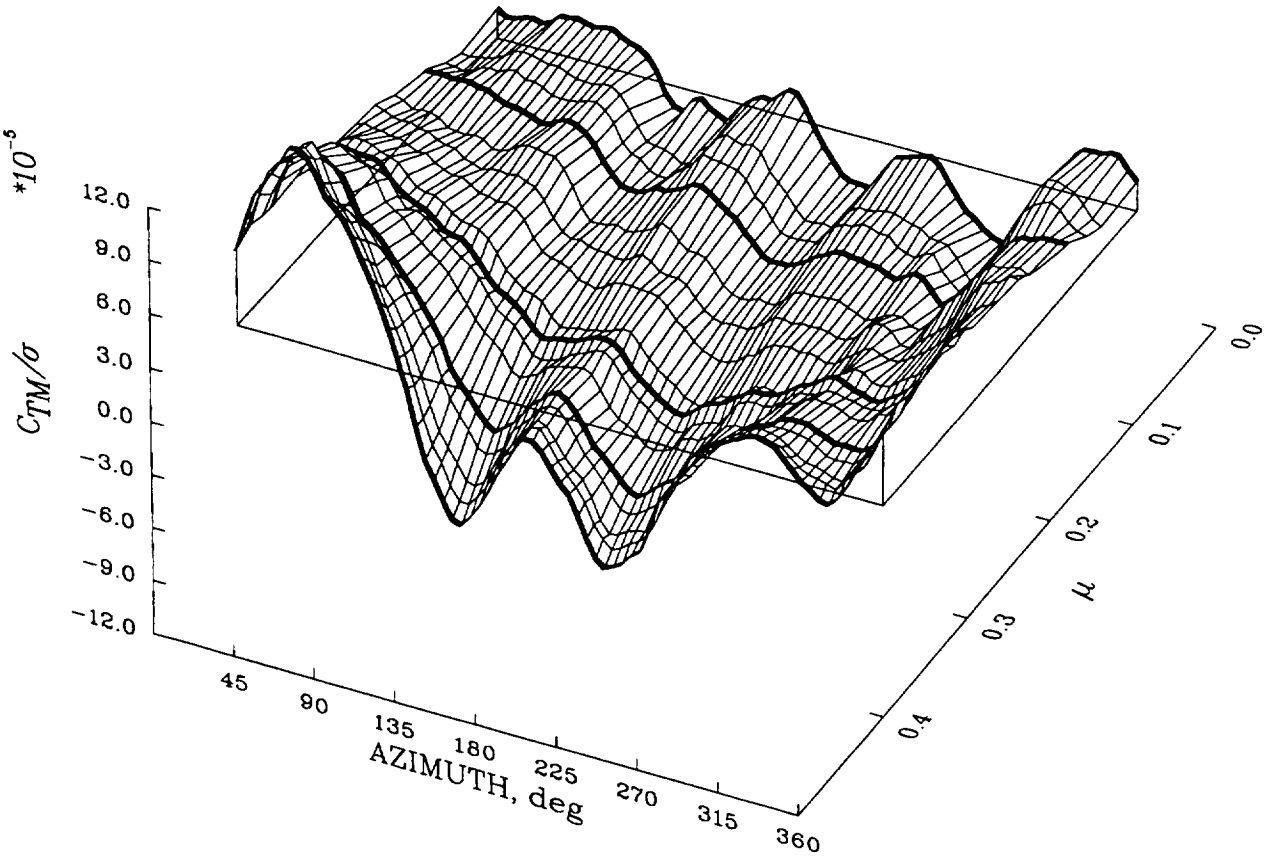


Figure 72. Torsion moment distribution as a function of azimuth and advance ratio; $0.126R$, 1–32 harmonics.

advancing side of the disk is very similar to the aerodynamic moment seen near the blade tip, for instance figure 63. Torsion moment measurements were obtained at only three radial stations so the distribution is more difficult to interpret than for the flap bending moment case. Figure 73 shows the torsion distribution for the low- and high-speed conditions and, as was apparent in figure 72, the torsion amplitude is quite low at $\mu = 0.098$. However, at high speed the torsion loads are quite high and the advancing side loading is, apparently, a direct consequence of the aerodynamic moment at the blade tip.

The variation in the pitch-link loads with airspeed is shown in figure 74. These loads appear nearly identical to the root torsion moment shown in figure 72 and, just as in that case, are a consequence of the aerodynamic loading induced at the blade tip.

The distribution of the blade geometric pitch angle as measured at the blade root and calculated at $0.75R$ using the built-in twist is shown in figure 75. The pitch angle distribution is relatively smooth and, as expected, shows an increase in the 1/rev cyclic pitch variation as advance ratio increases. At high speed the blade pitch angle is near zero on the advancing side because of the dynamic balance around the flap hinge. As a consequence, compressibility drag is minimized. The collective pitch for the airspeed sweep is shown in figure 76 and the lateral (cosine) and longitudinal (sine) pitch angles are shown in figure 77. The collective pitch angle increases with airspeed, particularly above $\mu = 0.2$ and, as expected, the lateral cyclic angle varies only slightly over the advance ratio range while the longitudinal cyclic becomes progressively more negative with airspeed. The measured collective and cyclic control positions are not used in the analytical efforts to specify the rotor trim and, therefore, the correlation of analysis with these measurements provides a test of the accuracy of the rotor trim computation. The reference here to first harmonic cosine and sine components assumes a conventional Fourier series.

The blade pitch angle was measured at the location of the blade pitch bearing. Some knowledge of control system flexibility may be obtained by examining this pitch angle measurement after removing the steady and first harmonic components which are the control angles. Figure 78 shows this measurement for the maximum airspeed condition and it can be seen that the amount of flexibility in the control system is fairly small, less than $\pm 0.4°$, and that the motion in the control system is largely at 3/rev. The swashplate fixed-system actuators for the Puma are spaced equidistantly around the swashplate and are located at 60°, 180°, and 300°. These locations coincide fairly closely with the most positive pitch angles and suggest that most of the flexibility in this control system is in the swashplate.

Blade flapping was measured by a potentiometer at the flapping hinge on three of the four blades. The distribution of blade flapping with azimuth and advance ratio is shown in figure 79. Particularly at high speed there is more 2/rev and 3/rev content in the measurement than 1/rev. The first harmonic flapping is shown in figure 80 as a function of advance ratio. This figure compares the flapping measurements from all three blades with the trim values specified for the five correlation cases.

The blade lead-lag angle was measured with a potentiometer around the lead-lag hinge. The distribution of blade lead-lag angle with azimuth and advance ratio is shown in figure 81. There is little harmonic content in the lead-lag angle measurement and this is undoubtedly a consequence of the lead-lag damper. The steady lag angle increases with airspeed because of the increasing steady drag on the blade. However, it appears that the offset is erroneous for these measurements and the steady lag angle is more like 10° than the 14° or 15° shown here. This will be discussed in Section 5.4.1.

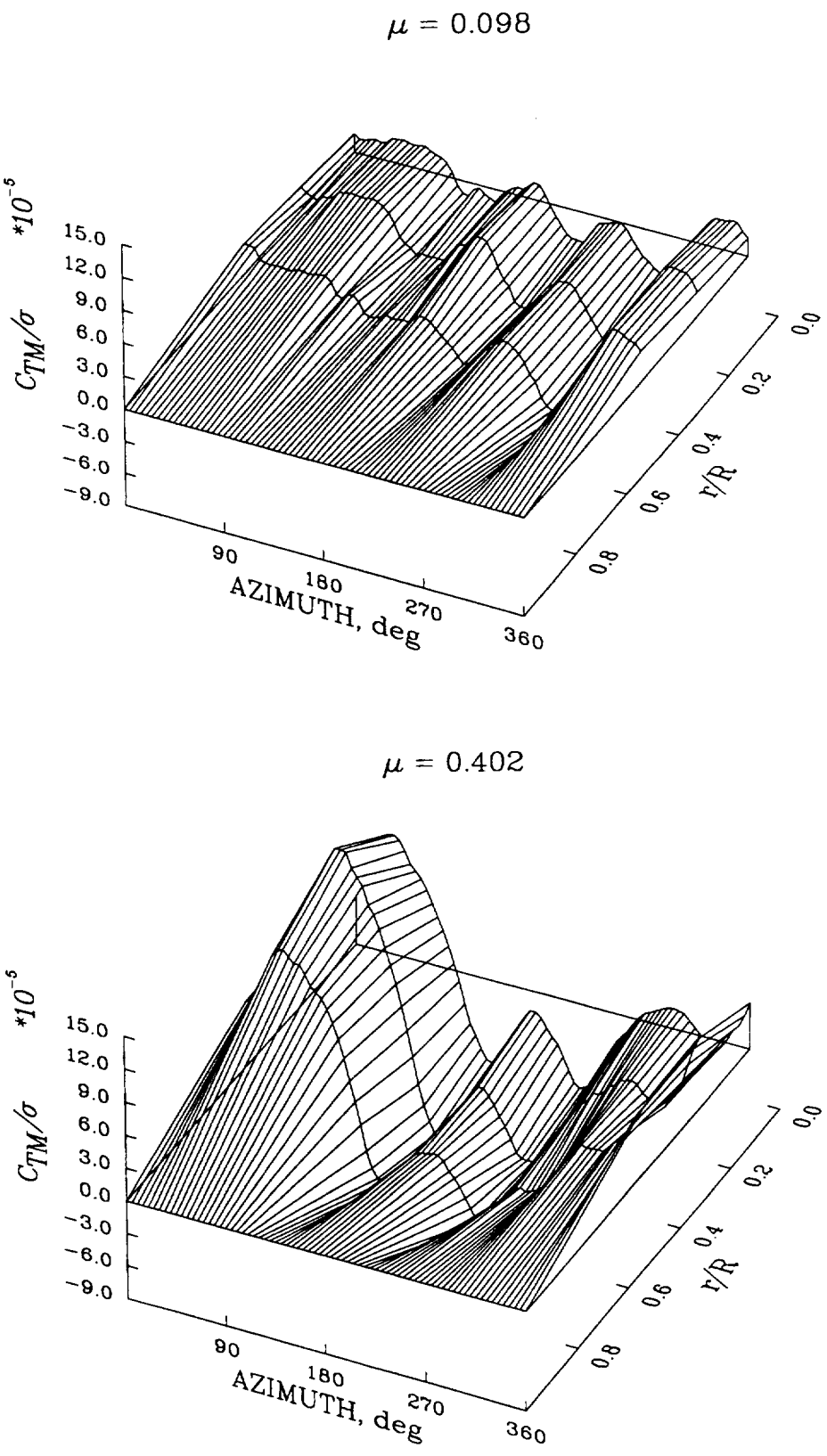


Figure 73. Torsion moment distribution as a function of azimuth and blade radius for $\mu = 0.098$ and 0.402, 1–32 harmonics.

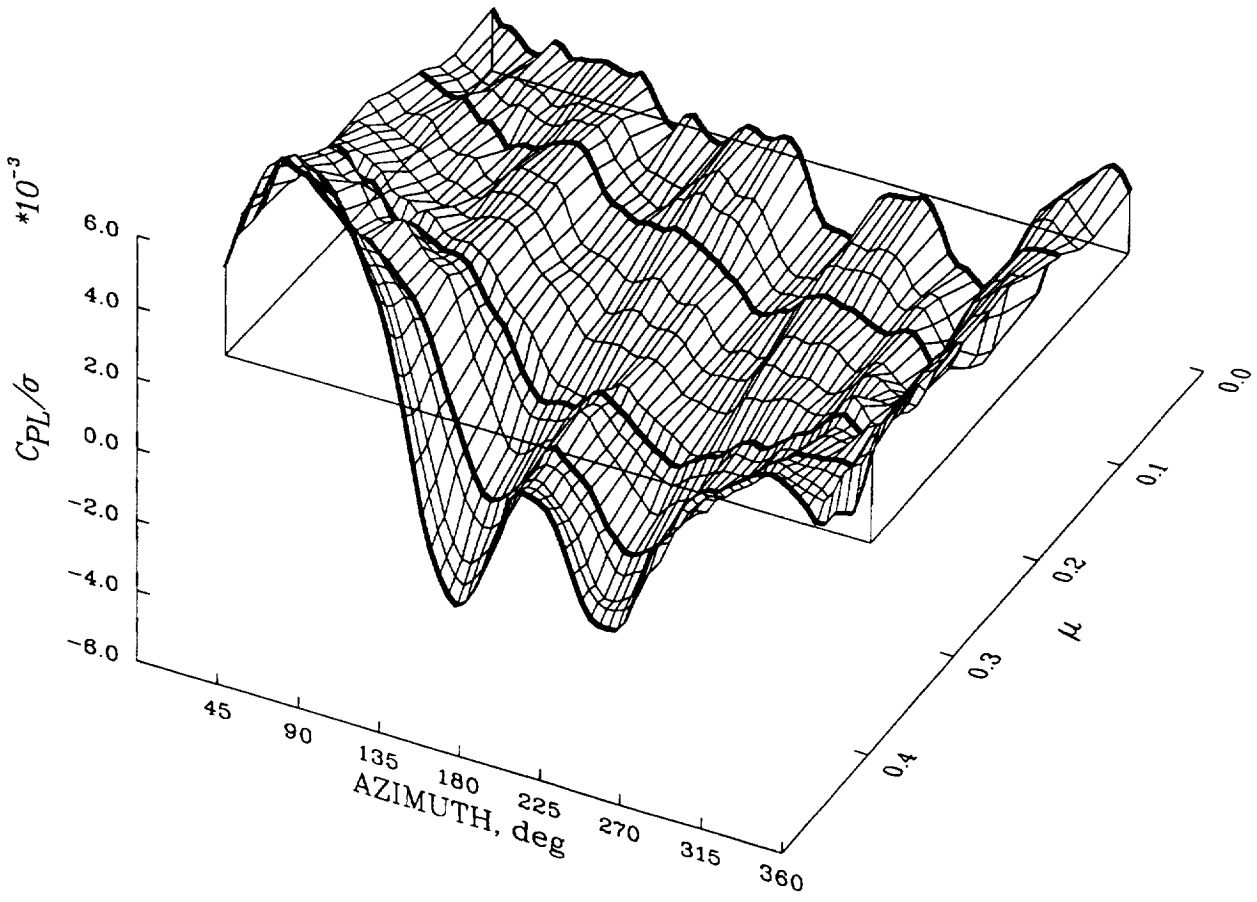


Figure 74. Pitch-link load distribution as a function of azimuth and advance ratio, 1–32 harmonics.

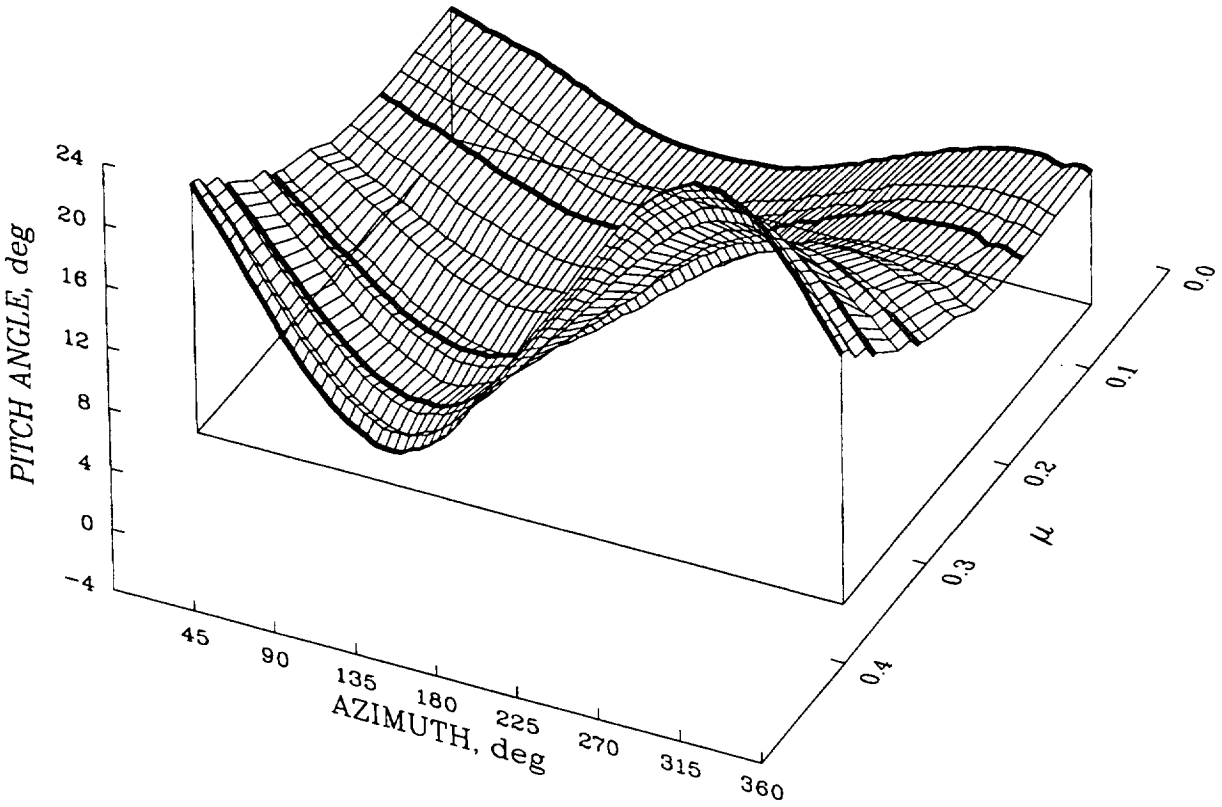


Figure 75. Blade pitch angle distribution at $0.75R$ as a function of azimuth and advance ratio.

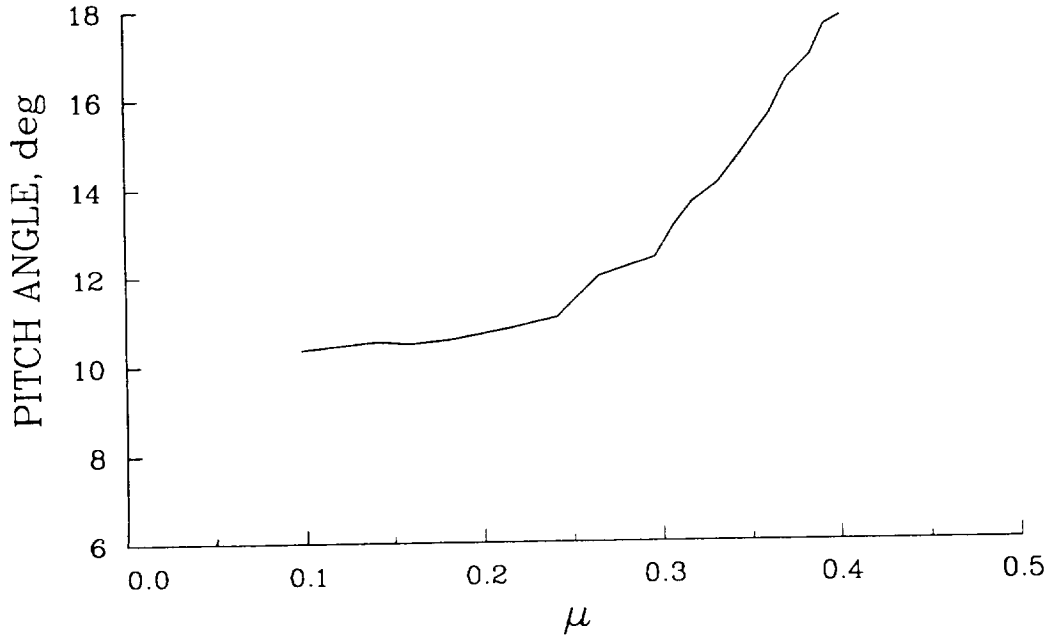


Figure 76. Collective pitch angle at $0.75R$ as a function of advance ratio.

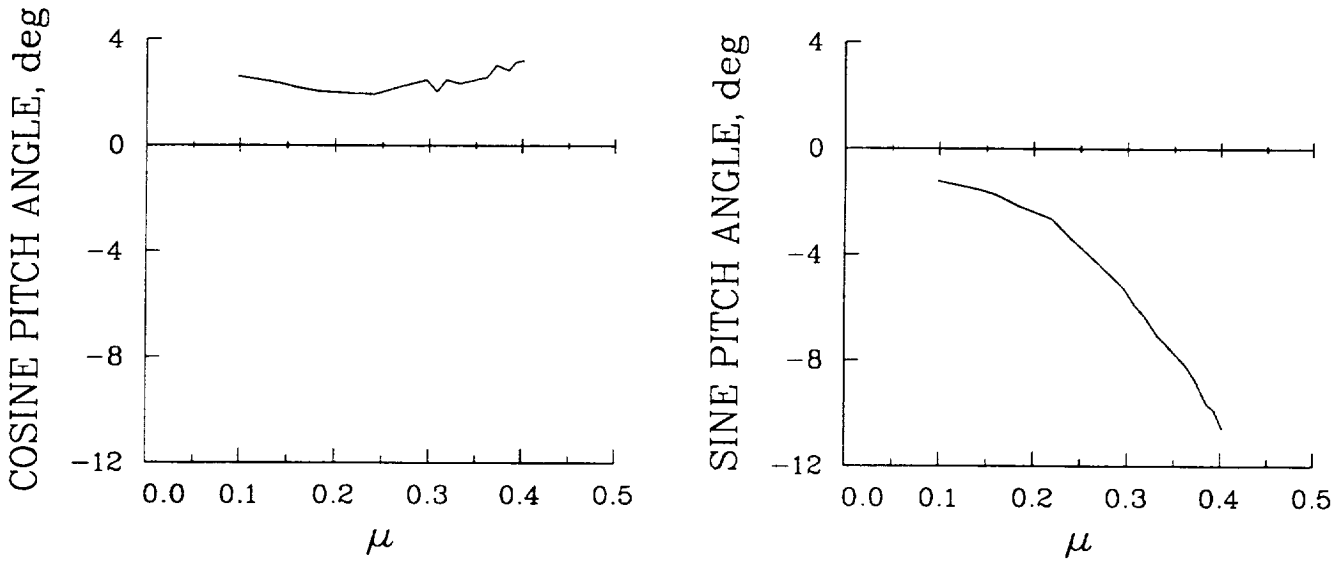


Figure 77. Lateral and longitudinal pitch angles as a function of advance ratio.

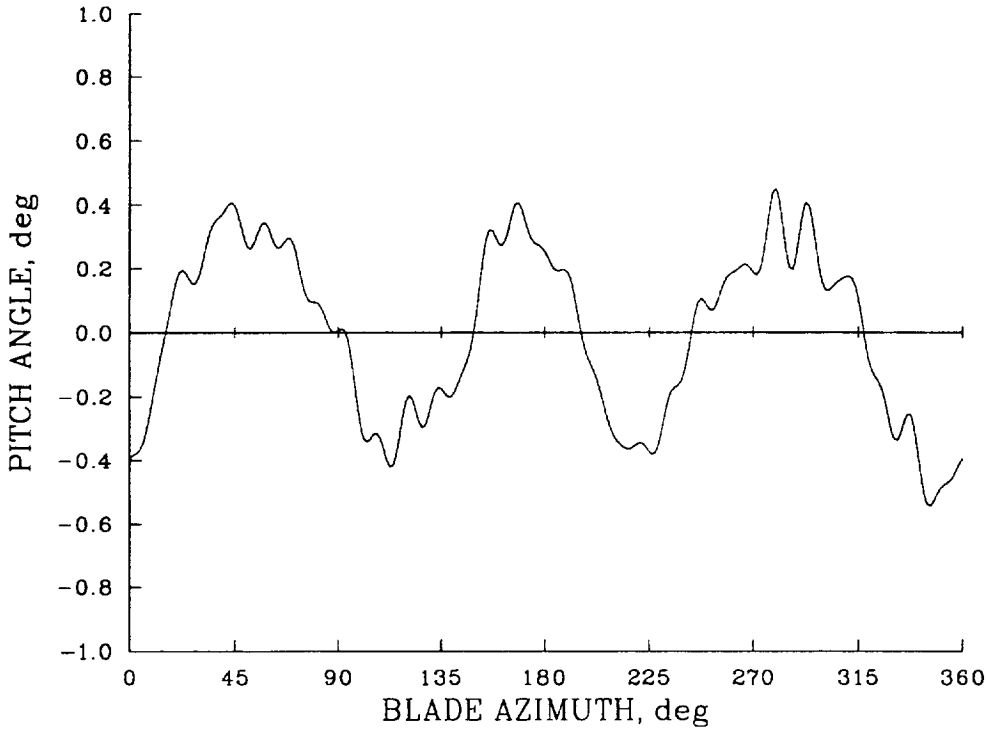


Figure 78. Pitch angle with control motions removed; 2–32 harmonics.

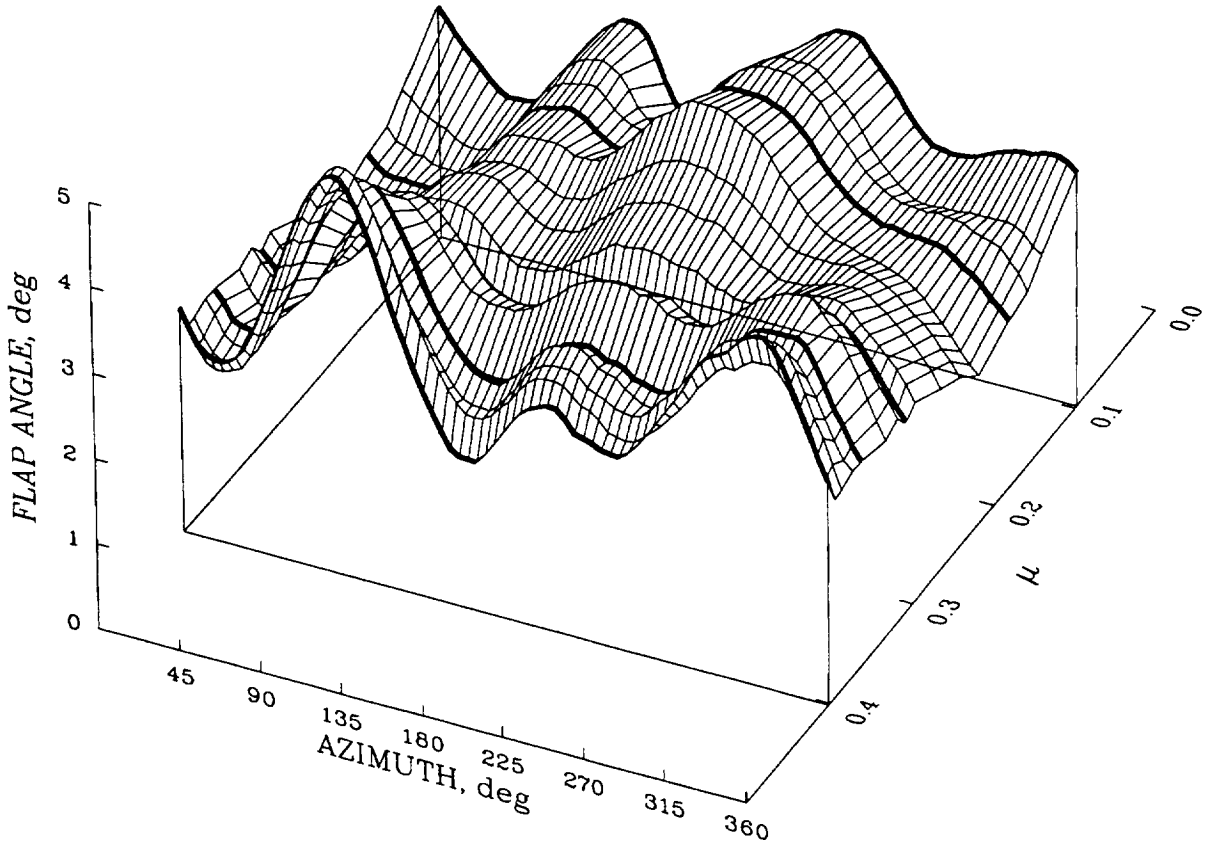


Figure 79. Flap angle distribution as a function of azimuth and advance ratio for Blade 1.

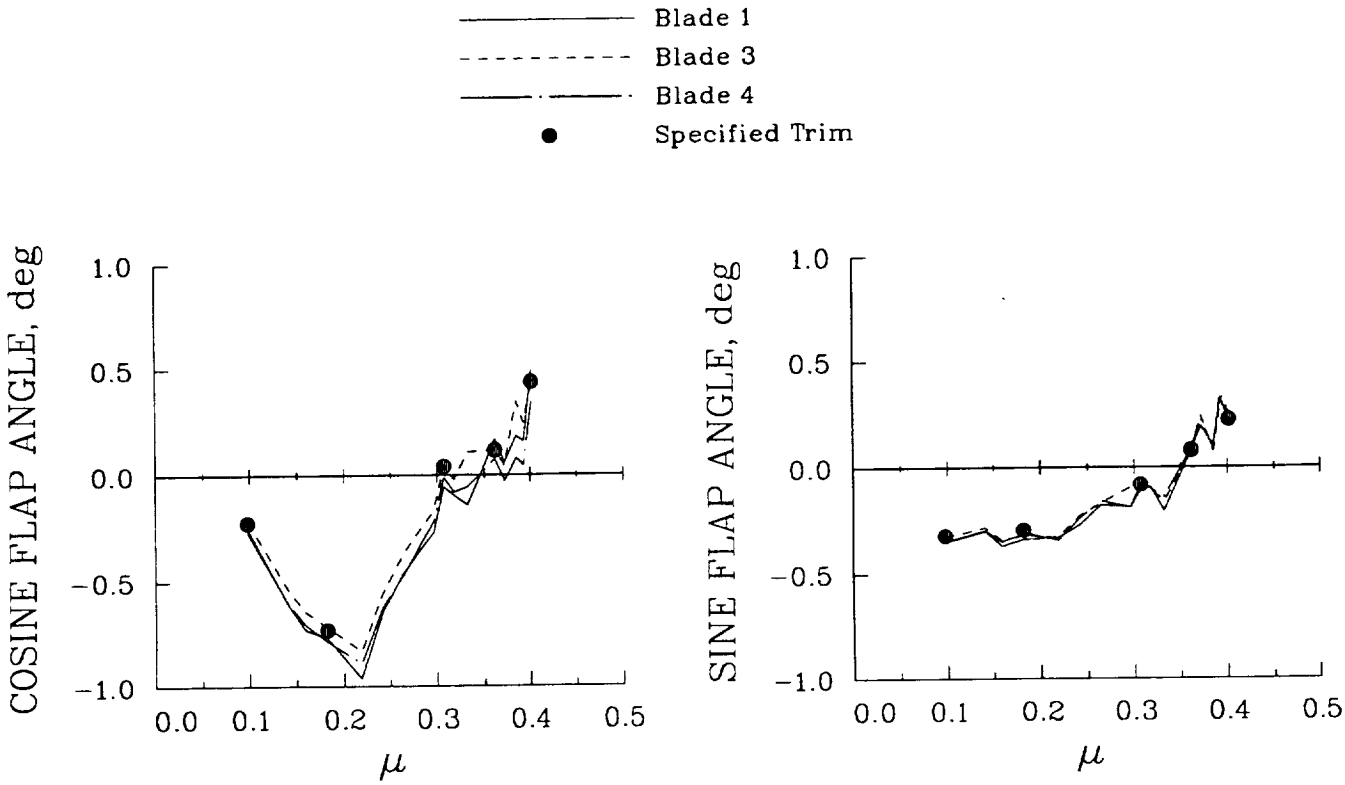


Figure 80. First harmonic blade flapping as a function of advance ratio.

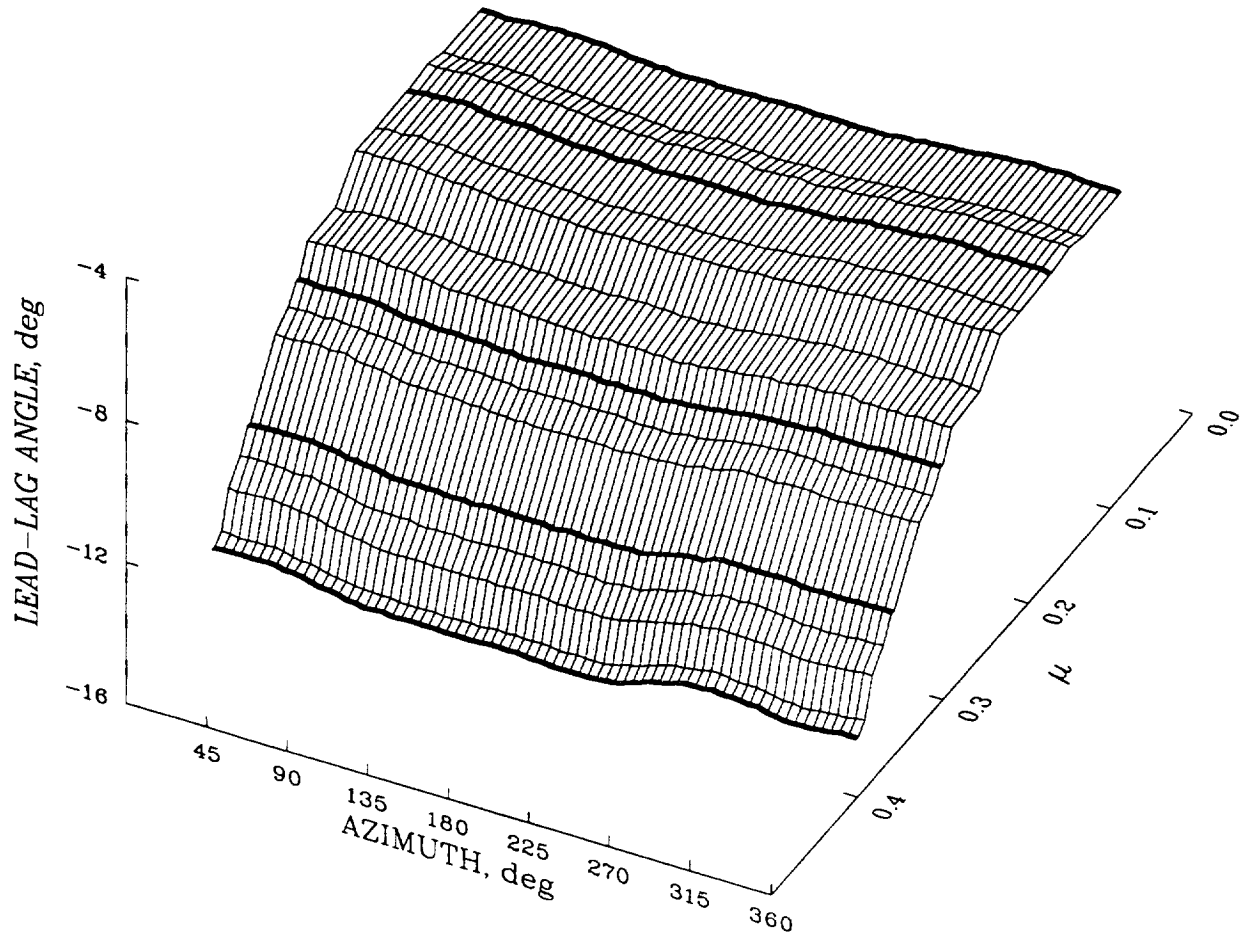


Figure 81. Lead-lag angle distribution as a function of azimuth and advance ratio for Blade 1.

The measured shaft angles for the Flight 525 airspeed sweep are shown in figure 82. Three different methods were used to measure the shaft angle in flight: a pitch vane mounted on the test boom, a pitch angle gyro, and a pitch angle measurement based on a pendulum device. The specified trim values used for the five correlation cases were determined from a shaft-angle schedule based on multiple flight test cases and, as shown here, agree quite well with the pitch pendulum measurement. The source of the discrepancy with the pitch vane measurement, which is about $0.43R$ in front of the aircraft nose, is not known.

### 5.2.2 Comparison of Analysis and Experiment

#### 5.2.2.1 *Trim and Performance*

The specified trim parameters that were used for the analytical computations were airspeed, aircraft thrust, shaft angle of attack, and first harmonic cosine and sine flapping; see table 17 presented previously.

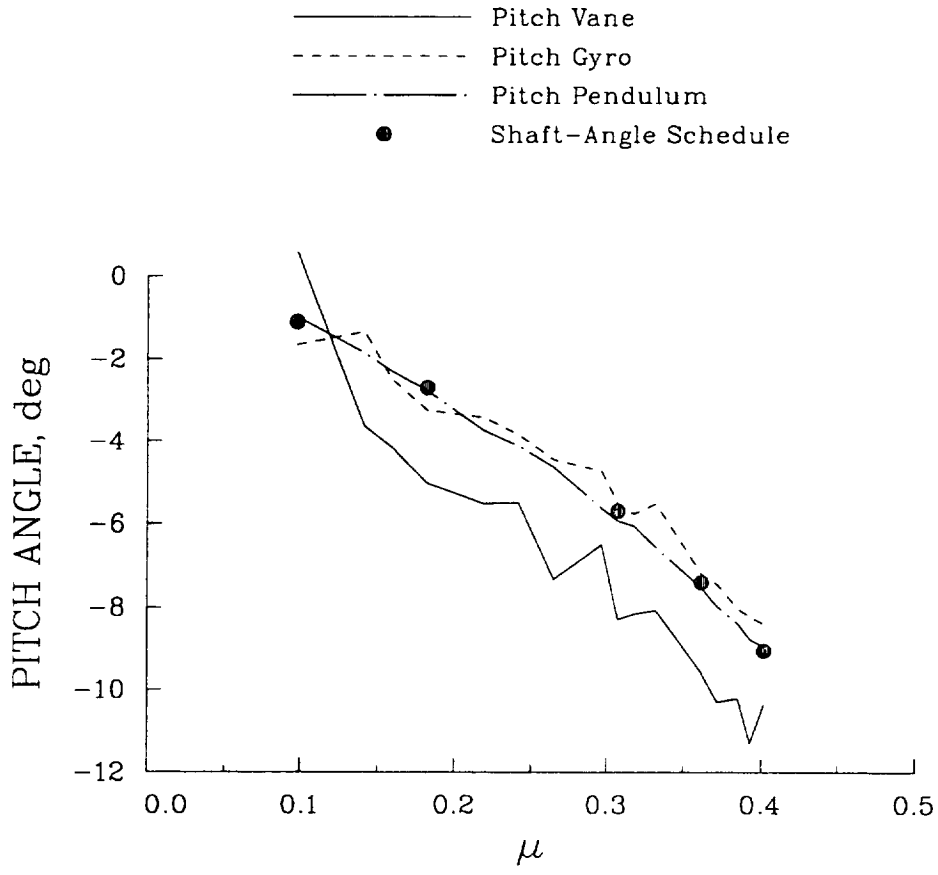


Figure 82. Shaft angle as a function of azimuth for three different measurements.

It was expected that these variables would be achieved exactly by the analyses but discrepancies occurred in rotor thrust and harmonic flapping and these differences are discussed below.

The trim rotor thrust computed by the four analyses is compared to the measured aircraft weight in figure 83. The decrease in rotor thrust with advance ratio is a consequence of fuel burnoff during the test flight. CAMRAD, CAMRAD/JA and RAE/WHL are trimmed with the thrust equal to the calculated aircraft weight. However, METAR/R85 is trimmed with the rotor lift, that is, the vertical component of thrust, equal to the weight. As the advance ratio increases, the propulsive force becomes larger and its effect on rotor thrust is no longer negligible. At high speed, therefore, the trimmed thrust is greater than the aircraft weight by about 1.5% for this analysis.

The specified and computed first harmonic flapping angles are compared in figure 84. The calculated first harmonic cosine flapping angle shows generally good agreement with the measured root flapping, but the sine flapping angle calculated by the RAE/WHL, CAMRAD, and METAR/R85 analyses is offset by about half a degree from the measurements. The difference is a consequence of the flapping angle definition that is used by the analyses. Each of the methods assumes that the input (experimental)

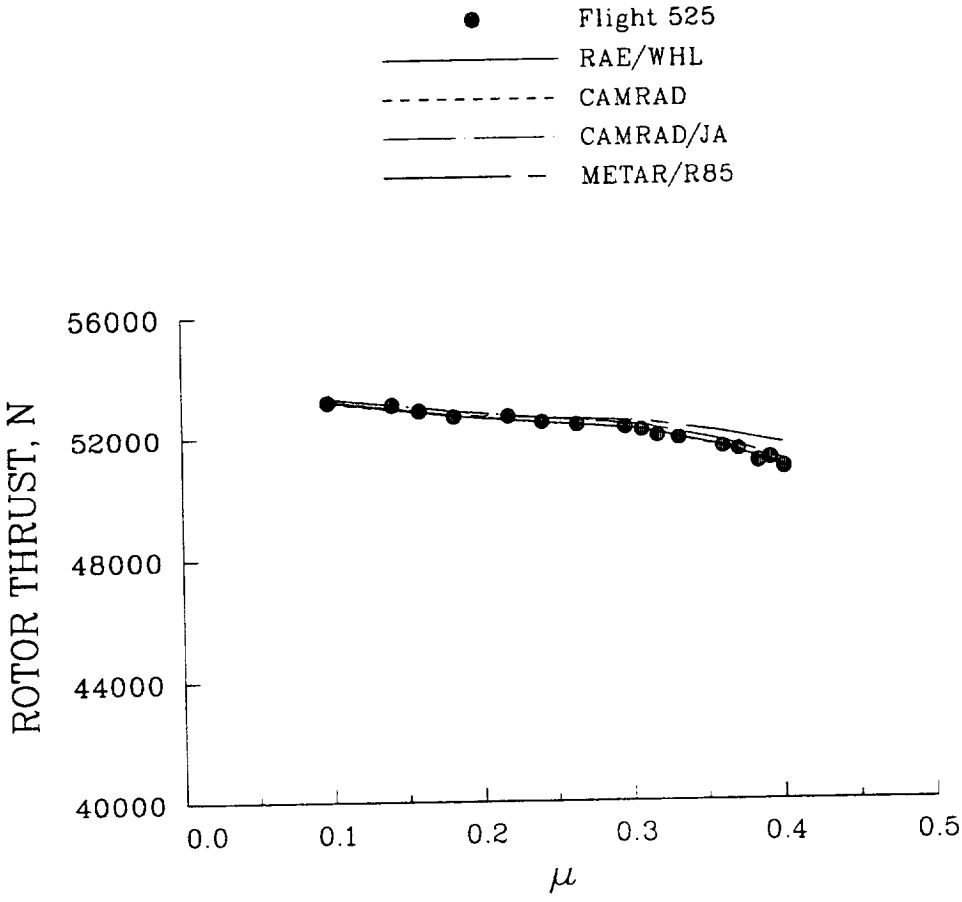


Figure 83. Computed trim rotor thrust compared to aircraft gross weight as a function of advance ratio.

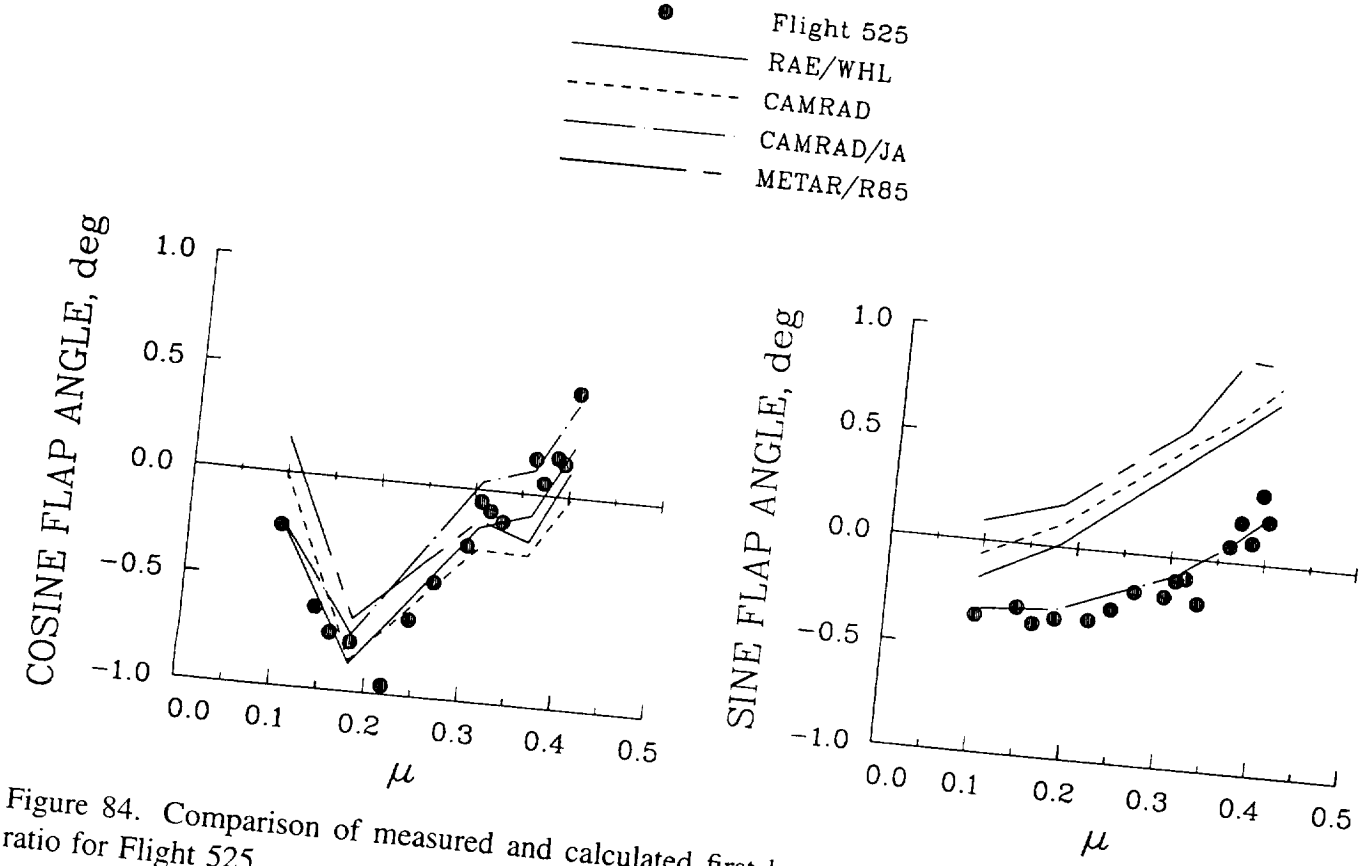


Figure 84. Comparison of measured and calculated first harmonic flapping as a function of advance ratio for Flight 525.

flapping angles define a tip path plane; hence the flapping angle is defined by a straight line between the blade tip and the flapping hinge. This approximation neglects elastic bending of the blade. The calculated flapping angles shown in figure 84 are not the angles based on the tip-path-plane definition but have, instead, been calculated from the modal solution. As shown here, there is approximately a half degree difference between the specified sine flapping angle and the value that is calculated at the blade flap hinge but no difference in the cosine flapping. Unlike the other analyses the trim solution for CAMRAD/JA was obtained iteratively by repeating the solution until the computed root flap angle matched the specified root flap angle.

The assumption that the rotor thrust is the same as the aircraft weight introduces an error in the computed solutions to the degree that these two quantities differ. The force balance equation for the Z-force is

$$T\cos\alpha_s + L + L_s - W = 0 \tag{5-2}$$

where $T$ is the rotor thrust, $\alpha_s$ is the shaft angle of attack, $L$ is the fuselage lift, $L_s$, is the stabilizer lift, and $W$ is the aircraft weight. Appendix A provides aerodynamic equations for the Puma based on wind tunnel measurements (Samoni, 1975) which allows the calculation of the $L$ and $L_s$. The sum of the aircraft weight, the fuselage lift (download), and the stabilizer lift (download) is shown in figure 85. For comparison, an estimate of rotor thrust based on blade coning is also shown in this figure. Based on calculation the effect of fuselage and stabilizer download is to increase the thrust that is required as airspeed increases. At the maximum speed this increment is approximately 9%. The estimated rotor thrust based on blade coning shows the same functional behavior with airspeed as the sum of aircraft

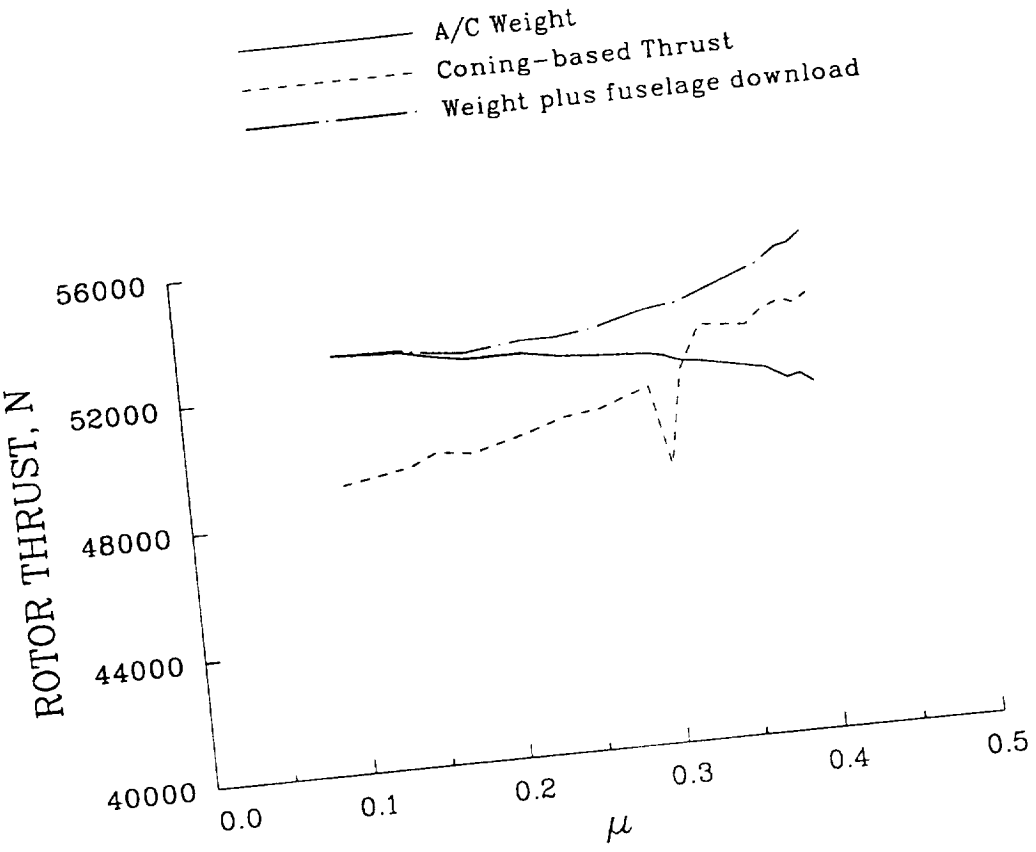


Figure 85. Aircraft gross weight, gross weight plus fuselage and stabilizer download, and coning-based thrust as functions of advance ratio.

weight and download but is offset by about 4000 N. Based on this comparison the specified rotor thrust used in the trim solution will be increasingly in error at higher speeds and this will influence the calculated solutions.

The comparisons for the specified trim parameters are a first step in the assessment of the lifting-line methods. The agreement is, in general, quite good and is expected. Comparison of the analytical predictions with measurements of resultant or unspecified trim parameters such as the blade control angles provides a much more rigorous test of these analyses and provides insight into their accuracy.

Figure 86 compares the computed collective pitch angle at the blade pitch bearing with the measured values for the Flight 525 airspeed sweep. The measured and computed values are compared in table for the five correlation cases. At the lowest advance ratio, differences between the computed collective pitch and the measurement are as large as 2.1°, but at higher speeds quite good agreement is observed particularly for the RAE/WHL, CAMRAD/JA, and METAR/R85 analyses which are within 0.4° to 0. It seems likely that the discrepancies at lower speed are related to the wake model.

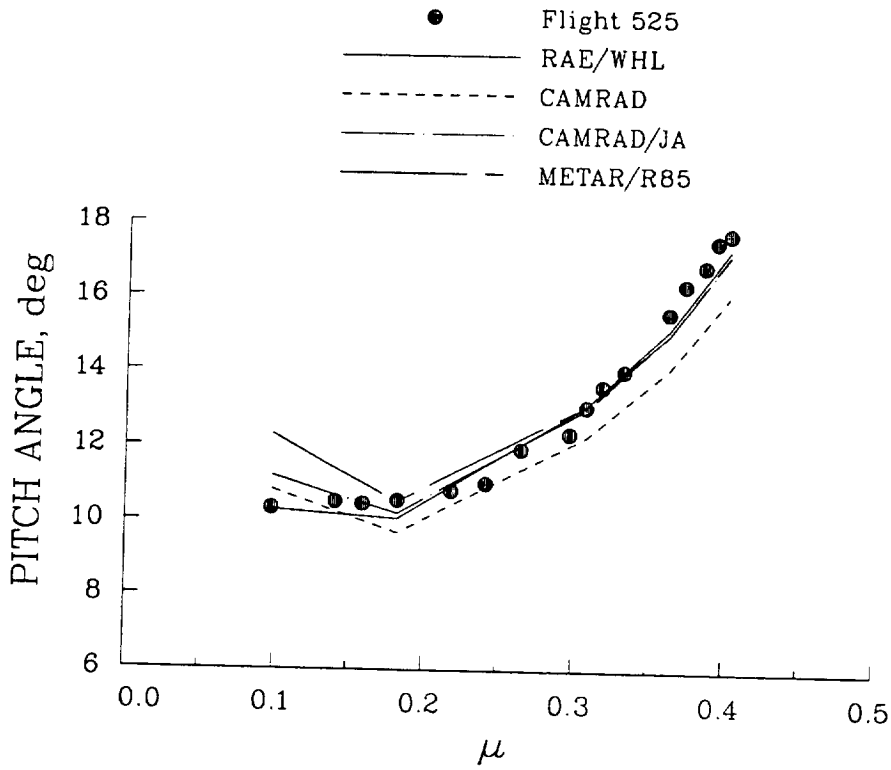


Figure 86. Comparison of measured and calculated collective pitch angle at blade pitch bearing as a function of advance ratio for Flight 525.

Table 19. Measured and calculated collective pitch angles for Flight 525

| Counter | $\mu$ | Flight 525 | RAE/WHL | CAMRAD | CAMRAD/JA | METAR/R85 |
|---|---|---|---|---|---|---|
| 03 | 0.098 | 10.35 | 10.84 | 10.84 | 11.21 | 12.32 |
| 07 | 0.182 | 10.56 | 10.07 | 9.70 | 10.22 | 10.53 |
| 12 | 0.307 | 13.09 | 13.12 | 12.29 | 13.04 | 13.12 |
| 17 | 0.362 | 15.61 | 15.17 | 14.10 | 15.03 | 15.02 |
| 21 | 0.402 | 17.77 | 17.36 | 16.09 | 17.20 | 17.20 |

The analytical modeling comparison for a rectangular-tipped blade, discussed in Section 4.3.1, showed a fairly large divergence in the predicted collective pitch values at $\mu = 0.381$, approximately 3° between the RAE/WHL and CAMRAD/JA analyses. However, for this swept-tip rotor at $\mu = 0.362$ the RAE/WHL, CAMRAD/JA, and METAR/R85 analyses are all within 0.2° and the reasons for the closeness in these predictions for the swept tip as compared to the rectangular tip are not clear.

The comparison of the collective pitch measured at the pitch bearing, $0.0573R$, with the collective pitch determined in the lifting-line methods is not straightforward. At any radial station the pitch angle is expressed as:

$$\theta(r) = \theta_C + \theta_s + \theta_t(r) + \theta_e(r) \tag{5-3}$$

where $\theta_C$ is the control angle input at the swashplate actuators; $\theta_s$ is elastic deflection in the swashplate, pitch link, and pitch horn; $\theta_t(r)$ is the built-in twist; and $\theta_e(r)$ is the elastic twist in the blade. At the blade pitch bearing, where the pitch angle measurement is made, the only terms that are effective are

the control angles and any elastic deformation in the control system between the actuators and the pitch bearing. Thus,

$$\theta(0.0573R) = \theta_C + \theta_s \tag{5-4}$$

Within the lifting-line methods, collective and cyclic pitch angles do not include torsional deformation so as to separate the control input from the response for the trim algorithm used to obtain force and moment balance. Hence, the calculated collective pitch angle, $\theta_{coll}$, is

$$\theta_{coll} \equiv \theta_C + \theta_t(0.75R) \tag{5-5}$$

and, based on equation (5-3), the angle at the pitch bearing is

$$\theta(0.0573R) = \theta_{coll} - \theta_t(0.75R) + \theta_s \tag{5-6}$$

where

$$\theta_t(0.0573R) \equiv 0.0 \tag{5-7}$$

For the Puma, the built-in twist between the pitch bearing and $0.75R$ is $-4.16°$. The swashplate and control system deformation, $\theta_s$, was calculated to vary from $-0.07°$ to $0.15°$ over the airspeed range for the RAE/WHL analysis. For CAMRAD and CAMRAD/JA this deformation was estimated from the calculated elastic deformation and varied between $-0.52°$ and $-0.36°$ for CAMRAD and $-0.28°$ and $-0.21°$ for CAMRAD/JA. The METAR/R85 solutions do not include a torsion mode so this deformation is zero. These corrections were used in calculating the angles at the pitch bearing that are shown in figure 86. Although not required for these corrections it is noted that the steady elastic deformation between the pitch bearing and $0.75R$ calculated by CAMRAD and CAMRAD/JA is about $0.2°$.

The calculated lateral cyclic pitch (cosine harmonic) and longitudinal cyclic pitch (sine harmonic) are compared with the pitch bearing measurements in figure 87. The calculated and measured values for the correlation cases are shown in tables 20 and 21. As before, the calculated cyclic angles were corrected for elastic deformation across the swashplate although these corrections were slight. The calculated lateral cyclic is generally within a degree of the data while the longitudinal cyclic calculations are quite close at low advance ratios but larger differences are seen at high speed. The Task 3 calculations, discussed in Section 4.3.1, provide some insight into these differences. The more negative longitudinal pitch of RAE/WHL appears to be a result of swept flow corrections and torsion deflection, whereas for CAMRAD/JA it is caused by the larger inflow gradients.

The measured root coning is compared with values derived from the three analyses in figure 88. The coning is obtained from the analytical methods using the flap displacement at the most inboard solution station and assuming that there is no deformation inboard of this station. This approach is quite accurate for METAR/R85 where the most inboard station is quite close to the flapping hinge, but less so for the CAMRAD analyses where the most inboard station is at $0.264R$. In general, the methods show a decrease in blade coning with advance ratio which is not surprising since the trim thrust was set to the aircraft weight. METAR/R85 shows a slightly higher value of coning and in part this is a result of including the effect of propulsive force on the trim thrust. The $0.4°$ to $0.8°$ offset between the measured coning and the derived values is unexplained.

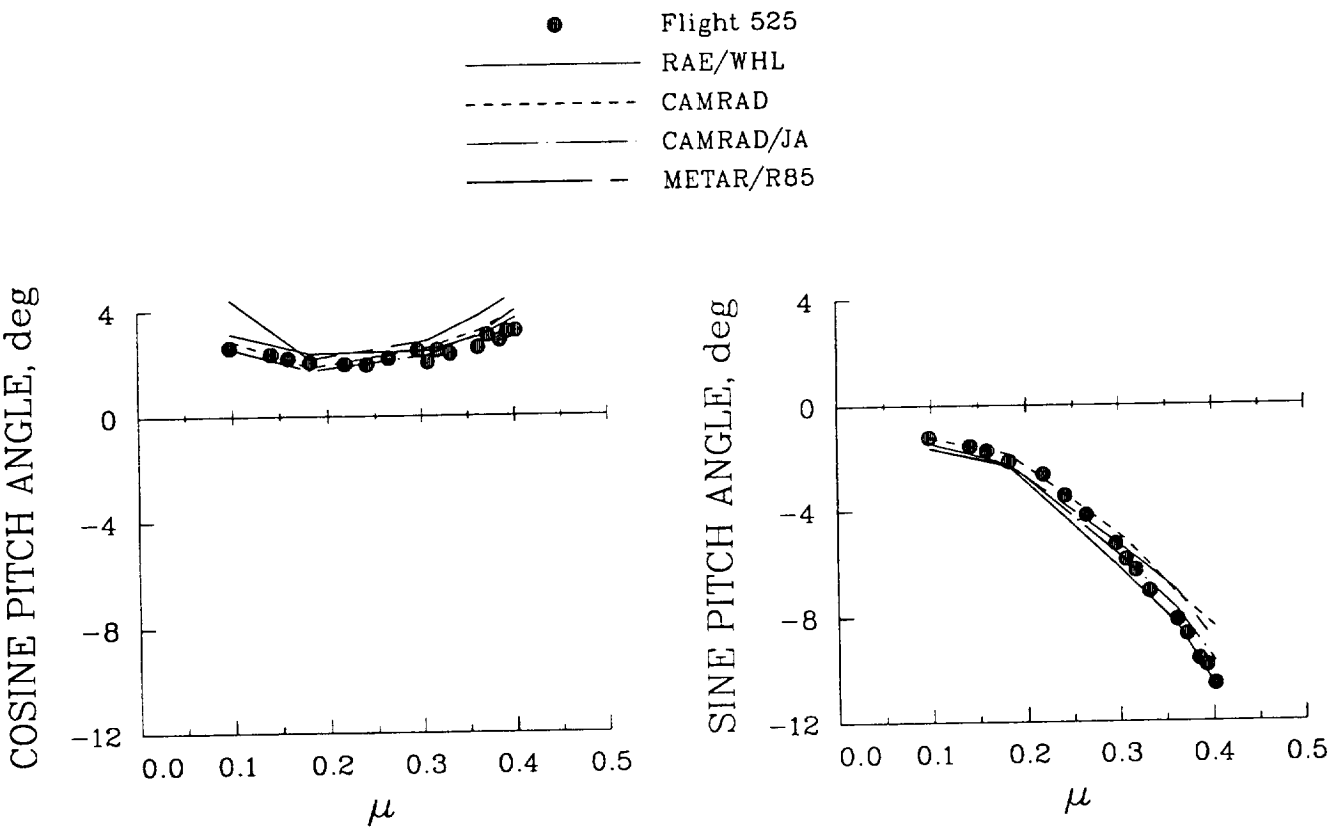


Figure 87. Comparison of measured and calculated cyclic pitch angles at the blade pitch bearing as a function of advance ratio for Flight 525.

Table 20. Measured and calculated cosine (lateral) cyclic pitch for Flight 525

| Counter | $\mu$ | Flight 525 | RAE/WHL | CAMRAD | CAMRAD/JA | METAR/R85 |
|---|---|---|---|---|---|---|
| 03 | 0.098 | 2.60 | 3.13 | 2.87 | 2.56 | 4.41 |
| 07 | 0.182 | 2.04 | 2.36 | 1.84 | 1.72 | 2.15 |
| 12 | 0.307 | 2.03 | 2.46 | 2.56 | 2.29 | 2.83 |
| 17 | 0.362 | 2.57 | 2.97 | 3.18 | 3.03 | 3.75 |
| 21 | 0.402 | 3.19 | 3.67 | 3.97 | 3.97 | 4.60 |

Table 21. Measured and calculated sine (longitudinal) cyclic pitch for Flight 525

| Counter | $\mu$ | Flight 525 | RAE/WHL | CAMRAD | CAMRAD/JA | METAR/R85 |
|---|---|---|---|---|---|---|
| 03 | 0.098 | −1.21 | −1.62 | −1.22 | −1.44 | −1.64 |
| 07 | 0.182 | −2.14 | −2.34 | −1.86 | −2.34 | −2.27 |
| 12 | 0.307 | −5.87 | −6.43 | −5.12 | −5.92 | −5.49 |
| 17 | 0.362 | −8.15 | −8.36 | −7.19 | −7.77 | −7.05 |
| 21 | 0.402 | −10.58 | −10.69 | −8.43 | −9.70 | −9.03 |

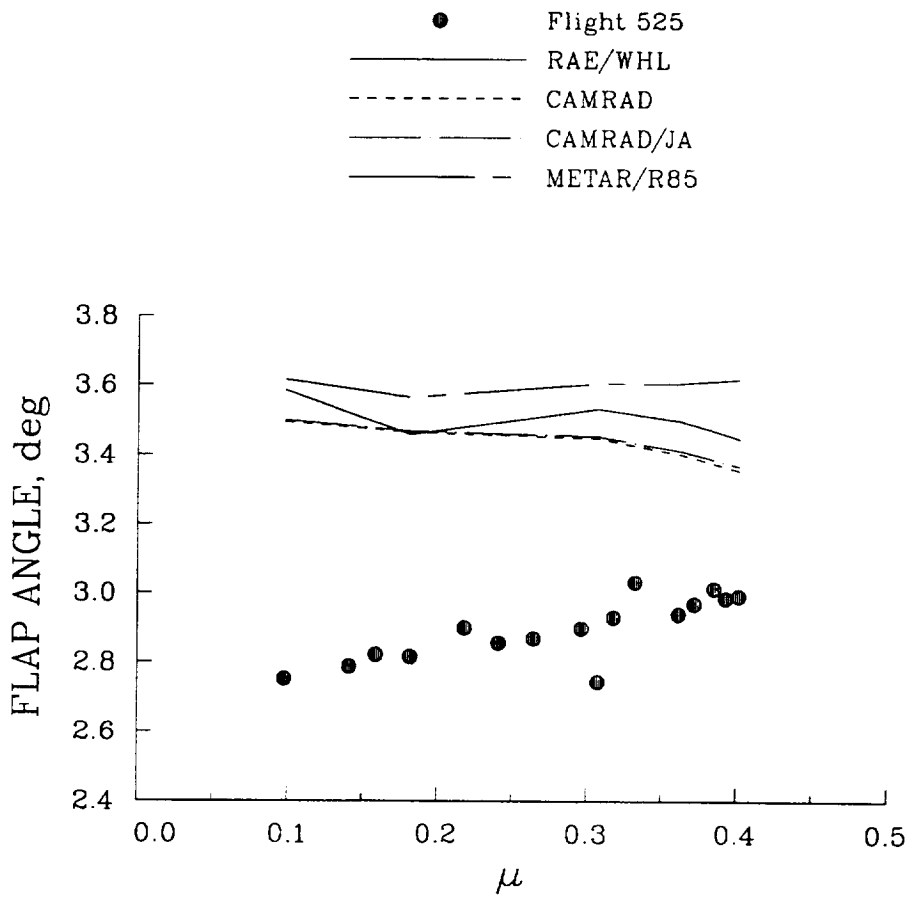


Figure 88. Comparison of measured and calculated blade coning as a function of advance ratio for Flight 525.

The calculated steady lag angles are compared with the measured values in figure 89. An offset between 3° and 6° is seen between the calculations and the data and, as will be discussed in Section 5.4.1, it is believed that there is a bias error in the measurements of approximately 4°. Over most of the speed range the RAE/WHL and CAMRAD analyses are offset from the measured values by the same amount and are believed correct. The METAR/R85 analysis shows less steady lag deflection than the other analyses, and this is believed to be a result of lag hinge restraint added to the model to increase the curvature near the lag hinge (see Section 3). Thus, there is less hinge rotation and the root deflection is smaller for a given tip deflection in the METAR/R85 solution.

The computed cosine and sine first harmonic lead-lag angles are compared with the measurements in figure 90. The RAE/WHL analysis represents the hydraulic lead-lag damper (see Appendix A) by incorporating 80% structural damping in the first lead-lag mode. The other analyses represent the damper as an equivalent linear viscous damper. Despite these modeling differences all of the analyses show fairly good agreement with the measurements. As before, the METAR/R85 angles are reduced slightly by the introduced hinge restraint.

The rotor thrust is a specified trim value, as discussed above, but the other steady hub forces and moments are not specified and provide an additional test of the accuracy of the four analyses. Except for the shaft torque, however, there are no direct aircraft measurements that can be compared with the

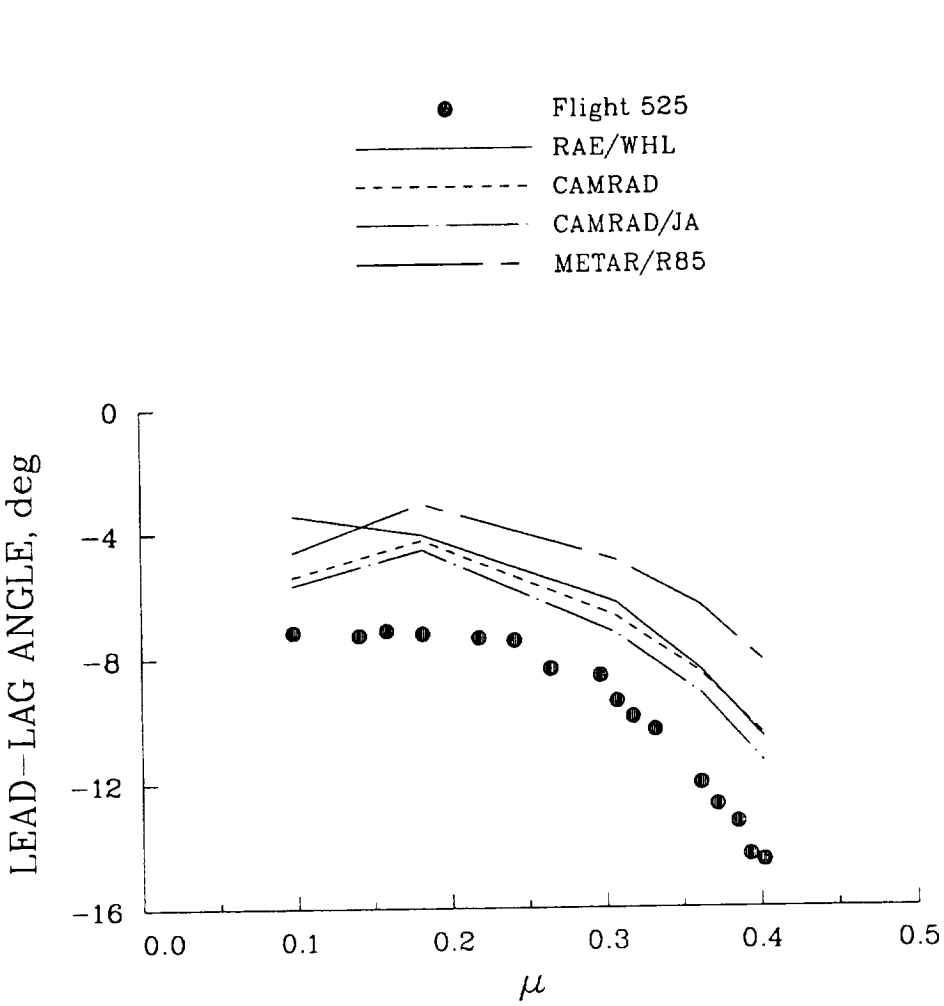


Figure 89. Comparison of measured and calculated blade steady lag angle as a function of advance ratio for Flight 525.

analyses and, therefore, the comparisons shown here are largely comparisons between methods rather than with data.

Figures 91 and 92 compare the computed values of the X-force (positive forward) and Y-force (positive to the right) in the shaft axes. Both sets of prediction are somewhat similar to the trim flapping angles which is not surprising as a tilting of the thrust vector by half a degree will result in approximately 550 N of X- or Y-force. Good agreement is observed between the analyses for the X-force, but less so for the Y-force where greater differences were observed in the computation of the sine flapping trim (see figure 84).

The hub pitch and roll moments are compared in figures 93 and 94. These figures also include roll and pitch moments derived from measured flap bending moments and flapping angles as will be discussed in Section 5.2.2.4. The analyses show similar trends in the pitch moment variation with airspeed except for CAMRAD/JA. This variation is similar to the first harmonic cosine flap angle which suggests that most of the moment is a result of vertical shear at the flap hinge. Reasonably good agreement is also seen with the derived pitch moment values.

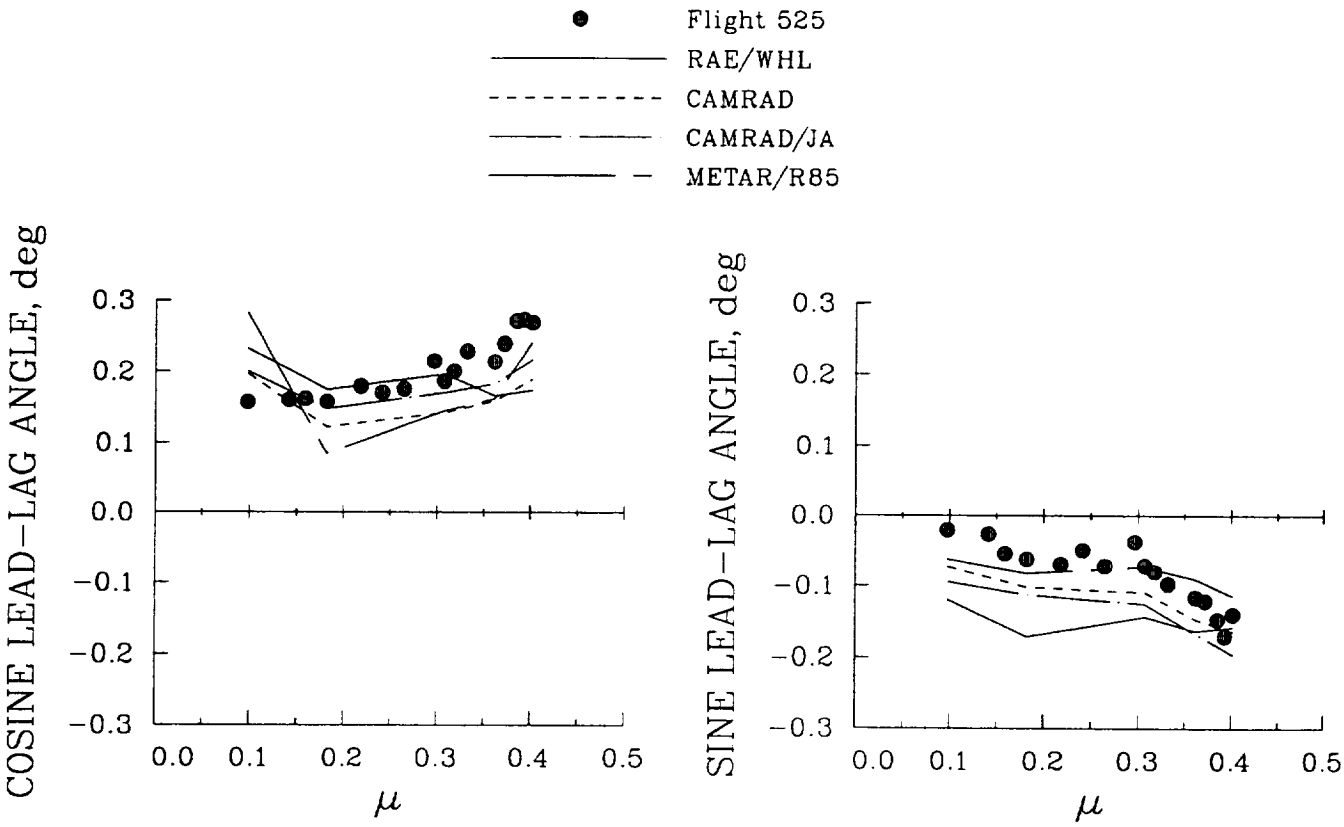


Figure 90. Comparison of measured and calculated first harmonic lead-lag angles as functions of advance ratio for Flight 525.

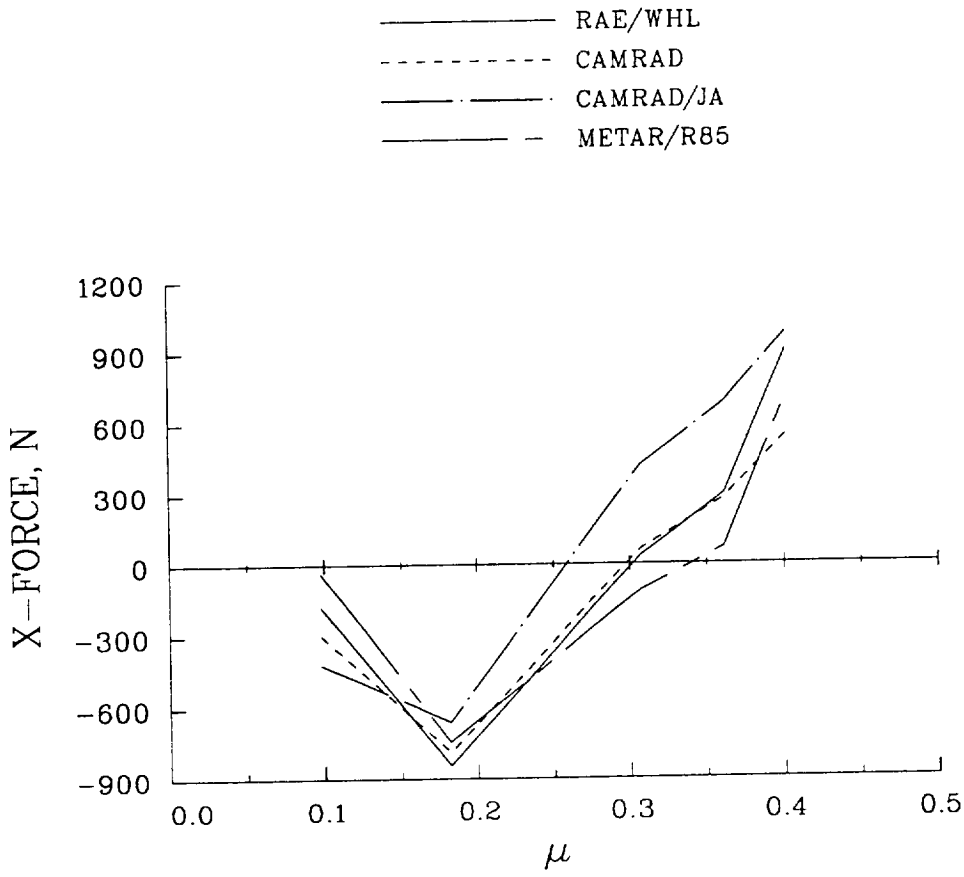


Figure 91. Comparison of calculated X-forces as a function of advance ratio for Flight 525.

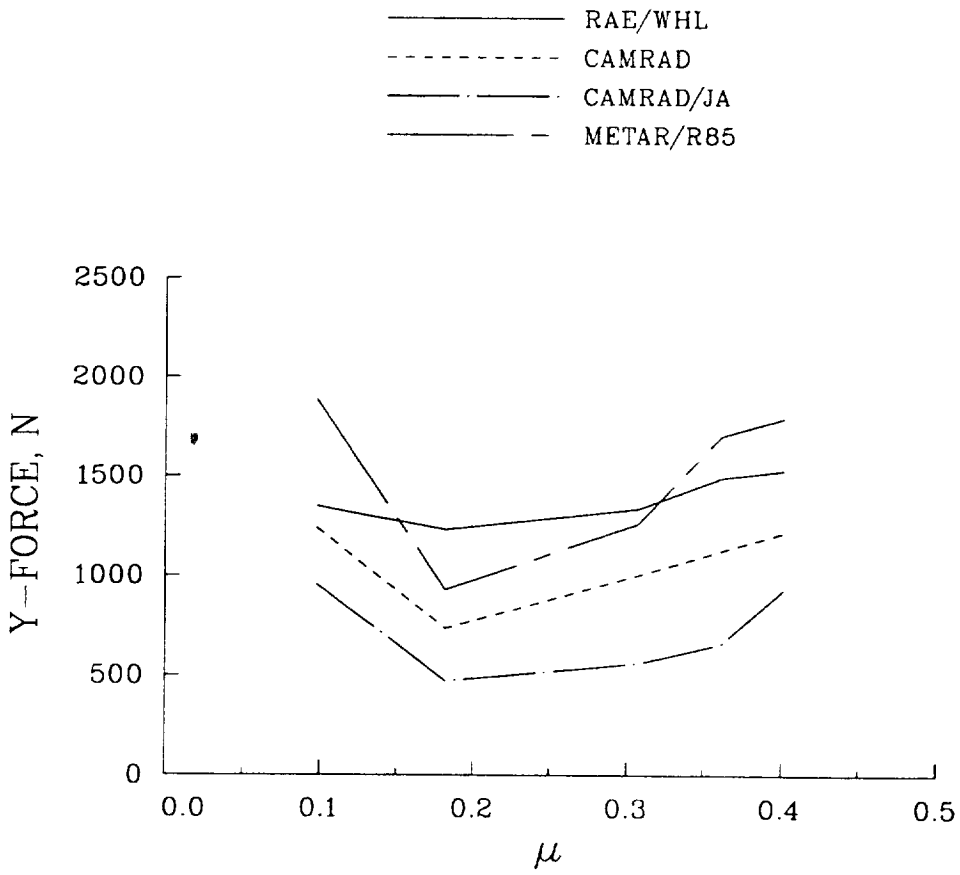


Figure 92. Comparison of calculated Y-forces as a function of advance ratio for Flight 525.

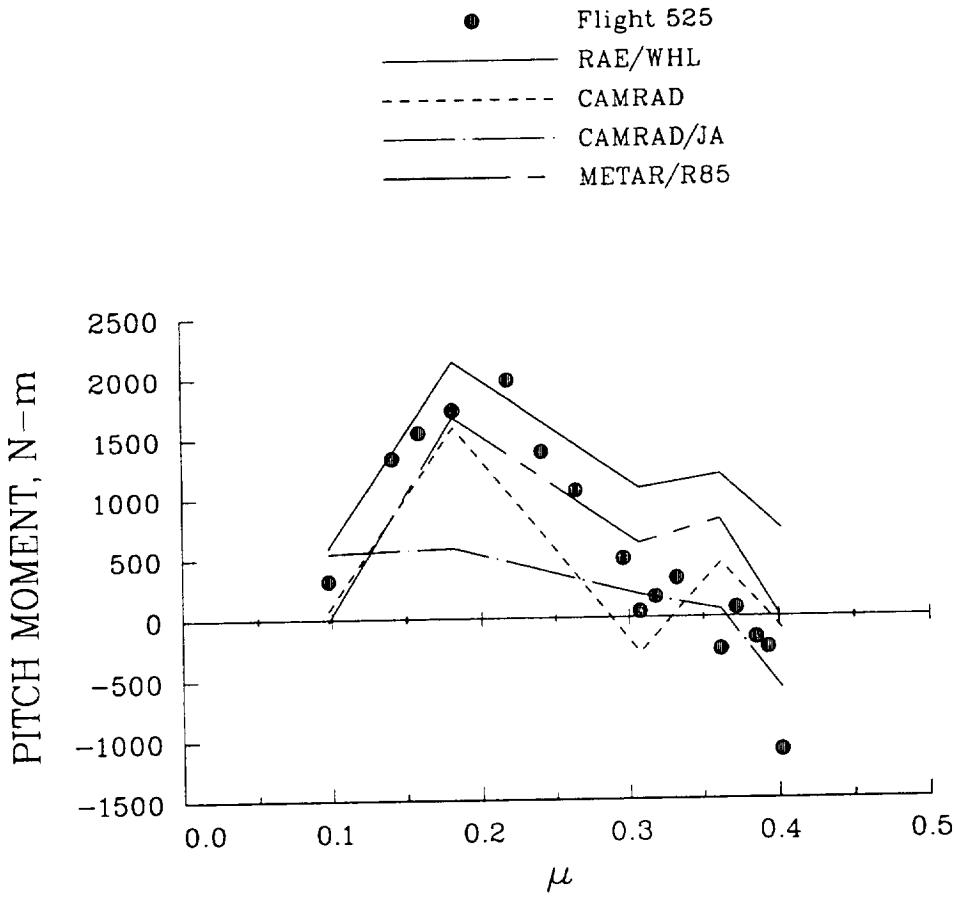


Figure 93. Comparison of calculated pitch moments with values derived from test data as functions of advance ratio for Flight 525.

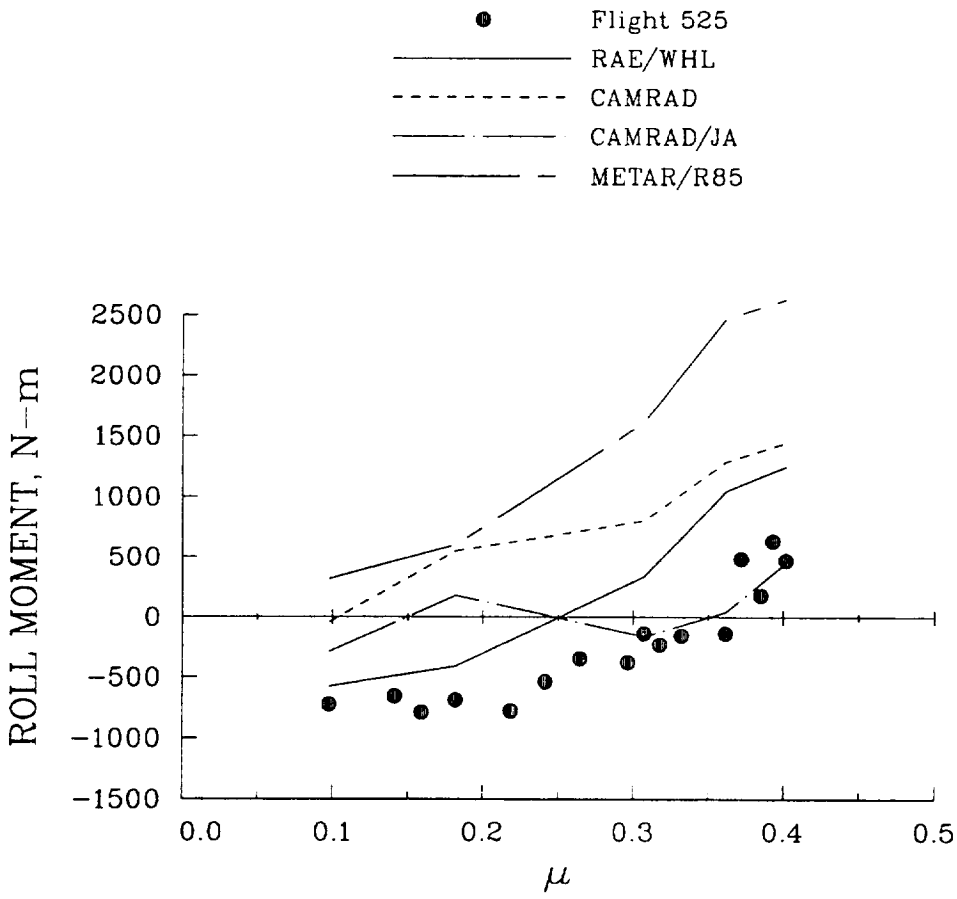


Figure 94. Comparison of calculated roll moments with values derived from test data as functions of advance ratio for Flight 525.

The analyses show the same trend in advance ratio for the roll moment as do the derived values, but there is considerable offset between the four analyses. This differs from first harmonic sine flap angle cases where the RAE/WHL, CAMRAD and METAR/R85 analyses were very similar.

The comparison of the analyses with the derived pitch and roll moments provides some confidence in the accuracy of the predictions. However, these derived values do not result from a direct measurement but instead depend upon accurate blade and hub data and a reliable modal calculation. A direct measurement using shaft bending gages or a wind tunnel balance is probably essential to demonstrate which methods achieve the greater accuracy.

The calculated and measured shaft torques for the Flight 525 airspeed sweep are compared in figure 95. There is generally good agreement between the analyses except at low speed, but all of the analyses underpredict the measured shaft torque at high speed.

The large error in power prediction cannot be explained solely in terms of the additional thrust required by download on the fuselage and stabilizer. A 4000 N error in the trim thrust would result in only, perhaps, a 6000 N-m underestimation of torque, that is, half the difference seen here between the codes and the measurement. It would take more than a $2^\circ$ error in disk angle of attack to explain the other half.

#### 5.2.2.2 *Blade Airloads*

The section normal force obtained by integrating the measured surface pressures at $0.95R$ is shown in figure 96 as a function of azimuth and advance ratio and is compared to the calculations made by the four lifting-line methods. The measurements are shown for 17 flight test points and the calculations are shown for five of these advance ratios. At the lowest speed, $\mu = 0.098$, the section normal force shows a rapid down-up change in force in the first quadrant and then an up-down change in the fourth quadrant. This force variation is caused by rapid changes in the inflow that are the result of the vorticity in the wake from the previous blades. This vortex loading diminishes as advance ratio increases but remnants of this loading can be seen out to $\mu \sim 0.3$, particularly on the retreating side. Each of the lifting-line models shows this basic behavior although the first and fourth quadrant loading at low speed is reduced for the RAE/WHL method which uses a vortex-ring model. Both CAMRAD and CAMRAD/JA use a free-wake calculation for the two lower speed cases shown here. A careful examination of the lifting-line predictions for the low-speed condition shows a reduction in lift over the forward part of the disk where the measurements show little variation.

As advance ratio increases, the basic character of the blade lift near the tip changes from a relatively steady load with the vortex loading superimposed to a reduction in lift that occurs in the second quadrant and, at the highest speeds, shows negative lift over a portion of the blade tip. Each of the computational methods shows this general character although the METAR/R85 analysis fails to predict negative loading at this radial station. Qualitatively, all of the lifting-line analyses are quite similar to the measurements and the correlation is good.

The section pitching moments are compared in the same fashion as the normal force at $0.95R$ in figure 97. At low speed the flight data again show evidence of vortex-induced loads on both the advancing and retreating sides and, as advance ratio increases, these pitching moments are reduced and

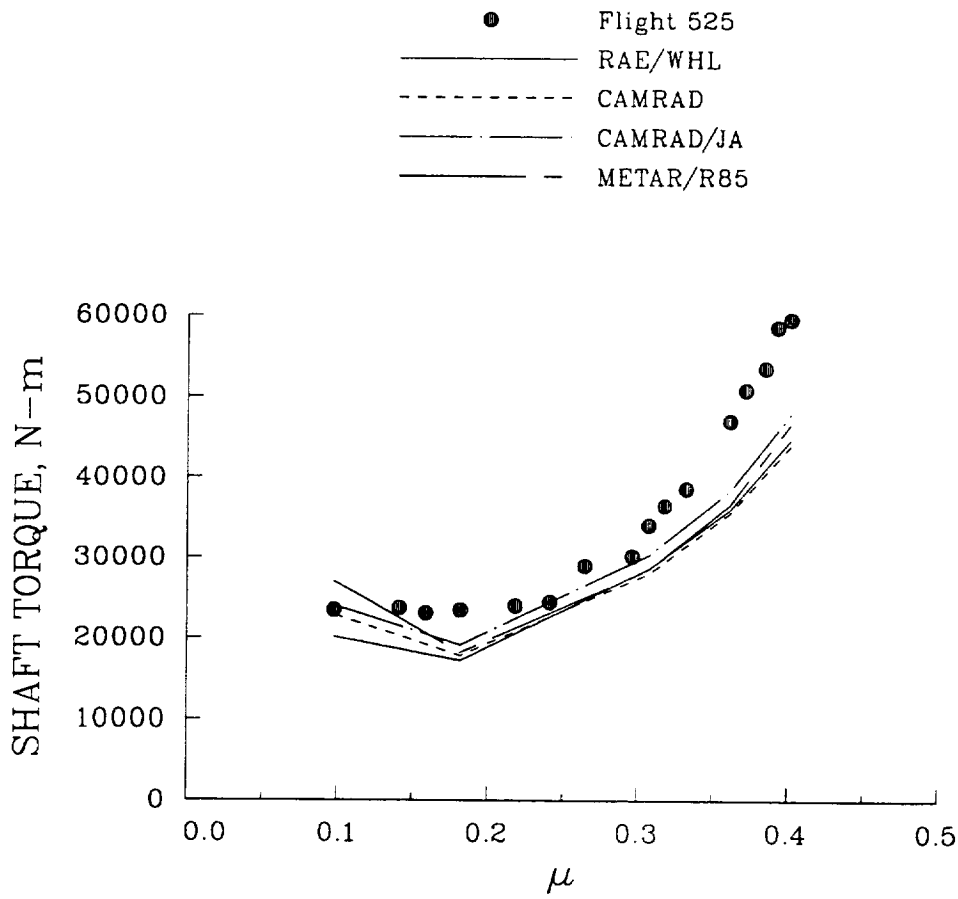


Figure 95. Comparison of measured and calculated shaft torque as a function of advance ratio for Flight 525.

disappear. At high speed, an area of positive pitching moment is observed in the first quadrant and, at about 90°, this rapidly changes to an area of negative moment in the second quadrant. Then, over the retreating side of the disk, the pitching moment returns to a positive value.

None of the lifting-line methods predict the vortex loading at low speed and this is not surprising as these methods model the inflow changes induced by previous blades' vorticity as an angle of attack change at 0.25$c$. The measurements clearly show the effects of this vorticity and it is likely that the correct modeling of these effects would require a lifting-surface analysis or one based on a CFD model. At high speed, CAMRAD, CAMRAD/JA, and METAR/R85 show section pitching moments similar in behavior to the measurements, but much reduced in amplitude. Within these analyses the positive-negative moment change is caused by both steady and unsteady effects as was discussed in Section 4.3.2 (see figure 41). The RAE/WHL analysis, on the other hand, shows pitching moment changes comparable to the flight data, although the most rapid change occurs in the middle of the fourth quadrant rather than at the beginning of the second. This increased section pitching moment for the RAE/WHL predictions is caused primarily by modeling of swept-tip effects as will be shown below by comparison with calculations for the reference rectangular-tip blade in Section 5.3.3.2.

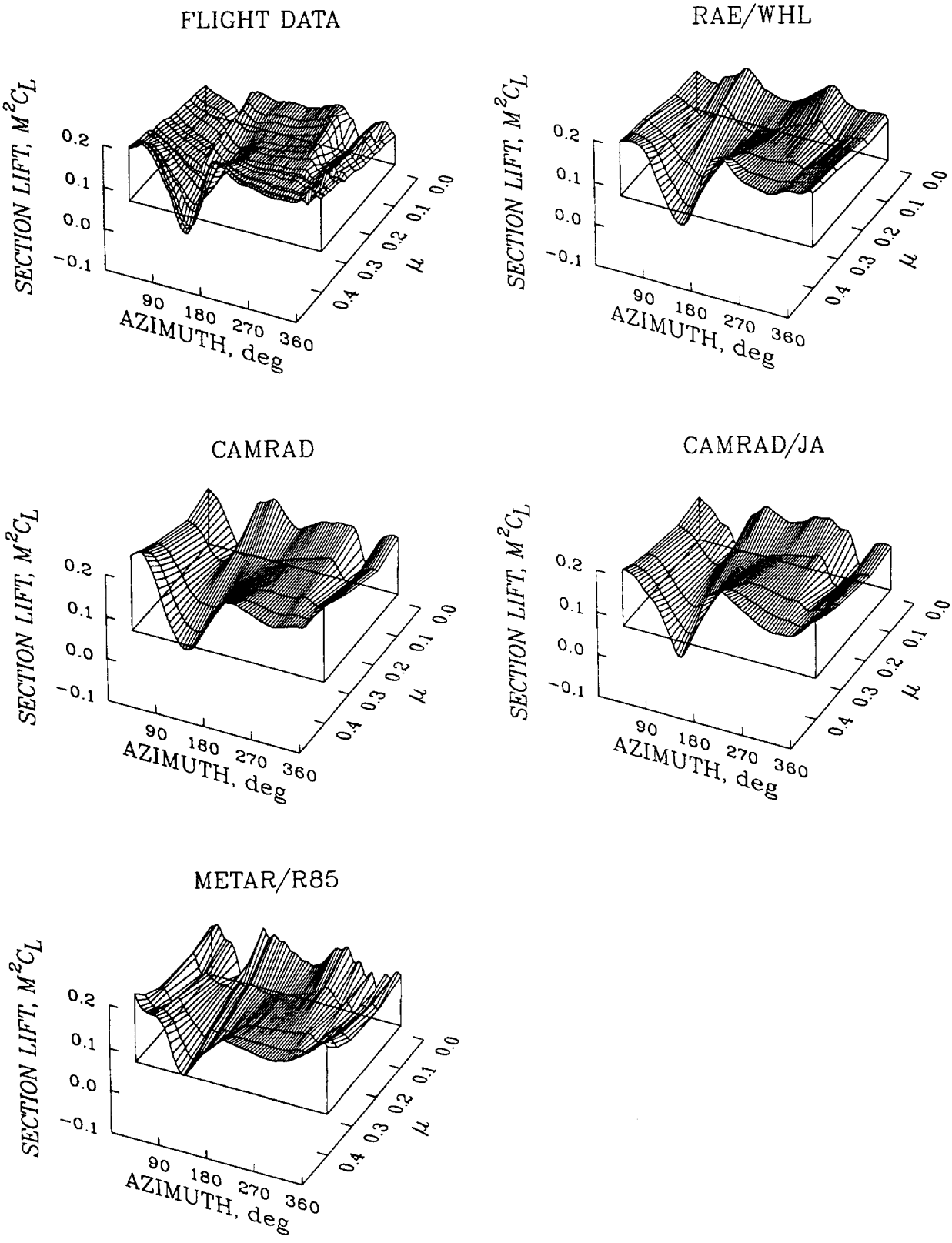


Figure 96. Comparison of measured and calculated section normal force as a function of azimuth and advance ratio; $0.95R$, Flight 525.

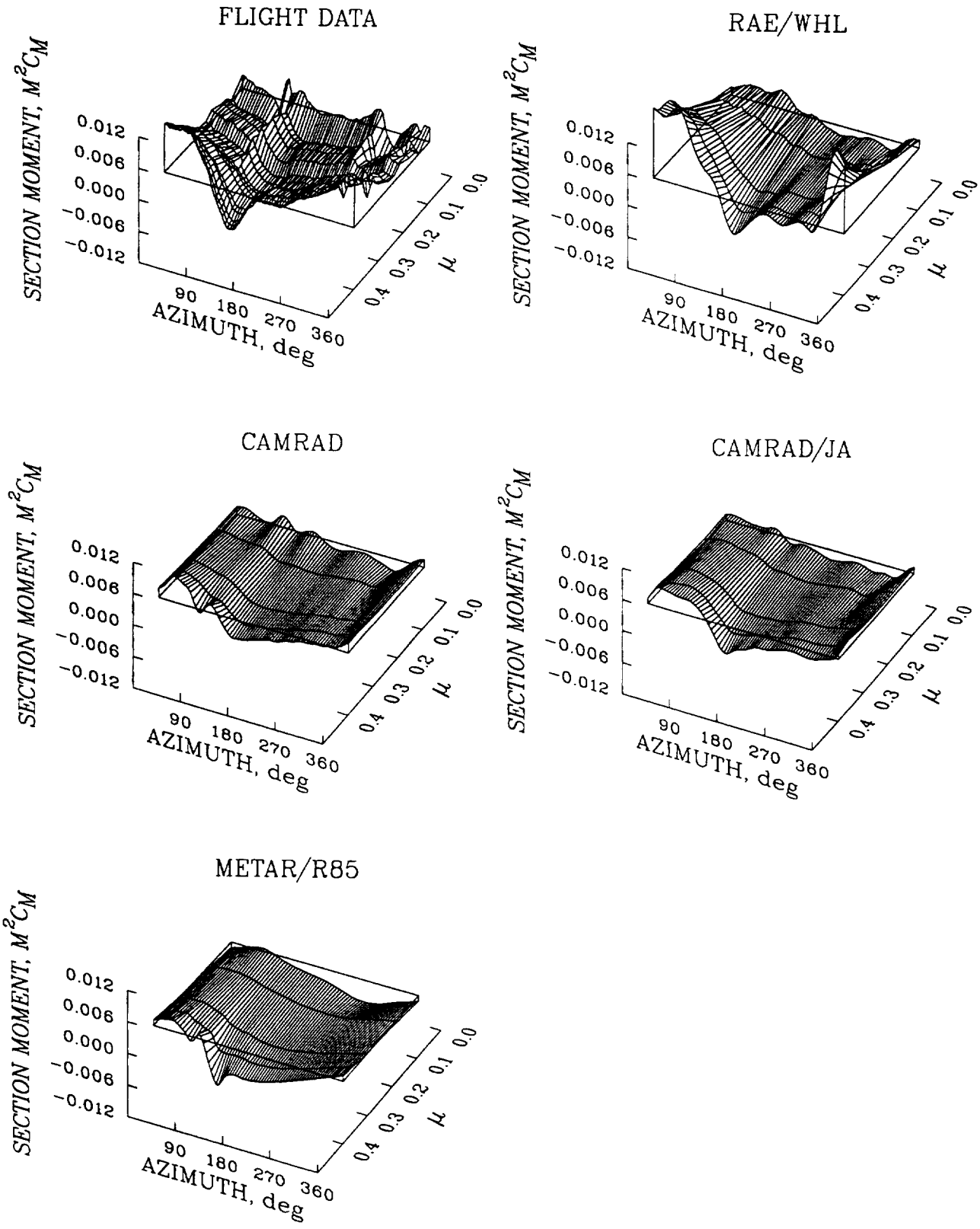


Figure 97. Comparison of measured and calculated section pitching moment as a function of azimuth and advance ratio; $0.95R$, Flight 525.

The underprediction of the section moment at the blade tip is typical of lifting-line analyses and is related to difficulties in the modeling of three-dimensional flows near the blade tip and the correct calculation of unsteady effects. The influence of planform is slight as shown by Maier and Bousman (1992) who compared pitching moment measurements obtained on earlier tests of the Puma using both a swept tip and a rectangular tip (Riley and Miller, 1983). The reason why the RAE/WHL analysis shows such a strong effect of the tip planform in comparison to the other methods, however, is not understood.

A detailed comparison of the predicted and measured section lift at $0.95R$ is shown in figures 98–102. Figure 98 shows that the normal force at this radius is dominated by the vortical loading from the previous blades. The vortex ring model used by the RAE/WHL analysis as well as the prescribed wake calculation that is included with the CAMRAD/JA prediction do not correctly represent the vortex wake at this airspeed. The CAMRAD and CAMRAD/JA free wake models provide a fairly accurate representation of the azimuthal location of the vortical loading although away from these azimuths the lift is overpredicted, particularly by CAMRAD. The METAR/R85 calculation, which uses a prescribed wake, is also able to capture some of the characteristics of the vortical loading in the first and fourth quadrants.

At $\mu = 0.182$ the vortical loading on the advancing and retreating sides of the rotor disk is still evident, as can be seen in figure 99, and the RAE/WHL and METAR/R85 computations provide a better prediction of the loading than was seen for the lower advance ratio case. CAMRAD continues to use the free wake model, but the advantages of this wake model over the other methods are no longer obvious. CAMRAD/JA uses both a free wake and a prescribed wake at this advance ratio and achieves similar results.

There is a reduction of section lift apparent in the second quadrant at $\mu = 0.307$ as shown in figure 100. Each of the analyses shows this reduction in lift and the phase is well predicted by the RAE/WHL and CAMRAD analyses and less so by CAMRAD/JA and METAR/R85. The slight drop in lift at about 270° is caused by retreating side vortical loading and is fairly well predicted by all of the analyses. The apparent impulsive-type load at about 330° is believed the result of a slip-ring failure at this station (as discussed before in Section 5.2.1).

At $\mu = 0.362$, in figure 101, the lift on the advancing side goes to zero at about 105°. The four lifting-line analyses also show this lift reduction and the CAMRAD analyses, in particular, calculate the phase and amplitude of the advancing side lift quite well. The RAE/WHL analysis shows a small phase delay and a greater extent of negative lift while METAR/R85 indicates an earlier phase in the minimum, and the lift always remains positive. CAMRAD indicates too much lift over the rear of the disk, but the other methods show quite good predictions in this region.

Figure 102 compares the measured lift and the calculated values for the highest speed condition. There is now a substantial area of negative lift in the second quadrant and this is well predicted by RAE/WHL and CAMRAD/JA. Neither CAMRAD nor METAR/R85 shows the proper extent of the negative lift region and METAR/R85, as at the other speeds, shows too much lead in the phase. The RAE/WHL and CAMRAD/JA analyses provide good predictions of the lift over the rest of the azimuth although the rapid increase in lift in the second quadrant is not well predicted.

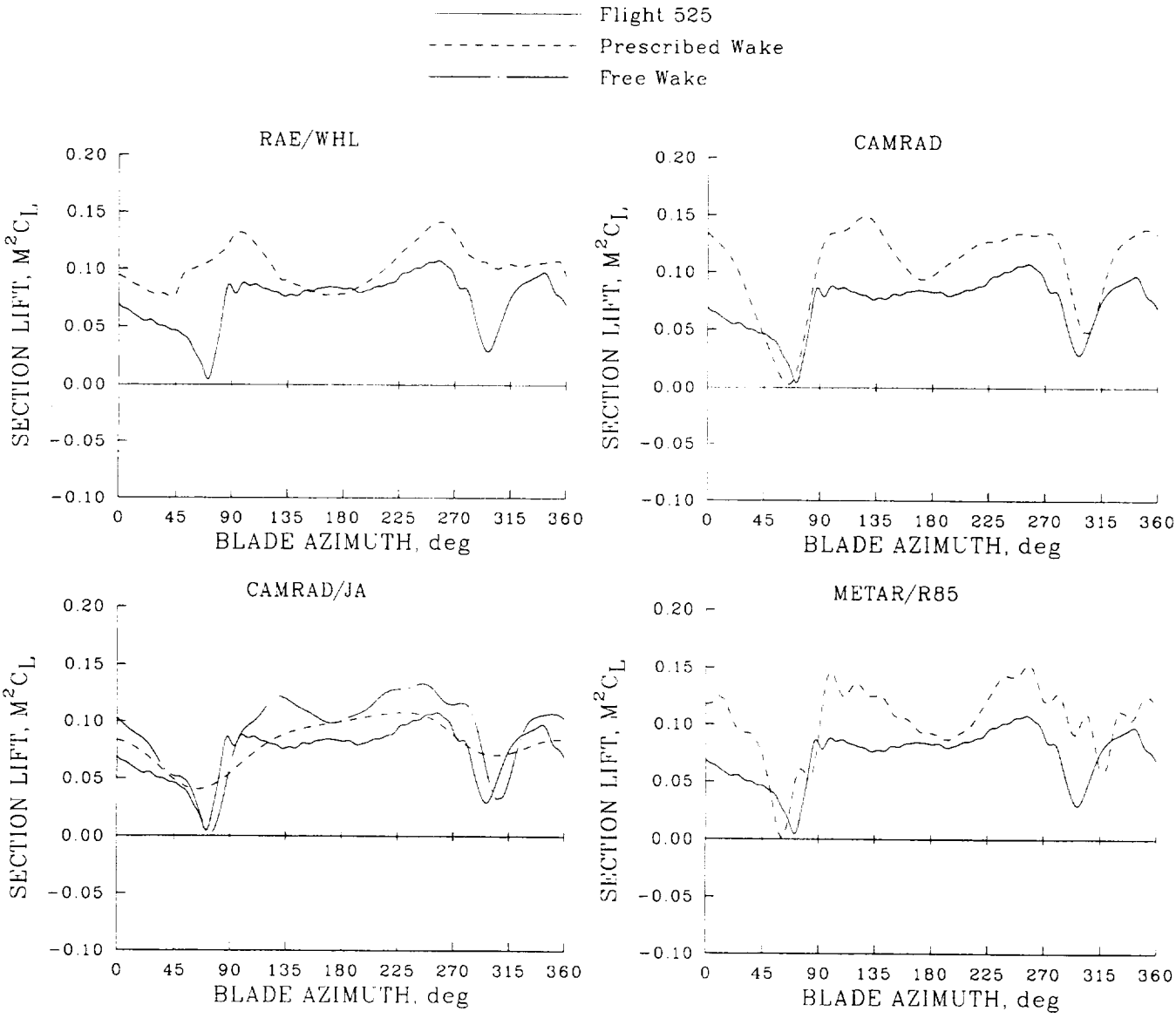


Figure 98. Comparison of measured and calculated section normal force as a function of azimuth; $\mu = 0.098$, $0.95R$, Flight 525.

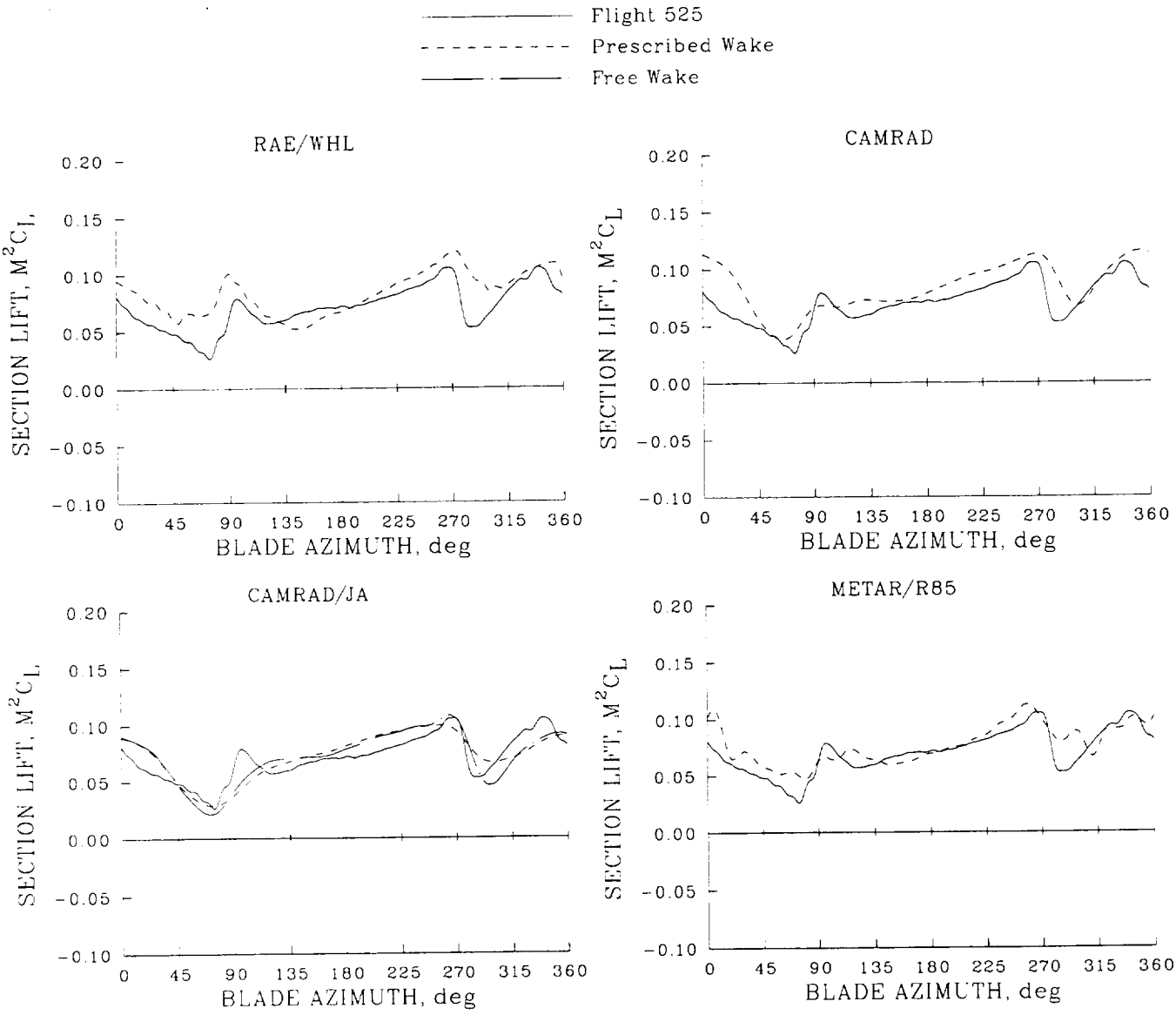


Figure 99. Comparison of measured and calculated section normal force as a function of azimuth; $\mu = 0.182$, $0.95R$, Flight 525.

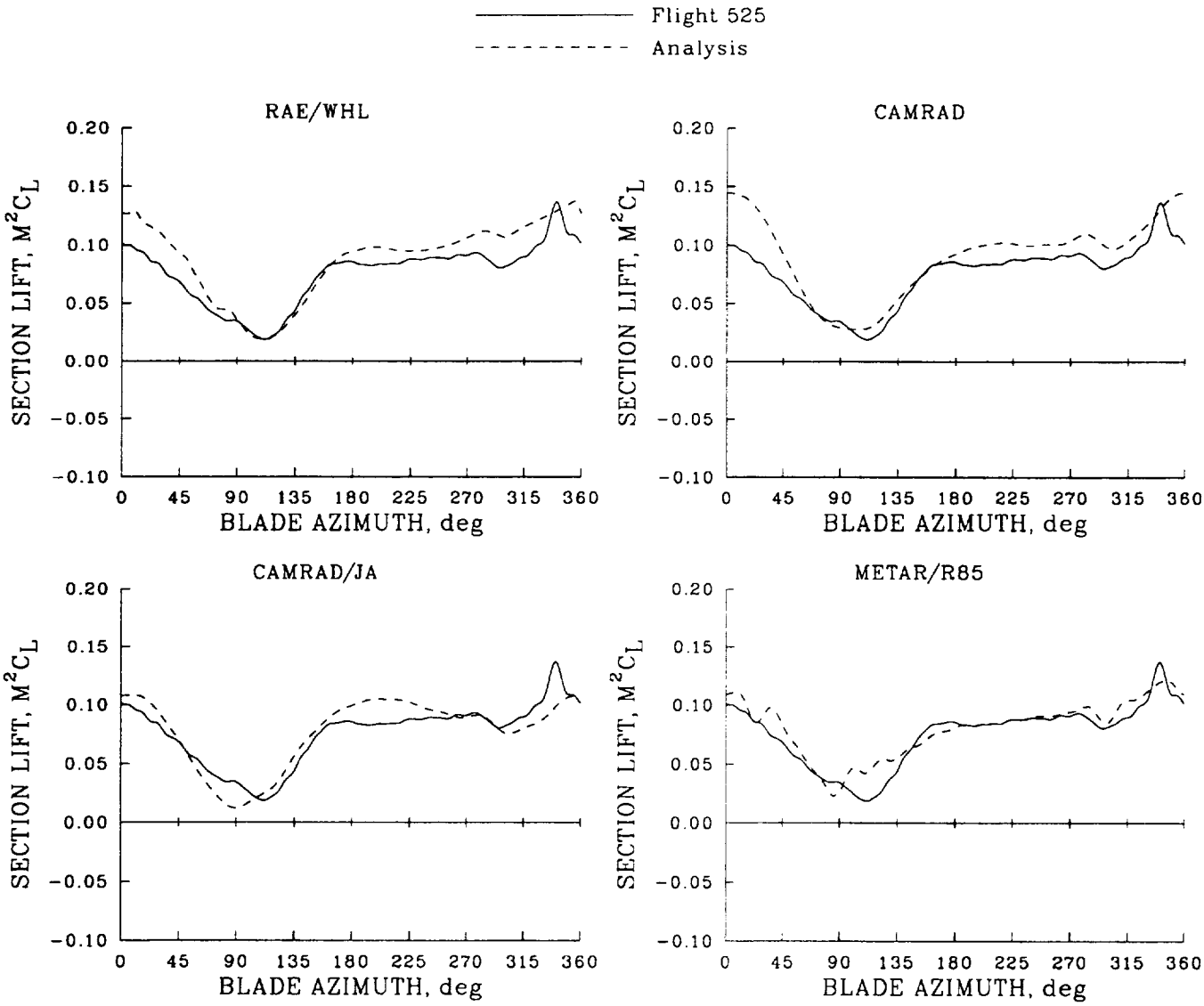


Figure 100. Comparison of measured and calculated section normal force as a function of azimuth; $\mu = 0.307$, $0.95R$, Flight 525.

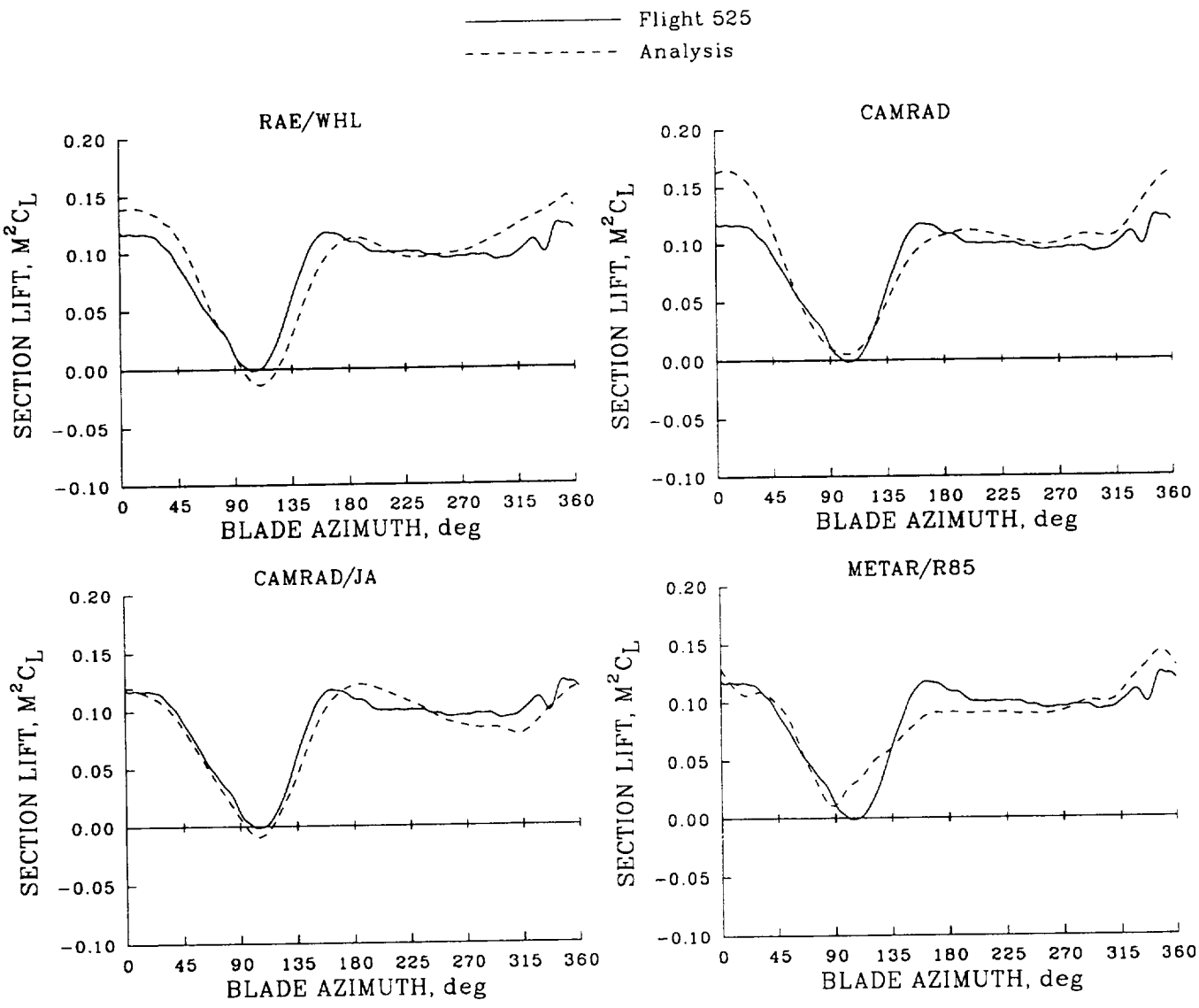


Figure 101. Comparison of measured and calculated section normal force as a function of azimuth; $\mu = 0.362$, $0.95R$, Flight 525.

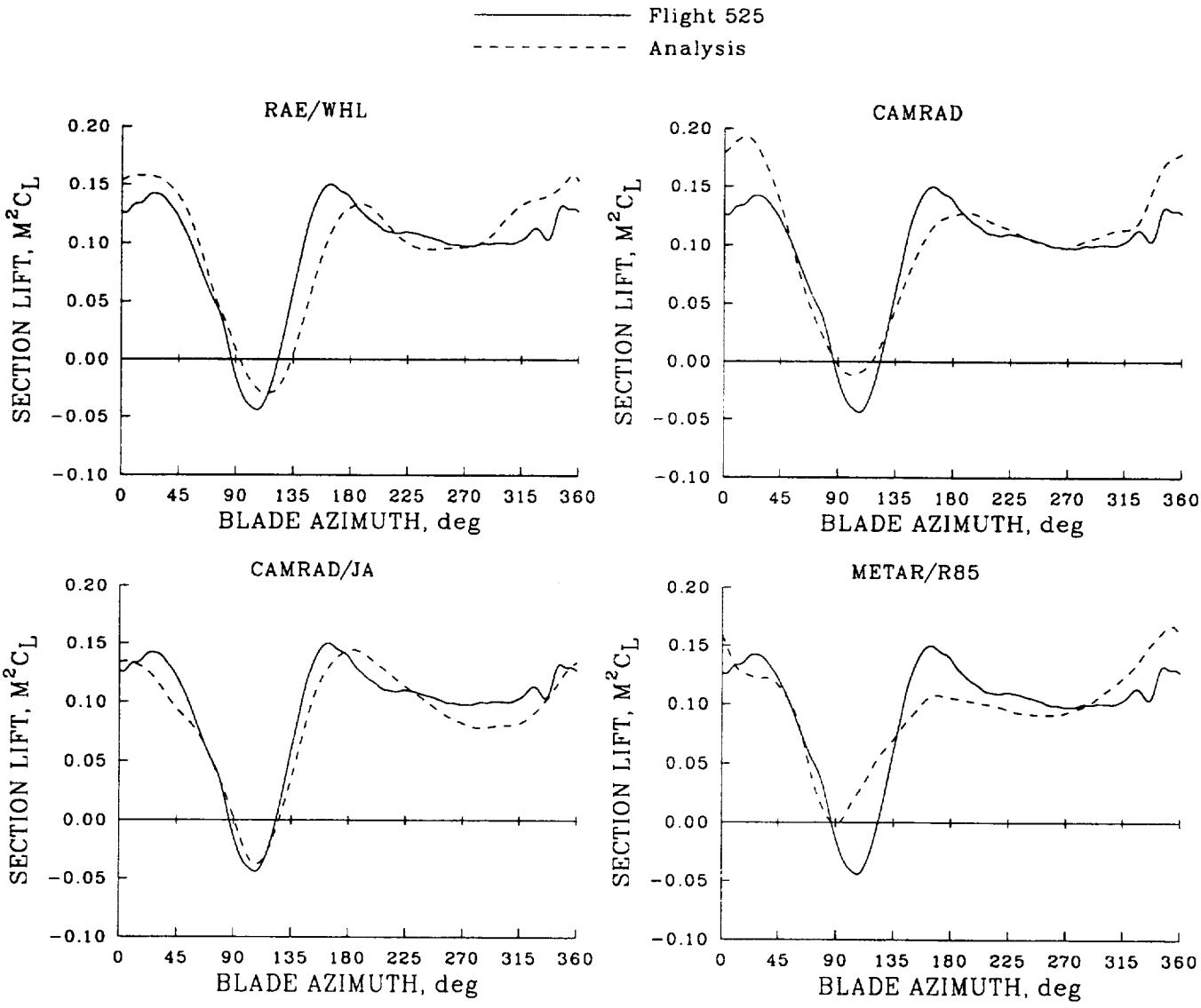


Figure 102. Comparison of measured and calculated section normal force as a function of azimuth; $\mu = 0.402$, $0.95R$, Flight 525.

The radial prediction of lift over the blade tip is examined in figure 103 for the high-speed case at four representative azimuths. At $\psi = 40°$, which is near the first quadrant peak in loading, there is a rapid reduction in lift towards the blade tip that is captured quite well by the RAE/WHL and CAMRAD/JA analyses. The CAMRAD analysis show no reduction in lift and METAR/R85 shows an initial reduction followed by an oscillation and then divergence in lift. This divergence is thought to be caused by the very large sweep angle in the most outboard sections. At these sections the swept flow correction takes on unrealistic values when the yaw angle approaches or even exceeds 90°. At $\psi = 110°$, which is near the peak of the negative lift region, the RAE/WHL analysis shows the best agreement and CAMRAD/JA and CAMRAD less so. METAR/R85 does not calculate any negative lift in this region. All of the methods are relatively close to the experimental measurements at $\psi = 180°$, which is at the lift maximum that occurs at the end of the second quadrant. On the retreating side of the disk, at $\psi = 270°$, the analyses show zero lift inboard of $0.40R$ as expected, and all provide a good prediction of the lift at the blade tip.

The measured and calculated pitching moments at $0.95R$ are compared over the airspeed range in figures 104–108. At the lowest speed conditions, as shown in figure 104, the measured section moments, a result of vortical loading, are simply not predicted by the lifting-line methods shown here. These methods compute the section moments based on angle-of-attack changes at the quarter chord and cannot account for angle-of-attack or velocity variations along the chord, as might be induced by near vortex passage.

At $\mu = 0.182$ the vortical loading on the advancing and retreating sides of the rotor disk is still evident, as can be seen in the pitching moment data in figure 105. The lifting-line methods do not show any effect of the vortical wake and the predicted moments are caused by the steady and unsteady values of angle of attack induced by geometric pitch changes.

There is a progressive increase in the oscillatory pitching moment at $0.95R$ as the advance ratio increases from 0.307 to 0.402, as shown in figures 106–108. The CAMRAD, CAMRAD/JA, and METAR/R85 analyses show this increase but at all airspeeds predict only about half the amplitude. The crossover point, from positive to negative pitching moment at the end of the first quadrant, is delayed in the CAMRAD analyses, but is better predicted by METAR/R85. Unlike the other lifting-line methods, the RAE/WHL analysis shows an increasing oscillatory moment that is greater than the measurements. The predicted moment is similar to the measurements on the advancing side of the rotor, but on the retreating side the rate of change in pitching moment is substantially greater than that observed in flight.

The calculated distributions of pitching moment over the blade tip are compared with the measurements at four azimuths in figure 109. The radial distributions at $\psi = 0$ and $40°$ are representative of the positive moment loading in the first quadrant. At both azimuths there is a rapid increase in the measured moment towards the blade tip and this increase is also seen in the RAE/WHL analysis, although in an exaggerated fashion. The other analyses, however, show hardly any increase in the moment and are clearly unsatisfactory. At $\psi = 140°$, where the most negative section moments occur, the experimental results do not clearly distinguish between the various methods. On the retreating side of the blade, at $\psi = 270°$, the moments are quite low and, again, the measurements do not distinguish between the various calculations.

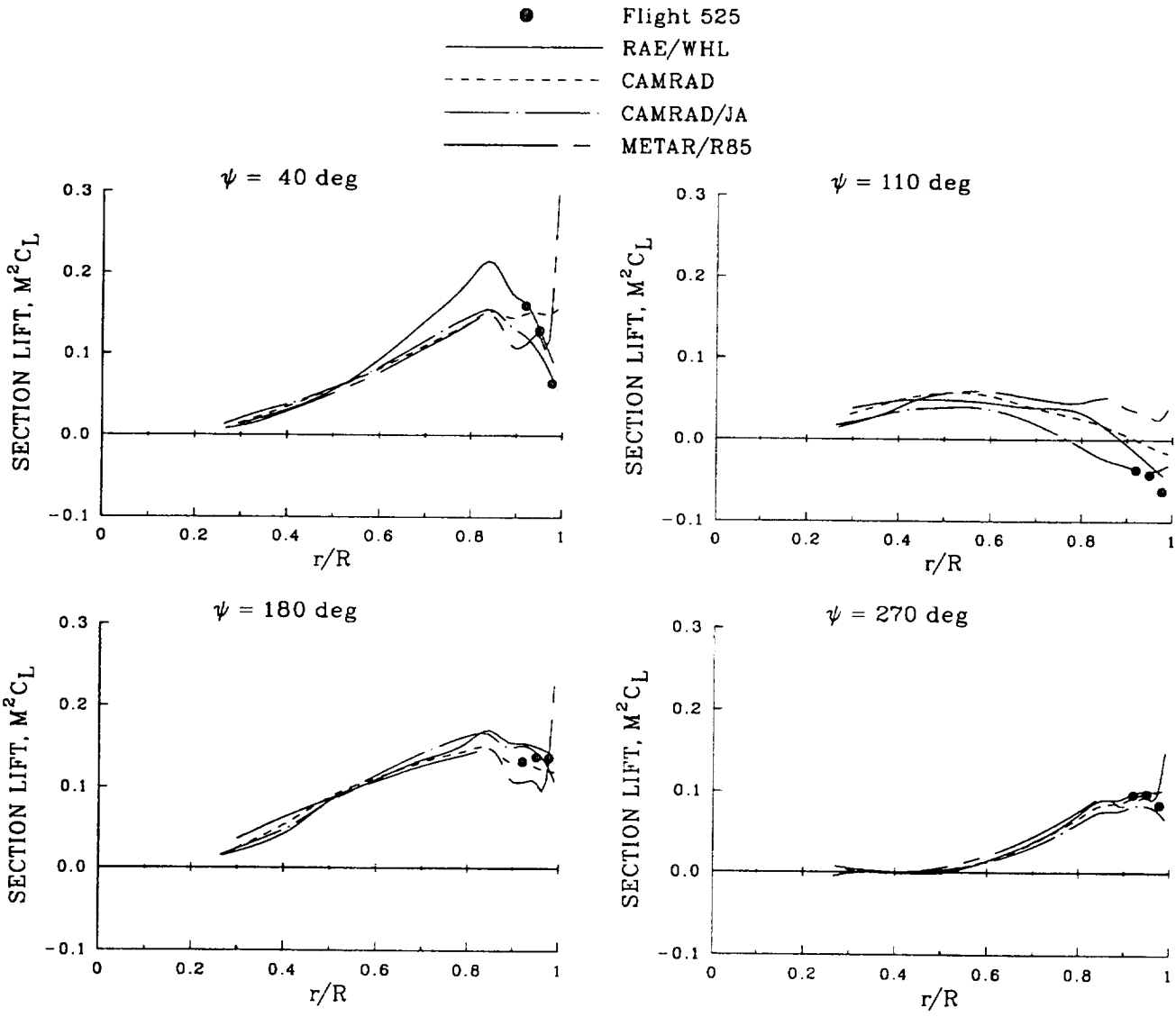


Figure 103. Comparison of measured and calculated section normal force as a function of radius at four azimuths; $\mu = 0.402$, Flight 525.

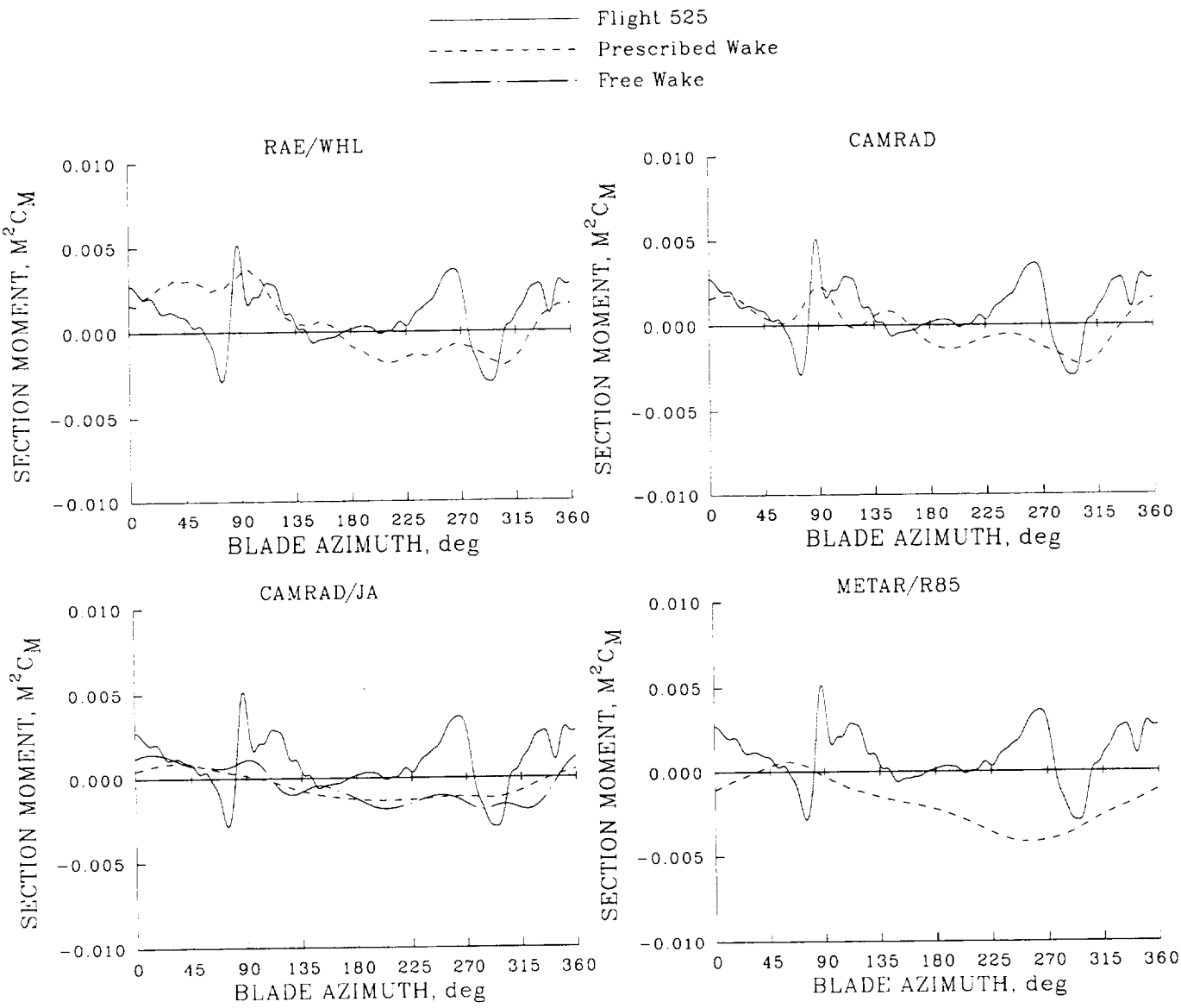


Figure 104. Comparison of measured and calculated section pitching moment as a function of azimuth; $\mu = 0.098$, $0.95R$, Flight 525.

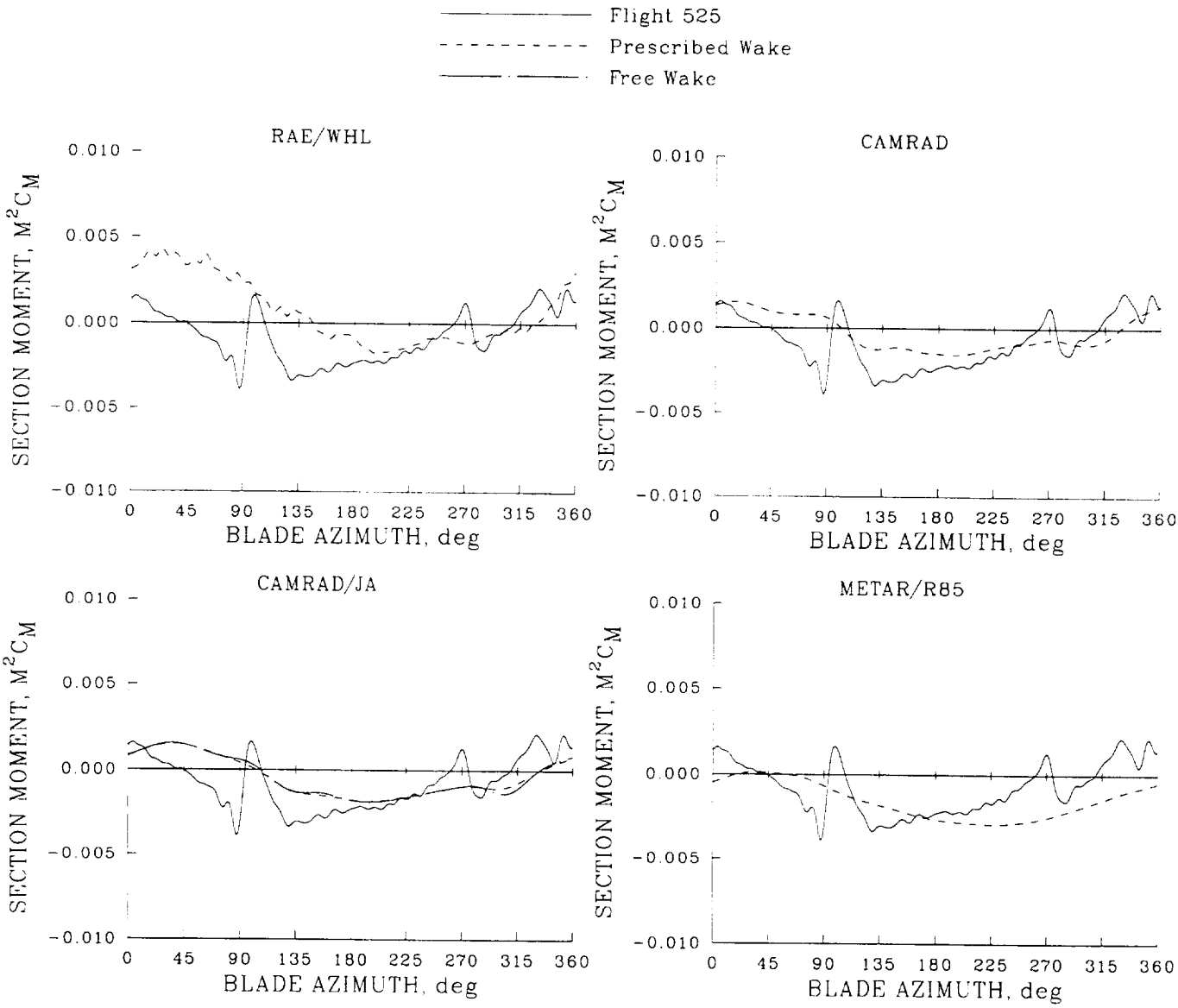


Figure 105. Comparison of measured and calculated section pitching moment as a function of azimuth; $\mu = 0.182$, $0.95R$, Flight 525.

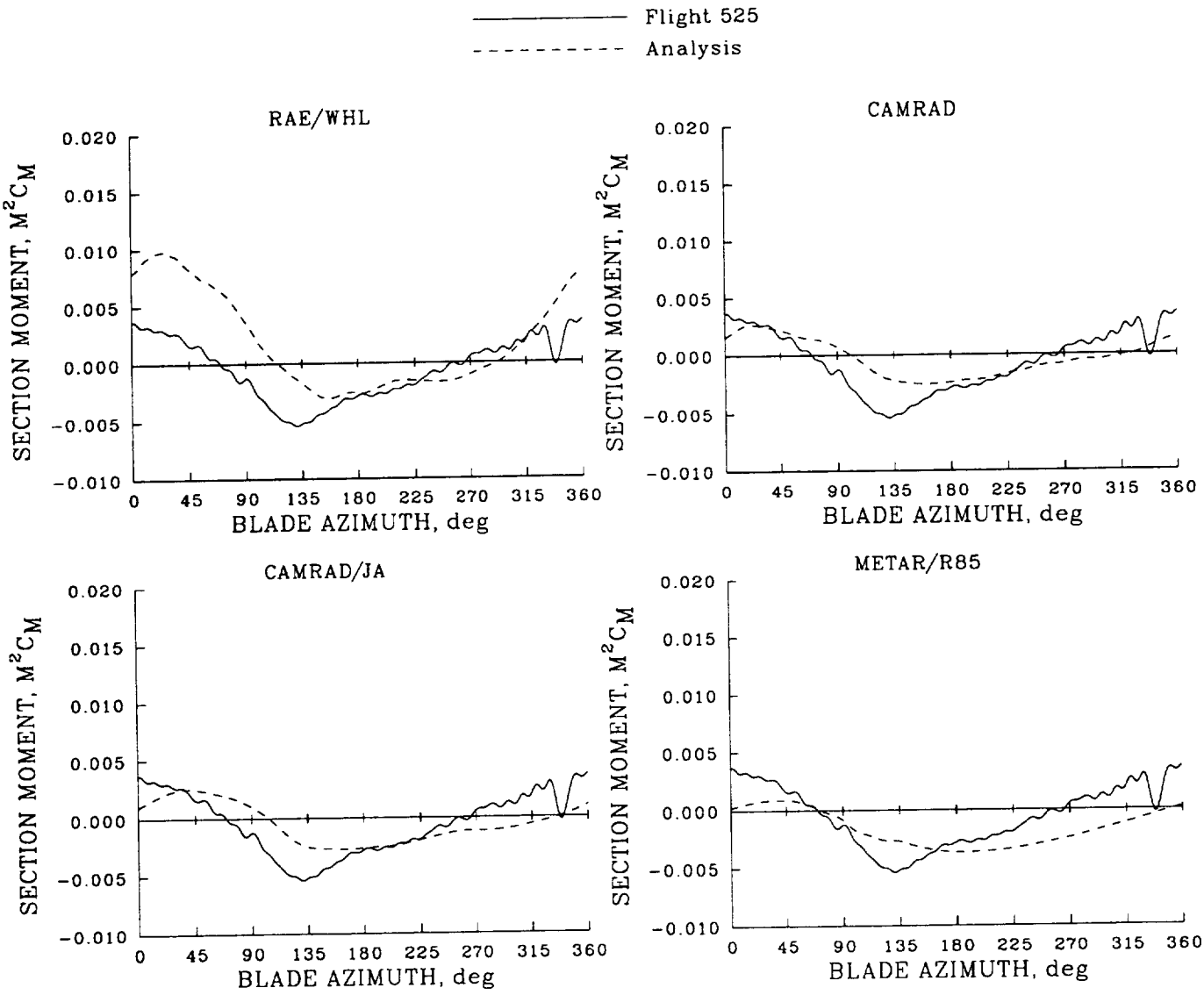


Figure 106. Comparison of measured and calculated section pitching moment as a function of azimuth; $\mu = 0.307$, $0.95R$, Flight 525.

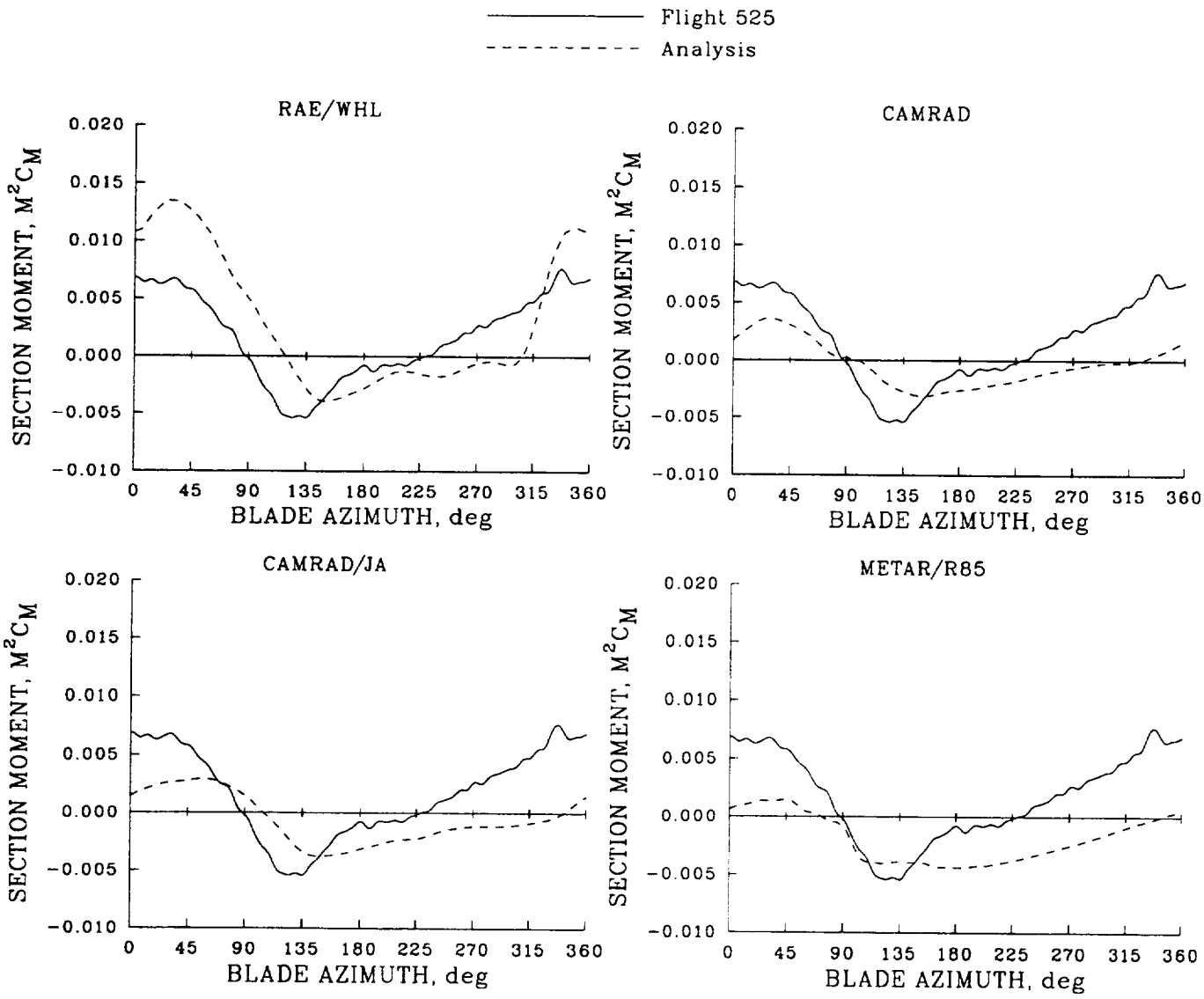


Figure 107. Comparison of measured and calculated section pitching moment as a function of azimuth; $\mu = 0.362$, $0.95R$, Flight 525.

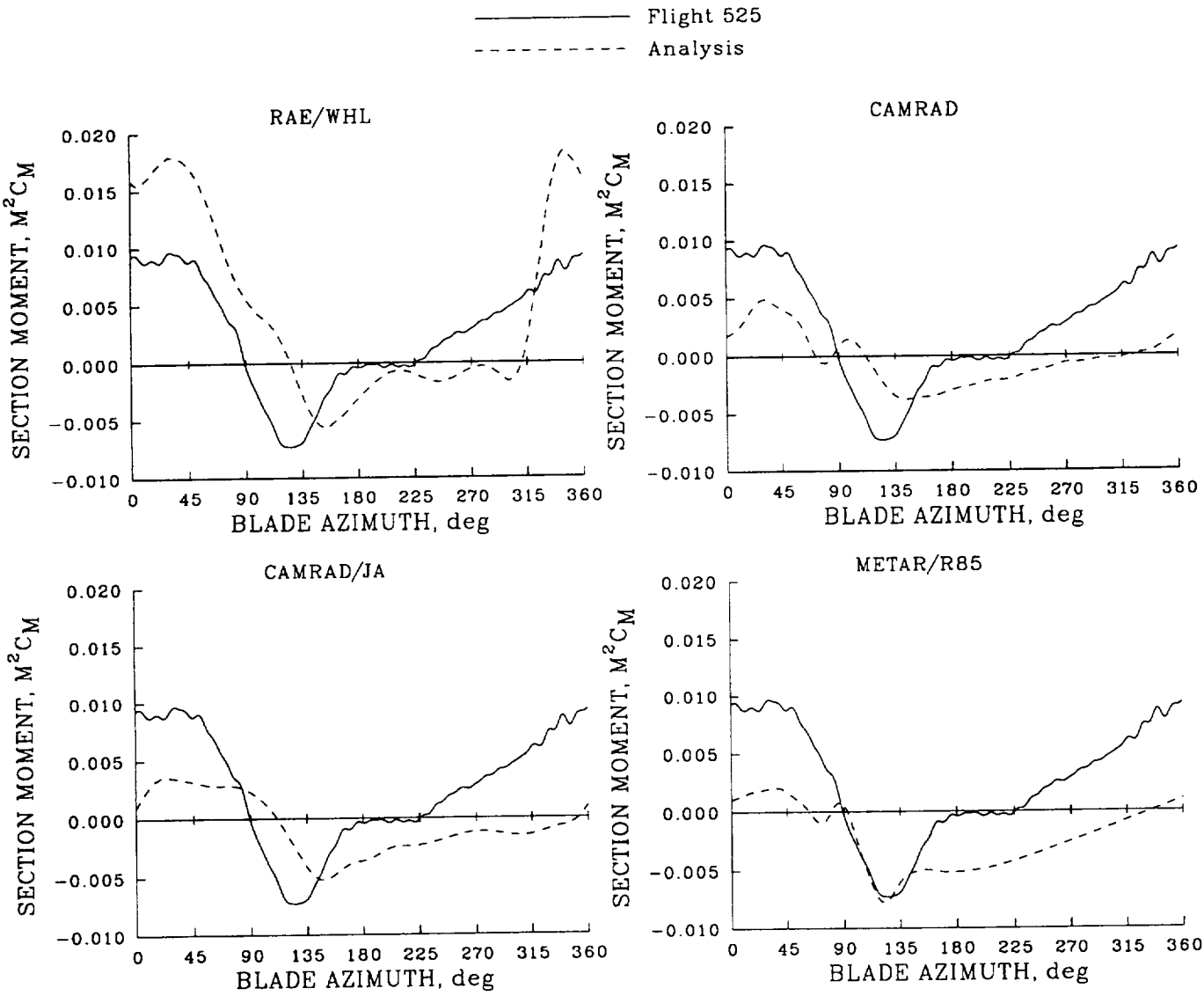


Figure 108. Comparison of measured and calculated section pitching moment as a function of azimuth; $\mu = 0.402$, $0.95R$, Flight 525.

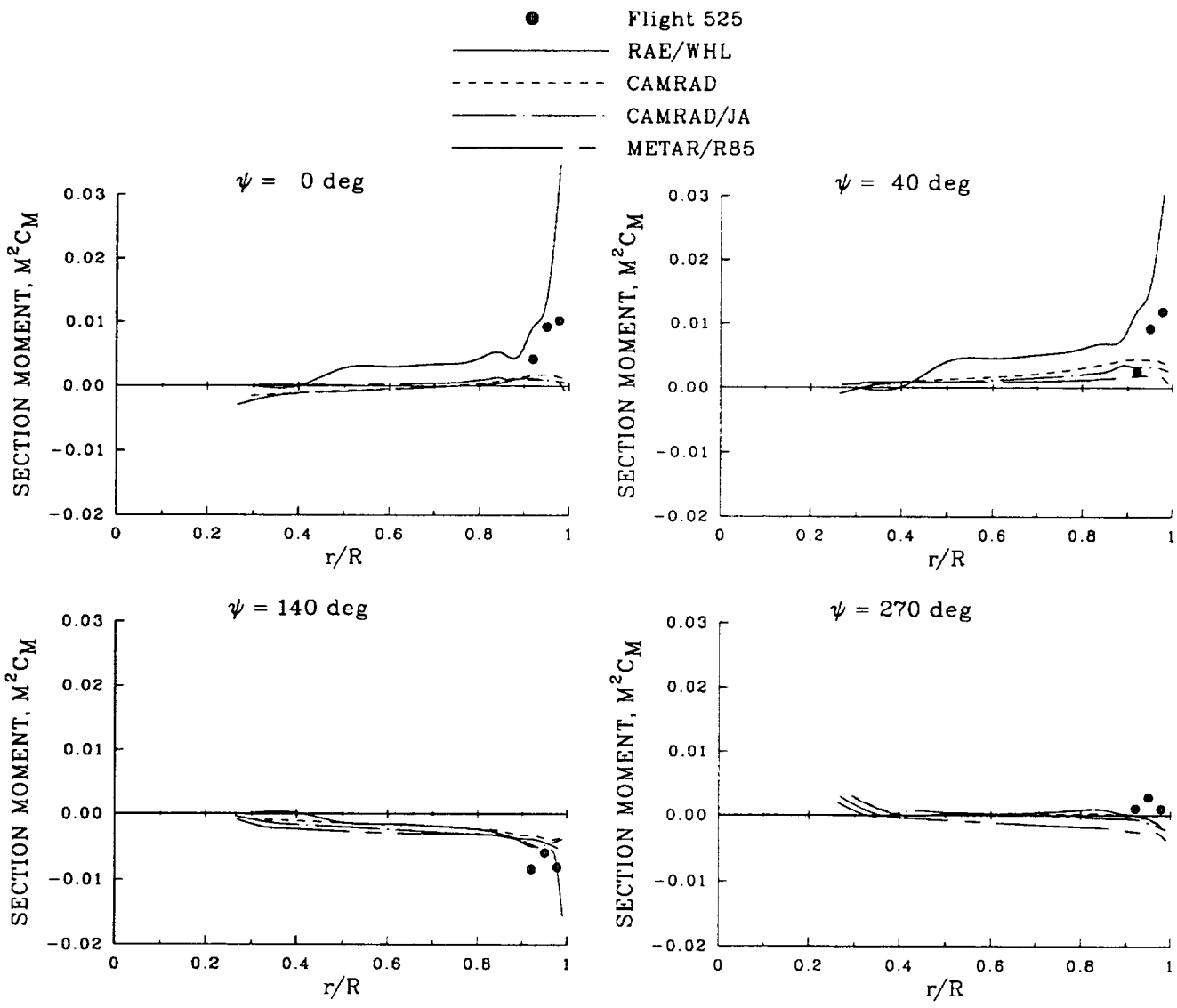


Figure 109. Comparison of measured and calculated section pitching moment as a function of radius at four azimuths; $\mu = 0.402$, Flight 525.

It is useful to compare the lifting-line method predictions over the entire blade, to better understand areas of agreement and disagreement, even though there are no measurements inboard of $0.92R$. Figure 110 compares the calculated section normal force at $\mu = 0.098$ for the four methods. The RAE/WHL and CAMRAD/JA analyses show the expected increase in lift moving outboard on the blade with the peak lift at about $0.80R$ and then a reduction in lift to the blade tip. The CAMRAD prediction extends the lift farther outboard which is expected (see figure 24 and the previous discussion in Section 4.3.2). The METAR/R85 calculation shows the greatest lift at the most outboard station, $0.991R$, and, as discussed above, this appears to be the result of swept flow corrections at the very large sweep angles near the tip.

The loading from the vortical structures on the advancing and retreating sides extends well inboard as can be seen in the RAE/WHL, CAMRAD, and CAMRAD/JA analyses. The inboard section of the blade for the RAE/WHL calculation shows rapid fluctuations in loading that are caused by close passage of the vortex rings that represent the vorticity in the wake. For the CAMRAD analyses the vorticity loading is quite smooth on the inboard part of the blade and this is caused, in part, by wake model changes that expand the tip vortex core inboard of $0.88R$. The inboard loading calculated by METAR/R85 appears quite chaotic at this advance ratio and the vortex-induced loading is difficult to identify, particularly on the retreating side.

The calculated section pitching moments are quite small at $\mu = 0.098$ over all of the blade as shown in figure 111. Almost no effect of vortex loading is seen in these calculations.

For the high-speed case, $\mu = 0.402$, the comparison of the four methods in figure 112 shows the reduction in lift in the second quadrant and, for the RAE/WHL and CAMRAD/JA calculations, a maximum in the radial lift at about $0.80R$. The lift is maintained towards the blade tip for the CAMRAD computation, while for the METAR/R85 analysis the lift abruptly increases near the tip. Comparing these latter results with the analytical comparisons that were done in Section 4.3.2 for a rectangular tip, figure 22, it is apparent that neither of these methods is adequately computing the normal force on the swept tip at its outboard end.

Figure 113 compares the predicted pitching moments for the high-speed case, $\mu = 0.402$. CAMRAD shows a moderate positive pitching moment in the first quadrant that increases slightly towards the blade tip. The effects of the reverse flow region are seen at the blade root, as expected, and a double oscillation is seen on the advancing side at the blade tip which is related to the high Mach number at this point and the reversal in angle of attack. CAMRAD/JA shows similar behavior although an oscillation near the blade root is believed a consequence of computational problems and no double oscillation is seen at the blade tip. METAR/R85 also shows the large pitching moment in the reverse flow regime and, at the outboard radial location, $0.991R$, a surprisingly large pitching moment. The RAE/WHL analysis shows very large pitching moments at the most outboard blade station. Pitching moment calculations have been made for a rectangular-tip planform on the Puma and have been shown above in the section on the analytical modeling task, Section 4.3.2, figure 40; further results will be shown in the discussion of the reference flight case in Section 5.3.3.2, figure 159. These calculations do not show the very large moments at the most outboard stations which suggests that the RAE/WHL and METAR/R85 analyses do not fully accommodate the swept-tip planform used here.

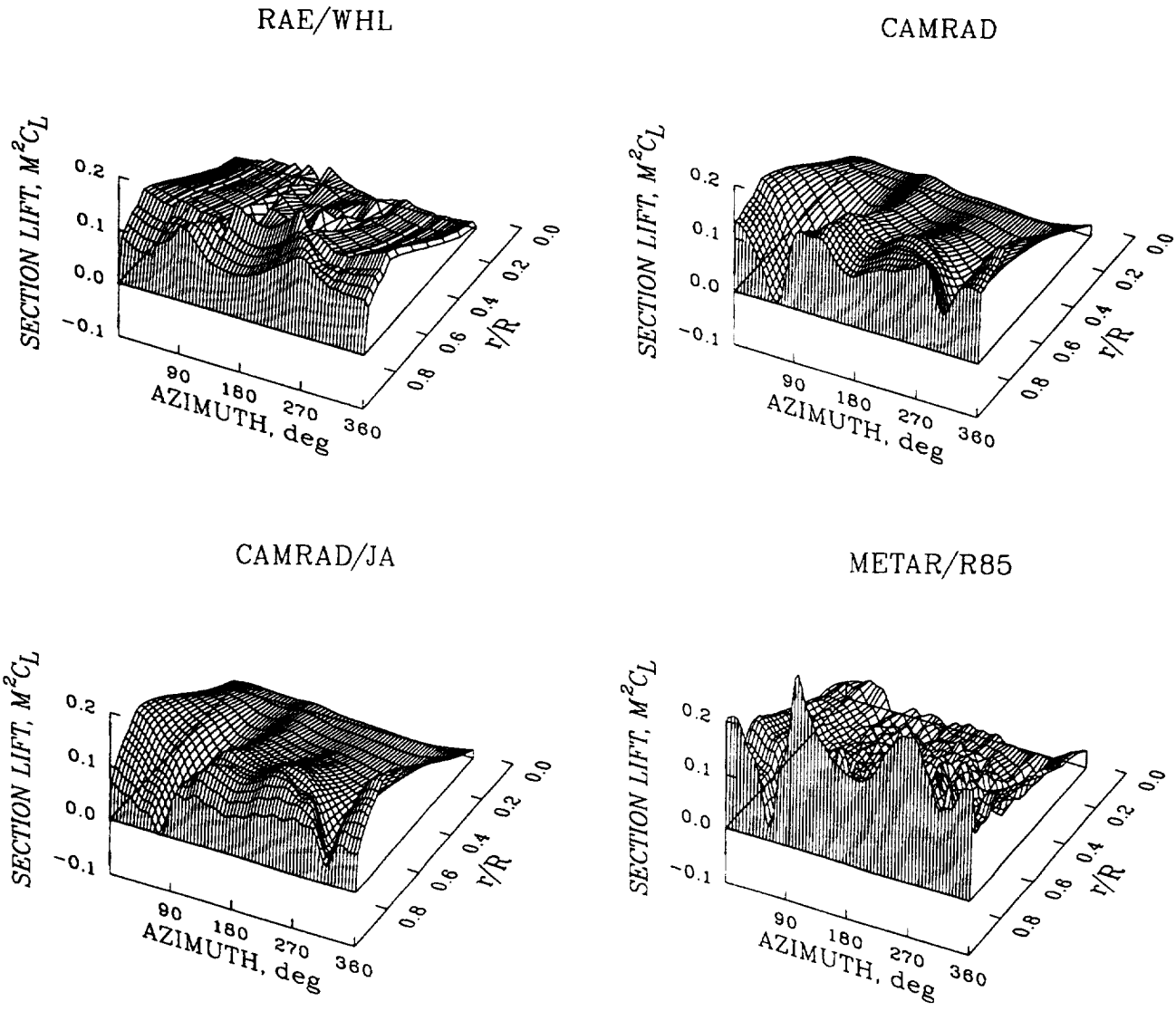


Figure 110. Comparison of calculated section normal force as a function of azimuth and radial station at $\mu = 0.098$; Flight 525.

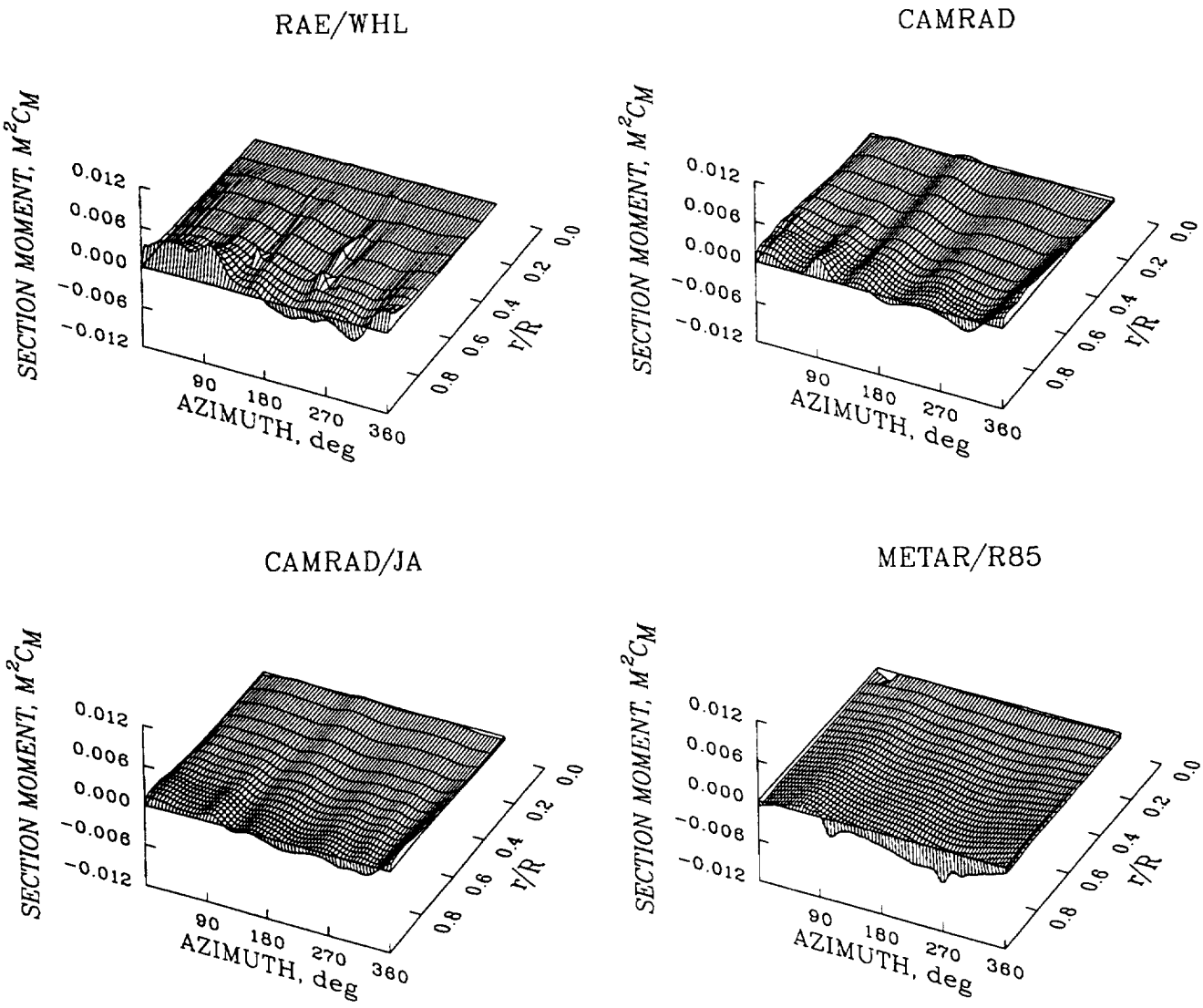


Figure 111. Comparison of calculated section pitching moment as a function of azimuth and radial station at $\mu = 0.098$; Flight 525.

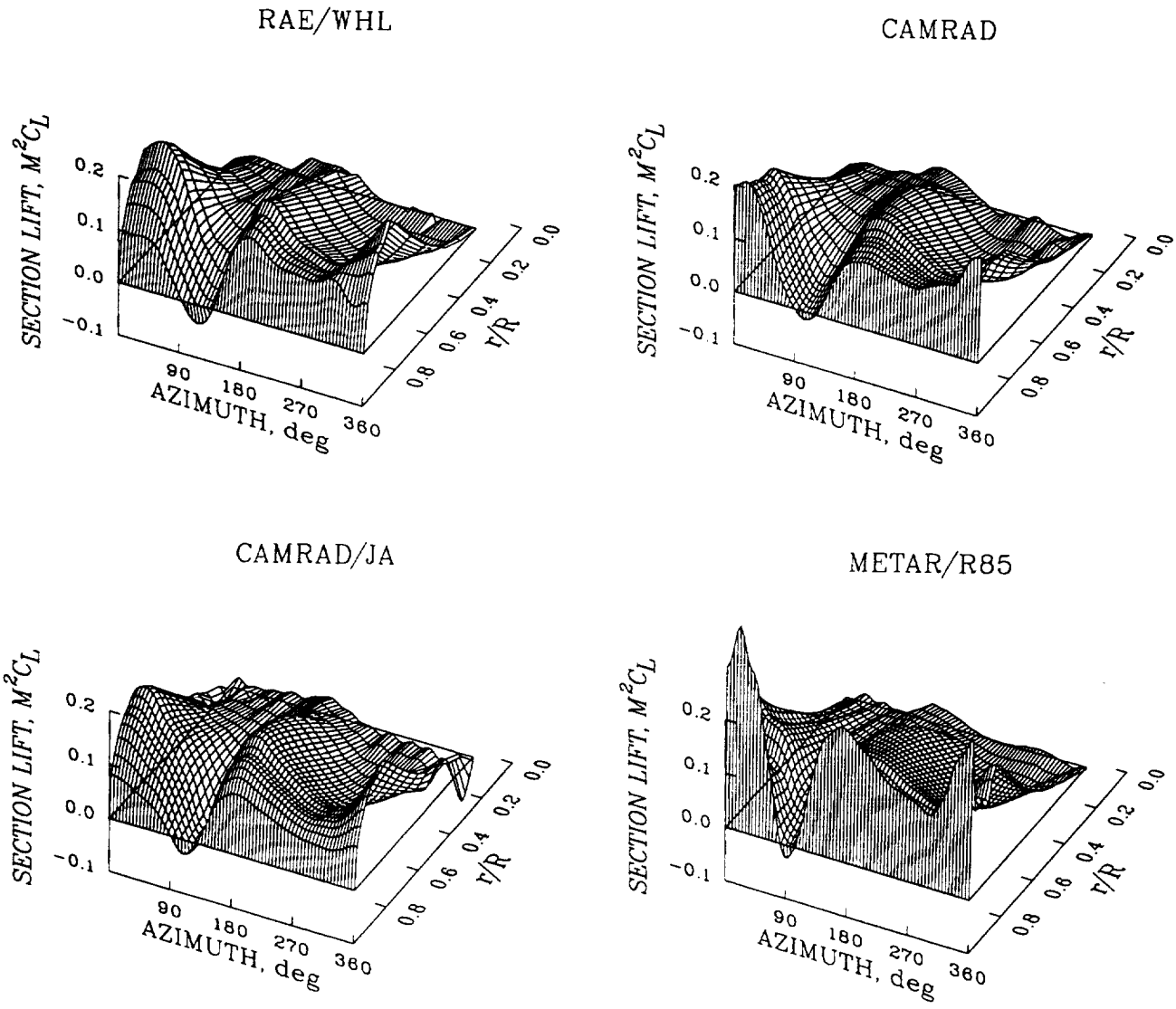


Figure 112. Comparison of calculated section normal force as a function of azimuth and radial station at $\mu = 0.402$; Flight 525.

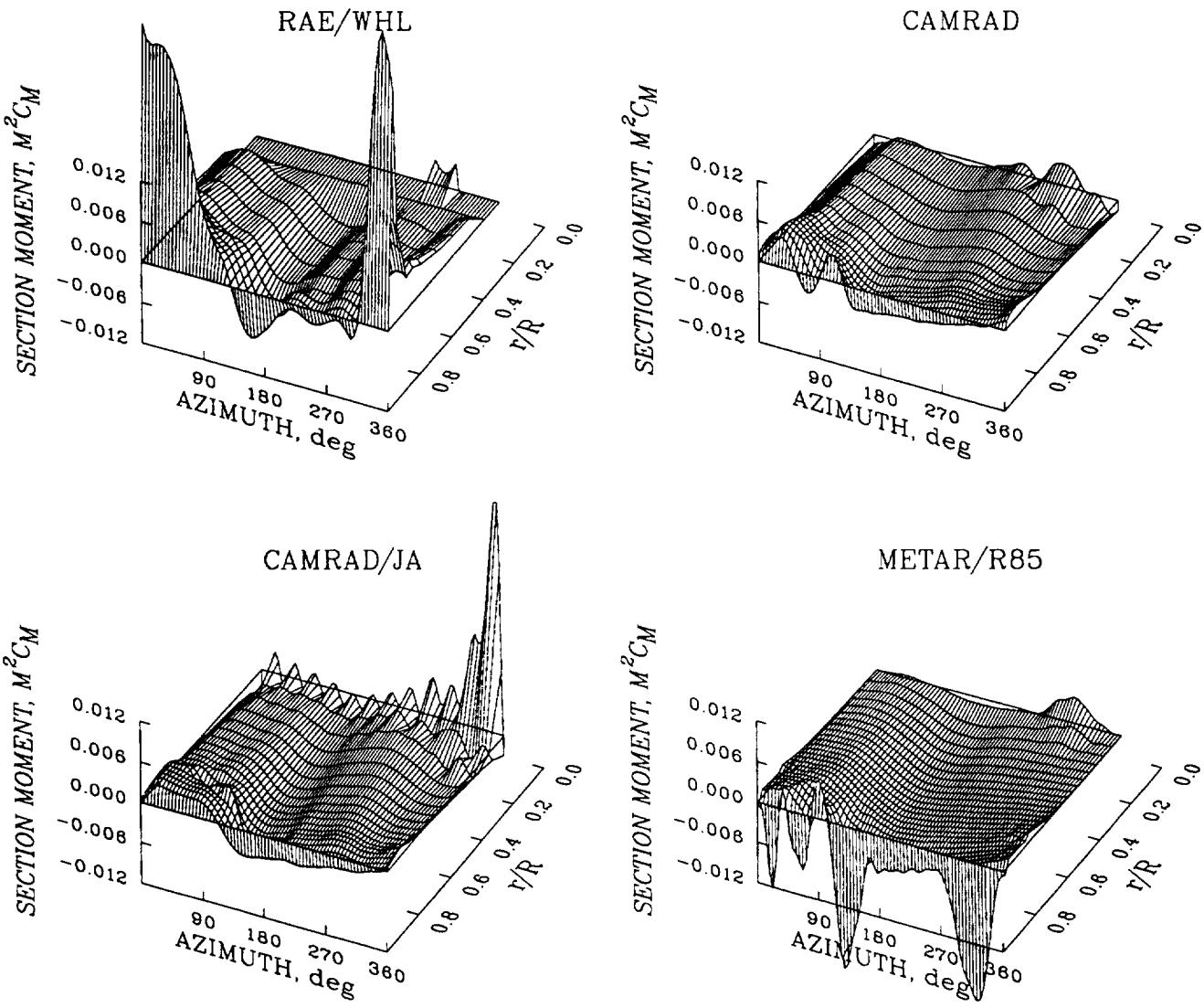


Figure 113. Comparison of calculated section pitching moment as a function of azimuth and radial station at $\mu = 0.402$; Flight 525.

5.2.2.3 *Blade Response, Moments, and Loads*

The analyses used to calculate the blade response, moments, and loads for Flight 525 were the RAE/WHL analysis, CAMRAD and CAMRAD/JA with both prescribed and free wakes, and the Aérospatiale R85 analysis with the METAR wake. Moments and loads were only computed for the two highest advance ratios for the METAR/R85 analysis. The free wake in CAMRAD and CAMRAD/JA is used for the two lowest advance ratio cases and the prescribed wake is used for the higher speeds.

*Blade Response*

The measured and calculated blade flapping are compared in figure 114 as a function of blade azimuth and advance ratio. The flight measurements show that blade flapping is primarily 3/rev in character and, as advance ratio increases, the basic behavior is modified with additional 1/rev and 5/rev components and a shift in phase of these components. Qualitatively, the RAE/WHL, CAMRAD, and CAMRAD/JA analyses each show this general behavior. CAMRAD and CAMRAD/JA show better agreement at low speed, a consequence of the free wake model, while the RAE/WHL analysis shows better agreement at high speed. Although qualitatively similar, the METAR/R85 analysis shows only fair agreement with the measurements.

A similar comparison of the lead-lag angle measurements and calculations is shown in figure 115. The measured and calculated angles are quite small and considerable noise is seen in the former. Good qualitative agreement is seen between the data and the CAMRAD methods. A better match is obtained with METAR/R85, particularly at high speed. The RAE/WHL calculated values show poorer agreement which is a result of modeling the viscous damper with structural damping in the first blade mode.

*Moments and Loads, Advance Ratio = 0.098*

The low advance ratio case provides a severe test for the analyses, particularly with regard to the modeling of the rotor wake. Comparisons between the analyses and the measurements of the flap bending moments are made at $0.20R$, $0.57R$, and $0.78R$. The test data contain a glitch near an azimuth of $15^\circ$ which produces a local peak at $0.20R$ and a trough at $0.78R$, but the data at $0.57R$ appear unaffected.

The comparison of the measured and calculated flap bending moment at $0.20R$ is shown in figure 116. The measured waveform has a predominant 3/rev variation from the forcing in the second flap mode, with smaller components at 5 and 6/rev arising from the third flap mode and the coupled flap/torsion mode at calculated frequencies of 5.3 and 5.6/rev respectively.

The RAE/WHL analysis predicts only half the measured value of the third harmonic component and the correlation with the test data is poor. The level of performance is not surprising as the RAE/WHL predictions of the blade loading at the tip of the blade, figure 98 in Section 5.2.2.2, were not good. The effect of the strong vortex interaction on the advancing side of the disk is more diffuse than in the measurements while the change in the magnitude of the loading is underestimated on the retreating side. The problem is due to the strength of the tip vortex from the complete vortex rings in the wake model which takes a smoothly varying prescribed value inappropriate to the type of loading observed in practice at low advance ratio.

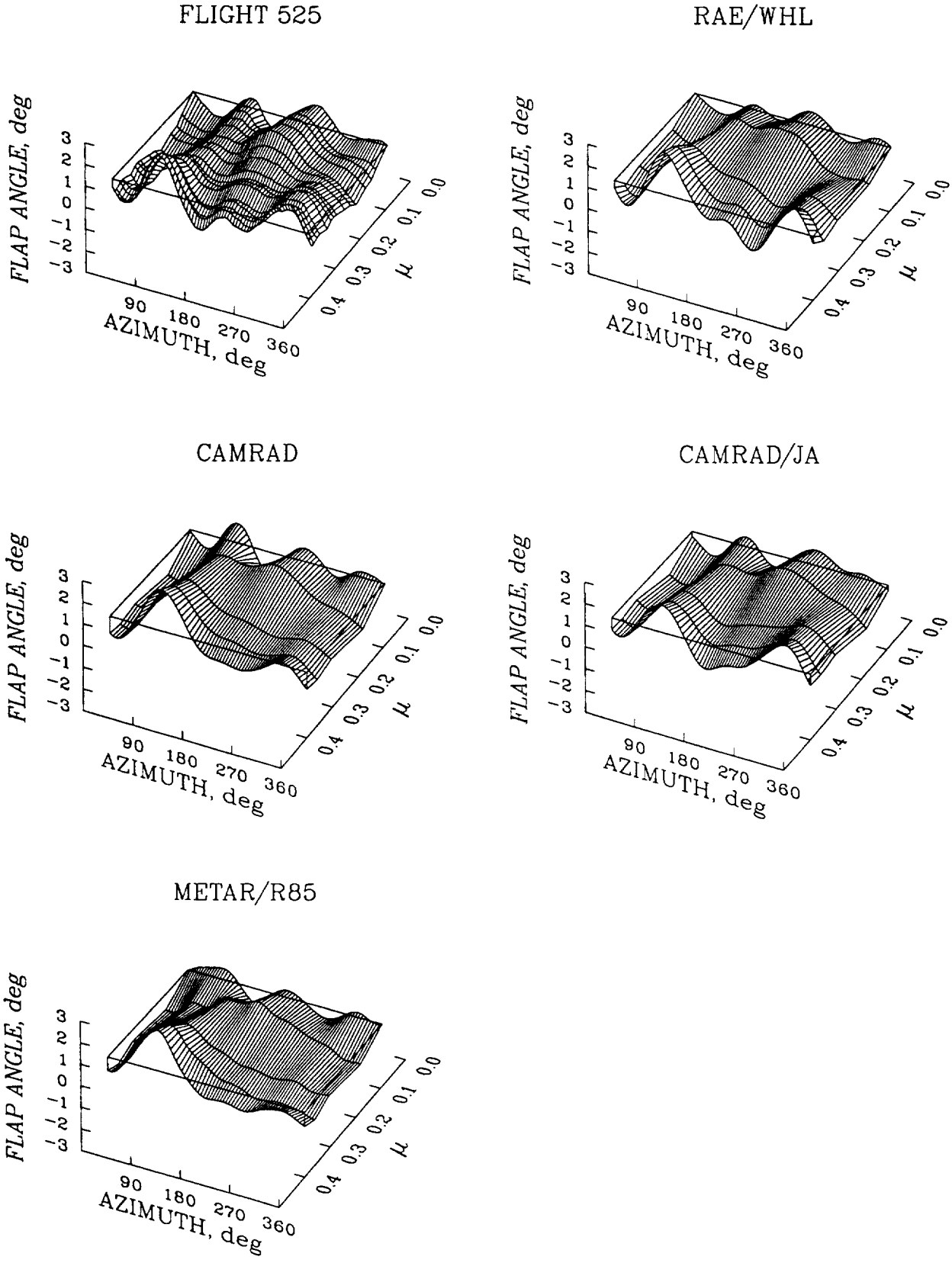


Figure 114. Comparison of measured and calculated blade flapping as a function of azimuth and advance ratio for Flight 525; 1–36 harmonics.

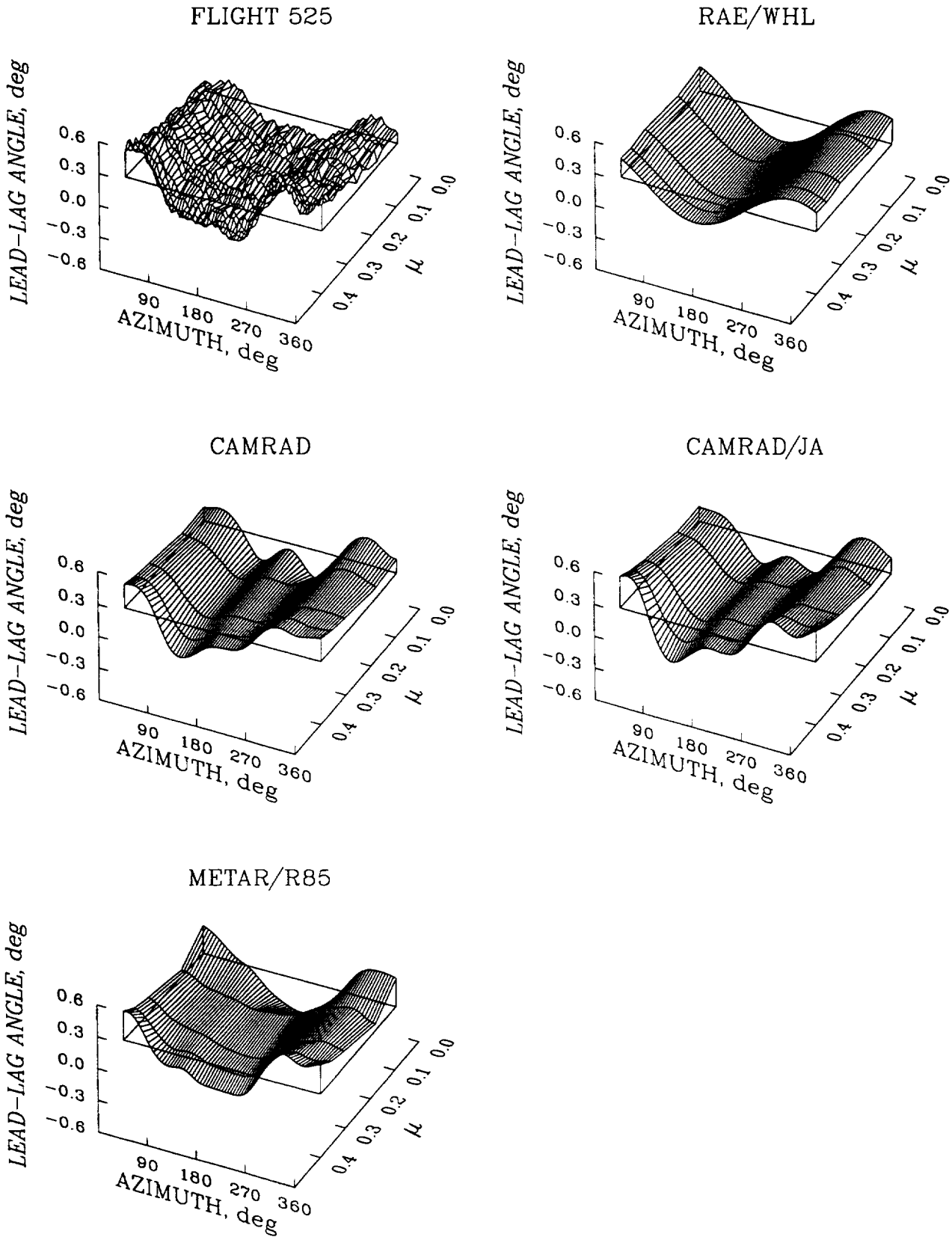


Figure 115. Comparison of measured and calculated blade lead-lag motion as a function of azimuth and advance ratio for Flight 525; 1–36 harmonics.

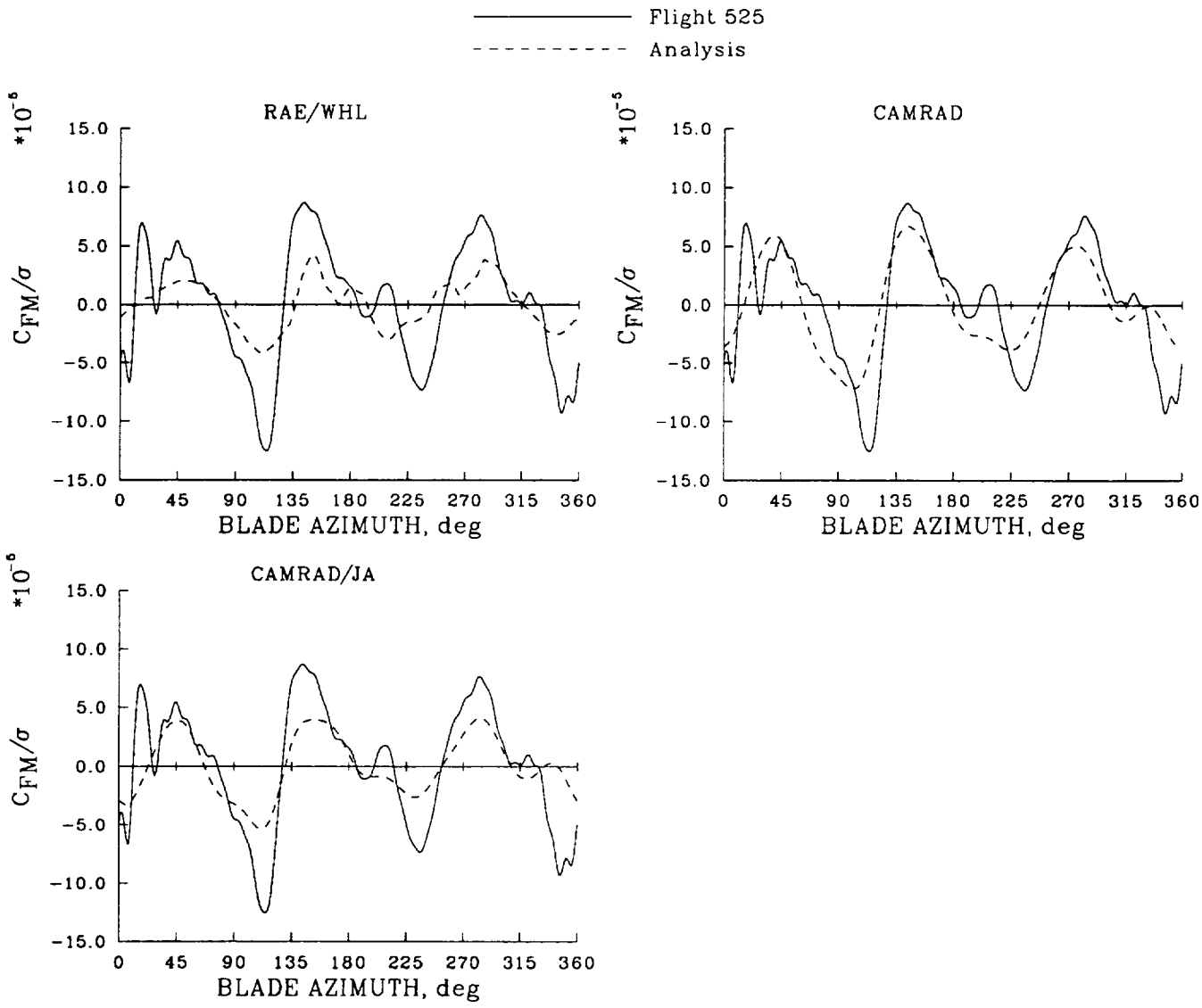


Figure 116. Comparison of measured and calculated flap bending moment as a function of azimuth at $0.20R$; $\mu = 0.098$, Flight 525, 1–36 harmonics.

The bending moment calculated by CAMRAD and CAMRAD/JA with the free wake model is in better agreement with the measurements than the RAE/WHL analysis. The third, fifth and sixth harmonics are slightly underestimated but the comparison is better than with the prescribed wake, particularly with regard to the third harmonic. The free wake model used by these two methods shows good agreement with the airloads measurements, particularly on the advancing side (see figure 98).

The measured flap bending moments at $0.57R$, figure 117, is dominated by the same 3/rev oscillation seen at the inboard position. The RAE/WHL calculation again underpredicts the magnitude of the third harmonic component but the level of correlation appears better than at $0.20R$. CAMRAD/JA shows the best correlation with the measurements and accurately predicts the magnitude of the third harmonic variation.

The azimuthal variation of the measured bending moment changes shape at $0.78R$, figure 118, compared to the inboard positions. As mentioned previously, the trough at about $15^\circ$ is spurious. The magnitude of the first and second harmonic components is almost as large as the third and there are significant contributions at 5, 6, 7 and 8/rev. The correlation between the test data and the RAE/WHL calculation is fairly good on the advancing side of the disk but the magnitude of the peak on the retreating side is underestimated. The free wake calculations of CAMRAD and CAMRAD/JA reproduce all of the features observed in the test data even though the magnitude of the third harmonic component is too large, particularly for CAMRAD.

The measured and calculated chord bending moments are compared at $0.122R$ and $0.55R$. The inboard station is near the lag damper attachment point so the stress is strongly influenced by the forces exerted by the damper. The level of correlation to be expected, therefore, depends on how the damper is represented and how the analyses calculate the resulting moments. The RAE/WHL analysis does not model the lag damper physically, but instead includes the damping effect of the damper as augmentation of the structural damping in the first lag mode. For this reason the predictions of this analysis are expected to be poor. CAMRAD and CAMRAD/JA represent the damper using a linear model (see Appendix A), but use modal summation to calculate the stresses. Nonlinearities in the lag damper and the inability to compute damper effects using a modal summation are both expected to degrade the predictive capability of these analyses.

The measured chord bending moment at $0.122R$, figure 119, has large first and third harmonic components with smaller contributions at 4 and 5/rev. The first and third harmonics arise from the lag damper which is reacting to the Coriolis forcing and the higher harmonic stresses are probably due to the response of the second lag mode. The RAE/WHL analysis, as expected, does not predict the stress to any degree of accuracy with only the fifth harmonic having the correct magnitude. CAMRAD, with its free wake model, predicts the magnitude of all the harmonics up to the fifth accurately, but the phasing is incorrect. CAMRAD/JA, however, underpredicts the amplitude of the third harmonic component.

The effect of the lag damper diminishes rapidly away from the attachment point and the measured chord bending moment at $0.55R$, figure 120, changes from largely 3/rev to 4/rev. The Fourier analysis, figure 121, shows this large 4/rev component with the amplitude of the other components reducing as the harmonic number increases or decreases away from the fourth harmonic.

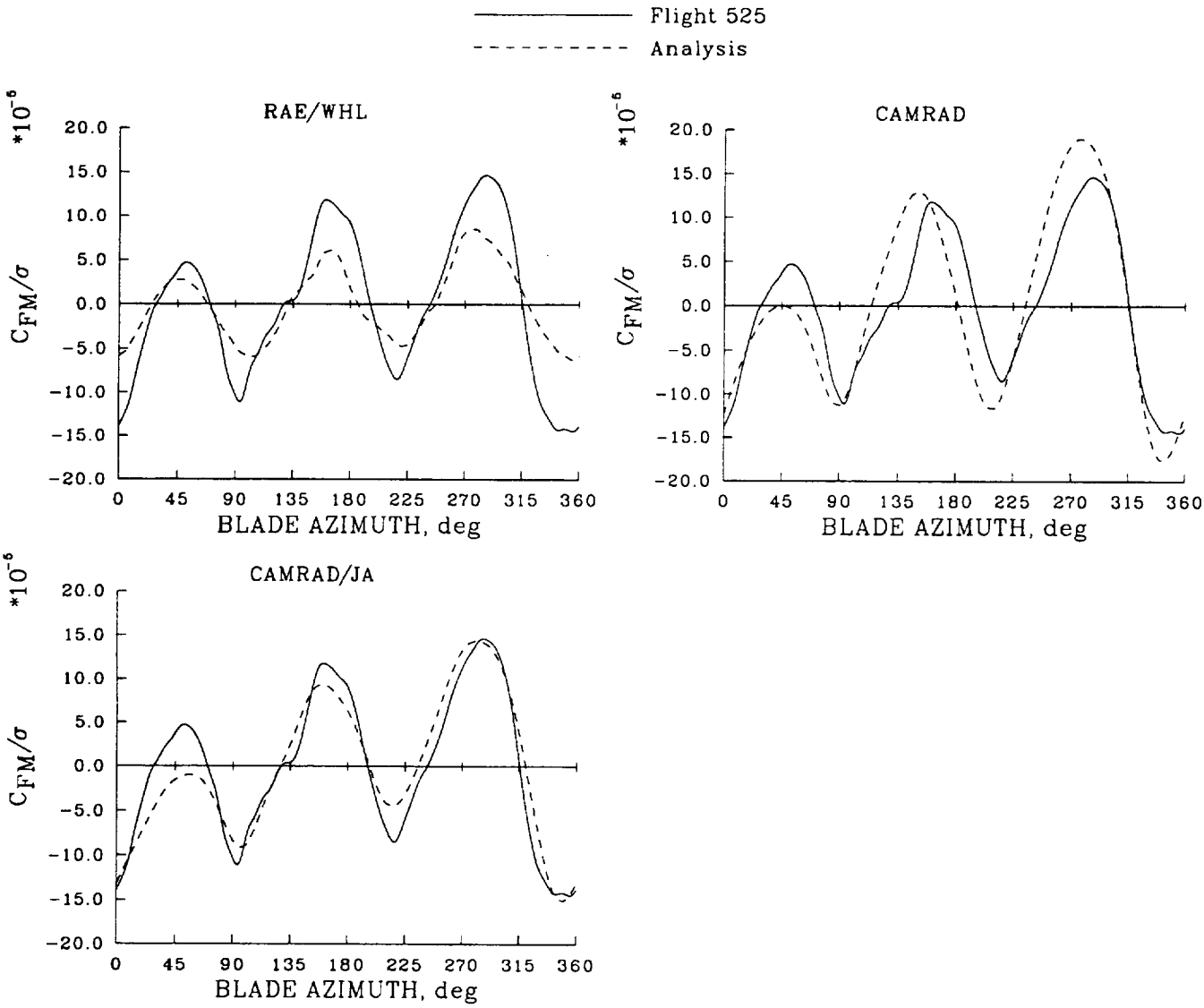


Figure 117. Comparison of measured and calculated flap bending moment as a function of azimuth at $0.57R$; $\mu = 0.098$, Flight 525, 1–36 harmonics.

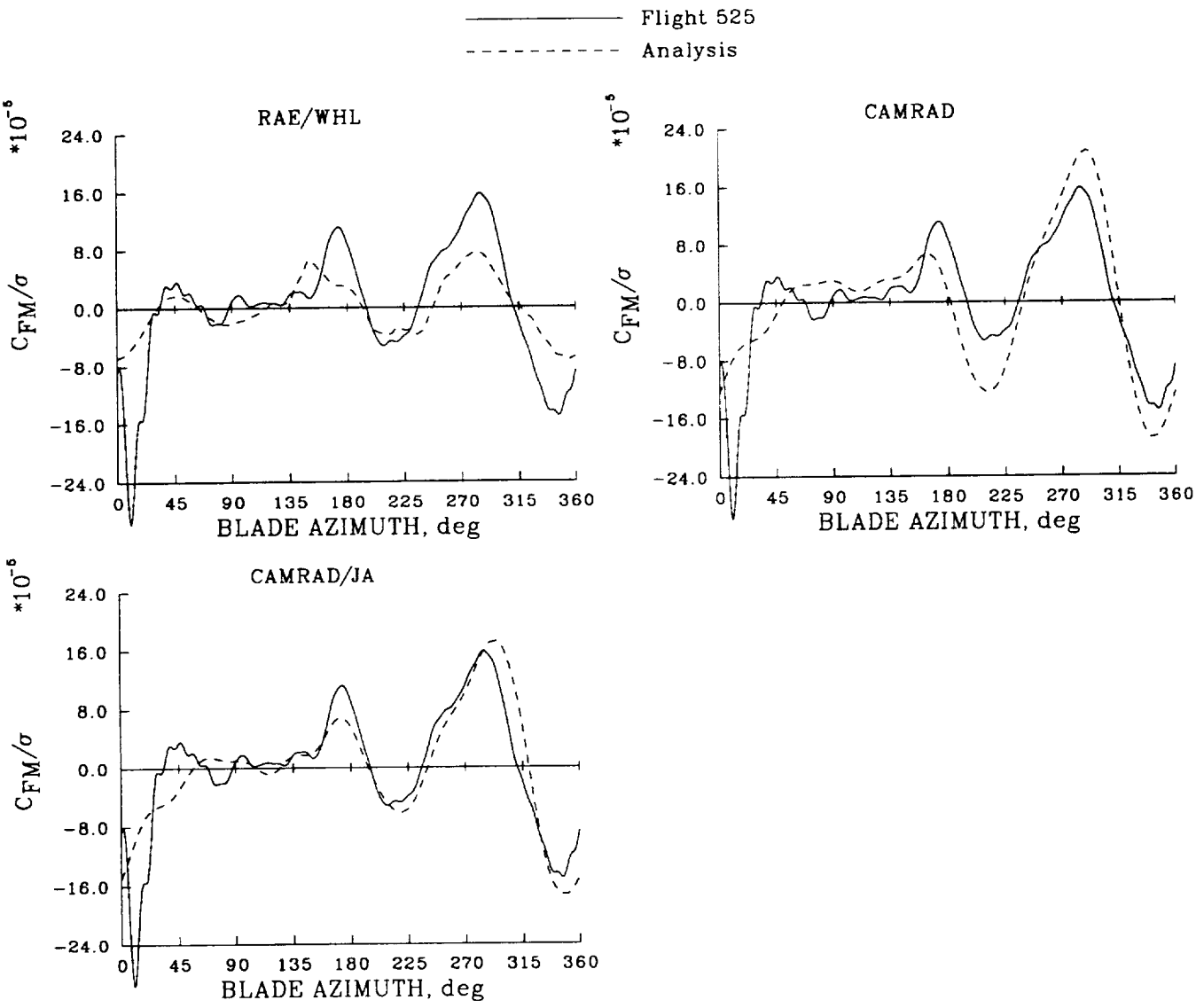


Figure 118. Comparison of measured and calculated flap bending moment as a function of azimuth at $0.78R$; $\mu = 0.098$, Flight 525, 1–36 harmonics.

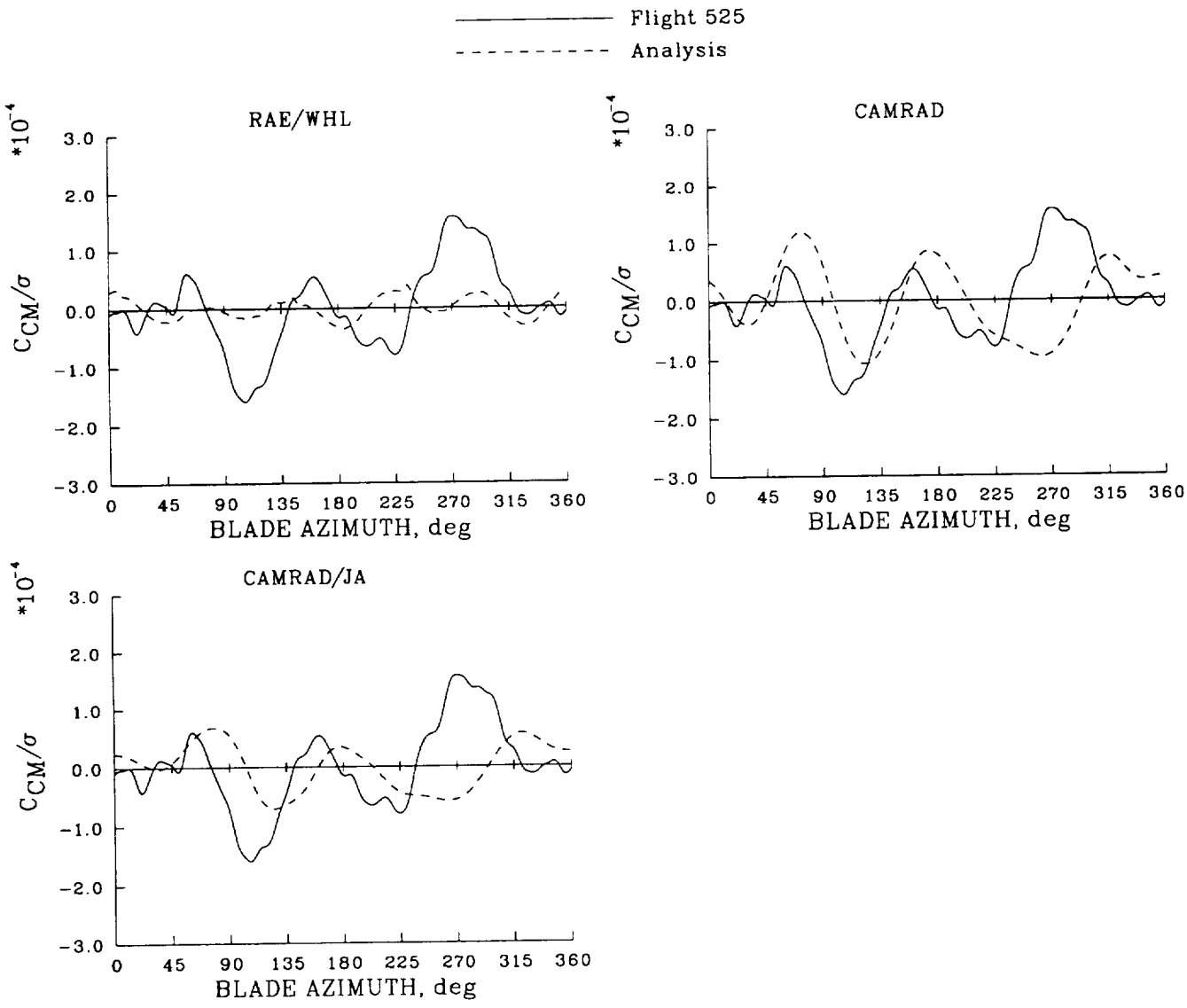


Figure 119. Comparison of measured and calculated chord bending moment as a function of azimuth at $0.122R$; $\mu = 0.098$, Flight 525, 1–36 harmonics.

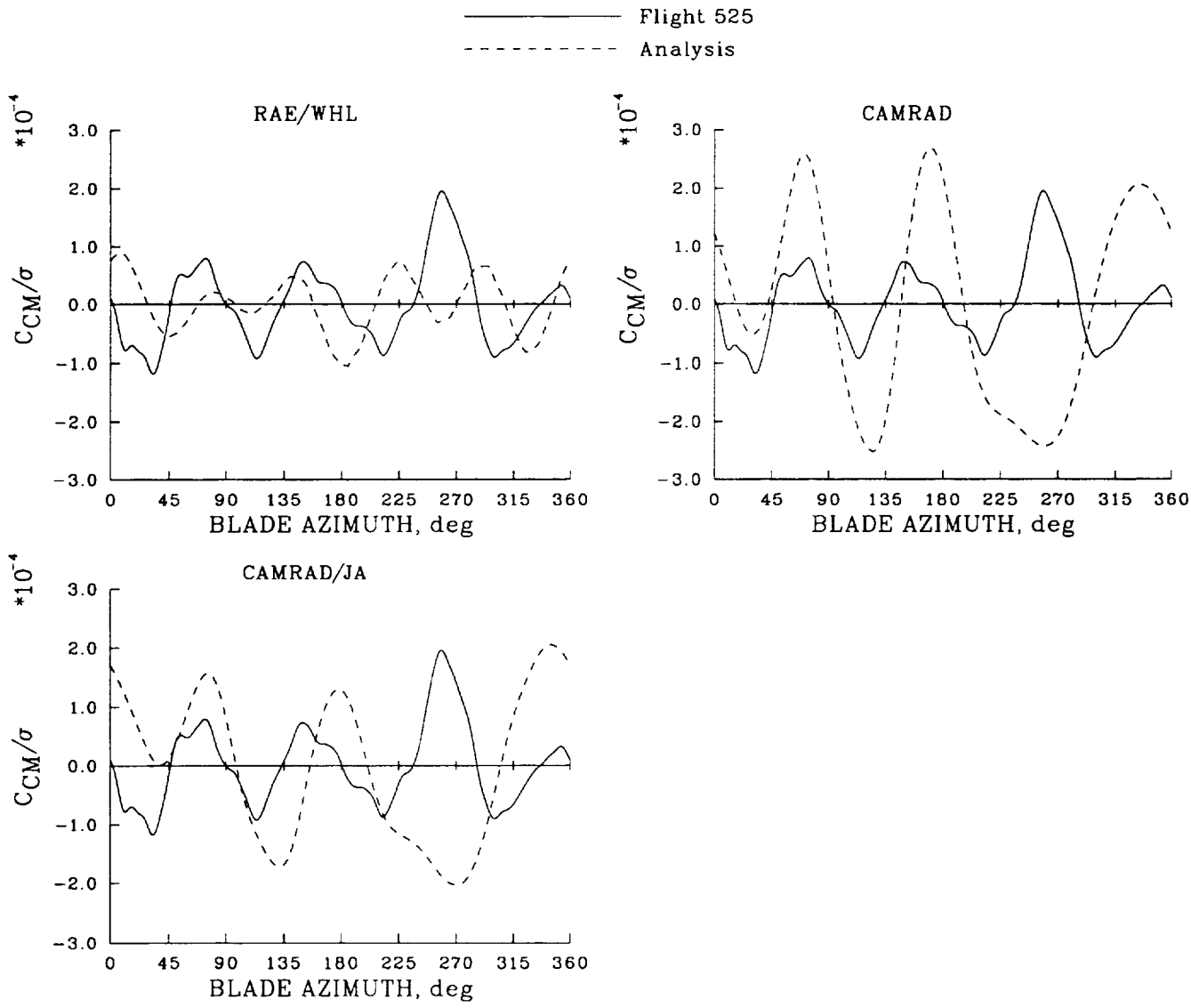


Figure 120. Comparison of measured and calculated chord bending moment as a function of azimuth at $0.55R$; $\mu = 0.098$, Flight 525, 1–36 harmonics.

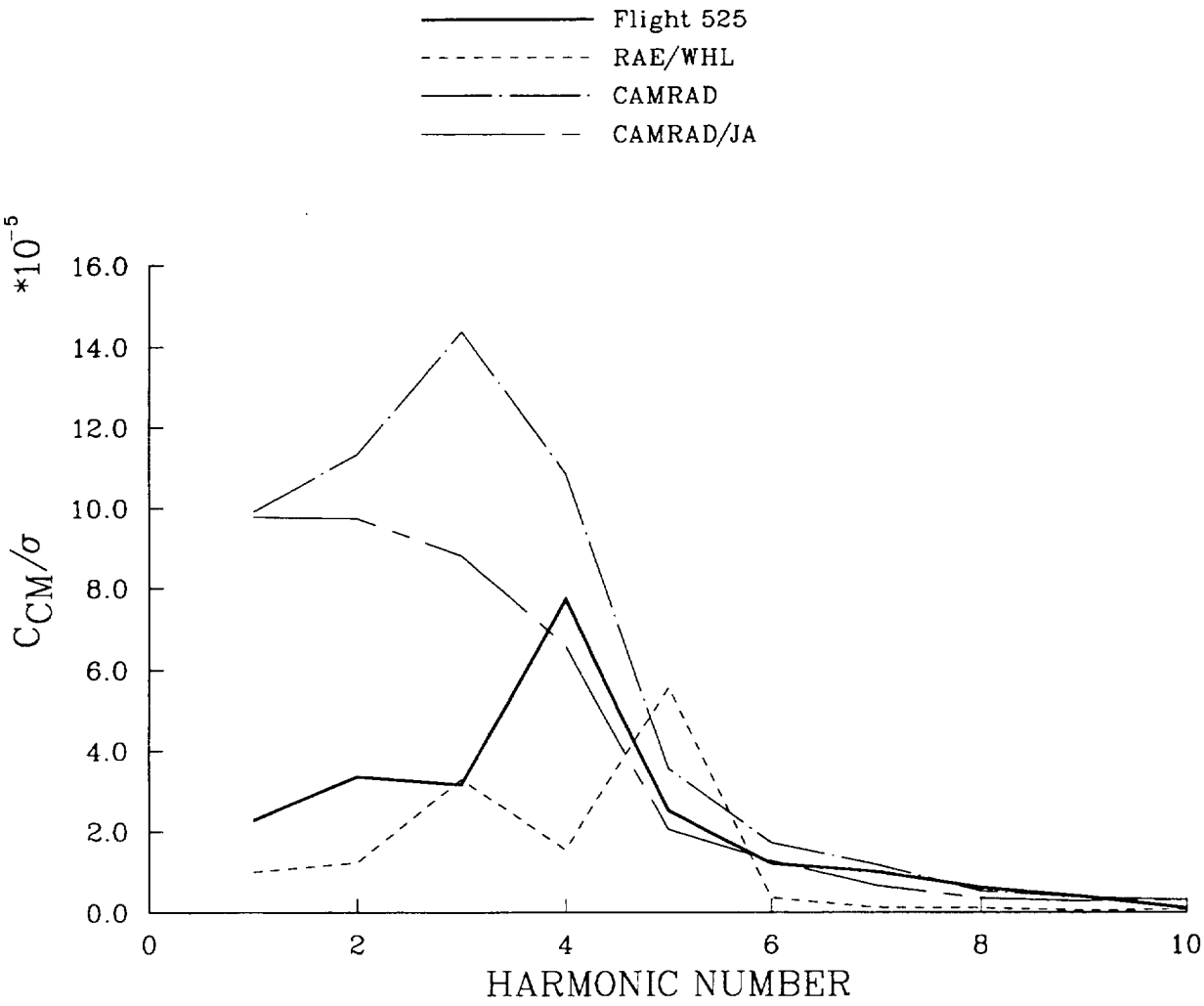


Figure 121. Comparison of measured and calculated harmonic amplitude of chord bending moment at $0.55R$; $\mu = 0.098$, Flight 525.

The harmonic analysis of the stress calculated by the RAE/WHL analysis shows that there are only significant components up to the fifth, which is also the largest. The correlation between the calculation and the test data is poor. The low order harmonic components are overestimated by the CAMRAD analyses, CAMRAD being worse in this respect than CAMRAD/JA, and the comparisons with the test data are not good.

The major source of forcing in the torsion modes arises from the aerodynamic pitching moment. Reference to the comparisons between the measured and calculated blade pitching moments presented

in Section 5.2.2.2 is worthwhile, therefore, before examining the torsional moments and pitch-link loads here.

The RAE/WHL analysis generally follows the trend of the measured pitching moment at $0.95R$, figure 104, but the sudden changes in the moment due to the vortex interactions are absent. The unsteady aerodynamic model used for the calculations does not include the impulsive moment required to predict the vortex loading effects. Although a free-wake model is used by the CAMRAD analyses they also do not compute the impulsive pitching moments associated with the vortex loading.

The comparisons between the measured and calculated torsion moments are shown at $0.126R$ and $0.55R$. The pitch-link loads are also considered to see if the dynamics of the control system have an appreciable effect on the predictions.

The calculated torsion moment at $0.126R$ is compared with the test data in figure 122. The largest harmonic contributions to the measured moment are the first, second and fourth, all of which are underestimated by the RAE/WHL analysis. The CAMRAD prediction has a large 3/rev component which is absent in the CAMRAD/JA calculation and overall CAMRAD/JA produces the best correlation with the test data.

The test data at $0.55R$, figure 123, have a greater amount of second and third harmonic contributions than at the inboard position which changes the waveform considerably. The RAE/WHL analysis reflects the change quite well but the amplitude of the oscillation remains underestimated. The first and third harmonic components predicted by CAMRAD are much reduced relative to the levels at $0.126R$ and the overall correlation is good, better than with CAMRAD/JA.

The measured pitch-link loads, figure 124, shows azimuthal variation similar to the torsion moment near the root of the blade although there are some minor differences such as the local peaks in the pitch-link load at about 35° and 130°. The RAE/WHL analysis underpredicts the magnitude of the pitch-link load as was the case for the torsion moment at the inboard position but the variation with azimuth for both the load and the moment are similar. The similarity is to be expected as the control system is modeled by a linear spring at the end of a rigid rod and the displacement in the rod is directly due to the torsional deflection. The prediction of the pitch-link load by CAMRAD, however, shows a completely different azimuthal variation to the torsion moment. The large 3/rev component is absent in the calculated pitch-link load and the magnitude of the oscillation is underestimated whereas the peak-to-peak moment is too large in the calculated moment. The way in which the control system is modeled in CAMRAD differs, therefore, from that in the RAE/WHL analysis. The relation between the blade moment and the pitch-link load is the same in the CAMRAD/JA predictions giving the better correlation with the test data although the peak-to-peak blade moment is overestimated while the peak-to-peak pitch-link load is underestimated.

The similarity in the pitch-link load and the torsion moment at the root in the test data means that the control system load need not be considered for the other flight cases.

The comparisons between theory and experiment presented in this section show how the analyses performed in low speed flight conditions. All the analyses have some strengths and weaknesses and

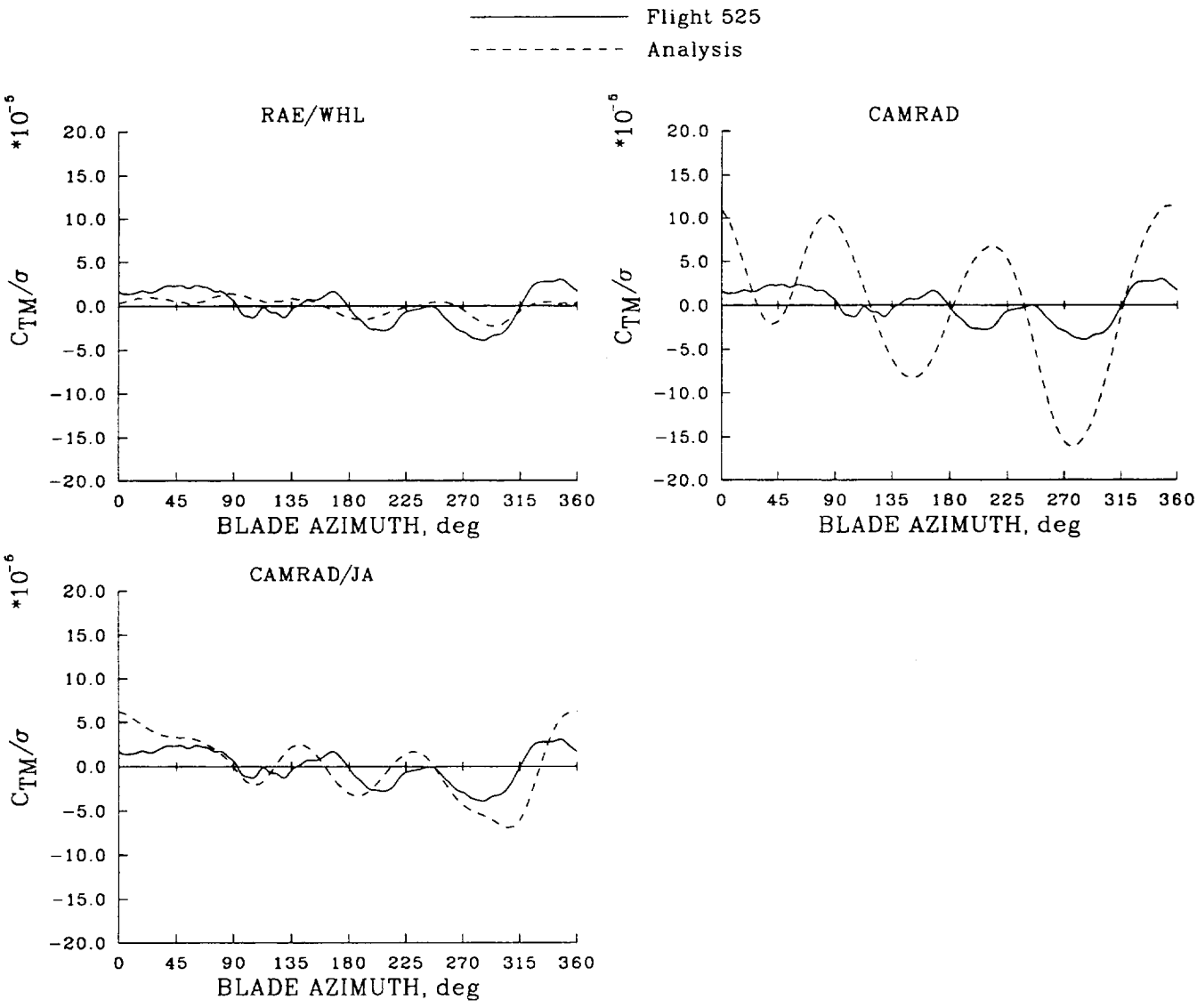


Figure 122. Comparison of measured and calculated torsion moment as a function of azimuth at $0.126R$; $\mu = 0.098$, Flight 525, 1–36 harmonics.

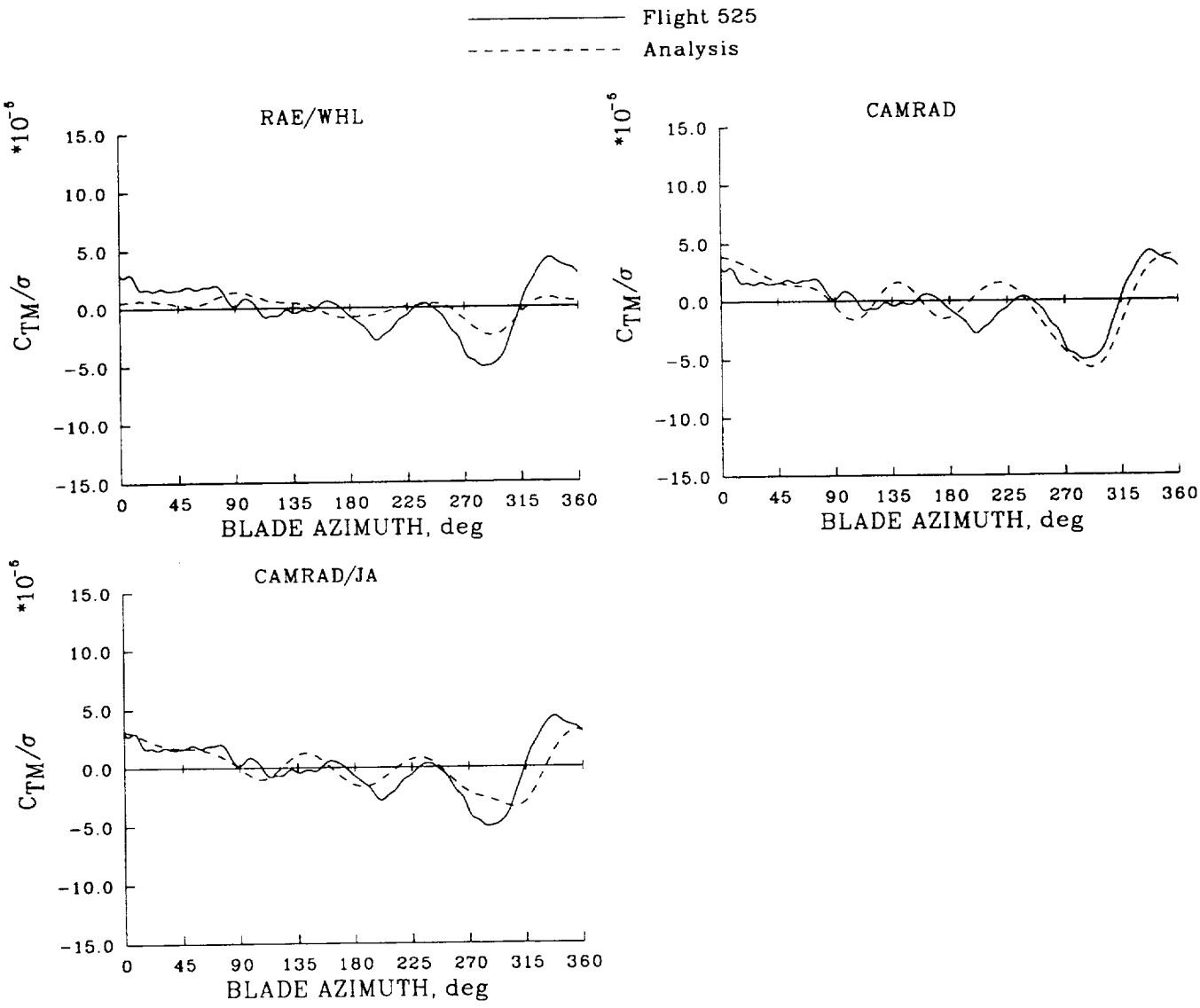


Figure 123. Comparison of measured and calculated torsion moment as a function of azimuth at $0.55R$; $\mu = 0.098$, Flight 525, 1–36 harmonics.

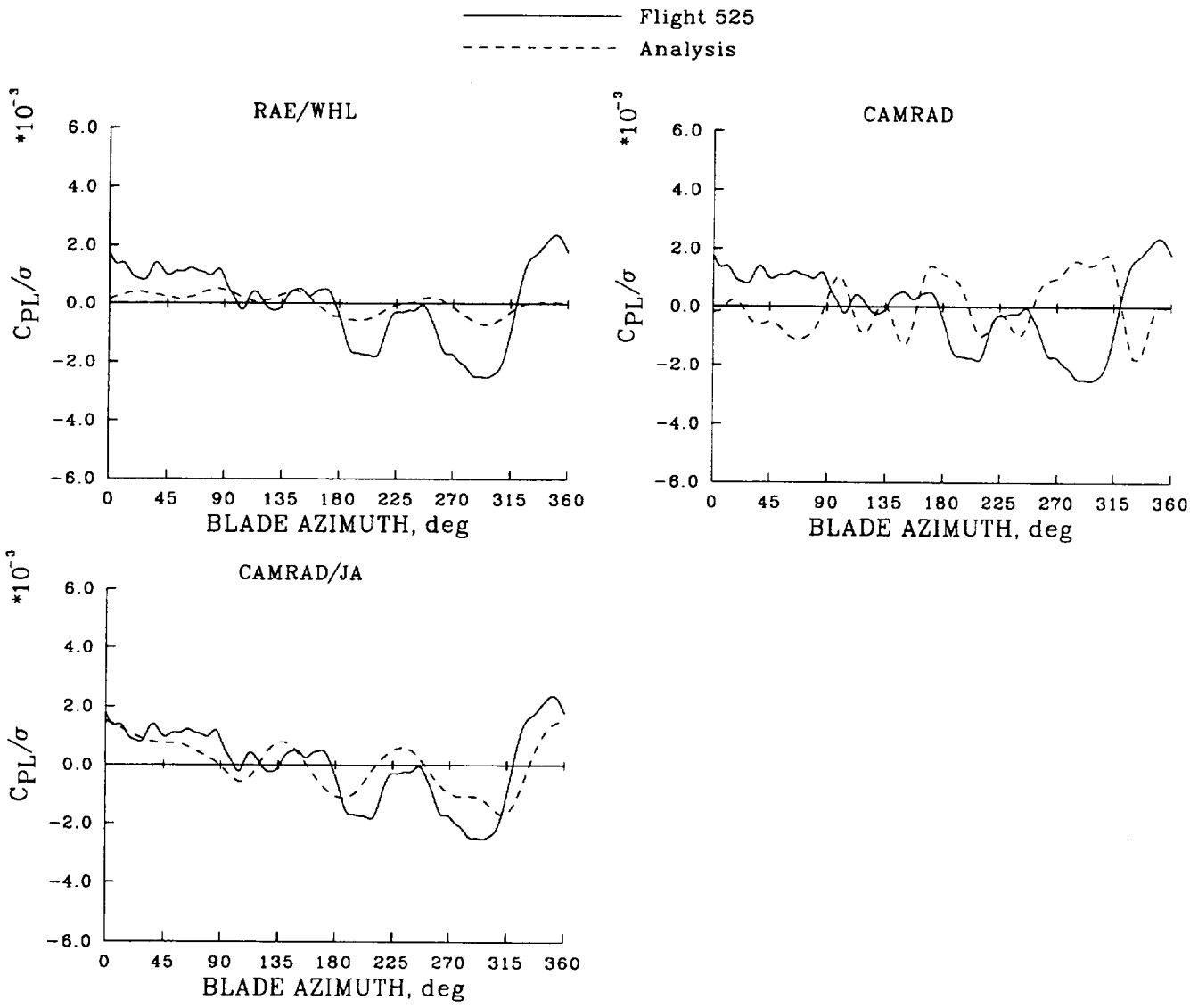


Figure 124. Comparison of measured and calculated pitch-link load as a function of azimuth; $\mu = 0.098$, Flight 525.

it is not possible to say that one analysis was consistently better than all the others for all the stress components.

*Moments and Loads, Advance Ratio = 0.182*

The second flight test case considered has an advance ratio of 0.182 and the measured normal force coefficients presented in figure 100 of Section 5.2.2.2 show evidence of two strong vortex interactions, although these are reduced in strength relative to the low advance ratio case. The modeling of the rotor wake remains a major factor therefore in the analytical methods.

The measured and calculated flap bending moment is compared at $0.20R$ and $0.67R$ in figures 125 and 126 respectively. The test data at both radial stations are dominated by the 3/rev oscillation as at the lower advance ratio. The RAE/WHL analysis, at $0.20R$, predicts the magnitude of the predominant harmonic well but there are also contributions at the sixth, ninth, and tenth harmonics arising from the third and fourth flap modes which have calculated frequencies of 5.8 and 9.7/rev. The test data have a measurable component at 5/rev but the contributions at the higher harmonics are small. CAMRAD and CAMRAD/JA correlate better with the test data than the RAE/WHL analysis but the peak at the front of the disk is underestimated.

The test data at $0.67R$, figure 126, show that the peak on the retreating side of the disk increases in magnitude compared to the inboard station. The waveform shows also a reduced amount of higher harmonic content and the nature of the peaks on the advancing side of the disk changes character. The RAE/WHL analysis retains the high frequency content that is seen at $0.20R$ but the magnitude of the lower order harmonics is underestimated. The overall level of correlation is reasonable, however, although the peak in the first quadrant and that on the retreating side of the disk occur later in the azimuth cycle. CAMRAD and CAMRAD/JA do not do as well as the RAE/WHL analysis on the advancing side of the disk but the position of the peak on the retreating side is positioned more accurately by CAMRAD/JA.

None of the calculation methods predict the chord bending moment at $0.55R$ accurately, as shown in figure 127. The peak-to-peak moment is adequately estimated by the RAE/WHL method but shows a dominant fifth harmonic contribution instead of the fourth harmonic response seen in the data. The CAMRAD and CAMRAD/JA calculations, on the other hand, show a large third harmonic component rather than the fourth harmonic, much as was seen at $\mu = 0.098$.

The correlation between the calculated torsion moment at $0.33R$ and the test data is only fair, figure 128, reflecting the poor prediction of the aerodynamic pitching moment. The RAE/WHL analysis underpredicts the magnitude of the oscillation and, as for the flap bending moment, has a higher harmonic content that is not observed in the measurements. The peak-to-peak level is calculated better by CAMRAD but only the lower order harmonics are present and overall CAMRAD/JA provides the most successful prediction of torsion moment.

Generally the analyses calculated the flap bending moment more accurately than at the lower advance ratio but there is no significant improvement in the prediction of the chord bending moment or torsion moment at the higher speed.

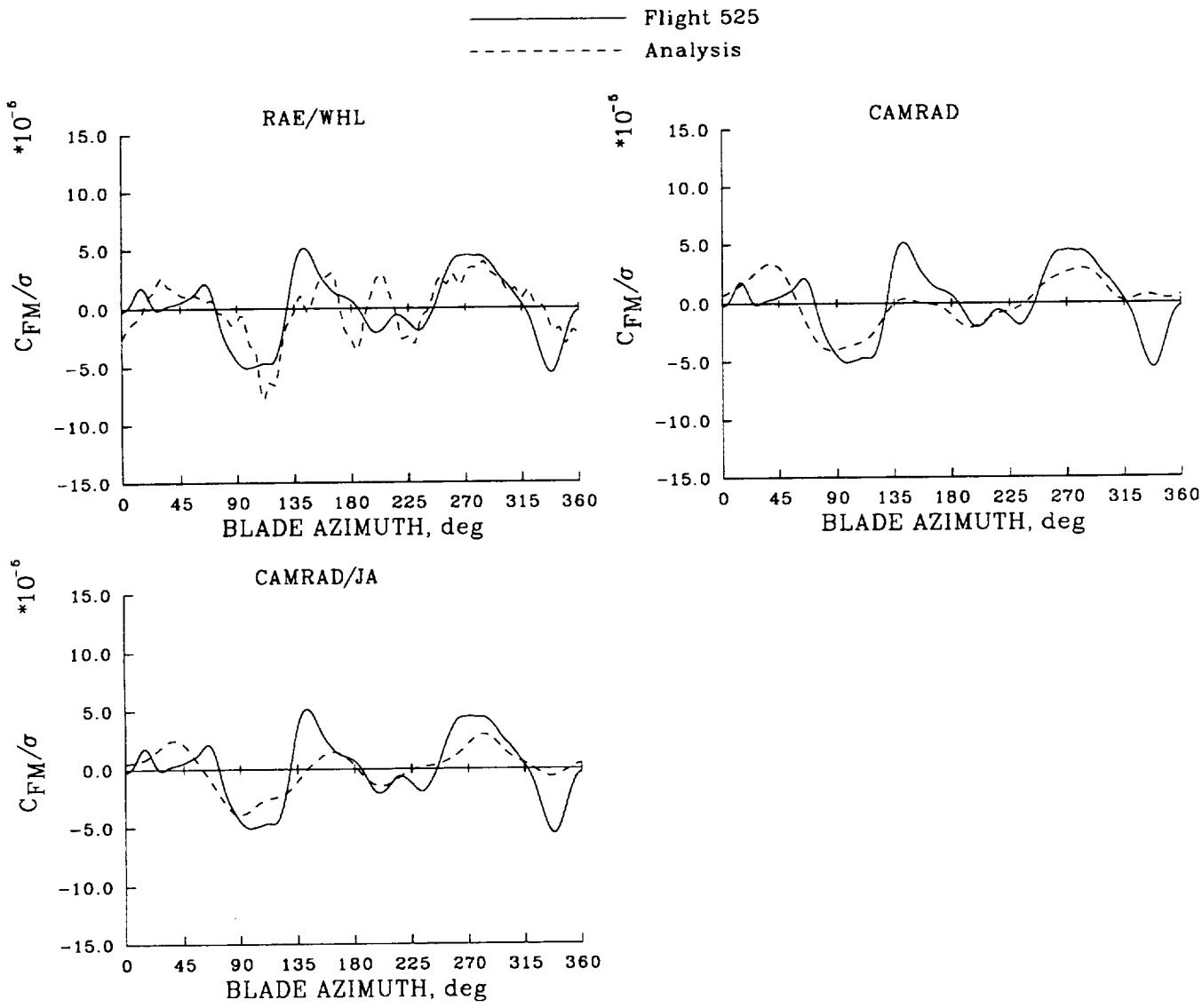


Figure 125. Comparison of measured and calculated flap bending moment as a function of azimuth at $0.20R$; $\mu = 0.182$, Flight 525.

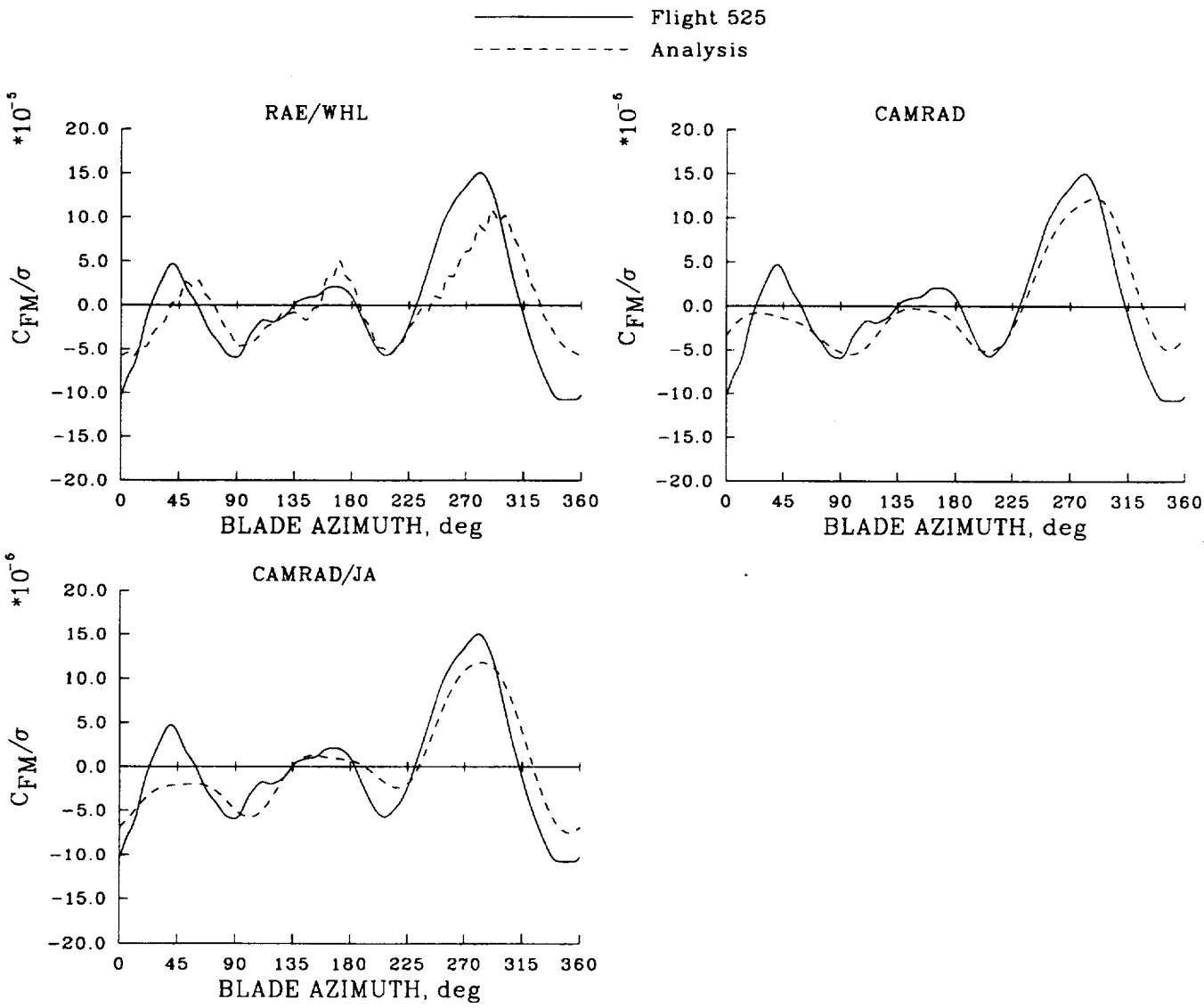


Figure 126. Comparison of measured and calculated flap bending moment as a function of azimuth at $0.67R$; $\mu = 0.182$, Flight 525.

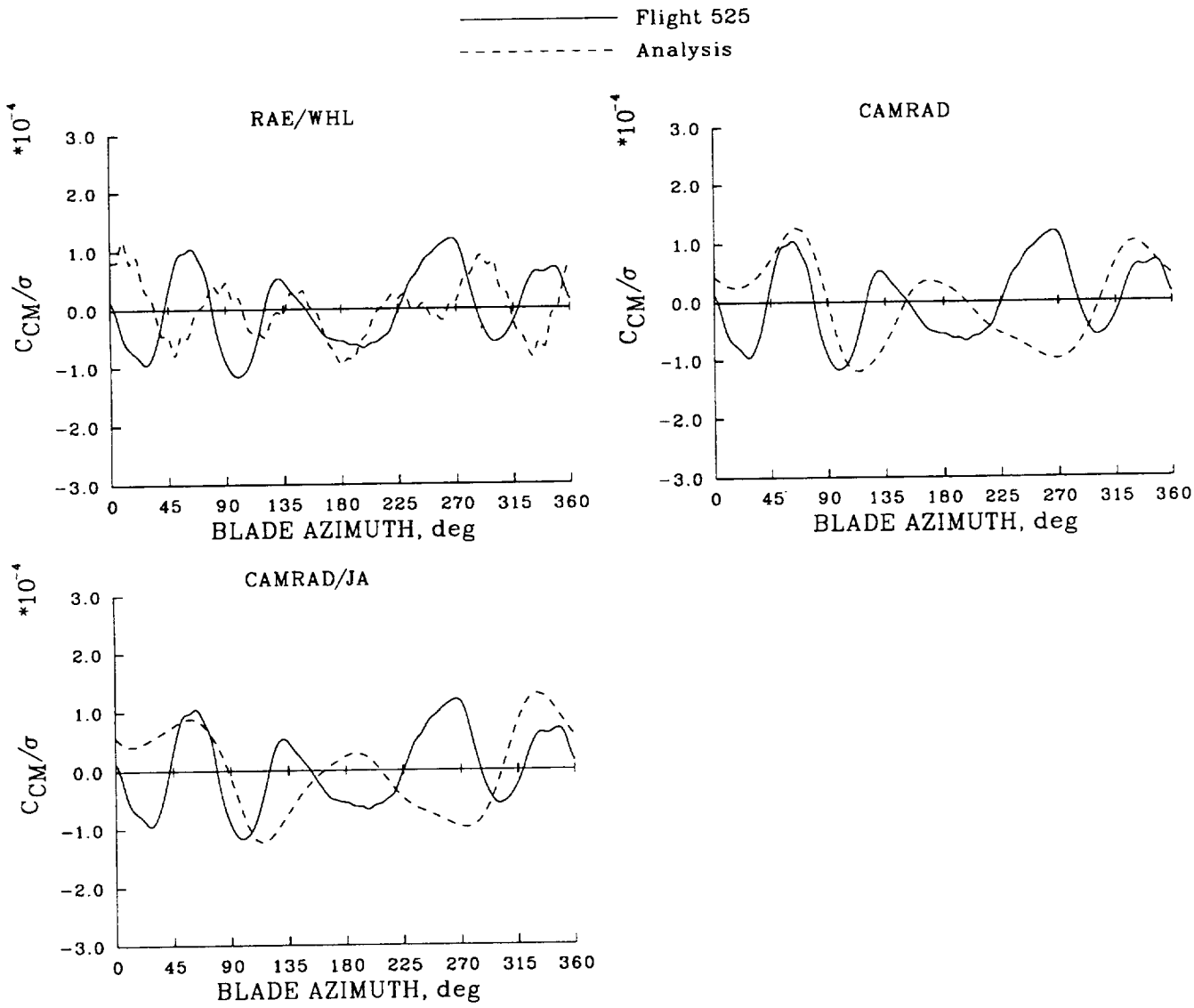


Figure 127. Comparison of measured and calculated chord bending moment as a function of azimuth at $0.55R$; $\mu = 0.182$, Flight 525.

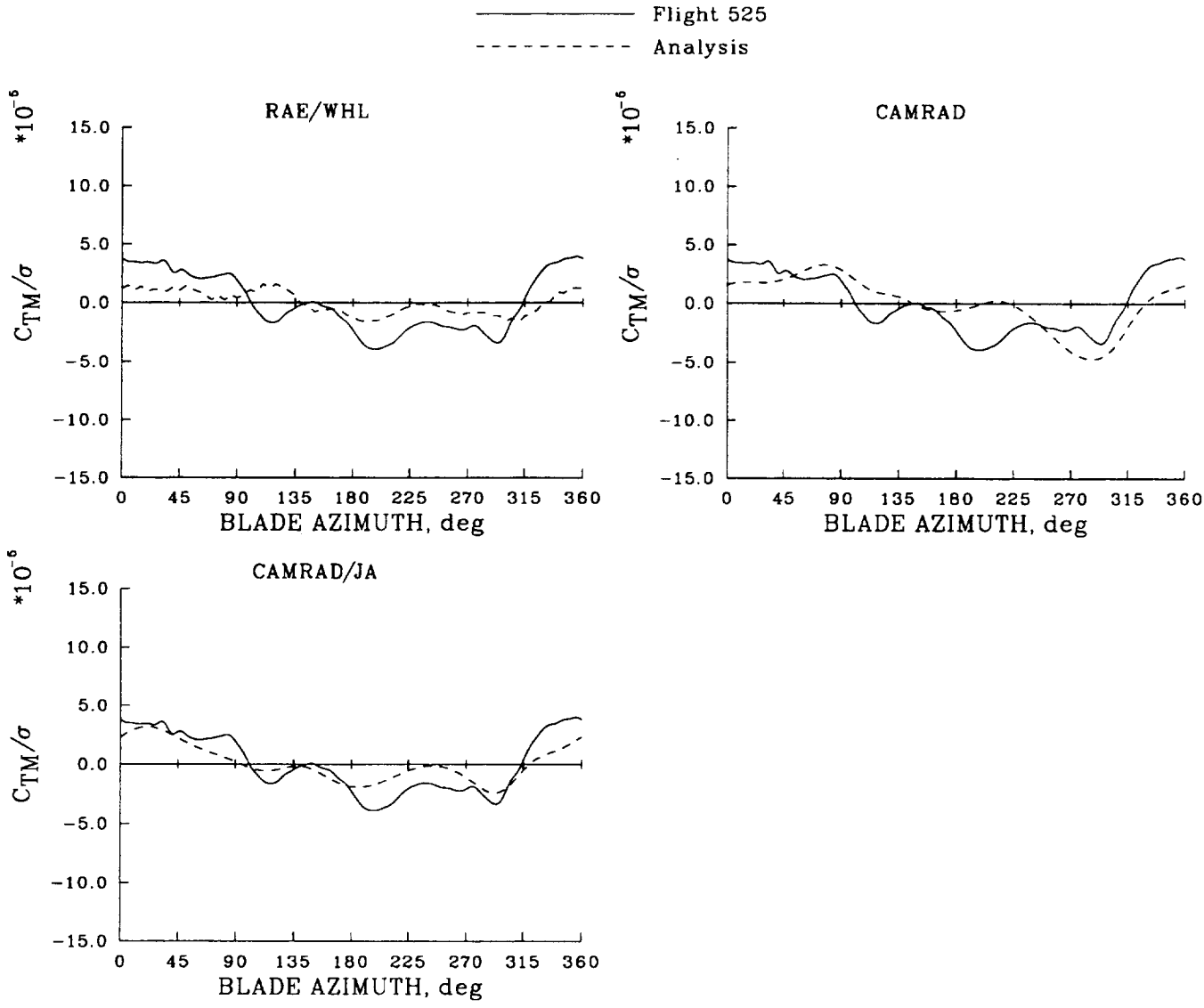


Figure 128. Comparison of measured and calculated torsion moment as a function of azimuth at $0.33R$; $\mu = 0.182$, Flight 525.

*Moments and Loads, Advance Ratio = 0.307*

The measured and calculated blade moments at an advance ratio of 0.307 are presented as three-dimensional surface plots showing the moment distribution over the complete span of the blade as a function of the azimuth angle. The surface plots give a more qualitative comparison between the test data and the calculations compared to the azimuthal variation at a single radial position used at the two lower advance ratios. Moreover, some features can be seen better in the surface plots because they provide a complete picture of the conditions on the rotor.

The measured and calculated radial distribution of the flap bending moment at an advance ratio of 0.307 is shown in figure 129. The predominant 3/rev oscillation is as clearly seen in the surface plot of the test data as it is at an individual azimuthal plot at one radial station. The magnitude of the 3/rev component at $0.67R$, for example, is slightly lower at this higher advance ratio, 333 N-m, compared with 374 N-m in obtained for the case at $\mu = 0.182$, figure 126, but there is a phase shift of 40°. The effect of the change in the phase is most readily seen around the front of the disk where the peak is more sharply defined.

The RAE/WHL analysis predicts the observed phase change with the result that the correlation with the test data is improved greatly around the front of the disk. The use of the free wake in the CAMRAD analyses has little effect above an advance ratio of 0.2 and both calculations are made with the prescribed wake model. The phase change is correctly predicted by CAMRAD and CAMRAD/JA but the magnitude of the 3/rev contribution remains too low at about 200 N-m.

The correlation of the measured and calculated flap bending moments therefore is improved at an advance ratio of 0.307 compared to the two lower advance ratios with the RAE/WHL analysis but both CAMRAD methods show poorer agreement with experiment because of an underprediction of the magnitude of the dominant harmonic component.

The surface plots of the measured and calculated chord bending moments are shown in figure 130. None of the analyses correlate well with the test data. The amplitude of the oscillation is underpredicted by the RAE/WHL analysis while CAMRAD and CAMRAD/JA have a dominant 3/rev variation instead of 4/rev seen in the measurements.

The RAE/WHL analysis underestimates the torsion moment over the complete blade span, figure 131, and CAMRAD/JA does little better except close to the blade root. CAMRAD predicts a much larger moment than CAMRAD/JA but the shape of the waveform is incorrect especially near the blade root.

The trends in the performance of the analyses at an advance ratio of 0.307 are similar to those at the lower speeds. The flap bending moment tends to be better predicted as speed increases using the RAE/WHL analysis. The CAMRAD analyses continue to show good qualitative agreement in the flap bending moment behavior but the predicted amplitudes are lower than the measurements. None of the analyses show any improvement in calculating the chord bending or torsional moment.

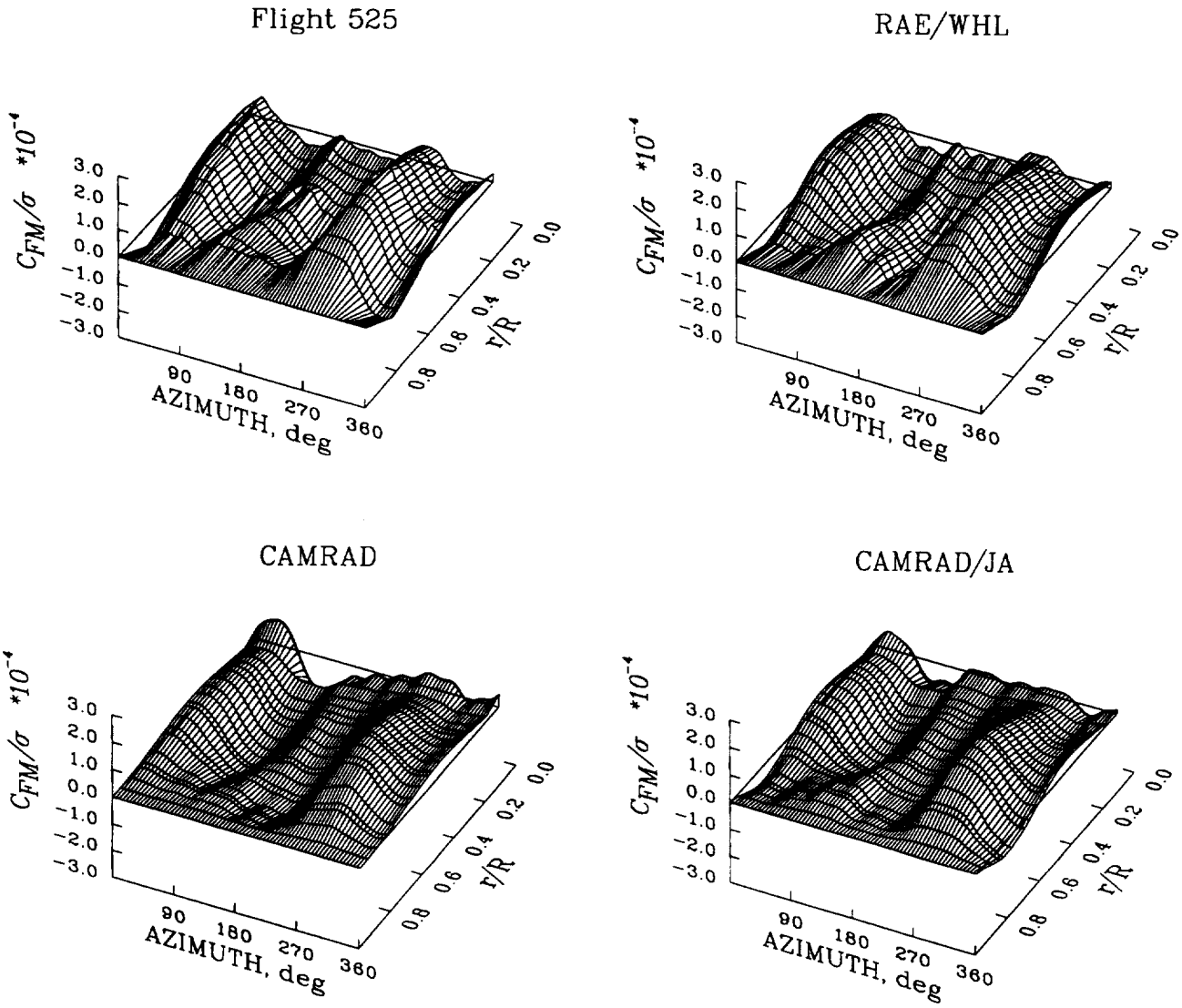


Figure 129. Comparison of measured and calculated flap bending moment as a function of azimuth and blade radius; $\mu = 0.307$, Flight 525.

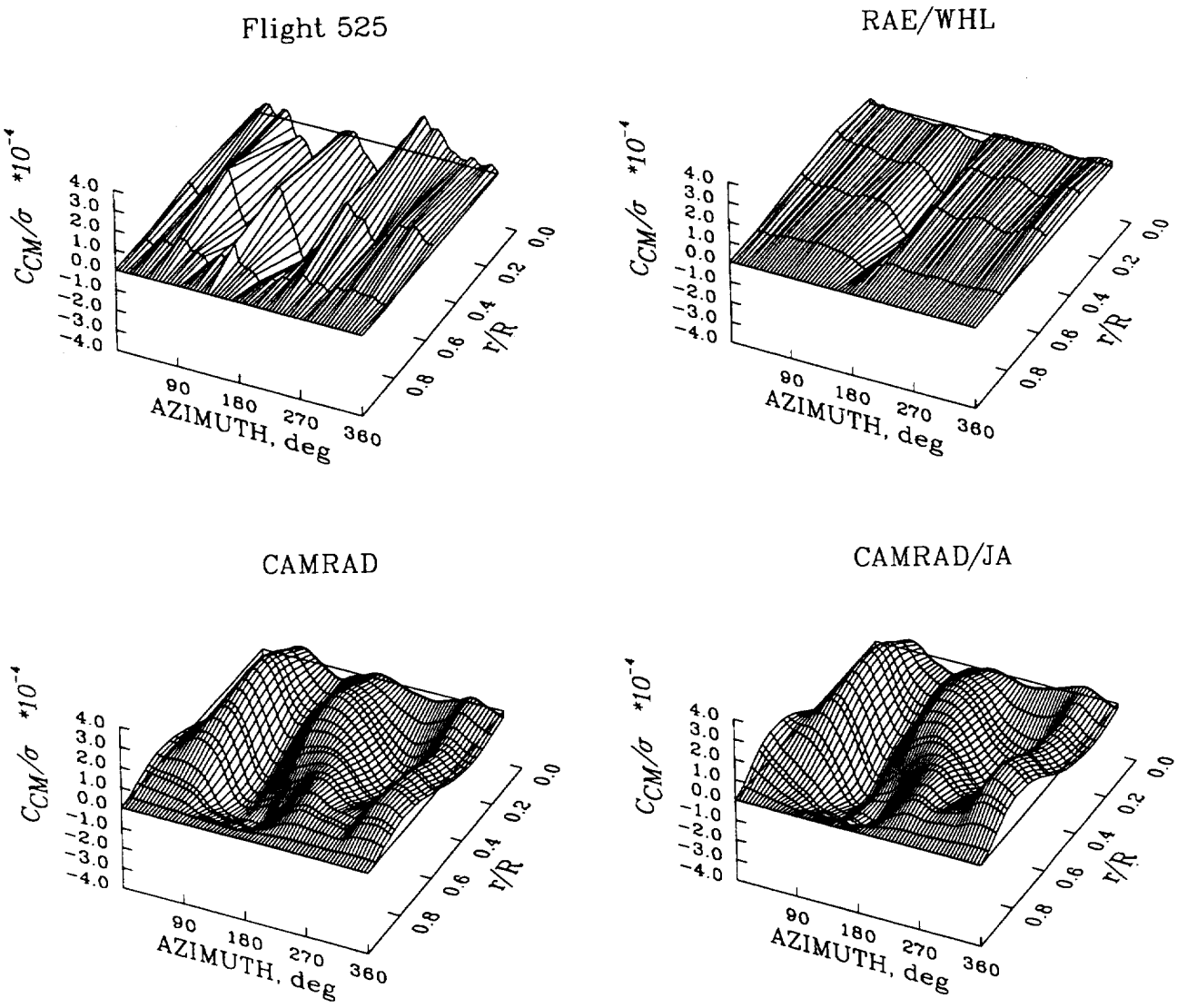


Figure 130. Comparison of measured and calculated chord bending moment as a function of azimuth and blade radius; $\mu = 0.307$, Flight 525.

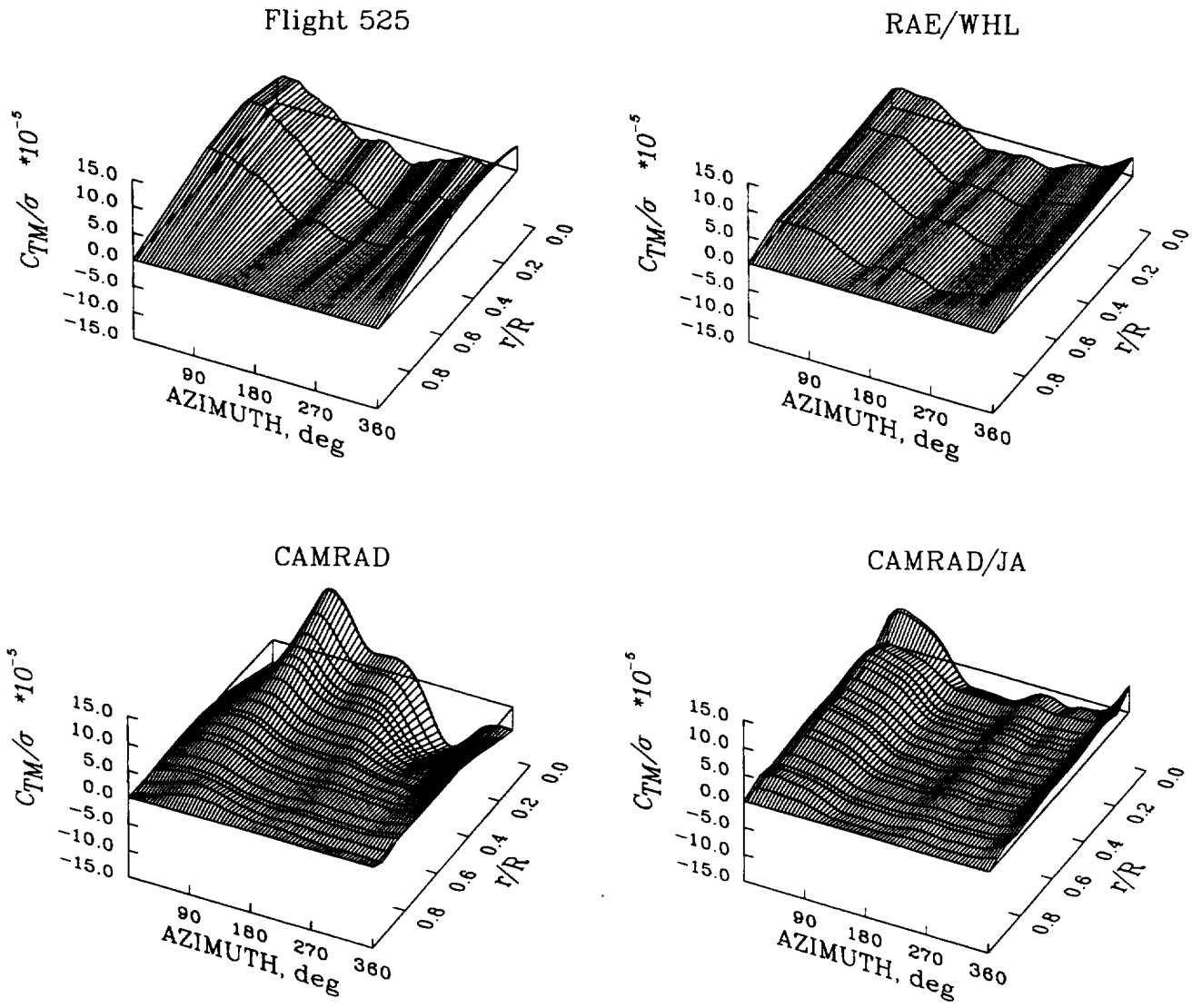


Figure 131. Comparison of measured and calculated torsion moment as a function of azimuth and blade radius; $\mu = 0.307$, Flight 525.

*Moments and Loads, Advance Ratio = 0.362*

Surface plots are used to compare the test data with the measurements at an advance ratio of 0.362 as in the previous section at the lower speed. Calculations are available for this case for the Aérospatiale R85 analysis with the METAR prescribed wake model.

The calculated flap bending moment over the blade span is compared with the test data in figure 132. The RAE/WHL analysis generally correlates well with the test data even at the most inboard positions although there is some doubt about the accuracy of the measurement at $0.20R$ for the advance ratio under consideration. CAMRAD and CAMRAD/JA predict similar bending moments except close to the blade root but the level of correlation with the measurements is not as good as the RAE/WHL prediction because of the underestimate of the 3/rev oscillation. The METAR/R85 analysis shows a 6/rev oscillation at the blade root which decreases in magnitude as the mid-span is approached to be replaced by a predominantly 3/rev oscillation towards the tip and the level of agreement with the test data is poor.

The measured and calculated chord bending moments are shown in figure 133. The trends apparent at the lower forward speeds are still present in that the RAE/WHL analysis fails to predict the magnitude of the oscillation, while CAMRAD and CAMRAD/JA have a large 3/rev component instead of the large 4/rev component visible in the test data. The METAR/R85 analysis uses force integration to calculate the chord bending moment and is perhaps the most successful of the analyses but the moment in the mid-span of the blade is underestimated and there is a significant 6/rev contribution.

The ability of the analyses to predict the torsion moment along the blade does not improve as the advance ratio increases and the comparisons with the test data made in figure 134 generally show a very poor level of correlation.

*Moments and Loads, Advance Ratio = 0.402*

The highest advance ratio in level flight at which comparisons are made of the measured and calculated blade moment is 0.402, but the Mach number at the tip of the advancing blade is only 0.826 because of the reduced rotor speed of the aircraft.

The measured and calculated oscillatory flap bending moments for this case are shown in figure 135. The trends observed at the lower advance ratios continue with the increasing 3/rev contribution well represented in the RAE/WHL calculation. CAMRAD/JA shows better agreement with the test data than CAMRAD especially towards the tip of the blade. The METAR/R85 calculation compares poorly with the test data with almost a complete absence of the dominant vibratory harmonic components.

None of the analyses predict the chord bending moment to any degree of accuracy as is seen in figure 136. The METAR/R85 calculation shows a 5/rev oscillation while CAMRAD and CAMRAD/JA retain the strong 3/rev oscillation seen at the lower advance ratios although a 4/rev contribution is visible. The RAE/WHL analysis displays the 5/rev component that is present throughout the range of speeds.

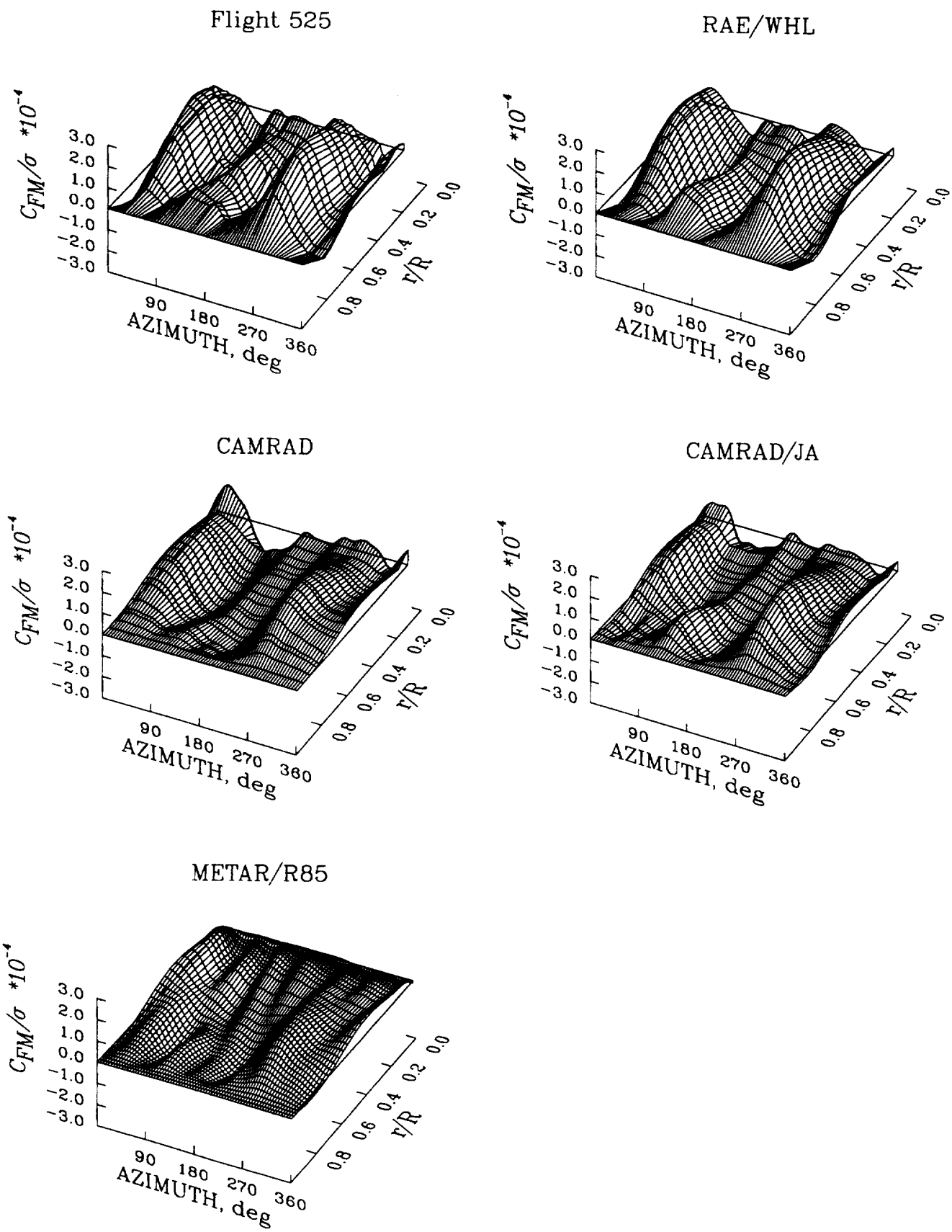


Figure 132. Comparison of measured and calculated flap bending moment as a function of azimuth and blade radius; $\mu = 0.362$, Flight 525.

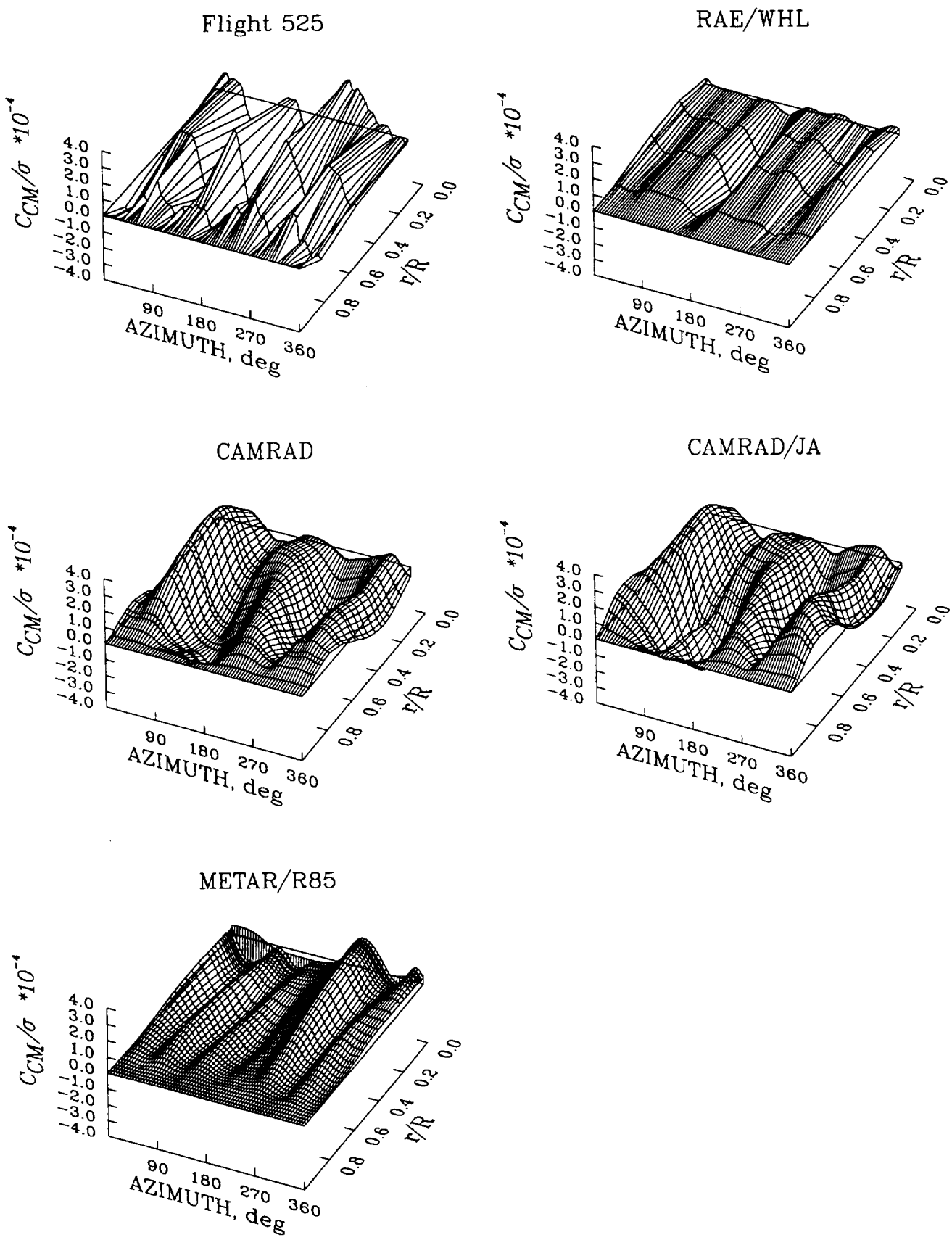


Figure 133. Comparison of measured and calculated chord bending moment as a function of azimuth and blade radius; $\mu = 0.362$, Flight 525.

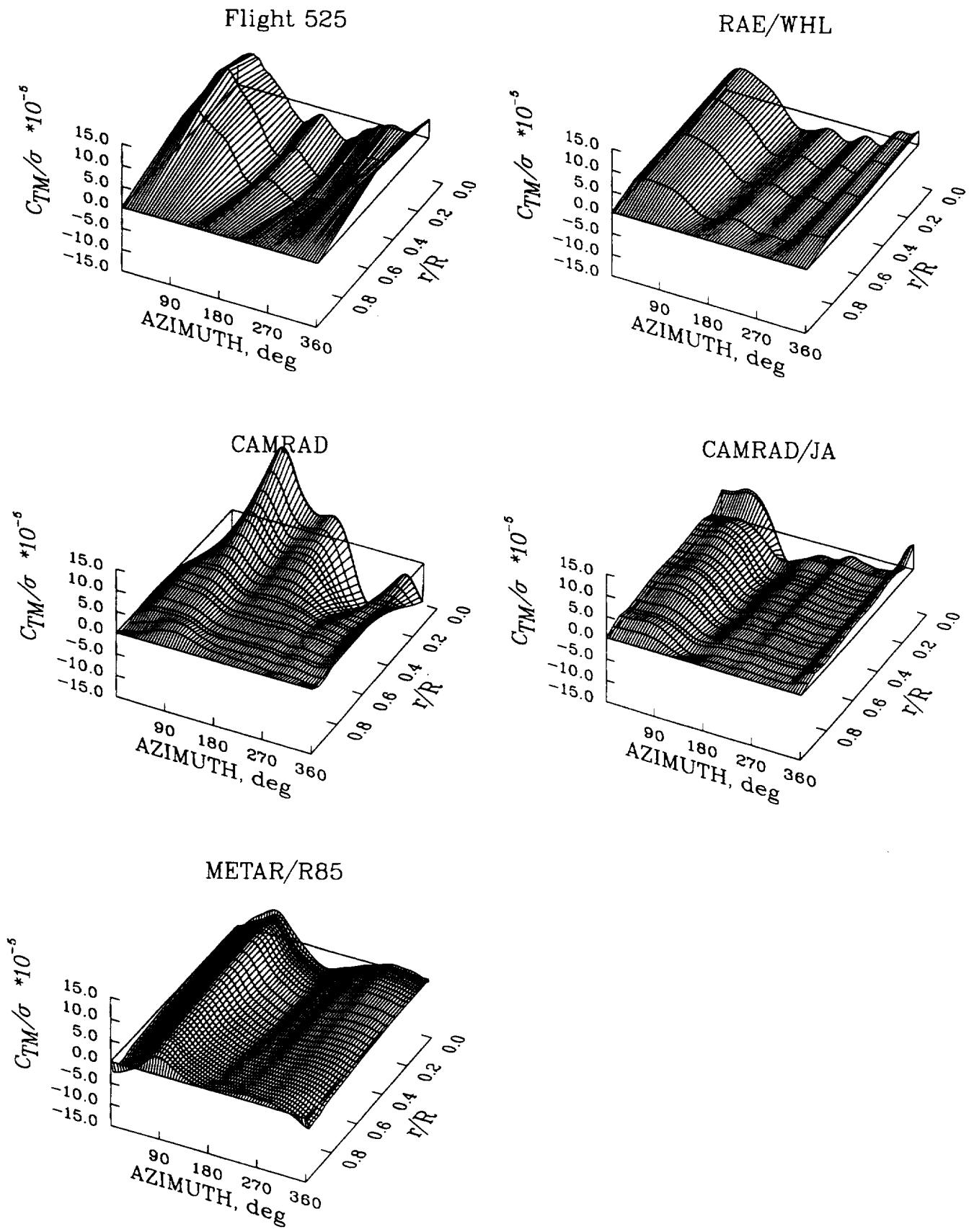


Figure 134. Comparison of measured and calculated torsion moment as a function of azimuth and blade radius; $\mu = 0.362$, Flight 525.

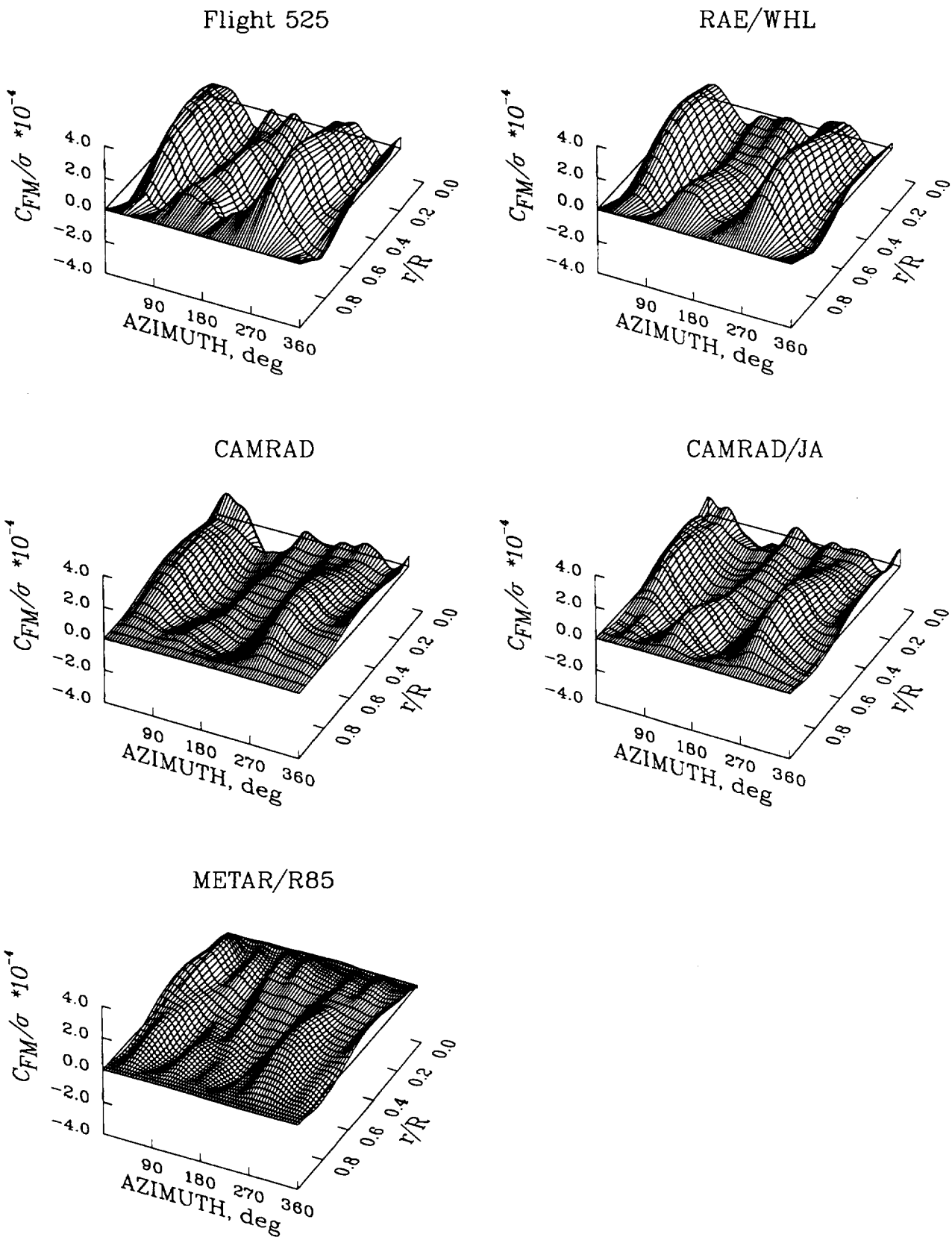


Figure 135. Comparison of measured and calculated flap bending moment as a function of azimuth and blade radius; $\mu = 0.402$, Flight 525.

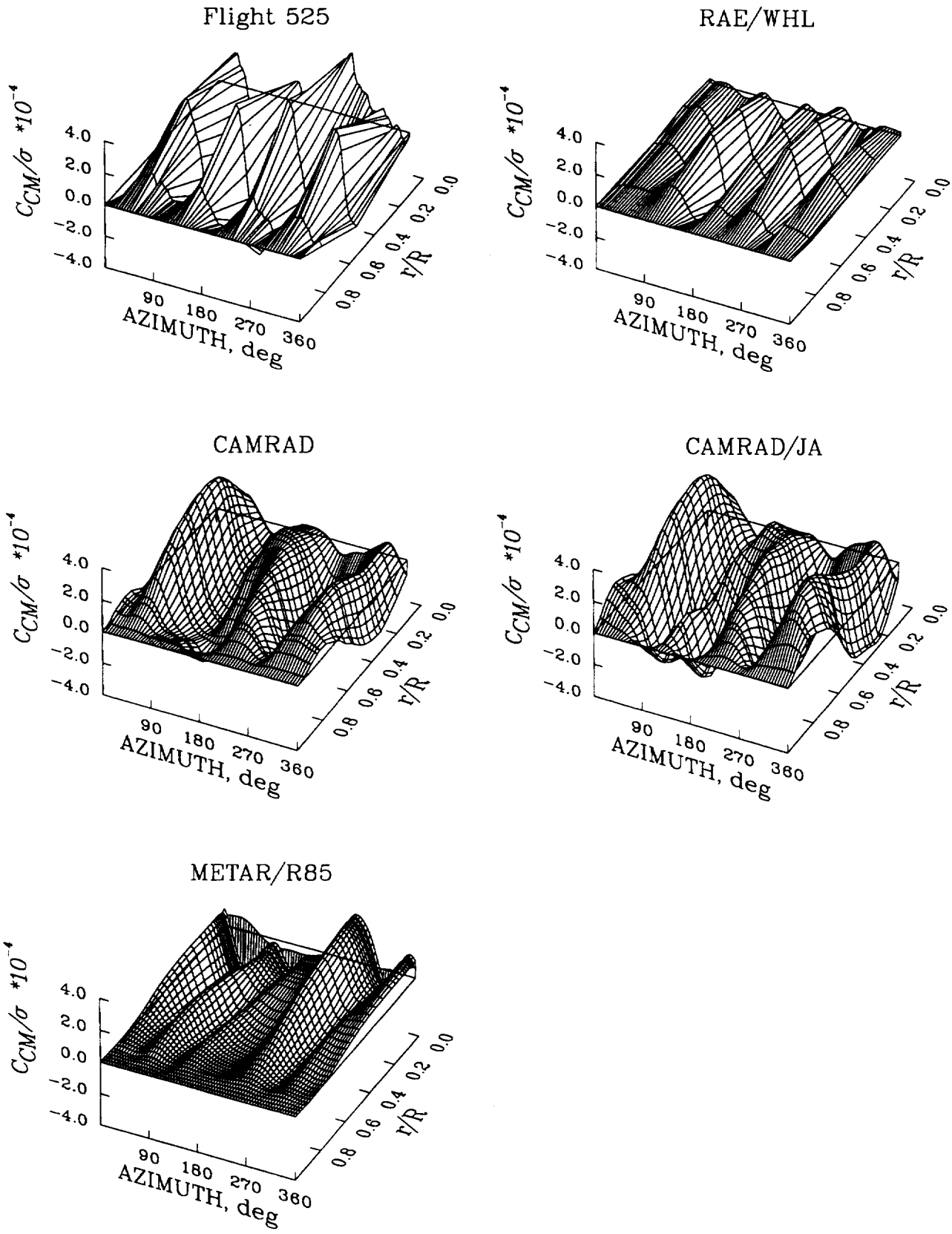


Figure 136. Comparison of measured and calculated chord bending moment as a function of azimuth and blade radius; $\mu = 0.402$, Flight 525.

The prediction of the torsion moment also leaves much to be desired. The CAMRAD and CAMRAD/JA calculations show large differences between each other and with the test data in figure 137. The RAE/WHL analysis underestimates the peak value in the first quadrant and the behavior around the retreating side of the disk differs from the measurements. The METAR/R85 calculation shows a peak on the advancing side of the disk at a greater azimuth angle than the test data but the magnitude of the moment is almost invariant with the radial position. The variation around the rest of the disk does not correlate well with the measurements.

The highest speed flight test case, therefore, confirms the trends that have become apparent as the advance ratio is increased. The flap bending moment is the most successfully predicted of the three moments with the RAE/WHL analysis showing good agreement with the test data. CAMRAD and CAMRAD/JA give acceptable levels of correlation with the flap bending moment but there is an apparent problem with the METAR/R85 method. None of the theories are very good at predicting the chord bending or torsional moments for the Puma rotor and further work is needed to improve the predictive capabilities of the analyses.

5.2.2.4 *Vibratory Loads*

Calculations of the vibratory fixed-system loads at the hub were made by all of the analyses. However, for METAR/R85, these computations were made only at the two highest advance ratios. No direct measurements of hub vibratory loads were obtained on the research Puma. However, blade flap bending moments and blade flapping were used to identify the uncoupled modal flap response of the rotor and these values were used to estimate the vibratory vertical shears and hub moments. No attempt was made to use the chord bending measurements in an equivalent approach to estimate the inplane shears.

The calculated 4/rev X-forces are compared in figure 138. A positive X-force is forward, towards the nose of the aircraft. Generally good agreement is seen between the four analyses; however, the RAE/WHL analysis shows a negative sine component at higher speeds, unlike the other analyses. The X-force amplitude calculated by METAR/R85 is lower than the other analyses and this is thought to be a result of lower response in the flap modes at 3/rev as observed in Section 5.2.2.3.

The lateral or Y-force analytical comparisons are shown in figure 139. A positive force is to the right of the aircraft. The agreement between the analyses is not as good for the cosine component of the Y-force as for the X-force, but is better for the sine component. The METAR/R85 analysis, for the two airspeed calculations made, again shows a reduced 4/rev amplitude.

The calculated 4/rev vertical shears are shown in figure 140 and are compared with estimates of the 4/rev shears based on modal fitting of the flap angle and flap bending moment measurements. The measured 4/rev vertical shear exhibits a large amplitude in the transition region (advance ratio less than 0.15), a large amplitude at high speed (advance ratio greater than 0.35), and a wide region of relatively smooth operation between the two regimes. In the low-speed regime each of the analyses shows a trend of increasing 4/rev shear as the advance ratio is reduced to 0.1 and the prediction of phase is reasonable as well. However, there is a factor of 3 difference between the analytical predictions and only the CAMRAD analysis shows good agreement with the derived values.

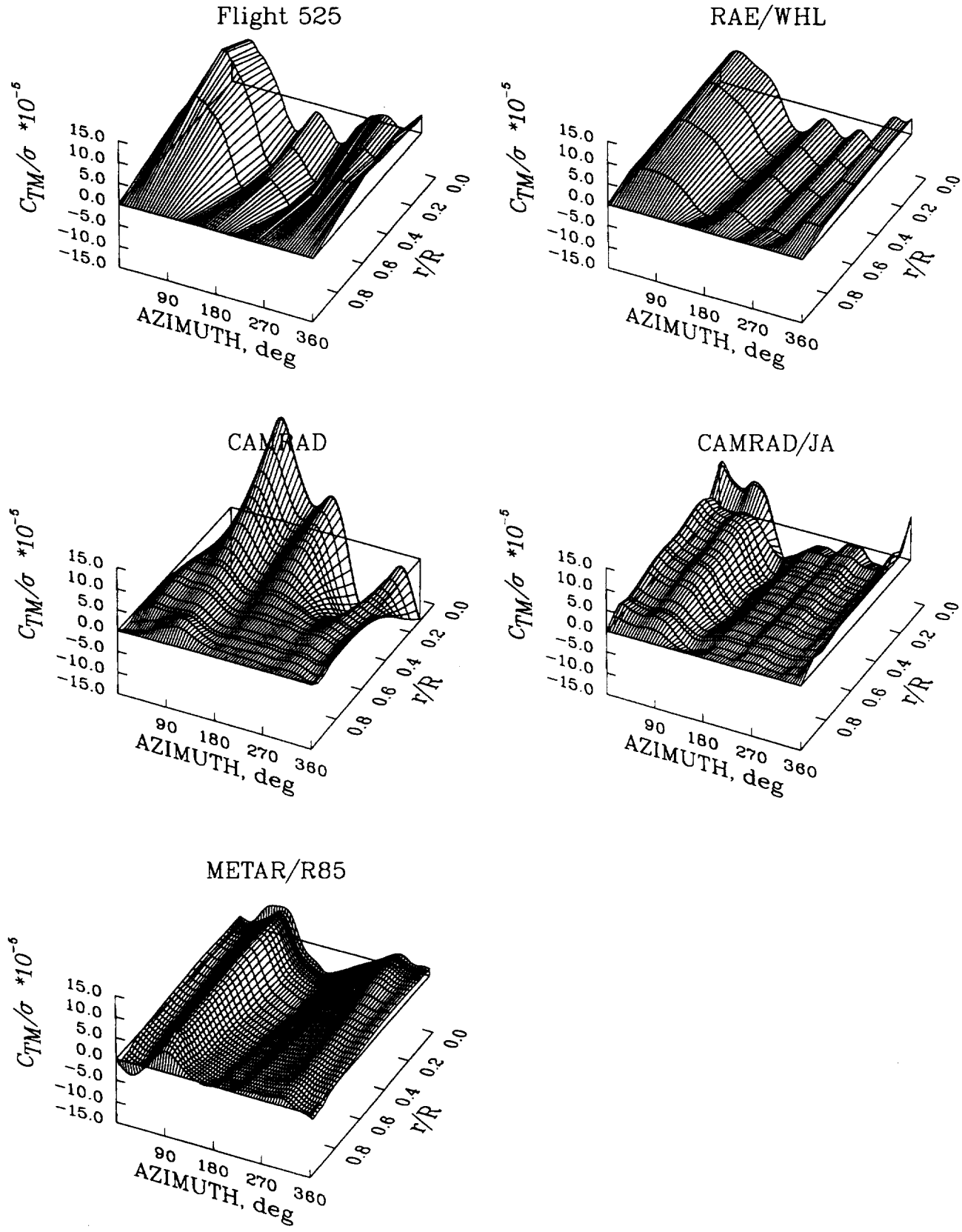


Figure 137. Comparison of measured and calculated torsion moment as a function of azimuth and blade radius; $\mu = 0.402$, Flight 525.

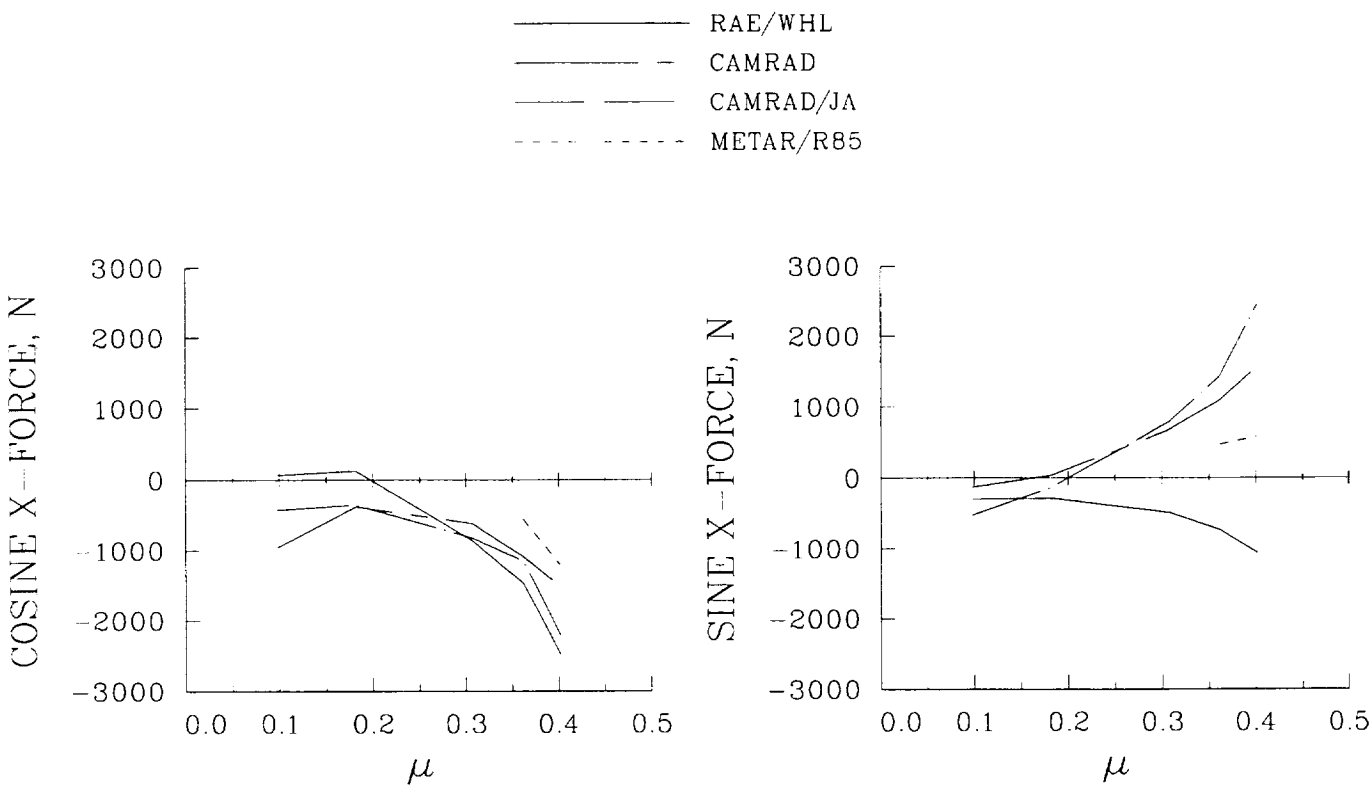


Figure 138. Comparison of calculated hub 4/rev X-force as a function of advance ratio for Flight 525.

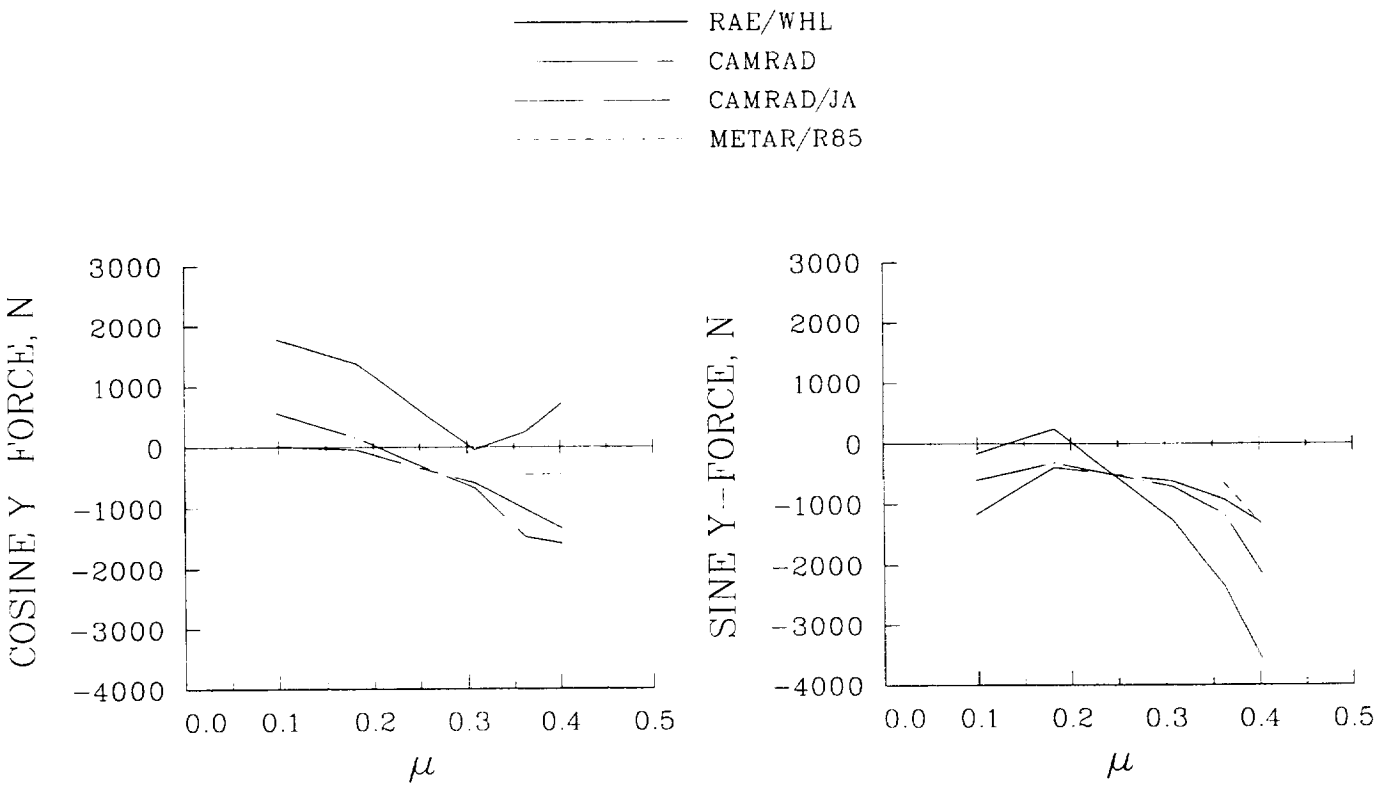


Figure 139. Comparison of calculated hub 4/rev Y-force as a function of advance ratio for Flight 525.

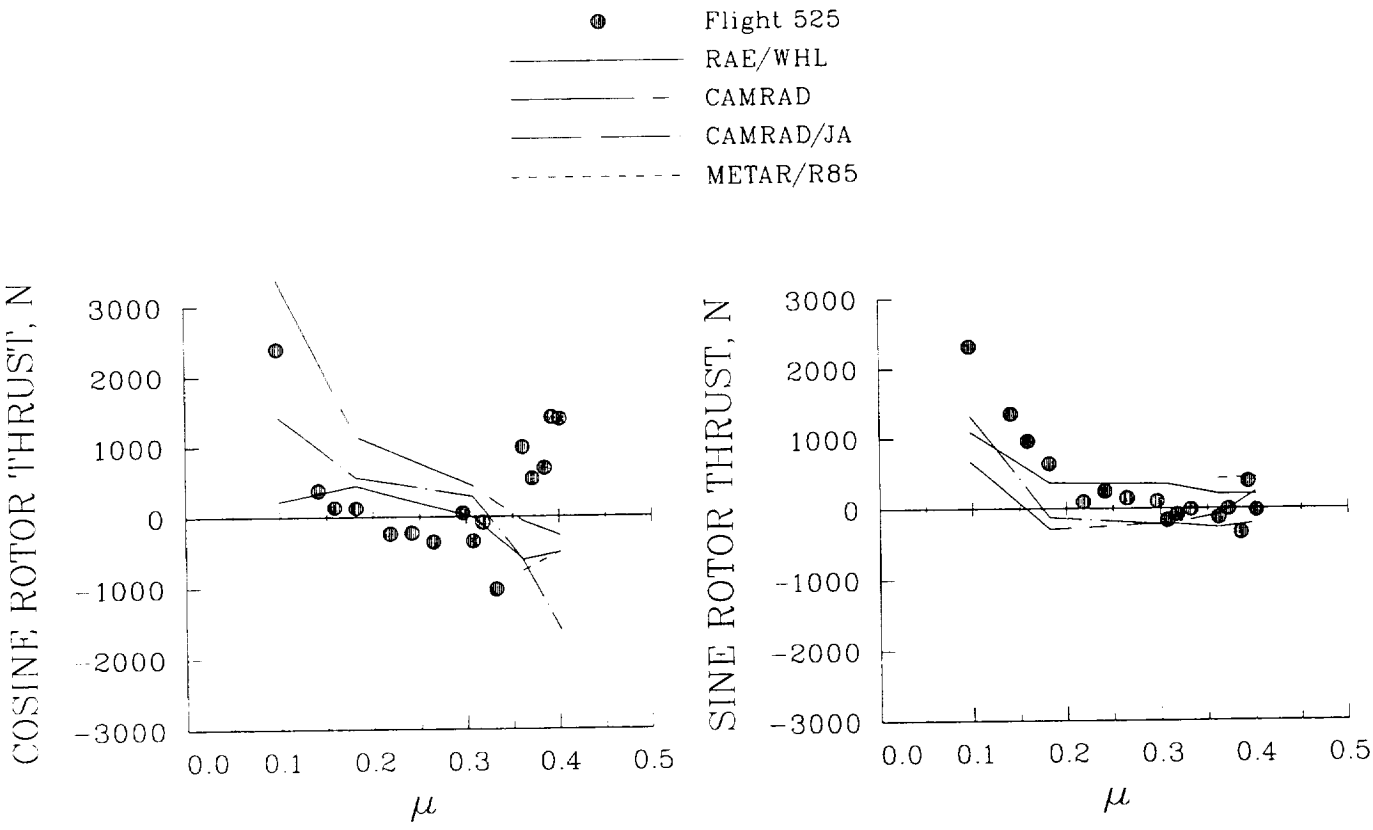


Figure 140. Comparison of calculated hub 4/rev vertical shears and values derived from blade measurements as a function of advance ratio for Flight 525.

The transition regime vibratory loading is a consequence of the rapid variation in the airloads near the blade tip on the advancing and retreating sides, as was discussed in Section 5.2.2.2. At high speed, however, the vibratory loading is largely a consequence of aircraft trim, as was discussed in Section 4. Except for CAMRAD/JA, the analyses predict a small or relatively constant 4/rev vertical shear at high speed and this is contrary to the data that show a substantial increase in the shear (cosine component). The increase predicted by CAMRAD/JA, although similar in size to the measurements, is opposite in phase.

The 4/rev vertical shears shown in figure 140 that were derived from flight test data were obtained by fitting nine flapping modes, calculated in a vacuum, to the measured flap angle and flap bending moments (Bousman, 1987). The fitting process is based on a least squares approach (Gaukroger and Hassal, 1978), with the flap angle fit obtained in an iterative fashion. Once the modal amplitudes are identified the solution of the entire state vector is obtained and the 3, 4, and 5/rev vertical shears at the hinge point may be used to compute the hub 4/rev vertical shear, pitch moment, and roll moment. The same process may be used, as in Section 5.2.2.1, for the 1/rev pitch and roll moment as well. An example of the bending moment fit for the first five harmonics of data at $\mu = 0.402$ is shown in figure 141. Because the modal fit used here is only for the flap degree of freedom, radial and inplane shears at the hub are not obtained.

The calculations for the 4/rev hub roll moment are compared with values derived from flight test data in figure 142 and the 4/rev pitch moment calculations and derived values are compared in figure 143. The 4/rev hub moments are primarily a result of the 3/rev flap bending moments and the comparisons in these figures are analogous to comparisons that were shown in Section 5.2.2.3. In the low-speed or transition regime, CAMRAD and CAMRAD/JA, which include a free wake in the model, show better agreement in amplitude, although not in phase angle. Over the mid-range of advance ratios, where the vibratory moments are less, all of the analyses show good agreement with the flight test derived values. At high speed, however, neither the CAMRAD analyses nor METAR/R85 shows a satisfactory calculation of the moment amplitudes, while the RAE/WHL analysis does provide a good estimate of both the amplitude and phase.

The calculations of the 4/rev component of shaft torque are compared in figure 144. At low speed the CAMRAD analyses show a higher 4/rev level than the RAE/WHL analysis for the cosine component, but at higher speeds there is better agreement between these calculations. The METAR/R85 computation at the two highest advance ratios, however, shows a much greater 4/rev vibration. Considering the poor calculation of the chord bending moments that has been shown by all of the analyses, good agreement in the vibratory shaft torque is too much to expect.

The comparisons of calculated hub vibratory loads and values derived from flight test in figures 140, 142, and 143 presume that the fuselage impedance is represented identically for the calculation and the vibratory load estimate. In fact, the calculations were obtained for an isolated rotor with an infinite hub impedance while the derived values, although based on isolated rotor vacuum modes, will include any effects of fuselage or hub flexibility. In this respect, the agreement shown in these figures suggests that fuselage flexibility is not important for this aircraft for these particular hub vibratory loads.

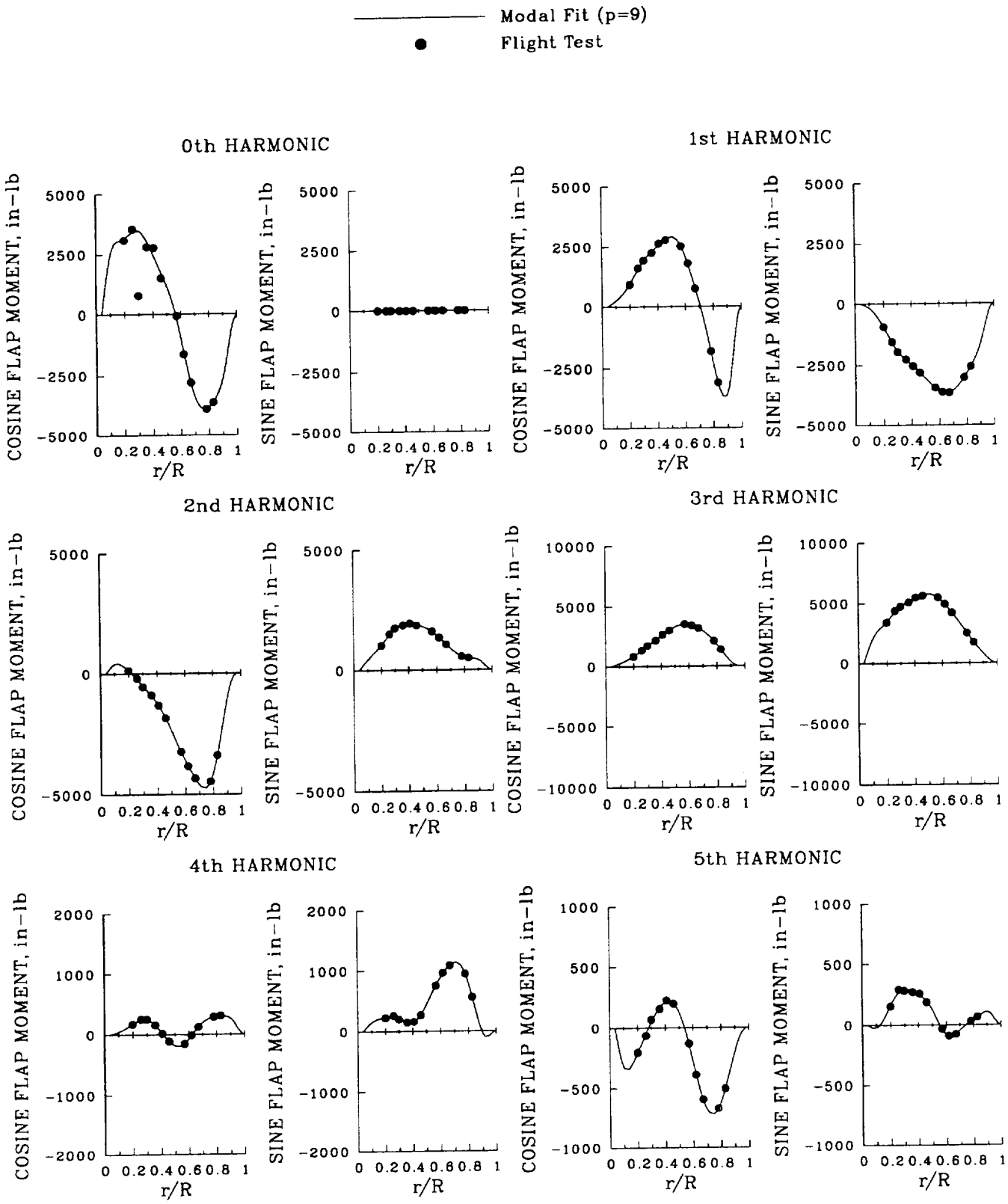


Figure 141. Modal fit of blade flap bending moment data using nine calculated modes; $\mu = 0.402$.

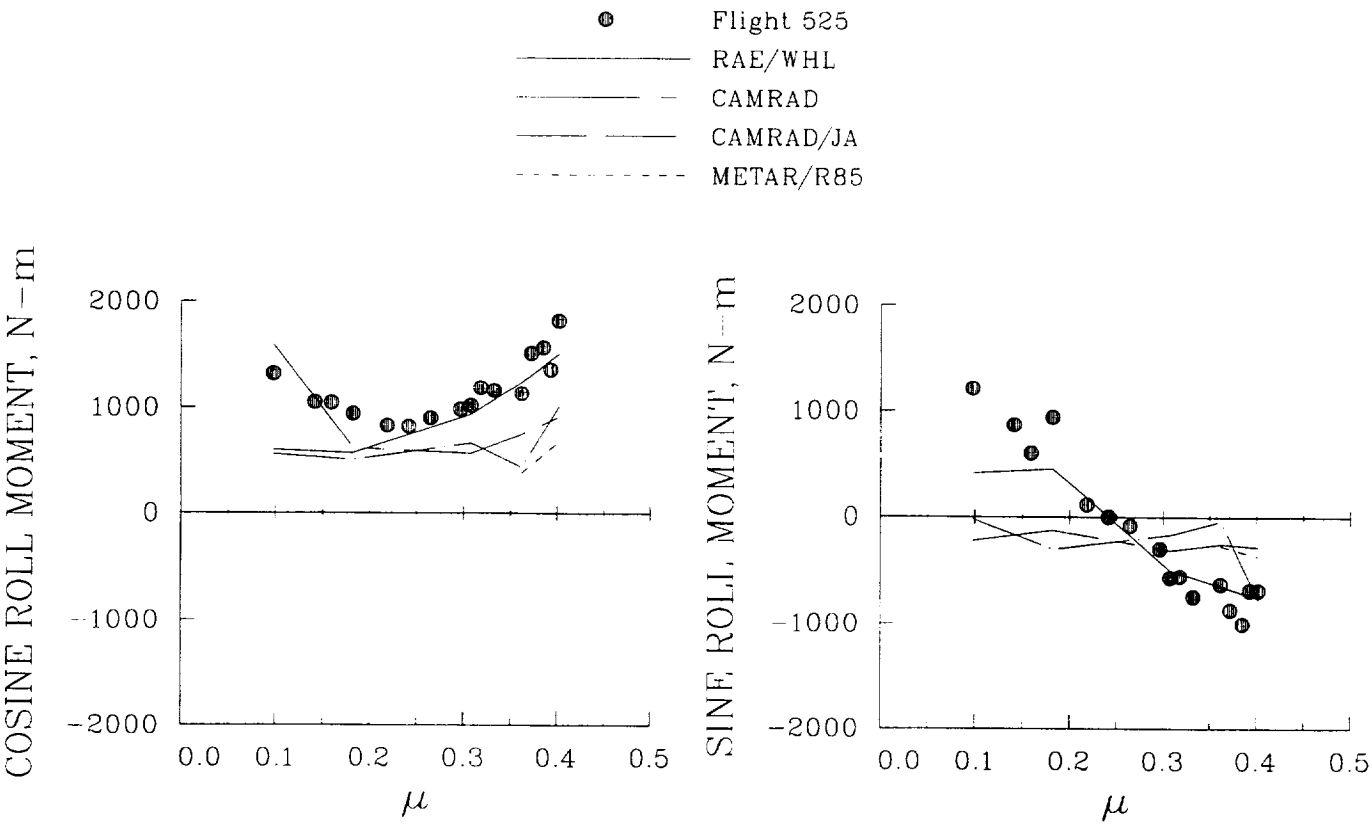


Figure 142. Comparison of calculated hub 4/rev roll moment and values derived from blade measurements as a function of advance ratio for Flight 525.

### 5.2.3 Summary of Advance Ratio Sweep (Flight 525) Comparisons

*Trim and Performance*

The four lifting-line methods were used to predict the performance, airloads, blade response and moments, and vibratory loads for advance ratios from 0.098 to 0.402 with the exception that the METAR/R85 analysis computed the airloads and structural response only for the two high-speed cases.

The trim parameters selected for the airspeed sweep were aircraft weight, shaft angle of attack, and first harmonic blade flapping. The analysts were able to match the specified trim parameters although there were slight differences. Whereas the RAE/WHL, CAMRAD, and CAMRAD/JA analyses equated the rotor thrust to the gross weight, the METAR/R85 analysis set rotor lift to gross weight which differs by $\cos\alpha_s$. In achieving blade flapping trim each of the analyses defined the flap angles as appropriate for a rigid blade rather than a flexible one. This had little effect on the longitudinal flapping, $\beta_{1c}$, but caused approximately a half degree out of trim condition for the lateral flapping, $\beta_{1s}$.

Although the specified trim parameters were achieved by all of the analyses, the assumption that the rotor thrust (or lift) is the same as aircraft weight was a poor one as it does not account for fuselage and stabilizer download. At the highest speed condition, based on wind tunnel measurements of the

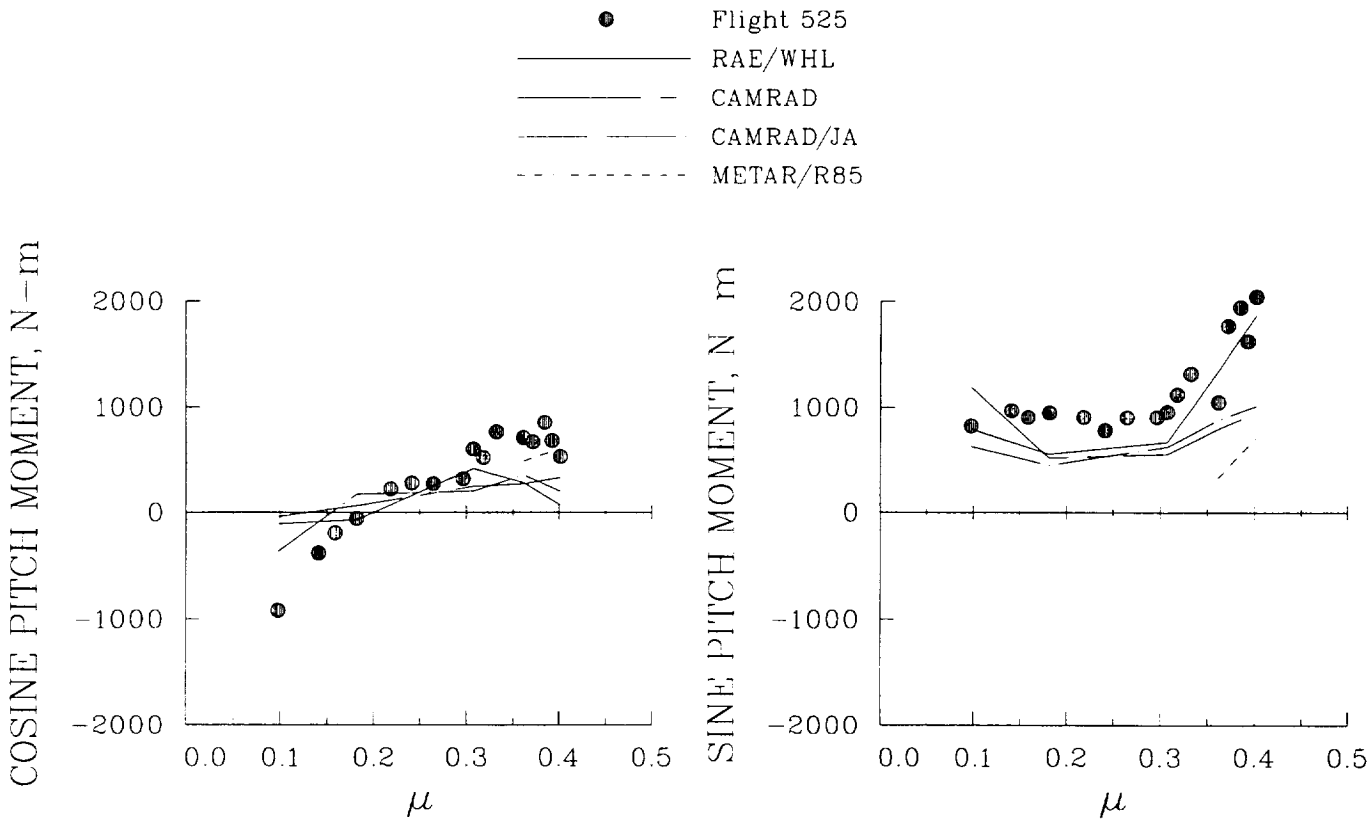


Figure 143. Comparison of calculated hub 4/rev pitch moment and values derived from blade measurements as a function of advance ratio for Flight 525.

fuselage characteristics, this represents approximately a 9% underprediction of the true rotor thrust. Thus, it is expected that the analyses should underpredict the power required at high speed as well as the airloads and structural response.

The prediction of the unspecified controls, that is, collective and cyclic angles, was fair to good. At low speed, where the wake modeling is important, differences between measurement and calculation were as high as 2°. Except for CAMRAD, the analyses showed good agreement in collective at high speed. The RAE/WHL analysis was able to calculate the cyclic angles to within 0.5° in most cases. The CAMRAD/JA cyclic angles, in some cases, showed differences up to 1°, while the other two analyses predicted cyclic angles that differed from the measurements by as much as 2°.

All of the analyses underpredicted the measured main rotor torque, particularly for the highest speed where the calculated torques were 20 to 26% low. In part it is believed that these differences are a consequence of underestimating the rotor thrust, but this does not explain all of the difference that is observed.

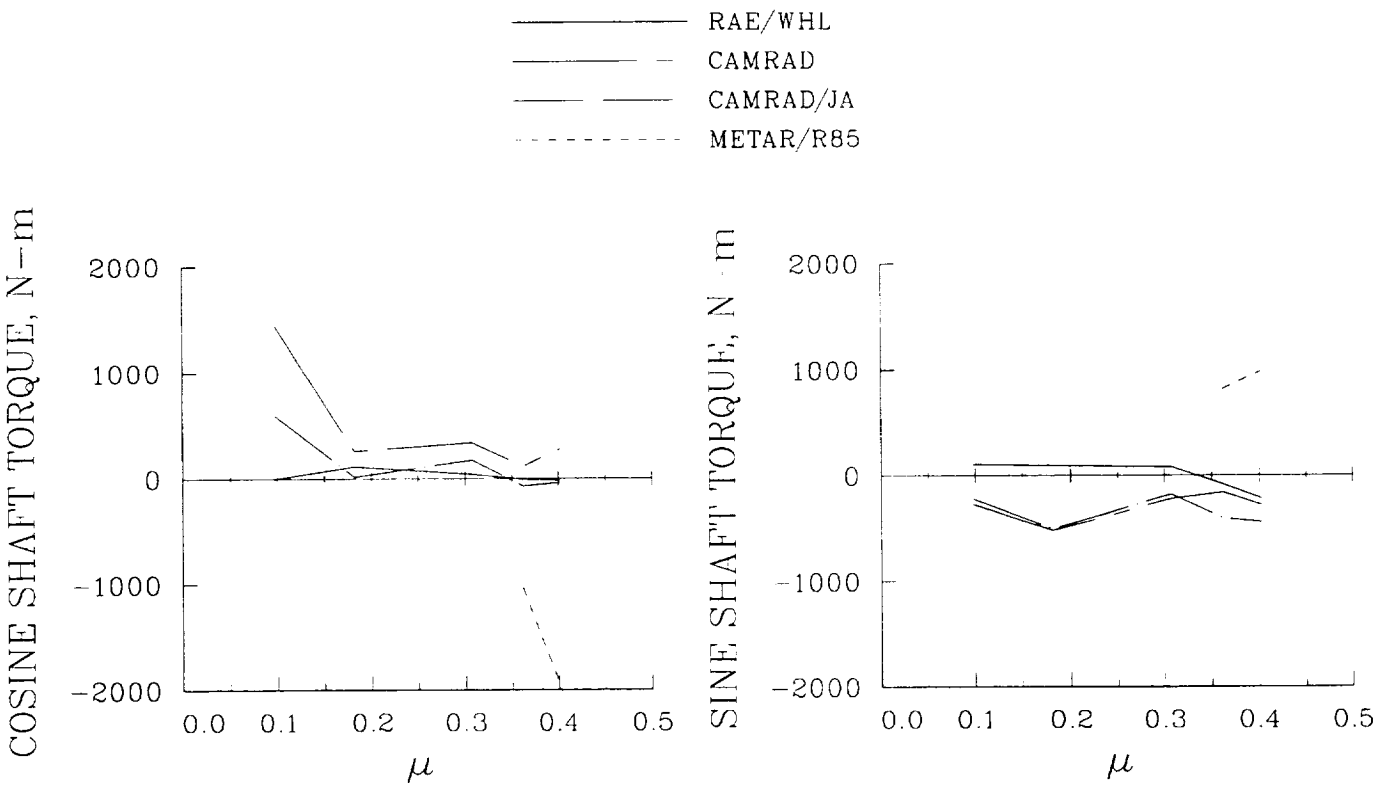


Figure 144. Comparison of calculated 4/rev shaft torque as a function of advance ratio for Flight 525.

*Blade Airloads*

Each of the four lifting-line methods provided good qualitative predictions of the blade normal force or lift near the tip where measurements were made. At low speed, the free wake included in the CAMRAD and CAMRAD/JA analyses provides a good prediction of the vortical loading. At higher speeds the free wake is no longer important and the best predictions were obtained by the RAE/WHL and CAMRAD/JA analyses. Both the CAMRAD and METAR/R85 analyses have difficulties predicting the lift close to the tip.

The prediction of the section pitching moment near the blade tip is, in general, poor. At low speed none of the analyses show the influence of vortical loads on pitching moment. At high speed, where the torsional loading is greatest, the CAMRAD analyses and METAR/R85 underpredict the loading. The RAE/WHL code predicts oscillatory loads as large as those observed in flight, but the character is different.

*Blade Response and Loads*

In general the various methods provide a good qualitative prediction of the flap response as well as the flap bending moments. The exception to this is that the METAR/R85 code, while providing a good prediction of the flap response over the speed range, does not predict the 3/rev loads well at

high speed. This deficiency is believed to be caused by the incorrect modeling of the geometry of the swept tip within the flexible blade model and the lack of torsion deformation in the calculation. Substantial improvements in both of these areas have been made subsequent to the workshop (Arnaud and Beaumier, 1992). Detailed examination of the flap bending moments shows that at low speed the CAMRAD analyses provide a better prediction of the flap moments and this is clearly a consequence of the free wake model. At high speed, the RAE/WHL, CAMRAD, and CAMRAD/JA analyses show the correct 3/rev character of the loading, but the CAMRAD analyses underpredict the magnitude of the loads while the RAE/WHL analysis provides an accurate computation.

The good prediction of the flap bending moments is in direct contrast to the poor prediction of the chord bending moments. Although the oscillatory amplitudes are similar to the flight measurements, the frequencies and phase behavior are substantially different and the computations are unsatisfactory. The reasons for the poor predictions are not clear and further work is needed to understand the influence of coupling with flap bending, the chord airloading, the effects of the lag damper at the root, and the root-end boundary conditions.

The torsional loading, unlike flap and chord, is not dominated by a particular frequency. In general, all of the analyses underestimate the torsional loads and the predicted characteristics do not show good agreement with the measurements. The correlation is best described as poor.

*Rotor Vibratory Loads*

The predicted hub vibratory loads, in general, show good qualitative agreement with each other. There are no measurements of the aircraft vibratory loads at the hub. However, it is possible to estimate the hub vertical shears and pitch and roll moments by fitting blade modes to the extensive flap bending moment measurements. This fit does not account for any motion or stiffness in the hub or aircraft. Comparison of the calculated 4/rev hub pitch and roll moments with the estimated moments is quite good and mirrors, to a degree, the comparisons for the flap bending moments. This is not surprising as these moments are largely due to the 3/rev flap bending moments, although the good agreement suggests that hub impedance is not important for this aircraft for these loads. The comparison of the 4/rev vertical shears is not as good as for the moments and this is particularly true at high speed. No attempt was made to estimate the hub inplane shears from blade measurements.

## 5.3 Reference Case (Flight 123)

### 5.3.1 Introduction

The Flight 123 case was selected to provide a reference or baseline case with the standard Puma blade without the swept tip. The use of a reference case is valuable in a number of respects. First, by comparing swept-tip and rectangular-tip flight test data it is possible to identify conditions in which the swept tip significantly changes the blade loading. Second, by comparing swept-tip and rectangular-tip analyses it is possible to identify modeling differences that are affected by the swept-tip. Finally, by comparing the analytical methods with the experimental data from the reference case it is possible to identify modeling deficiencies that are unrelated to the swept-tip blade. All of these approaches are used within this section.

### 5.3.2 Flight Data

Five counters were examined from Flight 123 that correspond roughly to the Flight 525 airspeed sweep; that is, the advance ratio varied from 0.097 to 0.377. One counter from this airspeed sweep, $\mu = 0.321$, was selected as the reference case and is compared in table 22 with the Flight 525 counter at $\mu = 0.307$ which was one of the correlation cases used in Section 5.2. Although the match is quite good on the basis of nondimensional thrust (based on aircraft weight), the advance ratio is 4% less for the Flight 525 case and the rotor speed is 5% less and this provides an 8% drop in the tip Mach number on the advancing side.

Table 22. Comparison of Flight 123 and 525 counters

| Case | Flight 123 (Counter 9) | Flight 525 (Counter 12) |
|---|---|---|
| $\mu$ | 0.321 | 0.307 |
| $M_{90}$ | 0.837 | 0.770 |
| $C_T/\sigma$ | 0.0695 | 0.0701 |
| $\alpha_s$, deg | −6.00 | −5.70 |
| $\beta_{1c}$, deg | 0.42 | 0.04 |
| $\beta_{1s}$, deg | −0.14 | −0.08 |
| $\Omega$, rpm | 267.4 | 253.9 |

A planform view of the instrumented blade is shown in figure 145. Flap bending moment measurements were obtained at eight radial stations: $0.35R$, $0.45R$, $0.55R$, $0.65R$, $0.75R$, $0.83R$, $0.90R$, and $0.95R$. Valid measurements of chord bending moment were obtained at a single station, $0.73R$, and the torsion moment at two stations, $0.33R$ and $0.73R$. Flap, pitch, and lead-lag angles were measured on one blade, but no measurement of pitch-link loads was obtained.

The same aircraft trim parameters are used for the reference case as were used for the Flight 525 calculations, that is, rotor thrust (aircraft weight), shaft angle of attack, and first harmonic of flap angle. Figure 146 compares the Flight 123 measured shaft angle of attack with the trim shaft angle-of-attack schedule used for the Flight 525 analytical models. The agreement between the two flights is quite good, particularly at the advance ratio of the reference case. The harmonic flapping angles for Flight 123 are compared with measurements on three blades from Flight 525 in figure 147. The cosine (longitudinal) flapping is offset by about a half degree between the two flights, but sine (lateral) flapping is similar for both flights.

A comparison of unspecified rotor trim parameters between flights 123 and 525 is also useful. The blade collective pitch angle, measured at the pitch bearing, is compared in figure 148 and good agreement is seen between the two flights. The measurements of the cyclic pitch angle for Flight 123 are compared with Flight 525 in figure 149. The cosine (lateral) cyclic angle agrees well for the two flights at lower speeds, but an increasing difference is observed at the higher advance ratio. The sine (longitudinal) cyclic angles, however, show improved agreement at the higher speeds. These differences are largely differences in phase with the Flight 123 data leading the Flight 525 data by about 40° at low speed and 15° at high speed.

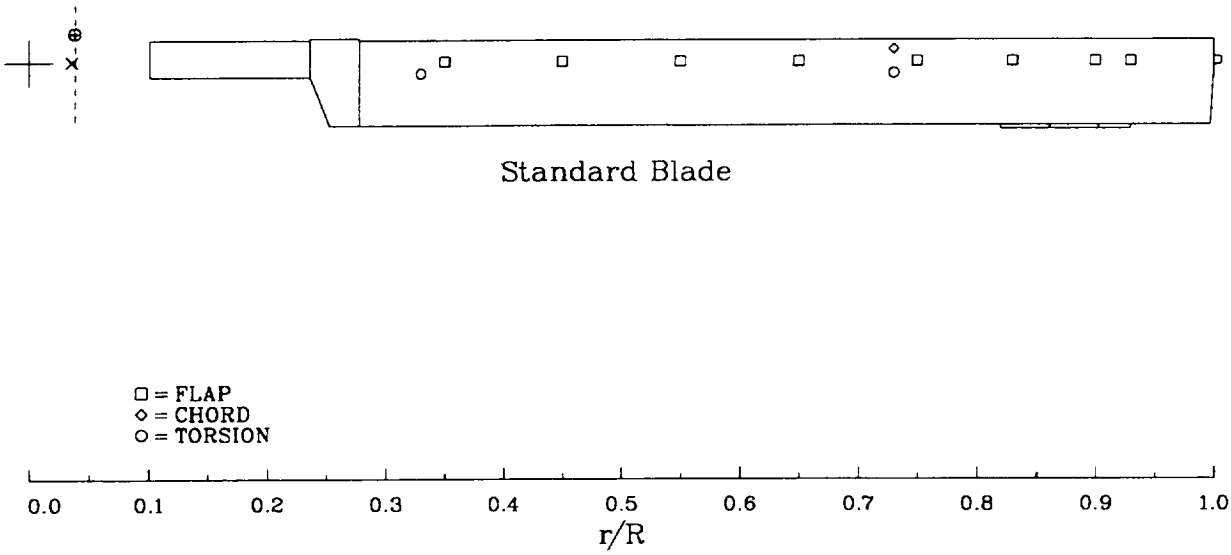


Figure 145. Structural instrumentation on the standard Puma blade.

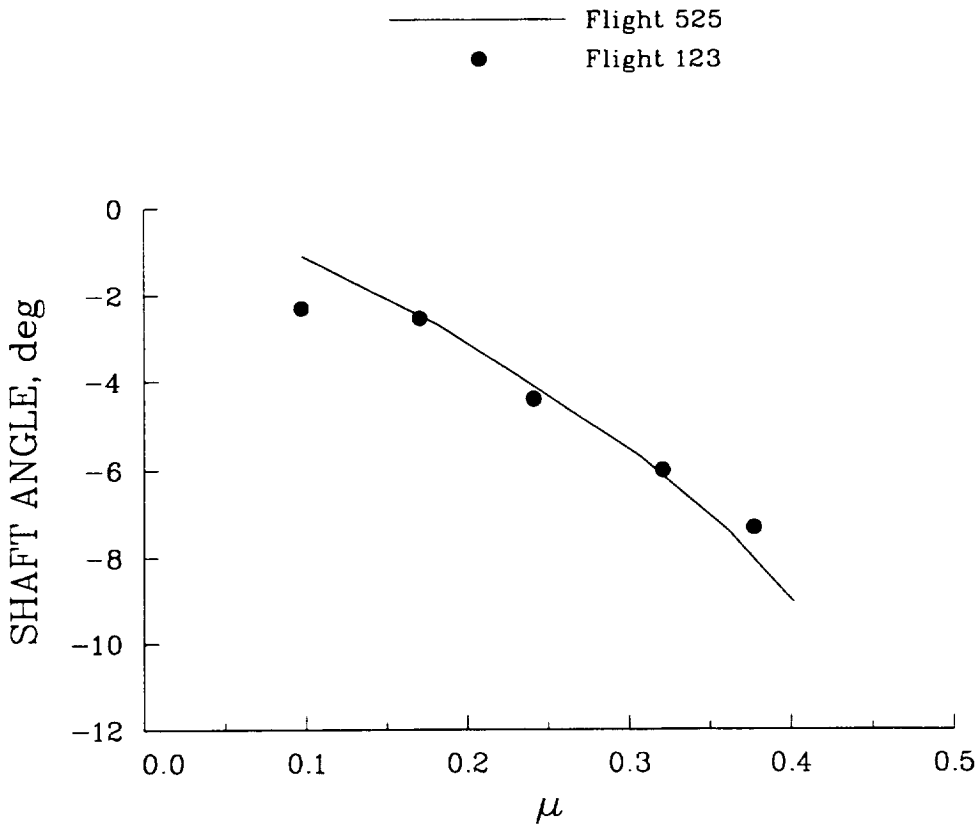


Figure 146. Shaft angle of attack for Flight 123 compared with Flight 525 angle-of-attack schedule.

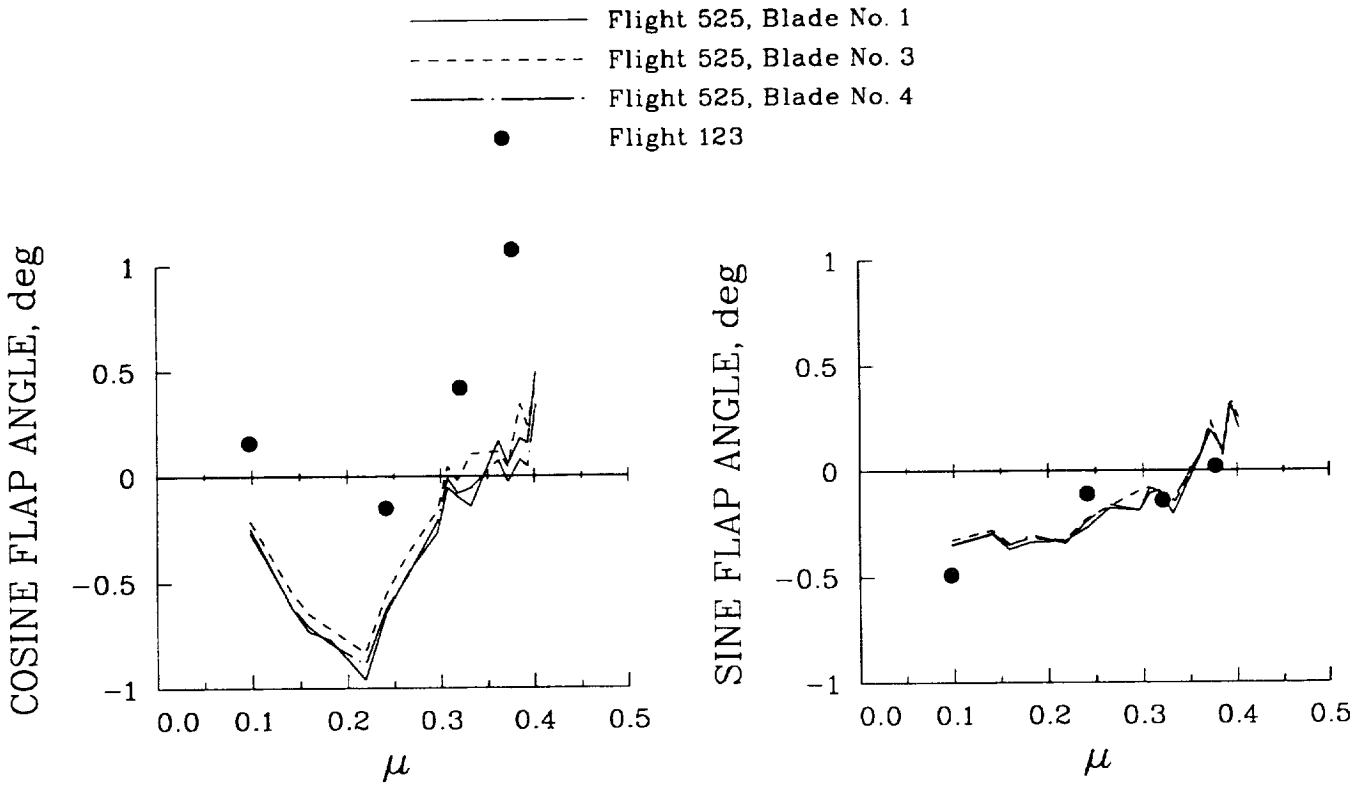


Figure 147. Flight 123 first harmonic flapping compared with Flight 525 values.

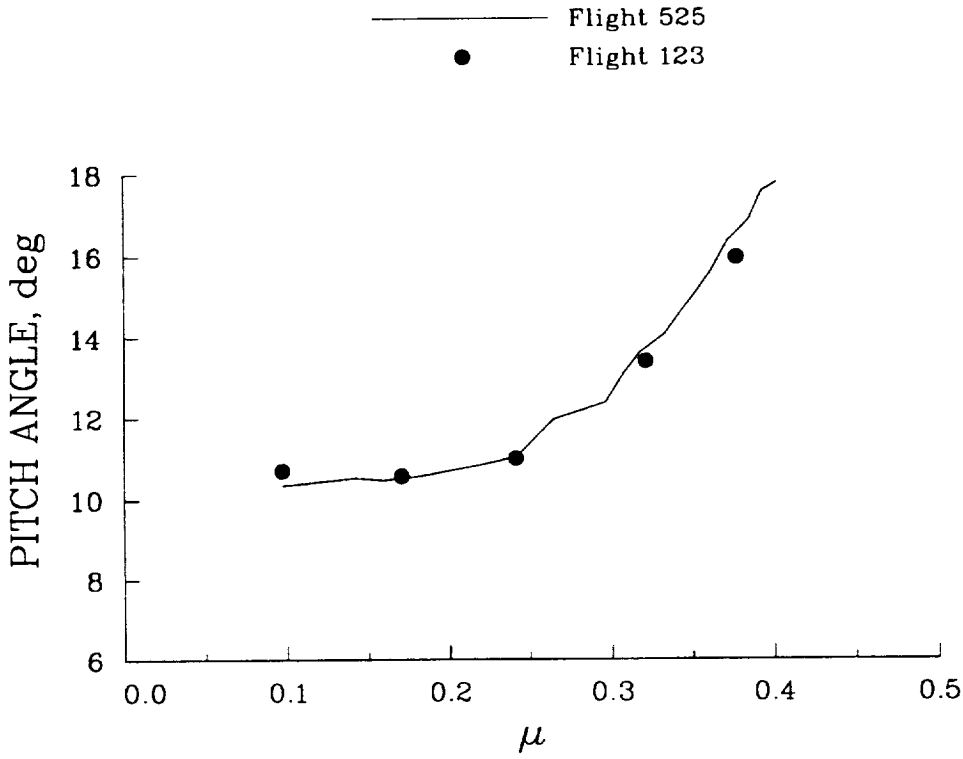


Figure 148. Flight 123 collective pitch angles compared with Flight 525 values.

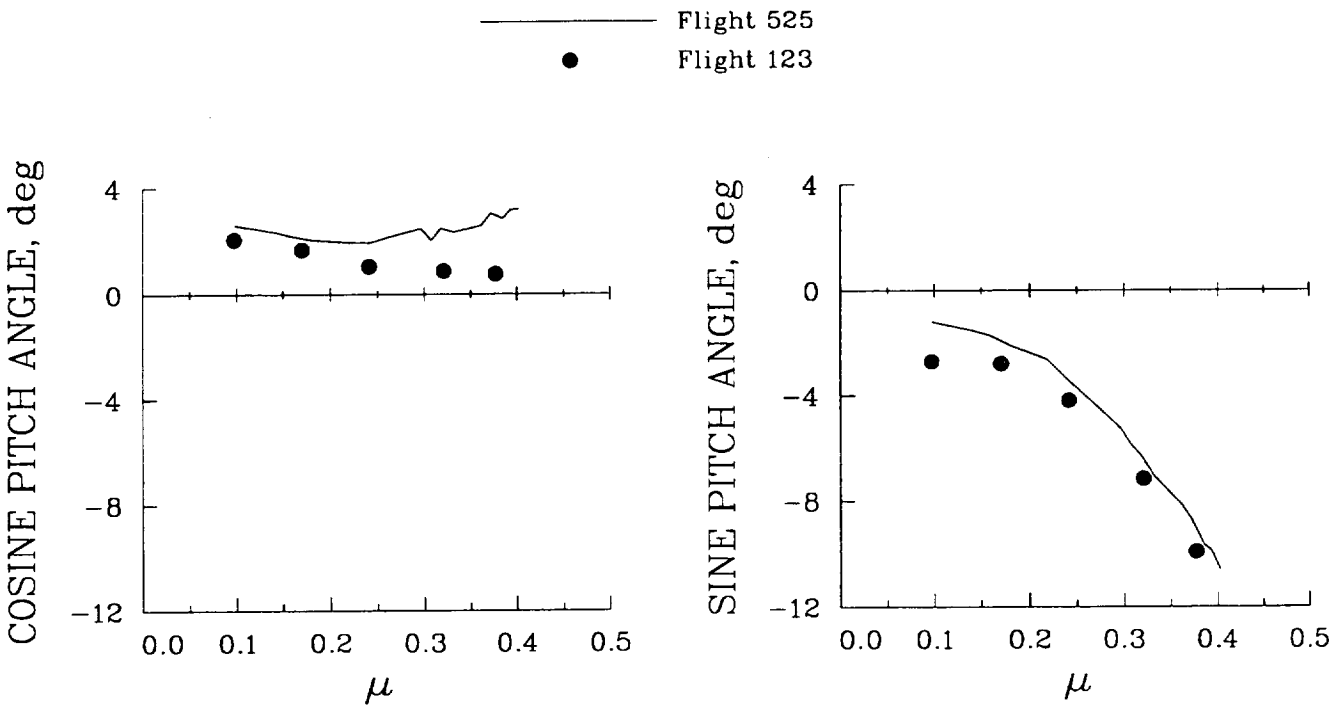


Figure 149. Flight 123 cyclic pitch angles compared with Flight 525 values.

The coning angles recorded on Flight 123 are compared with the Flight 525 measurements in figure 150. The Flight 123 coning is slightly lower than the mean position recorded for Flight 525 and this is probably a result of the slightly higher rotor speed. The cause of the negative coning jump at the $\mu = 0.307$ point in the Flight 525 data is unknown. Obvious changes in other parameters at this advance ratio have not been observed in the data.

The lag angle measurements obtained on Flight 123 are compared with the measurements on Flight 525 in figure 151. As mentioned previously in Section 5.2.1, the Flight 525 measurements appear to have a bias error of about $-4°$. Equating the measured shaft torque on Flight 525 to an equivalent lag angle, however, suggests that the bias error is between $-1.5°$ and $-2.0°$. These discrepancies remain unresolved.

Pressure instrumentation was not installed on the standard blade of the Puma for Flight 123 so there can be no comparison of airloads between the two flights. A comparison of the flap bending moments measured at midspan is shown in figure 152 as a surface plot where the bending moments are functions of blade azimuth and advance ratio. A thickened line is used to highlight the comparison cases. The Flight 525 data contain 16 advance ratio points, and the evolution of flap bending moment as advance ratio changes is quite smooth. Flight 123 includes only five advance ratio cases and the data appear less smooth. Nonetheless, the dominant 3/rev character of the flap bending moment is apparent for both flights.

The radial distributions of the measured flap bending moments for the comparison cases are shown in figure 153. The Flight 525 data extend farther inboard than the Flight 123 data, to $0.20R$ compared

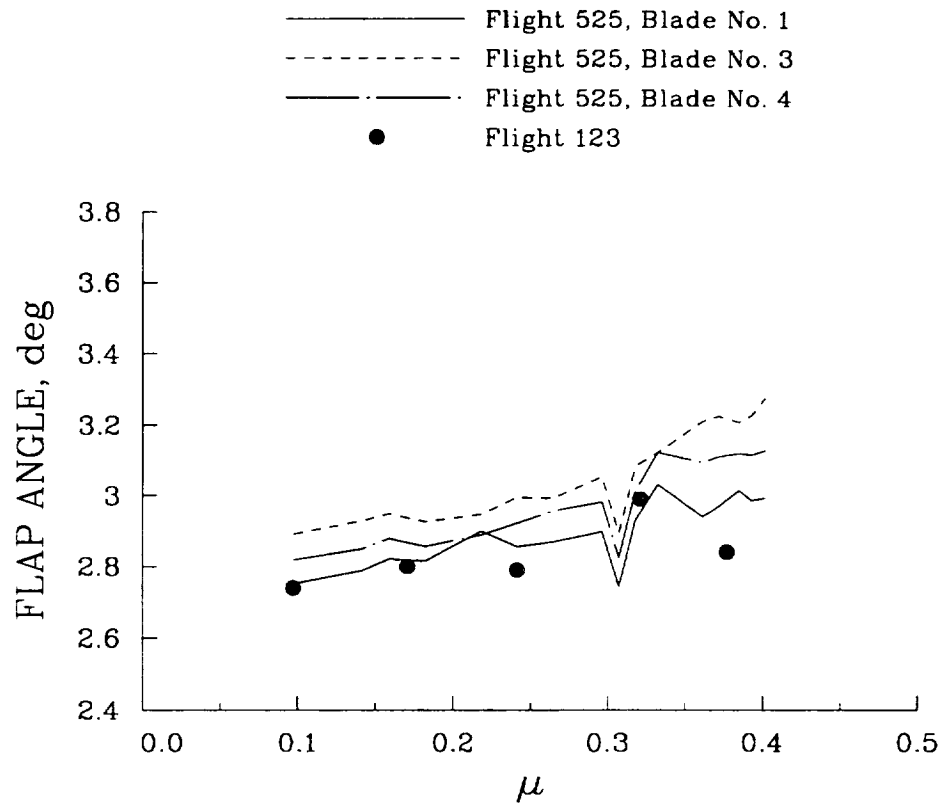


Figure 150. Flight 123 coning angles compared with Flight 525 values.

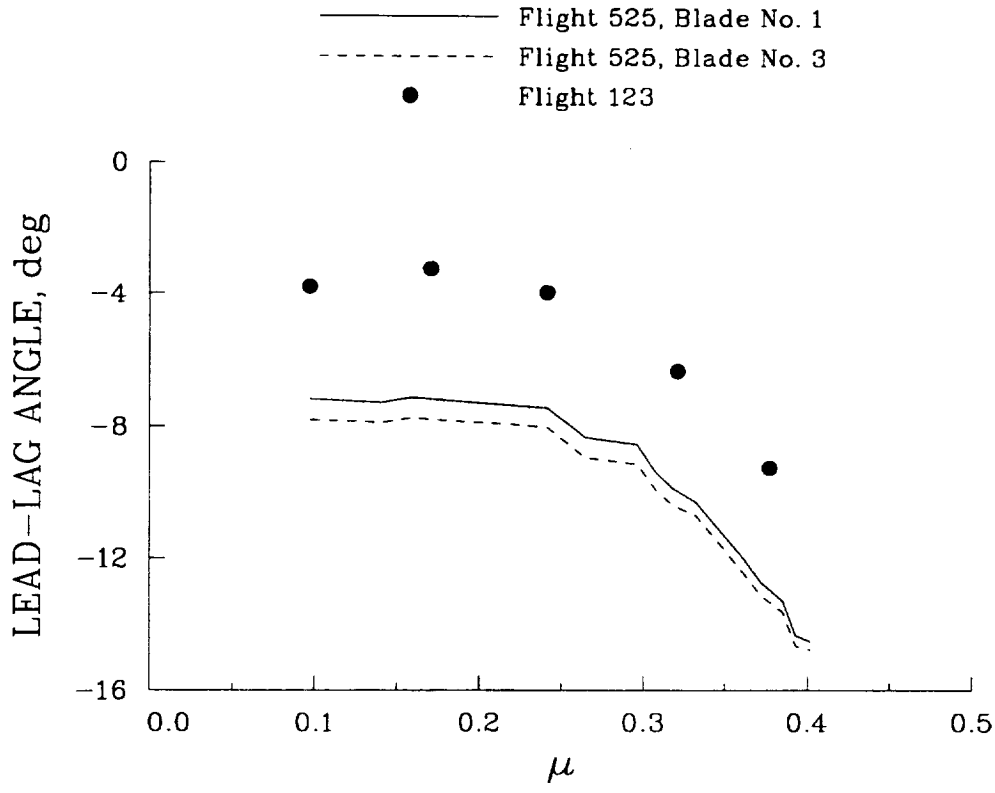


Figure 151. Flight 123 lead-lag angles compared with Flight 525 values.

Flight 525
r/R = 0.57

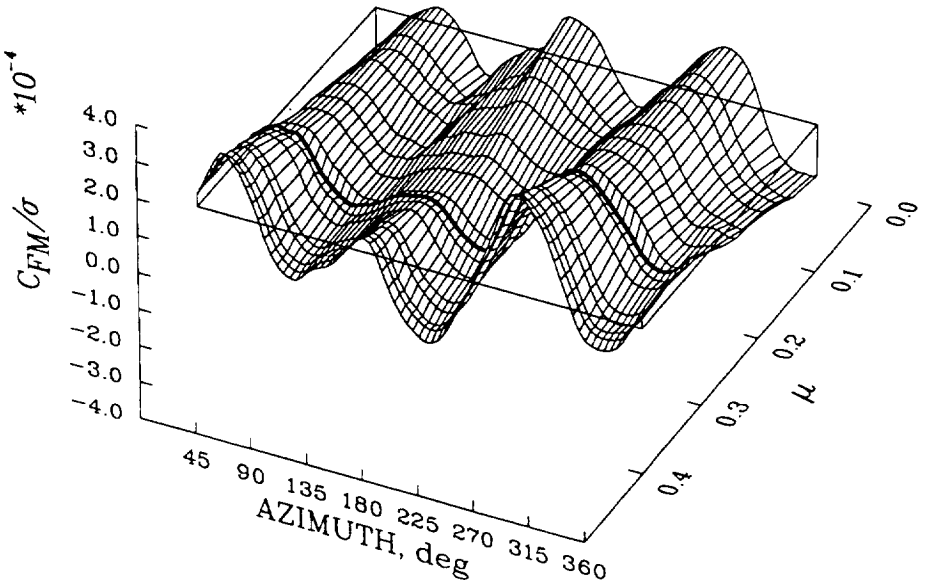


Flight 123
r/R = 0.55

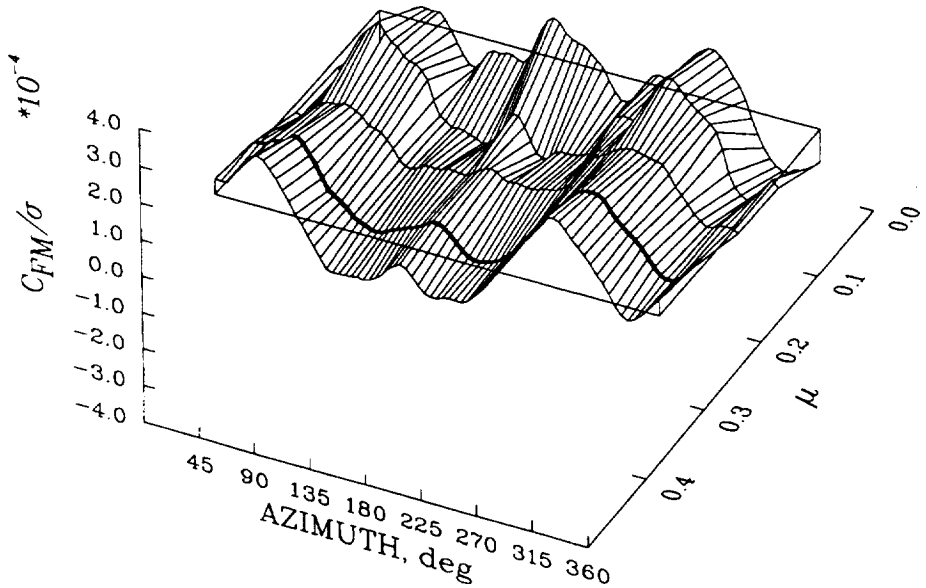


Figure 152. Comparison of midspan flap bending moment distributions for flights 525 and 123 as functions of azimuth and advance ratio. Comparison cases shown with a thickened line.

Flight 525, $\mu = 0.307$

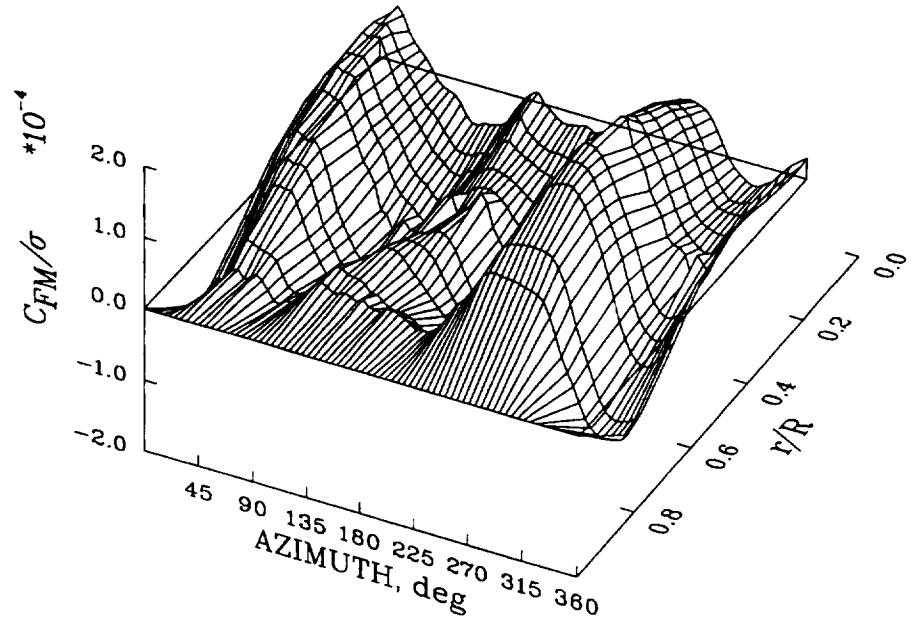


Flight 123, $\mu = 0.321$

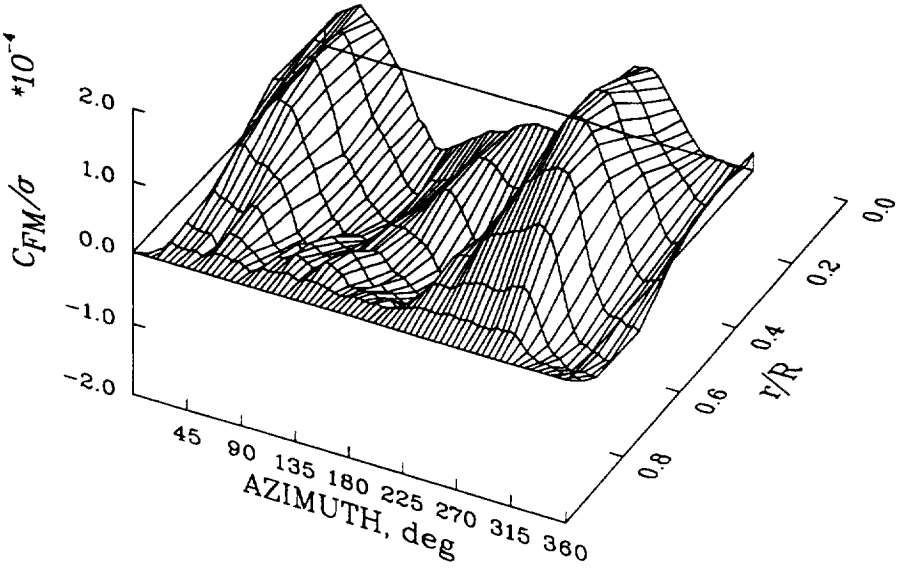


Figure 153. Comparison of flap bending moment radial distribution for flights 525 and 123; $\mu = 0.307$ (Flight 525), $\mu = 0.321$ (Flight 123).

to $0.35R$, but in general there is good qualitative agreement between the two cases. The flap bending moment measurements are compared at $0.35R$ and $0.55R$ in figure 154. As the flap bending moment measurements were not obtained at identical radial stations for the two flights the comparisons here are based on linear interpolation of the Flight 525 data. Good agreement is observed between the two flights in both the general behavior and in the amplitudes. There does appear to be a phase difference between the two cases with the Flight 525 data leading the Flight 123 data by about 10° to 15°. It is unclear whether this phase difference is related to the modified swept tip used on the research Puma, but it is clear that the aerodynamics of the swept tip have not significantly modified the amplitude or basic character of the flap bending moments.

The limited data available for the chord bending moments for Flight 123 make surface plot comparisons, such as were used for the flap bending moments, impossible. The chord bending moment measured on Flight 123 at $0.73R$ can be compared with interpolated values from Flight 525, however, and this comparison is shown in figure 155. The data from both rotors show the same general character with a clear 4/rev component observed in the time histories. The amplitudes of the chord bending moments are similar. As was seen in the case of the flap bending moment comparison in figure 154, the Flight 525 data lead the Flight 123 data by 10° to 15°.

The most inboard torsion measurement available on Flight 123 is at $0.33R$ and this measurement is compared with interpolated data from Flight 525 in figure 156. There are noticeable differences between the torsion moments on the swept-tip blade flown on Flight 525 and the standard, rectangular-tipped blade flown on Flight 123. The amplitude of the swept-tip blade is about 40% higher than the amplitude of the standard blade and the character of the oscillations on the retreating side of the disk is different. These differences are believed to be largely a result of the increased blade area at the tip rather than an effect of the swept planform geometry (Maier and Bousman, 1992).

### 5.3.3 Comparison of Analysis and Experiment

#### 5.3.3.1 *Trim and Performance*

The analyses were trimmed to the aircraft weight, shaft angle of attack, and first harmonic flapping angles for Flight 123; the same trim procedure as was used for Flight 525. The unspecified trim parameters and shaft torque that were computed for Counter 9 of Flight 123 are compared with flight measurements in table 23. No measurement of the shaft torque was obtained on the flight test aircraft.

The RAE/WHL, CAMRAD, and METAR/R85 analyses all predict a collective pitch value that is only slightly below the measurement. CAMRAD/JA, on the other hand, predicts a higher value for collective pitch and this situation is similar to the analytical model calculations (Case 10) discussed in Section 4.3.1. The predicted cyclic pitch angles are within a degree or a degree and a half of each other. Much of the difference that is seen between the measured and computed cyclic angles is a phase difference. The predicted phase of the cyclic pitch angle lags the measured values by 12° to 18°. The cyclic pitch amplitude predicted by the CAMRAD and METAR/R85 analyses are about 15% below the measured value, the RAE/WHL analysis is about 2% low, and the CAMRAD/JA prediction is within 1% of the measurement.

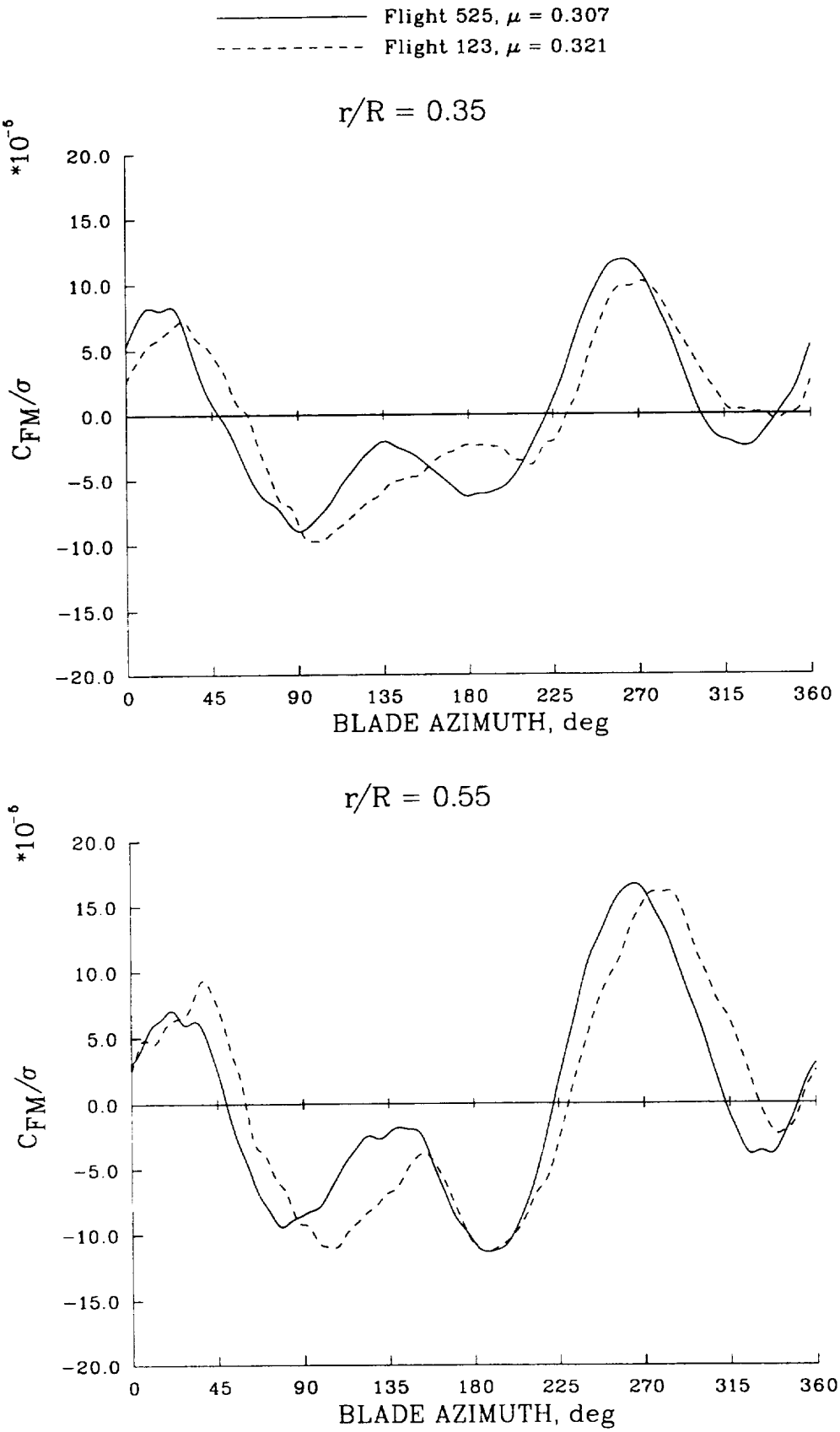


Figure 154. Comparison of measured flap bending moments for flights 525 and 123 at $0.35R$ and $0.55R$; $\mu = 0.307$ (Flight 525), $\mu = 0.321$ (Flight 123).

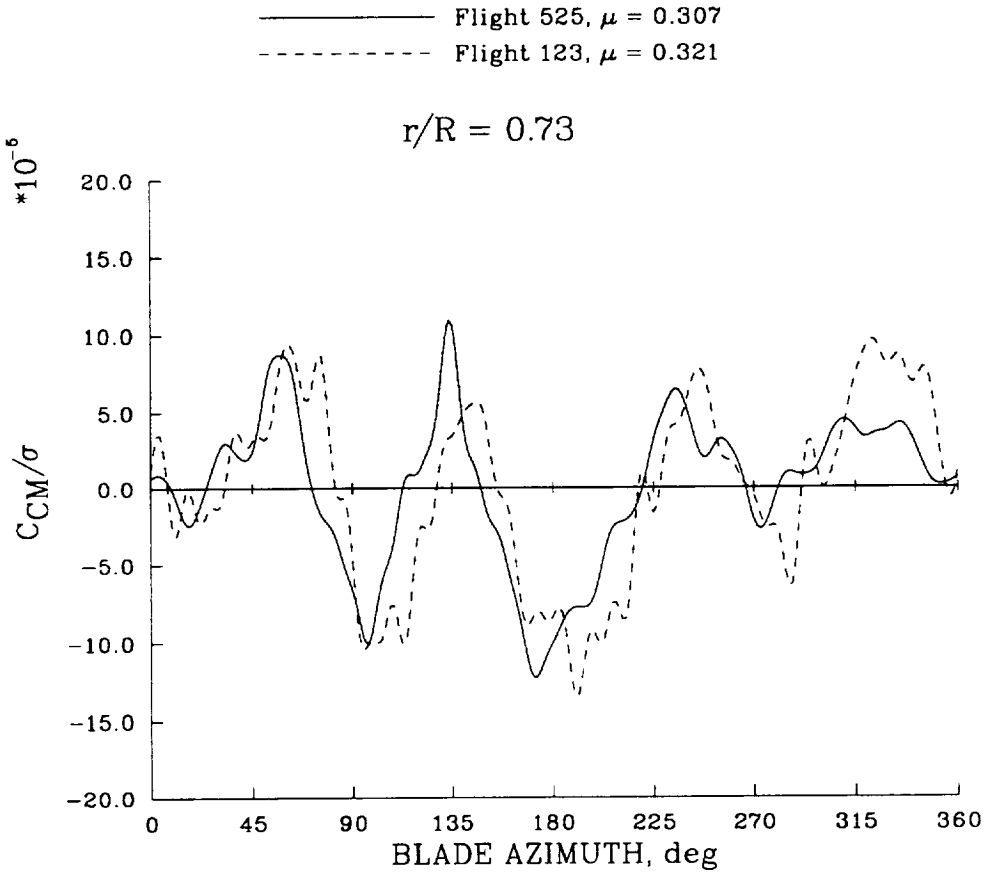


Figure 155. Comparison of measured chord bending moments for flights 525 and 123 at $0.73R$; $\mu = 0.307$ (Flight 525), $\mu = 0.321$ (Flight 123).

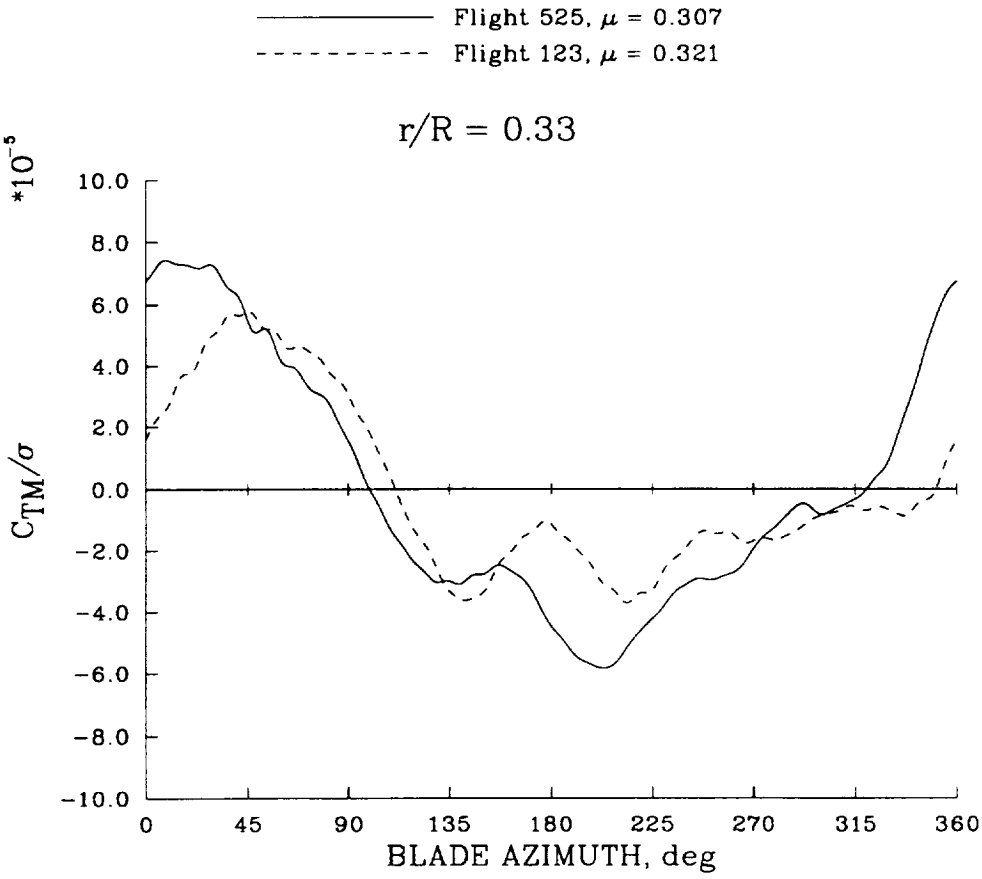


Figure 156. Comparison of measured torsion moments for flights 525 and 123 at $0.33R$; $\mu = 0.307$ (Flight 525), $\mu = 0.321$ (Flight 123).

Table 23. Unspecified trim parameters and shaft torque for Flight 123, Counter 9

| Parameter | Flight 123 | RAE/WHL | CAMRAD | CAMRAD/JA | METAR/R85 |
|---|---|---|---|---|---|
| Collective Pitch, deg | 12.40 | 13.26 | 13.04 | 14.11 | 13.05 |
| Cosine Cyclic Pitch, deg | 0.88 | 1.72 | 2.60 | 2.31 | 2.80 |
| Sine Cyclic Pitch, deg | −7.16 | −6.82 | −5.54 | −6.76 | −5.60 |
| Coning, deg | 2.99 | 3.46 | 3.46 | 3.44 | 3.53 |
| Lag Angle, deg | −6.33 | −7.02 | −7.06 | −7.85 | −5.80 |
| Shaft Torque, N-m | – | 28,166 | 27,845 | 30,990 | – |

The calculated coning angles are within 3% of each other but are significantly greater than the measured coning. A similar disparity was seen in the Flight 525 comparisons shown in figure 88 in Section 5.2.2.1. The calculated lag angles differ by as much as two degrees and, again, similar differences were seen for Flight 525.

As was seen in the analytical model calculations in Section 4.3.1 and the Flight 525 calculations in Section 5.2.2.1, the shaft torque computed by CAMRAD/JA is considerably greater than the other analyses, approximately 10% for this case.

5.3.3.2 *Blade Airloads*

The RAE/WHL, CAMRAD, CAMRAD/JA and METAR/R85 calculated airloads are compared in figure 157 for Flight 123 at an advance ratio of 0.321. No experimental data are available for this case, and only the similarities and differences between the methods can be discussed. The figure shows three-dimensional surface plots of the section lift evolution versus spanwise station and azimuth. The general trends are similar for all the methods as well as for the lift computed for the swept-tip blade discussed previously in Section 5.2.2.2. The major effects seen are a dominant 1 and 2/rev load variation around the azimuth, with a reduced loading on the advancing blade side at the tip and on the retreating side at the root, due to the rotor trim conditions.

A close examination of figure 157 reveals a number of differences between the predictions. First, there is a strong variation in the computed tip loading between the various methods. Ranking the methods from the lower to the larger tip loading gives CAMRAD/JA, METAR/R85, RAE/WHL and CAMRAD. These differences were also seen in the Task 3 analytical modeling comparisons discussed in Section 4.3.2 and are a consequence of the coupling of the prescribed wake model with the blade distribution of lift.

A second feature that is noted is that METAR/R85, and to a lesser extent RAE/WHL, computes higher harmonic components of the loading, which may be partly a consequence of the fact that CAMRAD and CAMRAD/JA include only the first 12 harmonics in the solution, while METAR/R85 uses 18 harmonics and RAE/WHL uses 36.

Figure 158 shows the loads evolution versus the azimuth at $0.95R$. The top part of the figure shows the higher harmonic part of the loads, that is, without the mean value and the first two harmonics which constitute the main part of the signal, while the lower part of the figure shows the fully computed

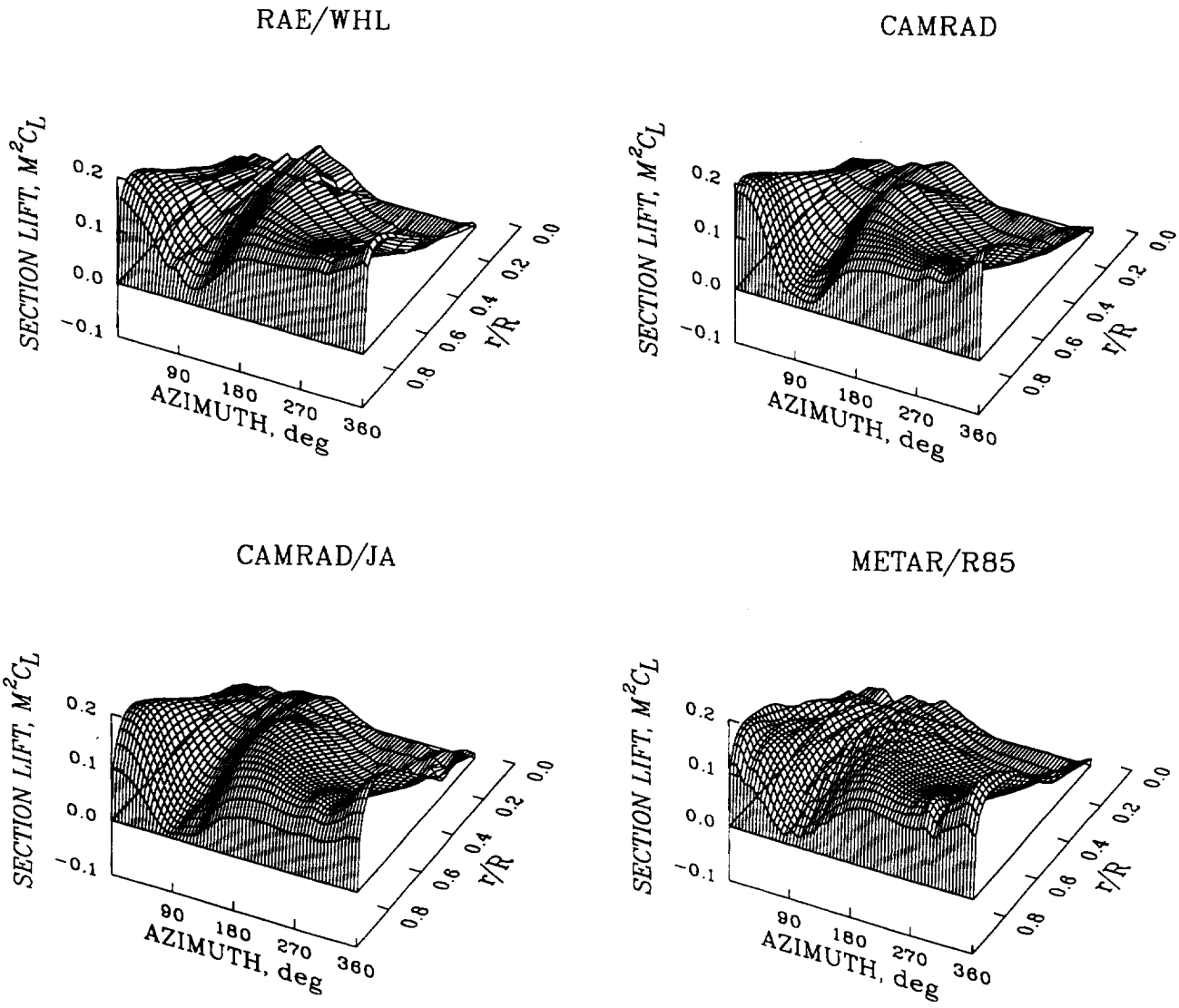


Figure 157. Calculated normal force as a function of azimuth and blade radius; Flight 123, $\mu = 0.321$.

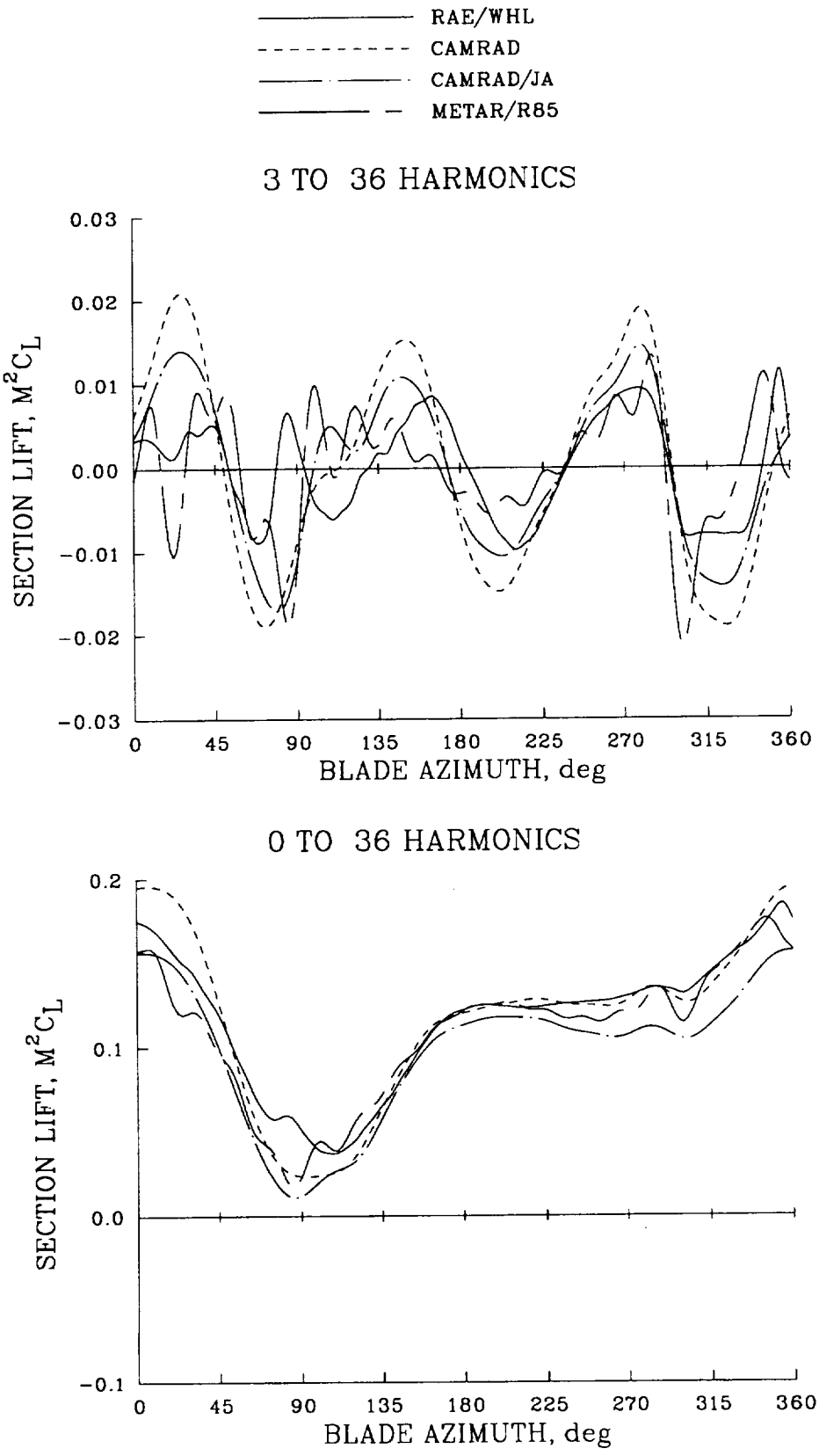


Figure 158. Calculated normal force as a function of azimuth at $0.95R$; Flight 123, $\mu = 0.321$.

airloads. This figure confirms the comments made above, but they also indicate that, for this blade section: the CAMRAD calculations give a higher lift for the rear part of the rotor disk; the RAE/WHL code computes less lift reduction on the advancing blade side; all of the methods show the dominant 3/rev component in the higher harmonic part of the lift; and the peak-to-peak amplitude of the higher harmonics component is greater in the CAMRAD computations.

Similar comparisons are shown in figures 159 and 160 for the section pitching moments. Figure 159 shows the surface plots of the section moment evolution versus azimuth and spanwise station. Qualitatively, all the methods give the same tendencies, with a section moment dominated by a 1/rev component. However, larger differences between the analytical predictions are seen here than were observed for the section lift. The RAE/WHL code gives a large positive section moment in the first quadrant, which extends from inboard up to the tip. The two most inboard sections show zero section moment as the $\dot{\alpha}$ terms have been switched off to avoid oscillations induced by the reversed flow region. CAMRAD and CAMRAD/JA compute less positive section moment in magnitude and extent, and a larger region of negative section moment. Furthermore, the advancing side moment variation decreases smoothly from blade tip to root and, at the blade root, large moment variations are found for the reversed flow region, with a strong positive peak around 270° azimuth. METAR/R85 gives a different section moment evolution, with a large part of the rotor disk having negative section moments, especially near the blade tip and only very small portions of the rotor disk have low positive section moment values.

Figure 160 compares the computed pitching moments at $0.95R$, substantiating the comments made above. However, this figure shows more clearly that the METAR/R85 calculation is fairly close to the CAMRAD and CAMRAD/JA results with the exception of the unusual behavior between 90° and 135° azimuth. In this azimuth range small differences in angle of attack will have strong effects on the moment coefficient due to the occurrence of transonic flow regions on the blade. This is also consistent with the larger lift value calculated by METAR/R85 for this portion of the rotor disk in figure 158. The RAE/WHL computed moment is different from the other calculations on the advancing blade side; this code also computes a large lift value all along the advancing blade side, and it seems difficult to explain this difference, because negative section moments would be expected in this case. Again, the METAR/R85 calculations give larger higher harmonic components, which is consistent with the lift values.

The computations for this flight condition were originally undertaken to understand computationally the differences between the rectangular-tip blade tested on Flight 123 and the swept-tip blade on Flight 525. In this respect it is useful to compare the calculations for these two conditions even though no pressure measurements are available for Flight 123. Figure 161 compares the radial distribution of lift, computed at $\psi = 0°$, for each analysis. The lift distributions are shown in nondimensional form, $M^2C_L$, and dimensional form. Although the radial distributions are similar inboard for the two flight conditions, outboard, where the swept-tip blade has a greater chord, there are differences seen in the nondimensional lift that are, in a sense, an artifact of the nondimensionalization used. The dimensional lift shows a relatively smooth and continuous distribution of lift near the blade tip while the nondimensional lift shows a lift decrement that coincides with the increased blade chord. Similar effects have been seen experimentally and computationally on the BERP blade tested as a fixed wing (Duque, 1989). In this sense comparisons based on dimensional lift are considered more appropriate for this section.

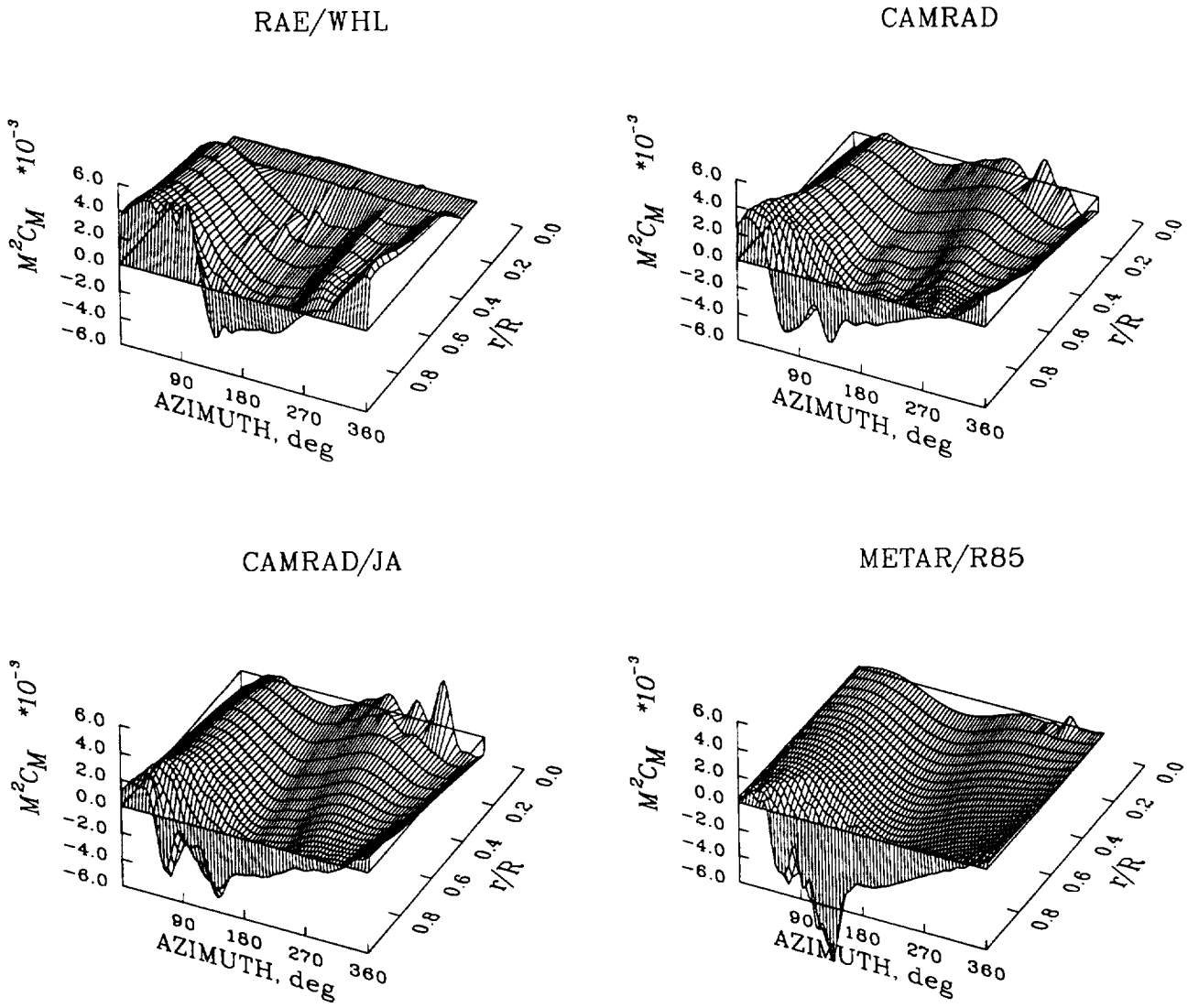


Figure 159. Calculated pitching moment as a function of azimuth and blade radius; Flight 123, $\mu = 0.321$.

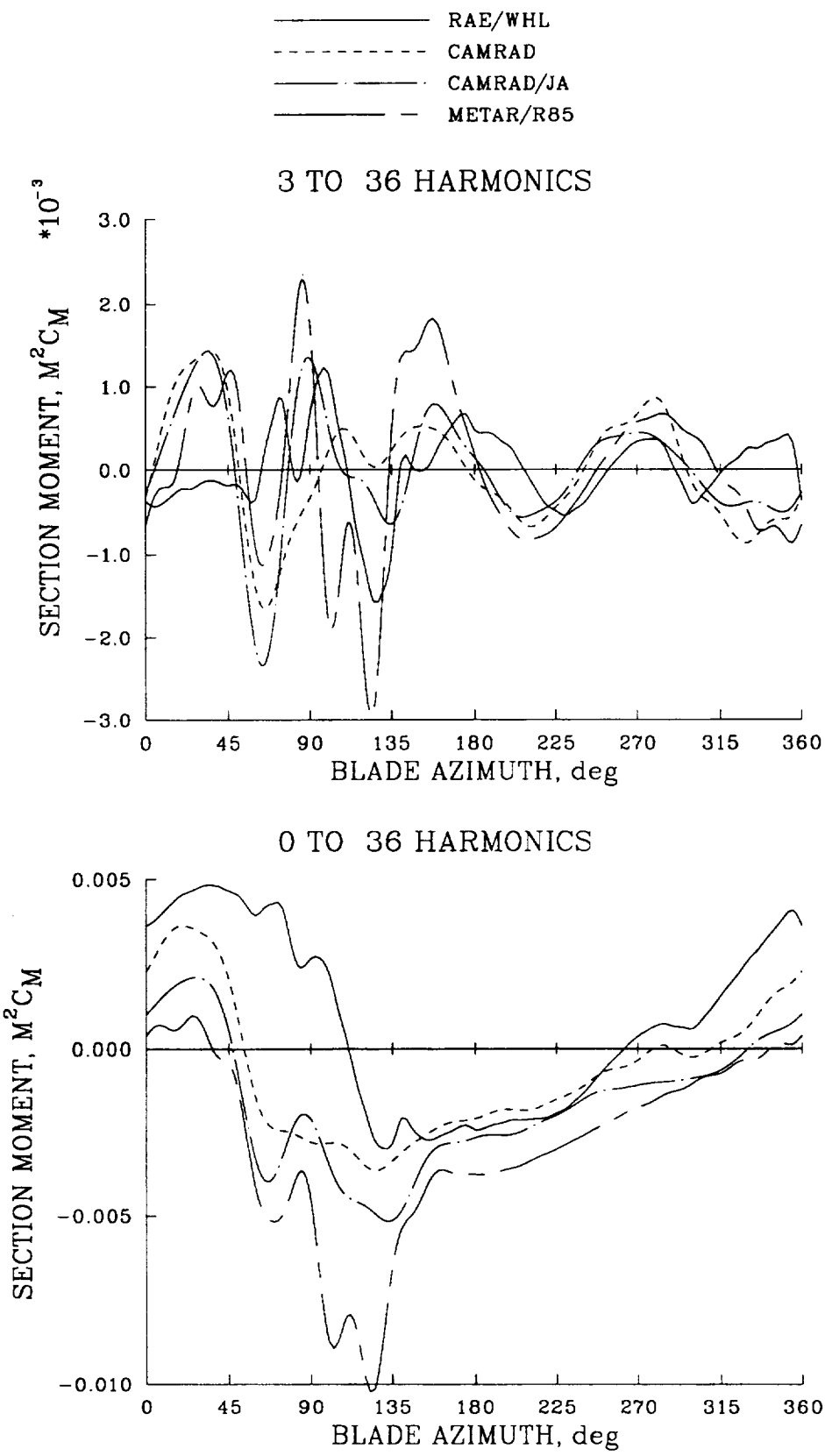


Figure 160. Calculated pitching moment as a function of azimuth at $0.95R$; Flight 123, $\mu = 0.321$.

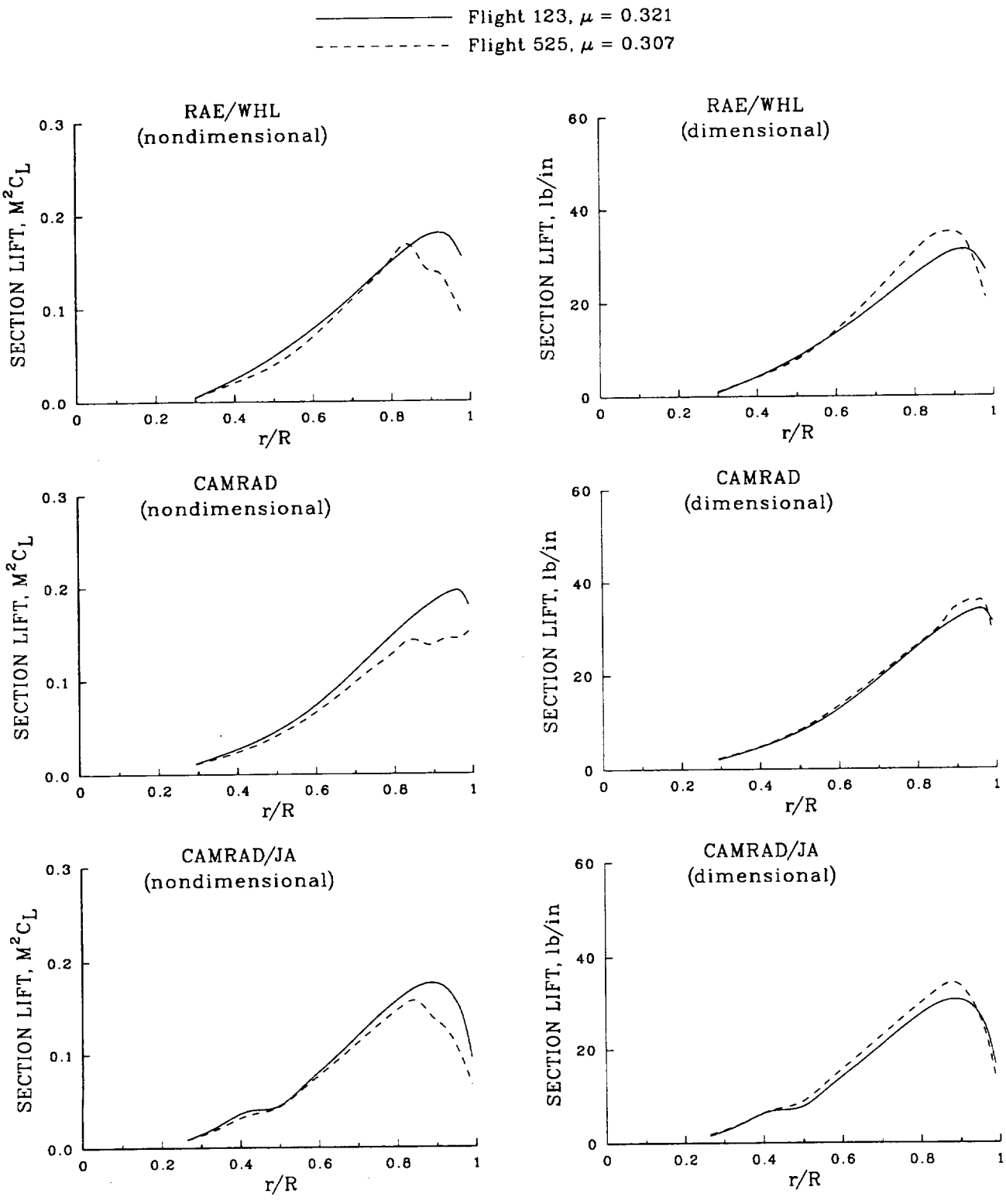


Figure 161. Comparison of calculated radial distributions of lift for a rectangular-tip and swept-tip blade; $\psi = 0°$.

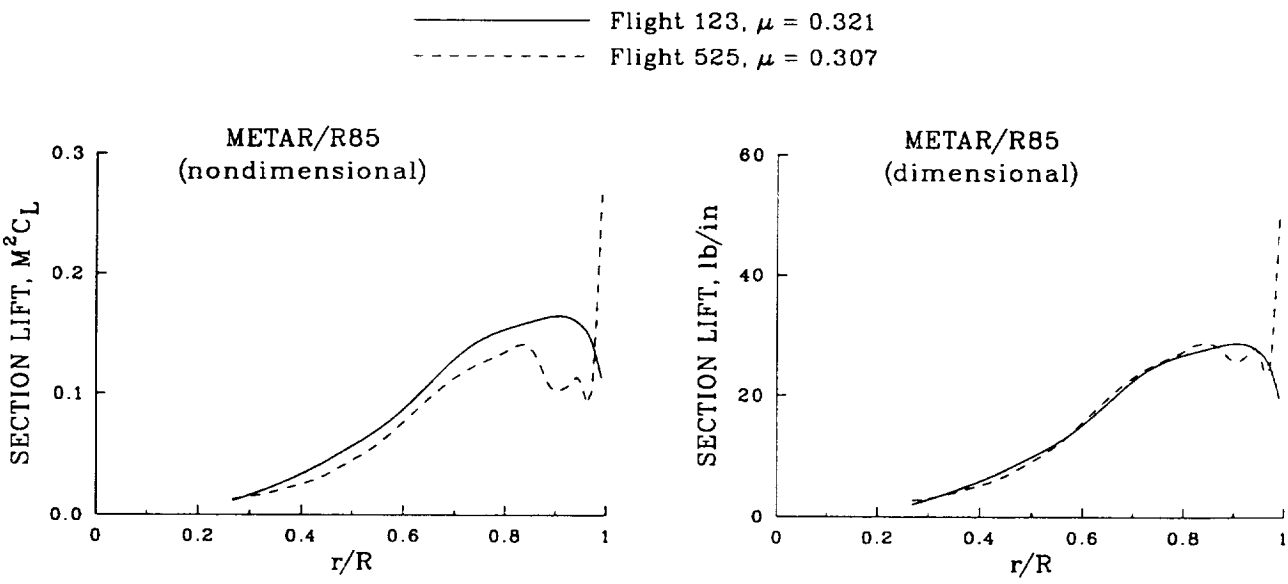


Figure 161. Concluded.

The lift distribution no longer appears singular at the tip for the METAR/R85 calculation of the rectangular-tip blade of Flight 123 compared to the swept-tip blade. As discussed previously in Section 5.2.2.2, the swept-tip singularity is related to modeling of the yawed flow at very large sweep angles and these are only associated with the swept tip.

The calculated section lift distributions at $0.95R$ are compared in figure 162 for the two flight conditions. The lift distributions calculated by each analysis are quite similar for the swept and rectangular-tip blades, although there are substantial differences seen between analyses. These comparisons suggest that tip sweep, at least based on these analyses, has a relatively small effect upon the section lift distribution of these two rotors.

An examination of the vibratory airloads, for harmonics 3 and above, as shown in figure 163, accentuates the conclusion relative to the influence of swept-tip effects on section lift. At this radial station there is very little difference between the two blade tips for any of the analyses. However, there are significant differences between the analyses, which suggests that modeling problems beyond tip sweep are the cause of the differences seen.

Figure 164 compares the section pitching moments computed by the four analyses for the two rotor blade tips. Unlike the calculation of section lift the effect of sweep does have a significant influence on the pitching moment prediction. The RAE/WHL analysis shows a significant increase in the section moment in the first and fourth quadrants and the peak-to-peak moment is doubled or tripled in comparison to the rectangular-tip blade. This provides better agreement with flight test measurements, see Section 5.2.2.2, but the cause of the increased loading is not understood. The effect of tip sweep for the CAMRAD analyses and METAR/R85 is to moderate and delay the negative loading on the

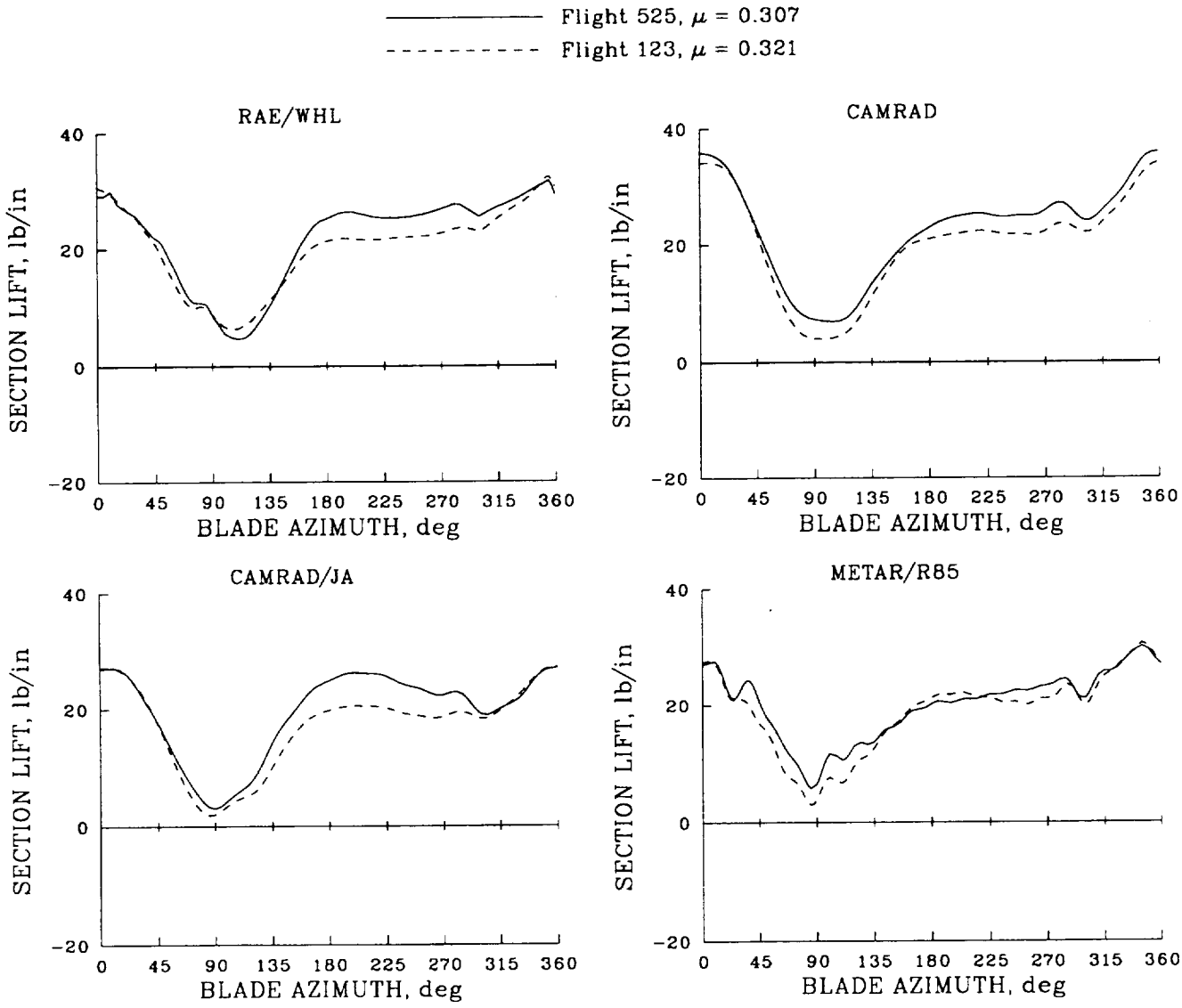


Figure 162. Comparison of section lift for a rectangular-tip and swept-tip blade; $0.95R$.

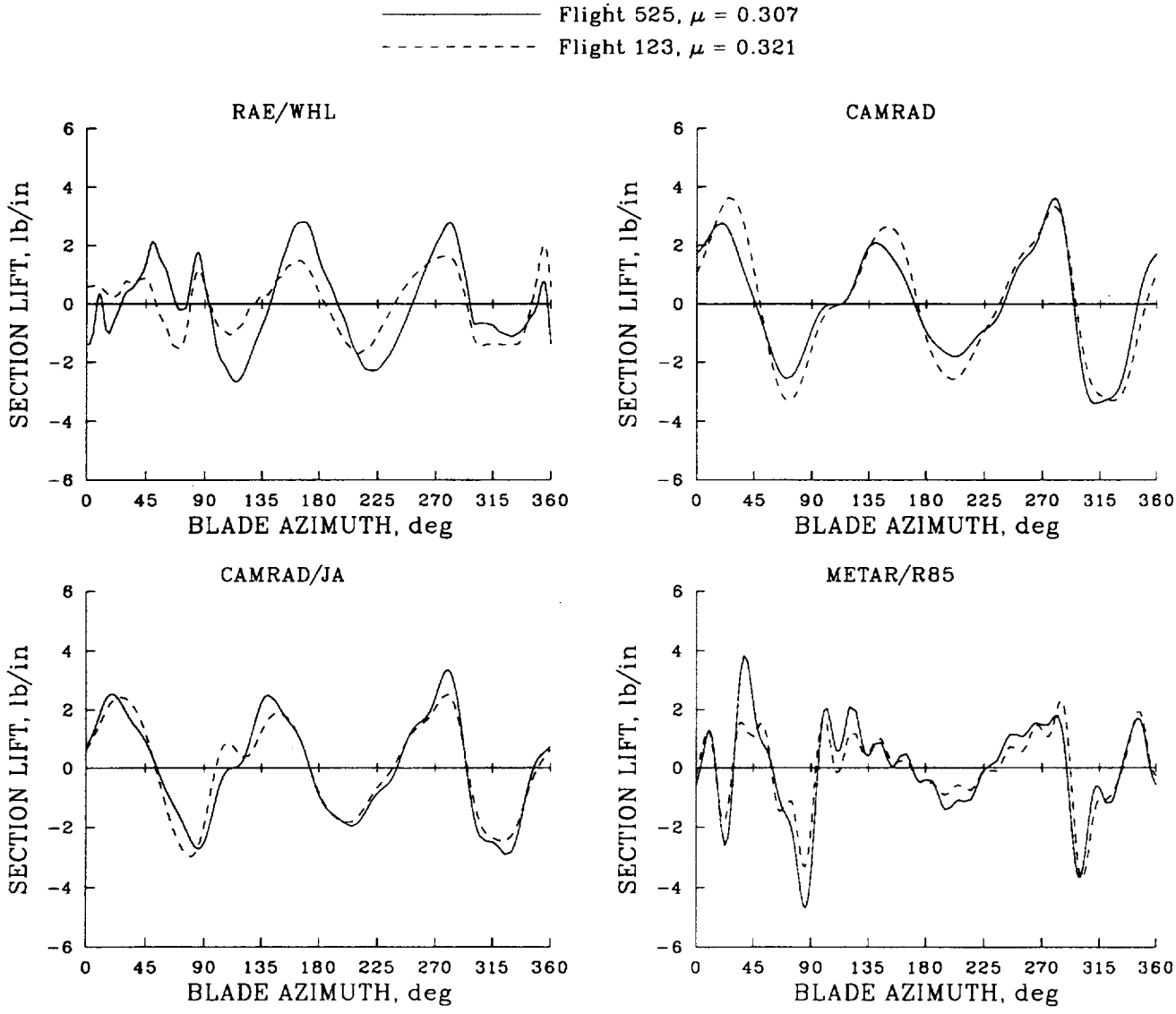


Figure 163. Comparison of vibratory section lift for a rectangular-tip and swept-tip blade; $0.95R$, harmonics 3 and above.

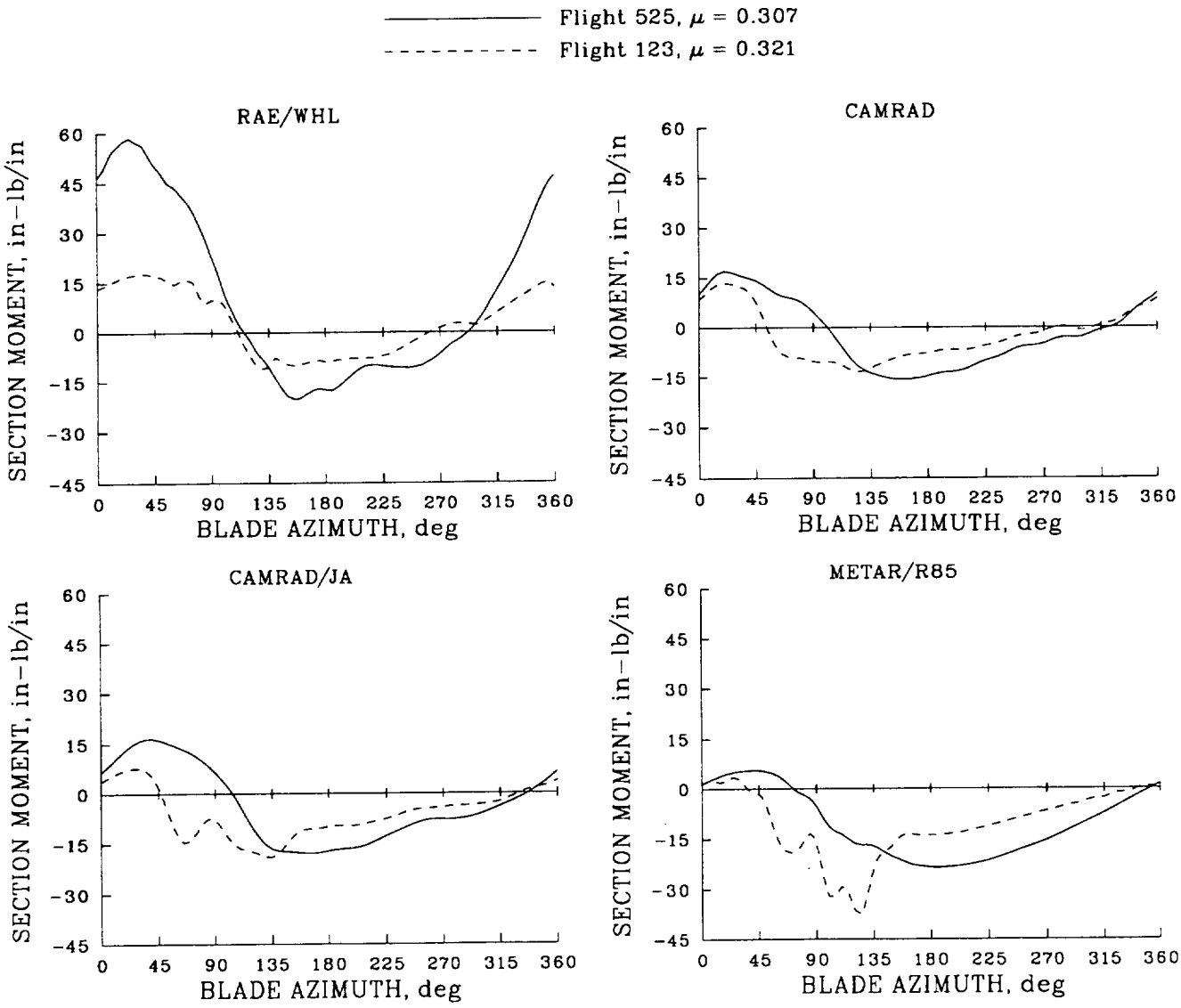


Figure 164. Comparison of section pitching moment for a rectangular-tip and swept-tip blade; $0.95R$.

advancing side. These analyses incorporate the aerodynamics of tip sweep by computing the Mach number that is normal to the local quarter chord, rather than the Mach number normal to the blade's feather axis and it is this local Mach number that is used to determine the section properties from the two-dimensional look-up tables. The effect of tip sweep, therefore, is to reduce the Mach number in the first quadrant and increase it slightly in the second. However, the peak-to-peak variation in the predicted pitching moments is largely unchanged.

5.3.3.3 *Blade Moments and Loads*

The moments measured on the blade for Flight 123 were the flap bending moment at $0.35R$, $0.45R$, $0.55R$, $0.65R$, $0.75R$, $0.83R$, $0.90R$ and $0.95R$, the chord bending moment at $0.33R$ and $0.73R$, and the torsional moment at $0.33R$ and $0.73R$. The chord moment strain-gauge at $0.33R$ radius failed, however, and no useful data were obtained at this position. The steady component of the blade moments has been removed since the zero readings were taken with the blade resting on the flapping stops of the helicopter. The analyses used to correlate with the test data are the RAE/WHL analysis, CAMRAD and CAMRAD/JA.

The measured and predicted flap bending moment at $0.35R$ is presented in figure 165. The correlation between the test data and the RAE/WHL analysis is generally good although the harmonic analysis, figure 166, shows that the third harmonic component is underestimated. The CAMRAD/JA prediction is slightly better than that of CAMRAD, particularly on the advancing side of the disk but the azimuthal variation of the moment on the retreating side is not accurate in either calculation.

The flap bending moment for an articulated rotor is a maximum at about $0.75R$ radius and figure 167 compares the measured and calculated moments at this station. The peak on the retreating side of the disk is underestimated by all the analyses but the RAE/WHL method is generally the best on the advancing side of the disk.

The chord bending moment for an articulated rotor is harder to predict accurately than the flap bending moment. The Puma rotor has a hydraulic lag damper which cannot be modeled in the calculation of the blade modes and its effect on the rotor has to be included in the solution of the forced response equation. A lag damper is not modeled in the RAE/WHL analysis but a linear model is included in the other methods. The force that the damper exerts near the blade root cannot be calculated if modal summation is used to calculate the bending moment and recourse must be made to the force integration method or the unified method of Hansford (1985). The flexibility in the gearbox and other elements of the transmission system must be accounted for as well although obtaining the relevant data is difficult.

The measured and calculated chord bending moments at $0.73R$ are compared in figure 168 and the harmonics are presented in figure 169. The test data have a pronounced 4/rev component and there are smaller oscillations at 6 and 10/rev. The prediction by the RAE/WHL analysis does not compare well with the measurements. The first harmonic variation is underestimated and there is a 5/rev oscillation which is consistent with the calculated chord mode frequency of 4.78/rev. CAMRAD and CAMRAD/JA overestimate the magnitude of the oscillatory bending moment, particularly the second and third harmonic components for CAMRAD and the first, second and third harmonics for CAMRAD/JA. The 4/rev oscillation is not predicted by any of the analyses even when the damper is

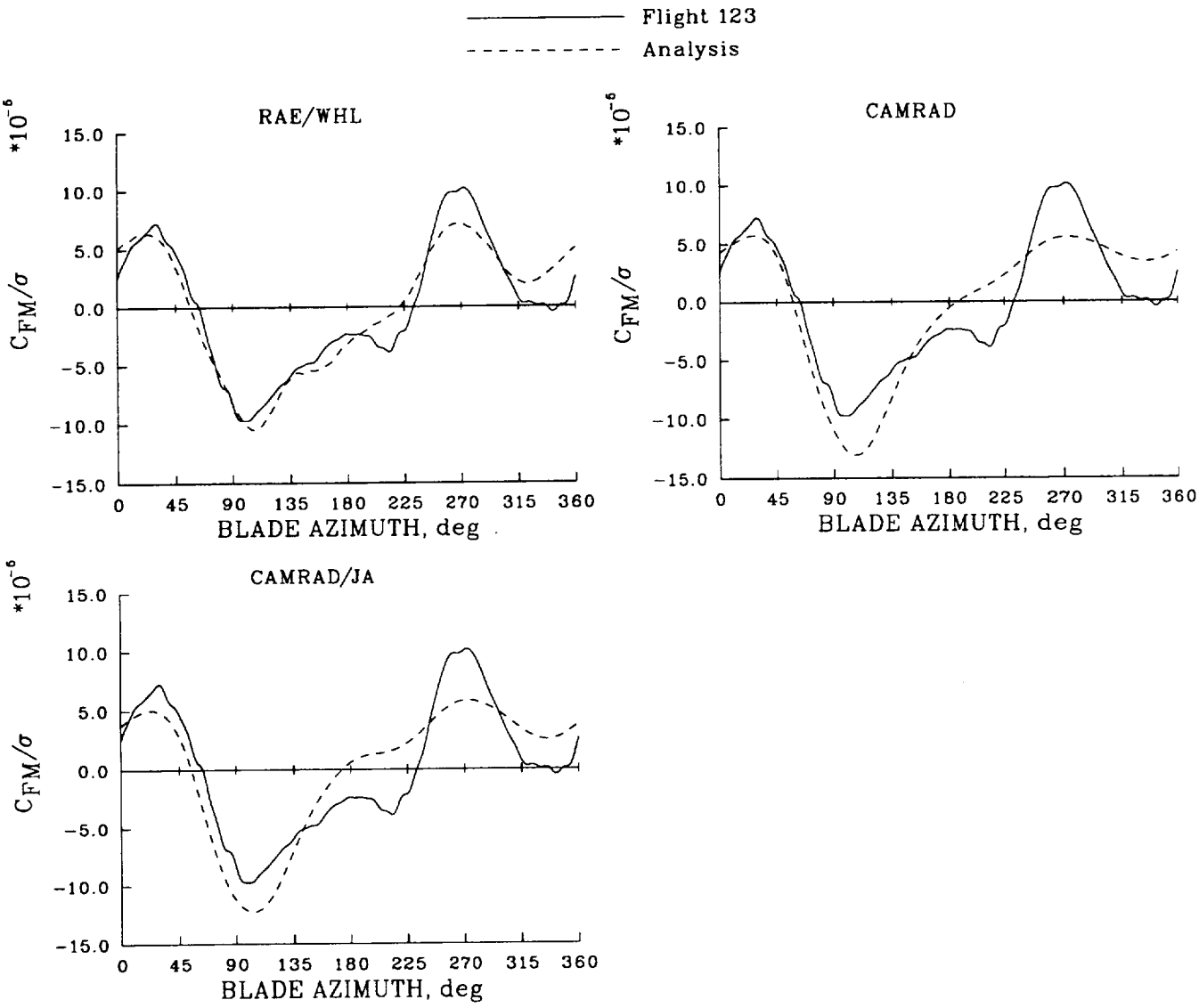


Figure 165. Comparison of measured and calculated flap bending moments as a function of azimuth for Flight 123; $0.35R$, $\mu = 0.321$.

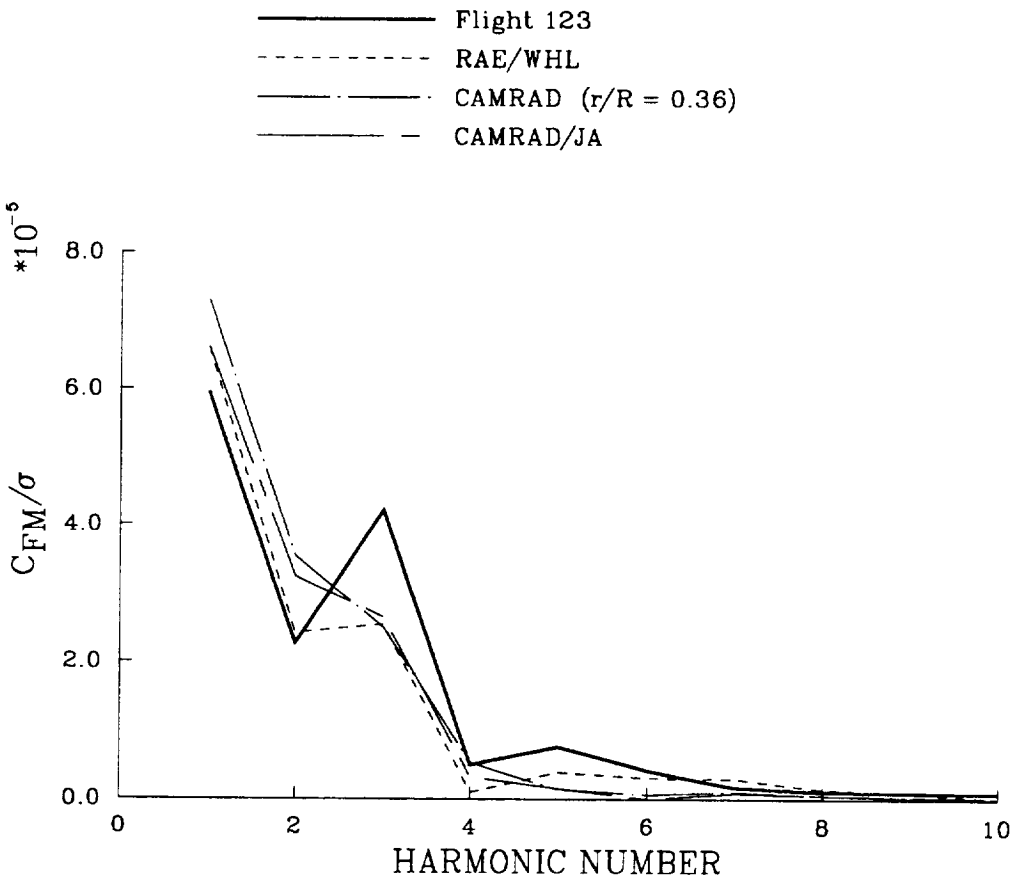


Figure 166. Comparison of measured and calculated flap bending moment harmonics for Flight 123; $0.35R$, $\mu = 0.321$.

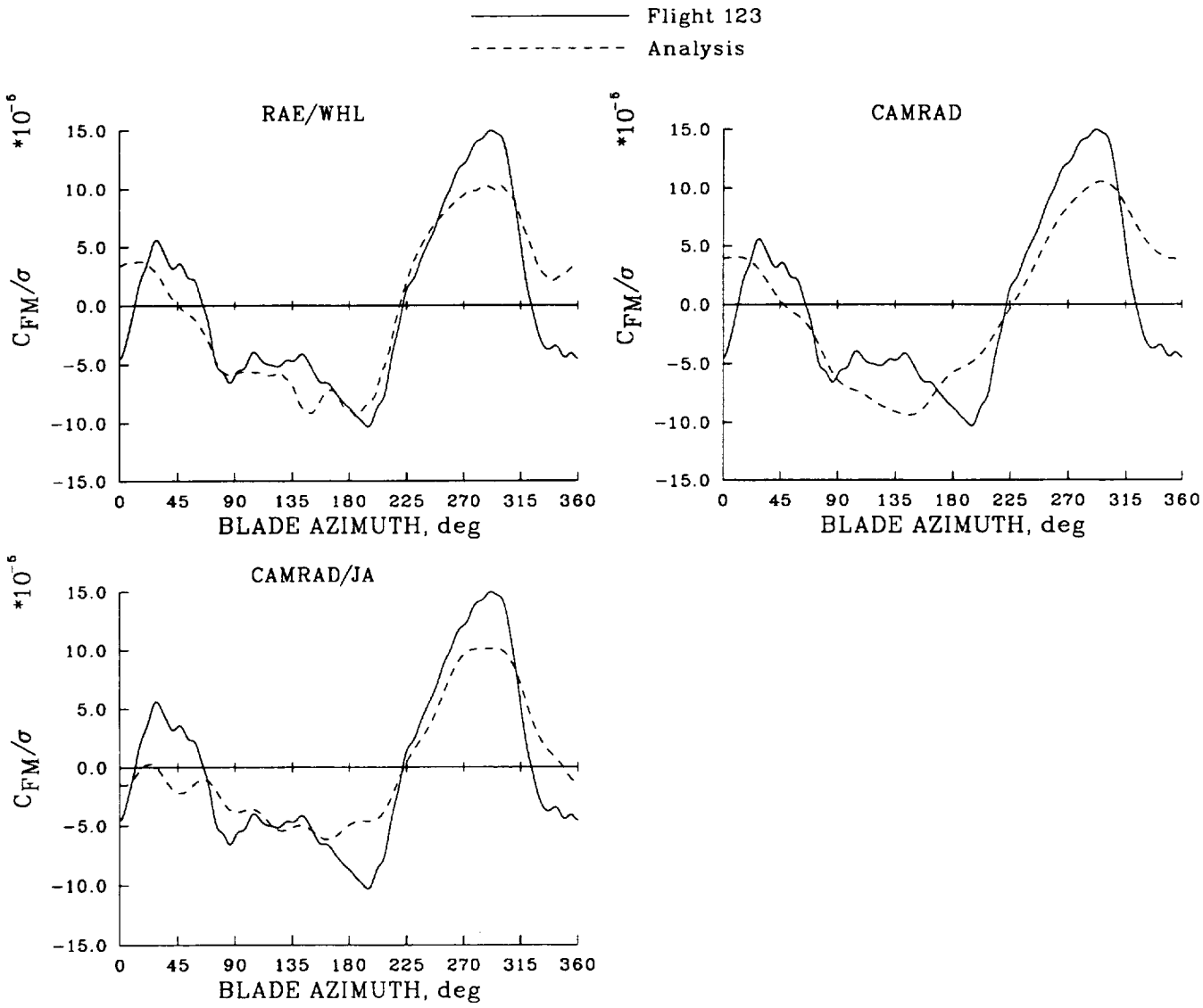


Figure 167. Comparison of measured and calculated flap bending moments as a function of azimuth for Flight 123; $0.75R$, $\mu = 0.321$.

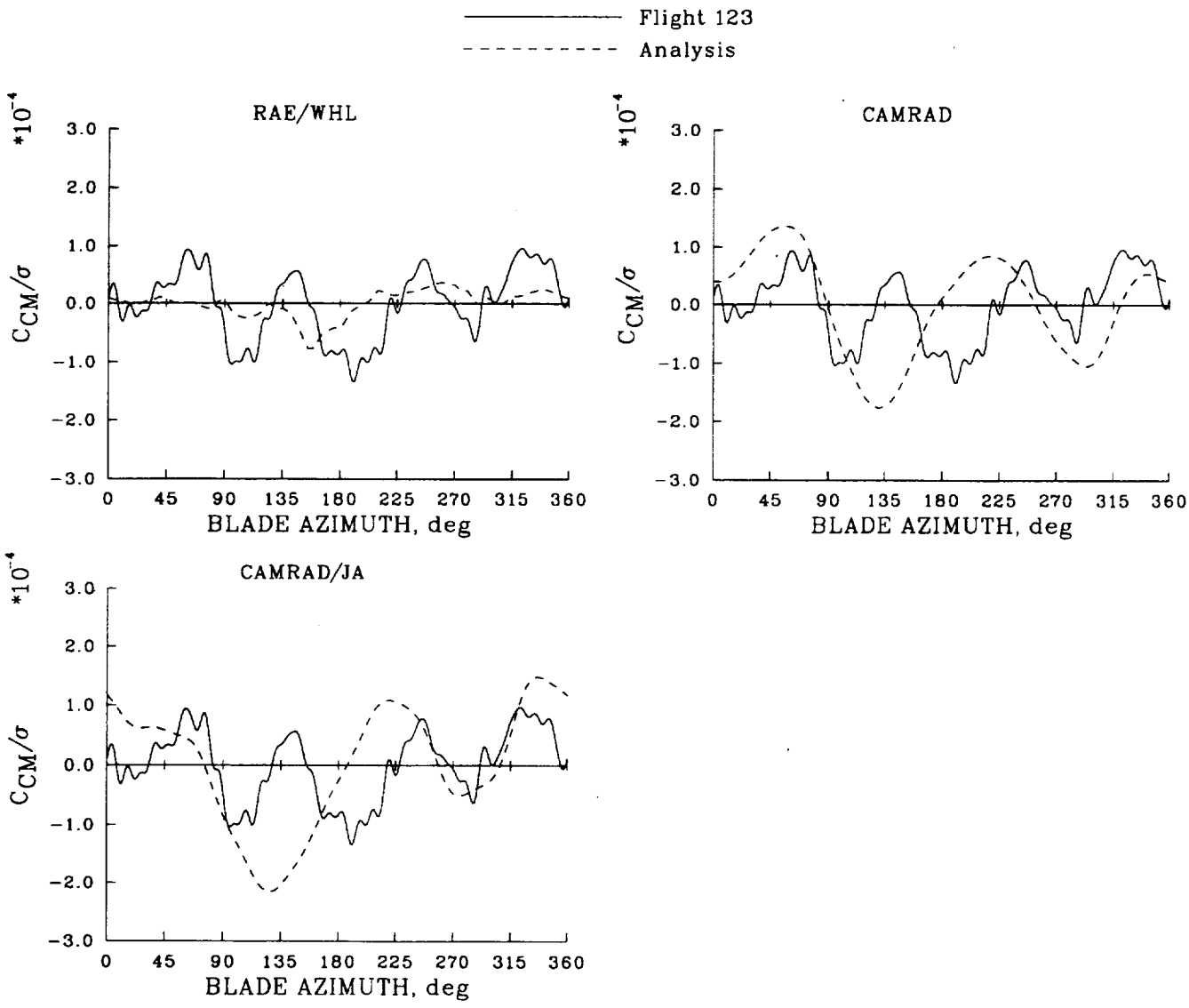


Figure 168. Comparison of measured and calculated chord bending moments as a function of azimuth for Flight 123; $0.73R$, $\mu = 0.321$.

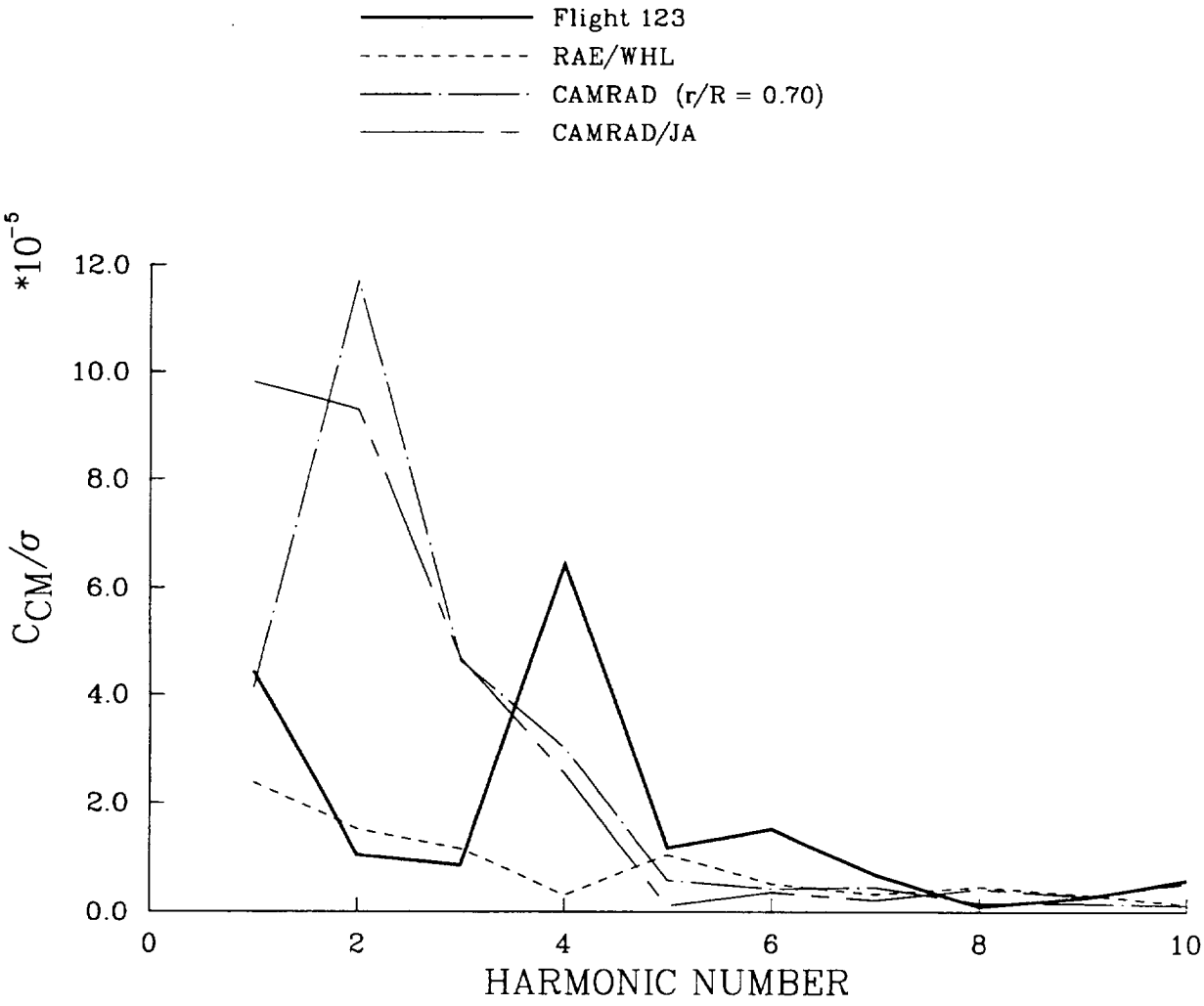


Figure 169. Comparison of measured and calculated chord bending moment harmonics for Flight 123; $0.73R$, $\mu = 0.321$.

included which suggests that the calculated second lag mode frequency is too high and that there is some flexibility in the transmission that detunes the mode.

The prediction of the torsional moment can, like the edgewise moment, present problems for rotor analysts. Much depends on the relative stiffness of the blade to the control system. A blade that is fairly flexible coupled to a stiff control system appears to present few problems and difficulties arise as the control system stiffness is reduced. The control system of the Puma is midway between the two extremes of low blade stiffness coupled to a high stiffness control system and a high blade stiffness blade with a soft control system. The RAE/WHL modal calculation shows that about half the torsional displacement at the blade tip occurs at the feathering bearing with the other half developing along the blade.

The torsional moment was measured at two radial stations for Flight 123 but only the inboard position, at $0.33R$, is considered as the variation with azimuth is similar farther outboard but of smaller magnitude. The test data and the calculations are compared in figure 170. The prediction using the RAE/WHL analysis does not agree with the measurements very well and a Fourier analysis shows that the first six harmonic components are only about half the experimental values. CAMRAD predicts the oscillatory torsion moment quite accurately as the first harmonic component is in good agreement with the test data. The shape of the waveform is wrong, however, since the second to fifth harmonic components are underpredicted. The CAMRAD/JA predictions are similar to those of the RAE/WHL analysis.

It is useful to compare the computed moments for the rectangular-tip blade (Counter 9, Flight 123) with the moments for the swept-tip blade (Counter 12, Flight 525) just as was done for the computed airloads in Section 5.3.3.2. This comparison is enhanced for the moments as experimental data are available in this case and can be compared at the same time. Figures 171 and 172 compare the predictions of the RAE/WHL, CAMRAD, and CAMRAD/JA analyses as well as the measured values for the flap bending moments at two radial stations. The measured flap bending moments are quite similar between the two flights and, therefore, the effect of tip sweep is not highly important. At the more outboard station it appears that there is a slight reduction for the bending moments for Flight 525 although this may be a consequence of the reduced advance ratio. The analytical predictions show fair-to-good agreement with the data as has been discussed previously in Section 5.2.2.3 and in this section. The comparison between flight cases, based on the analytical computations, shows only small differences and it appears that tip sweep has less of an influence on the moments than modeling differences between the analyses.

A comparison of the chord bending moments at $0.73R$ for the two flight test cases is shown in figure 173. None of the analyses predict the chord bending moments well, as has been discussed previously, and it is clear that tip sweep has little to do with this poor prediction of the chord bending.

The torsion moments at $0.33R$ are compared for the two flight cases in figure 174. There is an increase in the torsion moments for Flight 525 for the blade with a swept tip and this is seen in both the measurements and the calculations. As discussed previously, all of the analyses underpredict the torsion load amplitudes and the CAMRAD analysis shows a significant phase error as well. It is clear from this comparison that modeling assumptions used for the swept tip are not a primary contributor

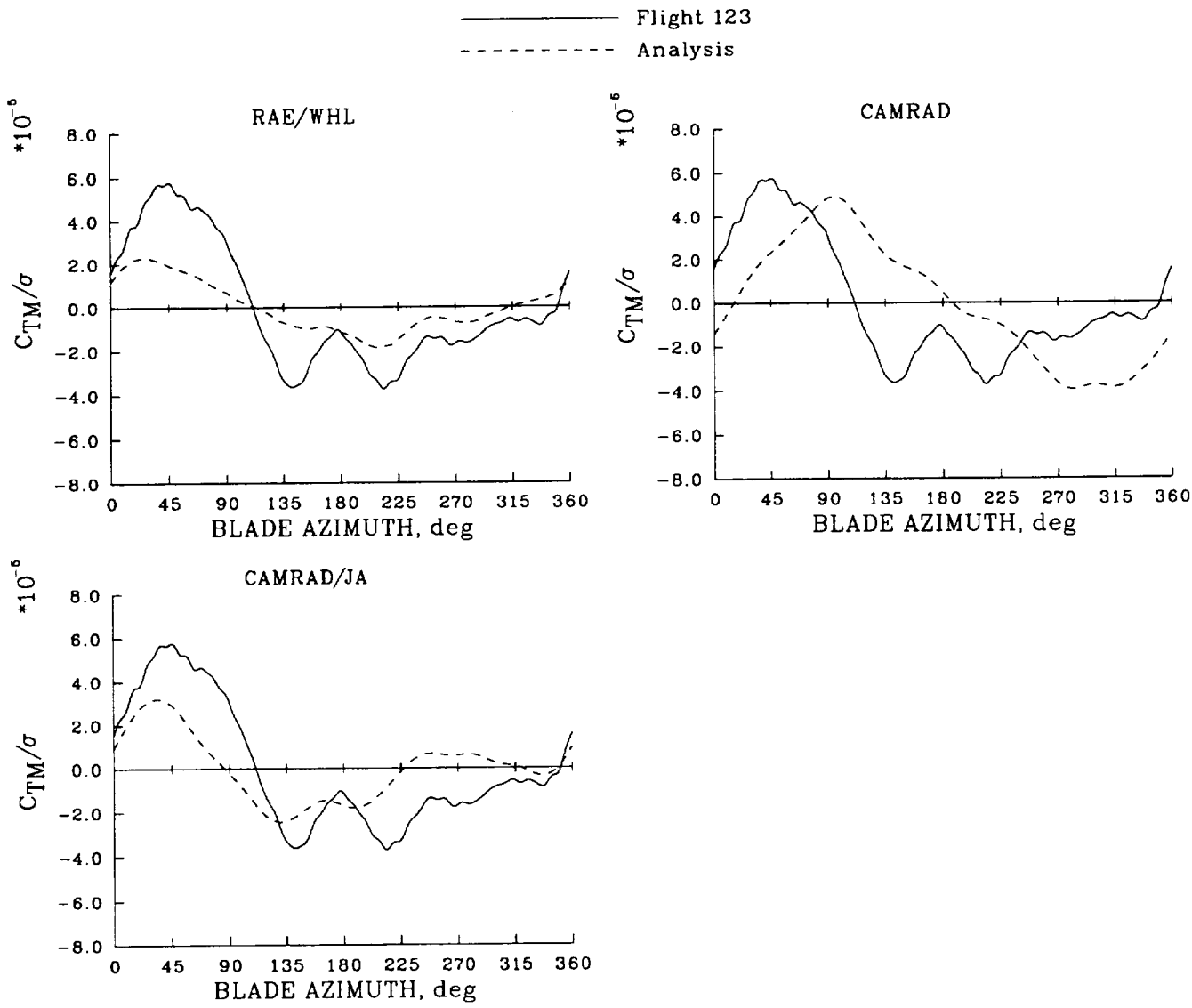


Figure 170. Comparison of measured and calculated torsion moments as a function of azimuth for Flight 123; $0.33R$, $\mu = 0.321$.

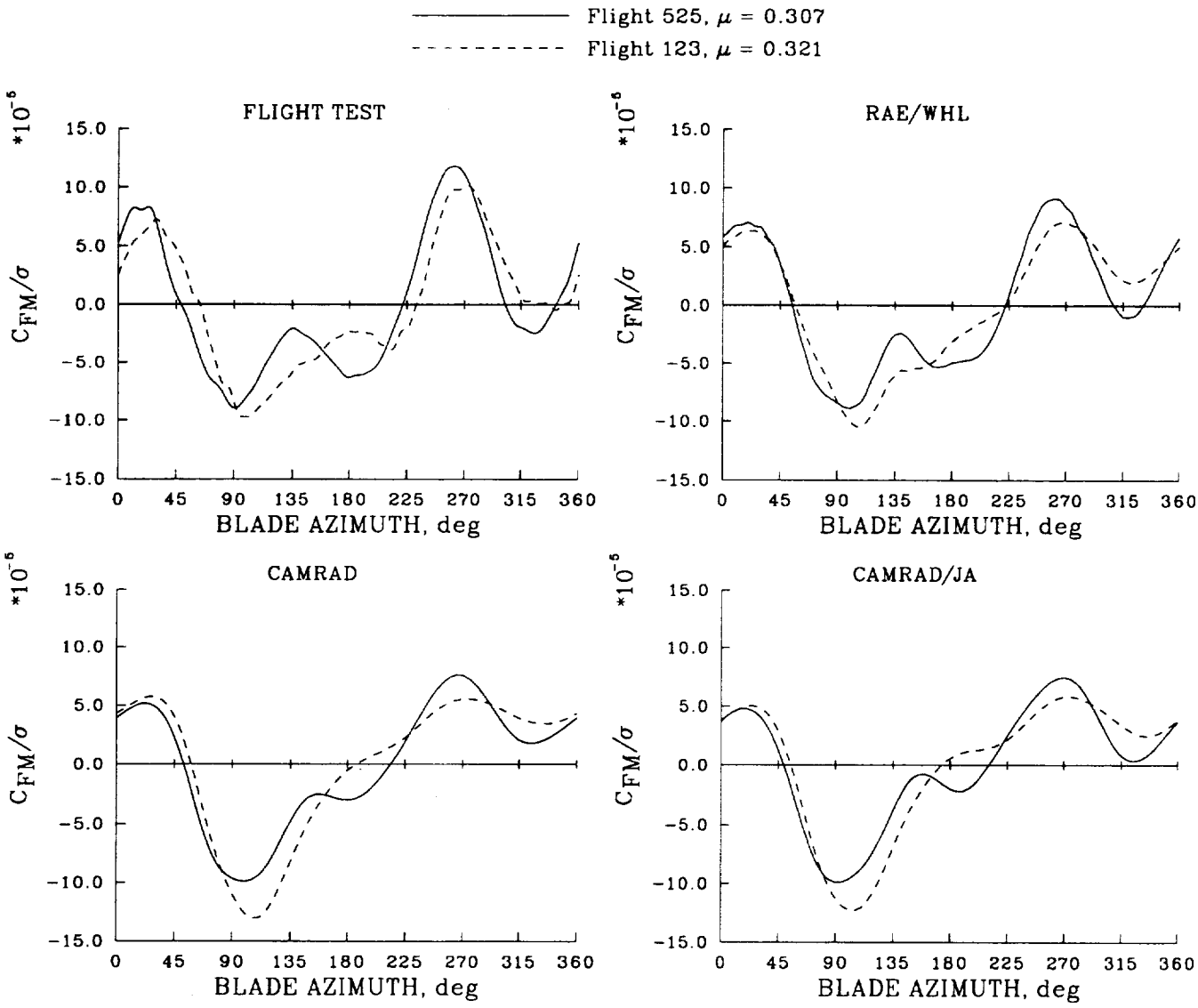


Figure 171. Comparison of measured and predicted flap bending moments for flights 525 and 123; $0.35R$.

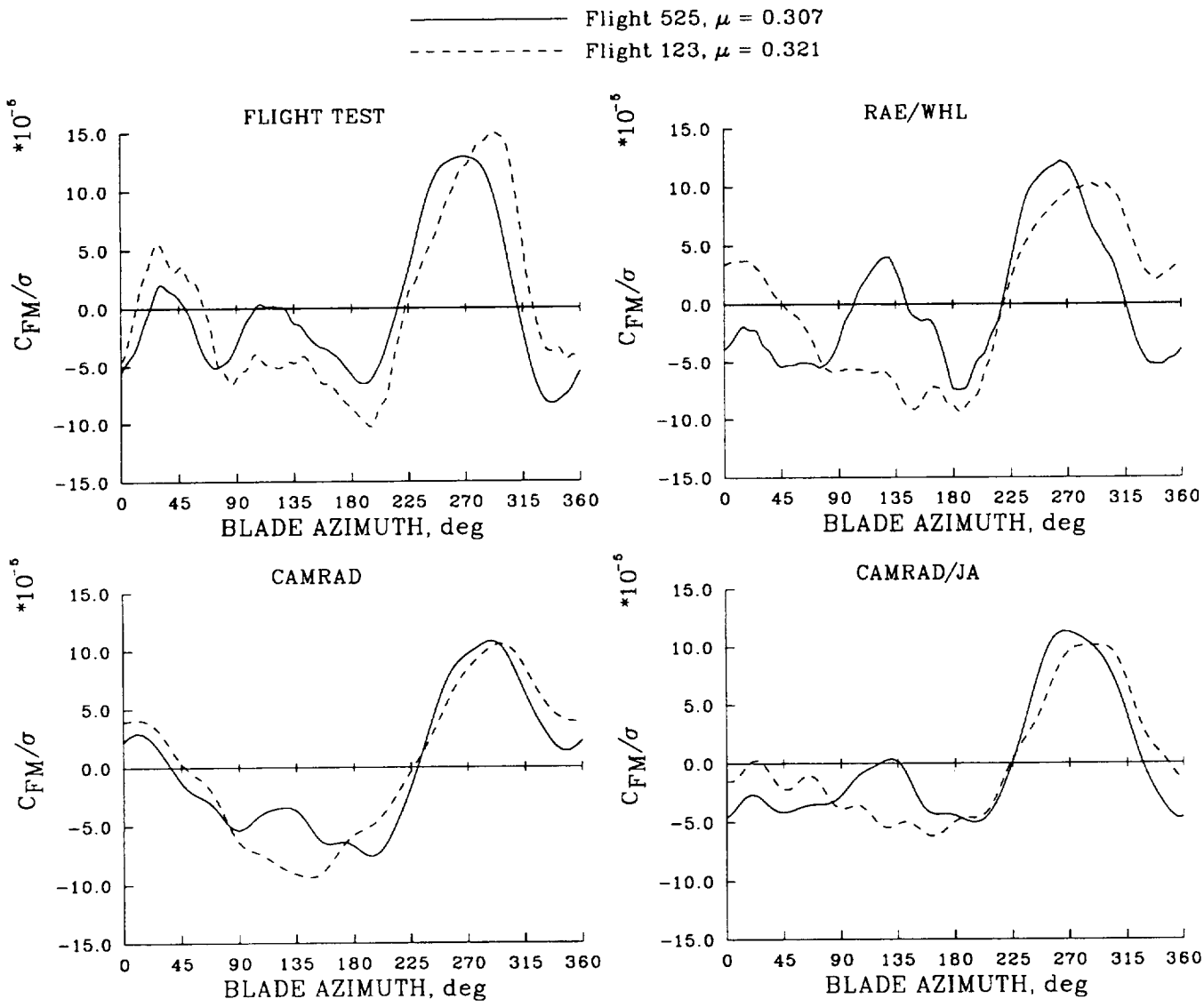


Figure 172. Comparison of measured and predicted flap bending moments for flights 525 and 123; $0.75R$.

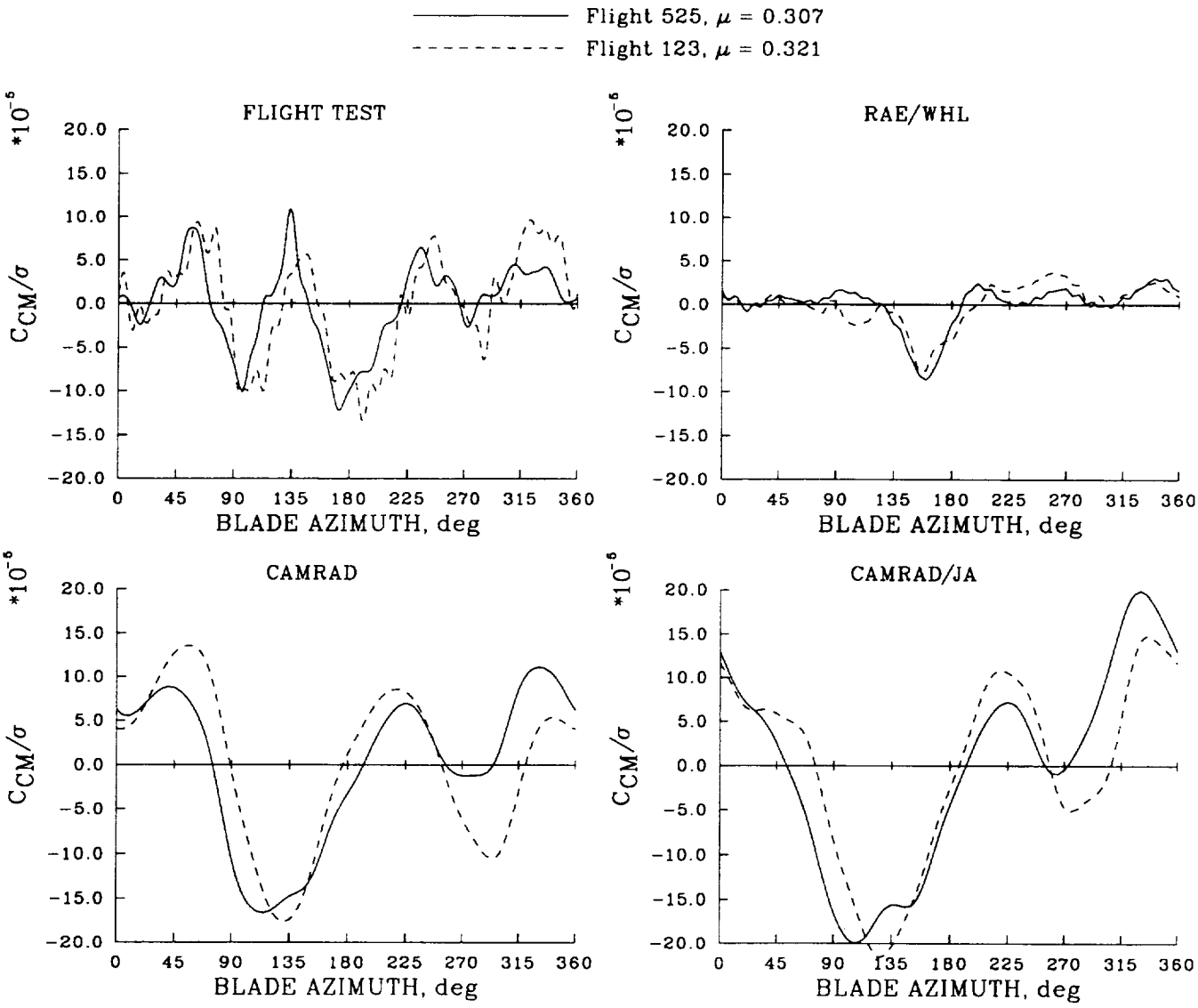


Figure 173. Comparison of measured and predicted chord bending moments for flights 525 and 123; $0.73R$.

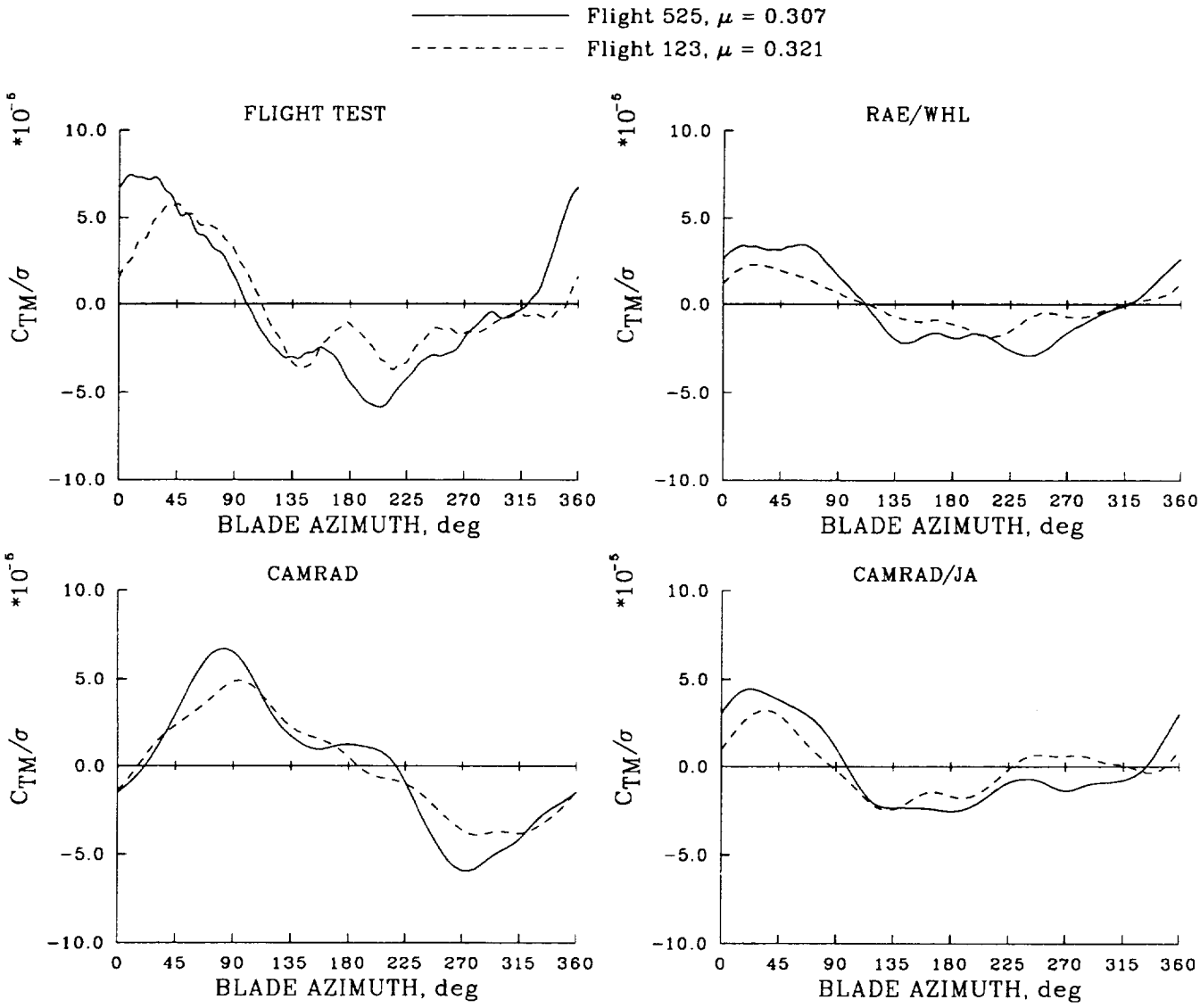


Figure 174. Comparison of measured and predicted torsion moments for flights 525 and 123; $0.33R$.

to the unsatisfactory predictions; rather there are more fundamental problems with the prediction of the torsional loads.

### 5.3.4 Summary of Reference Case Investigation

Experimental blade moment data from Flight 123, a test of the standard Puma blade with a rectangular tip, were included in the joint study to provide a reference case to better understand the effects of the swept tip on the airloads and structural loads of the Puma. This reference case has been helpful in sorting out the influence of the swept tip and where it is important and where it is not.

The comparison of the calculated airloads (there are no measured airloads for Flight 123) suggests that tip sweep has only a minor effect on the distribution of the section normal force and the differences between analyses in the prediction of normal force are significantly greater than the differences between a rectangular or swept tip for any one analysis. This conclusion does not hold, however, for the section pitching moment. The RAE/WHL analysis shows a significant increase in the oscillatory pitching moment induced by tip sweep while the other analyses show modification to the pitching moment distribution because of the lower effective Mach number over the blade tip.

The comparison of blade moments between the swept-tip cases and the reference case is enhanced over the case of the airloads in that experimental data are compared as well as the analytical predictions. All of the analyses correlate fairly well with the test data for the flap bending moment and differences that are observed between the swept tip and the rectangular tip experimentally are, in general, smaller than differences that are seen between the analytical methods. None of the calculation methods calculated the chord bending moment accurately. The large fourth harmonic component was absent in the calculations probably because the frequency of the second lag mode was too high. For these calculations it is clear that the effect of sweep has little to do with understanding the differences between measurement and analysis. The RAE/WHL and CAMRAD/JA analyses underpredicted the magnitude of the torsional moment while CAMRAD, although estimating the magnitude correctly, was unable to predict the shape of the waveform. The inability of the analyses to calculate the torsion accurately was possibly due to the lack of an azimuthal variation in the control system stiffness or the use of a collective torsion mode when coupled rotor modes, that is, collective and cyclic modes, are required instead.

## 5.4 Autorotational Case (Flight 487)

### 5.4.1 Flight Data

A single test point was selected from Flight 487 where the aircraft was in an autorotational dive and the rotor speed was increased to create a high advancing blade tip Mach number. The conditions for this case, Counter 11, are tabulated in table 24.

A planform view of the instrumented blade is shown in figure 175. The pressure instrumentation is the same as for Flight 525; however, the number of working strain gauges was considerably reduced for this flight. Satisfactory measurements of the flap bending moment were obtained at $0.46R$, chord bending moments at $0.33R$ and $0.55R$, and torsion moment at $0.126R$, $0.33R$, and $0.55R$. The measurements

Table 24. Trim conditions for Counter 11, Flight 487

| Parameter | Flight 487 (Counter 11) |
|---|---|
| $\mu$ | 0.429 |
| $M_{90}$ | 0.922 |
| $C_T/\sigma$ | 0.0731 |
| $\alpha_s$, deg | 5.77 |
| $\beta_{1c}$, deg | −2.19 |
| $\beta_{1s}$, deg | −1.22 |
| $\Omega$, rpm | 273.2 |

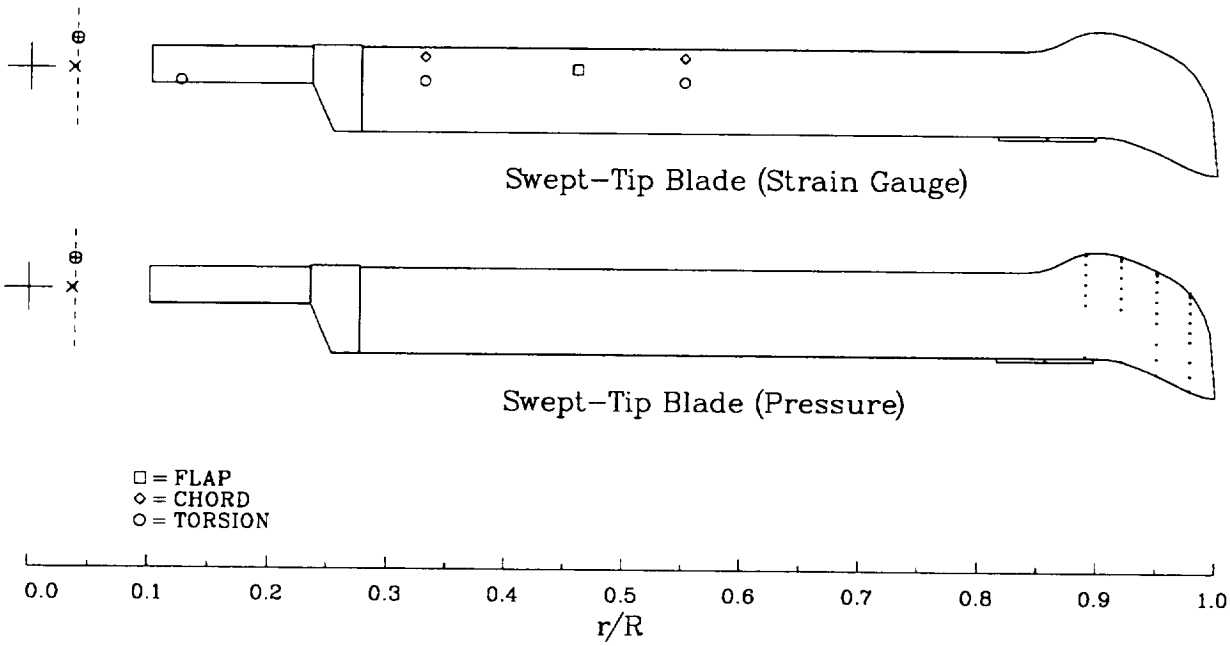


Figure 175. Instrumentation on Flight 487.

of the blade root angles were contaminated by noise and no satisfactory measurements of the pitch-link loads were obtained.

The collective and cyclic pitch angles were substantially reduced for the Flight 487 autorotational dive condition and the blade flapping changed relative to level flight so that the disk plane was tilted back. Figure 176 compares the pitch angle for the Flight 487 autorotational case with Counter 21 of Flight 525, the highest speed condition from that flight. Substantial contamination is seen in the root pitch angle measurement for Flight 487 but it appears that a representation of the contaminated signal, using only the steady and first harmonics, provides a reasonable approximation to the root pitch angle. Based on the 0th and 1st harmonics representation the collective pitch is reduced from 17.77° for Flight 525 to 5.45° for Flight 487 and the cyclic pitch is reduced from ±11.05° to ±3.39°. The blade flapping is changed, as well, as shown in figure 177. Again, substantial contamination is seen

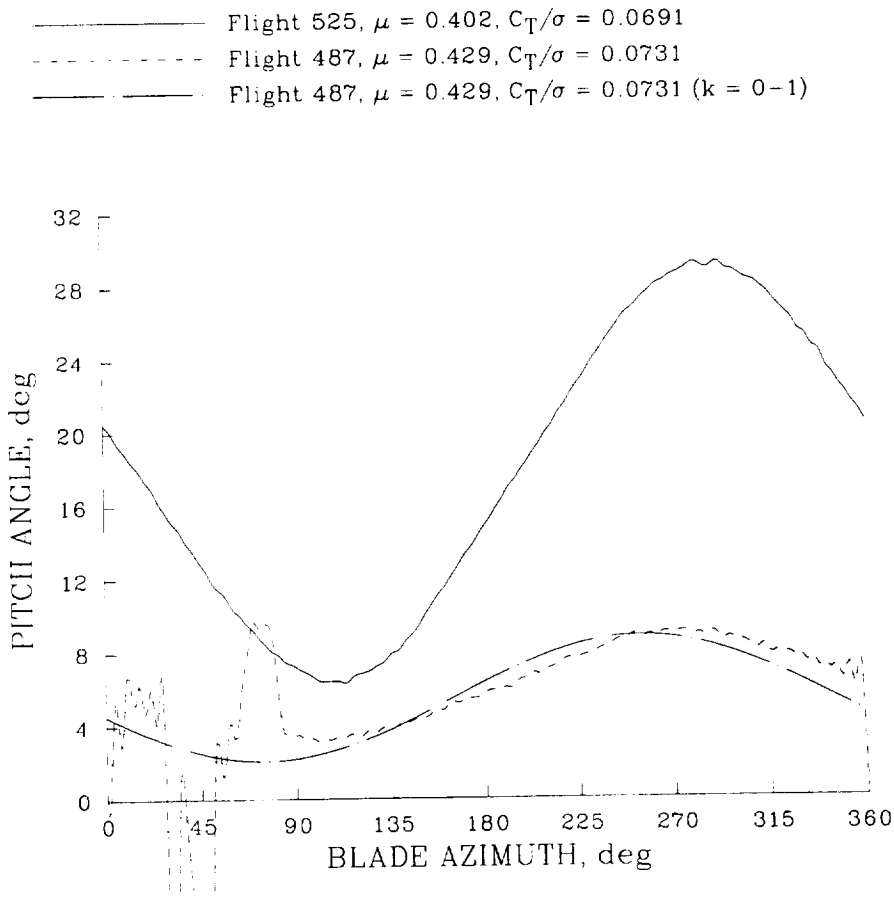


Figure 176. Comparison of root pitch angle for flights 487 and 525. Zeroth and first harmonic approximation included for Flight 487.

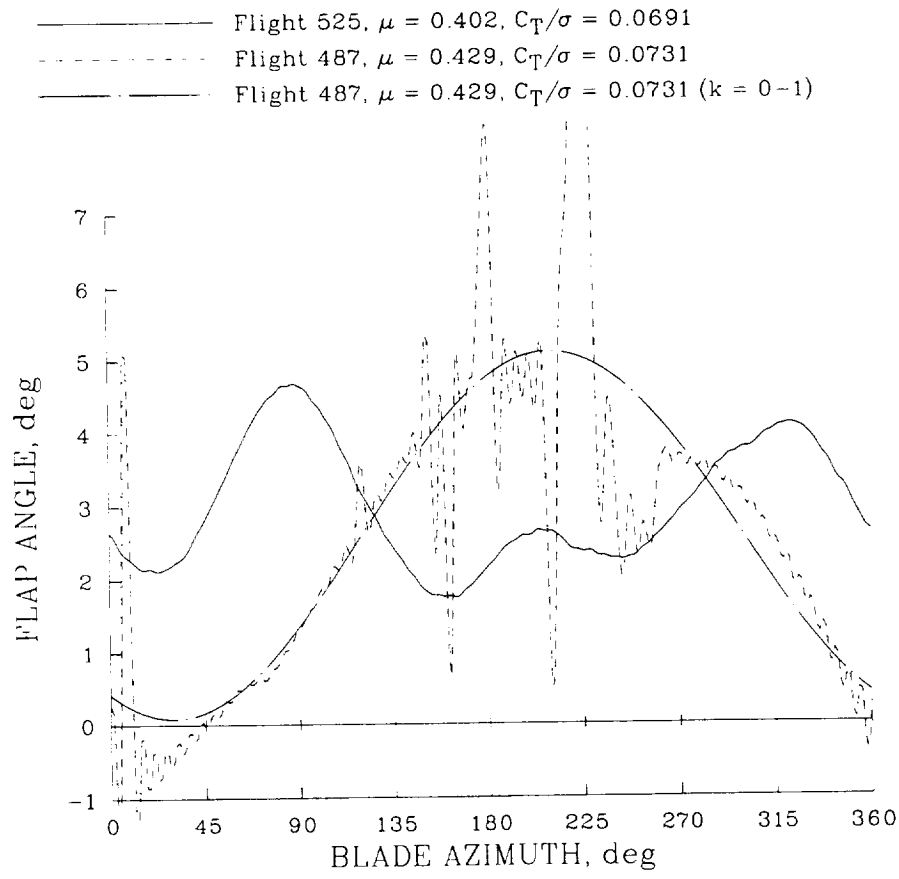


Figure 177. Comparison of blade flapping for flights 487 and 525. Zeroth and first harmonic approximation included for Flight 487.

in the Flight 487 data, but it appears from the approximation based on the zeroth and first harmonics of the measurement that the flapping is largely 1/rev and the disk is tilted towards the rear of the aircraft. Defining the disk angle of attack as $\alpha_d = \alpha_s - \beta_{1c}$, then, the angle of attack for Flight 487 is $7.95^\circ$ compared to $-9.49^\circ$ for Flight 525. It appears that there is is little 2/rev or 3/rev content in the Flight 487 blade flapping.

The section normal force and pitching moment at the three outboard stations for the Flight 487 autorotational case are compared in figure 178. The section normal force and the pitching moment data show large, higher harmonic oscillations, particularly on the advancing side. These oscillations are more noticeable for the pitching moment and are partly a consequence of the rapid movement of shocks on the upper and lower surfaces of the blade. In some cases the oscillations observed are partly an artifact of transducer sparseness. The loading variation that is seen at the rear of the disk, however, is a result of tip vortex induced loads. In the figures that follow, all of these features are discussed in detail because of the importance of this case for the CFD calculations in Section 6.

The upper surface pressures, from the leading edge to $0.55c$, are shown as a function of blade azimuth at $0.95R$ in figure 179. The sonic line or critical $M^2C_p$ is shown in this figure with a heavy dashed line. On the advancing side the upper surface pressures forward of $0.10c$ are subcritical, but aft of that point the shock passage over the pressure transducers is clearly seen and an area of supercritical flow exists on the airfoil surface as far back as $0.55c$. Although not shown in this figure, the supercritical flow does not extend as far back as $0.70c$, the next transducer location. On the retreating side the flow remains subcritical except for a small azimuthal range from about $330^\circ$ to $360^\circ$ where the flow is supercritical over the first 2% of the airfoil. A rapid variation in pressure is seen here and also at about $10^\circ$ in the first quadrant.

The azimuthal pressure behavior in figure 179 is shown in a different format in figure 180 where the pressure azimuthal histories are offset and ordered from front to rear on the airfoil. From $0.10c$ to $0.55c$ a region of supercritical flow develops over the upper surface in the last part of the first quadrant and the first half of the second quadrant. By $0.20c$ or $0.30c$ the passage of the shock over the transducer is clearly apparent as it first moves aft and, in the second quadrant, moves forward.

Pressure oscillations are also observed at the rear of the disk for this case. Wake calculations, such as by Egolf and Landgrebe (1983), suggest that these oscillations are related to the tip vortex of the previous blade that is "pinched off" and appears at the rear of the disk at this advance ratio for a four-bladed rotor. The first pressure peak, between $350^\circ$ and $360^\circ$, includes a region of supercritical flow and the azimuthal behavior indicates a convective event and it may be that the previous blade tip vortex has induced dynamic stall locally on the blade and the shedding of a small dynamic-stall vortex. The second pressure peak, at about $10^\circ$, appears to occur simultaneously along the upper surface and is induced by the previous blade's tip vortex. Vortex interactions of this nature were not observed for Flight 525 (Section 5.2.1), as the rotor disk was tilted forward and the trailed tip vortex wake was convected well away from the blade.

Vortices from the previous blade are also expected at the end of the first quadrant on the advancing side (Egolf and Landgrebe, 1983). However, no evidence of vortex intersections is seen in the pressure data and it seems likely that these vortices have been convected well away from the blade by the rotor inflow.

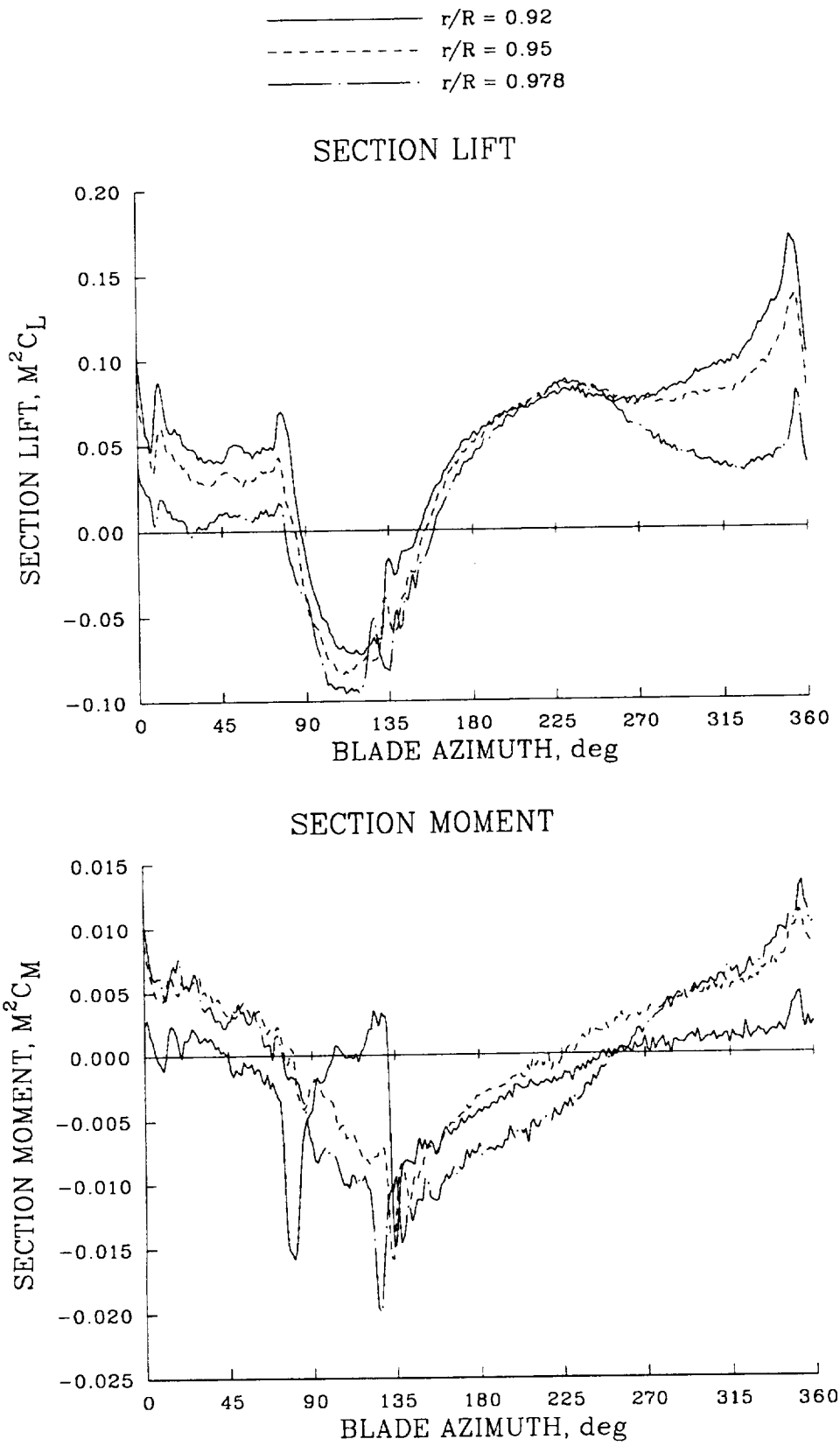


Figure 178. Section normal force and pitching moments; Flight 487.

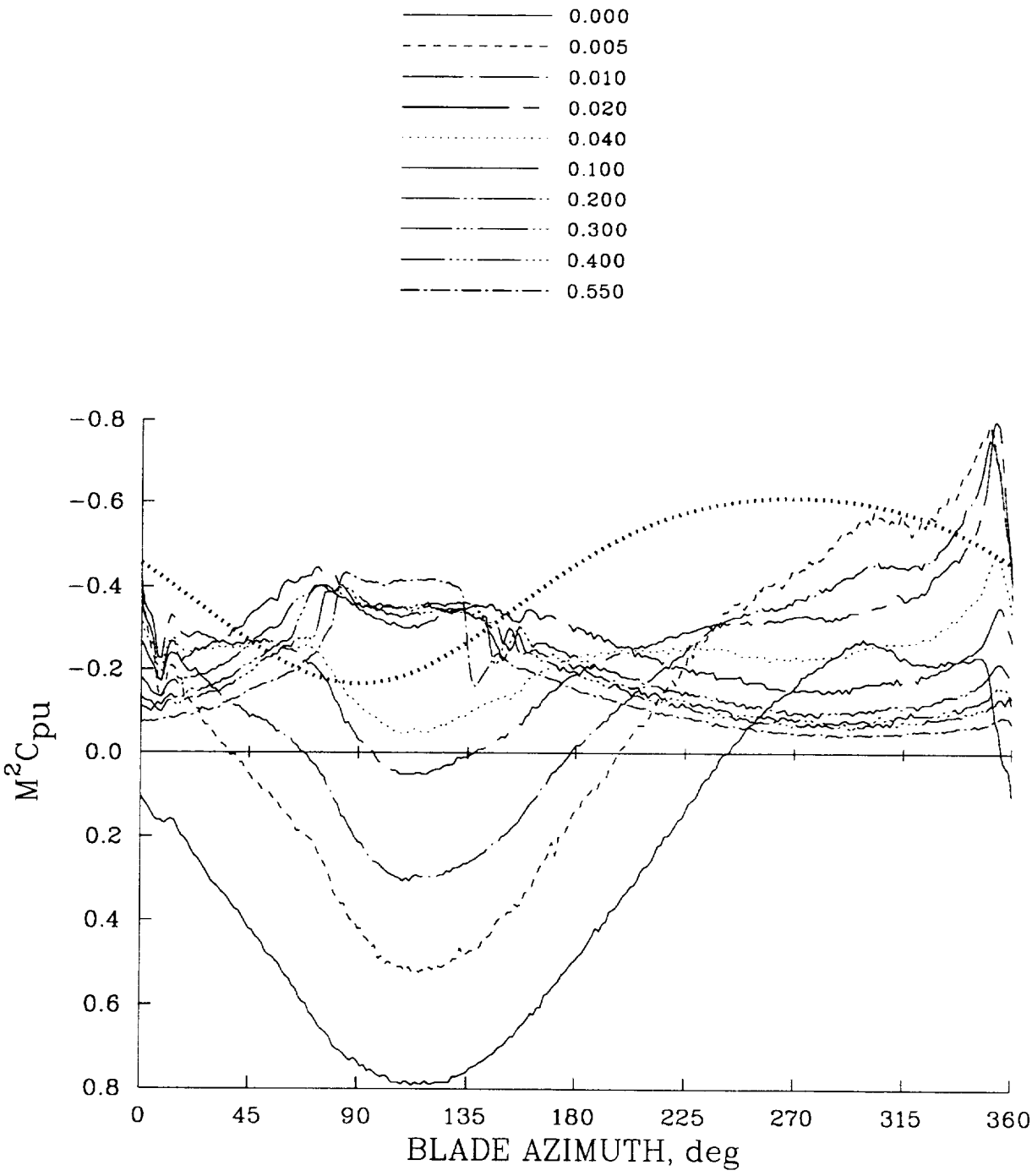


Figure 179. Upper surface pressures as a function of azimuth; $0.95R$, Flight 487. Sonic line shown as heavy dashed line.

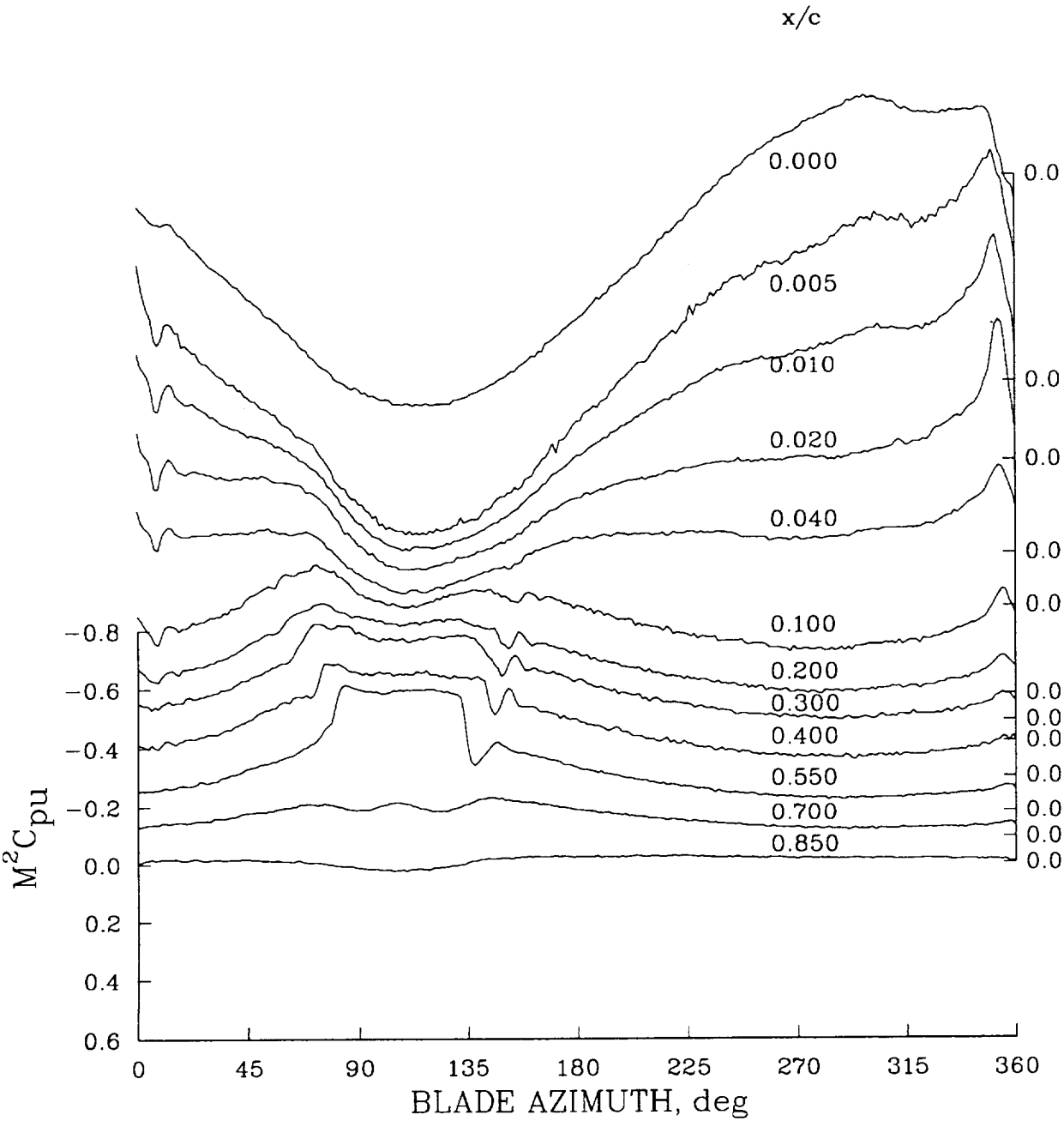


Figure 180. Offset plot of upper surface pressures as a function of azimuth; $0.95R$, Flight 487.

The distribution of the pressure on the lower surface at $0.95R$ is similar to the upper surface distribution as shown in the normal azimuthal plot, figure 181, and in an offset plot, figure 182. These figures show a region of supercritical flow at the end of the first quadrant and the beginning of the second that is similar to that seen on the upper surface. The effect of the previous blade's tip vortex is also apparent at the rear of the rotor disk, although the absence of pressure tranducers forward of $0.10c$ makes it difficult to determine whether the interaction is more intense on the upper or lower surface. A careful examination of the supercritical flow regions on both surfaces shows that these regions move fore and aft nearly simultaneously but slight differences in amplitude and phase between the two surfaces cause some of the higher harmonic oscillations that are seen on the advancing side in figure 178. These oscillations are probably accentuated by the lack of resolution in transducer spacing on the rear of the airfoil although the actual effect of the tranducer discretization is difficult to estimate. It is clear, however, that the large excursion in pitching moment at $0.92R$ that is seen in figure 178 on the advancing side is largely a result of an absence of transducers at $0.70c$ and $0.85c$ (see table 18).

The section normal force and pitching moment for the autorotational case in figure 178 are different from the maximum level flight speed case as can be seen by comparing the two conditions in figure 183 for the data at $0.95R$. The largest difference appears to be a reduction in normal force near the blade tip for the autorotational case and, by inference, a redistribution of the lift inboard. The normal force at $0.95R$ is substantially reduced in the first quadrant and is negative over most of the second quadrant. The change in lift from the first to second quadrants occurs more quickly for this flight case than seen in Flight 525 and this rapid change in lift is examined in more detail in figures 184 and 185. The chordwise pressure distributions at $\psi = 78^\circ$ in figure 184 show extensive regions of supercritical flow and the normal force is clearly positive at the three outboard stations. The $\psi = 78^\circ$ azimuth corresponds to the small peak in the normal force distribution seen in figure 178 just before the lift becomes negative. Seven degrees later the normal force distribution has changed substantially as shown in figure 185. The flow is still supercritical over the airfoil, but the normal force changes from positive at $0.92R$ to negative at $0.978R$. Within the azimuthal region where large supercritical flows occur, small changes in angle of attack can result in large changes in normal force and pitching moment and this will clearly be a challenge for the analytical methods.

The flap bending moment at $0.46R$ for Flight 487, Counter 11, is compared with interpolated data from the high-speed, level flight case in figure 186. The amplitude of the oscillatory loads is similar for both cases but the 3/rev loading is reduced for the autorotational case. A similar comparison is shown for the chord bending moment at $0.55R$ in figure 187 and it can be seen that the oscillatory loading has been reduced by about 20% with respect to Flight 525, largely because of a reduction in the 4/rev loads. At the same time the 5/rev loading has increased. The chord bending moment at $0.33R$ on Flight 487 is quite similar to the moment shown here at $0.55R$.

The torsion moment at $0.33R$ on Flight 487 is compared with the high-speed case from Flight 525 in figure 188. The oscillatory torsion moment for Flight 487 is decreased by about 30% with respect to the level flight case and, in particular, the large positive loading in the first quadrant is substantially reduced.

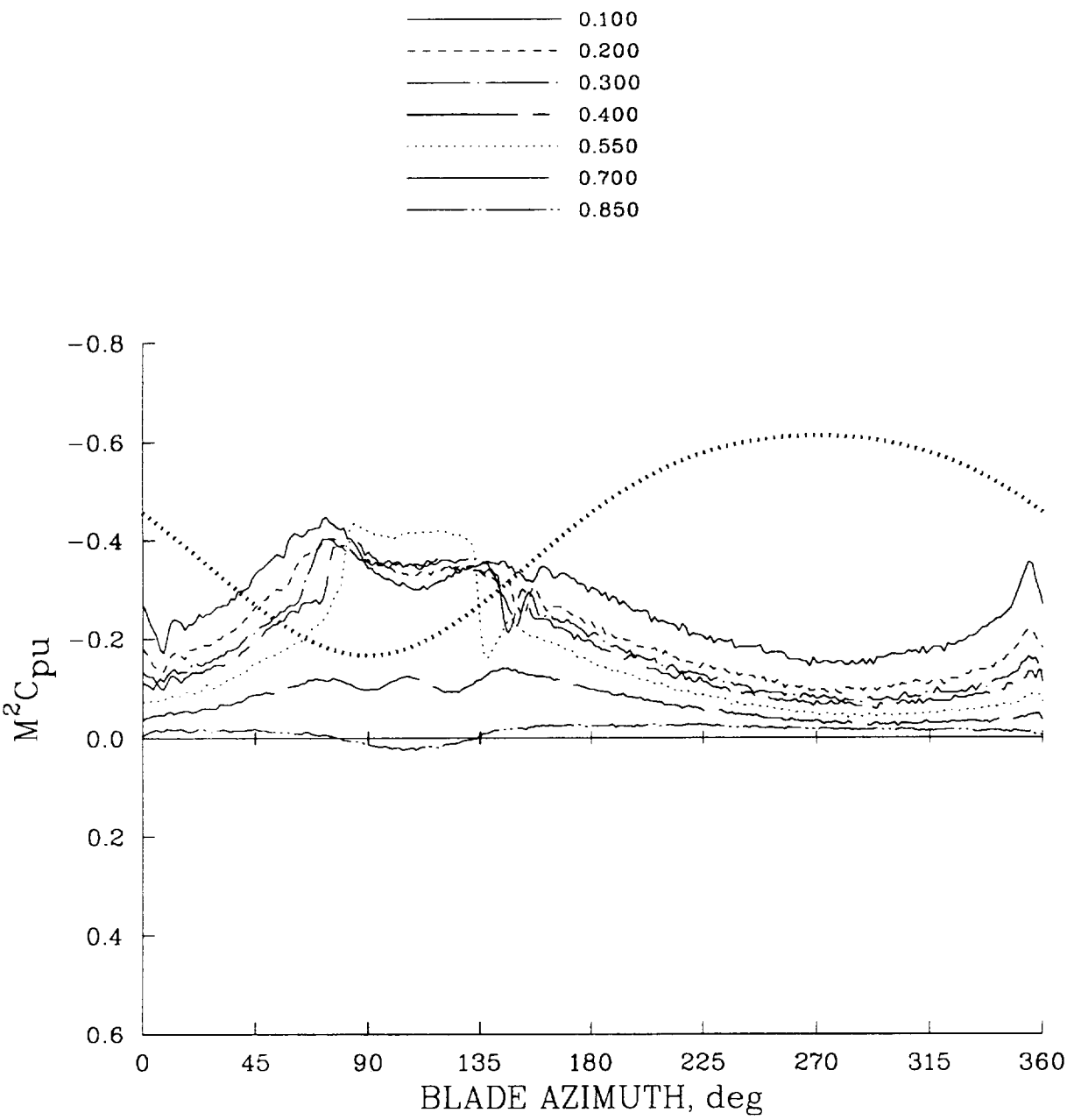


Figure 181. Lower surface pressures as a function of azimuth; $0.95R$, Flight 487. Sonic line shown as heavy dashed line.

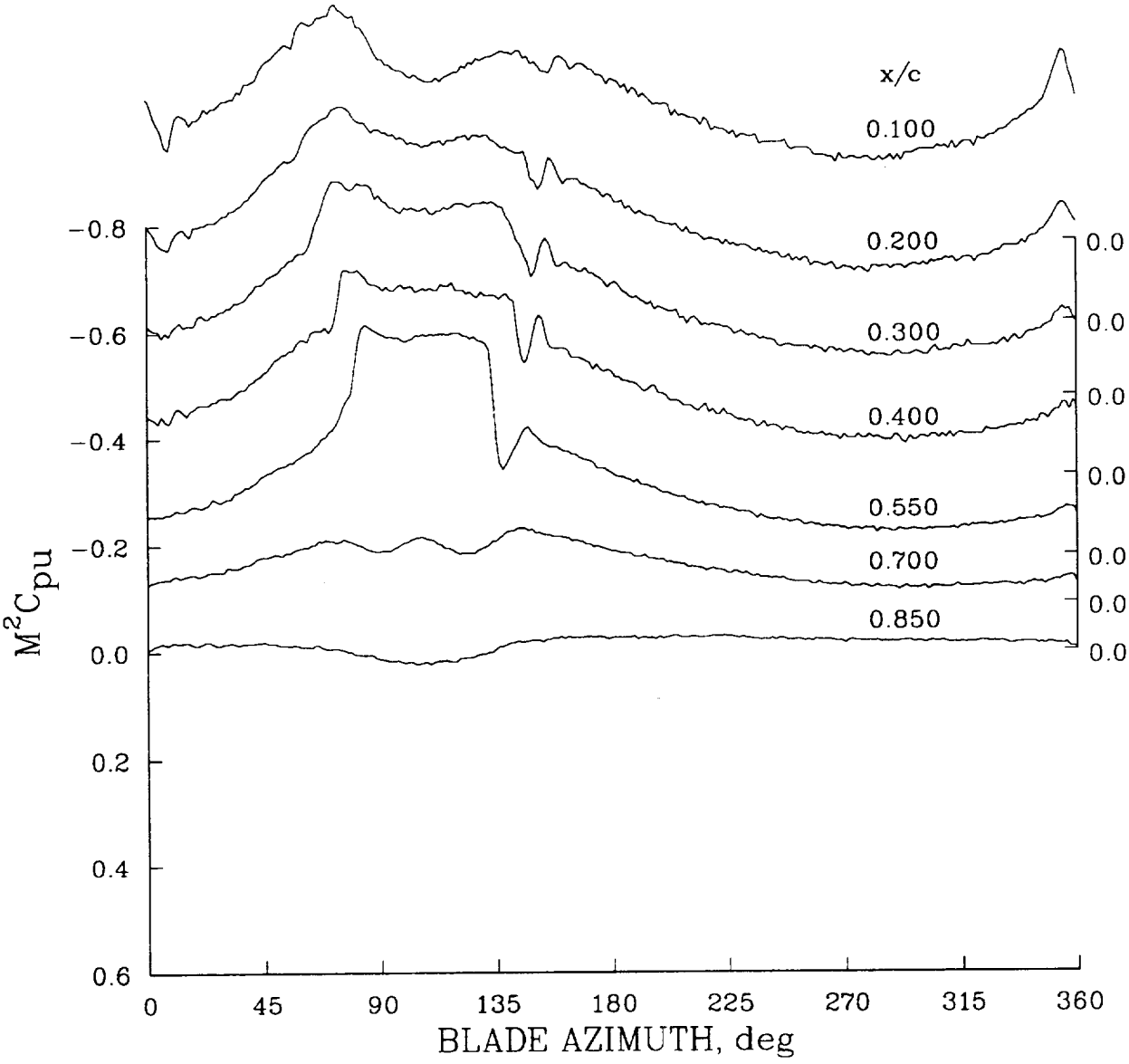


Figure 182. Offset plot of lower surface pressures as a function of azimuth; $0.95R$, Flight 487.

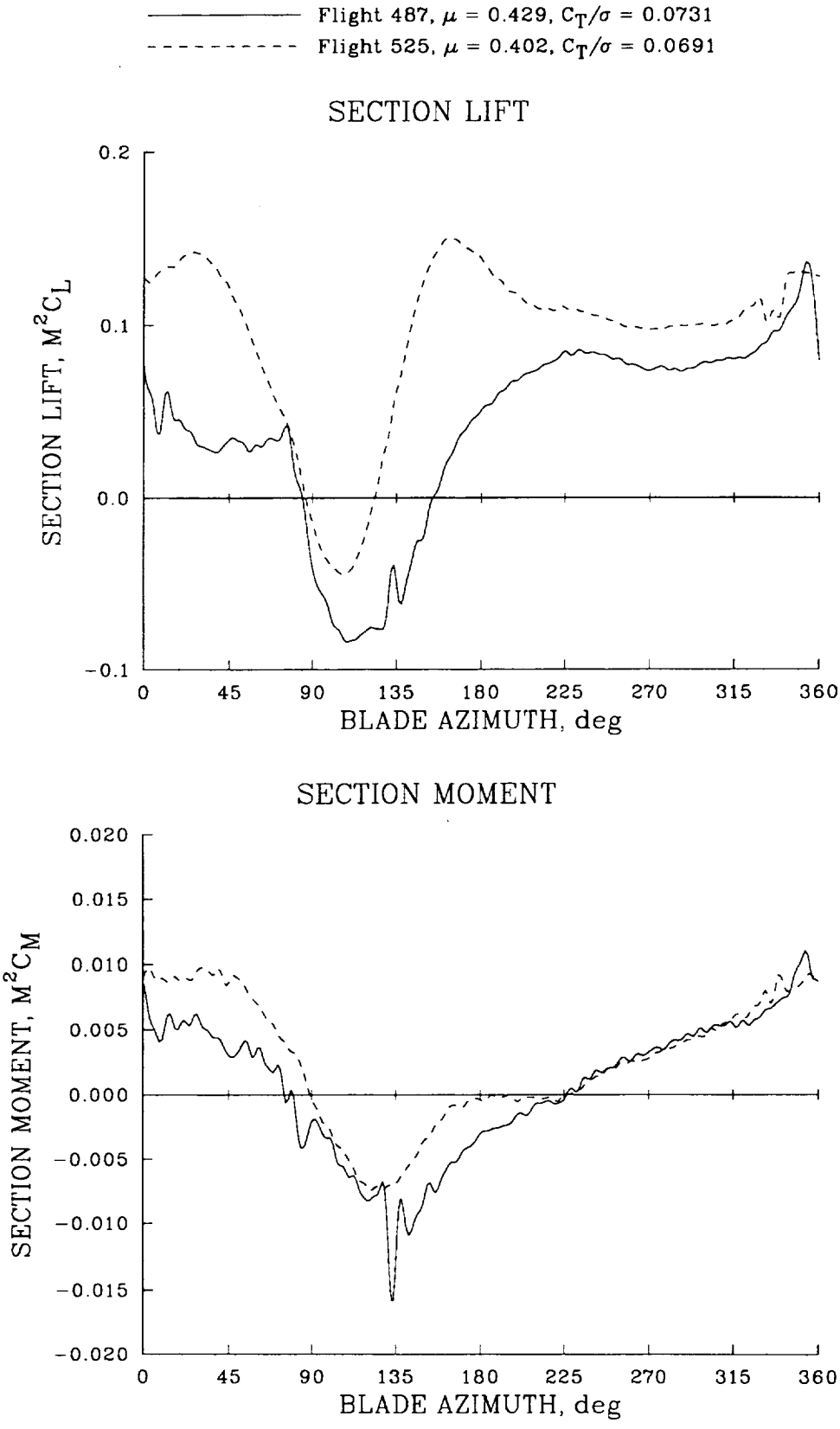


Figure 183. Comparison of normal force and pitching moment for flights 487 and 525; $0.95R$.

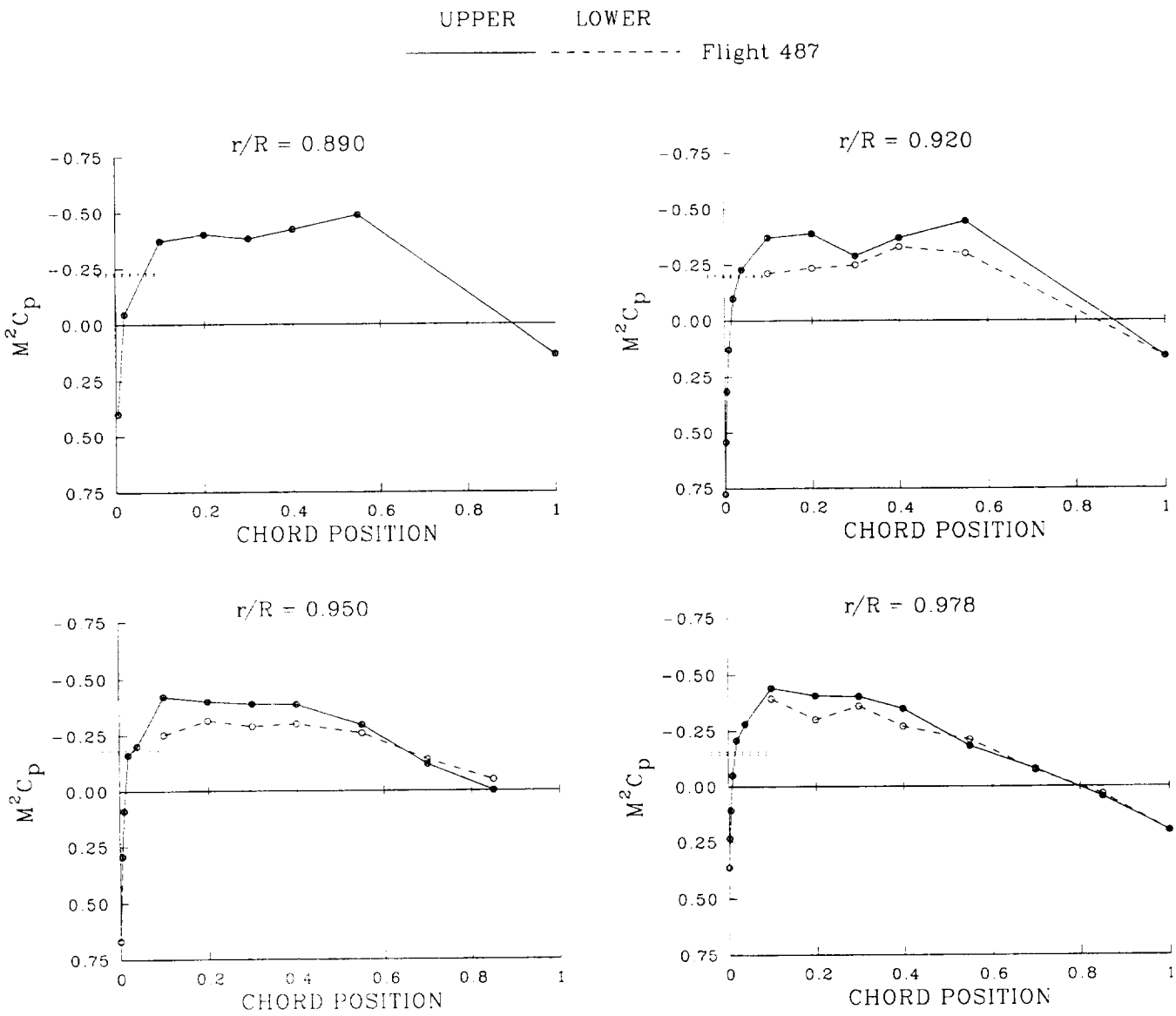


Figure 184. Chordwise pressure distributions at four radial stations; $\psi = 78°$, Flight 487. Critical $M^2C_p$ shown as heavy dashed line on y-axis.

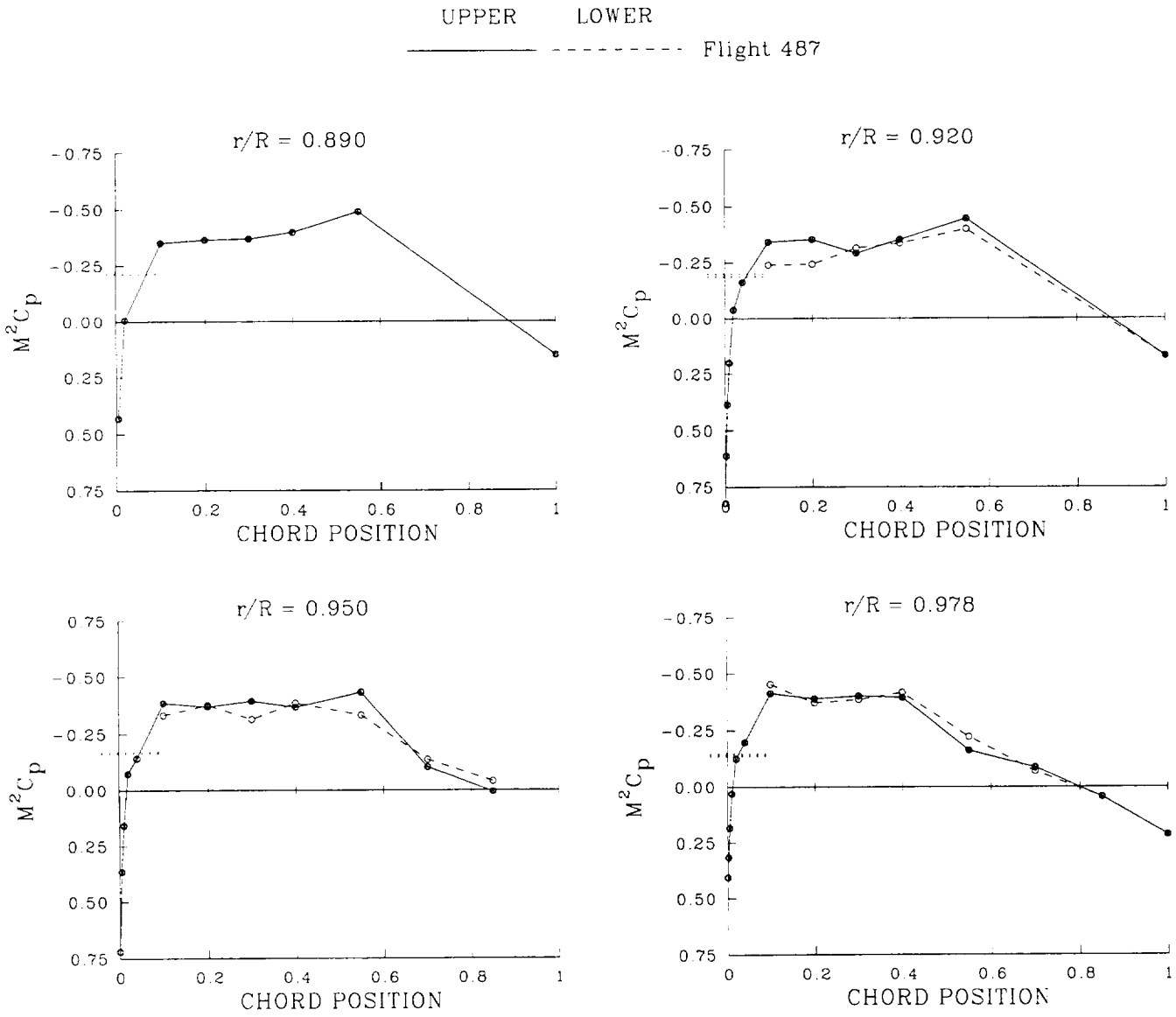


Figure 185. Chordwise pressure distributions at four radial stations; $\psi = 85°$, Flight 487. Critical $M^2C_p$ shown as heavy dashed line on y-axis.

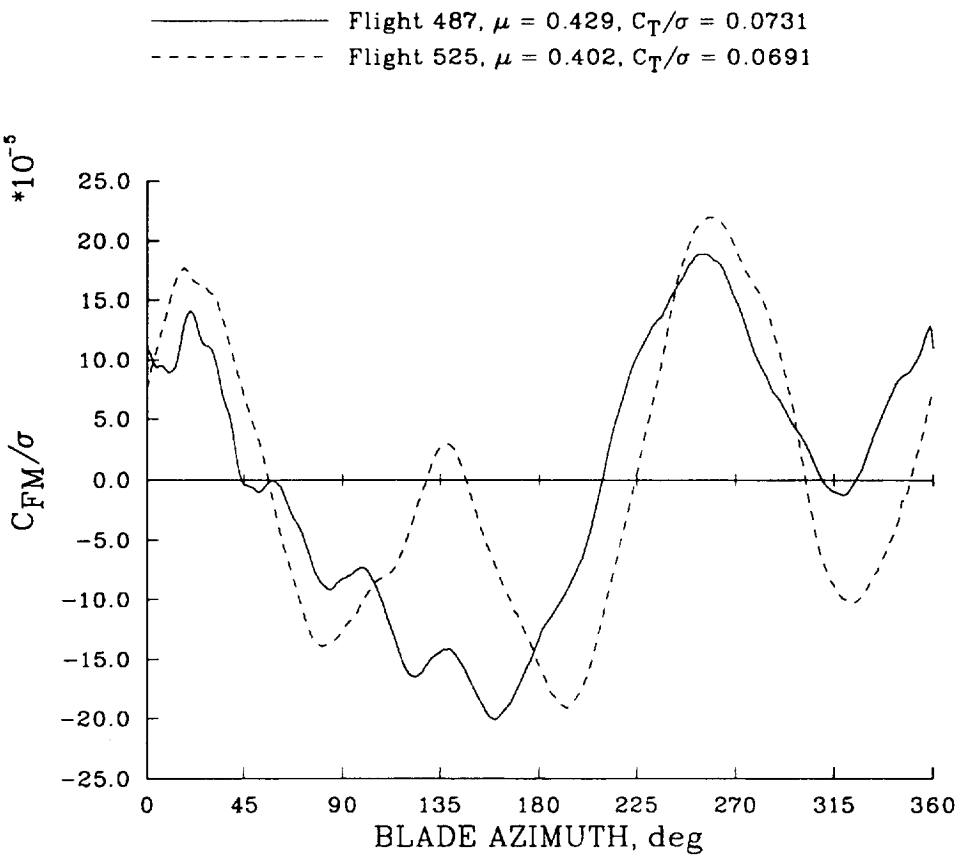


Figure 186. Comparison of flap bending moments on flights 487 and 525; $0.46R$.

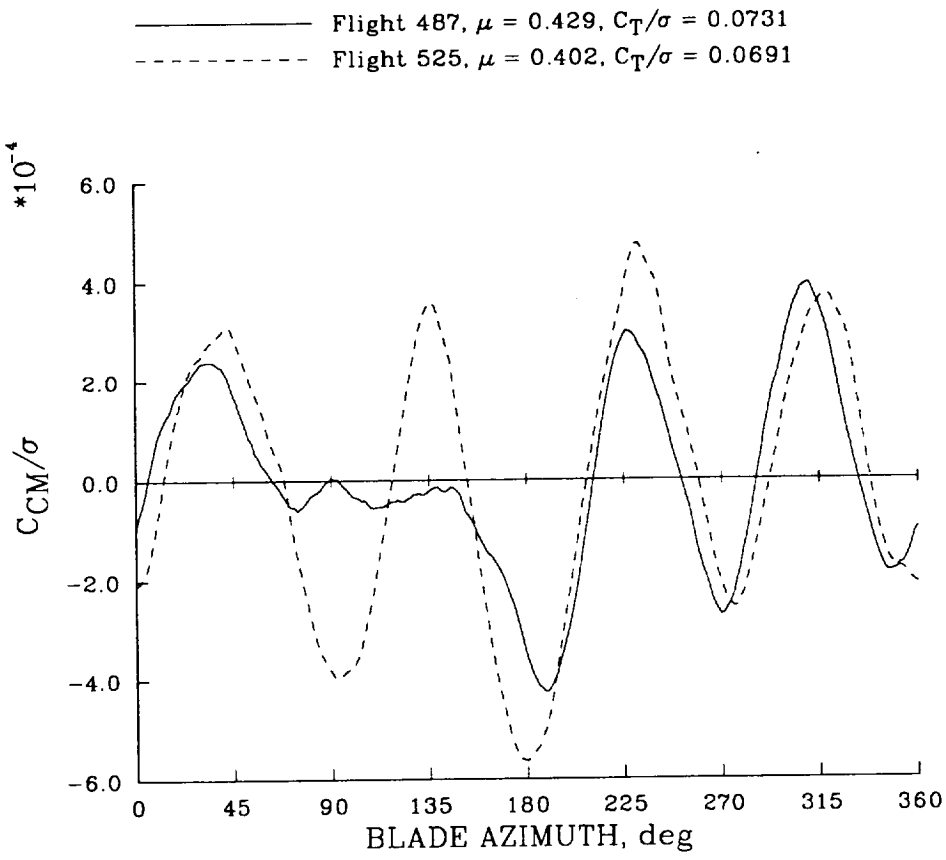


Figure 187. Comparison of chord bending moments on flights 487 and 525; $0.55R$.

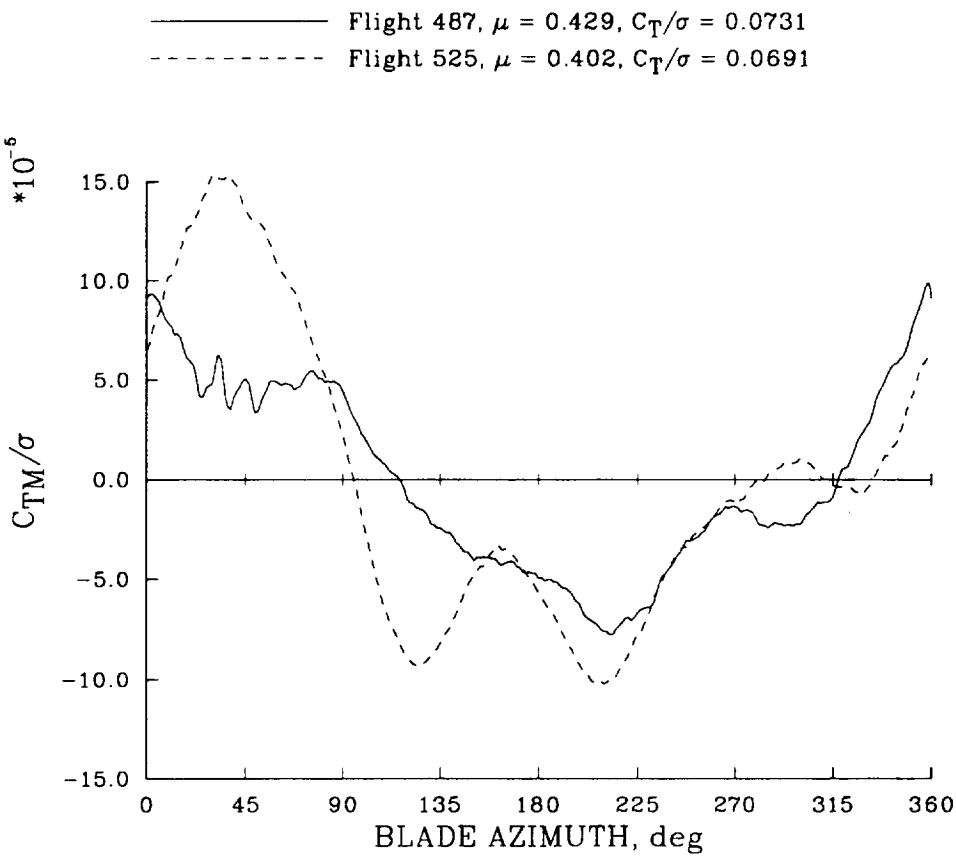


Figure 188. Comparison of torsion moments on flights 487 and 525; $0.33R$.

### 5.4.2 Comparison of Analysis and Experiment

#### 5.4.2.1 *Trim and Performance*

The analyses were trimmed to the aircraft weight, shaft angle of attack, and first harmonic flapping angles for Flight 487, Counter 11–the same trim as was used for the Flight 525 conditions. The flight condition was extreme with a rate of descent exceeding 6000 ft/min. The unspecified trim parameters and shaft torque for this case are compared with flight measurements in table 25. CAMRAD and METAR/R85 calculations were not required for this case and the unspecified trim calculations for the RAE/WHL analysis are not available.

Table 25. Unspecified trim parameters and shaft torque for Flight 487, Counter 11

| Parameter | Flight 487 | CAMRAD/JA |
|---|---|---|
| Collective Pitch, deg | 5.45 | 6.24 |
| Cosine Cyclic Pitch, deg | −0.92 | −0.77 |
| Sine Cyclic Pitch, deg | −3.27 | −2.52 |
| Coning, deg | 2.59 | 3.06 |
| Lag Angle, deg | 4.00 | 1.07 |
| Shaft Torque, N-m | −3,838 | −5,159 |

CAMRAD/JA predicts that the collective pitch angle at the pitch bearing is approximately 0.8° greater than the measurement and this overprediction is similar to what was seen for flights 525 and 123. There is very good agreement in phase for the cyclic pitch angles between CAMRAD/JA and the measurements, but the amplitude is underpredicted by about 23%. The calculated coning angle is about half a degree greater than the measurement and this difference is similar to what was seen on flights 525 and 123. The measured lag angle is positive for this counter and the shaft torque is negative indicating that the rotor is in a windmill state. The CAMRAD/JA predictions also show a positive lag angle and negative torque but there are substantial differences with the measurements.

#### 5.4.2.2 *Blade Airloads*

Only the RAE/WHL and CAMRAD/JA analyses were used to compute the airloads for the Flight 487 autorotational case and thereby provide the partial inflow angles required for the computations in Section 6.2. Figure 189 compares the section lift computed by the two methods to the experimental section lift obtained by pressure integration. The data at three radial stations are shown, $0.92R$, $0.95R$, and $0.978R$, and similar behavior is observed at each station. The CAMRAD/JA calculation shows a minimum in the lift on the advancing blade side that precedes the measured minimum by about 30°. The RAE/WHL calculation on the other hand, provides a much better prediction of the azimuth angle for minimum lift. Neither analysis, however, predicts the minimum level that is measured on the advancing side.

The lift evolution in the first quadrant is not well captured by either of the calculations. The measurements show a slowly time-varying lift followed by a sudden lift loss at 90°. The calculations,

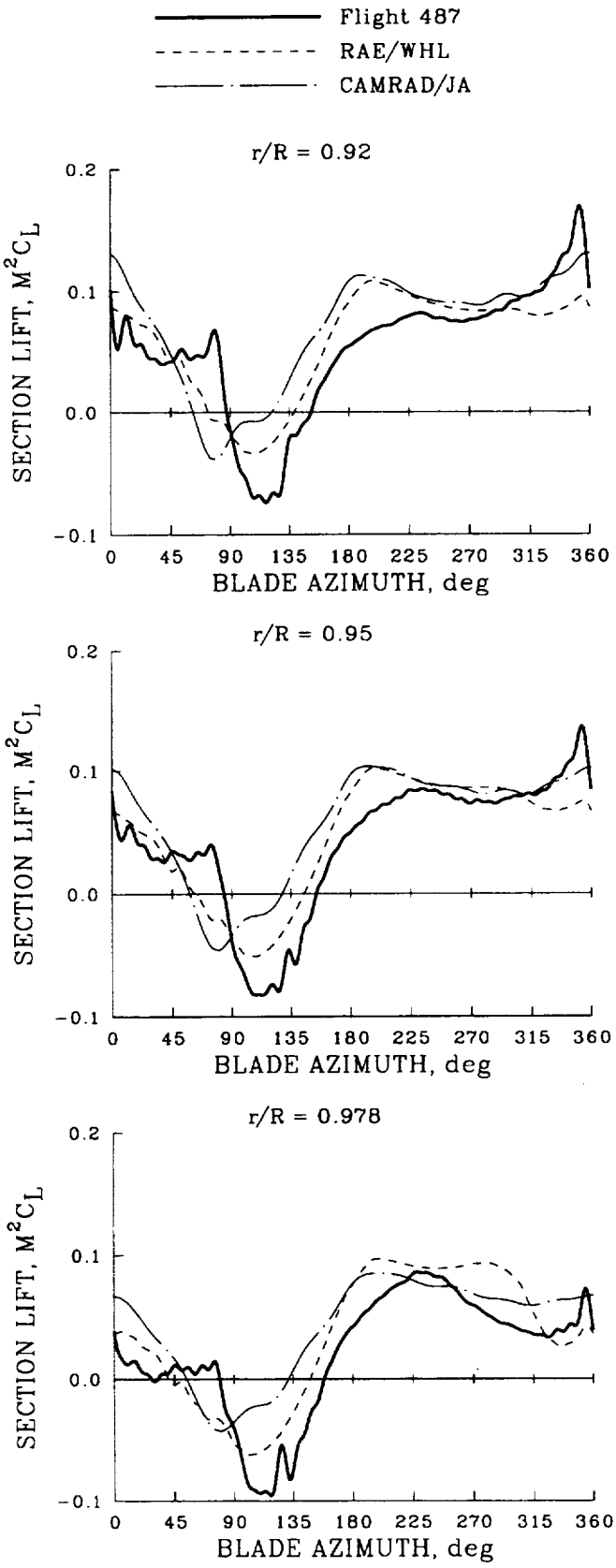


Figure 189. Comparison of experiment and calculation section normal force for the Flight 487 condition.

on the other hand, give a regularly decreasing lift value all along the first quadrant. As discussed previously in Section 5.4.1 this rapid change in lift is closely associated with changes in angle of attack with large areas of supercritical flow on each surface of the blade. As the lifting-line methods compute transonic flow effects only through the use of steady airfoil data it is, perhaps, not surprising that the methods do not predict these highly unsteady conditions. The positive peak found in the experiment just before 360° is a consequence of a blade-vortex interaction that is not captured in the calculations.

Figure 190 shows the correlation between measurements and theory for the section moments. Larger discrepancies are found for this quantity as compared with the section lift. The measured section moment at $0.92R$ is probably not trustworthy on the advancing side, as discussed before in Section 5.4.1, but the section moments at the two outboard locations are considered trustworthy. The measured moments for these two stations are quite different from the calculations and the correlation is poor. This poor agreement illustrates the difficulty of computing the section moment, a small quantity, which yet may have a large influence on the blade torsional dynamics.

5.4.2.3 *Blade Moments and Loads*

The autorotational flight case was taken from an early series of flight tests with the swept-tip blades and some of the settings in the data acquisition system were not adjusted correctly. As a consequence many of the strain-gauge channels show limiting and, therefore, only a few can be used for comparison with analysis.

The flap bending moment measured at $0.46R$ is compared with the RAE/WHL and CAMRAD/JA calculations in figure 191. Both analyses show the largely 1/rev character seen in the data and the RAE/WHL code slightly overpredicts the amplitude levels while CAMRAD/JA underpredicts the loading level. The accuracy of the flap bending moment calculation is not as good as was seen at high speed for Flight 525, Section 5.2.2.3, but good correlation is still achieved.

The chord bending moment comparison is shown in figure 192. Neither analysis predicts the general load behavior or the oscillatory amplitudes that were measured and are, in general, unsatisfactory. The poor predictive capability here is similar to what was seen in comparing the chord bending moments with measurements for the Flight 525 airspeed sweep and it is believed that the lack of a good lag damper model and knowledge of the root boundary conditions contribute to the poor predictions.

The RAE/WHL and CAMRAD/JA analyses underpredict the torsion moment for this case as shown in figure 193. The Flight 487 torsion data show much the same character as observed in the section pitching moments at the blade tip (see figure 190). The RAE/WHL prediction, on the other hand, is basically out of phase with the measured values, whereas the CAMRAD/JA analysis, while showing the correct 1/rev behavior, shows substantial differences for the higher harmonic loading. This poor prediction of the torsional loading was also seen for the Flight 525 airspeed sweep and it is difficult to see how the correct torsional deformation can be obtained until an improved calculation of the blade pitching moment is obtained.

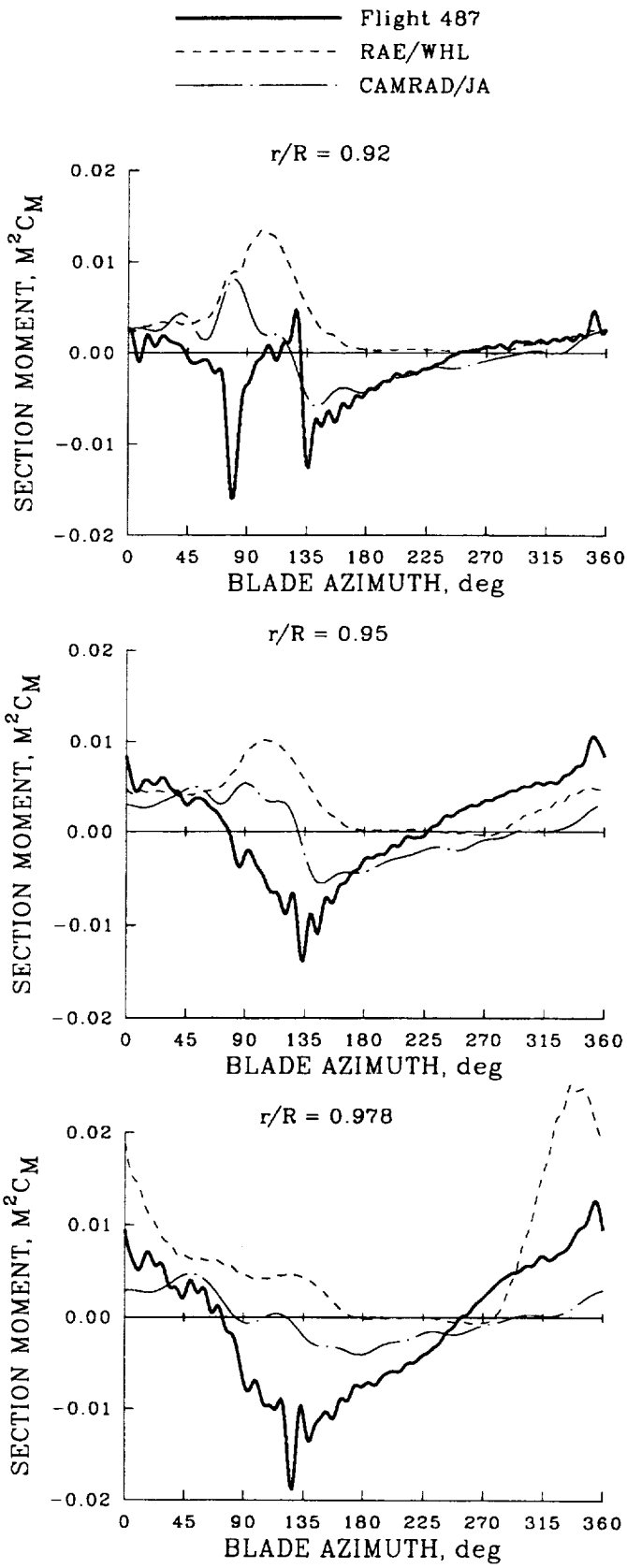


Figure 190. Comparison of experiment and calculation section pitching moment for the Flight 487 condition.

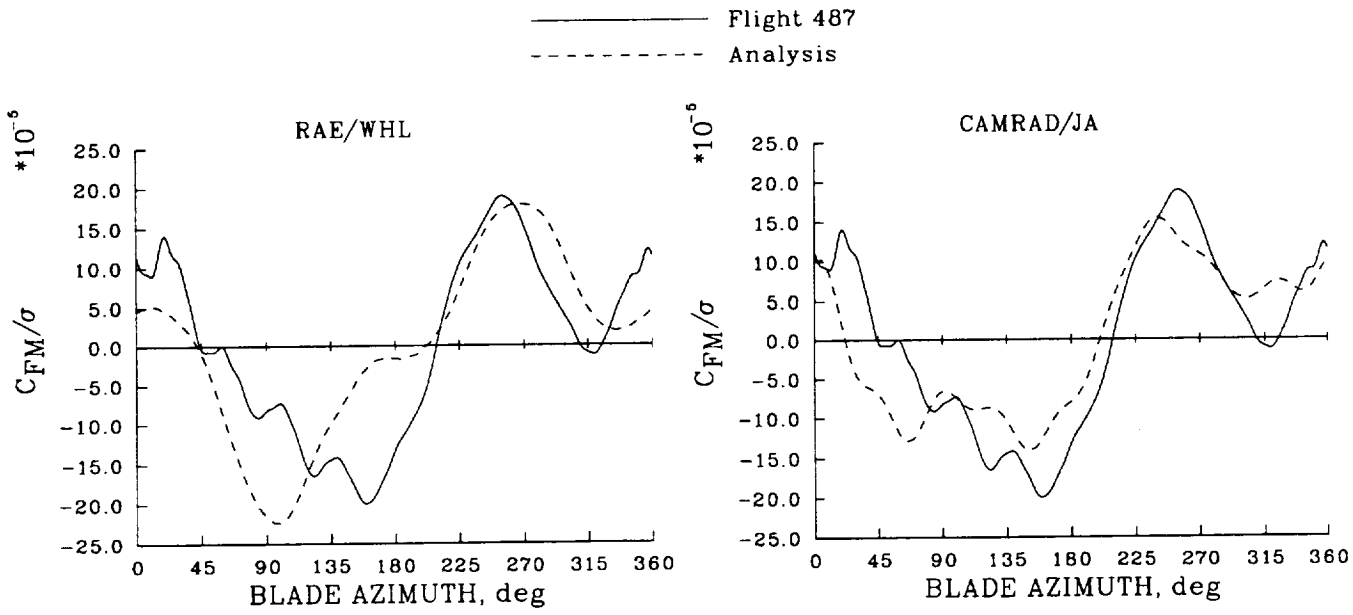


Figure 191. Comparison of measured and calculated flap bending moments for Flight 487; $0.46R$.

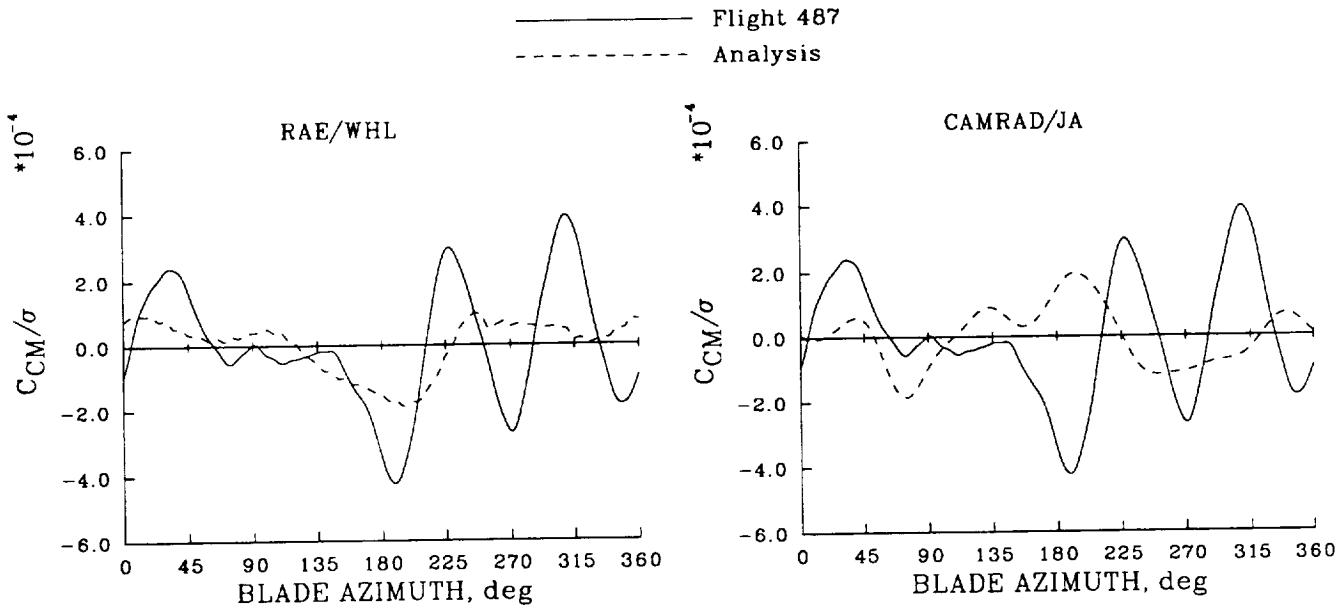


Figure 192. Comparison of measured and calculated chord bending moments for Flight 487; $0.55R$.

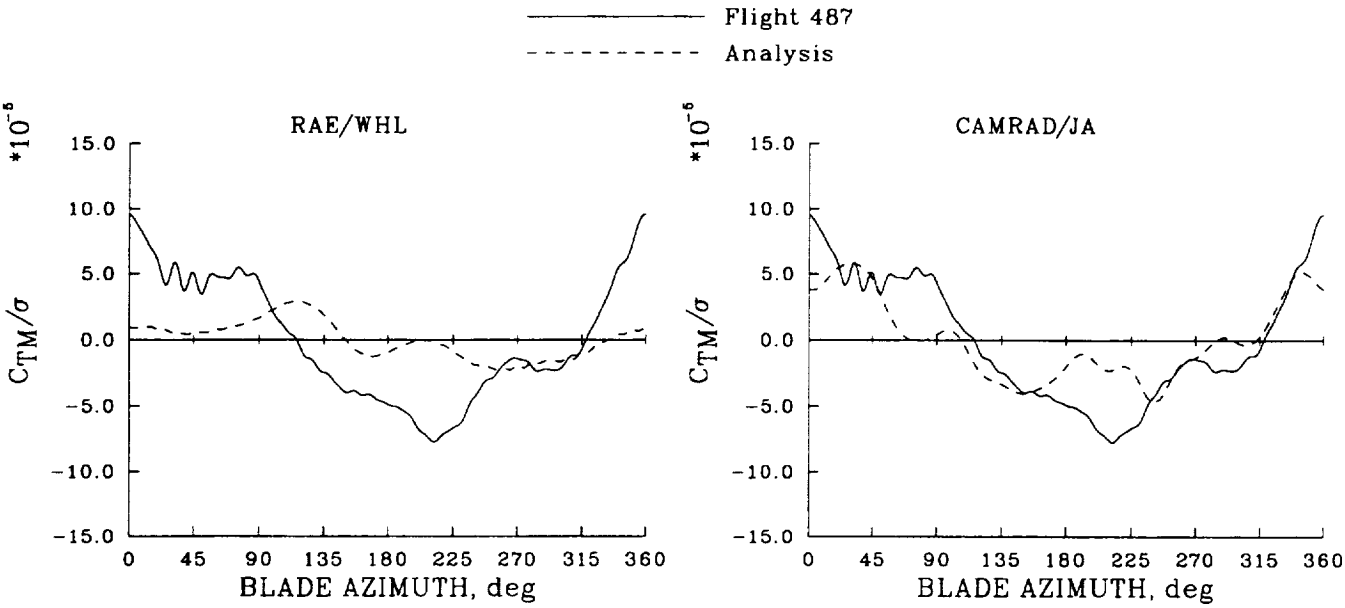


Figure 193. Comparison of measured and calculated torsion moments for Flight 487; $0.33R$.

### 5.4.3 Summary of Autorotational Flight Case Calculations

The autorotational case, Flight 487, Counter 11, was selected as a test case for CFD calculations (see Section 6.2) because of the high advance ratio and extensive regions of transonic flow at the blade tip. The RAE/WHL and CAMRAD/JA analyses were used to determine partial angle-of-attack distributions for this case to be used by the TSP and FPR codes in a hybrid calculation of the airloads. The comparisons shown in this section between the lifting-line methods and the experimental measurements provide some insight into the suitability of the partial angles of attack as a basis for CFD prediction.

The lifting-line predictions of section normal force appear deficient in two respects. First, the delayed decrease in lift observed in the experimental measurements in the first quadrant, a "plateau-like" effect, is not observed in the computations. It seems likely that this normal force delay and rapid decrease in thrust are related to nonlinear and unsteady characteristics of the transonic flow over the blade and, to a substantial extent, these cannot be correctly computed by the lifting-line methods. Second, an area of vortical loading is observed at the rear of the rotor disk that is clearly a result of a close passage of the tip vortex of the previous blade and this is not captured by the lifting-line methods.

The lifting-line prediction of section pitching moment is also unsatisfactory. At $0.95R$ the predicted phase of the moment is opposite that of the measurements, while at $0.978R$ the RAE/WHL analysis strongly overpredicts the pitching moment while CAMRAD/JA underpredicts the moment. The incorrect prediction of the pitching moment leads to an underprediction of the blade torsional motion and consequent errors in the partial angles of attack.

The trim parameters used for the lifting-line calculations for this case may not be as accurate as used for the Flight 525 cases. For Flight 525 it appears that the actual rotor thrust was greater than the gross weight of the aircraft because of fuselage and stabilizer download. For the present calculations the same differences are possible, although the angle of attack of the fuselage with respect to the air mass is less accurately known. Blade flap angle measurements were obtained on only one blade for Flight 487 and were contaminated by noise. In this regard the precision of the trim flapping angles is considered to be reduced from the Flight 525 airspeed sweep where good flapping angle measurements were obtained on three blades.

The deficiencies in the lifting-line methods for this case suggest that the partial angle-of-attack distributions that are used by the TSP and FPR codes will not be completely satisfactory. However, when the lifting-line and CFD methods are coupled, that is, the lift calculated by the CFD methods is fed back to the lifting-line calculation, then some of these deficiencies may be eliminated.

## 5.5 Puma Airfoil

### 5.5.1 Introduction

The basis for the research Puma rotor was a standard Puma blade with a rectangular planform and a constant airfoil section similar to a NACA 0012. The blade tip was then modified to add sweep to the planform in such a way that a section of forward sweep inboard was balanced by a section of backward sweep outboard so that the blade torsion moments induced by the offset of the center of lift from the feathering axis were canceled. The modified tip planform of the research Puma is illustrated in figure 194 and this figure also shows the location of the four pressure measurement stations and the blade feather axis coincident with the quarter chord of the blade inboard of $0.84R$.

The blade chord was extended outboard of $0.84R$ to provide the additional area at the blade tip. This was accomplished at each section by translating the airfoil profile along its line of symmetry and fairing the upper and lower surfaces between the original and translated profiles as shown in figure 195. This method of construction provides a slightly greater airfoil thickness over the outer 16% of the blade, but the increase in chord is such that the thickness to chord ratio is reduced from 0.111 to 0.104. This new section profile is referred to here as the Puma airfoil.

The CFD calculations performed for this rotor and discussed in Section 6 used section profile and planform geometry derived from a theoretical model of the modified tip. The accuracy of this geometric model is addressed in Section 5.5.2 by comparing profile measurements made on the research Puma blade with the theoretical model. Section 5.5.3 examines the adequacy of the NACA 0012 airfoil deck that was used for all of the lifting-line calculations presented in this study, by comparing airfoil characteristics for the NACA 0012 profile with the Puma airfoil using both inviscid and viscous two-dimensional calculations. Summary comments are provided in Section 5.5.4.

### 5.5.2 Puma Airfoil Measurements

Following construction of the modified blades for the research Puma, templates were made for one blade at each of the four radial stations where pressure measurements were to be obtained. Each of the

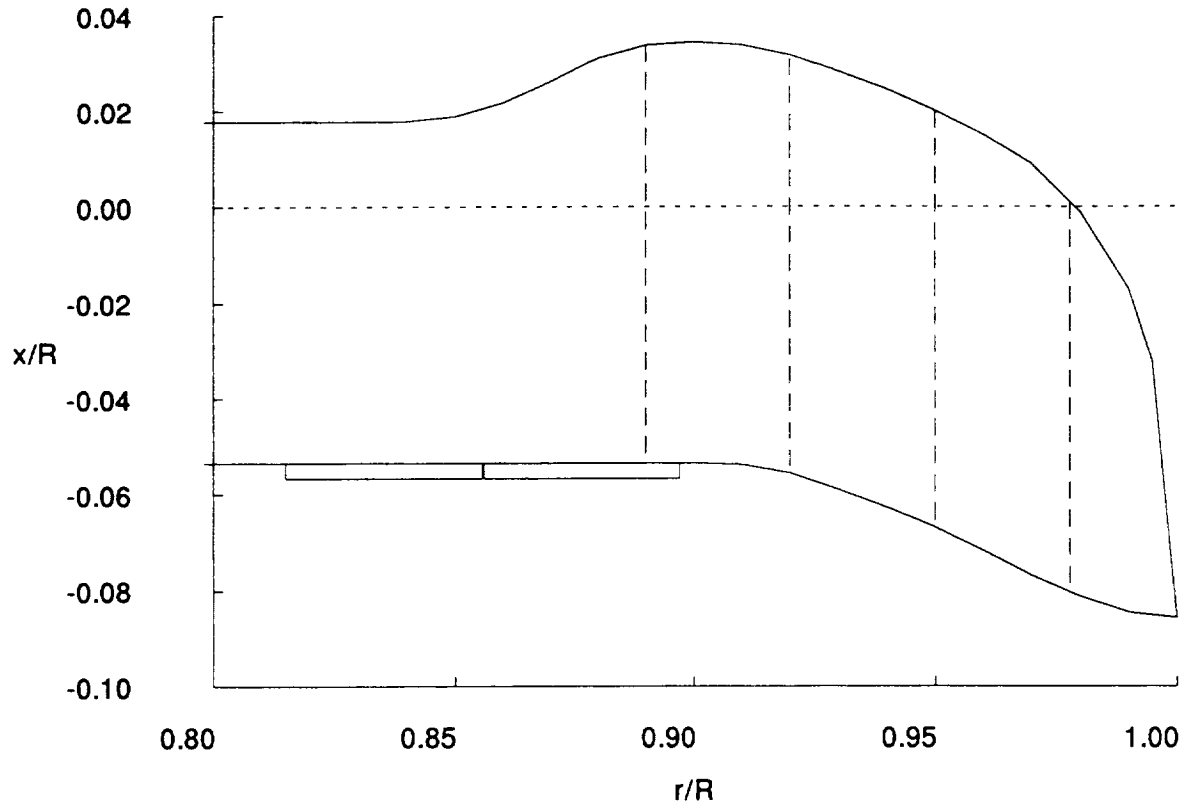


Figure 194. Swept tip planform of research Puma. Chordwise pressure transducer sections shown by dashed lines and feather axis by dotted line.

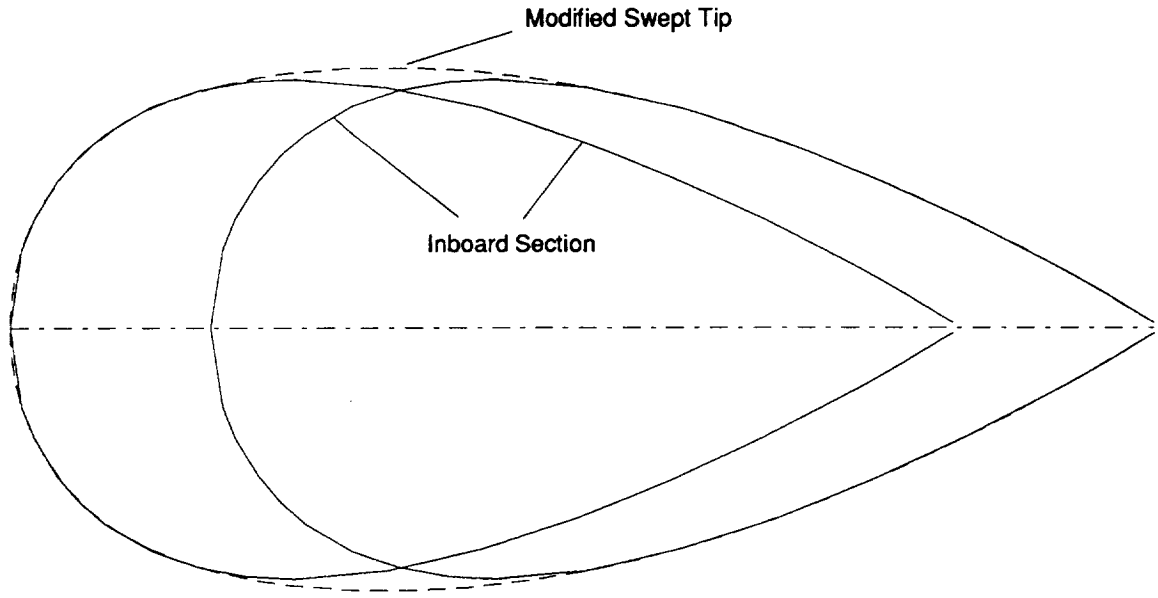


Figure 195. Puma section profile created by translation of inboard profile and fairing; $0.95R$, vertical scale 4.4 X horizontal scale.

templates was measured by the Inspection Department at RAE Bedford in 1982, gauging the thickness at 35 points along the airfoil. The measured thickness was reduced by 0.10 mm to compensate for tape that had been placed on the airfoil during the template construction. Figure 196 compares the measurements at the four radial stations with the theoretical values used for the CFD calculations. The agreement between the measurements and the theoretical geometry is quite good, at this scale, for the two inboard profiles. At $0.95R$ the measurements show a slight thickening of the profile over the last 10 or 20% of the airfoil, while at $0.978R$ the measurements show a thinning of the airfoil near the trailing edge and the airfoil stops at about 96% of the theoretical chord. The anomalous thickness measurement at $0.80c$ for this station is believed to be spurious. The maximum airfoil thickness measured was greater than the theoretical value for all four sections. The incremental increase at each station in terms of $t/c$ was 0.0016, 0.0005, 0.0025, and 0.0013 for the radial stations $0.89R, 0.92R, 0.95R$, and $0.978R$ respectively. The physical differences ranged from 0.4 mm to 1.7 mm.

As a part of the present collaboration a new mold was made of the blade profile at $0.95R$ and measurements of the upper and lower surface thickness were made in 1989 for approximately 100 chordwise stations. The 1982 and 1989 measurements are compared with the theoretical model in figure 197 for $0.95R$. This exploded view shows that the 1982 and 1989 measurements are very similar and indicate that the actual blade profile was slightly thicker than the the theoretical model.

### 5.5.3 Airfoil Analysis

The Puma airfoil, as described above, was obtained by translating the inboard profile in the $x$-direction and fairing the section in between. The fairing increases the dimensional thickness of the airfoil, but because of the increased chord the thickness to chord ratio is decreased.

All of the lifting-line calculations for the Puma rotor presented in this report assume that NACA 0012 airfoil data, either as two-dimensional tables or as formulas, can be used to provide realistic section properties. This has been done because experimental airfoil tables do not exist for the actual airfoils used, either the standard inboard section or the modified tip. The purpose of the present computational study is to assess the effects of this approximation on the lifting-line aerodynamics.

The differences between the Puma airfoil sections and the the standard NACA 0012 section are illustrated in figure 198. Both the standard inboard and the modified tip sections on the Puma are thinner than the NACA 0012. The inboard section on the Puma has its maximum thickness slightly forward of the NACA 0012 and the aft portion of the airfoil is thinner by comparison. The modified tip section, although thinner than the NACA 0012, shows a similar chordwise thickness distribution.

To understand the differences between these airfoil sections calculations were made for the modified tip section and the NACA 0012 section using two different methods. No calculations were made for the inboard standard airfoil section. The first method used is an inviscid, nonconservative full-potential code called FLO 6 (Jameson, 1974). This code has the advantage of being computationally fast and robust. It can be run many times in order to identify conditions of similarity and dissimilarity between the two airfoil sections.

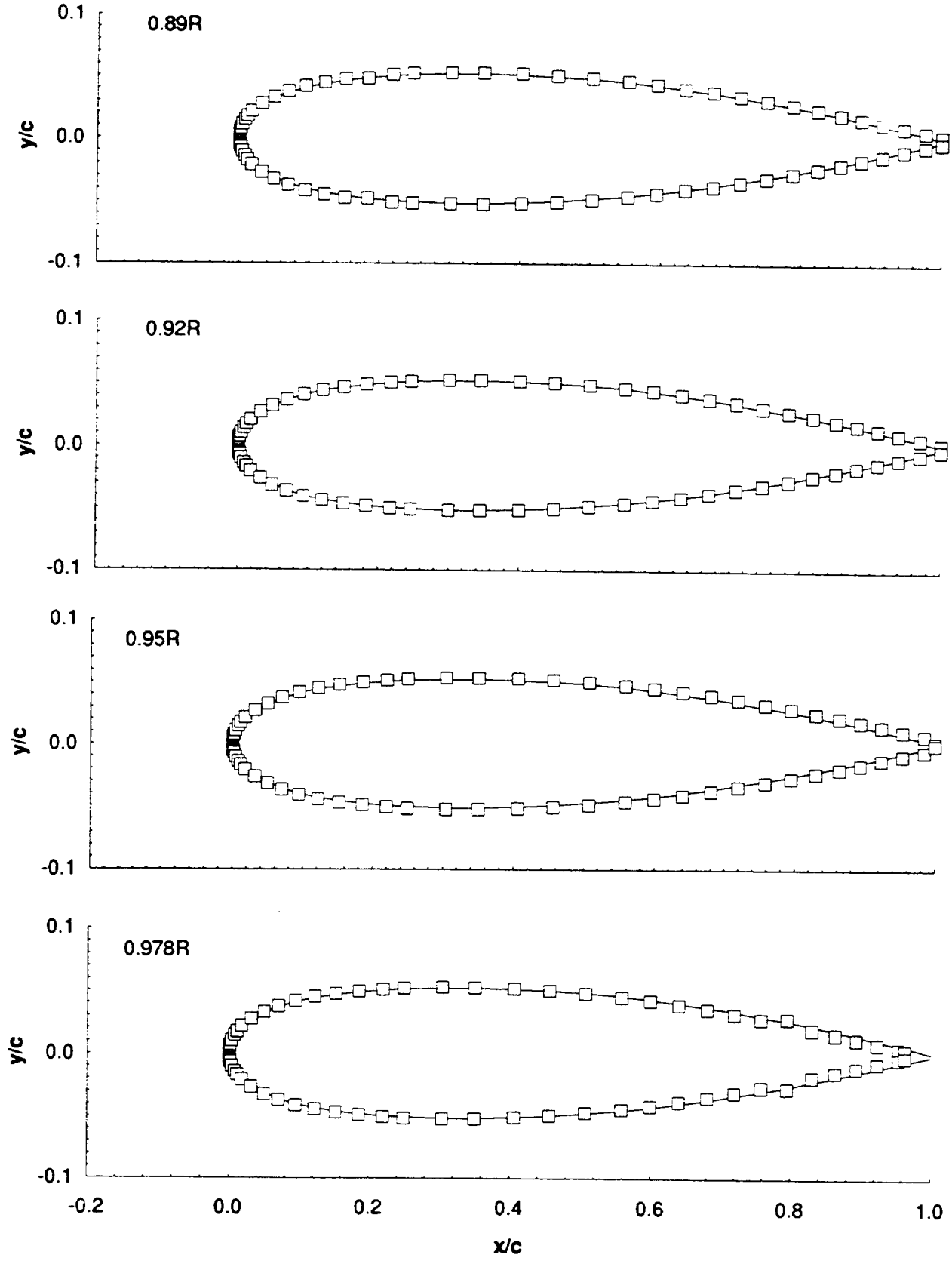


Figure 196. Comparison of theoretical profiles and 1982 measurements for four stations. Vertical scale 1.7 X horizontal scale.

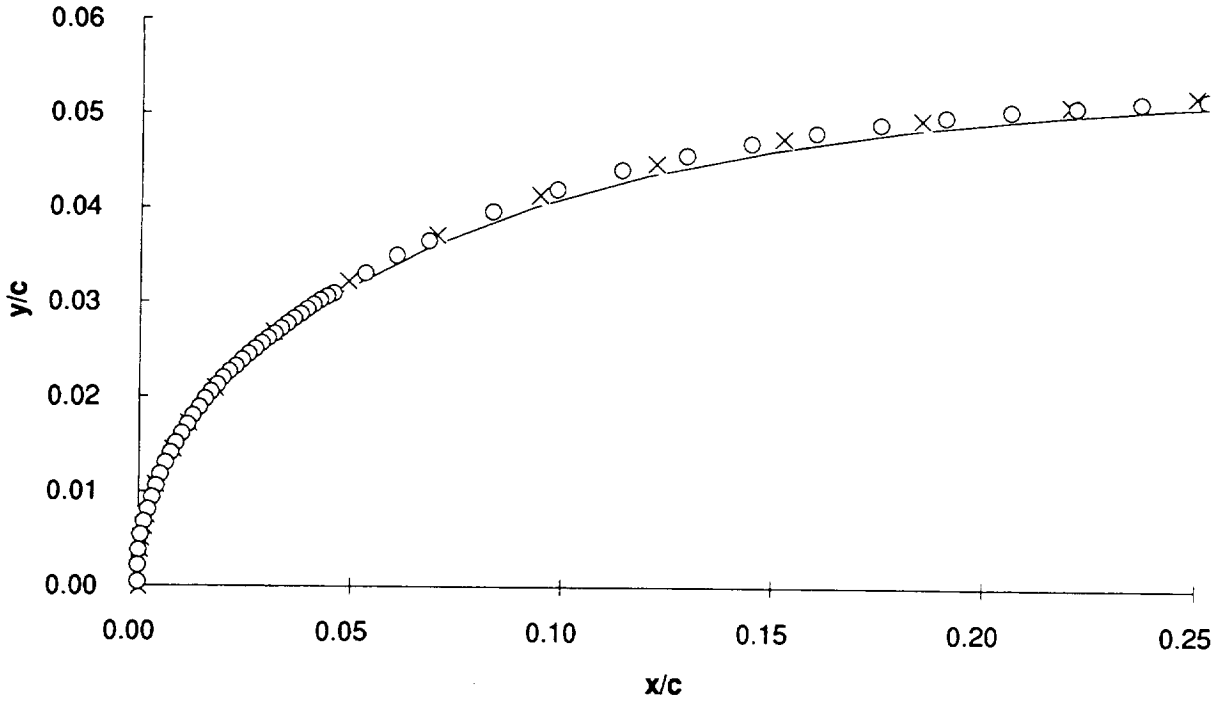


Figure 197. Comparison of theoretical profile with 1982 and 1989 measurements; $0.95R$. Vertical scale 2.4 X horizontal scale.

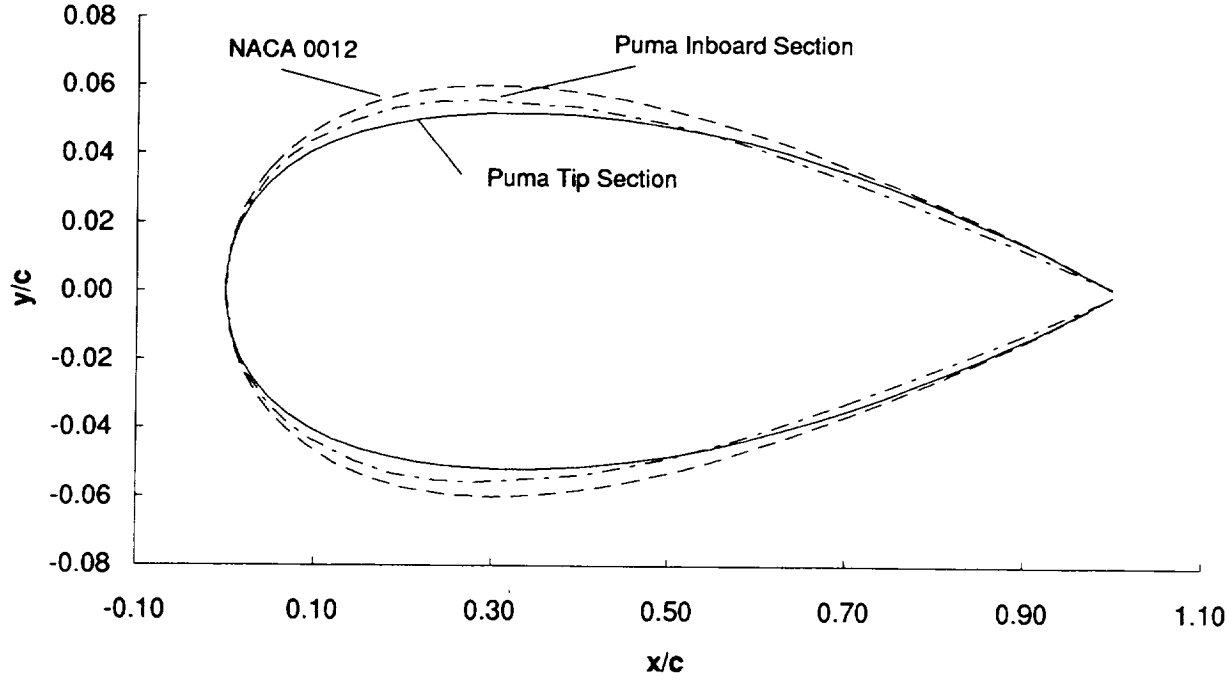


Figure 198. Comparison plot of the Puma airfoil sections and the NACA 0012 section. Vertical scale 3.8 X horizontal scale.

The second computer code used in this investigation is ARC2D (Steger, 1978), developed at NASA Ames Research Center by Pulliam and Steger. ARC2D solves the compressible, time-averaged, thin-layer Navier-Stokes equations in two dimensions. It has been used by McCroskey et al. (1985) to compute airfoil characteristics for high tip-speed rotor applications. It uses an algebraic turbulence model and requires significantly more computer resources to run than the inviscid code (~5 minutes CPU time on a CRAY YMP). Reynolds numbers were chosen to correspond to the Puma flight tests.

Results from all of the calculations are summarized in table 26. The inviscid calculations were used to identify areas where the greatest differences existed between the two airfoils. Viscous calculations were then performed for three cases that are representative of the differences between the two airfoils in different transonic flow conditions.

All of the results show that for subcritical flow conditions, there is very little difference between the two airfoils. This is because they both behave according to thin airfoil theory until there is significant transonic flow. Since both airfoils are symmetric, the pitching moments are very small unless strong shocks are present. Both viscous and inviscid calculations were performed for two of the transonic cases. In both cases, results from the two methods show substantial differences. These differences are most likely the result of viscous effects on the shock location.

Table 26. Summary of airfoil comparison cases

| $\alpha$ | $M_\infty$ | $Re^a$ | Puma airfoil | | | NACA 0012 | | |
|---|---|---|---|---|---|---|---|---|
| | | | $C_l$ | $C_d$ | $C_m$ | $C_l$ | $C_d$ | $C_m$ |
| 0.0 | 0.2 | – | 0.0000 | −0.000012 | 0.00001 | 0.0000 | −0.000013 | 0.00001 |
| 5.0 | 0.2 | – | 0.6108 | −0.000007 | −0.00621 | 0.6167 | −0.000008 | −0.00664 |
| 0.0 | 0.4 | – | 0.0000 | 0.000000 | 0.00000 | 0.0000 | 0.000000 | 0.00000 |
| 2.0 | 0.4 | – | 0.2638 | −0.000065 | −0.00276 | 0.2667 | −0.000063 | −0.00291 |
| 4.0 | 0.4 | – | 0.5281 | −0.000099 | −0.00506 | 0.5339 | −0.000093 | −0.00538 |
| 6.0 | 0.4 | – | 0.7936 | −0.000232 | −0.00632 | 0.8023 | −0.000191 | −0.00691 |
| 8.0 | 0.4 | – | 1.0638 | 0.001763 | −0.00525 | 1.0738 | 0.000178 | −0.00653 |
| 5.0 | 0.55 | – | 0.7502 | 0.002257 | −0.00197 | 0.7599 | 0.000998 | −0.00237 |
| 7.0 | 0.55 | – | 1.0636 | 0.026982 | 0.00240 | 1.0803 | 0.020683 | 0.00299 |
| 0.0 | 0.6 | – | 0.0000 | −0.000101 | 0.00000 | 0.0000 | −0.000010 | 0.00000 |
| 2.0 | 0.6 | – | 0.3135 | −0.000143 | −0.00268 | 0.3187 | −0.000136 | −0.00267 |
| 4.0 | 0.6 | – | 0.6358 | 0.000181 | −0.00148 | 0.6462 | 0.000944 | −0.00155 |
| 6.0 | 0.6 | – | 0.9683 | 0.026649 | 0.00151 | 0.9889 | 0.021917 | 0.00280 |
| 6.0 | 0.6 | $10 \times 10^6$ | 0.7840 | 0.023489 | 0.02904 | 0.8244 | 0.023330 | 0.02612 |
| 0.0 | 0.8 | – | 0.0000 | 0.001274 | 0.00000 | 0.0000 | 0.009191 | 0.00000 |
| 2.0 | 0.8 | – | 0.4989 | 0.024035 | −0.04254 | 0.4780 | 0.033514 | −0.05527 |
| 2.0 | 0.8 | $6 \times 10^6$ | 0.4599 | 0.030222 | −0.02514 | 0.4379 | 0.040470 | −0.03931 |
| 0.0 | 0.825 | – | 0.0000 | 0.006088 | 0.00000 | 0.0000 | 0.020498 | 0.00000 |
| 1.0 | 0.825 | – | 0.2723 | 0.014627 | −0.03382 | 0.2474 | 0.026801 | −0.04250 |
| 0.5 | 0.84 | $6 \times 10^6$ | 0.1469 | 0.022219 | −0.02649 | 0.1175 | 0.042160 | −0.02706 |

[a] ARC2D computations.

For transonic cases, the difference in thickness between the two airfoils causes differences in the lift, drag and moment. Three representative flow conditions were computed by the ARC2D code and the results are shown in figures 199–201. Figure 199 shows a transonic condition with a high angle of attack, $\alpha = 6°$, and a low Mach number, $M_\infty = 0.6$. Here, the lift of the Puma airfoil is about 5% lower than the NACA 0012 value. The drag for both airfoils is almost equal and the moments are also very close. This is because the shock is located close to the leading edge of both airfoils, where the two profiles are very similar.

Figure 200 shows a case where the shock is located farther aft on the Puma airfoil in the faired region. Here, the thickness difference between the two airfoils is more important. The angle of attack is 2° for this case and the Mach number is 0.8. The lift for the two airfoils is similar, but both the drag and the moment are much higher for the NACA 0012 airfoil.

Figure 201 shows a higher Mach number case with a lower angle of attack, $M_\infty = 0.84, \alpha = 0.5°$. Here, the Puma airfoil shows about 25% more lift than the NACA 0012. The transonic drag for the Puma airfoil is about half that of the NACA 0012. The moment values between the two are similar. The rapid rise in drag for the thicker NACA 0012 airfoil shows the difference in the drag divergence Mach number for the two airfoils: the thinner Puma airfoil has better drag divergence characteristics.

### 5.5.4 Puma Airfoil Summary

The comparison of measured and theoretical aerodynamic profiles in Section 5.5.2 shows, for the most part, only slight differences between the physical blade and the theoretical model. However,

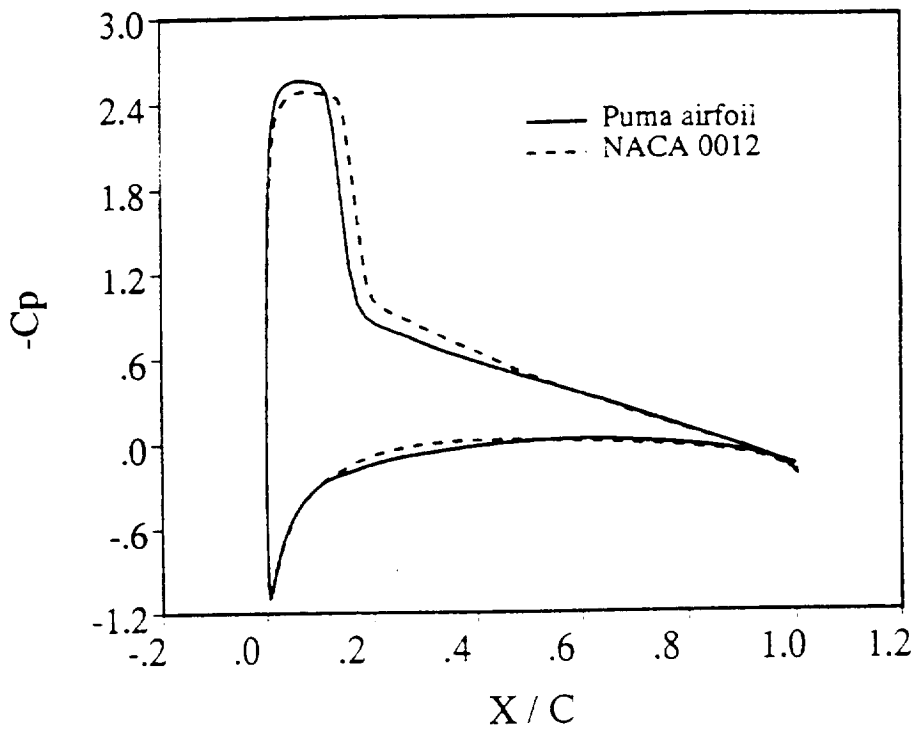


Figure 199. Viscous calculation results; $M_\infty = 0.60$, $\alpha = 6.0°$. NACA 0012: $C_l = 0.8244$, $C_d = 0.02333$, $C_m = 0.02612$; Puma airfoil: $C_l = 0.7840$, $C_d = 0.02349$, $C_m = 0.02904$.

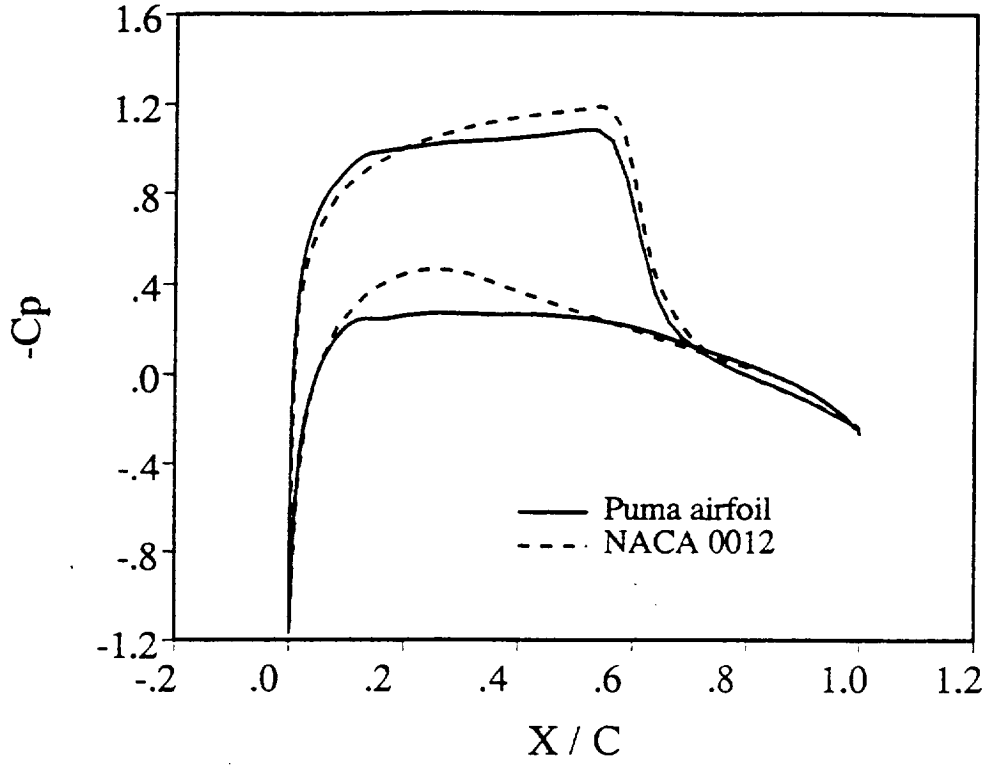


Figure 200. Viscous calculation results; $M_\infty = 0.80$, $\alpha =$; Puma airfoil: $C_l = 0.4599$, $C_d = 0.03022$, $C_m = -0.02514$.

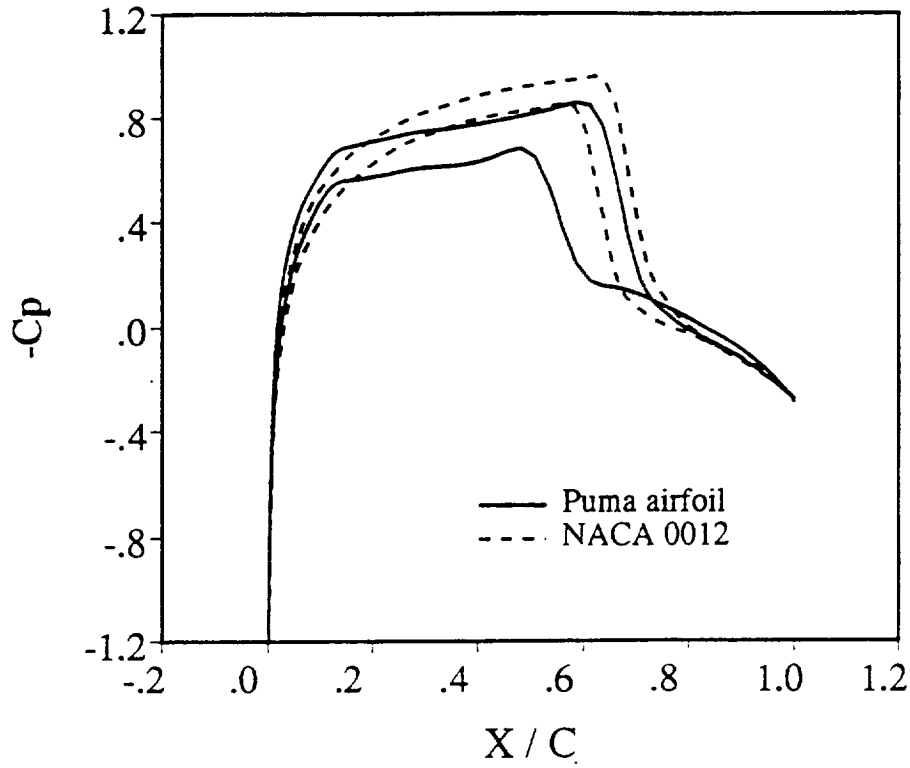


Figure 201. Viscous calculation results; $M_\infty = 0.84$, $\alpha = 0.5°$. NACA 0012: $C_l = 0.1175$, $C_d = 0.04216$, $C_m = -0.02706$; Puma airfoil: $C_l = 0.1469$, $C_d = 0.02222$, $C_m = -0.02649$.

the measurements indicate that the blade thickness at the measurement stations is 1–3% greater than the theoretical model, but the effect of this thickness difference is expected to be slight, based on the analysis presented in Section 5.5.3. The measurements at the most outboard station, $0.978R$, show some thinning of the measured contour near the blade trailing edge and a reduction in chord length as compared to the theoretical ordinates.

The comparison of the 12% thick NACA 0012 and the 10.4% thick Puma airfoil in Section 5.5.3 shows very similar behavior for all subsonic cases. The transonic performance can be very different depending on the particular combination of Mach number and angle of attack that are present. The three test cases in the first Puma correlation workshop had limited transonic flow on the rotor blades and, for those conditions, there should be little effect of using NACA 0012 airfoil tables for the predictions. For the higher speed cases examined in the present study, however, the choice of airfoil tables, plus the accuracy of these tables in the nonlinear flow regions, will have a greater effect on the overall results.

# 6 COMPARISON OF HYBRID METHODS WITH FLIGHT TEST DATA (TASK 2)

## 6.1 Introduction

Typically, aerodynamic models for comprehensive rotor codes are based on lifting-line methods. Nonlinear sectional lift, moment, and drag are based on two-dimensional experimental airfoil data and are incorporated in the lifting-line methods in a straightforward manner. Approximate methods are used to correct for unsteady aerodynamics and three-dimensional effects near the blade tip. The rotor wake is modeled with discrete vortex segments that are tracked in a Lagrangian framework. Wake-induced inflow to the rotor disk is computed with a Biot-Savart integration. The rotor-wake, aerodynamics, and dynamics solutions are coupled together in an iterative trim solution in order to balance the forces for the entire helicopter. The four comprehensive codes described in Section 2.1 of this report are examples of this type of analysis.

Alternatives to lifting-line models for blade aerodynamics are computational fluid dynamics (CFD) schemes that compute the full three-dimensional transonic flow around rotor blades. These methods typically solve the Navier-Stokes, Euler, or potential flow equations. CFD methods have an advantage over other methods because they are designed to model accurately the three-dimensionality and the transonic flow nonlinearities that are associated with high-speed advancing rotors. However, the disadvantage of these methods is that their computational speed and storage requirements are too great to allow for a large number of iterative CFD computations in the trim loop of the comprehensive code. In addition, the complexities of resolving the rotor wake system with adequate grid resolution are typically beyond the capabilities of current CFD codes.

To surmount these problems, computationally efficient hybrid schemes have been developed that replace the lifting-line aerodynamic models in helicopter comprehensive codes with aerodynamic loads that are computed with CFD. The major difficulty with such schemes is how to integrate the CFD-computed airloads efficiently into the trim loop of the comprehensive code. The first successful hybrid approach of this type was developed by Tung et al. (1986) who iteratively coupled the CFD-computed lift from a small-disturbance potential code to the CAMRAD comprehensive analysis (Johnson, 1981a; Johnson, 1981b). The CFD solution was placed outside the CAMRAD trim loop, and the CFD-computed lift was gradually introduced into the calculation with a clever relaxation algorithm.

Figure 202 illustrates the basic Tung et al. (1986) coupling method for the CAMRAD/JA comprehensive code and the FPR CFD code. Note that the two-dimensional airfoil lift values in the CAMRAD/JA trim solution eventually go to zero and that only the CFD-computed lift is used once convergence has been reached. The main point is that the computationally-intensive CFD simulation sits outside of the CAMRAD/JA trim loop, thereby allowing rapid trim solutions at each iteration of the comprehensive code. Typical trimmed calculations using the scheme in figure 202 require approximately three runs each of the CFD solver and the CAMRAD/JA code.

The basic Tung et al. (1986) coupling methodology has been used with a number of different CFD methods and comprehensive rotorcraft codes (Strawn and Tung, 1987; Yamauchi et al., 1988; Chan and Tung, 1985; Kim et al., 1991; Tran and Desopper, 1988). Typically, these efforts have focused on

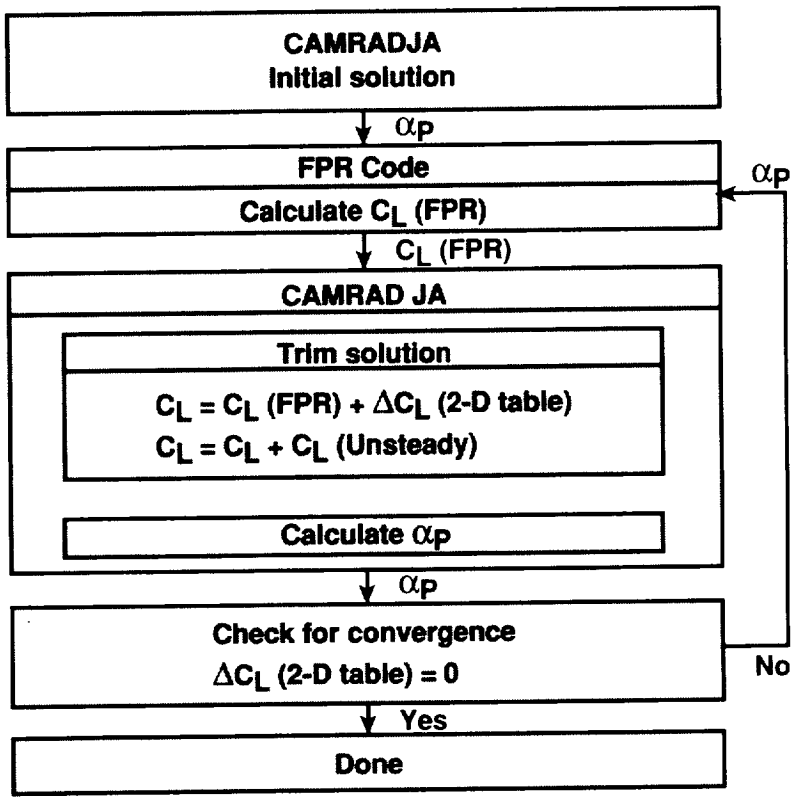


Figure 202. Schematic of the combined rotor airloads prediction scheme of Tung et al. (1986).

the development of the CFD methods rather than the details of the comprehensive analyses and CFD coupling scheme.

The advantage of this type of hybrid analysis is that the CFD-computed aerodynamic loads should model unsteady transonic effects and blade three-dimensionality more accurately. These schemes are not without their problems, however. Their major drawback is that an approximate boundary condition is used to couple the CFD airloads to the comprehensive code. The blade motion and wake inflow are modeled in the CFD solver as radially varying angle-of-attack boundary conditions. This procedure ignores some important unsteady effects that influence the rotor airloads. In addition, the fact that the CFD code sits outside the trim loop in the comprehensive code means that the two codes are "loosely coupled." This loose coupling can lead to stability and convergence problems for the overall scheme. This is particularly true when CFD-computed moments and drag are introduced into the comprehensive code. Note that all of the hybrid efforts cited above use only the CFD-computed lift in the comprehensive analyses.

This section of the report presents results from the CFD analyses after coupling with their comprehensive code counterparts. The two hybrid analyses combine the Full-Potential Rotor code (FPR) with CAMRAD/JA, and the Transonic Small Perturbation code (TSP) with the RAE/WHL code. Results from the Transonic Small Disturbance code (TSD) coupled to the ONERA comprehensive analysis were not available for the workshop. The two hybrid analyses are compared with the measurements obtained in the autorotational dive condition of Flight 487 in Section 6.2. The advancing tip Mach number in this case is approximately 0.92 and the ability of CFD methods to compute unsteady, transonic flows in this case should offer advantages. The two analyses are compared with experimental data for the

high-speed flight condition from Flight 525 in Section 6.3. Although the tip Mach number in this case is only 0.83, the impressed airfoil pitch rate (cyclic pitch angle) has increased from the Flight 487 value of $\pm 3.4^\circ$ to $\pm 11.0^\circ$ and this will force greater unsteadiness in pitching motion. In Section 6.4, the hybrid analyses are compared with the predictions of the lifting-line methods alone for the two cases to assess the advantages and disadvantages of these hybrid methods. Section 6.5 discusses modifications to the CFD lifting-line coupling methods that offer some improvement in prediction accuracy. Finally, summary remarks are provided in Section 6.6.

It should be noted in the comparisons shown in Sections 6.2 to 6.4 that the hybridization or coupling of FPR and CAMRAD/JA represents a relatively mature approach that has evolved from the work of Tung et al. (1986). The hybridization between the TSP method and the RAE/WHL analysis, however, has not been done before and the work reported here is the first attempt at linking the methods, and no modifications or improvements have been performed. The effect is, in all cases, a degradation of the comparison of the calculated results with flight data, even though a convergence in the hybrid scheme has been obtained.

## 6.2 Autorotational Case (Flight 487, Counter 11)

A comparison of the CFD hybrid prediction methods with experimental measurements was made for the high-speed, autorotational case from Flight 487. This case was chosen because it has significant three-dimensional and transonic flow on the advancing side of the rotor disk. The expectation was that the CFD methods should provide a better model for the transonic unsteadiness in the aerodynamic forces than two-dimensional airfoil tables in the lifting-line analyses.

### 6.2.1 Azimuthal Histories of Section Lift

Figure 203 shows azimuthal histories of section lift at three radial locations on the blade. All sectional lift values are scaled by the square of the local Mach number to remove the dependence on local dynamic pressure from the comparisons.

The experimental data at the three radial locations show a large negative lift in the second quadrant on the advancing side of the rotor disk as discussed in Section 5.4.1. This negative lift is accompanied by strong shocks on both the upper and lower surfaces of the rotor. The strong transonic effects pose a challenge for the CFD codes and also for the weak boundary condition that couples the CFD codes to the comprehensive analyses. Recall that the entire effect of the unsteady blade motion and wake is modeled with a radially varying angle-of-attack boundary condition on the rotor blade.

The TSP-RAE/WHL and the FPR-CAMRAD/JA results show large differences in their computed lift predictions. The FPR-CAMRAD/JA results show higher lift near $0^\circ$ azimuth than TSP-RAE/WHL except at the most outboard radial station. The experimental data tend to split the two predictions at this aft edge of the rotor disk. In the third and fourth quadrants the experimental data show better agreement with FPR-CAMRAD/JA predictions.

The two predictions do not show good agreement with the experimental data in the negative lift region of the second quadrant. Here, the FPR-CAMRAD/JA prediction shows more negative lift than

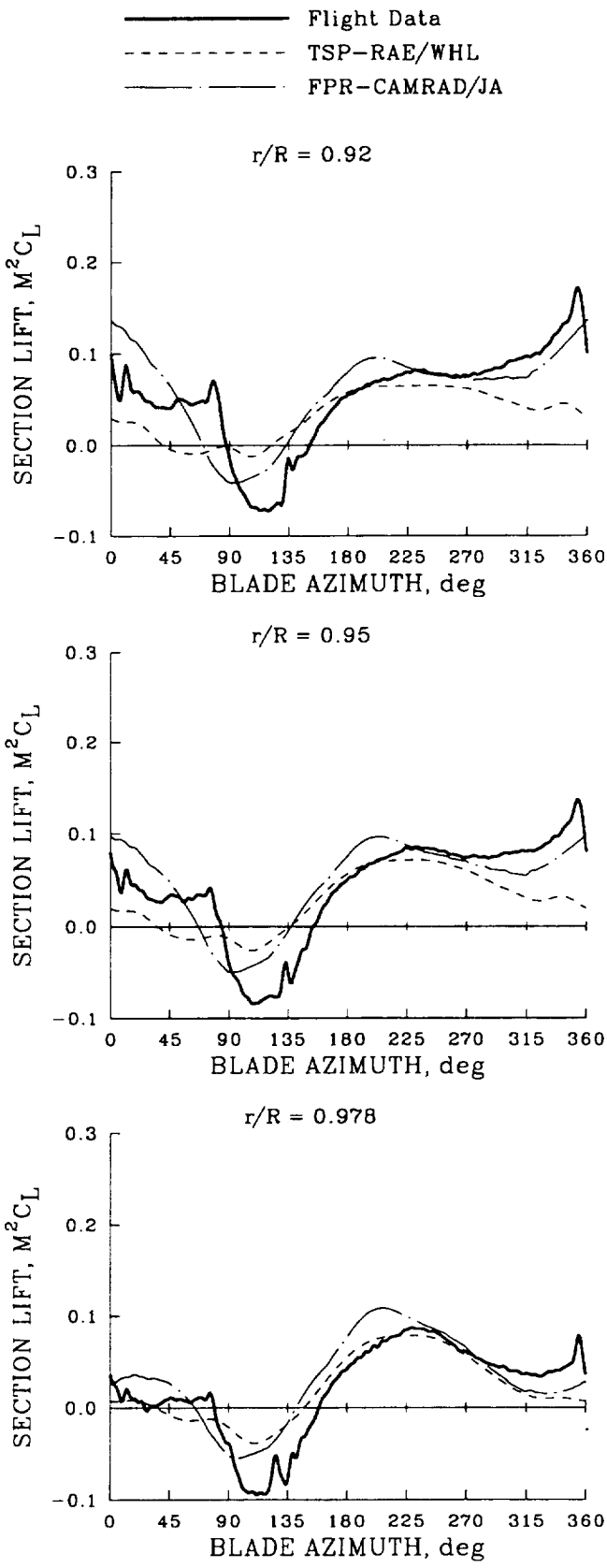


Figure 203. Comparison of hybrid CFD analyses with experiment for section lift; Flight 487.

the TSP-RAE/WHL result although neither shows good agreement with the data. It is not surprising that the TSP-RAE/WHL and the FPR-CAMRAD/JA predictions are different in this region as the FPR code computes a time-accurate solution for the rotor blades while the TSP code uses a quasi-steady analysis. One would expect that the FPR code would provide a better prediction in the second quadrant where unsteady shock motion is important. The fact that neither CFD prediction shows good agreement with the experimental data here means that other factors, not modeled well by either analysis, are important in this region.

Trying to isolate the causes for discrepancies between the predictions and the experimental data is very difficult for this case. This is because the CFD results are iteratively coupled into the trim of the comprehensive codes. Differences in computed results reflect the specifics of the comprehensive codes, the specifics of the CFD analyses, and the specifics of the hybrid coupling algorithms. It is not possible to separate these effects in a meaningful way without additional calculations.

### 6.2.2 Azimuthal Histories of Section Moment

Figure 204 shows computed and experimental values of sectional moment at the three radial stations. As was the case for the lift comparisons, the moment values are scaled by the local free-stream Mach numbers to remove the dependence on local dynamic pressure. Although the computed moment values from the two CFD codes are plotted in this figure, these values were not part of the coupling process with the comprehensive codes. The aerodynamic moment values in the comprehensive codes were obtained from 2-D airfoil tables, modified to account for unsteady effects. Thus the computed moment values in this figure have no effect on the rotor trim.

The data at $0.92R$ are not considered trustworthy on the advancing side because of the absence of pressure transducers towards the rear of the airfoil (see Section 5.4.1). The two hybrid calculations are substantially different between 60° and 180°, although because of limitations of the pressure integration it is not possible to state which provides better accuracy. On the retreating side, however, the TSP-RAE/WHL predictions show better agreement with the data.

Both of the CFD predictions show poor agreement with the experimental data at $0.95R$ and $0.978R$. The TSP-RAE/WHL predictions follow the trend of the data on the advancing side but the magnitude of the predicted moment is underestimated at $0.978R$. The FPR-CAMRAD/JA method does not predict the negative moment in the second quadrant, but the trend of the predictions improves after about 200° azimuth. Such discrepancies between experiment and computation are not surprising for these cases since it is much more difficult to predict aerodynamic moment than aerodynamic lift with a CFD code. This is because aerodynamic moment is much more sensitive to the accurate treatment of the leading and trailing edge regions as well as the effects of transonic shocks. Both the FPR and TSP CFD codes are inviscid and will not give good predictions near the trailing edge of the rotor blade. This affects the aerodynamic moment much more than it affects the aerodynamic lift. Accurate prediction of aerodynamic moment is extremely difficult, even with a CFD code that includes viscous effects. Furthermore, accurate CFD computation of blade moments requires realistic blade-motion boundary conditions. In the present calculations, blade-motion effects were modeled with an inflow angle boundary condition which does not give the correct results for unsteady moments, even with a perfect CFD code.

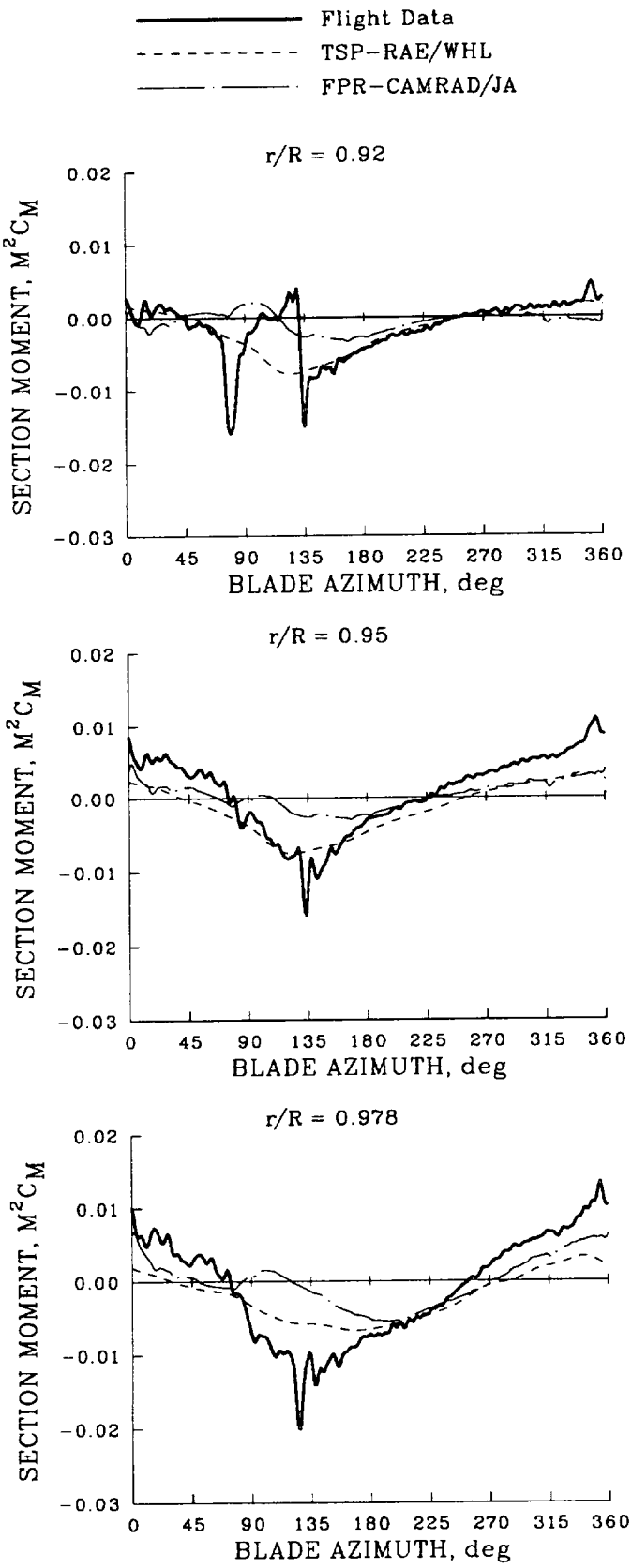


Figure 204. Comparison of hybrid CFD analyses with experiment for section moment; Flight 487.

### 6.2.3 Chordwise Pressure Distributions

Figure 205 compares the experimental and computed chordwise pressure distributions at four radial locations for an azimuth of 30°. The $C_p$ values are scaled by the square of the local free-stream Mach number. For this azimuth in the first quadrant of the rotor the flow is mostly subsonic and significant differences are observed between the CFD predictions and the experimental data. The FPR-CAMRAD/JA predictions generally show better agreement with the data and it appears that most of the difference could be corrected with inflow angle changes to the surface boundary conditions. However, this is not the case with the TSP predictions. As an example, at $0.92R$, the TSP-RAE/WHL prediction shows good agreement with the lower surface pressures, but the prediction of the upper surface pressure is substantially in error. An inflow-angle boundary condition change to the TSP code will not improve this situation.

Figures 206 and 207 compare the CFD hybrid predictions with the experimental data in the transonic region on the advancing side of the rotor disk. The two computations show reasonable agreement with each other at 90°, particularly for the three inboard radial stations. The computed shocks have similar locations and both codes show reasonably good agreement with the experimental data. At 120°, however, the TSP-RAE/WHL code does not show a strong shock at the three inboard radial stations. Both the experimental data and the FPR-CAMRAD/JA result show a shock in this region. The explanation for this is that the TSP code does not include unsteady terms within its solution and therefore cannot properly model transonic flow-field unsteadiness. The FPR code solves the unsteady full-potential equation and is able to capture the unsteady motion of the transonic shock. At $0.978R$ and 120° azimuth, both CFD hybrid predictions show poor agreement with the experimental data. It does not appear that this poor agreement would be remedied by changes to the inflow-angle boundary conditions in either CFD code.

Comparison of the hybrid CFD calculations and the measurements shows similar trends at all azimuths on the retreating side of the disk. Figure 208 shows the comparison at 270°. The FPR-CAMRAD/JA computations show good agreement with the experimental data, with a slight underprediction of the leading edge suction peak at the outboard stations. The TSP-RAE/WHL predictions, however, show worse agreement with experiment. The lower surface pressures are predicted fairly well, but the leading edge suction peaks are significantly underpredicted at all radial stations. This deficiency is typical of CFD predictions based on the transonic small disturbance equation. When the sectional inflow angles are high, the suction peaks on the leading edge are underpredicted. This problem cannot be corrected with changes to the inflow-angle boundary conditions provided by the comprehensive code. The fact that these leading edge suction peaks are underpredicted will then affect the final trim that is obtained in the TSP-RAE/WHL computation.

## 6.3 High-Speed Level Flight Case (Flight 525, Counter 21)

A comparison of the CFD hybrid prediction methods with experimental measurements was made for the high-speed level flight case from Flight 525. This case was chosen because it has significant three-dimensional and unsteady flows due to pitch rate in comparison to the autorotational case of Section 6.2. However, the advancing blade tip Mach number is reduced from 0.92 to 0.83 and the influence of transonic flow is correspondingly diminished.

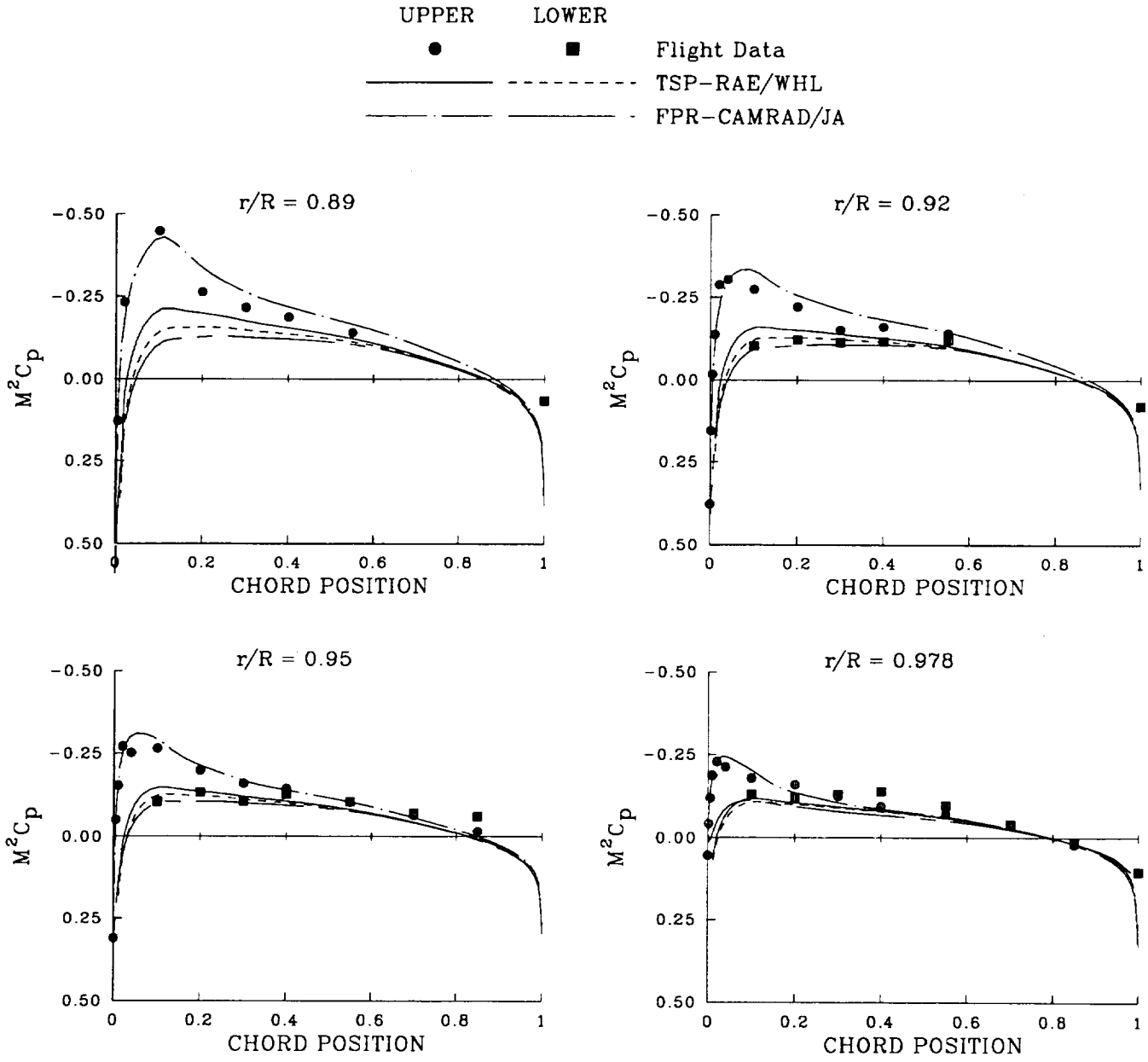


Figure 205. Chordwise pressure comparison of experimental measurements and CFD hybrid predictions for Flight 487; $\psi = 30°$.

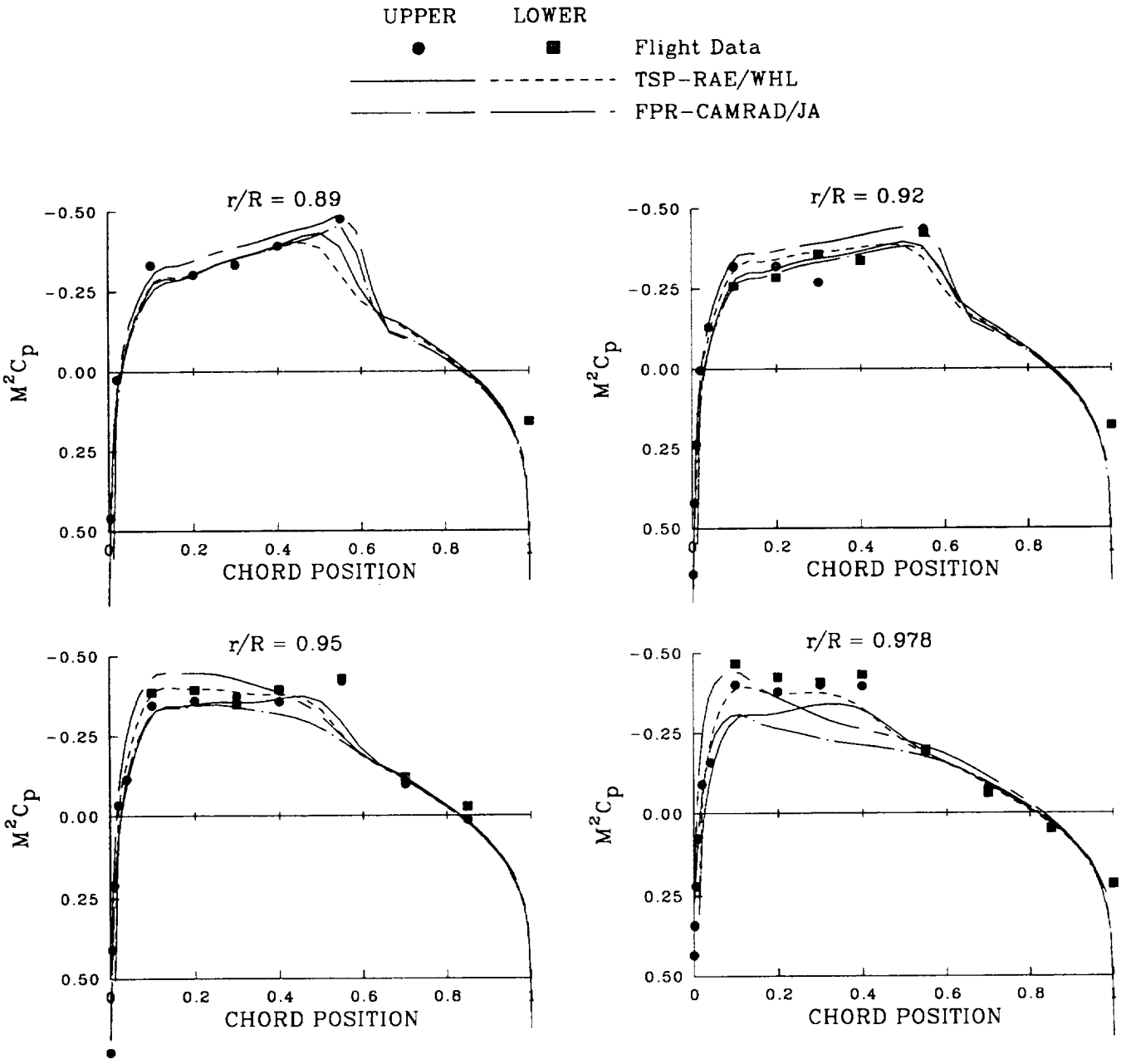


Figure 206. Chordwise pressure comparison of experimental measurements and CFD hybrid predictions for Flight 487; $\psi = 90°$.

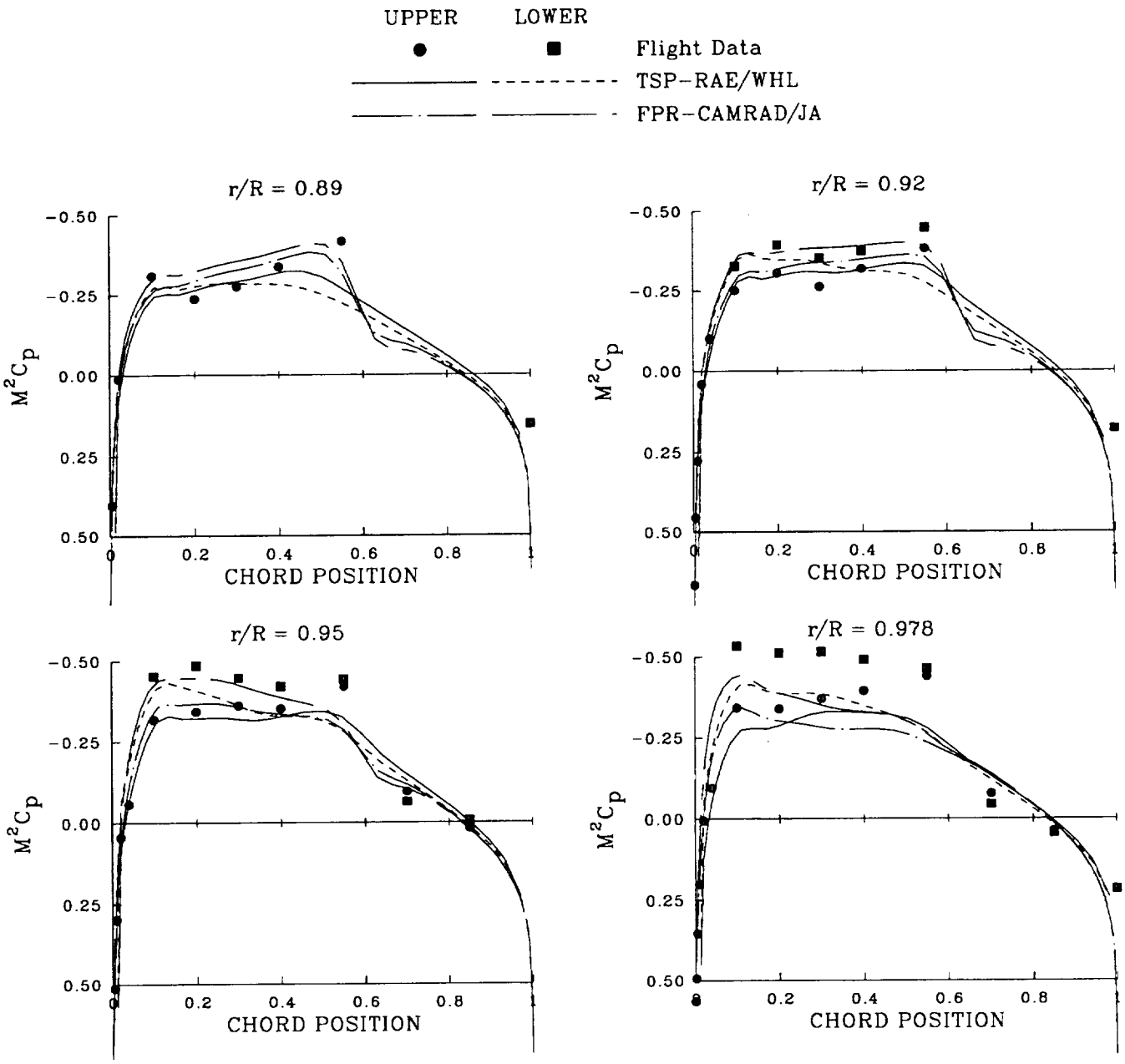


Figure 207. Chordwise pressure comparison of experimental measurements and CFD hybrid predictions for Flight 487; $\psi = 120°$.

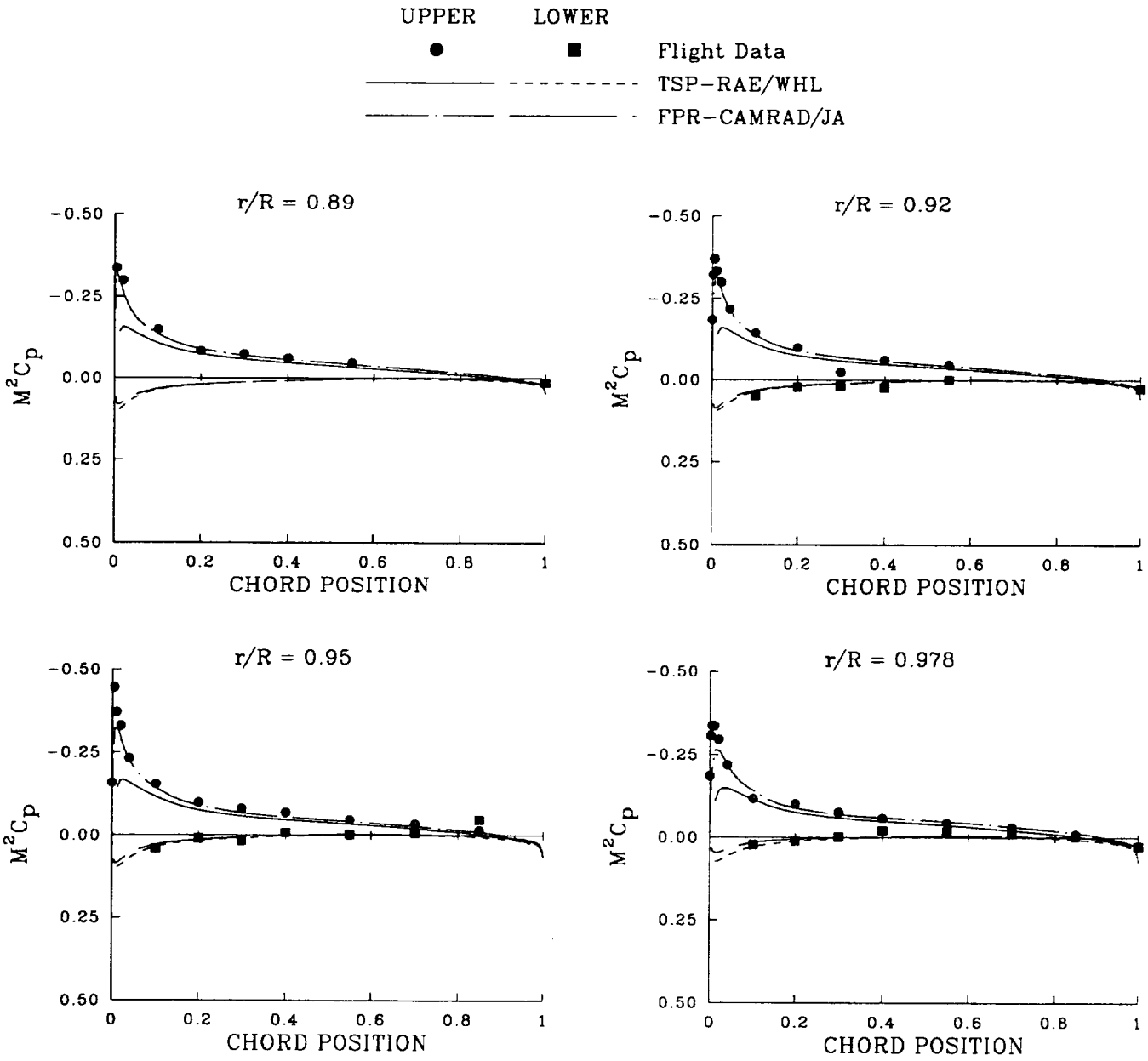


Figure 208. Chordwise pressure comparison of experimental measurements and CFD hybrid predictions for Flight 487; $\psi = 270°$.

### 6.3.1 Azimuthal Histories of Section Lift

In figure 209 plots of section lift, $M^2C_L$, are shown against azimuth for the three radial stations at which flight measurements were obtained: $0.92R$, $0.95R$, and $0.978R$. The FPR-CAMRAD/JA results show a reasonably good comparison with the flight data, with lift maxima and minima occurring with slight discrepancies in azimuth angle. The position of the minimum lift at the beginning of the second quadrant is predicted most accurately, while the first maximum near 30° appears slightly early and the second maximum, in the second quadrant, is predicted late. The actual values of lift are closest around the advancing side, with over- and under-predictions at the rear and front of the disk respectively. The TSP-RAE/WHL results show much less variation in lift values. The minimum at 90° is more obvious than the maxima at about 30° and 180°. Interestingly, the TSP-RAE/WHL results do show a feature at 340° to 355° which reflects the shape of the flight data, albeit at a displaced value of section lift, which the FPR-CAMRAD/JA results do not demonstrate at all. The TSP-RAE/WHL predictions do not vary much across the three radial stations, whereas for FPR-CAMRAD/JA, the maximum at the rear of the disk decreases substantially with increasing radius, following the flight data, and the maximum at the front of the disk increases a little, improving the comparison with flight data at the most outboard station.

### 6.3.2 Azimuthal Histories of Section Moment

The section moment is plotted against azimuth in figure 210, for the same stations as before. The TSP-RAE/WHL results show a trend which is similar to the flight data, but without matching their magnitudes at the maxima and minima. The FPR-CAMRAD/JA results behave similarly over the second half of the azimuth range, and are particularly good in this region at $0.978R$. On the advancing side of the rotor, however, the predicted moments at each radial station have a local maximum where the flight data show a minimum. The section moment values are not easily compared with flight data for these CFD codes, because of the absence of any viscous modeling. Also, the inflow-angle boundary conditions to the CFD codes neglect unsteady effects caused by blade motion. These unsteady effects are very important for accurate moment calculations.

### 6.3.3 Chordwise Pressure Distributions

The calculated chordwise pressure distributions from the hybrid calculations are compared with the measured pressures at $\psi = 30°$ in figure 211. The figures on each plot show the pressure distributions at the four flight data measurement stations: $0.89R$, $0.92R$, $0.95R$, and $0.978R$. With the poor prediction of lift distribution shown by the TSP-RAE/WHL method previously, it is to be expected that the related pressure distributions do not compare favorably with the flight data and this is indeed the case. The FPR-CAMRAD/JA results, on the other hand, are much nearer the flight data, and the corresponding pressure distributions should show better agreement. The full-potential formulation should also show a better prediction of the suction peaks near the leading edge than the TSP method.

These expectations are certainly demonstrated in the pressure distributions at 30°. At $0.89R$ and $0.92R$ the FPR-CAMRAD/JA results slightly underpredict the upper surface pressures, while at $0.95R$ and $0.978R$ the pressure is well predicted over most of the chord, with the minimum pressure at the leading edge not quite achieved. The TSP-RAE/WHL results, however, are not very good for either the upper or lower surface values, except for the lower surface at the radial station nearest the tip.

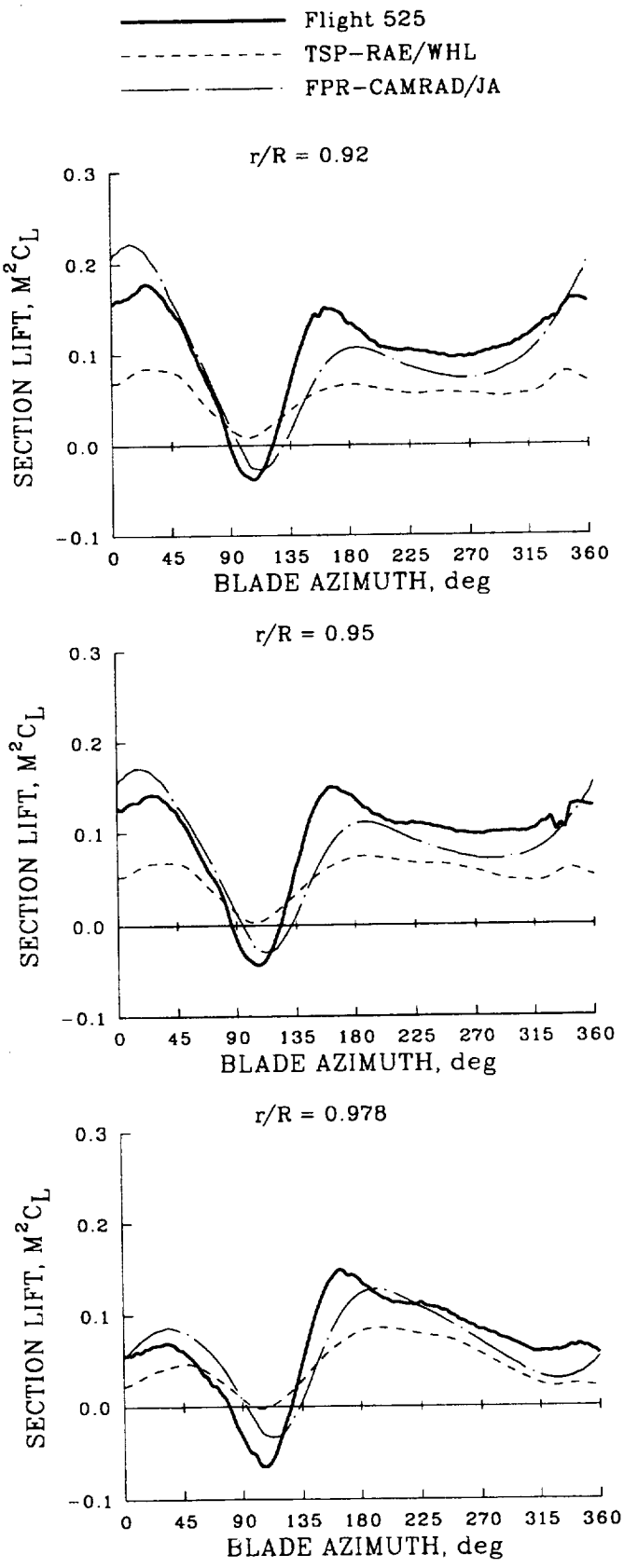


Figure 209. Comparison of hybrid CFD analyses with experiment for section lift; Flight 525.

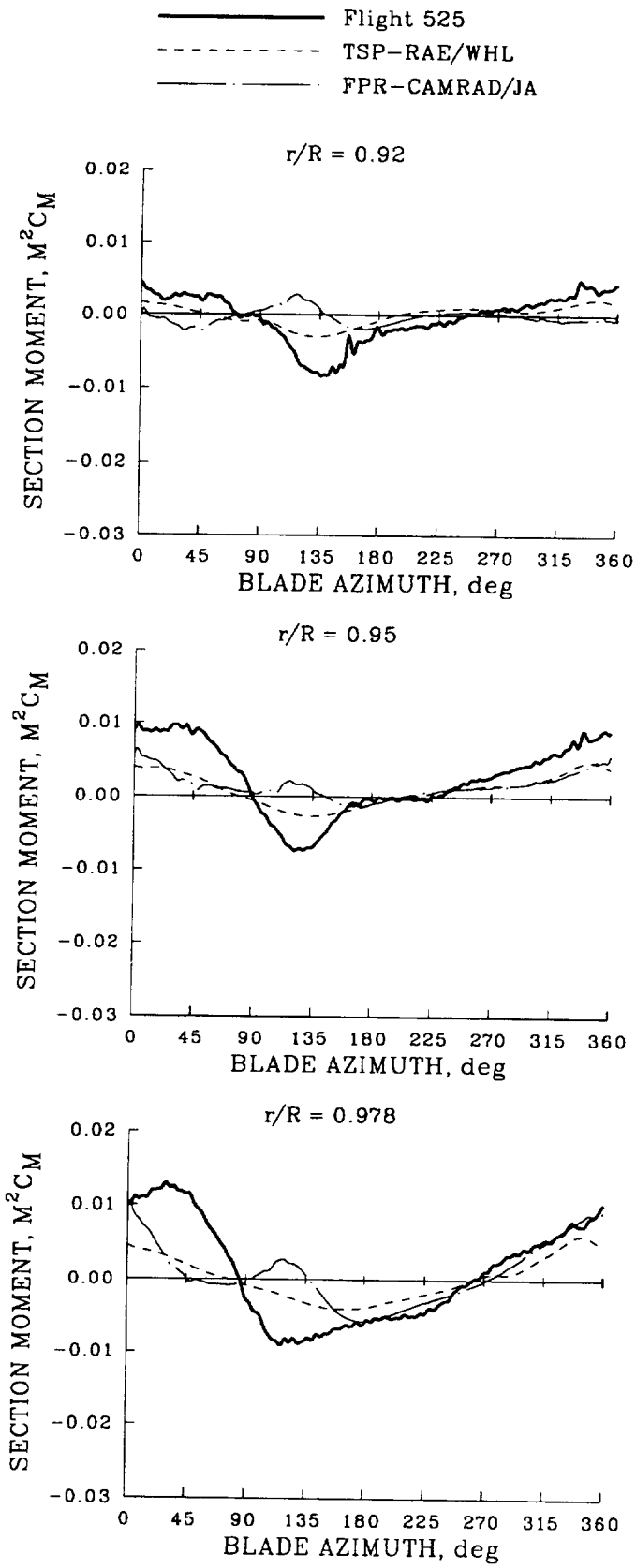


Figure 210. Comparison of hybrid CFD analyses with experiment for section moment; Flight 525.

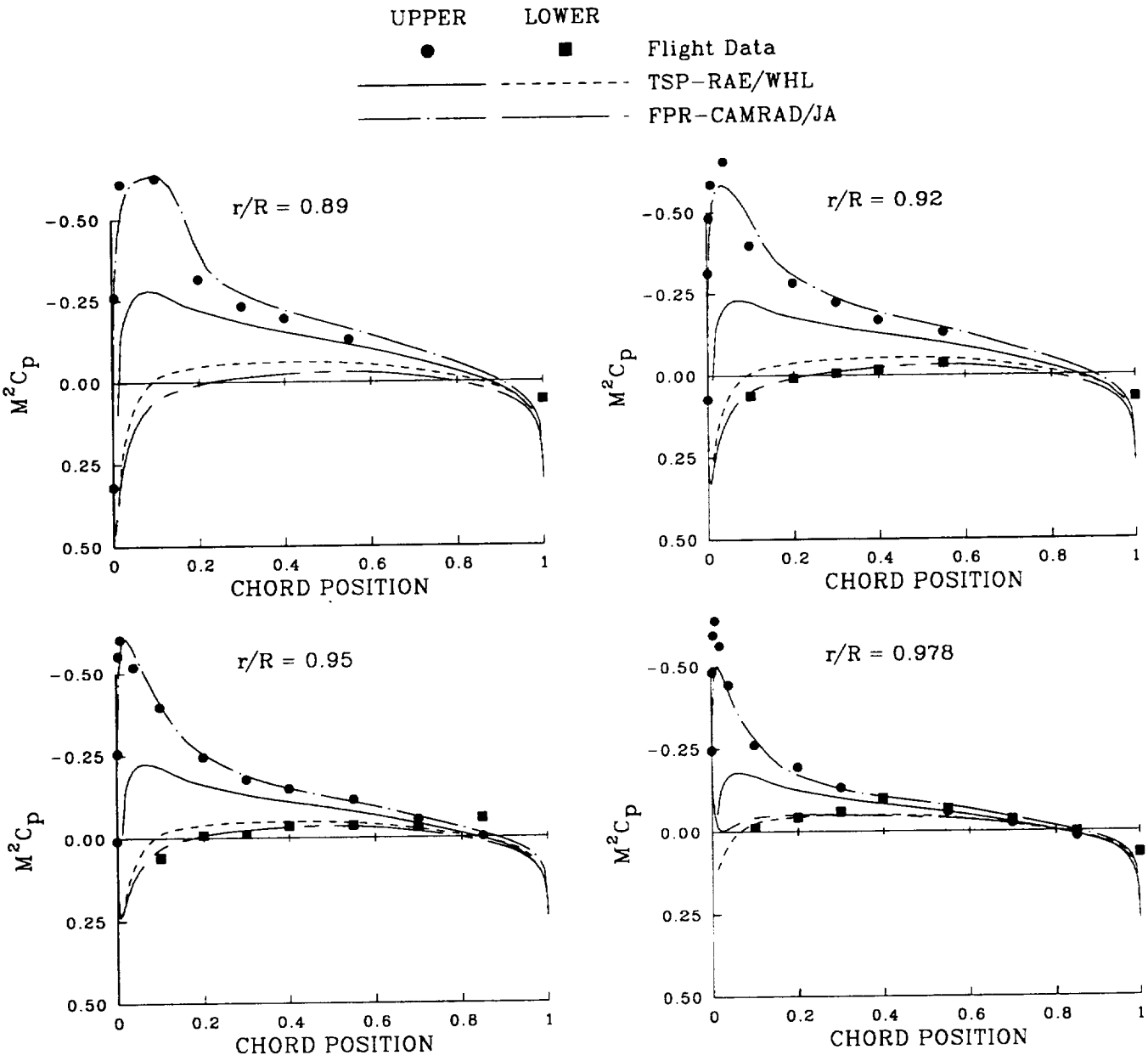


Figure 211. Chordwise pressure comparison of experimental measurements and CFD hybrid predictions for Flight 525; $\psi = 30°$.

At $\psi = 120°$, as shown in figure 212, the lift is negative for both the flight data and FPR-CAMRAD/JA, while the TSP-RAE/WHL results are at positive lift. This azimuth position corresponds to the point where the FPR-CAMRAD/JA results move from slightly overpredicting the lift to slightly underpredicting the lift, so the lift prediction is good at this point, but this is also where the comparison of section moment was at its worst. The reason can now be seen–for the flight data the suction surface appears to cross from the lower surface to the upper surface around mid-chord, thus creating the peak negative moment, but the calculations do not follow this pattern.

At 150° azimuth, figure 213, the lift is again positive everywhere, but this is one of the regions with the greatest discrepancy of section lift between the calculations and the flight data. The predicted lower surface pressures from both codes improve with increasing radius–but otherwise the comparison is poor.

The comparison of the hybrid CFD predictions and measured pressures changes little over the retreating side of the disk; an example at $\psi = 270°$ is shown in figure 214. The FPR-CAMRAD/JA analysis predicts the pressure distributions well on the retreating side of the disk, only missing the tip of the suction peak near the leading edge. Although TSP-RAE/WHL predicts the lower surface pressure correctly, it fails to predict the upper surface pressure and, in particular, only poorly predicts the leading edge suction peak.

## 6.4 Comparison of Hybrid CFD Methods with Lifting-Line Calculations

Hybrid CFD calculations have been compared with two sets of experimental flight data in Sections 6.2 and 6.3 and the accuracy of these methods has been assessed. In the present section these comparisons are extended to include the lifting-line predictions as well and in this fashion assess to what degree the coupling of the CFD methods improves predictive capability.

Figure 215 compares the CAMRAD/JA and FPR-CAMRAD/JA predictions of the section normal force and pitching moment at two radial stations with the experimental results for the high-speed, autorotational case. Neither method predicts the "plateau-like" effect of the normal force in the first quadrant, the extent of the negative lift region in the second quadrant, nor the vortex-induced flows at the rear of the disk. However, the FPR-CAMRAD/JA calculation does show a phase shift in the negative lift region that is an improvement over that predicted by CAMRAD/JA alone. Neither method predicts the section moments adequately.

The CAMRAD/JA and FPR-CAMRAD/JA calculations for the level flight case, Flight 525, Counter 21, are compared with the data in figure 216 for the two radial stations shown previously. For this level-flight case, the lift predictions show much better agreement with the flight data than was seen for the autorotational dive case. There are azimuths for both radial stations where the hybrid CFD computation shows better agreement with the data than the lifting-line method, just as there are azimuths where the converse is true. It is not obvious that the hybrid CFD computation is an improvement over the lifting-line method based on these comparisons with the section lift. Neither method provides a good prediction of the pitching moments although the character of the lifting-line computation is more like the measured behavior, particularly on the advancing side.

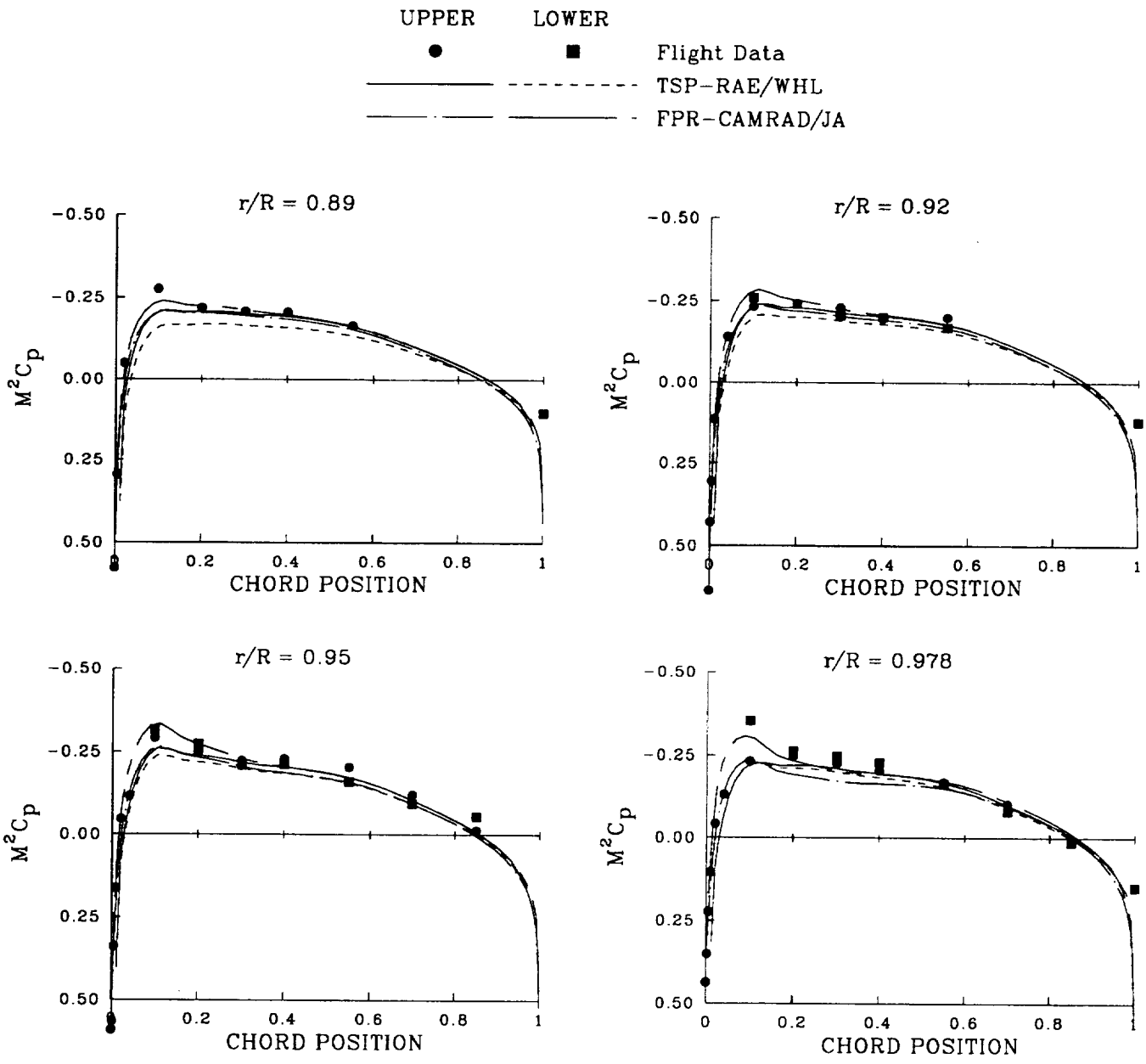


Figure 212. Chordwise pressure comparison of experimental measurements and CFD hybrid predictions for Flight 525; $\psi = 120°$.

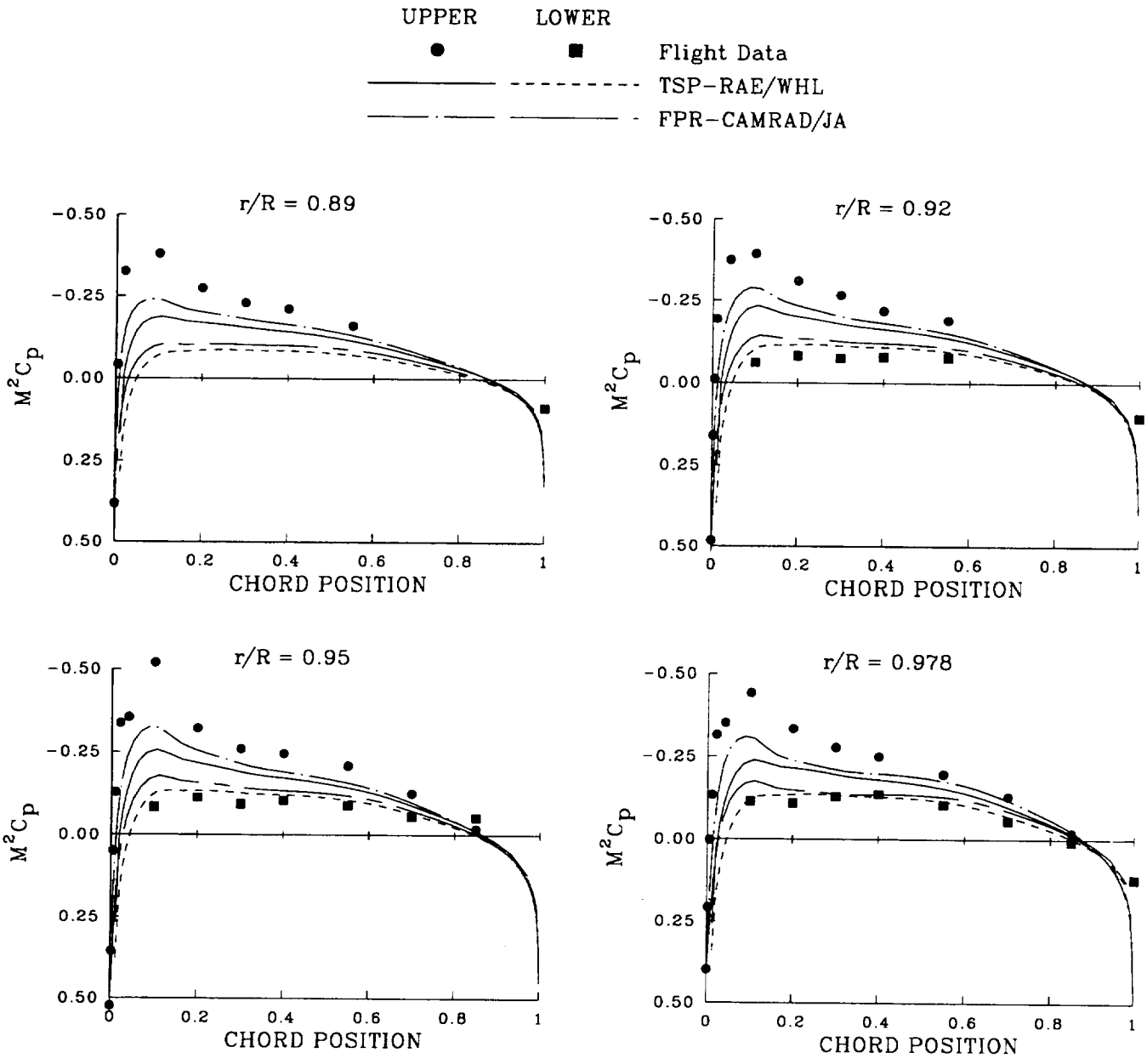


Figure 213. Chordwise pressure comparison of experimental measurements and CFD hybrid predictions for Flight 525; $\psi = 150°$.

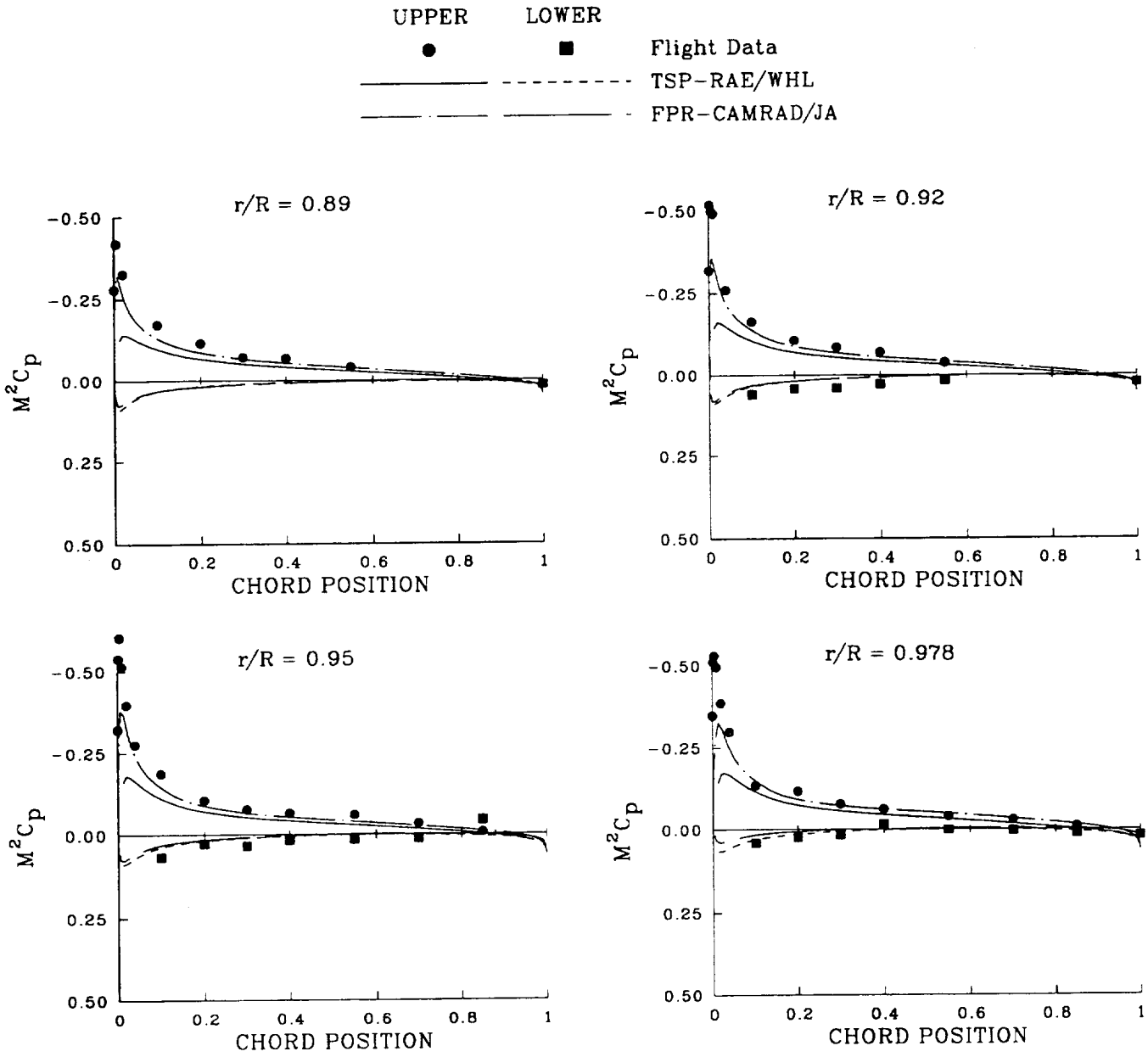


Figure 214. Chordwise pressure comparison of experimental measurements and CFD hybrid predictions for Flight 525; $\psi = 270°$.

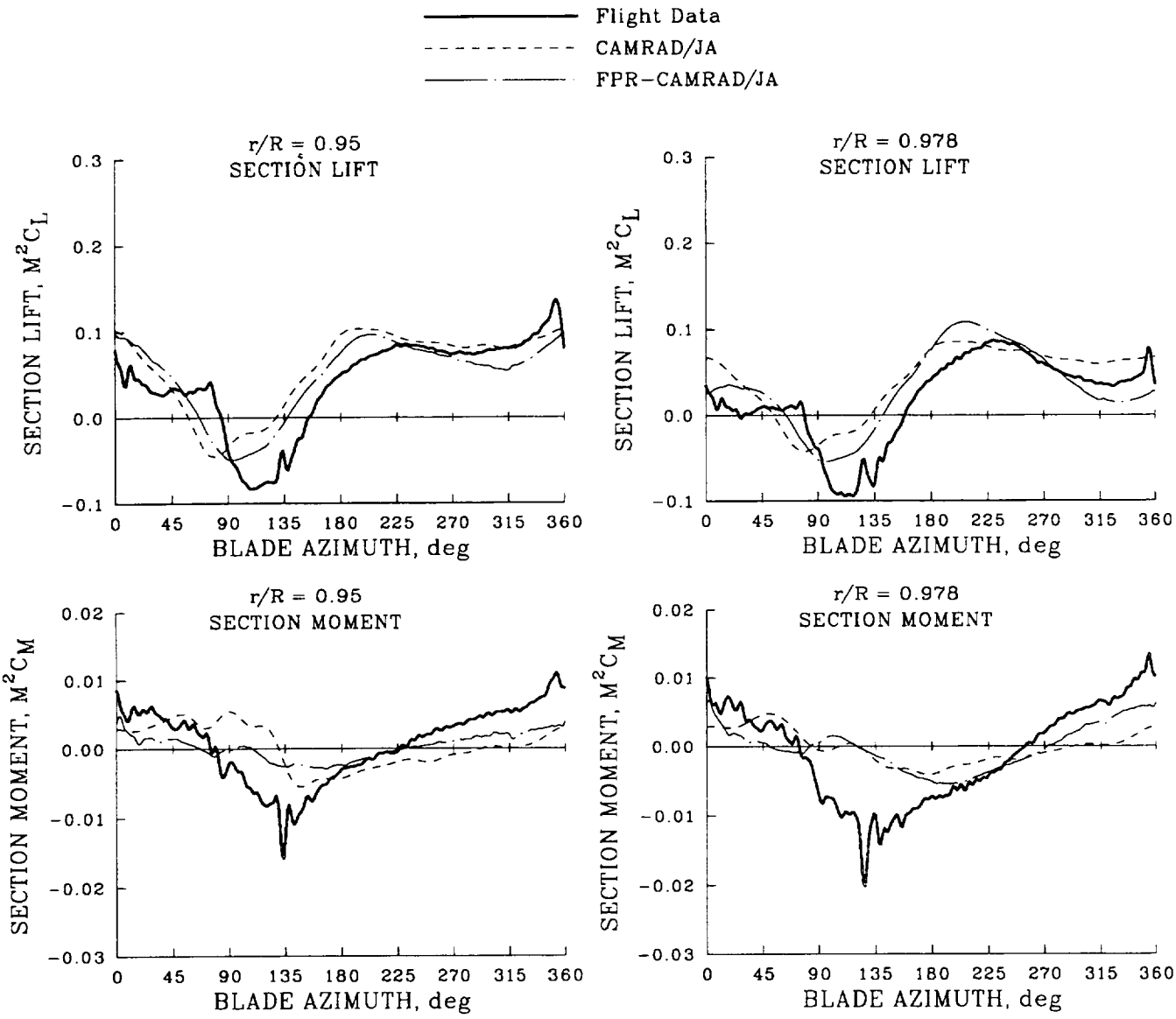


Figure 215. Comparison of CAMRAD/JA and FPR-CAMRAD/JA with flight test measurements at $0.95R$ and $0.978R$; Flight 487, Counter 11.

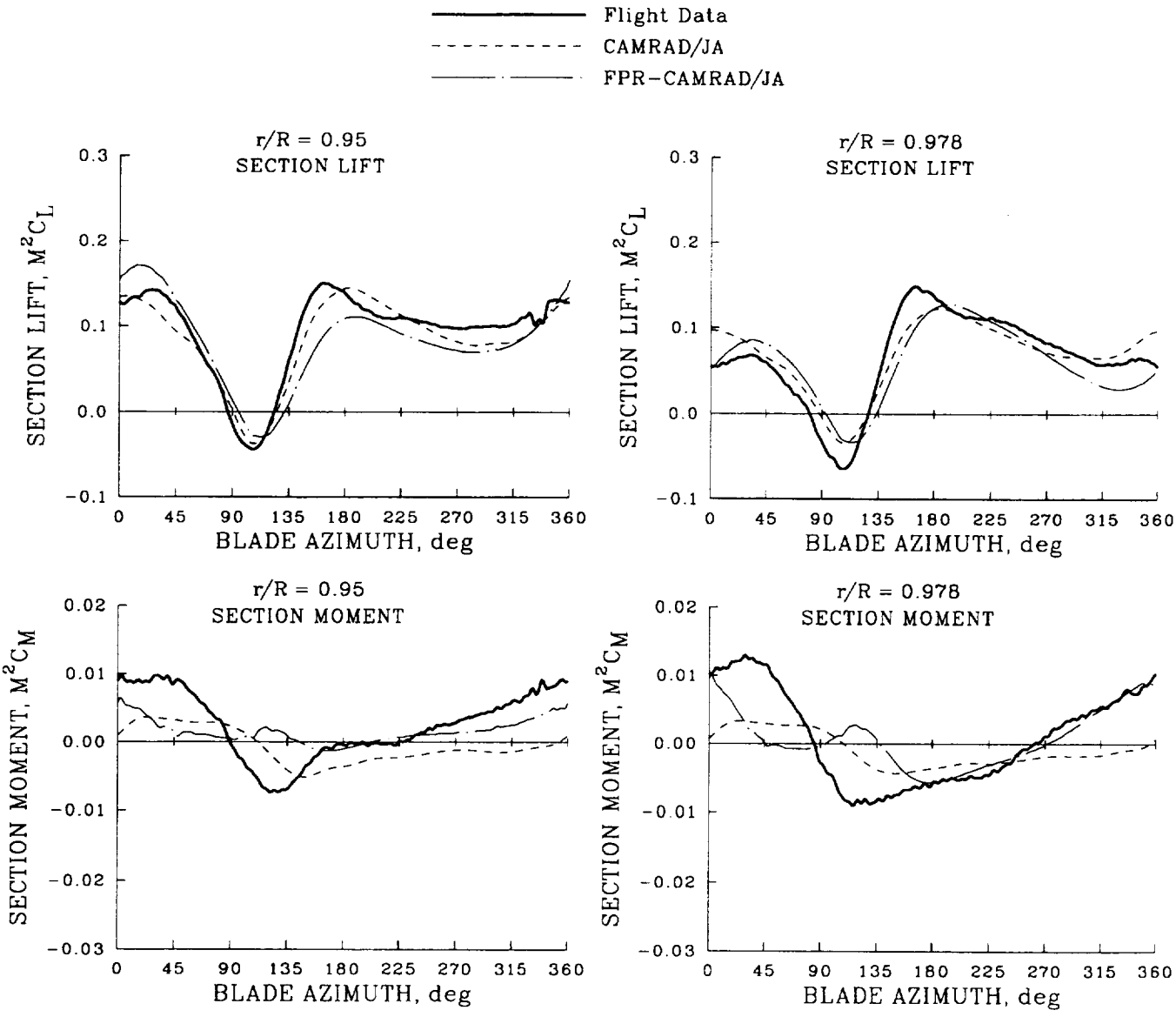


Figure 216. Comparison of CAMRAD/JA and FPR-CAMRAD/JA with flight test measurements at $0.95R$ and $0.978R$; Flight 525, Counter 21.

The RAE/WHL and TSP-RAE/WHL calculations are compared with measurements for the high-speed autorotational case in figure 217. The lifting-line prediction is better than the hybrid method in the prediction of the section lift and also shows a slight improvement in the phase of the negative lift region compared to figure 215. The hybrid calculation shows less lift variation around the azimuth than the lifting-line analysis it is coupled to and is clearly less accurate. The pitching moment predictions are not good, but are better for the CFD calculation than the lifting-line computation, with the general trend being much better predicted even though the magnitudes are not correct. The lifting-line computation shows sizeable excursions in the pitching moment that are substantially different from the measurements and these excursions become more extreme closer to the blade tip.

Comparing the RAE/WHL and TSP-RAE/WHL predictions with the high-speed, level flight case, Flight 525, Counter 21, in figure 218 shows that the lifting-line prediction of the section lift is relatively good, much like was seen in figure 216 for CAMRAD/JA. However, the hybrid calculation shows only about half the section lift and is clearly unsatisfactory. The predicted pitching moments, however, show a better trend for the hybrid calculation than for the lifting-line one, with the extreme excursions in moment near the blade tip predicted by the lifting-line computation being replaced by much more moderate behavior which anticipates the positive and negative regions of the moment correctly. The predicted size of the moment is however too small.

The lack of clear improvement in the hybrid calculations for the cases shown here, particularly for the section moments, is not too surprising. The lifting-line methods in the comprehensive codes use two-dimensional data that include viscous effects while the CFD methods do not include the effects of viscosity and this is especially important for the moment calculations. The lifting-line methods employ unsteady correction terms to accommodate unsteady blade motions while these effects are approximated by the inflow-angle boundary condition in the CFD methods. Neither approach provides a superior prediction of the lift and moment behavior and the limiting effects of the various assumptions is not clearly understood.

## 6.5 Coupling Method Improvements (Flight 488, Counter 9)

As a follow-up to the results presented above, a second study was initiated to evaluate the iterative coupling process between the comprehensive and CFD codes. The results of this study have been published (Strawn and Bridgeman, 1991) and are briefly summarized below.

One of the problems with the Tung et al. (1986) coupling technique shown in figure 202 is that all of the blade motion and wake effects are represented as an inflow angle-of-attack boundary condition at the blade surface. This simplified boundary condition does not model many important unsteady aerodynamic effects that are present for real helicopter blades. A second problem is that previous efforts using the Tung et al. (1986) scheme only make use of the CFD-computed lift in the comprehensive code solution. The computed aerodynamic moment has not been used.

Strawn and Bridgeman (1991) developed improved aerodynamic boundary conditions that more rigorously represent the effects of unsteady rotor blade motion. Just as for the present work, the FPR and CAMRAD/JA codes were used for these studies. The modified analysis was used to compute one of the Puma flight-test cases from the first Puma workshop (Strawn et al., 1989). The effects of unsteady

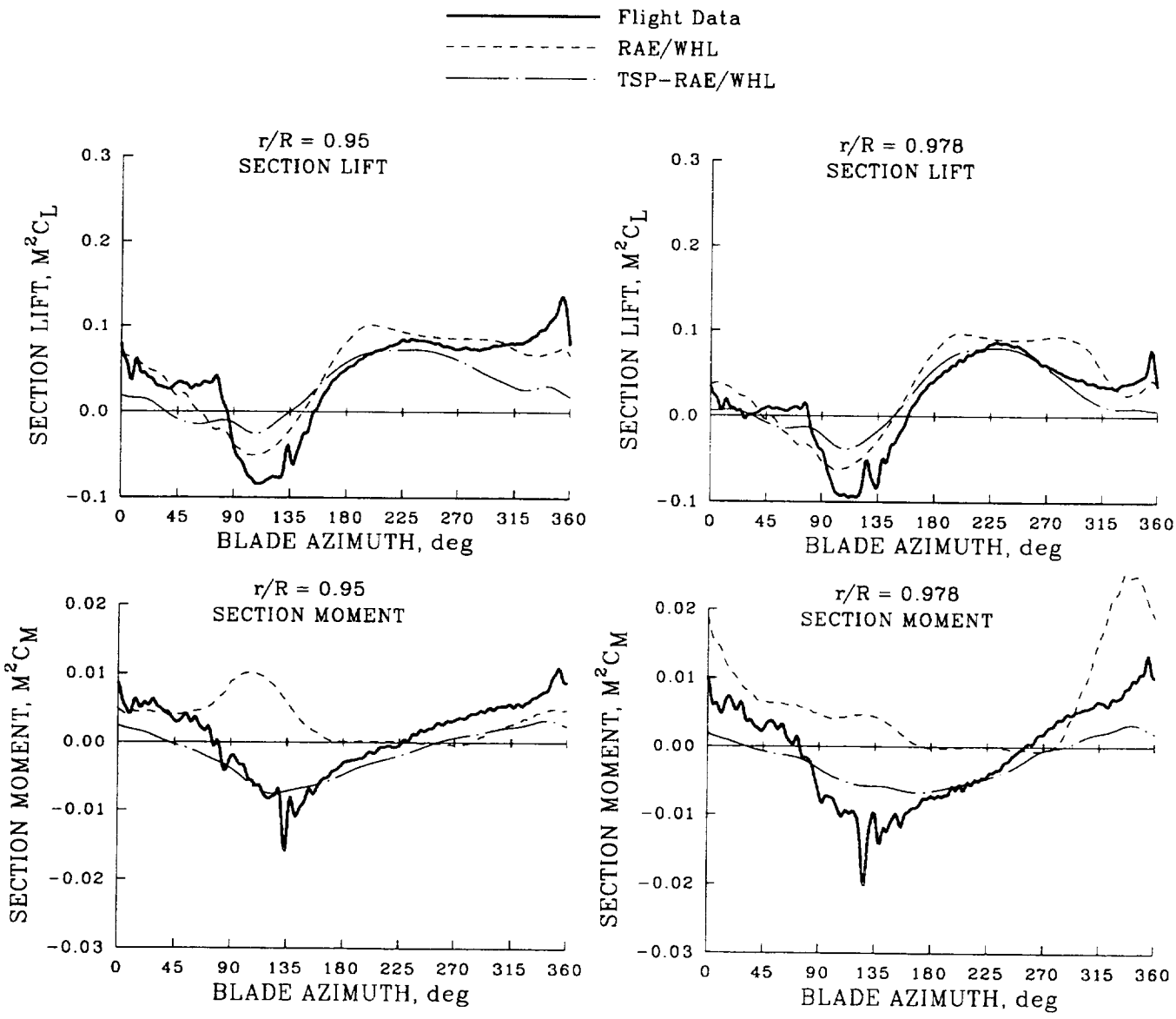


Figure 217. Comparison of TSP and TSP-RAE/WHL with flight test measurements at $0.95R$ and $0.978R$; Flight 487, Counter 11.

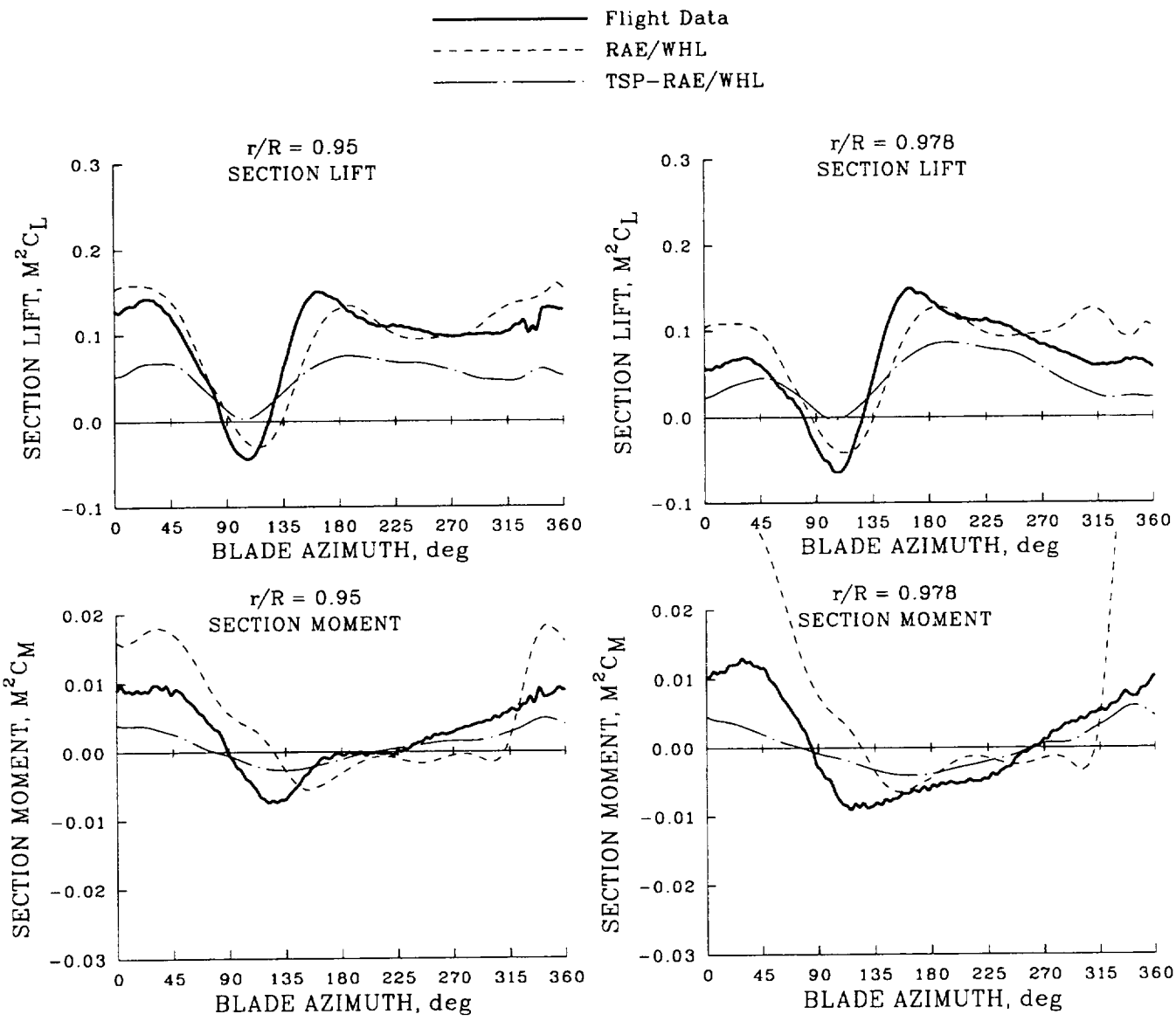


Figure 218. Comparison of TSP and TSP-RAE/WHL with flight test measurements at $0.95R$ and $0.978R$; Flight 525, Counter 21.

pitch were described as a chordwise-varying inflow angle at each spanwise section of the rotor blade. Also, the effects of unsteady lead and lag were directly introduced into the prescribed blade motion for the FPR code. These boundary condition changes resulted in improved correlations with experimental data for both aerodynamic lift and moment. This was particularly the case near 90° azimuth where there is a significant amount of negative lift near the blade tip. The computed moment values were also improved when the unsteady blade motion terms were included in the calculation.

The major drawback with these unsteady boundary conditions was that they led to convergence problems between the CAMRAD/JA and FPR codes. This is because the CFD and comprehensive codes are loosely coupled in the Tung et al. (1986) iteration scheme. The coupling works well as long as the CFD results are not too different from those in the lifting-line aerodynamic tables. Since the lifting-line 2-D tables do not contain any blade unsteady effects, they are most similar to the CFD results when the simplified inflow-angle boundary conditions are used. The nonlinear effects from the unsteady boundary conditions cause convergence problems with the overall scheme.

In addition to the effects of flow-field unsteadiness on the aerodynamic lift, the unsteadiness has an even larger effect on CFD-computed moment values. Moment forces from the FPR code were included in the CAMRAD/JA analysis with the same Tung et al. (1986) coupling scheme that had previously been used only for aerodynamic lift. Once again, the iterative coupling procedure failed to converge.

Several conclusions can be drawn from the Strawn and Bridgeman (1991) study. First, the effects of aerodynamic unsteadiness play a large role in the aerodynamic forces for the Puma flight test cases and this unsteadiness is not accurately modeled in the hybrid CFD calculations for the workshop. Second, it is extremely difficult to improve the boundary conditions for the iterative coupling between the CFD and comprehensive code. Any attempt to improve the modeling of nonlinear unsteady aerodynamic effects degrades the iterative convergence of the "loose" coupling between the two codes.

A new coupling scheme must be developed if these effects are to be accurately modeled. One such scheme is to compute both the aerodynamics and dynamics solutions in the time domain. Time steps would alternate between the aerodynamics and dynamics codes. The dynamics code would provide the complete blade motion to the CFD code, and the CFD code would provide the complete aerodynamic forces and moments to the dynamics code. These boundary conditions would be lagged one time step in each code. This procedure gives a more tightly coupled solution between the aerodynamics and dynamics than the Tung et al. (1986) method. It should be stable at all times, but it is unknown whether the rotor blade forces could be trimmed within a reasonable amount of computer time. Other coupling techniques may be possible and these should be explored in further research efforts.

## 6.6 Summary of Hybrid CFD Calculations

CFD and lifting-line methods were combined in a hybrid scheme (Tung et al., 1986) and compared to two flight cases: a high-speed, autorotational case with $M_{90} = 0.92$ and a level flight case with $M_{90} = 0.83$. The coupling of the FPR and CAMRAD/JA analyses is an evolutionary development from the original work of Tung et al. (1986), but the coupling of the TSP and RAE/WHL analyses was done for the first time as part of this correlation effort.

The FPR-CAMRAD/JA hybrid analysis, in general, shows predictions of the section lift that are as good as, and in some cases better than, that predicted by the conventional lifting-line approach. The prediction of the section pitching moment, however, is unsatisfactory as is the lifting-line prediction. The TSP-RAE/WHL predicted lift is considered poor for all cases, but the moment, although not strong enough, shows improvement over that predicted by the lifting-line calculation.

The hybrid scheme used to couple the CFD and lifting-line methods is based on an iteration method where the lift computed by the CFD code is used as a replacement of the 2-D tables that are integral to the lifting-line methods. Details of the coupling still require refinement, as discussed in Section 6.5, and it has been shown (Strawn and Bridgeman, 1991) that these improvements will provide lift predictions that are as good as the best from a lifting-line prediction. However, this iteration approach does not converge when unsteady blade-motion effects are added to the CFD analysis nor when the CFD-computed pitching moment is coupled to the comprehensive code using the same scheme as used with the blade lift.

The largest pitching moments are observed to occur near the blade tip and it is in this region, within a blade chord or two of the tip, that the lifting-line methods become inaccurate in the calculation of moment (Bousman et al., 1989). It is difficult to accurately compute the blade pitching moments in this region with a CFD code. In addition, even if accurate CFD pitching moments were computed, it does not appear that they could be iteratively coupled to the comprehensive analyses using the method of this study (see figure 202).

# 7 CONCLUSIONS

Conventional lifting-line methods and hybrid lifting-line/CFD analyses have been used to predict the airloads and structural loads on a research Puma in forward flight and have been compared with measurements obtained on that aircraft. Under Task 1 of the collaboration the predictive accuracy of the lifting-line methods has been assessed by comparing calculations with airload measurements, blade bending moments, pitch-link loads, and aircraft trim measurements for a range of advance ratios from 0.098 to 0.402. These comparisons provide a general assessment of the lifting-line methods over a range of flight speeds. In Task 2, two flight conditions have been selected for detailed comparisons of the predictive accuracy of the hybrid lifting-line/CFD methods, including the prediction of pressure distributions on the blade under transonic flow conditions.

In addition to the comparisons of analysis and measurement in the two primary tasks a third task, Task 3, was designed to examine the lifting-line method predictions as modeling complexity was increased in a stepwise manner. In this way it was possible to conclude, in examining the predictions of Task 1, the source of differences between the analysis and the measurements. Task 3, as discussed in Section 4, was augmented by a number of other investigations that addressed particular modeling issues or questions. These investigations included a comparison of modal frequency predictions as a means of comparing the structural models in the lifting-line analyses (Section 3), a comparison of the airfoil tables used in the lifting-line calculations with wind tunnel measurements (Section 4.2) and calculation (Section 5.2.2), calculations and measurements on a rectangular-tip blade to provide insight into the swept-tip blade behavior (Section 5.3), and measurements of the blade profile and comparison with the theoretical blade ordinates used in the CFD calculations (Section 5.5.1).

This conclusion section will focus on the most significant results obtained from the collaboration and will not, in general, repeat all of the summary material in Sections 4.4, 5.2.3, 5.3.4, 5.4.3, 5.5.4, and 6.6. In presenting these conclusions, the section will integrate results obtained in all of the collaborative tasks.

*Normal Force*

Qualitatively, the lifting-line methods provide a good prediction of the normal force on the blade near the blade tip. It is clear from the modeling investigations for Task 3 (Section 4) that the rotor wake and the coupling of the wake with the lifting-line analysis is by far the most important aspect of these calculations. At low speeds the wake vorticity must be correctly modeled to obtain a good calculation of the normal force and this was achieved by the methods that include a free wake model. At higher speeds the use of a prescribed wake model is suitable for all of the calculations.

The detailed comparisons for normal force show that, in most of the flight conditions examined here, the best of the lifting-line methods are able to provide an accurate prediction of the normal force. The worst case is the autorotational dive condition (Section 5.4) and although part of the difficulty these methods encounter is related to the unsteady transonic loads at this high Mach number condition it appears that most of the difficulty is related to the inability of these methods to calculate the torsional response of the rotor blades properly.

The prediction of the normal force with the best hybrid lifting-line/CFD calculation is neither better nor worse than the lifting-line prediction alone. The hybrid calculation does, of course, provide details of the blade pressure distribution and in many cases these results show quite good agreement with measurements and provide confidence that these analytical tools can correctly model the transonic flow behavior.

The analytical modeling investigation in Section 4 shows that the correct calculation of normal force at the speed and thrust conditions examined in this task is largely a consequence of the correct modeling of the rotor wake and, to a substantially lesser degree, the blade aeroelastic behavior. Nonlinear aerodynamics, as represented by blade stall or transonic effects beyond the Prandtl-Glauert corrections, are not important for these conditions nor are unsteady aerodynamics.

*Section Pitching Moment*

Qualitatively, the prediction of section pitching moment at the blade tip by the lifting-line methods is poor. At low speed, as was seen in the case of the normal force, the dominant effect is vorticity in the rotor wake, while at high speed, the dominant effects appear to be related to unsteadiness and three-dimensionality. The poor low-speed predictions are a consequence of the single lifting line of the analytical methods. The rapid inflow change induced by vorticity from previous blades is applied at only a single point and, hence, there is little effect on the section moment. Thus the physics of the rotor flow are absent in the calculation, but as these section moments are relatively small and of high frequency the torsional loading is not strongly affected.

The largest section moments are seen at high speed. This is also true for the torsional loading and there is a direct correspondence between the measured section moments and the torsional response. The analytical modeling calculations in Section 4 show that these loads are a consequence of both steady effects incorporated in the nonlinear aerodynamic look-up tables and unsteady effects that are derived theoretically. The data for the swept-tip rotor clearly show an increase in these section moments towards the blade tip and only the RAE/WHL analysis shows a comparable increase. The other lifting-line methods substantially underpredict this loading. A comparable moment is not obtained by the RAE/WHL analysis for a rectangular blade calculation (Section 5.3.2.2) and hence the moment calculation is sensitive to tip planform, an effect that is contrary to experimental measurements previously obtained on the Puma with a mixed-bladed rotor (Maier and Bousman, 1992).

A part of the discrepancy in pitching moments at high speed appears to be related to inadequacies in the section pitching moment tables used by the CAMRAD analyses and METAR/R85. The comparison of these tables in Section 4.2 with experimental data and the equations used by the RAE, which are based on an independent set of data, show that the section moments are positive and nonzero for $M \leq 0.70$. Calculations show that these nonzero values do have a significant effect upon the prediction of the blade pitching moments. However, the difference in section pitching moment tables, although important for the inboard portion of the blade where two-dimensional flow is dominant, does not appear to influence the discrepancy in moments near the blade tip.

The hybrid TSP-RAE/WHL method shows an improvement in the prediction of the section moments at the blade tip, although the results are still not good, but the FPR-CAMRAD/JA hybrid calculation does not show any substantial improvement. These methods should be able to model accurately both

three-dimensional and unsteady effects and the cause of their poor performance is unknown. Comparison of a full-potential method and a thin-layer Navier-Stokes calculation for the prediction of steady, two-dimensional pitching moment in Section 5.5.3 shows the necessity of some sort of boundary-layer model for the prediction of steady moments and the lack of a viscous model is clearly part of the problem. Another deficiency is the fact that the unsteady effects due to rotor blade motion are not adequately represented in the boundary conditions for the CFD codes. Finally, the method of weak coupling of the lifting-line and CFD methods through the section normal force calculation is unlikely to allow improved moment calculations to be fed back into the lifting-line computation.

*Performance*

The rotor was trimmed to aircraft gross weight and the prime measure of performance was the main rotor shaft torque. The four lifting-line methods, in general, show good agreement with each other, but underpredict the measured values. This underprediction is greatest at high speed and, undoubtedly, some of the discrepancy is related to the fact that the effect of fuselage and stabilizer download is not included in specifying the rotor thrust. However, it does not appear that the incorrect download modeling can explain more than half the discrepancy and the cause of the rest of this difference is unknown. The drag coefficient data used in the airfoil tables compare quite well with wind tunnel measurements, as shown in Section 4.2, and it seems unlikely that the incorrect calculation of profile drag can explain the discrepancy in main rotor torque. The ordinates of the modified tip used on the research Puma have been measured (Section 5.5.1) and two-dimensional CFD calculations using these ordinates (Section 5.5.2) are close to the values used in the lifting-line analyses' look-up tables and equations. Analytical modeling investigations (Section 4) indicate that the blade is largely unstalled for these conditions.

*Blade Flap Moment*

The blade flap bending moments, computed by the lifting-line methods, are qualitatively quite good. This is particularly true in the midspan section of the blade and at high speed where the loading is dominated by the first and second flap bending modes. In the root section of the blade the influence of higher blade modes is observed and the calculations are less accurate. The accuracy of the flap bending moment amplitudes is closely related to the accuracy observed in the calculation of normal force. Thus, at low speed, where the wake vorticity influences the inflow angles, the CAMRAD analyses, using a free wake model, show better predictions of the flap bending moments. At high speed, the RAE/WHL code provides a more accurate prediction of the blade bending moments.

Modal frequency and shape information is provided in Section 3 for some of the lifting-line methods and these results indicate that the structural models implemented in these analyses are essentially identical. Thus, observed differences in the lifting-line predictions are likely to be a result of aerodynamic modeling difficulties or other aspects rather than structural modeling problems.

*Blade Chord Moment*

The lifting-line calculations of chord bending moment are uniformly poor. The peak-to-peak loadings that are calculated are similar to the flight measurements, but the frequency content is substantially

different and it is clear that the present models are inadequate for the prediction of chord bending moments, deformations, or shears.

It is useful to note, for a high-speed condition, that the best of the lifting-line methods are predicting the phase of the 3/rev flap bending moments to within a few degrees and the moment amplitudes are predicted nearly exactly by the RAE/WHL analysis although they are underpredicted by the other methods. Yet for the identical condition and radial station the chord bending moment calculations and measurements show entirely different frequency content and behavior. Comparing the two sets of predictions, for flap bending and chord bending, it is difficult to believe that they are in any way related.

The calculation of the chord bending moments is sensitive to both the normal and chord airloads and the structural response may be caused as much by coupling with the flap degree of freedom as by direct response to the chord airloads which are much smaller than the normal airloads. In addition the response calculation must include the effects of the blade root-end fixity in terms of the boundary conditions. In this respect both the drive train (or rotor shaft impedance) and the lag damper may be important. The modal comparisons in Section 3 do not consider either the effect of the shaft impedance or the lag damper and are, therefore, not useful in understanding the poor chord bending moment prediction. Clearly a great deal of work remains to be done to understand the correct modeling of the chord bending degree of freedom.

*Blade Torsion Moment*

The blade torsion moments, particularly at high speed, are underpredicted by all of the analyses except CAMRAD. However, an examination of the azimuthal time histories suggests that the CAMRAD predictions are largely spurious as they bear little relation to the data. On the other hand, the general character of the RAE/WHL and CAMRAD/JA analyses is similar to the data, but with an oscillatory amplitude only half what is measured in flight. The METAR/R85 analysis shows similar amplitudes, but the frequency content and phase of the computation is degraded from that of the other analyses, most likely because of the lack of blade torsion deflection in the analysis.

The underprediction of the torsional moments leads to an underprediction of the torsional deformation as well. From the experimental data, it is estimated that the elastic deformation at the blade tip at high speed is approximately $\pm 3^\circ$ and this suggests that the underprediction in the torsional moment calculation will lead to errors of up to one and a half degrees in angle of attack at the tip.

*Hub Vibratory Loads*

Predictions were made of the hub 4/rev vibratory loads by each of the lifting-line methods assuming that the rotor was mounted to a hub of infinite stiffness. No direct measurements of the hub vibratory loads were obtained in the test program, but the 4/rev vertical shears, pitch moments, and roll moments have been estimated from flap bending moment and angle measurements using calculated in-vacuum modes to fit the data. The lifting-line methods show reasonable agreement with the vibratory pitch and roll moments and this agreement roughly parallels the agreement seen in the prediction of the flap bending moments. The prediction of the 4/rev shears is less satisfactory, particularly at high speed, and this is a result of the poorer prediction of the 4/rev flap bending moments.

No attempt was made to estimate the inplane shears based on the limited chord bending moment measurements so it is not possible to assess the predictive capability of the methods for these loads. However, the poor calculation of the chord bending moments discussed above probably applies also to the calculation of the 4/rev inplane shears.

Although hub vibratory loads were not computed as a part of the analytical modeling effort in Section 4, that section is useful in clearly demonstrating that at high speed, the source of the 3/rev and 4/rev vibratory loads in the rotor is aircraft trim. These loads may be decreased slightly or increased slightly through aeroelastic effects, but the high-speed vibration is trim-induced and is a fundamental part of a conventional helicopter's existence.

*Puma Airfoil Characteristics*

A number of separate efforts were undertaken as a part of this collaboration to assess both the modified and unmodified Puma airfoil characteristics. Measurements were made of the modified airfoil ordinates at the time of the original flight tests and, with greater resolution, as a part of the collaboration. The results in Section 5.5.2 indicate that the swept tip as flown is quite close to the theoretical ordinates used for the CFD calculations. It appears that the actual airfoil is slightly thicker but this is not expected to affect any of the results. At the most outboard measurement station, $0.978R$, there is a slight shortening of the actual airfoil and the effect of this change is unclear.

Two-dimensional calculations have been made in Section 5.5.3, both with an inviscid model and, for a few extreme cases, with a viscous model and the results compared with a standard NACA 0012 profile (the lifting-line methods have used the section aerodynamics of the NACA 0012 for all calculations). Although some effects are seen on pitching moment and drag at high Mach numbers and angles of attack, these are relatively slight and should not significantly affect the calculated results. More important is the comparison of the aerodynamic tables with experimental measurements in Section 4.2 which shows that the section moments for $M \leq 0.70$ are too small in the tables used by the CAMRAD analyses and METAR/R85. The equations in the RAE/WHL model show good agreement with the wind tunnel data.

# 8 RECOMMENDATIONS

*CFD Modeling*

The hybrid lifting-line/CFD method results presented in this collaboration are feasible only because of the relatively rapid solution of the trim problem by the lifting-line calculation and the provision of this information to the CFD analysis. At least for the research Puma, the prediction of normal force by the lifting-line methods appears relatively satisfactory and the hybrid methods used here did not show a clear improvement over their lifting-line counterparts. However, the weak coupling scheme and simplified inflow-angle boundary conditions used with the hybrid methods are a major cause of inaccuracy in the CFD methods. The coupling scheme of Tung et al. (1986) will most likely have to be abandoned to make more effective use of the CFD results. Unfortunately, any improved coupling scheme will probably require that the CFD codes be coupled directly into the rotor trim analysis, with resulting high computational cost. This may also require that the integration and convergence schemes in the comprehensive codes be restructured to accommodate the computational overhead of the CFD analysis.

*Aerodynamic Moments*

The failure of the lifting-line methods to predict the aerodynamic pitching moments near the blade tip is not surprising as the accuracy of these methods should decrease as the tip is approached. There may be a number of analytical approaches that can extend or modify the lifting-line approach without going to the computational burden that CFD analyses currently require and these should be pursued. It is also clear that when CFD analyses are used for airloads computations they must include some viscous representation to properly represent the aerodynamic pitching moments. Improving the accuracy of CFD methods for the prediction of aerodynamic pitching moments must remain a primary focus in their future development.

*Torsional Deformation*

The elastic deformation of the blade in torsion is the single most important aeroelastic problem in the calculation of aerodynamic loading and performance. Depending upon the fuselage and control system design more or less of this deformation will take place on the blade or in the fixed system. These effects are largely unquantified and experimental efforts should be advanced that can use extensive measurements of torsion moments and loading to accurately estimate the torsional deformation at all radial stations. Methods exist today to accomplish this task, but little work has been published that clearly shows the accuracy of these methods. Future experiments with aeroelastic rotors in wind tunnels and flight should consider the "measurement" of the torsional deformation as an essential part of any test.

*Chord Bending Moment Calculation*

The poor chord bending moment predictions shown here may have their basis in a number of areas. It is possible that an improved understanding of some of these areas can be obtained through careful experimentation in flight, but a better approach, perhaps, would be to examine a simplified model-scale

rotor where the root-end boundary conditions could be carefully controlled and quantified and chord bending moment measurements could be used as a basis of correlation and improved understanding.

*Articulated Rotors and Bending-Torsion Coupling*

The hinges of articulated rotors were added in the early development of helicopters to relieve the blades of the high moments that will occur in trimmed level flight for a hingeless rotor. With the improvement in materials it is now possible to design and operate hingeless rotors where the primary loading is caused by rotor trim. For these rotors the blade loading includes a 1/rev trim load and, because of bending-torsion coupling, this large 1/rev load is seen in the chord bending and torsion moments as well. These large 1/rev loads can obscure many of the higher harmonic loads seen on articulated rotors that have been the focus of this study. With proper structural modeling of a hingeless rotor it is possible to calculate the 1/rev trim loads quite accurately and, in doing so, lose sight of the higher harmonic loading and its importance to vibration. To the degree that the 1/rev loads on a hingeless rotor obscure its higher harmonic loading, an articulated rotor is a more sensitive assay of analytical methods and remains an important test in the further improvement of these methods.

*Rotor Thrust in Flight*

The equating of rotor lift or thrust to vehicle weight is a convenient way of defining trim, but is counterproductive when differences between the rotor thrust and weight are of the same order as the predictive accuracy of the methods. In this case the inaccuracy in the trim specification will confound the assessment of the accuracy of the predictions of other rotor properties. Future computation of forward flight conditions needs to focus more clearly on the exact determination of rotor thrust.

# APPENDIX A

# RESEARCH PUMA DOCUMENTATION

William G. Bousman

## Puma Research Aircraft Configurations

The data used in this study were obtained from measurements on two rotor configurations tested on the research Puma at RAE Bedford. The first configuration was a Puma (AS 330) rotor with unmodified production blades while the second configuration used blades that were modified to provide a swept planform at the blade tip. The planforms of these two configurations are compared in figure A-1.

The standard (unmodified) Puma blade includes a tether or tie-down ring at its tip and this tether ring is also used for tracking of the blades in hover. The swept-tip blades did not require a tether ring and, therefore, were made slightly larger in radius so that the blade plus a small tab would match the standard blade during mixed-blade rotor tests (Riley and Miller, 1983). Very little of the outer spar of the blade was removed in building the swept-tip blade and the only properties changed by the modification were the blade mass distribution, center of gravity (c.g.) offset, torsional stiffness, and torsional inertia.

The structural changes required for the swept-tip blades were made by Aérospatiale while the final tip planform and contour was built at the RAE using balsa wood and a fiberglass skin (Riley and Miller, 1983). One of the four blades that was built was extensively instrumented with pressure transducers on four chord lines near the blade tip. In addition, the outermost tracking tab was removed for the swept-tip blade.

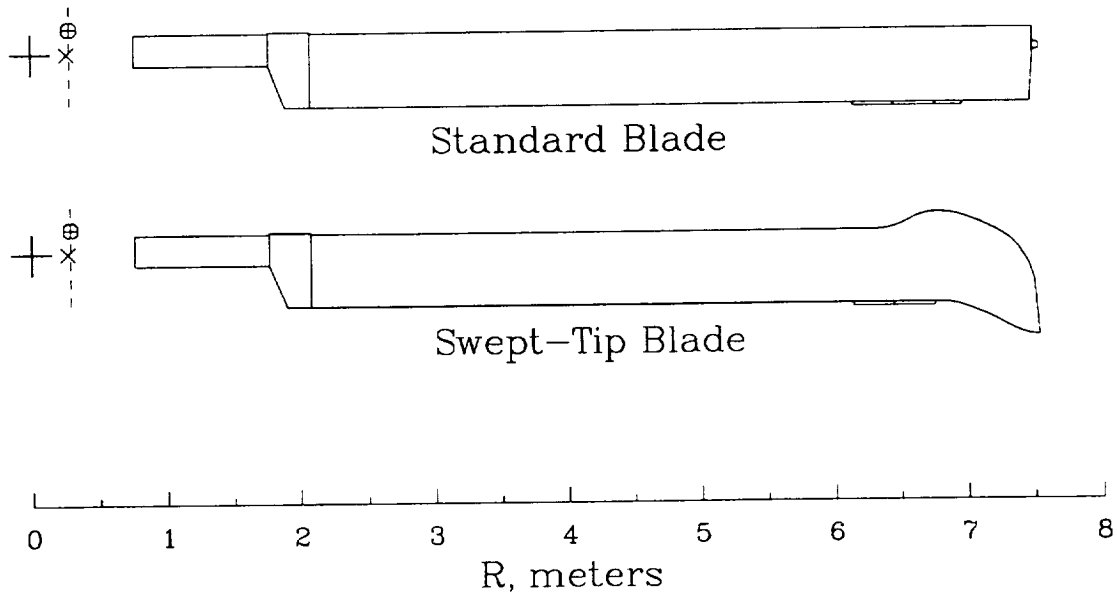


Figure A-1. Comparison of standard Puma blade and modified swept-tip blade.

Except for some details of the swept-tip construction all of the rotor properties were determined by Aérospatiale and provided to RAE under the original AFARP agreement (Young et al., 1991). Blade properties in the format used in the RAE/WHL analysis were provided to the US and Australian collaborators prior to the workshop. Miscellaneous details about the Puma rotor were also provided by the workshop collaborators at RAE Bedford. In a number of instances the analysts used slightly different values for rotor properties and, where known, these differences are noted below. None of these differences are considered significant for the comparisons shown in this report.

## Rotor Geometry

The basic geometry of the two rotor configurations is described in table A-1. There is some ambiguity in the definition of the root cutout and the tabulated value was used in the CAMRAD analyses while 1.72 m was used in the RAE/WHL analysis and 1.757 m in the METAR/R85 calculations. The radius of the standard Puma blade without the tether ring (shown in figure A-1) is the value given in table A-1. However, the radial dimension used in METAR/R85 is 7.536 m, which includes the tether ring. The solidity is calculated on the basis of the inboard or root chord for both rotors and, therefore, makes no allowance for the increased blade area at the tip of the swept-tip blade. The feather axis is coincident with the airfoil quarter chord.

Table A-1. Puma blade geometry

| Parameter | Unmodified | Swept tip |
|---|---|---|
| Root Cutout, m | 2.080 | 2.080 |
| Chord, m | 0.537 | 0.537 |
| Radius, m | 7.490 | 7.536 |
| Solidity | 0.09129 | 0.09073 |

Geometric parameters describing hinge locations, pitch-link attachments and so forth are shown in table A-2. Hub drawings show that the pitch sleeve extends from 0.432 m to 0.528 m and the inner edge of the sleeve was used as the location of the pitch bearing in the CAMRAD analyses. The METAR/R85 analysis used a value of 0.59 m. The pitch-link attaches to the pitch horn on the leading edge of the blade. The attachment point distance from the quarter chord used by the RAE/WHL and CAMRAD analyses is 0.181 m while a value of 0.165 m is used by METAR/R85. The pitch link is mounted vertically so that the lower rod end has the same span and chord location as the upper rod end when the blade pitch is set to zero.

Table A-2. Puma hub/blade geometry

| Parameter | Radial Location | | |
|---|---|---|---|
| | m | $(r/R)_u$ | $(r/R)_s$ |
| Lag Hinge Axis | 0.269 | 0.0359 | 0.0357 |
| Flap Hinge Axis | 0.289 | 0.0386 | 0.0383 |
| Pitch Link | 0.289 | 0.0386 | 0.0383 |
| Pitch Bearing | 0.432 | 0.0577 | 0.0573 |
| Root Cutout | 2.080 | 0.2777 | 0.2760 |
| Radius (unmodified) | 7.490 | 1.0000 | – |
| Radius (swept tip) | 7.536 | – | 1.0000 |

The twist distribution for the two blades is shown in figure A-2 and the values are tabulated in table A-3. The unmodified Puma blade was designed to have a nominal $-8^\circ$ linear twist from centerline to tip. The twist departs from a linear distribution outboard of the root cutout and the structure inboard of the cutout is untwisted. The swept-tip blade modification extended the linear twist as is shown in table A-3. The twist at the outboard end of the standard blade, as modeled by the RAE/WHL and CAMRAD analyses, also follows the linear twist characteristic. However, METAR/R85 treats the blade as untwisted outboard of 7.34 m ($0.98R$) based on Aérospatiale documentation. The twist change from $0.75R$ to the pitch bearing where the pitch angle is measured is $-4.11^\circ$ for the standard blade and $-4.16^\circ$ for the swept-tip blade.

## Structural Properties

Figures A-3 and A-4 show respectively the blade mass distributions and the c.g. location. The tabulated data are shown in tables A-4 and A-5. For the swept-tip blade the mass is increased over the standard blade outboard of $0.89R$ and initially the c.g. of the swept-tip blade is forward of the quarter chord and then moves aft of the quarter-chord location (the reference point for the c.g.).

The extensional stiffness or EA distribution is shown in figure A-5 and the data are tabulated in table A-6. The flap and chord stiffnesses are shown in figures A-6 and A-7 and the data are in table A-7. The flap and chord stiffnesses are identical for the unmodified and swept-tip blades as shown here. The structural modifications required to install the fiberglass skins for the swept-tip blade may have changed the section stiffnesses slightly at the tip, but it is assumed that these changes can be neglected and do not affect the blade response.

The torsional stiffness or GJ distributions are shown in figure A-8 and the torsional inertias are shown in figure A-9. The data are tabulated in tables A-8 and A-9. The shell of the swept-tip blade has increased the torsional stiffness significantly on the outer portion of the blade as well as increasing the torsional inertia (relative to the section shear center). From 1.11 m to 1.26 m the METAR/R85 analysis used a value of 0.039 for the torsional inertia while the other analyses used the tabulated value.

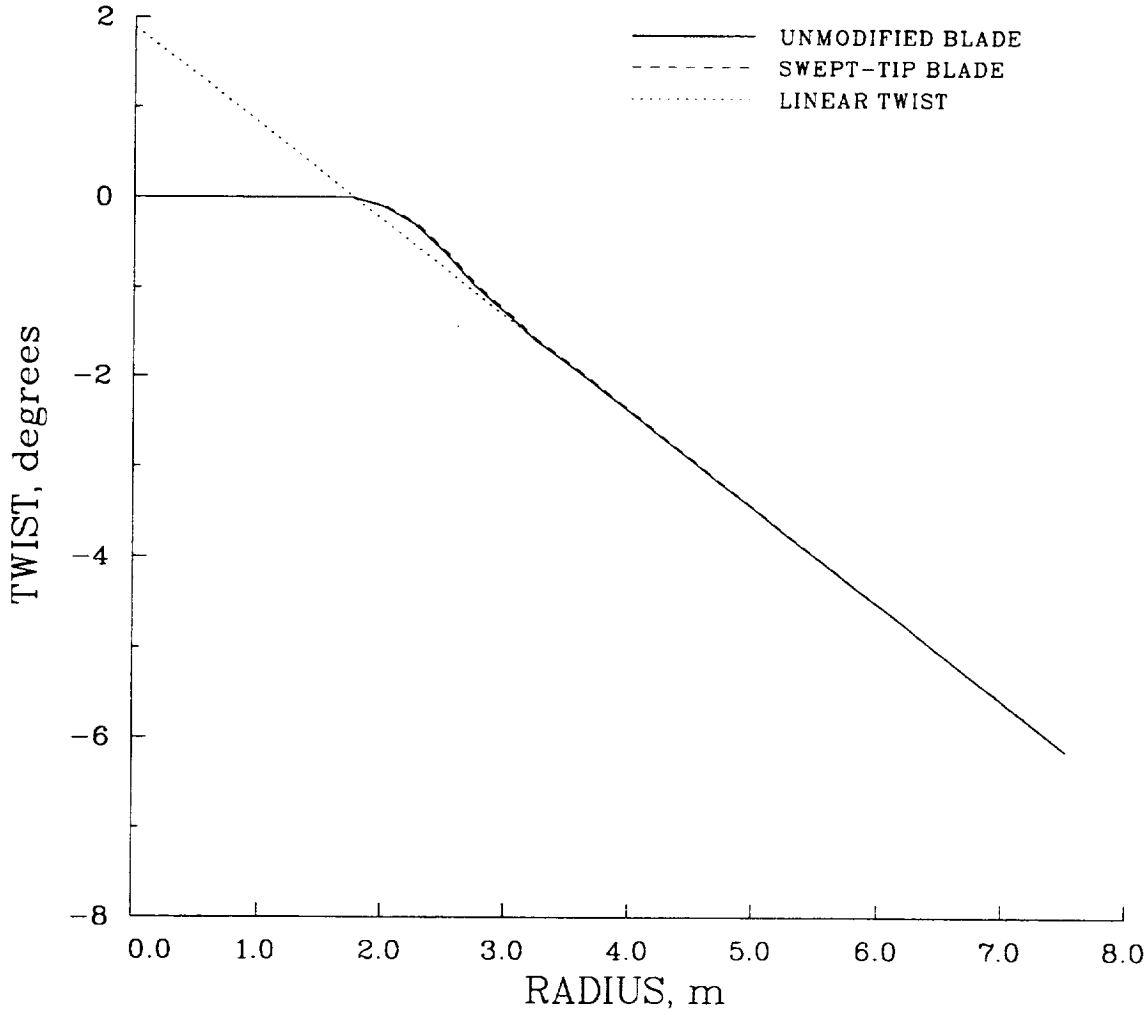


Figure A-2. Standard and swept-tip blade twist distribution.

Table A-3. Blade twist distribution

| Radial location | | | Twist | |
|---|---|---|---|---|
| $r$ | $(r/R)_u$ | $(r/R)_s$ | $\theta_u$ | $\theta_s$ |
| m | | | deg | deg |
| 0.000 | 0.000 | 0.000 | 0.000 | 0.000 |
| 0.760 | 0.101 | 0.101 | 0.000 | 0.000 |
| 1.757 | 0.235 | 0.233 | 0.000 | 0.000 |
| 2.007 | 0.268 | 0.266 | −0.100 | −0.100 |
| 2.257 | 0.301 | 0.299 | −0.300 | −0.300 |
| 2.507 | 0.335 | 0.333 | −0.617 | −0.617 |
| 2.757 | 0.368 | 0.366 | −0.983 | −0.983 |
| 3.007 | 0.401 | 0.399 | −1.283 | −1.283 |
| 3.257 | 0.435 | 0.432 | −1.600 | −1.600 |
| 3.507 | 0.468 | 0.465 | −1.867 | −1.867 |
| 6.257 | 0.835 | 0.830 | −4.800 | −4.800 |
| 6.296 | – | 0.835 | – | −4.838 |
| 6.360 | – | 0.844 | – | −4.906 |
| 6.467 | – | 0.858 | – | −5.021 |
| 6.531 | – | 0.867 | – | −5.089 |
| 6.574 | – | 0.872 | – | −5.137 |
| 6.629 | – | 0.880 | – | −5.191 |
| 6.682 | – | 0.887 | – | −5.252 |
| 6.736 | – | 0.894 | – | −5.307 |
| 6.779 | – | 0.900 | – | −5.354 |
| 6.843 | – | 0.908 | – | −5.422 |
| 6.897 | – | 0.915 | – | −5.476 |
| 6.950 | – | 0.922 | – | −5.537 |
| 7.005 | – | 0.930 | – | −5.592 |
| 7.058 | – | 0.937 | – | −5.653 |
| 7.112 | – | 0.944 | – | −5.707 |
| 7.165 | – | 0.951 | – | −5.768 |
| 7.182 | – | 0.953 | – | −5.776 |
| 7.219 | – | 0.958 | – | −5.823 |
| 7.273 | – | 0.965 | – | −5.884 |
| 7.326 | – | 0.972 | – | −5.938 |
| 7.380 | – | 0.979 | – | −5.998 |
| 7.434 | – | 0.986 | – | −6.053 |
| 7.488 | – | 0.994 | – | −6.108 |
| 7.490 | 1.000 | – | −6.117 | – |
| 7.514 | – | 0.997 | – | −6.138 |
| 7.536 | – | 1.000 | – | −6.159 |

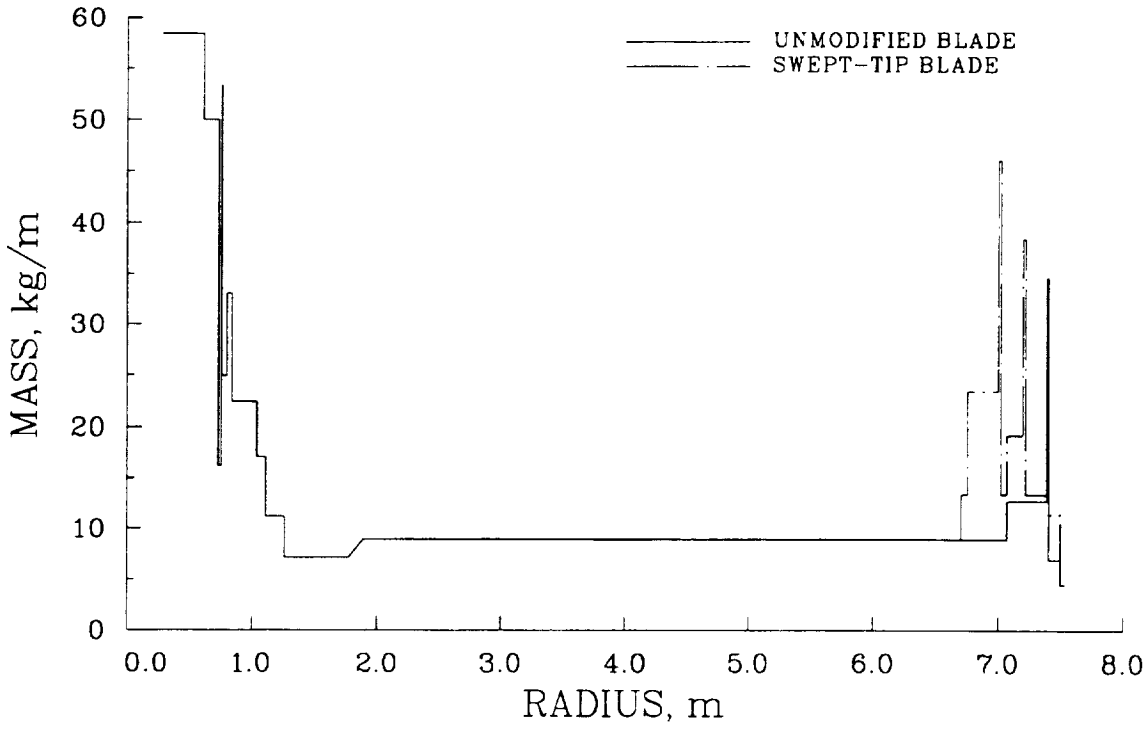


Figure A-3. Standard and swept-tip blade mass distribution.

Table A-4. Mass distribution

| Radial location | | | Running mass | |
|---|---|---|---|---|
| $r$ | $(r/R)_u$ | $(r/R)_s$ | $m_u$ | $m_s$ |
| m | | | kg/m | kg/m |
| 0.280 | 0.037 | 0.037 | 58.400 | 58.400 |
| 0.610 | 0.081 | 0.081 | 58.400 | 58.400 |
| 0.610 | 0.081 | 0.081 | 50.000 | 50.000 |
| 0.730 | 0.097 | 0.097 | 50.000 | 50.000 |
| 0.730 | 0.097 | 0.097 | 16.175 | 16.175 |
| 0.754 | 0.101 | 0.100 | 16.175 | 16.175 |
| 0.754 | 0.101 | 0.100 | 53.333 | 53.333 |
| 0.760 | 0.101 | 0.101 | 53.333 | 53.333 |
| 0.760 | 0.101 | 0.101 | 24.949 | 24.949 |
| 0.800 | 0.107 | 0.106 | 24.949 | 24.949 |
| 0.800 | 0.107 | 0.106 | 33.100 | 33.100 |
| 0.840 | 0.112 | 0.111 | 33.100 | 33.100 |
| 0.840 | 0.112 | 0.111 | 22.400 | 22.400 |
| 1.040 | 0.139 | 0.138 | 22.400 | 22.400 |
| 1.040 | 0.139 | 0.138 | 17.110 | 17.110 |
| 1.110 | 0.148 | 0.147 | 17.110 | 17.110 |
| 1.110 | 0.148 | 0.147 | 11.225 | 11.225 |
| 1.260 | 0.168 | 0.167 | 11.225 | 11.225 |
| 1.260 | 0.168 | 0.167 | 7.150 | 7.150 |
| 1.770 | 0.236 | 0.235 | 7.150 | 7.150 |
| 1.770 | 0.236 | 0.235 | 7.150 | 7.150 |
| 1.887 | 0.252 | 0.250 | 8.929 | 8.929 |
| 5.546 | 0.740 | 0.736 | 8.929 | 8.929 |
| 6.707 | – | 0.890 | – | 8.929 |
| 6.707 | – | 0.890 | – | 13.429 |
| 6.758 | – | 0.897 | – | 13.429 |
| 6.758 | – | 0.897 | – | 23.429 |
| 7.000 | – | 0.929 | – | 23.429 |
| 7.000 | – | 0.929 | – | 46.079 |
| 7.020 | – | 0.932 | – | 46.079 |
| 7.020 | – | 0.932 | – | 13.429 |
| 7.070 | 0.944 | 0.938 | 8.929 | 13.429 |
| 7.070 | 0.944 | 0.938 | 12.754 | 19.253 |
| 7.196 | – | 0.955 | – | 19.253 |
| 7.196 | – | 0.955 | – | 38.429 |
| 7.216 | – | 0.958 | – | 38.429 |
| 7.216 | – | 0.958 | – | 13.429 |

Table A-4. Concluded.

| Radial location | | | Running mass | |
|---|---|---|---|---|
| $r$ | $(r/R)_u$ | $(r/R)_s$ | $m_u$ | $m_s$ |
| m | | | kg/m | kg/m |
| 7.390 | 0.987 | – | 12.754 | – |
| 7.390 | 0.987 | – | 34.600 | – |
| 7.402 | 0.988 | 0.982 | 34.600 | 13.429 |
| 7.402 | 0.988 | 0.982 | 6.930 | 11.430 |
| 7.490 | 1.000 | – | 6.930 | – |
| 7.499 | – | 0.995 | – | 11.430 |
| 7.499 | – | 0.995 | – | 4.500 |
| 7.536 | – | 1.000 | – | 4.500 |

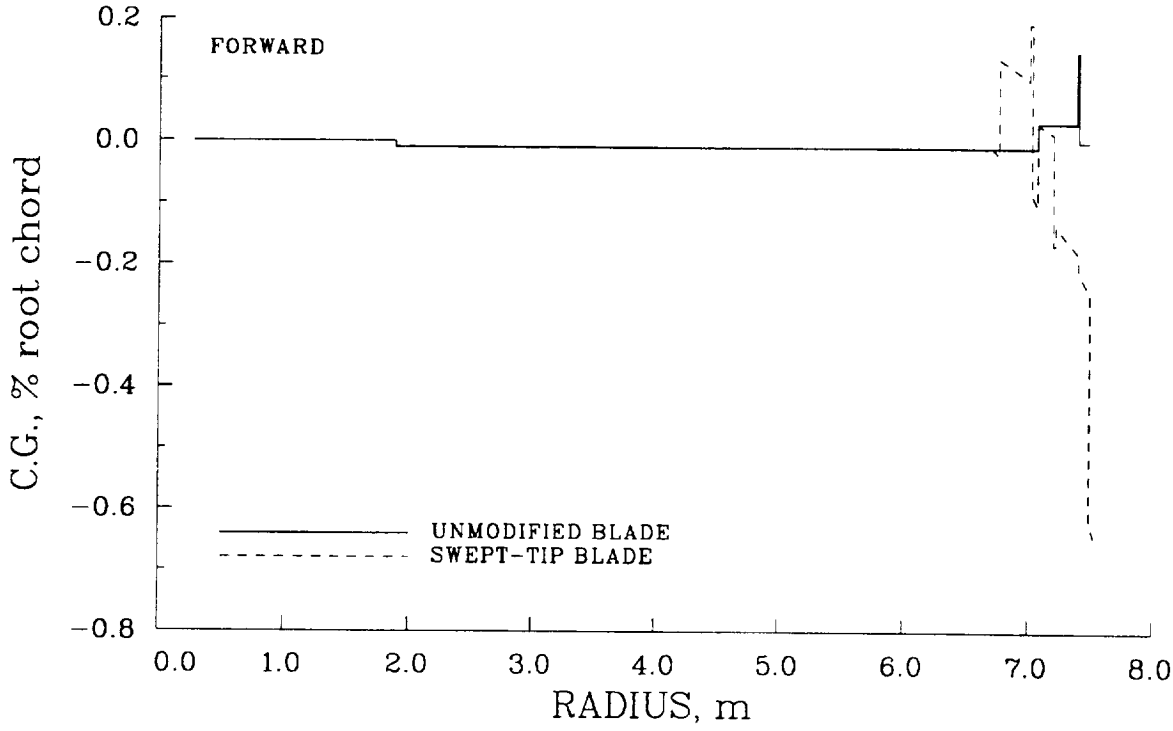


Figure A-4. Standard and swept-tip blade c.g distribution with respect to root quarter chord.

Table A-5. Blade c.g. offset

| Radial location | | | C.g. offset[a] | |
|---|---|---|---|---|
| $r$ | $(r/R)_u$ | $(r/R)_s$ | $(x/c)_u$ | $(x/c)_s$ |
| m | | | | |
| 0.280 | 0.037 | 0.037 | 0.000 | 0.000 |
| 1.887 | 0.252 | 0.250 | 0.000 | 0.000 |
| 1.887 | 0.252 | 0.250 | −0.010 | −0.010 |
| 6.707 | – | 0.890 | – | −0.010 |
| 6.758 | – | 0.897 | – | −0.022 |
| 6.758 | – | 0.897 | – | 0.135 |
| 7.000 | – | 0.929 | – | 0.100 |
| 7.000 | – | 0.929 | – | 0.194 |
| 7.020 | – | 0.932 | – | 0.194 |
| 7.020 | – | 0.932 | – | −0.084 |
| 7.070 | 0.944 | 0.938 | −0.010 | −0.105 |
| 7.070 | 0.944 | 0.938 | 0.030 | 0.029 |
| 7.196 | – | 0.955 | – | 0.013 |
| 7.196 | – | 0.955 | – | −0.167 |
| 7.216 | – | 0.958 | – | −0.167 |
| 7.216 | – | 0.958 | – | −0.136 |
| 7.390 | 0.987 | – | 0.030 | – |
| 7.390 | 0.987 | – | 0.147 | – |
| 7.402 | 0.988 | 0.982 | 0.147 | −0.182 |
| 7.402 | 0.988 | 0.982 | 0.000 | −0.211 |
| 7.490 | 1.000 | – | 0.000 | – |
| 7.499 | – | 0.995 | – | −0.247 |
| 7.499 | – | 0.995 | – | −0.615 |
| 7.536 | – | 1.000 | – | −0.646 |

[a]With respect to root quarter-chord, positive forward.

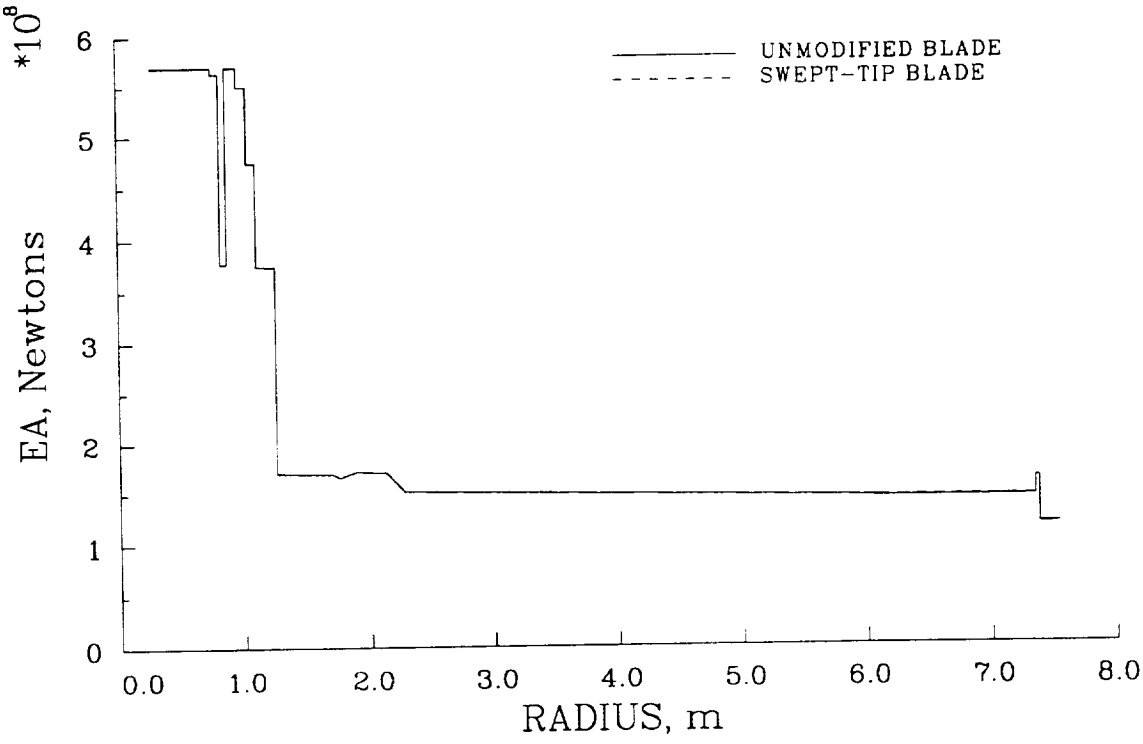


Figure A-5. Standard and swept-tip blade EA distribution.

Table A-6. Extensional stiffness distribution

| Radial location | | | Extensional stiffness | |
|---|---|---|---|---|
| $r$ | $(r/R)_u$ | $(r/R)_s$ | $(EA)_u$ | $(EA)_s$ |
| m | | | $10^8$ N | $10^8$ N |
| 0.280 | 0.037 | 0.037 | 5.69 | 5.69 |
| 0.760 | 0.101 | 0.101 | 5.69 | 5.69 |
| 0.760 | 0.101 | 0.101 | 5.63 | 5.63 |
| 0.820 | 0.109 | 0.109 | 5.63 | 5.63 |
| 0.820 | 0.109 | 0.109 | 3.77 | 3.77 |
| 0.873 | 0.117 | 0.116 | 3.77 | 3.77 |
| 0.873 | 0.117 | 0.116 | 5.69 | 5.69 |
| 0.965 | 0.129 | 0.128 | 5.69 | 5.69 |
| 0.965 | 0.129 | 0.128 | 5.50 | 5.50 |
| 1.040 | 0.139 | 0.138 | 5.50 | 5.50 |
| 1.040 | 0.139 | 0.138 | 4.74 | 4.74 |
| 1.111 | 0.148 | 0.147 | 4.74 | 4.74 |
| 1.111 | 0.148 | 0.147 | 3.74 | 3.74 |
| 1.260 | 0.168 | 0.167 | 3.74 | 3.74 |
| 1.260 | 0.168 | 0.167 | 1.70 | 1.70 |
| 1.697 | 0.227 | 0.225 | 1.69 | 1.69 |
| 1.757 | 0.235 | 0.233 | 1.65 | 1.65 |
| 1.880 | 0.251 | 0.249 | 1.71 | 1.71 |
| 2.128 | 0.284 | 0.282 | 1.70 | 1.70 |
| 2.278 | 0.304 | 0.302 | 1.51 | 1.51 |
| 5.250 | 0.701 | 0.697 | 1.45 | 1.45 |
| 5.800 | 0.774 | 0.770 | 1.44 | 1.44 |
| 6.110 | 0.816 | 0.811 | 1.43 | 1.43 |
| 7.350 | 0.981 | 0.975 | 1.43 | 1.43 |
| 7.350 | 0.981 | 0.975 | 1.61 | 1.61 |
| 7.382 | 0.986 | 0.980 | 1.61 | 1.61 |
| 7.382 | 0.986 | 0.980 | 1.16 | 1.16 |
| 7.490 | 1.000 | – | 1.16 | – |
| 7.536 | – | 1.000 | – | 1.16 |

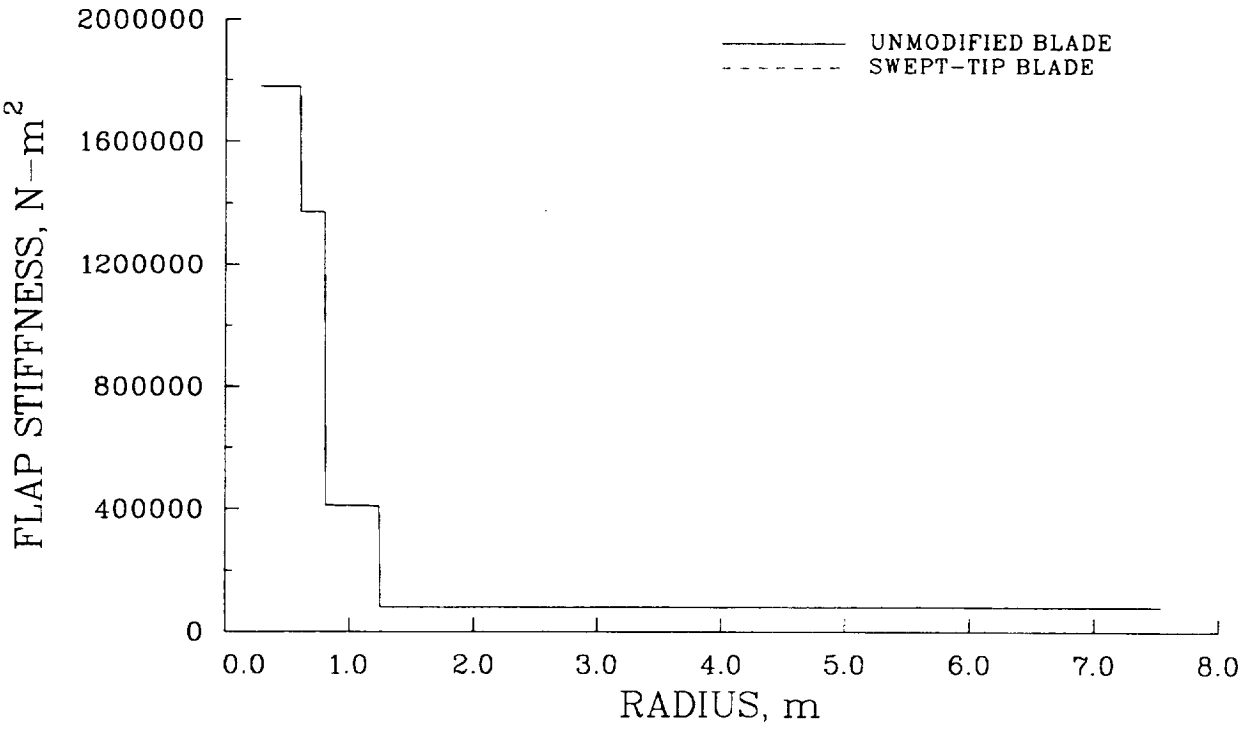


Figure A-6. Standard and swept-tip blade flap stiffness distribution.

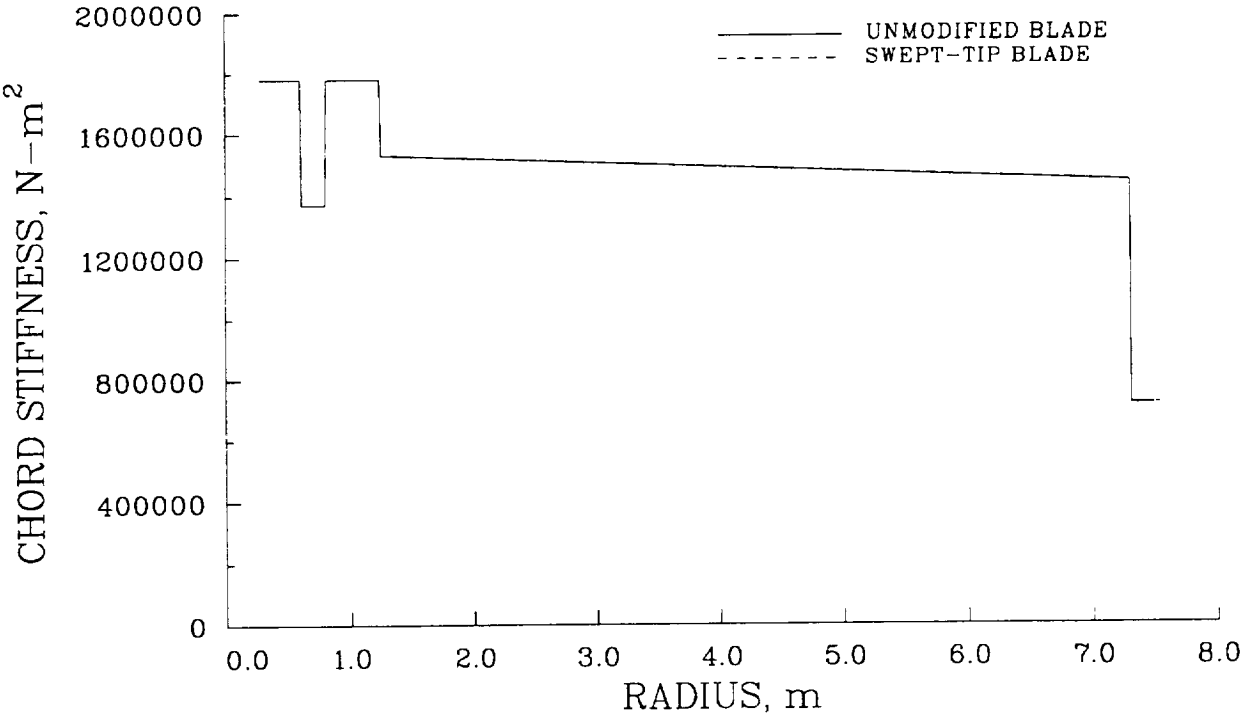


Figure A-7. Standard and swept-tip blade chord stiffness distribution.

Table A-7. Flap and chord stiffness distribution

| Radial location | | | Flap stiffness | | Chord stiffness | |
|---|---|---|---|---|---|---|
| $r$ | $(r/R)_u$ | $(r/R)_s$ | $(EI_f)_u$ | $(EI_f)_s$ | $(EI_c)_u$ | $(EI_c)_s$ |
| m | | | $10^4$ N-m$^2$ | $10^4$ N-m$^2$ | $10^4$ N-m$^2$ | $10^4$ N-m$^2$ |
| 0.280 | 0.037 | 0.037 | 178.00 | 178.00 | 178.00 | 178.00 |
| 0.600 | 0.080 | 0.080 | 178.00 | 178.00 | 178.00 | 178.00 |
| 0.610 | 0.081 | 0.081 | 137.00 | 137.00 | 137.00 | 137.00 |
| 0.800 | 0.107 | 0.106 | 137.00 | 137.00 | 137.00 | 137.00 |
| 0.810 | 0.108 | 0.107 | 41.20 | 41.20 | 178.00 | 178.00 |
| 1.240 | 0.166 | 0.165 | 41.00 | 41.00 | 178.00 | 178.00 |
| 1.250 | 0.167 | 0.166 | 8.10 | 8.10 | 153.00 | 153.00 |
| 7.300 | 0.975 | 0.969 | 8.10 | 8.10 | 144.00 | 144.00 |
| 7.310 | 0.976 | 0.970 | 8.20 | 8.20 | 71.50 | 71.50 |
| 7.490 | 1.000 | – | 8.20 | – | 71.50 | – |
| 7.536 | – | 1.000 | – | 8.20 | – | 71.50 |

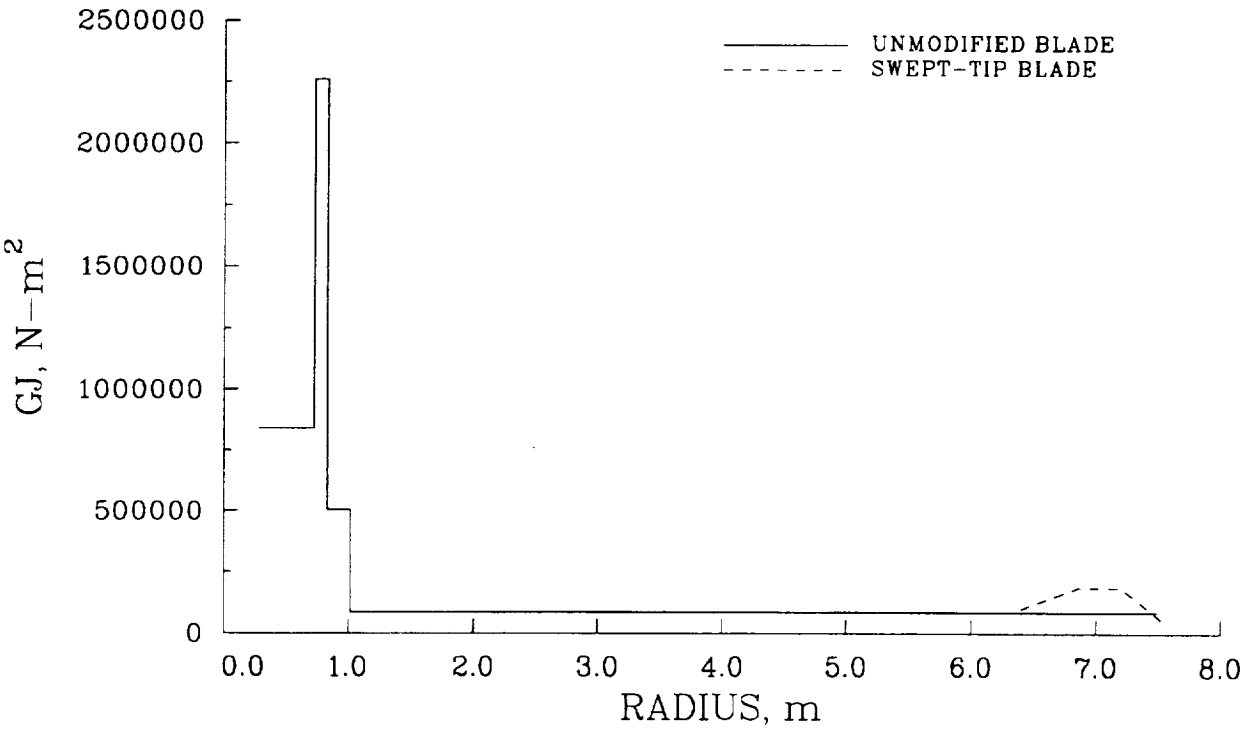


Figure A-8. Standard and swept-tip blade torsional stiffness distribution.

Table A-8. Torsional stiffness distribution

| Radial location | | | Torsional stiffness | |
|---|---|---|---|---|
| $r$ | $(r/R)_u$ | $(r/R)_s$ | $(GJ)_u$ | $(GJ)_s$ |
| m | | | $10^4$ N-m$^2$ | $10^4$ N-m$^2$ |
| 0.280 | 0.037 | 0.037 | 84.00 | 84.00 |
| 0.725 | 0.097 | 0.096 | 84.00 | 84.00 |
| 0.725 | 0.097 | 0.096 | 226.00 | 226.00 |
| 0.828 | 0.111 | 0.110 | 226.00 | 226.00 |
| 0.828 | 0.111 | 0.110 | 50.50 | 50.50 |
| 1.017 | 0.136 | 0.135 | 50.50 | 50.50 |
| 1.017 | 0.136 | 0.135 | 8.50 | 8.50 |
| 6.330 | – | 0.840 | – | 8.50 |
| 6.858 | – | 0.910 | – | 18.50 |
| 7.196 | – | 0.955 | – | 18.50 |
| 7.241 | 0.967 | – | 8.50 | – |
| 7.241 | 0.967 | – | 8.70 | – |
| 7.490 | 1.000 | – | 8.70 | – |
| 7.536 | – | 1.000 | – | 5.00 |

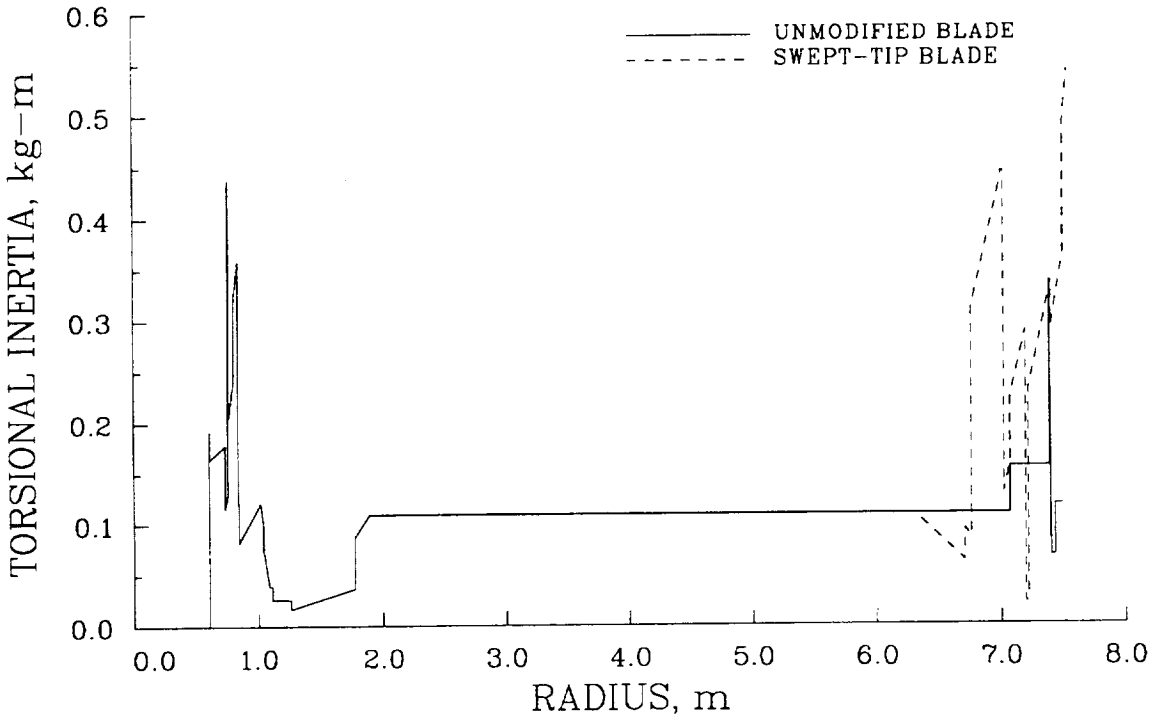


Figure A-9. Standard and swept-tip blade torsional inertia with respect to section shear center.

Table A-9. Torsional inertia distribution

| Radial location | | | Torsional inertia | |
|---|---|---|---|---|
| $r$ | $(r/R)_u$ | $(r/R)_s$ | $(I_\theta)_u$ | $(I_\theta)_s$ |
| m | | | kg-m | kg-m |
| 0.280 | 0.037 | 0.037 | 0.000 | 0.000 |
| 0.604 | 0.081 | 0.080 | 0.000 | 0.000 |
| 0.604 | 0.081 | 0.080 | 0.192 | 0.192 |
| 0.610 | 0.081 | 0.081 | 0.192 | 0.192 |
| 0.610 | 0.081 | 0.081 | 0.164 | 0.164 |
| 0.730 | 0.097 | 0.097 | 0.178 | 0.178 |
| 0.730 | 0.097 | 0.097 | 0.116 | 0.116 |
| 0.754 | 0.101 | 0.100 | 0.130 | 0.130 |
| 0.754 | 0.101 | 0.100 | 0.427 | 0.427 |
| 0.760 | 0.101 | 0.101 | 0.438 | 0.438 |
| 0.760 | 0.101 | 0.101 | 0.205 | 0.205 |
| 0.800 | 0.107 | 0.106 | 0.240 | 0.240 |
| 0.800 | 0.107 | 0.106 | 0.318 | 0.318 |
| 0.836 | 0.112 | 0.111 | 0.359 | 0.359 |
| 0.837 | 0.112 | 0.111 | 0.120 | 0.120 |
| 0.840 | 0.112 | 0.111 | 0.121 | 0.121 |
| 0.840 | 0.112 | 0.111 | 0.082 | 0.082 |
| 1.017 | 0.136 | 0.135 | 0.121 | 0.121 |
| 1.040 | 0.139 | 0.138 | 0.098 | 0.098 |
| 1.040 | 0.139 | 0.138 | 0.075 | 0.075 |
| 1.085 | 0.145 | 0.144 | 0.040 | 0.040 |
| 1.110 | 0.148 | 0.147 | 0.040 | 0.040 |
| 1.110 | 0.148 | 0.147 | 0.026 | 0.026 |
| 1.260 | 0.168 | 0.167 | 0.026 | 0.026 |
| 1.260 | 0.168 | 0.167 | 0.017 | 0.017 |
| 1.770 | 0.236 | 0.235 | 0.037 | 0.037 |
| 1.770 | 0.236 | 0.235 | 0.087 | 0.087 |
| 1.887 | 0.252 | 0.250 | 0.109 | 0.109 |
| 5.546 | – | 0.736 | – | 0.109 |
| 6.302 | – | 0.836 | – | 0.109 |
| 6.707 | – | 0.890 | – | 0.063 |
| 6.707 | – | 0.890 | – | 0.094 |
| 6.758 | – | 0.897 | – | 0.085 |
| 6.758 | – | 0.897 | – | 0.309 |
| 7.000 | – | 0.929 | – | 0.437 |
| 7.000 | – | 0.929 | – | 0.444 |
| 7.020 | – | 0.932 | – | 0.444 |

Table A-9. Concluded.

| Radial location | | | Torsional inertia | |
|---|---|---|---|---|
| $r$ | $(r/R)_u$ | $(r/R)_s$ | $(I_\theta)_u$ | $(I_\theta)_s$ |
| m | | | kg-m | kg-m |
| 7.020 | – | 0.932 | – | 0.130 |
| 7.070 | 0.944 | 0.938 | 0.109 | 0.159 |
| 7.070 | 0.944 | 0.938 | 0.156 | 0.222 |
| 7.196 | – | 0.955 | – | 0.288 |
| 7.196 | – | 0.955 | – | 0.022 |
| 7.216 | – | 0.958 | – | 0.022 |
| 7.216 | – | 0.958 | – | 0.230 |
| 7.390 | 0.987 | – | 0.156 | – |
| 7.390 | 0.987 | – | 0.337 | – |
| 7.402 | 0.988 | 0.982 | 0.067 | 0.336 |
| 7.402 | 0.988 | 0.982 | 0.067 | 0.292 |
| 7.434 | 0.993 | – | 0.067 | – |
| 7.434 | 0.993 | – | 0.118 | – |
| 7.490 | 1.000 | – | 0.118 | – |
| 7.499 | – | 0.995 | – | 0.364 |
| 7.499 | – | 0.995 | – | 0.492 |
| 7.536 | – | 1.000 | – | 0.542 |

## Lag Damper

The damper on the Puma is a hydraulic damper where damping is obtained by forcing hydraulic fluid through an orifice. At displacement rates above approximately 16 mm/sec a spring-loaded bleed valve opens and the damping is reduced. Bench measurements have been made on used dampers at the 1/rev frequency (4.5 Hz). Results are shown in figure A-10 for the measured force as a function of displacement where the excitation is

$$x(t) = X\cos\omega t \tag{A-1}$$

and the response is

$$f(t) = F(X)\cos[\omega t - \phi(X)] \tag{A-2}$$

where both the force and phase angle are functions of the displacement $X$. The change in the damping force and phase between 0.4 and 0.9 mm is a result of the bleed valve opening. A linear approximation to the force characteristics is shown on this figure by the dashed line, where the resulting damping coefficient is 7000 N-m/rad/sec.

## Control System

The fixed system swashplate actuators are located at 60, 180, and 300° around the azimuth. A torsional natural frequency of 5.62/rev was observed in flight tests where the blade was undergoing dynamic stall-induced oscillations. The control stiffness was derived from this value by computing the blade modal frequencies as the root-end spring stiffness was varied until the first torsion mode frequency matched the in-flight value. For the RAE/WHL analysis the root-end stiffness was 33,032 N-m/rad while for CAMRAD/JA the derived value was 33,032 N-m/rad. In the case of METAR/R85, however, no solutions were obtained with the torsional degree of freedom.

## Fuselage Aerodynamic Force and Moments

Fuselage coefficient data are from the simulation program HELISTAB in use at the DRA Bedford, and are from a wind tunnel test reported by Samoni (1975). The drag force is

$$D = q\left(\frac{\pi R^2}{1000}\right)\left(11.0402 - 0.00765\alpha + 0.00274\alpha^2 + 0.00087\alpha^3\right) \tag{A-3}$$

where $q$ is the dynamic pressure, $R$ is the rotor radius, and $\alpha$ is the fuselage angle of attack in degrees. The drag is positive to the rear of the aircraft. The side force is

$$Y = q\left(\frac{\pi R^2}{1000}\right)\left(-2.0064\beta\right) \tag{A-4}$$

where $\beta$ is the sideslip angle in degrees and is positive nose right. The side force is positive to the left of the aircraft (advancing side). The fuselage lift is

$$L = -q\left(\frac{\pi R^2}{1000}\right)\left(-0.4512 - 0.37873\alpha + 0.00623\alpha^2 - 0.00021\alpha^3\right) \tag{A-5}$$

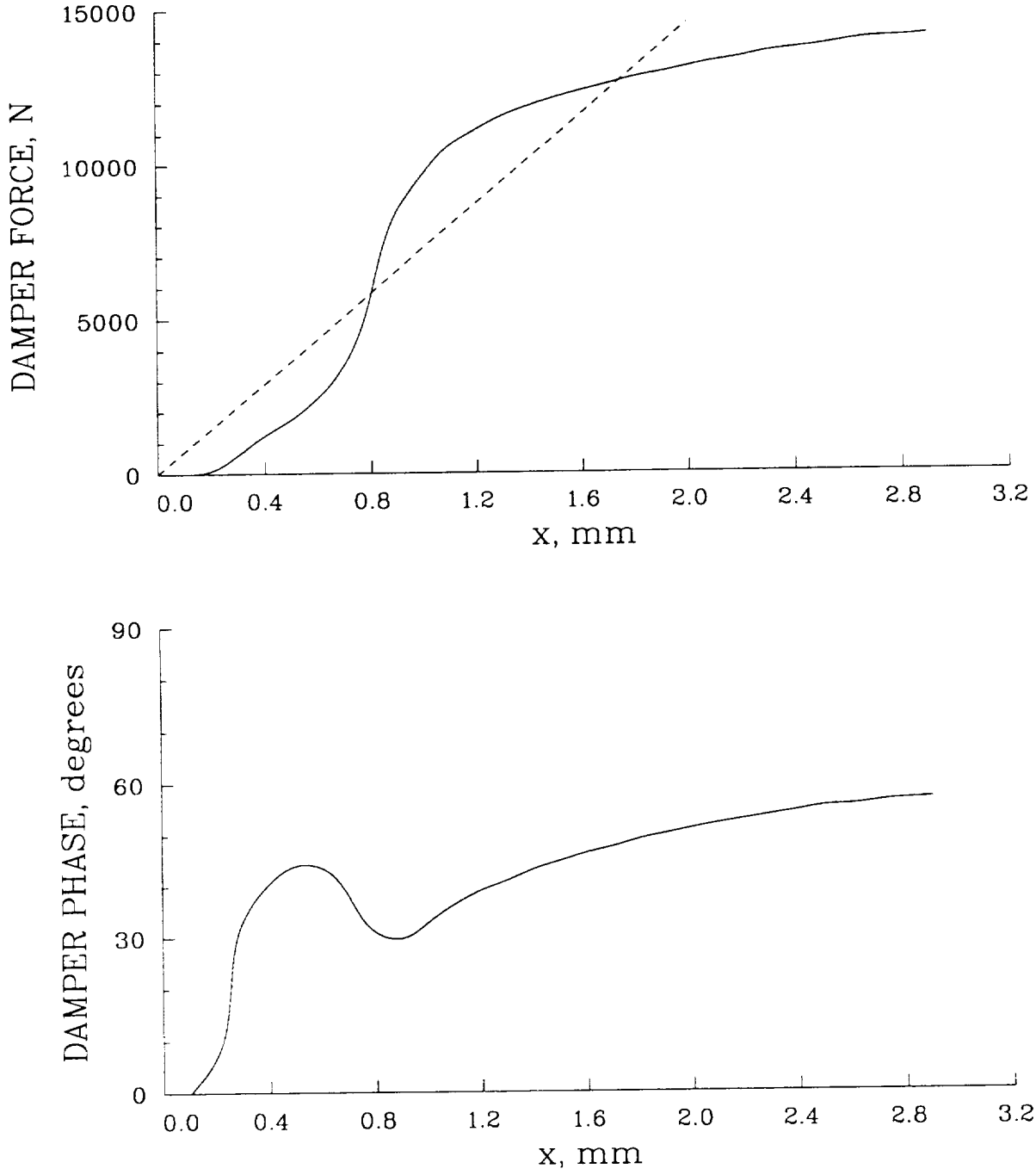


Figure A-10. Hydraulic damper force response characteristics from bench tests.

and is positive up. The pitching moment is

$$M_Y = q\left(\frac{\pi R^3}{1000}\right)\left(-1.3984 + 0.20043\alpha + 0.00499\alpha^2 - 0.00007\alpha^3\right) \tag{A-6}$$

and is positive nose up. The roll moment is zero. The yawing moment is

$$M_Z = q\left(\frac{\pi R^3}{1000}\right)\left(-0.55624\beta + 0.00068\beta^3\right) \tag{A-7}$$

and is positive in the clockwise direction.

Forces are also calculated for the horizontal stabilizer and vertical fin. The center of pressure of the stabilizer is at $X = 9.0075$ m, $Y = 0.0$ m, and $Z = 1.5$ m in a system where the rotor hub is at $X = Y = 0.0$ m and $Z = 2.157$ m. The stabilizer area, $A_s$, is 1.3395 m$^2$ and the lift is

$$L_s = qA_s\left(0.064575(\alpha + 1.5) + 7.709X10^{-5}(\alpha + 1.5)^2\right) \tag{A-8}$$

and is positive up. The stabilizer angle for zero lift is $-1.5°$. The center of pressure of the vertical fin is at $X = 9.0$ m, $Y = 0.0$ m, and $Z = 1.005$ m. The vertical fin area, $A_f$, is 1.3943 m$^2$ and the side force is

$$Y_f = -qA_f\left(2.07347X10^{-4}(\beta + 1.0)^3 - 4.8584X10^{-9}(\beta + 1.0)^5\right) \tag{A-9}$$

and the force is positive to the left. The zero lift angle for the fin is $-1.0°$.

# APPENDIX B

# POWER BREAKDOWN USING THE ENERGY METHOD

François Toulmay

The material system considered for the analysis is the rotor, that is, the hub and the blades. The rotor exchanges energy with the external world, that is, the air surrounding the blades and the helicopter body through the shaft. Only steady operation of the rotor is considered and it is assumed that structural dissipation (for example power dissipated by the lag damper) is negligible compared to exchanged energy. Thus there is neither production nor accumulation of energy in the rotor system, and the conservation of mechanical energy can be written:

$$W_{aero} + W_{body} = 0 \tag{B-1}$$

To develop the expression of $W_{aero}$ and $W_{body}$ consider cartesian coordinates in reference axes moving with the air mass upstream of the rotor (ground based coordinates for a helicopter flying in a calm atmosphere). The air velocity with respect to this reference frame is called the induced velocity $V_i$. The induced velocity may be large in the vicinity of the blades and in the wake, but vanishes at some distance upstream.

The mean power transferred from blades to the air during one revolution is:

$$W_{aero} = b \int_{azimuth} \frac{d\Psi}{2\pi} \int_{span} \int_{chord} -\vec{V}_m \cdot d^2\vec{F}_A \tag{B-2}$$

where $b$ is the number of blades, $\vec{V}_m$ is the velocity of a point at the blade surface, and $d^2\vec{F}_A$ is the force applied by the air onto the surface for an elementary area.

Call C the reference point at any blade station (generally chosen at the quarter chord where airfoil 2-D performance is known). Then,

$$\vec{V}_m = \vec{V}_C + \vec{\Omega}_C \times \vec{CM} \tag{B-3}$$

where $\vec{V}_C$ and $\vec{\Omega}_C$ are constant for a given station and can be factored out of the chordwise integral. The elementary power integrated over the chord now becomes

$$\begin{aligned} dW_A &= -\vec{V}_C \cdot \int_{chord} d^2F_A - \vec{\Omega}_C \cdot \int_{chord} \vec{CM} \times d^2F_A \\ &= -\vec{V}_C \cdot d\vec{F}_A - \vec{\Omega}_C \cdot d\vec{M}_A \end{aligned} \tag{B-4}$$

The second term, which combines the pitching motion with the aerodynamic pitching moment, $C_m$, is usually small compared to the first term for slender rotor blades (typically 0.2%). It can, nevertheless, be calculated.

For the term $-\vec{V}_C \cdot d\vec{F}_A$, two situations must be considered. First, if $d\vec{F}_A$ is obtained by means of a 3-D calculation, then the induced velocity has to match some boundary condition around the airfoil

contour. This term is varying continuously in the fluid domain and the concept of an "induced velocity at station C" has no meaning. As a consequence, the breakdown of power cannot be further detailed. Second, if $d\vec{F}_A$ is obtained using the lifting-line theory (matched asymptotic expansion of the 3-D problem), the inner problem consists of an airfoil in 2-D conditions moving in air with the relative velocity

$$\vec{V}_R = \vec{V}_C - \vec{V}_i \tag{B-5}$$

where $V_i$ is the induced velocity at station C, supposedly uniform in the inner field. $\vec{V}_i$ is obtained by solving the outer problem, that is, by integrating blade-induced and wake-induced 3-D effects.

Considering the second case, that of lifting-line theory, then the aerodynamic force can be broken down into lift and drag, where lift is defined as the component normal to $V_R$ and located in the airfoil plane (that is, not contributing to power in 2-D),

$$d\vec{F}_A = d\vec{L} + d\vec{D} \tag{B-6}$$

where $\vec{V}_R \cdot d\vec{L} = 0$. The elementary aerodynamic power can be written

$$dW_A = -\vec{V}_R \cdot d\vec{D} - \vec{V}_i \cdot (d\vec{L} + d\vec{D}) - \vec{\Omega}_C \cdot d\vec{M}_A \tag{B-7}$$

Coming back to equation (B-1), the power transferred from the rotor to the body can be expressed at any convenient point which is generally chosen as the rotor center:

$$W_{body} = \int_{azimuth} \frac{d\Psi}{2\pi} [\vec{V} \cdot \vec{T}(\Psi) + \vec{\Omega} \cdot \vec{Q}(\Psi)] \tag{B-8}$$

where $\vec{T}$ is the thrust and $\vec{Q}$ is the torque. As $\vec{V}$ and $\vec{Q}$ are constant, they can be factored out:

$$W_{body} = \vec{V} \cdot \vec{T} + \vec{\Omega} \cdot \vec{Q} \tag{B-9}$$

Bringing all terms of equation (B-1) together, we obtain:

$$\begin{aligned} -\vec{\Omega} \cdot \vec{Q} = &\vec{V} \cdot \vec{T} + b \int_{azimuth} \frac{d\Psi}{2\pi} \int_{span} -\vec{V}_R \cdot d\vec{D} + b \int_{azimuth} \frac{d\Psi}{2\pi} \int_{span} -\vec{V}_i (d\vec{L} + d\vec{D}) \\ &+ b \int_{azimuth} \frac{d\Psi}{2\pi} \int_{span} -\vec{Q}_C \cdot d\vec{M}_a \end{aligned} \tag{B-10}$$

The left-hand side of equation (B-10) is called *shaft power*:

$$W_S = -\vec{\Omega} \cdot \vec{Q} \tag{B-11}$$

The first term on the right-hand side could be called thrust power or propulsive power. It is traditionally called *parasite power* because, in the case of level flight, the propulsive force balances the fuselage parasite drag. Note:

$$W_T = \vec{V} \cdot \vec{T} \tag{B-12}$$

The second term on the right-hand side is called *profile power*:

$$W_P = b \int_{azimuth} \frac{d\Psi}{2\pi} \int_{span} -\vec{V}_R \cdot d\vec{D} \tag{B-13}$$

The third term on the right-hand side is called *induced power*:

$$W_i = +b \int_{azimuth} \frac{d\Psi}{2\pi} \int_{span} -\vec{V}_i (d\vec{L} + d\vec{D}) \tag{B-14}$$

The fourth term on the right-hand side can be called *feathering power*:

$$W_F = b \int_{azimuth} \frac{d\Psi}{2\pi} \int_{span} -\vec{Q}_C \cdot d\vec{M}_a \tag{B-15}$$

Since it is quite small, most analysts simply neglect it, or lump it implicitly with another term.

The connection between the power breakdown terms in equation (B-10) and those obtained in rotating coordinates by the RAE is developed here. The balance of forces on the rotor system can be written:

$$\vec{T} = b \int_{azimuth} \frac{d\Psi}{2\pi} \int_{span} (d\vec{L} + d\vec{D}) \tag{B-16}$$

Thus:

$$W_T = b \int_{azimuth} \frac{d\Psi}{2\pi} \int_{span} \vec{V} \cdot (d\vec{L} + d\vec{D}) \tag{B-17}$$

Substituting in equation (B-10), we obtain:

$$W_S = b \int_{azimuth} \frac{d\Psi}{2\pi} \int_{span} (\vec{V} - \vec{V}_C) \cdot (d\vec{L} + d\vec{D}) + W_F \tag{B-18}$$

The expression for $V_C$ is

$$\vec{V}_C = \vec{V} + \vec{\Omega} \times \vec{OC} + \vec{V}_m \tag{B-19}$$

where $\vec{V}_m$ is the contribution of the blades modes to the airfoil motion. Then:

$$\vec{V} - \vec{V}_C = -\vec{\Omega} \times \vec{OC} - \vec{V}_m \tag{B-20}$$

$$W_S = b \int_{azimuth} \frac{d\Psi}{2\pi} \int_{span} -\vec{\Omega} \cdot [\vec{OC} \times (d\vec{L} + d\vec{D})] - \vec{V}_m \cdot (d\vec{L} + d\vec{D}) + W_F \tag{B-21}$$

The term

$$b \int_{azimuth} \frac{d\Psi}{2\pi} \int_{span} -\vec{V}_m \cdot (d\vec{L} + d\vec{D}) \tag{B-22}$$

is power transferred from the air to the blade modes averaged over one revolution. Since the modes are conservative, that is, structural dissipation is neglected, this term has to vanish (although the instantaneous power at a given azimuth may be quite large because of rigid flap motion).

The power breakdown in rotating coordinates is given by:

$$W_S = W_L + W_D + W_F \tag{B-23}$$

with

$$W_L = -\vec{\Omega} \cdot b \int_{azimuth} \frac{d\Psi}{2\pi} \int_{span} \vec{OC} \times d\vec{L} \tag{B-24}$$

and

$$W_D = -\vec{\Omega} \cdot b \int_{azimuth} \frac{d\Psi}{2\pi} \int_{span} \vec{OC} \times d\vec{D} \tag{B-25}$$

$W_L$ is referred to as the thrust-dependent power and $W_D$ as the rotational power at the RAE. These components can be expressed in terms of the more classical parasite, induced and profile powers as

$$W_L = W_T - \vec{V} \cdot \vec{D} = W_i' \tag{B-26}$$

$$W_D = -\vec{V} \cdot \vec{D} + W_P + W_i' \tag{B-27}$$

where

$$\vec{D} = b \int_{azimuth} \frac{d\Psi}{2\pi} \int_{span} d\vec{D} \tag{B-28}$$

$$\vec{L} = b \int_{azimuth} \frac{d\Psi}{2\pi} \int_{span} d\vec{L} = \vec{T} - \vec{D} \tag{B-29}$$

$$W_i{}' = b \int_{azimuth} \frac{d\Psi}{2\pi} \int_{span} -\vec{V}_i \cdot d\vec{D} \tag{B-30}$$

$\vec{L}$ and $\vec{D}$ can be regarded as the breakdown of thrust $\vec{T}$ in out-of-plane and in-plane components respectively although this is only an approximation. $W_i'$ is an auxiliary induced power which is generally quite small since $V_i$ and $dD$ are both small and nearly orthogonal in usual situations.

It is not possible, however, to neglect $\vec{V} \cdot \vec{D}$. This power is always negative and represents the contribution of in-plane drag to power. As a consequence, the rotational power is smaller than the profile power, and the thrust-dependent power is larger than the sum of parasite and induced powers:

$$W_D < W_P \tag{B-31}$$

$$W_L > W_T + W_i \tag{B-32}$$

$$W_L + W_D = W_T + W_P + W_i \simeq W_S \tag{B-33}$$

# APPENDIX C

# DIFFERENCES BETWEEN CAMRAD AND CAMRAD/JA ROTOR WAKE MODELS

R. Toffoletto and N. E. Gilbert

In comparing the predictions made by CAMRAD with those of CAMRAD/JA for Case 3 in Section 4, significant differences were observed for section lift in the azimuthal range from 90° to 270° and the induced power calculated by CAMRAD was about 70 hp less than that computed by CAMRAD/JA. These differences remained even when the modeling capability of CAMRAD/JA was limited to that provided by CAMRAD, as far as it was possible to do so through user input. The uniform inflow solutions given by each code were found to be almost identical. For the prescribed wake model, the rolling-up and the far wake influence coefficients were almost identical, but there were differences in the near-wake influence coefficients. The purpose of this appendix is to examine these differences.

The general layout of the near-wake geometry is similar in both models as is shown in figure C-1. The near-wake is made up of vortex sheet panels, with the side edges coinciding with the mid-points of the aerodynamic panels defined on the blade. Both codes represent these near-wake panels with single trailed and shed vortex line segments. The position and core size of these line segments differ in a number of significant ways. In CAMRAD, a standard vortex sheet model is used, which consists of line segments passing through the mid-point of the panel. The core sizes are set to cover the entire panel. In CAMRAD/JA, the trailed line segments are positioned in-line with the edge of the aerodynamic panels, and the shed wake is moved to the rear by a quarter chord. The trailed line segments will have the same location in both codes for panels of uniform size, but will be offset when adjacent panels differ in width. The CAMRAD/JA shed vortex line segment will always be a quarter chord behind the CAMRAD line segment. The core sizes of the CAMRAD/JA vortex segments are set to one fifth the width of the

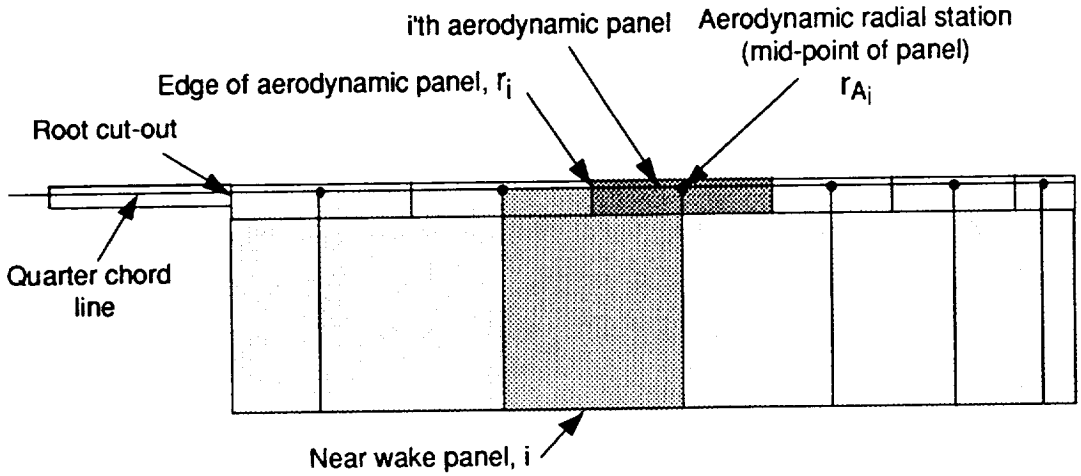


Figure C-1. General representation of near wake geometry.

wake panel. The differences between the two near wake panel models are illustrated in figure C-2. The blade tip and root edge panels are treated in the same way as the other panels in CAMRAD, but in CAMRAD/JA the trailing wake is located at the edge of the blade for these edge panels (the tip of the blade for the tip panel, and the root cut-out for the root panel). In addition to these near-wake panel differences, CAMRAD originates the tip vortex from the blade, whereas in CAMRAD/JA the tip vortex starts at the end of the near wake.

The various steps undertaken to reduce the differences between the two near-wake models are shown in table C-1. The only change made in going from Case 3 to Case 3a is that the near-wake shed vortex element in CAMRAD/JA is located at $L/2$ instead of $L/2 + c/4$. The aerodynamic segments

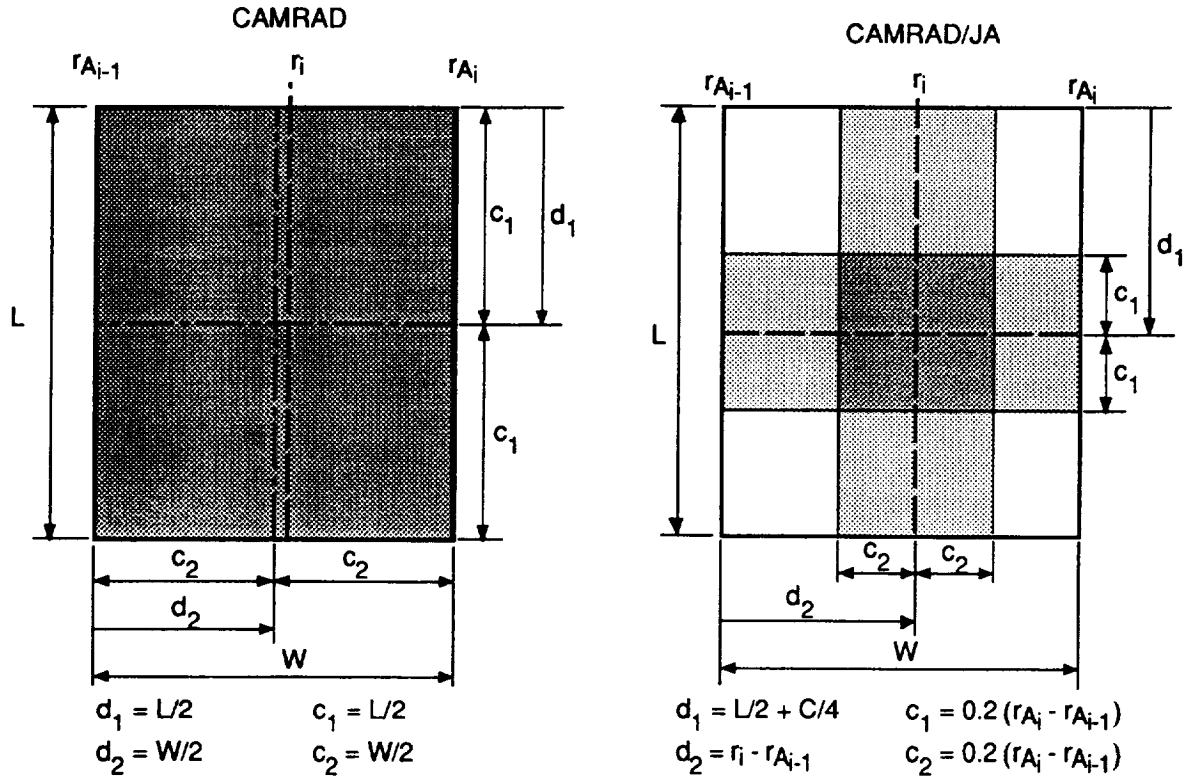


C = Chord of aerodynamic panel i

L = Length of vortex panel i

W = Width of vortex panel i

$d_1$ = Position of shed vortex line segment

$d_2$ = Position of trailed vortex line segment

$c_1$ = Core radius of shed vortex line segment

$c_2$ = Core radius of trailed vortex line segment

$r_{A_i}$ = Aerodynamic radial station i

$r_i$ = Edge of aerodynamic panel i

Figure C-2. CAMRAD and CAMRAD/JA representation of near-wake panel.

Table C-1. Modifications to reduce differences between CAMRAD and CAMRAD/JA near-wake models

| Case | $d_1$ | | $c_1$ | | $c_2$ | | Aero segments | |
|---|---|---|---|---|---|---|---|---|
| | CAMRAD | JA | CAMRAD | JA | CAMRAD | JA | CAMRAD | JA |
| 3 | $L/2$ | $L/2+c/4$ | $L/2$ | $L/5$ | $L/2$ | $L/5$ | variable | variable |
| 3a | $L/2$ | $L/2$ | $L/2$ | $L/5$ | $L/2$ | $L/5$ | variable | variable |
| 3b | $L/2$ | $L/2$ | $R/20$ | $R/20$ | $L/2$ | $L/5$ | variable | variable |
| 3c | $L/2$ | $L/2$ | $R/20$ | $R/20$ | $R/20$ | $R/20$ | variable | variable |
| 3d | $L/2$ | $L/2$ | $R/20$ | $R/20$ | $R/20$ | $R/20$ | constant | constant |

are reduced in length as the tip is approached, as shown in table C-2 for Cases 3 to 3c. For Case 3d, however, the aero segments are of constant length ($R/20$). In both codes, the core radius of the shed vortex, $c_1$, is set in Case 3b to $R/20$, and the core radius of the trailed vortex, $c_2$, is similarly set to $R/20$ in Case 3c. Finally, in Case 3d, the aero segments are made identical so that the trailed vortices are at the same radial location for all segments. In this final case the only remaining differences are the treatment of the tip vortex and the edge panels, as discussed above.

The near-wake geometry representation is directly related to the near-wake influence coefficients. These coefficients, together with the circulation strength, are used to calculate the induced velocity, which then affects the induced power. The relationship between induced velocity and power may be masked if any circulation or motion iterations are performed. Therefore, to determine the effect of the wake geometry differences, it is useful to compare the induced power for each model when they are run with no circulation or motion iterations for given control inputs (table C-3). The full number of decimal

Table C-2. Aerodynamic segment boundaries for CAMRAD and CAMRAD/JA models

| $r/R$ | |
|---|---|
| Cases 3–3c | Case 3d |
| 0.228 | 0.25 |
| 0.36 | 0.30 |
| 0.46 | 0.35 |
| 0.56 | 0.40 |
| 0.64 | 0.45 |
| 0.72 | 0.50 |
| 0.78 | 0.55 |
| 0.82 | 0.60 |
| 0.86 | 0.65 |
| 0.88 | 0.70 |
| 0.90 | 0.75 |
| 0.92 | 0.80 |
| 0.94 | 0.85 |
| 0.96 | 0.90 |
| 0.98 | 0.95 |
| 1.00 | 1.00 |

Table C-3. Effect of near-wake model changes on induced and total power for forward flight with circulation and motion iterations excluded

| Case | Power, hp | | | |
|---|---|---|---|---|
| | CAMRAD | | CAMRAD/JA | |
| | Induced | Total | Induced | Total |
| 3 | 36.508 | 1225.131 | 71.118 | 1248.956 |
| 3a | 36.508 | 1225.131 | 71.752 | 1249.493 |
| 3b | 36.943 | 1225.481 | 71.492 | 1249.295 |
| 3c | 39.065 | 1227.982 | 43.491 | 1230.876 |
| 3d | 39.416 | 1223.526 | 42.584 | 1225.578 |

places are given so that round-off effects can be distinguished. As can be seen, changing the trailed core size (Case 3c) has a major effect on the induced power calculated by CAMRAD/JA (induced power reduces from 71.492 hp in Case 3b to 43.491 hp in Case 3c) and a significant effect on that calculated by CAMRAD (induced power increases from 36.943 hp in Case 3b to 39.065 hp in Case 3c), with an overall reduction in the differences between the two codes (from 34.549 hp in Case 3b to 4.426 hp in Case 3c).

When circulation and motion iterations are included to obtain a trimmed solution for a given control input, the variables directly affected are the circulation distribution and the flap and lag angles (blade motion). To determine the effect of these iterations, all five cases were rerun with full circulation and motion trim, but without trimming the controls (table C-4). Although the induced power values are much larger, the same effects are seen, i.e., the induced power difference reduces from 71.886 hp in Case 3b to 17.060 hp in Case 3c. The difference in flap angles is also reduced.

Table C-4. Effect of near-wake model changes on induced and flap angles for forward flight with circulation and motion iterations included

| Case | CAMRAD | | | | CAMRAD/JA | | | |
|---|---|---|---|---|---|---|---|---|
| | Induced power | Flap angles, deg | | | Induced power | Flap angles, deg | | |
| | | $\beta_0$ | $\beta_{1c}$ | $\beta_{1s}$ | | $\beta_0$ | $\beta_{1c}$ | $\beta_{1s}$ |
| 3 | 219.705 | 4.2317 | −0.5643 | 1.8533 | 290.325 | 3.3658 | −0.7941 | 2.8058 |
| 3a | 219.705 | 4.2317 | −0.5643 | 1.8533 | 290.985 | 3.3627 | −0.7919 | 2.8100 |
| 3b | 220.911 | 4.2301 | −0.5653 | 1.8578 | 292.797 | 3.3606 | −0.8042 | 2.8303 |
| 3c | 245.997 | 4.1814 | −0.6221 | 1.9302 | 263.057 | 4.0806 | −0.6734 | 2.0160 |
| 3d | 247.210 | 4.1605 | −0.6129 | 1.9688 | 264.384 | 4.0784 | −0.6554 | 2.0606 |

Because there is no circulation variation with azimuth in hover, the influence of the shed wake is eliminated. Therefore, the only differences in the models will be due to the differences in trailed wake representation. For this reason, the models were compared in hover and the results are given in table C-5. In Case 3d the difference in induced power is almost eliminated (less than 2 hp in about 1360 hp).

Table C-5. Effect of near-wake model changes on induced power and coning angle for hover with circulation and motion iterations included

| | CAMRAD | | CAMRAD/JA | |
|---|---|---|---|---|
| Case | Induced power hp | Coning angle, $\beta_0$ deg | Induced power hp | Coning angle, $\beta_0$ deg |
| 3 | 1371.807 | 6.0000 | 1307.299 | 5.5998 |
| 3a | 1371.807 | 6.0000 | 1307.299 | 5.5998 |
| 3b | 1371.807 | 6.0000 | 1307.299 | 5.5998 |
| 3c | 1369.131 | 5.6777 | 1360.968 | 5.4852 |
| 3d | 1358.401 | 6.0714 | 1356.644 | 5.9231 |

It has been established that there are differences between CAMRAD and CAMRAD/JA in the near-wake representation which cannot be eliminated through user input. The progressive elimination of most of these differences through changes to the codes has shown that the differences in predictions can be significantly reduced. It is assumed that the two model differences which could not be removed, i.e., the treatment of the tip vortex and edge panels, are responsible for the residual differences in predictions.

# REFERENCES


Allongue, M.; and Krysinski, T.: Validation of a New General Aérospatiale Aeroelastic Rotor Model Through W1nd Tunnel and Flight Tests Data. Amer. Hel. Soc. 46th Annual Forum Proceedings, May 1990, pp. 389–402.

Arnaud, G.; and Beaumier, P.: Validation of R85/METAR on the Puma RAE Flight Tests. Eighteenth European Rotorcraft Forum, September 1992.

Arnaud, G.; Benoit, B.; and Toulmay, F.: Ameliorations du Modèle Aérodynamique du Code Rotor Hélicoptères R85 Validation et Applications. 28eme Colloque d'Aérodynamique Appliquée, AAAF, October 1991.

Beddoes, T. S.: A Synthesis of Unsteady Aerodynamic Effects Including Stall Hysteresis. 1st European Rotorcraft and Powered Lift Aircraft Forum, September 1975.

Beddoes, T. S.: Onset of Leading Edge Separation Effects Under Dynamic Conditions and Low Mach Number. WHL Research Paper 562, 1977.

Benoit, Bernard; and Arnaud, Gilles: Simultaneous Treatment of Flexion and Torsion in a Global Model Approach for the Calculation of Blade Deformations in the Comprehensive Rotor Code R85. Paper No. 68, Eighteenth Eur. Rotorcraft Forum, September 1992.

Bousman, William G.: Estimation of Blade Airloads from Rotor Blade Bending Moments. Paper No. 6-5, Thirteenth Eur. Rotorcraft Forum, September 1987.

Bousman, William G.; and Maier, Thomas H.: An Investigation of Helicopter Rotor Blade Flap Vibratory Loads. Amer. Hel. Soc. 48th Annual Forum Proceedings, June 1992, pp. 977–999.

Bousman, William G.; Young, Colin; Gilbert, Neil; Toulmay, François; Johnson, Wayne; and Riley, M. J.: Correlation of Puma Airloads – Lifting-line and Wake Calculation. Paper No. 21, Fifteenth European Rotorcraft Forum, September 1989.

Bridgeman, J. O.; Steger, J. L.; and Caradonna, F. X.: A Conservative Finite-Difference Algorithm for the Unsteady Transonic Potential Equation in Generalized Coordinates. AIAA Paper No. 82-1388, August 1982.

Bridgeman, John O.; Strawn, Roger C.; Caradonna, Francis X.; and Chen, Ching S.: Advanced Rotor Computations with a Corrected Potential Method. Amer. Hel. Soc. 45th Annual Forum Proceedings, May 1989, pp. 563–577.

Caradonna, F. X.: The Application of CFD to Rotary Wing Flow Problems. AGARD-R-781, 1990, pp. 5-1 to 5-38.

Chan, I-Chung; and Tung, C.: Numerical Solutions of the Full-Potential Equation for Rotors and Oblique Wings using a New Wake Model. AIAA Paper 85-0268, AIAA 23rd Aerospace Sciences Meeting, January 1985.

Cook, C. V.: Induced Flow Through a Helicopter Rotor in Forward Flight. WHL Research Paper 374, 1970.

Davis, John M.: Rotorcraft Flight Simulation with Aeroelastic Rotor and Improved Aerodynamic Representation, Volume II – User's Manual. USAAMRDL TR 74-10B, 1974.

Duque, Earl P. N.: A Numerical Analysis of the British Experimental Rotor Program Blade. Paper No. 10, Fifteenth Eur. Rotorcraft Forum, September 1989.

Egolf, T. Alan; and Landgrebe, Anton J.: Helicopter Rotor Wake Geometry and Its Influence in Forward Flight, Volume II – Wake Geometry Charts. NASA CR-3727, October 1983.

Egolf, T. A.; and Landgrebe, A. J.: Generalized Wake Geometry for a Helicopter Rotor in Forward Flight and Effect of Wake Deformation on Airloads. Amer. Hel. Soc. 40th Annual Forum Proceedings, May 1984, pp. 359–376.

Gaukroger, D. R.; and Hassal, G. J. W.: Measurement of Vibratory Displacements of a Rotating Blade. Vertica, vol. 2, 1978, pp. 111–120.

Grant, J.: The Prediction of Supercritical Pressure Distributions on Blade Tips of Arbitrary Shape over a Range of Advancing Blade Azimuth Angles. Vertica, vol. 3, 1979, pp. 275–292.

Hansford, R. E.: A Unified Formulation of Rotor Load Prediction Methods. Amer. Hel. Soc. 41st Annual Forum Proceedings, May 1985, pp. 73–83.

Harris, Charles D.: Two-Dimensional Aerodynamic Characteristics of the NACA 0012 Airfoil in the Langley 8-Foot Transonic Pressure Tunnel. NASA TM-81927, April 1981.

Jameson, A.: Iterative Solution of Transonic Flows over Airfoils and Wings Including Flows at Mach 1. Comm. Pure Appl. Math, vol. 27, 1974.

Johnson, Wayne: Development of a Comprehensive Analysis for Rotorcraft – I. Rotor Model and Wake Analysis. Vertica, vol. 5, 1981a, pp. 99–130.

Johnson, Wayne: Development of a Comprehensive Analysis for Rotorcraft – II. Aircraft Model, Solution Procedure and Applications. Vertica, vol. 5, 1981b, pp. 185–216.

Johnson, Wayne, Assessment of Aerodynamic and Dynamic Models in a Comprehensive Analysis for Rotorcraft. Computers & Mathematics with Applications, vol. 12A, no. 1, 1986.

Johnson, Wayne: CAMRAD/JA: A Comprehensive Analytical Model of Rotorcraft Aerodynamics and Dynamics; Johnson Aeronautics Version; Volume 1, Theory Manual. Johnson Aeronautics, Palo Alto, California, 1988.

Jones, Alan F.; Young, Colin; Miller, Judith V.; Riley, M. J.; Bousman, William G.; Strawn, Roger C.; Gilbert, Neil E.; Desopper, Andre; and Toulmay, François; Tripartite Workshop on the Prediction of the Pressure Distribution on Helicopter Rotor Blade Tips. Internal TTCP report, June 1990.

Kim, Ki-Chung; Desopper, Andre; and Chopra, Inderjit: Blade Response Calculations Using Three-Dimensional Aerodynamic Modeling. J. Am. Hel. Soc., vol. 36, no. 1, Jan. 1991, pp. 68–77.

Kocurek, J. David; and Tangler, James L.: A Prescribed Wake Lifting Surface Hover Performance Analysis. J. Amer. Hel. Soc., vol. 22, no. 1, January 1977, p. 235.

Leishman, J. G.; and Beddoes, T. S.: A Second Generation Model for Airfoil Unsteady Aerodynamic Behaviour and Dynamic Stall. WHL Research Paper 704, 1986.

Maier, Thomas H.; and Bousman, William G.: An Examination of the Aerodynamic Moment on Rotor Blade Tips Using Flight Test Data and Analysis. Paper No. 48, 18th Eur. Rotorcraft Forum, September 1992. Also: NASA TM-104006, October 1993.

McCroskey, W. J.: A Critical Assessment of Wind Tunnel Results for the NACA 0012 Airfoil. NASA TM-100019, October 1987.

McCroskey, W. J.; Baeder, J. D.; and Bridgeman, J. O.: Calculation of Helicopter Airfoil Characteristics for High Tip-Speed Applications. Amer. Hel. Soc. 41st National Forum Proceedings, May 1985, pp. 531–545.

Riley, M. J.: Measurements of the Performance of a Helicopter Swept Tip Rotor in Flight. Paper No. 35, Twelfth Eur. Rotorcraft Forum, September 1986.

Riley, M. J.; and Miller, Judith V.: Pressure Distributions on a Helicopter Swept Tip from Flight Tests and from Calculations. Paper No. 9, Ninth Eur. Rotorcraft Forum, September 1983.

Samoni, G.: Simulation Hélicoptère, Caractérisques du SA 330, Aérospatiale Note Technique 330.05.0080, 1975.

Steger, J. L.: Implicit Finite-Difference Simulation of Flow about Arbitrary Two-Dimensional Geometries. AIAA J., vol. 16, no. 7, July 1978, pp. 679–686.

Strawn, R. C.; and Bridgeman, J. O.: An Improved Three-Dimensional Aerodynamics Model for Helicopter Airloads Prediction. AIAA Paper 91-0767, AIAA 29th Aerospace Sciences Meeting, January 1991.

Strawn, R. C.; and Caradonna, F. X.: Conservative Full-Potential Model for Unsteady Transonic Rotor Flows. AIAA J., vol. 25, no. 2, February 1987, pp. 193–198.

Strawn, Roger C.; Desopper, Andre; Miller, Judith; and Jones, Alan: Correlation of Puma Airloads – Evaluation of CFD Prediction Methods. Paper No. 14, Fifteenth Eur. Rotorcraft Forum, September 1989.

Strawn, Roger C.; and Tung, Chee: Prediction of Unsteady Transonic Rotor Loads with a Full-Potential Rotor Code. Amer. Hel. Soc. 43rd Annual Forum Proceedings, May 1987, pp. 795–805.

Tran, C. T.; and Desopper, A.: An Iteration Technique Coupling 3-D Transonic Small Perturbation Aerodynamic Theory and Rotor Dynamics in Forward Flight. Fourteenth Eur. Rotorcraft Forum, September 1988.

Tung, Chee; Caradonna, Francis X.; and Johnson, Wayne R.: The Prediction of Transonic Flows on an Advancing Rotor. J. Am. Hel. Soc., vol. 31, no. 3, July 1986, pp. 4–9.

Yamauchi, G.; Heffernan, R.; and Gaubert, M.: Hub and Blade Structural Loads Measurements of an SA349/2 Helicopter. NASA TM-101040, 1988.

# REPORT DOCUMENTATION PAGE

Form Approved
OMB No. 0704-0188

Public reporting burden for this collection of information is estimated to average 1 hour per response, including the time for reviewing instructions, searching existing data sources, gathering and maintaining the data needed, and completing and reviewing the collection of information. Send comments regarding this burden estimate or any other aspect of this collection of information, including suggestions for reducing this burden, to Washington Headquarters Services, Directorate for information Operations and Reports, 1215 Jefferson Davis Highway, Suite 1204, Arlington, VA 22202-4302, and to the Office of Management and Budget, Paperwork Reduction Project (0704-0188), Washington, DC 20503.

| 1. AGENCY USE ONLY *(Leave blank)* | 2. REPORT DATE | 3. REPORT TYPE AND DATES COVERED |
|---|---|---|
| | October 1996 | Technical Memorandum |

**4. TITLE AND SUBTITLE**

A Comparison of Lifting-Line and CFD Methods with Flight Test Data from a Research Puma Helicopter

**5. FUNDING NUMBERS**

505-59-87

**6. AUTHOR(S)**

William G. Bousman,* Colin Young,† François Toulmay,‡ Neil E. Gilbert,§ Roger C. Strawn,* Judith V. Miller,‡ Thomas H. Maier,* Michel Costes,¶ and Philippe Beaumier¶

**7. PERFORMING ORGANIZATION NAME(S) AND ADDRESS(ES)**

Aeroflightdynamics Directorate, U.S. Army Aviation and Troop Command, Ames Research Center, Moffett Field, CA 94035-1000

**8. PERFORMING ORGANIZATION REPORT NUMBER**

A-962753

**9. SPONSORING/MONITORING AGENCY NAME(S) AND ADDRESS(ES)**

National Aeronautics and Space Administration
Washington, DC 20546-0001 and U.S. Army Aviation and Troop Command, St. Louis, MO 63120-1798

**10. SPONSORING/MONITORING AGENCY REPORT NUMBER**

NASA TM-110421
USAATCOM TR-96-A-008

**11. SUPPLEMENTARY NOTES**

Point of Contact: William G. Bousman, Ames Research Center, MS T12-B, Moffett Field, CA 94035-1000; (415) 604-3748

**12a. DISTRIBUTION/AVAILABILITY STATEMENT**

Unclassified–Unlimited Subject Category 01

*Aeroflightdynamics Directorate, U.S. Army Aviation and Troop Command, Ames Research Center, Moffett Field, California †Defence Research Agency (Aerospace Division), Farnborough, United Kingdom ‡Eurocopter France, Marignane, France §Aeronautical and Maritime Research Laboratory, Melbourne, Australia ¶ONERA, Châtillon, France

**12b. DISTRIBUTION CODE**

**13. ABSTRACT** ***(Maximum 200 words)***

Four lifting-line methods were compared with flight test data from a research Puma helicopter and the accuracy assessed over a wide range of flight speeds. Hybrid CFD methods were also examined for two high-speed conditions. A parallel analytical effort was performed with the lifting-line methods to assess the effects of modeling assumptions and this provided insight into the adequacy of these methods for load predictions.

| 14. SUBJECT TERMS | 15. NUMBER OF PAGES |
|---|---|
| Computational Fluid Dynamics, CFD, Helicopter, Rotor airloads | 359 |
| | 16. PRICE CODE: A16 |

| 17. SECURITY CLASSIFICATION OF REPORT | 18. SECURITY CLASSIFICATION OF THIS PAGE | 19. SECURITY CLASSIFICATION OF ABSTRACT | 20. LIMITATION OF ABSTRACT |
|---|---|---|---|
| Unclassified | Unclassified | | |

Young, C.: Development of the Vortex Ring Wake Model and Its Influence on the Prediction of Rotor Loads. AGARD CP-334, 1982.

Young, C.: A Basic Approach to Predicting the Power Required by a Helicopter. RAE Technical Report 89043, August 1989.

Young, Colin; Bousman, William G.; Maier, Thomas H.; Toulmay, François; and Gilbert, Neil: Lifting Line Predictions for a Swept Tip Rotor Blade. 47th Amer. Hel. Soc. Annual Forum Proceedings, May 1991, pp. 1345–1370.